GRANITE PETROGENESIS AND GEODYNAMICS

EDITED BY: J. Gregory Shellnutt, Steven W. Denyszyn and Kwan-Nang Pang
PUBLISHED IN: Frontiers in Earth Science

frontiers Research Topics

frontiers

ISSN 1664-8714
ISBN 978-2-88966-558-7
DOI 10.3389/978-2-88966-558-7

About Frontiers

Frontiers is more than just an open-access publisher of scholarly articles: it is a pioneering approach to the world of academia, radically improving the way scholarly research is managed. The grand vision of Frontiers is a world where all people have an equal opportunity to seek, share and generate knowledge. Frontiers provides immediate and permanent online open access to all its publications, but this alone is not enough to realize our grand goals.

Frontiers Journal Series

The Frontiers Journal Series is a multi-tier and interdisciplinary set of open-access, online journals, promising a paradigm shift from the current review, selection and dissemination processes in academic publishing. All Frontiers journals are driven by researchers for researchers; therefore, they constitute a service to the scholarly community. At the same time, the Frontiers Journal Series operates on a revolutionary invention, the tiered publishing system, initially addressing specific communities of scholars, and gradually climbing up to broader public understanding, thus serving the interests of the lay society, too.

Dedication to Quality

Each Frontiers article is a landmark of the highest quality, thanks to genuinely collaborative interactions between authors and review editors, who include some of the world's best academicians. Research must be certified by peers before entering a stream of knowledge that may eventually reach the public - and shape society; therefore, Frontiers only applies the most rigorous and unbiased reviews.
Frontiers revolutionizes research publishing by freely delivering the most outstanding research, evaluated with no bias from both the academic and social point of view. By applying the most advanced information technologies, Frontiers is catapulting scholarly publishing into a new generation.

What are Frontiers Research Topics?

Frontiers Research Topics are very popular trademarks of the Frontiers Journals Series: they are collections of at least ten articles, all centered on a particular subject. With their unique mix of varied contributions from Original Research to Review Articles, Frontiers Research Topics unify the most influential researchers, the latest key findings and historical advances in a hot research area! Find out more on how to host your own Frontiers Research Topic or contribute to one as an author by contacting the Frontiers Editorial Office: frontiersin.org/about/contact

GRANITE PETROGENESIS AND GEODYNAMICS

Topic Editors:
J. Gregory Shellnutt, National Taiwan Normal University, Taiwan
Steven W. Denyszyn, University of Western Australia, Australia
Kwan-Nang Pang, Institute of Earth Sciences, Academia Sinica, Taiwan

Citation: Shellnutt, J. G., Denyszyn, S. W., Pang, K.-N., eds. (2021). Granite Petrogenesis and Geodynamics. Lausanne: Frontiers Media SA.
doi: 10.3389/978-2-88966-558-7

Table of Contents

frontiers in Earth Science

EDITORIAL
published: 21 January 2021
doi: 10.3389/feart.2020.637729

Editorial: Granite Petrogenesis and Geodynamics

J. Gregory Shellnutt[1]*, *Steven W. Denyszyn*[2] *and Kwan-Nang Pang*[3]

[1]Department of Earth Sciences, National Taiwan Normal University, Taipei, Taiwan, [2]School of Earth and Environment, University of Western Australia, Perth, WA, Australia, [3]Institute of Earth Sciences, Academia Sinica, Taipei, Taiwan

Keywords: granite, tectonics, continental crust, geochemistry, geochronology, isotopes, metallogenesis

Editorial on the Research Topic

Granite Petrogenesis and Geodynamics

Granite, *sensu stricto*, is a coarse grained and granular igneous rock comprising 20–60 vol% quartz and 35–90 vol% total feldspar whereas a granitic rock, *sensu lato*, is texturally similar but has variable proportions of quartz, alkali feldspar, and plagioclase (Streckeisen, 1976). Granites have interested geologists for centuries because of their ubiquity on continents, association with ore deposits, and their use in the construction of ancient buildings. The origin and formation of granitic rocks was at the forefront of geological debate before and after the pioneering work of James Hutton and Charles Lyell, and played an important role in the development of continental drift theory (Wegener, 1924; Du Toit, 1937; Holmes, 1945; Bowen, 1948). Early concepts of granite formation include crystallization from a fluid, precipitation from a primordial ocean, or transformation of pre-existing rocks into granite (i.e., granitization) by metasomatism (Marmo, 1967). Furthermore, if granites were indeed derived from a fluid (e.g., a magma), then a question arises as to how such enormous space can be created in the crust to accommodate their emplacement (Marmo, 1967). It was not until the mid-20th century that the debate regarding the fundamental origin of granitic magma was resolved. The recognition that granite crystallizes from magma refuted many opposing theories including the granitization theory (Tuttle and Bowen, 1958).

Granitic magmas form by a variety of processes including melting of crustal lithologies at various depths in the presence or absence of fluids, fractional crystallization of mafic magmas, and mixing between magmas derived from the crust and from the mantle (Pitcher, 1997; Barbarin, 1999; Brown, 2013; Janoušek et al., 2020). Thus, studying the origins of granite (*sensu lato*) is a challenging proposition because of the complex relationship between the effects of magma crystallization superimposed on the varied source components that might have contributed to initial melt composition. Most granitic magmas are emplaced as plutonic to hypabyssal intrusions of various sizes at subduction zone settings and during orogenesis, whereas comparatively minor volumes are emplaced within stable cratons, sites of active continental rifting, and within oceanic crust (Pitcher, 1997; Barbarin, 1999; Bonin, 2007). Thus, the formation of granitic rocks is crucial for understanding the creation and recycling of continental crust (Brown, 2013).

With the advent of modern geochemical methods, it was recognized that there is a relationship between the composition of granite and tectonic setting (Pearce et al., 1984; Maniar and Piccoli, 1989; Bonin, 1990; Barbarin, 1999). Consequently, nomenclature of granitic rocks rapidly expanded and no fewer than 30 classification schemes have been developed (e.g., Streckeisen, 1976; Pearce et al., 1984; Maniar and Piccoli, 1989; Barbarin, 1999; Frost et al., 2001). Classification of granites is based on a number of factors including mineralogy, geology, and geochemistry, leading to the creation of the widely used but petrogenetically linked 'letter based' (e.g., I-type, M-type, S-type, A-type) classification scheme (Chappell and White, 1974; Loiselle and Wones, 1979; White, 1979). Non-genetic classification schemes based on major element geochemistry are also used, and have the

OPEN ACCESS

Edited and reviewed by:
Catherine Jeanne Annen, University of Bristol, United Kingdom

***Correspondence:**
J. Gregory Shellnutt
jgshelln@ntnu.edu.tw

Specialty section:
This article was submitted to Petrology, a section of the journal Frontiers in Earth Science

Received: *04 December 2020*
Accepted: *21 December 2020*
Published: *21 January 2021*

Citation:
Shellnutt J G, Denyszyn SW and Pang K-N (2021) Editorial: Granite Petrogenesis and Geodynamics. Front. Earth Sci. 8:637729. doi: 10.3389/feart.2020.637729

advantage of not being interpretive (Frost et al., 2001; Frost and Frost, 2011). The scientific benefits of granite classification are clear, but the debate around their application continues and new methods of classification are frequently proposed (c.f, Glazner et al., 2019; Bonin et al., 2020). Nevertheless, the discovery that there is an association between the type of granite and tectonic setting presents an opportunity to extrapolate the possible geodynamic processes that operated in the past, even in regions where a complete geological record is not preserved.

This Special Topic of Frontiers in Earth Science comprises papers that discuss the formation of granitic rocks and their relationship to the geodynamic evolution of continental crust. To address the outstanding issues regarding the formation of granitic rocks, the authors apply modern analytical techniques in geochronology, elemental geochemistry, and isotope geochemistry, coupled with geological and structural observations to quantify and constrain the tectonomagmatic processes associated with granite petrogenesis. The manuscripts present a variety of approaches that address the role of hydrothermal and hydromagmatic fluids in the formation of mineral deposits and magma emplacement, magma differentiation, and the importance of polygenetic (i.e., crust/mantle) sources in the formation of granitic melts. Moreover, the manuscripts provide critical insight on the importance of the geodynamic setting in creating juvenile crust and recycling of older continental crust. The manuscripts in this volume cover a broad range of subjects related to crustal evolution, formation of granite-hosted ore deposits, magma genesis, enclave textural variation, and structural controls during emplacement, and propose new views on the lithotectonic development of Eurasia, Western North America, and Africa. Below is a summary of the contents of this Special Topic.

Through field observations, petrography, and geochemistry Ardill et al. focus on formation mechanisms in the Tuolumne Intrusive Complex (TIC). Small scale (1 mm–1 m), local scale (1 m–1 km), and regional scale (10s of km) observations indicate there is evidence for crystal flow-sorting, magmatic faulting and folding, fluidization within a hydrogranular medium, and magma pulse-induced convection. The structural patterns are consistent with a magma mixing region of ~150 km^2 and that melt-present reservoirs were derived from multiple magma pulses.

Pang et al. document zircon U-Pb age, mineral compositional, elemental and Sr-Nd isotopic data for the Late Oligocene Takht batholith, Iran, which is part of the Arabia-Eurasia collision zone. Results show that the batholith is a Cordilleran-type batholith formed at ~25 Ma beneath a continental or transitional arc of normal crustal thickness. As no geochemical evidence is found for collision-induced crustal thickening, the implication is that Arabia and Eurasia might have collided in a diachronous manner.

Ji et al. explore the early evolution of the Himalayan Orogenic Belt and delineate an expanded Eocene magmatic belt that predates most Himalayan igneous activity. They accomplish this through LA-ICPMS and SIMS U-Pb geochronology of zircons and titanites, and this data is combined with major-, trace-, and radiogenic-element geochemistry to elucidate the petrogenesis of these granodiorites.

The Ladakh Batholith is one of the largest intrusions of the Alpine-Himalayan orogenic belt. It is composed of silicic and intermediate rocks and hosts a variety of mafic and microgranular enclaves. Kumar provides detailed field observations on the type, orientation, and mineralogy, of enclaves of the Ladakh Batholith. The diversity of enclaves suggests that the Ladakh Batholith developed over time via multi-stage interactions of mafic to hybrid magmas coeval with silicic magma pulses.

Asokan et al.'s contribution presents a close examination of the Kanker Granites, a suite of felsic intrusions in the Bastar Craton of central India, in the context of crustal growth and evolution. Emplaced at the geodynamically active Archean-Proterozoic transition time, the compositional variability of these granitic rocks preserves a complex history of melt and heat sources, and provides a geological record of a tectonically significant period of Earth history.

Shellnutt et al. present new zircon geochronology, mineral chemistry, whole rock and isotope geochemistry of spessartine-bearing biotite leucogranite from Macau Special Administrative Region, SE China. The leucogranites are Late Jurassic in age and compositionally similar to post-collisional S-type granite. The rocks are considered to be formed during decompressional melting associated with a period of crustal relaxation that occurred during the transition from low angle subduction to high angle subduction of the Paleo-Pacific plate.

Huang and Yeh present field mapping results, detailed structural data and petrographic analysis for granitic rocks in Kinmen Island, which occurs along the southeastern edge of the South China Block. By integrating the structural data with published radiometric ages and strain patterns, it is proposed that rollback of the subducting Paleo-Pacific plate changed from northeastward to southeastward at ~114–107 Ma.

Suga and Yeh examine published elemental data for Cretaceous granitic rocks from Kyushu, SW Japan to investigate compositional secular variations and evaluate the potential role played by subduction-related mélange rocks. Secular variations in aluminum saturation index and Sr-Nd isotopes during the Albian are taken to indicate a change of geodynamic setting from subduction-accretion to continental arc. Also, the Albian granitic rocks are consistent with derivation from mélange rocks as demonstrated by Rhyolite-MELTS modeling.

Dostal et al. investigate the Tukhum granitic pluton, a member of the Early Jurassic composite Khentei batholith, North-Central Mongolia. The Tukhum pluton is shallow-seated and comprises two distinct biotite-bearing post-collisional granites. The granites are considered to be derived from Neoproterozoic crustal sources but, the younger of the two intrusions was derived from a biotite/phlogopite-bearing source that was enriched in tungsten and tin. They suggest melting was related to the passage of a mantle plume across Central Asia.

Büttner et al. present the petrogenesis of Mesoproterozoic granites from the Namaqua Belt, South Africa. A petrographic, geochemical, and isotopic study of these granites tells a complex story of mantle enrichment, crustal contamination, and metasomatism during their formation, and identifies a prevailing regional tectonic setting that drove their emplacement.

Kwékam et al. explore the origin of the Late Ediacaran Batié granitic massif in western Cameroon. The massif is composed of biotite granite and amphibole granite that were emplaced during and

after the final collisional stages of the Central African Orogenic Belt. It is thought that the granites were likely derived by partial melting of Paleoproterozoic lower crust and that magma was subsequently mixed with felsic melts derived from the upper continental crust.

Pham et al. examine the biotite chemistry from a series of granitic plutons from the Guéra Massif (South-Central Chad) that were emplaced at: 595–590 Ma, ~570 Ma, and ~560 Ma. The older granites (595–590 Ma) are compositionally similar to collisional granites whereas the younger granites (≤570 Ma) are compositionally similar to post-collisional granites. The magmatic conditions display a broad secular change in their temperatures and pressures but their redox conditions appear to be spatially controlled.

AUTHOR CONTRIBUTIONS

JS, SD, and K-NP equally contributed to this editorial.

FUNDING

This project received support from Ministry of Science and Technology (Taiwan) through grant 107–2628-M-003–003-MY3 to JGS and Career Development Award, Academia Sinica (AS-CDA-109-M07) to KNP.

ACKNOWLEDGMENTS

We are grateful to the reviewers for providing timely and comprehensive reviews that ensured the efficient handling of the manuscripts. Editorial assistance was provided by Scott Whattam, Patrizia Fiannacca, and Paterno Castillo that handle manuscripts of the guest editors. Finally, we are indebted to Ursula Rabar, Emily Legge, Roshan Patel, and Camilla Imarisio at Frontiers Media SA for their tireless efforts in assisting us from the beginning of this endeavor to its successful conclusion.

REFERENCES

Barbarin, B. (1999). A review of the relationships between granitoid types, their origins and their geodynamic environments. *Lithos.* 46, 605–626. doi:10.1016/S0024-4937(98)00085-1\

Bonin, B. (2007). A-type granites and related rocks: evolution of a concept, problems and prospects. *Lithos*. 97, 1–29. doi:10.1016/j.lithos.2006.12.007

Bonin, B. (1990). From orogenic to anorogenic settings: evolution of granitoid suites after a major orogenesis. *Geol. J.* 25, 261–270. doi:10.1002/gj.3350250309

Bonin, B., Janoušek, V., and Moyen, J.-F. (2020). "Chemical variation, modal compositional and classification of granitoids," in *Post-archean granitic rocks: petrogenetic processes and tectonic environments*. Editors V. Janoušek, B. Bonin, W. J. Collins, F. Farina, and P. Bowden (Bath, UK: Geological Society of London Special Publication).

Bowen, N. L. (1948). The granite problem and the method of multiple prejudices. *Geol. Soc. Am. Mem.* 28, 79–90.

Brown, M. (2013). Granite: from genesis to emplacement. *Geol. Soc. Am. Bull.* 125, 1079–1113. doi:10.1130/B30877.1

Chappell, B. W., and White, A. J. R. (1974). Two contrasting granite types. *Pac. Geol.* 8, 173–174.

Du Toit, A. L. (1937). *Our wandering continents*. London: Oliver & Boyd.

Frost, B. R., Barnes, C. G., Collins, W. J., Arculus, R. J., Ellis, D. J., and Frost, C. D. (2001). A geochemical classification for granitic rocks. *J. Petrol.* 42, 2033–2048. 10.1093/petrology/42.11.2033

Frost, C. D., and Frost, B. R. (2011). On the ferroan (A-type) granitoids: their compositional variability and modes of origin. *J. Petrol.* 52, 39–53. 10.1093/petrology/egq070

Glazner, A. F., Bartley, J. M., and Coleman, D. S. (2019). A more informative way to name plutonic rocks. *GSA Today.* 29, 4–10. 10.1130/GSATG384A.1

Holmes, A. (1945). Natural history of granite. *Nature.* 155, 412–415. 10.1038/155412a0

Janoušek, V., Bonin, B., Collins, W. J., Farina, F., and Bowden, P. (2020). "Introduction," in *Post-archean granitic rocks: petrogenetic processes and tectonic environments*. Editors V. Janoušek, B. Bonin, W. J. Collins, F. Farina, and P. Bowden (Bath, UK: Geological Society of London Special Publication).

Loiselle, M. C., and Wones, D. R. (1979). Characteristics and origin of anorogenic granites. *Geol. Soc. Am. Abstracts with Programs.* 11, 468.

Maniar, P. D., and Piccoli, P. M. (1989). Tectonic discrimination of granitoids. *Geol. Soc. Am. Bull.* 101, 635–643. 10.1130/0016-7606(1989)101<0635:TDOG>2.3.CO;2

Marmo, V. (1967). On the granite problem. *Earth Sci. Rev.* 3, 7–29. doi:10.1016/0012-8252(67)90369-8

Pearce, J. A., Harris, N. B., and Tindle, A. G. (1984). Trace element discrimination diagrams for the tectonic interpretation of granitic rocks. *J. Petrol.* 25, 956–983. 10.1093/petrology/25.4.956

Pitcher, W. S. (1997). *The nature and origin of granite*. London: Chapman & Hall.

Streckeisen, A. L. (1976). To each plutonic rock its proper name. *Earth Sci. Rev.* 12, 1–33. doi:10.1016/0012-8252(76)90052-0

Tuttle, O. F., and Bowen, N. L. (1958). *Origin of granite in the light of experimental studies in the system NaAlSi3O8–KAlSi3O8–SiO2–H2O*. Washington: Geological Society of America.

Wegener, A. (1924). *The origin of continents and oceans*. London: Methuen.

White, A. J. R. (1979). Sources of granitic magma. *Geol. Soc. Am. Abstracts with Programs.* 11, 539.

Conflict of Interest: The authors declare that the research was conducted in the absence of any commercial or financial relationships that could be construed as a potential conflict of interest.

frontiers in Earth Science

ORIGINAL RESEARCH
published: 15 May 2020
doi: 10.3389/feart.2020.00095

Secular Variation of Early Cretaceous Granitoids in Kyushu, SW Japan: The Role of Mélange Rocks as a Possible Magma Source

Kenshi Suga and Meng-Wan Yeh*

Department of Earth Sciences, National Taiwan Normal University, Taipei, Taiwan

The Early Cretaceous volcanic-arc granitic rocks from Kyushu, SW Japan are contemporaneous with the granitic rocks of the Yanshan Orogeny (SE China) along the eastern Eurasian continental margin. The secular geochemical variations of the whole-rock major elemental and Sr–Nd isotope data of the Early Cretaceous granitic rocks from Kyushu, SW Japan, as well as the zircon and apatite saturation temperatures, shows distinct changes during the Albian (∼115 to ∼100 Ma) as: (1) the mASI value of the rocks (i.e., Shiraishino granodiorites) decreases below 1, (2) the Sr–Nd isotopic data are relatively constant [$^{87}Sr/^{86}Sr_i$ = 0.70471 to 0.70573; $\varepsilon_{Nd}(t)$ = + 0.2 to + 1.9] within different rock types including granites, granodiorites, tonalites, and adakitic rocks (i.e., the Shiraishino granodiorites), following the increase of $^{87}Sr/^{86}Sr_i$ and decrease of $\varepsilon_{Nd}(t)$ from Berriasian, and (3) higher maximum temperatures at ∼105 Ma. The secular changes indicate that important geodynamic changes occurred in the arc system of SW Japan as it changed from subduction-accretion during the Jurassic to continental arc during the Early Cretaceous. Thermodynamic partial melting modeling demonstrates that the Albian granitic rocks can be derived from mélange rocks, such as chlorite-actinolite schists, at moderate depth and variable redox conditions. It is concluded that the genesis of the Early Cretaceous granitic rocks from Kyushu, SW Japan, may be related to upwelling of the asthenosphere and hot corner flow into the mantle wedge caused by slab rollback, which followed a shallowing of the subduction angle and subsequent flat-slab subduction during the Late Jurassic. The resultant heat induced the partial melting of the mélange rocks that formed on and were transported from the subducted plate interface.

Keywords: granitoids, mélange, arc magma, partial melt, Early Cretaceous, SW Japan, Yanshan orogeny

OPEN ACCESS

Edited by:
Kwan-Nang Pang,
Institute of Earth Sciences, Academia Sinica, Taiwan

Reviewed by:
David R. Lentz,
University of New Brunswick Fredericton, Canada
J. Victor Owen,
Saint Mary's University, Canada

****Correspondence:***
Kenshi Suga
sgkenshi@ntnu.edu.tw

Specialty section:
This article was submitted to Petrology, a section of the journal Frontiers in Earth Science

Received: *20 January 2020*
Accepted: *19 March 2020*
Published: *15 May 2020*

Citation:
Suga K and Yeh M-W (2020) Secular Variation of Early Cretaceous Granitoids in Kyushu, SW Japan: The Role of Mélange Rocks as a Possible Magma Source. Front. Earth Sci. 8:95. doi: 10.3389/feart.2020.00095

INTRODUCTION

Convergent margin magmatism occurred along the eastern Eurasian continental margin during the Late Jurassic to Late Cretaceous as the Paleo-Pacific plate subducted. Magmatism extended from the Korean Peninsula in the north to Vietnam in the south and represents a major period of juvenile crust formation and recycling in East Asia (Xu et al., 2002; Nguyen et al., 2004; Zhou et al., 2006; Kiminami and Imaoka, 2013; Shellnutt et al., 2013; Kim et al., 2016). Alternating periods of crustal

shortening and extension accompanied by magmatism during the Late Mesozoic are collectively referred to as the Yanshan Orogeny (Wu, 2005; Zhou et al., 2006; Li and Li, 2007; Dong et al., 2018). The Yanshan Orogeny consists of an early period (∼170 to ∼135 Ma) of crustal shortening and a late (∼135 to ∼90 Ma) period of extension followed by a brief period (∼80 Ma) of weak crustal shortening (Dong et al., 2018). The majority of Early Cretaceous magmatic rocks from SE China, NE China, Korea, and SW Japan are compositionally similar to volcanic-arc granites and it appears that their emplacement migrated eastward toward the Eurasia margin over time (Chen and Jahn, 1998; Zhou and Li, 2000; Xu et al., 2002; Zhou et al., 2006; Kiminami and Imaoka, 2013; Kim et al., 2016).

The formation of Late Yanshanian granitic rocks is debated as there are different models proposed for different regions. On the one hand, plutons from SE China are thought to be related to extension-induced melting of mafic igneous protoliths at mid-lower crustal depths, due to the heat advection resulting from the underplating of basaltic magmas along the active continental margin (Zhou and Li, 2000; Zhou et al., 2006). On the other hand, the Early Cretaceous granitic rocks from the Korean Peninsula and SW Japan are explained by partial melting of lower continental crust, due to slab rollback (Kiminami and Imaoka, 2013; Kim et al., 2016), whereas, for NE China, by interaction of delaminated lower mafic continental crust with an upwelling asthenosphere (Xu et al., 2002; Hou et al., 2007; Lan et al., 2011). The difference in the melting regimes and tectonomagmatic models may be, in part, related to the paleoposition of Korea and Japan relative to China. Although there is along strike subduction, Early Cretaceous magmatism in NE Asia may be related to subduction of the Izanagi plate, whereas in eastern China, it is related to subduction of the Paleo-Pacific plate (Maruyama et al., 1997). Moreover, it is still debated whether the paleogeographic position of Korea and SW Japan belongs to the North China craton or the South China craton (Osanai et al., 1999, 2006; Ishiwatari and Tsujimori, 2003; Ernst et al., 2007; Oh and Kusky, 2007; Omori and Isozaki, 2011; Suga et al., 2017).

The upwelling of hot asthenosphere into the mantle wedge caused by slab rollback may have played a vital role in the formation of Early Cretaceous granitic rocks in NE Asia as this is thought to be the primary process that produces the adakitic rocks of SW Japan (Kamei, 2004; Imaoka et al., 2014; Kim et al., 2016). Alternatively, it is possible that the combination of asthenospheric upwelling and hot corner flow caused by slab rollback may have induced partial melting of mélange rocks, such as chlorite-actinolite schists, producing intermediate to silicic melts (Marschall and Schumacher, 2012; Hao et al., 2016). The Early Cretaceous granitic rocks, including adakitic rocks, in Kyushu, SW Japan, therefore, potentially provide an opportunity to investigate the genesis of granitic rocks related to the combination of asthenospheric upwelling and hot corner flow caused by slab rollback.

In this study, whole rock geochemical data from ∼150 granitic samples across Kyushu, SW Japan, are compiled in order to determine if there is a secular variation in the nature of the plutons and to assess the role subduction-related mélange rocks may play in their origin. Thermodynamic modeling using the program Rhyolite-MELTS is used to evaluate whether partial melting of mélange rocks is either partially or wholly responsible for the genesis of some Early Cretaceous felsic igneous rocks, including the adakitic plutons.

GEOLOGICAL BACKGROUND

The Japanese Islands comprise a number of subduction-related orogenic belts that were produced beneath the Eurasian continent over more than *c.* 500 Myr (Maruyama et al., 1997; Isozaki et al., 2010). The geotectonic framework in the inner zone of southwest Japan is made up of, from north to south, the Hida–Oki, Renge, Akiyoshi, Suo, Maizuru, Ultra-Tamba, Mino–Tanba, and Ryoke belts, with a tectonically downward-younging polarity that resulted from stepwise accretions during the Paleozoic to Mesozoic (Nishimura, 1998; **Figure 1**). In Kyushu, SW Japan, the Renge, Akiyoshi, Suo, and Ryoke belts occur on the northern side of Usuki–Yatsushiro tectonic line, where Cretaceous igneous rocks are distributed (**Figure 1**).

Cretaceous plutonic rocks in Kyushu consist mainly of granites, tonalites, and granodiorites with subordinate gabbro and diorites (**Figure 1**). They intruded metamorphic rocks of the Renge, Suo, Ryoke, and Higo belts, and sedimentary rocks of the Cretaceous Kanmon Group. Cretaceous andesites and dacite occur in and around Kyushu (Imaoka et al., 1993; Matsuura, 1998; Owada et al., 1999).

Published age dates of the granitic rocks using various methods (K–Ar, Rb–Sr, Sm–Nd, CHIME, U–Pb) on whole rock and minerals range from 143 to 75 Ma, whereas the mafic rocks yielded ages (K–Ar, Rb–Sr, U–Pb) that are comparatively more restricted and were emplaced from 123 to 97 Ma (Hattori and Shibata, 1982; Sasada, 1987; Osanai et al., 1993; Nakajima et al., 1995; Kamei et al., 1997, 2000, 2004; Matsuura, 1998; Hamamoto et al., 1999; Owada et al., 1999; Takagi et al., 2000, 2007; Sakashima et al., 2003; Nishimura et al., 2004; Fujii et al., 2008; Kouchi et al., 2011; Miyoshi et al., 2011; Adachi et al., 2012; Tiepolo et al., 2012; Miyazaki et al., 2018). In comparison, the dacite and andesite yielded K–Ar mineral ages of 107 ± 3 Ma (Imaoka et al., 1993) and from 110 to 102 Ma (Imaoka et al., 1993; Matsuura, 1998; Owada et al., 1999), respectively.

The Nagasaki high-*P* metamorphic rocks are distributed in western Kyushu (**Figure 1**). The rocks are a western extension of the high-*P* Sanbagawa metamorphic rocks of southwest Japan (Faure et al., 1988; Nishimura et al., 2004), which are the higher *P/T* members of a Cretaceous paired metamorphic belt that joins the high-*T* metamorphic rocks of the Ryoke plutono-metamorphic belt along the Median Tectonic Line. Toward the west, the Cretaceous plutonic rocks and related high-*T* metamorphic rocks, including the Higo high-*T* metamorphic rocks, are distributed throughout central to northern Kyushu.

The Nishisonogi unit of the Nagasaki metamorphic rocks forms a Late Cretaceous subduction complex that consists mainly of epidote-blueschist facies pelitic, psammitic, and mafic schists with minor serpentinite (Nishiyama, 1990; Mori et al., 2014). The serpentinite, which is in tectonic contact with the schists,

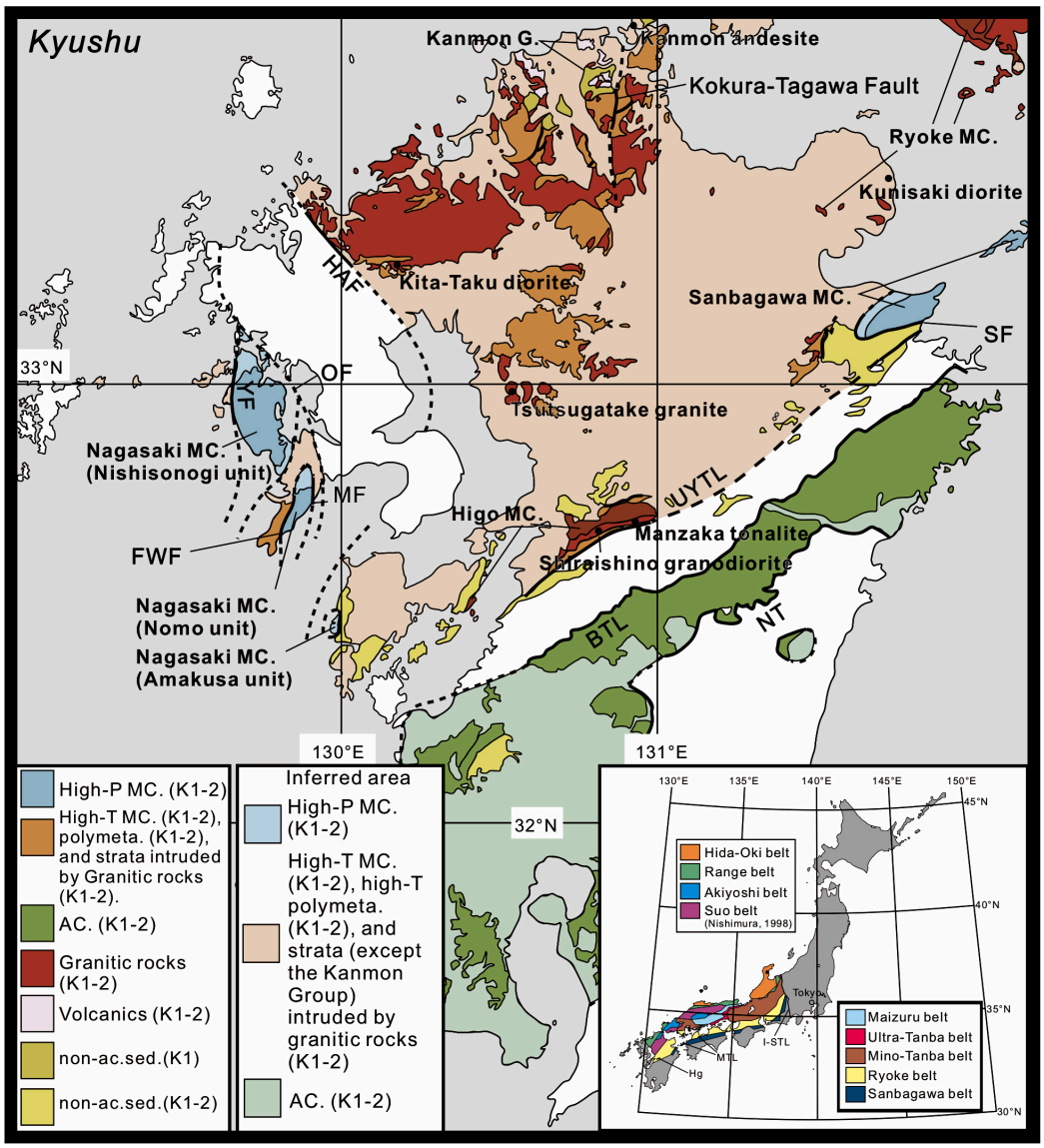

FIGURE 1 | Distribution of Cretaceous accretionary complex, metamorphic complex, plutonic rocks, volcanic rocks, and non-accretionary sedimentary rocks in Kyushu, SW Japan [modified from Miyazaki et al. (2016) based on the seamless geological map of Japan (1:200,000), Geological Survey of Japan, https://gbank.gsj.jp/seamless/index_en.html] with solid circle indicating the locality of granitic rock samples of which the thermodynamic modeling was modeled in this study. UYTL, Usuki–Yatsushiro Tectonic Line; BTL, Butsuzo Tectonic Line; SF, Sashu Fault; HAF, Hatashima–Ariake Fault; FWF, Fukabori–Wakimisaki Fault; OF, Omurawan–Amakusa Fault; YF, Yobikonoseto Fault; MF, Mogi Fault; NT, Nobeoka Thrust; MC, Metamorphic Complex; AC, Accretionary Complex; polymeta, polymetamorphic rocks; non-ac.sed., non-accretionary sedimentary rocks; K1–2, Early–Late Cretaceous; K1, Early Cretaceous. Inset-map showing a geotectonic map of SW Japan (modified form Nishimura, 1998 with permission). MTL, Median Tectonic Line; I–STL, Itoigawa–Shizuoka Tectonic Line; Hg, Higo belt.

occurs as pod-like bodies of < 150 m in diameter and ultramafic melanges of < 350 m in thickness (Mori et al., 2014). The ultramafic melanges contain tectonic blocks of metagabbro, mafic schist, pelitic schist, and albitite in a matrix of chlorite-actinolite schist, talc schist, and schistose serpentinite (Nishiyama, 1989, 1990). Small blocks (<5 m in diameter) of jadeitite, omphacitite, rodingite, and zoisitite are found locally (Nishiyama, 1978; Shigeno et al., 2005, 2012a,b; Mori et al., 2011). The mineral assemblages of the schists suggest the peak metamorphic *P–T* conditions of 8 kbar and 400°C (Mori et al., 2014). The peak metamorphic conditions for the jadeitites were estimated to be $P > 13$ kbar and $T > 400$°C (Shigeno et al., 2005).

Metamorphic age data (K–Ar, $^{40}Ar/^{39}Ar$, U–Pb) from the pelitic and psammitic schists range from 85 to 60 Ma (Hattori and Shibata, 1982; Faure et al., 1988; Miyazaki et al., 2019), 85–65 Ma ($^{40}Ar/^{39}Ar$, U–Pb) for the jadeitites (Mori et al., 2007, 2011; Yui et al., 2012), and 108–105 Ma (U–Pb) for the rodingites (Fukuyama et al., 2014). The youngest detrital zircon ages and metamorphism duration were estimated to be 97–79 Ma and 10 to 20 Myr, respectively (Miyazaki et al., 2019).

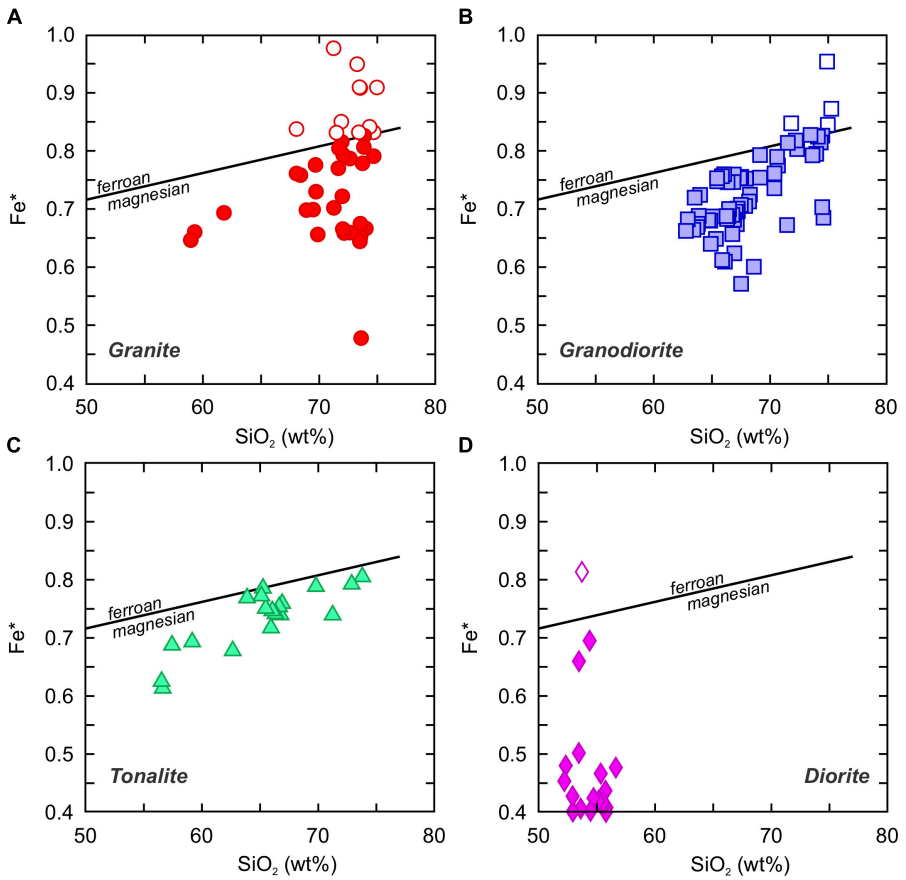

FIGURE 2 | Division of the Cretaceous **(A)** granites, **(B)** granodiorites, **(C)** tonalites, and **(D)** diorites from Kyushu into ferroan and magnesian compositions using the Fe* [FeOt/(FeOt + MgO)] vs. SiO_2 (wt%) discrimination of Frost et al. (2001).

GEOCHEMICAL CHARACTERISTICS OF CRETACEOUS GRANITOIDS IN KYUSHU, SW JAPAN

Whole-rock major elemental data published for 148 samples of granitic rocks from Kyushu were compiled (**Supplementary Table S1**) and plotted using the geochemical classification diagrams of granitic rocks reported by Frost et al. (2001; **Figures 2**, **3**) and Harker diagrams (**Figure 4**). The granites (n = 40) are peraluminous to metaluminous, ferroan to magnesian (Fe* = 0.48–0.98), and alkalic to calcic in composition with Mg# ranging from 4 to 66 and K_2O/Na_2O ratios of 0.5–1.6. The rocks have high SiO_2 contents as all but 3 samples have SiO_2 from 68.1 to 75.0 wt.%. The granodiorites (n = 65) are peraluminous to metaluminous, ferroan to magnesian (Fe* = 0.57–0.95), and calc-alkalic to calcic in composition with Mg# ranging from 8 to 57 and K_2O/Na_2O ratios of 0.2–1.5. The SiO_2 contents range from 62.8 to 75.3 wt.%. The tonalites (n = 19) are peraluminous to metaluminous, magnesian (Fe* = 0.61–0.80), and calc-alkalic to calcic in composition with Mg# ranging from 30 to 53 and K_2O/Na_2O ratios of 0.3–1.1. The SiO_2 contents range from 56.5 to 73.8 wt.%. The granite, granodiorite, and tonalite plutons have similar negative trends of TiO_2, Al_2O_3, CaO, and Mg#, and positive trends of $Na_2O + K_2O$, against SiO_2 (**Figure 4**). They also have similar loss on ignition (LOI) values of 0.0–1.8 wt.%.

By comparison, the diorites (n = 24), for the exception of 3 samples, are metaluminous, magnesian (Fe* = 0.36–0.50), and calc-alkalic to calcic in composition (**Figures 2–4**). They have higher Mg# ranging from 64 to 76 and lower SiO_2 contents of 52.2–59.4 wt.%, and have similar K_2O/Na_2O ratios of 0.3–0.9, compared to the granites, granodiorites, and tonalites. There is a weak positive trend of $Na_2O + K_2O$ against SiO_2. The trend line is extrapolated into the corresponding lines for the granites, granodiolites, and tonalites. LOI contents are 0.5–2.1 wt.%, which are similar to those of the granites, granodiorites, and tonalites.

Some or all trace elemental data were reported from 127 samples across all rock types. The trace element concentrations of the granites, granodiorites, and tonalites show broad similarities across all elements, but the diorites are somewhat unique. The concentration of transition metals (Sc $\leq$ 12 ppm, V = 2 to 178 ppm, Cr $\leq$ 56 ppm, Ni $\leq$ 22 ppm, Cu = 3 to 182 ppm, and Zn = 4 to 117 ppm) for the granites, tonalites, and granodiorites are similar. In contrast, the diorites have comparatively higher concentrations of V (125–231 ppm), Cr (5–1544 ppm), and Ni (10–259 ppm), but similar concentrations of Cu (18–116 ppm)

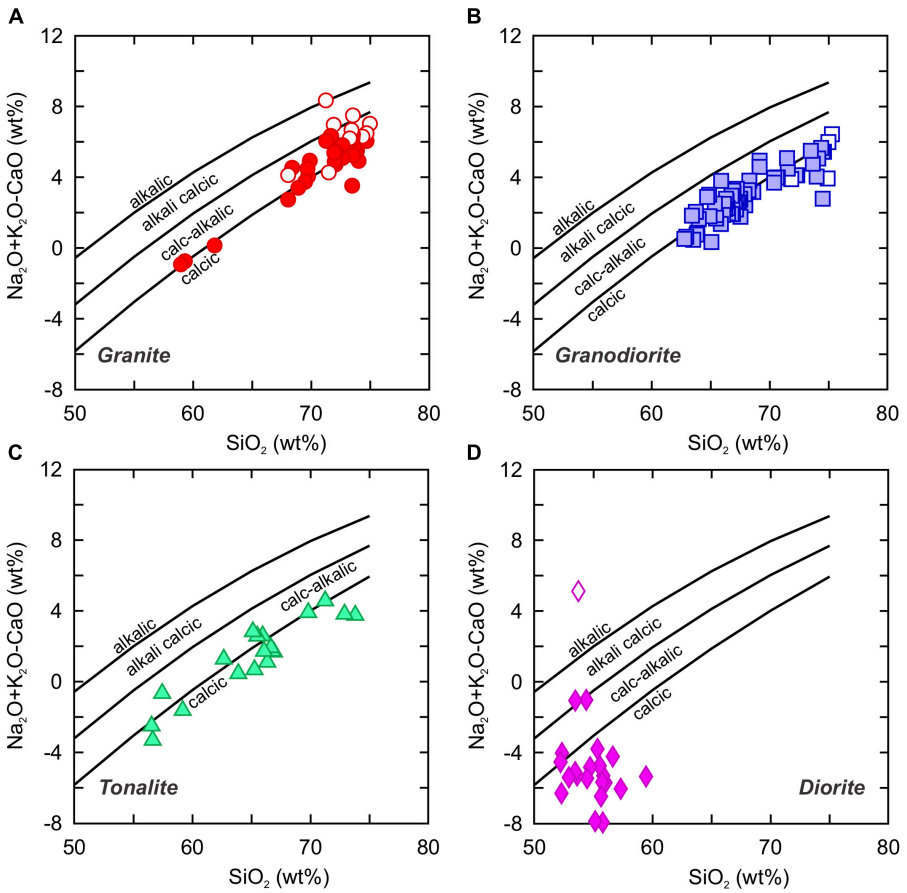

FIGURE 3 | Modified alkali-lime index ($Na_2O + K_2O - CaO$ wt%) vs. SiO_2 (wt%) of the Cretaceous **(A)** granites, **(B)** granodiorites, **(C)** tonalites, and **(D)** diorites from Kyushu (Frost et al., 2001). Symbols as in **Figure 2**.

and Zn (57–110 ppm). The large ion lithophile elements (Rb, Sr, and Ba) show more chemical variability in all rock types, but the diorites tend to have lower concentrations of Rb (10–74 ppm) and Ba (52–405 ppm) and similar Sr (75 to 864 ppm) compared to the granites, tonalites, and granodiorites (Rb = 38–186 ppm, Sr = 117–859 ppm, Ba = 214–1142 ppm). The concentrations of Y and Nb across all rock types are generally similar (Y = 5–39 ppm, Nb = 4–24 ppm), although the diorites tend to have lower concentrations of Zr (16–102 ppm) and the granites tend to have higher concentrations of Th (3–26 ppm), compared to other rock types (Zr = 47–218 ppm, Th = 0.9–23 ppm).

The primitive mantle normalization patterns show enrichment of the less incompatible elements over the incompatible elements but they also have prominent depletions of Ba, Nb, and Ti (**Figure 5**). The granodiorites have a subgroup of Hf depleted rocks but it is not certain if it is unique as Hf data was not reported for the diorites. The chondrite-normalized rare-earth element patterns of the granodiorites and tonalites show similar light rare-earth element (LREE) enrichment and tend to have high La/Yb_N ratios (5.6 to 35.4), whereas the diorites have moderately to slight LREE ($La/Yb_N < 5$) enrichment (**Figure 6**). Rare earth elemental data are not available for the granites. The rocks generally do not display prominent depletion of Eu as the tonalites, diorites and most of the granodiorites (all but 4) have Eu/Eu* values ≥ 0.8. The relatively high Eu/Eu* values indicate that the rocks probably did not experience significant plagioclase fractionation.

Strontium and Nd isotopic data are only available for the granites, granodiorites, and tonalites (**Supplementary Table S2**). There are more samples with Sr isotopes (123) reported than Nd isotopes (48). Moreover, the Sr isotopes cover nearly the entire Cretaceous (~145 to ~85 Ma), whereas there is an age gap (~140 to ~120 Ma) within samples that have Nd isotope data. The initial Sr isotope ratios ($^{87}Sr/^{86}Sr_i$) of granites (0.70404 to 0.70654), granodiorites (0.70471 to 0.70573), and tonalites (0.70430 to 0.70529) are similar and have relatively restricted ranges, although there are two outliers (0.70302 and 0.70620) within the granodiorites. The Nd isotopes, as expressed by the $\varepsilon_{Nd}(t)$ notation, show distinct negative values for the granites [$\varepsilon_{Nd}(t) = -4.7$ to $+ 1.0$] compared to the granodiorites [$\varepsilon_{Nd}(t) = + 0.5$ to $+ 1.6$] and tonalites [$\varepsilon_{Nd}(t) = + 0.2$ to $+ 3.1$]. The Nd depleted mantle model ages of the granites are 0.7–1.4 Ga, which are older than those of the granodiorites (0.6–1.1 Ga) and tonalites (0.8–1.2 Ga).

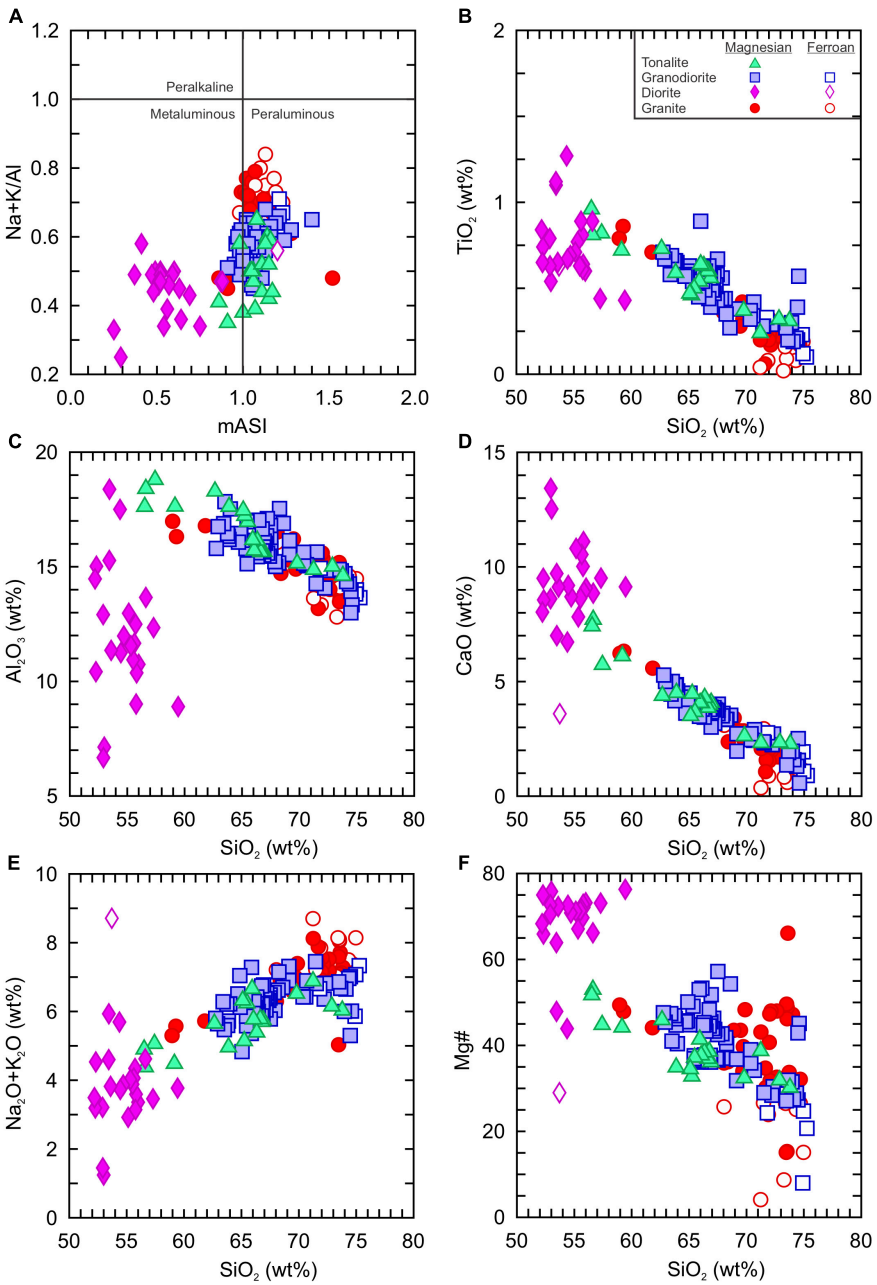

FIGURE 4 | Major element variation of the Cretaceous granites, granodiorites, tonalites, and diorites from Kyushu. **(A)** Alumina saturation index [mASI = molecular Al/(Ca − 1.67P + Na + K)] vs. alkali-alumina ratio [molecular (Na + K)/Al]. **(B)** TiO_2 (wt%) vs. SiO_2 (wt%). **(C)** Al_2O_3 (wt%) vs. SiO_2 (wt%), **(D)** CaO (wt%) vs. SiO_2 (wt%). **(E)** $Na_2O + K_2O$ (wt%) vs. SiO_2 (wt%). **(F)** Mg# [molecular Mg/(Mg + Fe)*100] vs. SiO_2 (wt%). The division of rocks into magnesian and ferroan is plotted in **Figure 2**.

DISCUSSION

Petrogenesis of the Early Cretaceous Granitic Rocks in Kyushu, SW Japan

Tectonomagmatic Classification

According to the classification scheme of Frost et al. (2001), the Early Cretaceous granitic rocks from Kyushu, are primarily magnesian, peraluminous to metaluminous, calc-alkalic to calcic in composition (**Figures 2–4**). Rocks of this composition are considered to be most commonly associated with subduction-zone settings. There are some rocks in the data set that are ferroan but they are also highly silicic (SiO_2 > 72 wt.%). Magnesian and ferroan rocks tend to overlap at highly silicic compositions within cogenetic rock suites due to chemical differentiation as intermediate magnesian magmas eventually become ferroan after

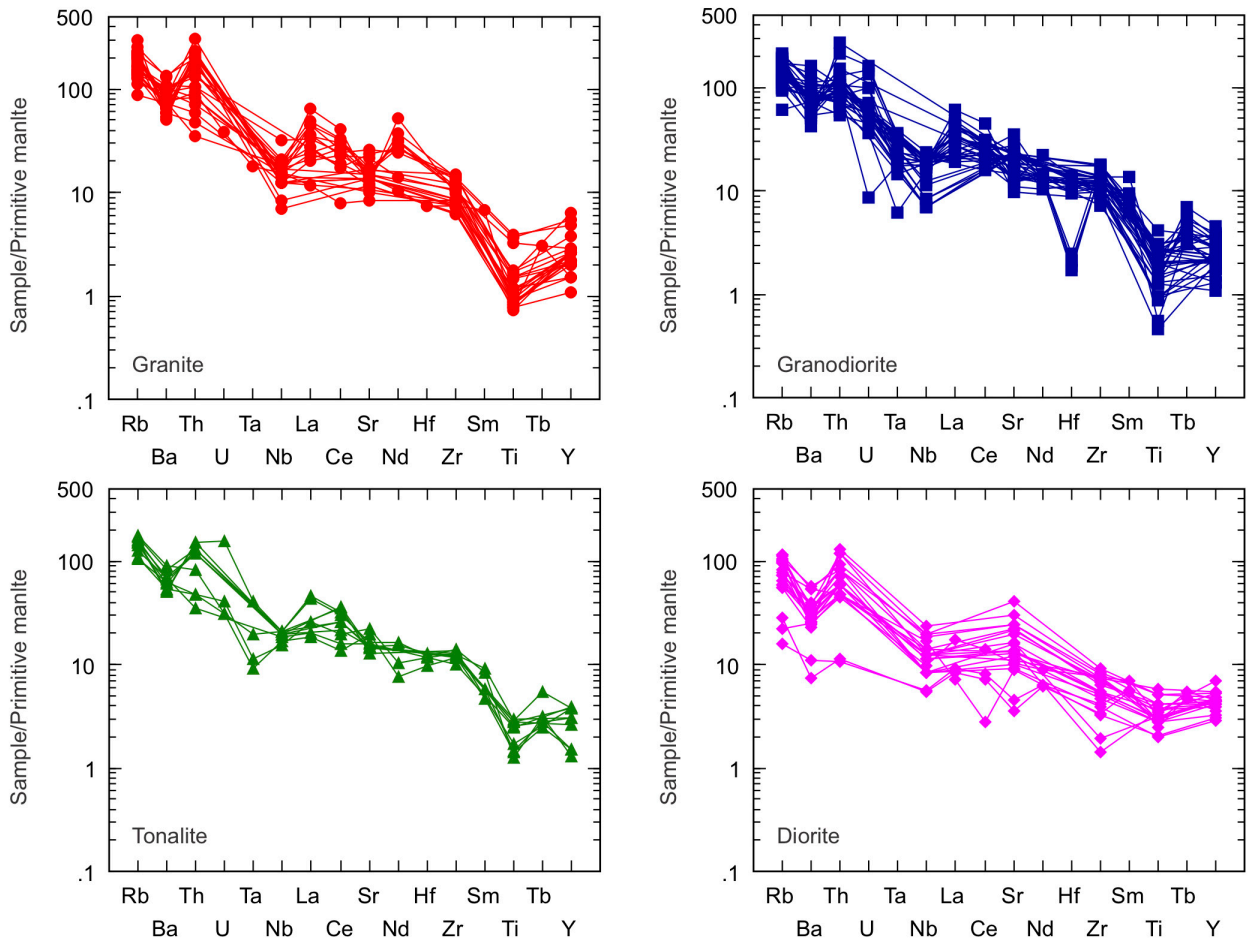

FIGURE 5 | Primitive mantle-normalized incompatible trace element diagrams of the Cretaceous **(A)** granites, **(B)** granodiorites, **(C)** tonalites, and **(D)** diorites from Kyushu. Normalizing values are from Sun and McDonough (1989).

extensive fractional crystallization (Frost et al., 2001). Given that the ferroan rocks in this study are highly silicic and that they fall along the same negative or positive trends of TiO_2, Al_2O_3, CaO, Mg#, and $Na_2O + K_2O$ against SiO_2 as the magnesian granitic rocks, they are likely the most evolved compositions of an original magnesian parental magma (**Figure 4**). The trace element compositions of all samples fall unambiguously within the volcanic-arc/I-type granite field of the Y + Nb–Rb discrimination diagram (Pearce et al., 1984; Christiansen and Keith, 1996) (**Figure 7**). Moreover, the results indicate that the chemical differentiation trends identified in some of the plutons did not have a significant effect on their Y, Nb, and Rb concentrations and thus did not cause 'elemental drift' across the field boundaries (Forster et al., 1997). In other words, the major and trace elemental compositions are mutually supportive of each other, and consistent with the fact that the Japanese Islands comprise a number of subduction-related orogenic belts over more than *c*. 500 Myr (Maruyama et al., 1997; Isozaki et al., 2010). Thus, there is little doubt that the Early Cretaceous granitic rocks of Kyushu were exclusively emplaced at a volcanic-arc setting.

Secular Compositional and Temperature Variations

The whole-rock major elemental and Sr–Nd isotope data, as well as zircon (T_{Zrc}) and apatite (T_{Apt}) saturation temperatures, of the granitic rocks are plotted against time (Ma), in order to evaluate the secular compositional and temperature variations during the Cretaceous (**Figures 8**, **9** and **Supplementary Tables S1, S2**). The ages of the rocks are reported from high closure temperature minerals (U–Pb zircon, Rb–Sr whole-rock isochoron, K–Ar hornblende) and are interpreted to be crystallization ages. The zircon (T_{Zrc}) and apatite (T_{Apt}) saturation temperatures were calculated using the whole rock major and trace element data available for the granitic rocks (Harrison and Watson, 1984; Boehnke et al., 2013).

There is clear secular variation in the major element compositions (**Figure 8**). The most distinct major element change is the decrease in the alumina saturation index (mASI) value at ∼105 Ma (i.e., Shiraishino granodiorites). All other intrusions have near constant mASI values of ∼1.1 to ∼1.2, whereas the Shiraishino granodiorites have a wide range but drop below 1 and become metaluminous (**Figure 8A**). In fact the Shiraishino

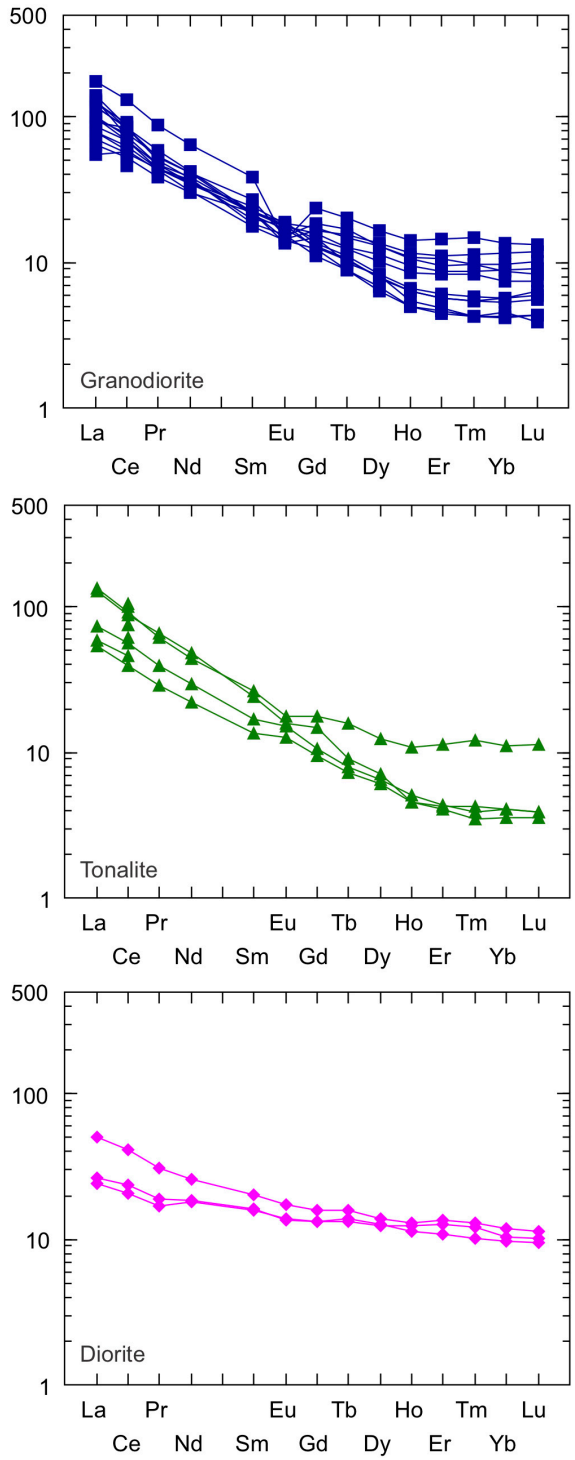

FIGURE 6 | Chondrite-normalized rare earth element patterns of the Cretaceous **(A)** granodiorites, **(B)** tonalites, and **(C)** diorites from Kyushu. Chondrite values are from Sun and McDonough (1989).

granodiorite is the most distinct intrusion as it has high TiO_2 (~0.66 wt.%) and low SiO_2 (~63.8 wt.%) contents and low K_2O/Na_2O ratios (~0.3) compared to the other granitic rocks. However, in spite of the Shiraishino granodiorite, the overall trends show an increase in the Mg# and TiO_2 and Al_2O_3 contents and a decrease in the K_2O/Na_2O ratio and SiO_2 over time (**Figures 8B–F**).

The Sr–Nd isotopes show two secular trends (**Figures 9A,B**). There are overall trends for both Sr and Nd, but they both show changes during the Albian (~115 to ~105 Ma). The $^{87}Sr/^{86}Sr_i$ ratio increases from the Early Cretaceous to the Late Cretaceous, which is mirrored by an overall negative trend in the $\varepsilon_{Nd}(t)$ values. However, between ~115 and ~105 Ma it is clear that the $^{87}Sr/^{86}Sr_i$ ratio flattens and becomes relatively constant (~0.7047 to ~0.7057) until it increases (~0.7065) after 105 Ma and then drops (~0.7051) at ~90 Ma. Although there is less Nd isotopic data, a similar pattern as the Sr isotopes is observed at ~115 to ~105 Ma. The $\varepsilon_{Nd}(t)$ values of the tonalites, granodiorites and some granites are constant (~ + 0.2 to ~ + 1.9) before dropping to the lowest values (−4.7) at ~95 Ma and increasing again (+ 0.4) at ~85 Ma. Unlike the major elements where most of the compositional variation at ~105 Ma is attributed to the Shiraishino granodiorites, the isotopic consistency between 115 and 105 Ma occurs within different rock types, implying a relatively uniform source for the Albian rocks. After ~105 Ma, the increase of the $^{87}Sr/^{86}Sr_i$ ratio and decrease of the $\varepsilon_{Nd}(t)$ values suggests a greater contribution of less radiogenic material was involved in the origin of the granites. It could be that these primitive magmas experienced crustal contamination during emplacement; or that the granites were derived by partial melting of the crust; or the source became more enriched due to an increase in subducted sediment into the mantle wedge. It would seem the first two options are more likely as the Sr and Nd isotopic values after 95 Ma return to the values observed during the Albian and some of the granites have higher Th/Nb_{PM} values (>20) (**Figure 10**).

The calculated T_{Zrc} and T_{Apt} for the granites, granodiorites, and tonalites are similar: T_{Zrc} = 653–740°C and T_{Apt} = 806–927°C for the granites, T_{Zrc} = 666–756°C and T_{Apt} = 803–1022°C for the granodiorites, T_{Zrc} = 674–739°C and T_{Apt} = 779–943°C for the tonalites. The diorites did not yield meaningful T_{Zrc} values, because their M values were outside (>1.9) of the experimental range (Miller et al., 2003), but T_{Apt} (584–896°C) estimates are the lowest of all rock types. The estimates of T_{Zrc} for each rock type are lower than those of T_{Apt}, implying the magma sources were undersaturated in Zr during partial melting and crystallization. In other words, the estimates of T_{Apt} represent the maximum temperatures experienced by the granitic rocks, whereas, for T_{Zrc}, are probably the minimum temperatures.

Over this time interval, the T_{Zrc} and T_{Apt} estimates of the granites, granodiorites, and tonalites increased from T_{Zrc} = ~660°C and T_{Apt} = ~810°C at 135 Ma and reached a peak of T_{Zrc} = ~750°C and T_{Apt} = ~960°C at ~105 Ma. This is followed by lower T_{Apt} temperatures to 840°C at 81 Ma. Both the higher peaks of T_{Zrc} and T_{Apt} estimates are recorded in the granodiorites (i.e., Shiraishino granodiorite).

The secular variations observed within the whole-rock major elemental and Sr–Nd isotope data, and zircon (T_{Zrc}) and apatite (T_{Apt}) saturation temperatures reveal important geodynamic changes in the development of the Cretaceous arc system of

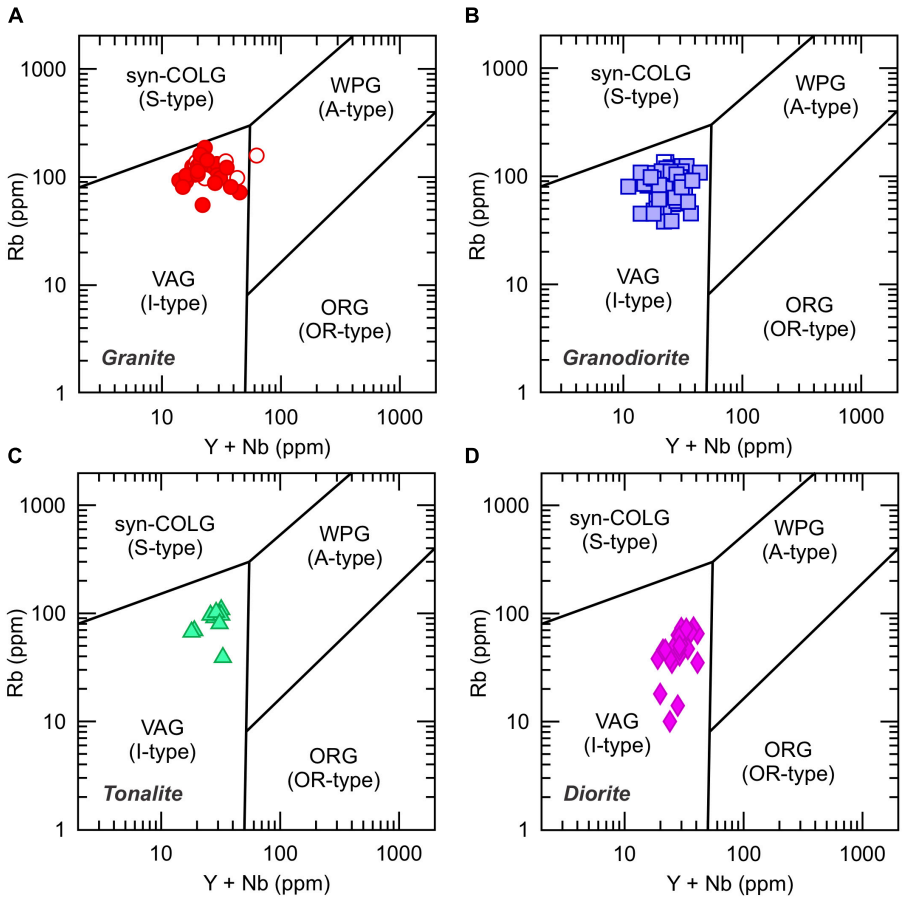

FIGURE 7 | Tectonomagmatic discrimination of the Cretaceous **(A)** granites, **(B)** granodiorites, **(C)** tonalites, and **(D)** diorites from Kyushu using Rb (ppm) vs. Y + Nb (ppm) criteria of Pearce et al. (1984) enhanced with Christiansen and Keith (1996). Symbols as in **Figure 2**. VAG, volcanic arc granites; ORG, ocean ridge granites; syn-COLG, syn-collisional granites; WPG, within-plate granites; OR, ocean ridge.

SW Japan. The rocks are principally magnesian and calc-alkalic, and have relatively high Eu/Eu* values (≥0.8). The magnesian nature of the rocks implies that their parental magmas were likely oxidized as this would lead to early crystallization of magnetite or Ti-rich magnetite and a relatively high Mg# (Osborn, 1959; Buddington and Lindsley, 1964). Moreover, the rocks are calc-alkalic to calcic and have relatively high Eu/Eu* values which is likely a consequence of water-rich magma systems as plagioclase crystallization is suppressed under hydrous conditions (Arculus, 2003). In this regard, the relative uniformity of the rocks is supportive of a long term volcanic-arc setting as oxidizing and water-rich conditions are expected at subduction zones (Arculus, 2003; Plank et al., 2013).

It is clear that the Albian rocks, and perhaps the older (Valanginian) and youngest (Coniacian) rocks, are derived from a relatively uniform source as they have similar $^{87}Sr/^{86}Sr_i$ ratios and $\varepsilon_{Nd}(t)$ values, as described above. The two exceptions are the oldest rocks (Berriasian) that are the most radiogenic and the ∼95 Ma rocks (Cenomanian) that are the most unradiogenic rocks. As mentioned previously, the Sr–Nd isotopic data of the ∼95 Ma rocks may reflect crustal contamination during emplacement, or partial melting of the crust. The fact that the Albian rocks are all less radiogenic than the Berriasian-Valanginian rocks in spite of their different rock types (granodiorite, tonalite, granite) indicates they are probably derived from a source that became slightly less radiogenic over time as a result of the material that was brought into the subduction system/mantle wedge. The T_{Zrc} and T_{Apt} estimates may also be supportive of the change in the subduction and melting geodynamics as the Albian rocks (i.e., Shiraishino granodiorite) have the higher mineral saturation temperatures, whereas older and younger rocks appear to have lower mineral saturation temperatures (**Figure 9D**). The higher temperatures for the granodiorites at Albian may imply the heat input into the magma source was higher during this time.

The magma source of the Shiraishino granodiorites was proposed to be subducted oceanic crust that melted due to asthenospheric upwelling and hot corner flow caused by slab rollback (Kamei, 2004; Kiminami and Imaoka, 2013; Imaoka et al., 2014; Kim et al., 2016). The proposed petrogenetic model is broadly consistent with the classification of the granodiorites as being related to slab failure using the Nb + Y–Nb/Y

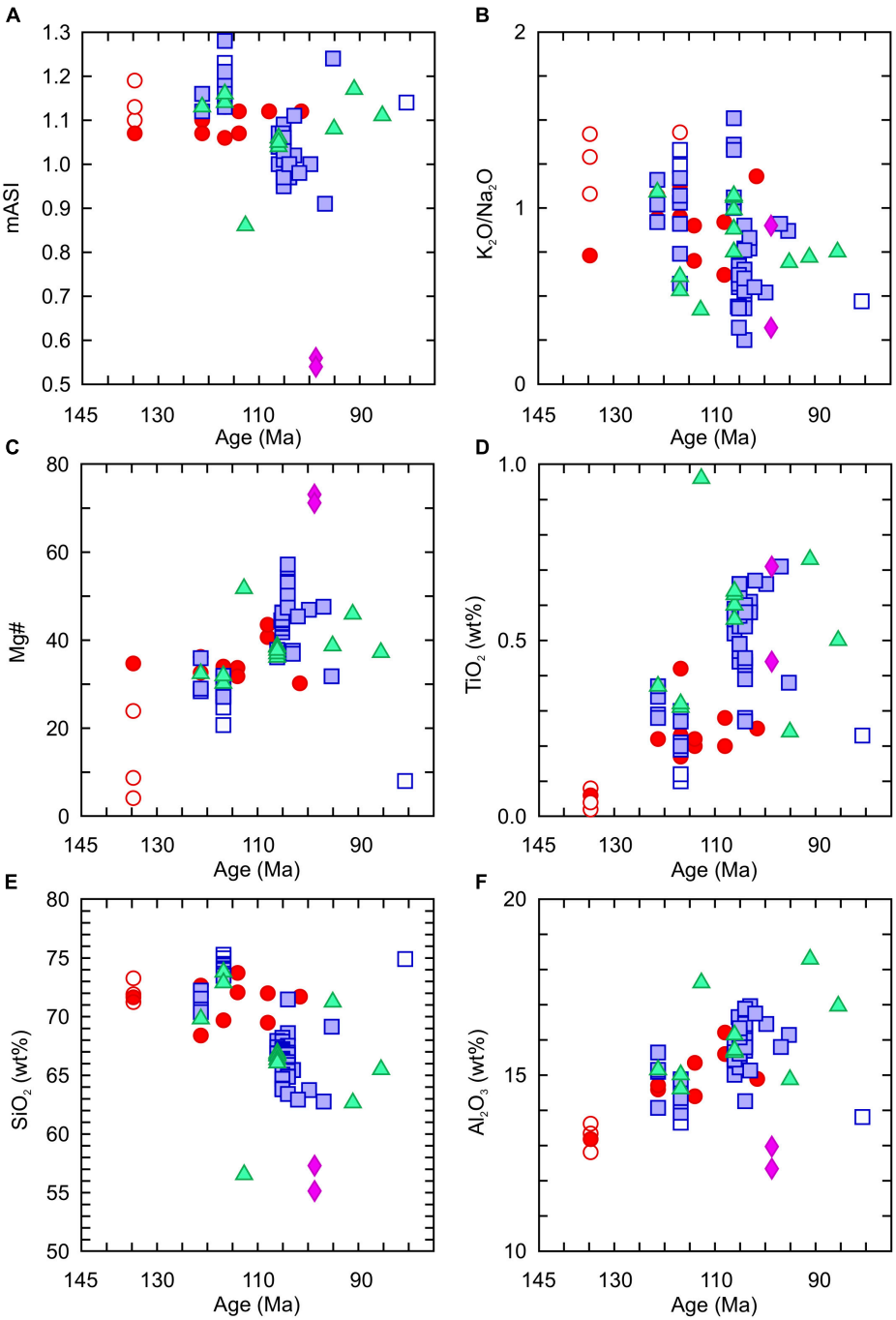

FIGURE 8 | Major element secular variability of the Cretaceous granitic (granties, granodiorites, tonalites, diorites) rocks from Kyushu. **(A)** mASI [molecular Al/(Ca − 1.67P + Na + K)], **(B)** K_2O/Na_2O, **(C)** Mg# [molecular Mg/(Mg + Fe)*100], **(D)** TiO_2 (wt%), **(E)** SiO_2 (wt%), and **(F)** Al_2O_3 (wt%). Symbols as in **Figure 2**.

discrimination diagram (**Figure 11**), which implies that they were derived from partial melting of the upper layers of oceanic crust (Whalen and Hildebrand, 2019). In contrast, the other granitic rocks are thought to be derived by partial melting of mafic lower continental crust (Kamei, 2004), tonalitic middle crust (Kamei, 2002), and young and hot subducted oceanic crust (Kamei et al., 2004). However, the other granitic rocks are also classified as slab failure-related (**Figure 11**), suggesting they were derived from the same source as the Shiraishino granodiorites. The model proposed for the genesis of the Shiraishino granodiorites, as well as the other granitic rocks, can be tested as there are constraints on the type of source material that is representative the upper part of subducted oceanic crust in the region. For example, the proximal Nishisonogi chlorite-actinolite schist is interpreted to

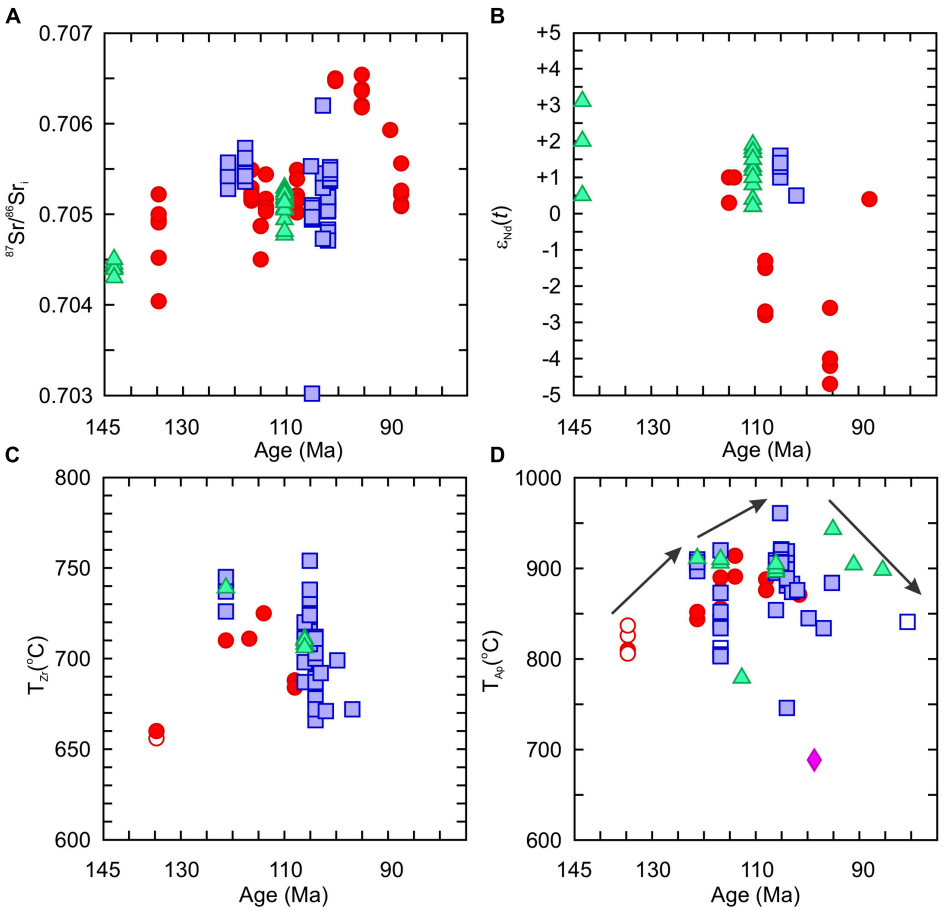

FIGURE 9 | Secular variation of **(A)** $^{87}Sr/^{86}Sr_i$, **(B)** $\varepsilon_{Nd}(t)$, **(C)** zircon saturation temperature (T_{Zrc} °C), and **(D)** apatite saturation temperature (T_{Apt} °C) in the Cretaceous granitic (granties, granodiorites, tonalites, diorites) rocks from Kyushu. Symbols as in **Figure 2**.

be a mélange sequence that was derived from the upper part of subducted oceanic crust and melting of these rock types are known to produce silicic melts (Marschall and Schumacher, 2012; Hao et al., 2016). In the following section, we present thermodynamic modeling in order to determine if granitic melts similar to the Albian rocks can be derived by partial melting of the Nishisonogi chlorite-actinolite schist.

Thermodynamic Modeling of the Albian Granitic Rocks

For this study, the origins of the Albian granitic rocks of Kyushu are evaluated as they appear to be derived from the same source (**Figures 9A,B**, **11**) as discussed above. Namely, the Tsutsugatake granite (Kamei et al., 2009), the Shiraishino granodiorites (Kamei, 2004), the Manzaka tonalite (Kamei, 2002), the Kunisaki and Kita-Taku high-Mg diorites (Kamei et al., 2004), and the Kanmon andesites (Imaoka et al., 1993) (**Figure 1**). The reported ages in previous studies are 117 ± 13 Ma for the Tsutsugatake granite (Osanai et al., 1993), 121–100 Ma for the Shiraishino granodiorite (Nakajima et al., 1995; Kamei et al., 1997, 2000), 113 ± 5 Ma for the Manzaka tonalite (Sakashima et al., 2003), 99 ± 5 Ma for the Kunisaki high-Mg diorite (Kamei et al., 2004), and 105–102 Ma for the Kanmon andesite (Imaoka et al., 1993; Matsuura, 1998). The age of the Kita-Taku high-Mg diorite, which occurs as a xenolith in the Kita-Taku gabbros (Oshima, 1961), is inferred to be *c.* 116 Ma, based on the geological relations of its host rocks with the surrounding granitic and metamorphic rocks (Owada et al., 1999; Kamei et al., 2004).

Equilibrium partial melting models were calculated using the Nishisonogi chlorite-actinolite schist as a proxy for mélange rocks in the region. Our goal is to determine if it is possible to derive some or all of the Albian granitic rocks from the Nishisonogo schist including: the Tsutsugatake granite, the Shiraishino granodiorites, the Manzaka tonalite, the Kunisaki and Kita-Taku high-Mg diorites, and the Kanmon andesites. We selected a starting composition that is typical of the Nishisonogi chlorite-actinolite schist (NK25; Mori et al., 2014; **Table 1**).

The thermodynamic modeling of granitic rocks can be modeled using the program Rhyolite-MELTS (Gualda et al., 2012). Rhyolite-MELTS as it is calibrated to the SiO_2–TiO_2–Al_2O_3–Fe_2O_3–Cr_2O_3–FeO–MnO–MgO–CaO–Na_2O–K_2O–P_2O_5–H_2O bulk composition system. The software is optimized for silicic systems and enables the user to adjust modeling parameters, such

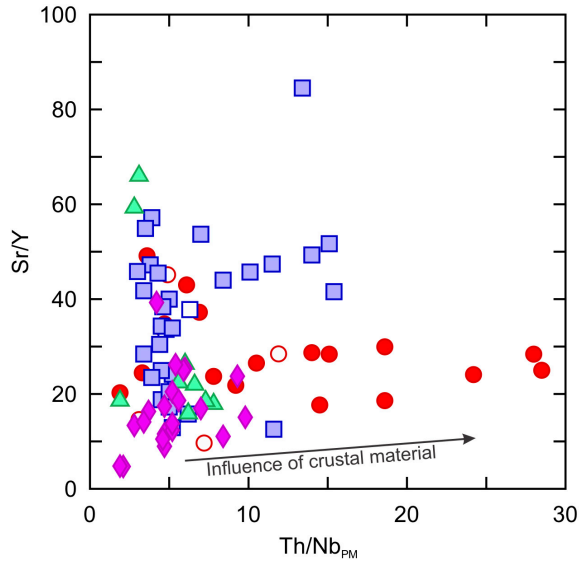

FIGURE 10 | Sr/Y vs. primitive mantle-normalized Th/Nb (Th/Nb$_{PM}$) plot of the Cretaceous granitic (granites, granodiorites, tonalites, diorites) rocks from Kyushu. Primitive mantle values are from Sun and McDonough (1989). Symbols as in **Figure 2**.

as pressure (bars), relative oxidation state (fO_2), and water (wt.%) content of the system being modeled, in order to constrain the possible conditions and processes (i.e., fractional crystallization or partial melting). The crust of Kyushu is comprised of the Paleozoic–Mesozoic high-*P* metamorphic rocks and Jurassic accretionary rocks, and its thickness is estimated to be ∼26 km (Arai et al., 2009). However, it is likely that the crust was thinner during the Cretaceous as it would not include the additional material added since the Cenozoic. Consequently, the initial pressure used for the modeling is 0.5 GPa (i.e., 5 kbar, ∼20 km thickness) which is based on the likely depth of melting for the rocks. The relative oxidation state of the parental rock assemblage is not constrained and therefore we ran models using oxidation conditions that range from relatively reducing to relatively oxidizing (i.e., FMQ − 1, FMQ + 1, and FMQ + 3) with water contents of 0.5 wt%.

The results are shown in **Figure 12** at 10°C intervals, with models represented by different colored dots (i.e., white dots = FMQ − 1; black dots = FMQ + 1; gray dots = FMQ + 3). The thermal window of the models for this study extends from 1300 to 700°C and represents ∼60 to ∼0.3% melting of the source. The results indicate that the source composition, under the melting conditions outlined in **Table 1**, can reasonably produce the compositions of the Shiraishino granodiorite, the

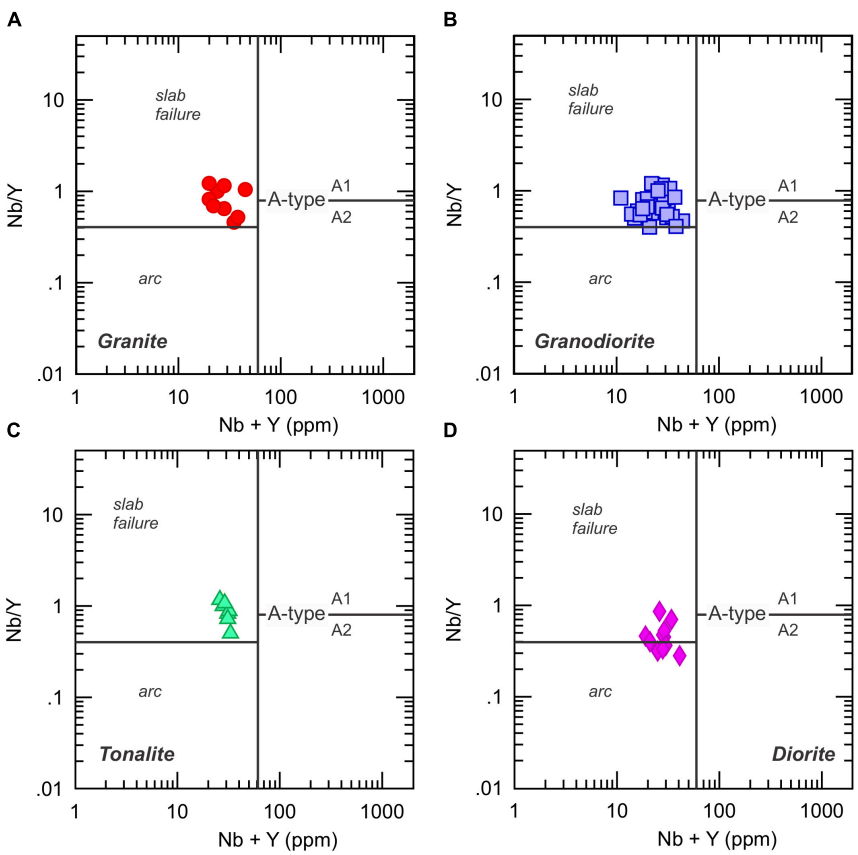

FIGURE 11 | Nb + Y (ppm) vs. Nb/Y discrimination plots used to separate arc, slab failure, and A-type (A1, A2) compositions of the Cretaceous **(A)** granites, **(B)** granodiorites, **(C)** tonalites, and **(D)** diorites from Kyushu (Whalen and Hildebrand, 2019). Symbols as in **Figure 2**.

TABLE 1 | Starting compositions used for equilibrium partial melting models and compositions for Albian granitic rocks from Kyushu.

	Starting composition				Albian granitic rocks from Kyushu					
Name	**Nishisonogi**				**Tsutsugatake**	**Shiraishino**	**Manzaka**	**Kunisaki**	**Kita-Taku**	**Kanmon**
Sample	**NK25**	**Model 1**	**Model 2**	**Model 3**	**05031803**	**Average (*n* = 12)**	**Average (*n* = 7)**	**98970505**	**93100506**	**CH905**
Lithology	**Chlorite-actinolite schist**				**Granite**	**Granodiorite**	**Tonalite**	**High-Mg diorite**	**High-Mg diorite**	**Andesite**
SiO_2 (wt.%)	51.98	54.25	54.25	54.25	74.69	66.21	56.53	55.14	52.93	57.62
TiO_2	0.33	0.34	0.34	0.34	0.17	0.54	0.96	0.71	0.63	0.65
Al_2O_3	5.33	5.56	5.56	5.56	14.02	15.81	17.62	12.97	6.67	17.17
Fe_2O_3t	8.83	9.22	9.22	9.22	1.26	3.61	6.58	7.75	9.84	6.80
MnO	0.16	0.17	0.17	0.17	0.04	0.08	0.13	0.16	0.22	0.05
MgO	19.00	19.83	19.83	19.83	0.30	1.64	3.95	9.65	13.23	3.07
CaO	8.58	8.95	8.95	8.95	1.18	3.88	7.41	10.81	13.43	5.02
Na_2O	0.93	0.97	0.97	0.97	3.43	3.88	3.46	2.21	1.09	5.26
K_2O	0.09	0.09	0.09	0.09	3.79	2.23	1.44	0.71	0.36	2.95
P_2O_5	0.11	0.11	0.11	0.11	0.03	0.16	0.14	0.07	0.11	0.13
H_2O		0.5	0.5	0.5						
Pressure		0.5 GPa	0.5 GPa	0.5 GPa						
fO_2		FMQ −1	FMQ + 1	FMQ + 3						

Data of the starting compositions from Mori et al. (2014), and the compositions of Tsutsugatake granite from Kamei et al. (2009), Shiraishino granodiorite from Kamei (2004), Manzaka tonalite from Kamei (2002), Kunisaki and Kita-Taku diorites from Kamei et al. (2004), and Kanmon andesite from Imaoka et al. (1993). FMQ, fayalite-magnetite-quartz buffer.

Manzaka tonalite, the Kunisaki and Kita-Taku high-Mg diorites, and the Kanmon andesites for the exception of K_2O. Moreover, the modeling results could not replicate the highly silicic Tsutsugatake granites suggesting an additional process (e.g., fractional crystallization, assimilation-fractional crystallization) or possibly source is required to generate highly evolved rocks.

The thermodynamic modeling demonstrates that equilibrium partial melting of chlorite-actinolite schists can produce the Early Cretaceous granitic rocks, except for the highly silicic Tsutsugatake granites (**Figure 12**). The compositions of the Manzaka tonalite (∼20 to ∼25% melting), the Kunisaki high-Mg diorite (∼30 to ∼37% melting), and the Kanmon andesite (∼20 to ∼25% melting) rocks are best replicated with a relatively reducing oxidation state (i.e., FMQ − 1), whereas the rocks from Shiraishino granodiorite (FMQ + 1 = ∼18% melting; FMQ + 3 = ∼9 to ∼13% melting) favor oxidizing conditions (FMQ + 1 or + 3), which is consistent with their relatively high Eu/Eu* (∼1.1). The Kita-Taku high-Mg diorite probably requires more melting (i.e., 65–70%), but the relative oxidation state does not appear exert a strong influence on the composition.

Although the models show that there is good agreement between the liquid evolution curves and the bulk composition of the granitic rocks, the K_2O content in each model is consistently too low (**Figure 12**). The explanations for the discrepancy between the model curves and the K_2O concentration are either related to the highly mobile nature of K^+ during metamorphism to hydrothermal alteration or to the fact that the Nishisonogi chlorite-actinolite schist is not a perfect analog of the mélange rocks that melted during the Albian (Wood et al., 1976; Kogiso et al., 1997; Zheng et al., 2011).

Tectonomagmatic Evolution of the Early Cretaceous Granitic Rocks

It is thought that slab rollback during the Early Cretaceous, following a shallowing of the subduction angle and subsequent flat-slab subduction during the Late Jurassic, changed the geotectonic setting of SW Japan from subduction-accretion to continental arc (Kiminami and Imaoka, 2013; Kim et al., 2016). As a result of the slab rollback, a slab gap could be created and filled with an upwelling asthenosphere, creating a 'hot corner' within the mantle wedge. The change in subduction geodynamics is expected to be reflected in the secular compositional and temperature variations of the granitic rocks.

The initiation of asthenospheric upwelling and hot corner flow caused by slab rollback likely began during the Berriasian as the tonalites have the most radiogenic Sr and Nd isotopic values [$^{87}Sr/^{86}Sr_i$ = 0.70430 to 0.70450; $\varepsilon_{Nd}(t)$ = + 0.5 to + 3.1; **Figures 9A,B**]. The magmatic source is likely juvenile or at least the rocks were derived from a radiogenic source under the lower continental crust or from subducted oceanic crust. Once slab rollback began, it is possible that the dip of the subducted slab increased and more sediments were transported along the subducted plate interface into the mantle wedge, likely causing a magma source to become more isotopically enriched. This is consistent with the increase of $^{87}Sr/^{86}Sr_i$ ratios and decrease of $\varepsilon_{Nd}(t)$ values of granitic rocks during Beriasian to Albian (**Figures 9A,B**). The maximum temperatures experienced by the granitic rocks (T_{Apt}) also increased over time, indicating that there may be higher heat flow or melting conditions due to the input of upwelling asthenosphere into the mantle wedge and development of hot corner flow (**Figures 9C,D**).

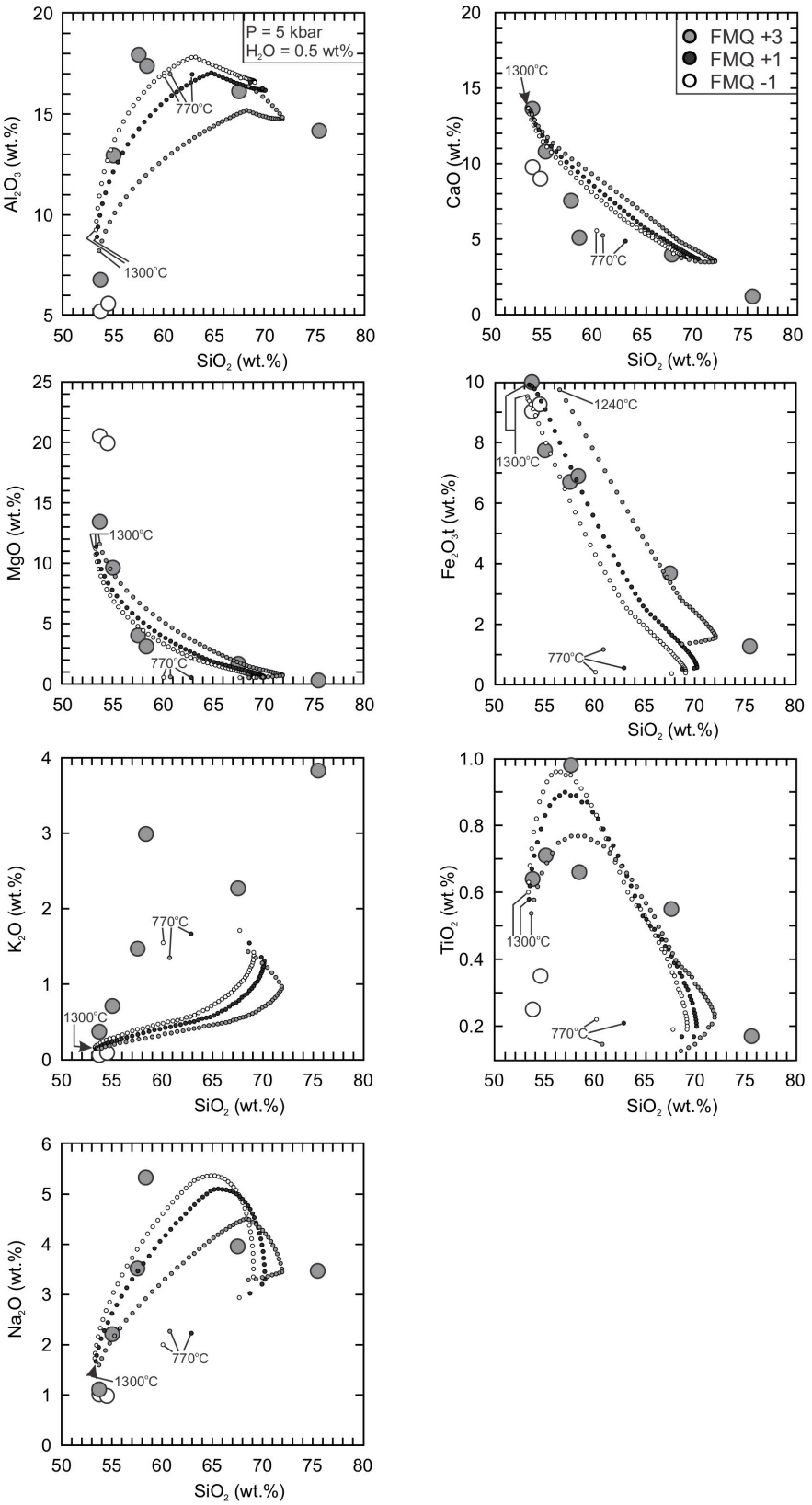

FIGURE 12 | (A–G) Results of equilibrium partial melting showing the liquid evolution paths of the Nishisonogi chlorite-actinolite schist with models represented by different colored dots (i.e., white dots = FMQ −1; black dots = FMQ + 1; gray dots = FMQ + 3). Each dot represents a 10°C interval of melting.

During the Albian and the Valanginian to Coniacian, the granitic rocks have similar $^{87}Sr/^{86}Sr_i$ ratios and $\varepsilon_{Nd}(t)$ values independent of rock type (**Figures 9A,B**) as described above, although some granites at ∼95 Ma have higher $^{87}Sr/^{86}Sr_i$ ratios and lower $\varepsilon_{Nd}(t)$ values, which might be explained by crustal contamination during emplacement or they were derived by partial melting of the crust as discussed above. The peak of maximum temperatures (T_{Apt}) occurred during the Albian, but the rate of temperature changes decreased in this period (**Figures 9C,D**). These lines of evidence suggest the inputs of heat and sediments into the mantle wedge may be close to 'steady state,' probably due to the subducted slab reaching a stable angle. The stable subduction angle was likely the key development that enabled the generation of melts from a relatively uniform source for the granodiorites, tonalites, and possibly the least evolved granitic rocks.

The magmatic source during the Albian could be similar to mélange rocks, such as chlorite-actinolite schists, which are intensely mixed and metasomatised rocks on the subducting plate interface, and contain the chemical components characteristic for the generation of arc magma at subduction zone settings (Marschall and Schumacher, 2012). The mélange rocks may be transported as a diapir or plume into the hot corner of the mantle wedge where the dehydration and partial melting of the mélange rocks could generate a range of fluid and melt compositions (Marschall and Schumacher, 2012). Equilibrium partial melting modeling of chlorite-actinolite schists suggests that it is possible that they could produce magma similar to the Albian rocks at moderate depth and variable redox conditions, indicating that this may be a viable process that produced some of the Kyushu granitic rocks (**Figure 12**).

CONCLUSION

The Early Cretaceous granitic rocks from Kyushu, SW Japan, formed in a volcanic-arc setting. Important geodynamic changes in the heat supply and magmatic sources occurred during the Berriasian to Albian. Upwelling of the asthenosphere and hot corner flow into the mantle wedge caused by slab rollback, following a shallowing of the subduction angle and subsequent flat-slab subduction during the Late Jurassic, likely supplied the heat for partial melting of upper plate mélange rocks or the initiation of diapirs that formed on the subducted plate-mantle interface. This process was likely responsible for dehydration and partial melting of the subducted slab. The partial melting of the mélange rocks such as chlorite-actinolite schists at high to moderate pressure can yield melts that are similar to the bulk compositions observed in the Albian granitic rocks including the adakitic rocks of the Shiraishino granodiorites. Melting of the same source could also explain the relative Sr–Nd isotopic homogeneity of the Albian rocks.

DATA AVAILABILITY STATEMENT

All datasets generated for this study are included in the article/**Supplementary Material**.

AUTHOR CONTRIBUTIONS

KS contributed to conception and design of the study and wrote the manuscript. M-WY contributed to interpretation of data for the work. Both authors contributed to manuscript revision, read and approved the submitted version.

ACKNOWLEDGMENTS

We thank Dr. Kwan-Nang Pan for handling of the manuscript and Profs. D. R. Lentz and J. V. Owen for their constructive comments. KS is grateful to Robert Hsieh for his assistance and Prof. J. G. Shellnutt for his guidance and support.

SUPPLEMENTARY MATERIAL

The Supplementary Material for this article can be found online at: https://www.frontiersin.org/articles/10.3389/feart.2020.00095/full#supplementary-material

REFERENCES

Adachi, T., Osanai, Y., Nakano, N., and Owada, M. (2012). LA-ICP-MS U–Pb zircon and FE-EPMA U–Th–Pb monazite dating of pelitic granulites from the Mt. Ukidake area, Sefuri Mountains, northern Kyushu. *J. Geol. Soc. Jpn.* 118, 39–52. doi: 10.5575/geosoc.2011.0022

Arai, R., Iwasaki, T., Sato, H., Abe, S., and Hirata, N. (2009). Collision and subduction structure of the Izu-Bonin arc, central Japan, revealed by refraction/wide-angle reflection analysis. *Tectonophysics* 475, 438–453. doi: 10.1016/j.tecto.2009.05.023

Arculus, R. J. (2003). Use and abuse of the terms calcalkaline and calcalkalic. *J. Petrol.* 44, 929–935. doi: 10.1093/petrology/44.5.929

Boehnke, P., Watson, E. B., Trail, T., Harrison, T. M., and Schmitt, A. K. (2013). Zircon saturation re-visited. *Chem. Geol.* 351, 324–334. doi: 10.1016/j.chemgeo.2013.05.028

Buddington, A. F., and Lindsley, D. H. (1964). Iron-titanium oxide minerals and synthetic equivalents. *J. Petrol.* 5, 310–357. doi: 10.1093/petrology/5.2.310

Chen, J. F., and Jahn, B. M. (1998). Crustal evolution of southeastern China: Nd and Sr isotopic evidence. *Tectonophysics* 284, 101–133. doi: 10.1016/s0040-1951(97)00186-8

Christiansen, E. H., and Keith, J. D. (1996). "Trace element systematics in silicic magmas: a metallogenic perspective," in *Trace Element Geochemistry of Volcanic Rocks: Applications for Massive Sulphide Exploration*, ed. D. A. Wyman (Canada: Geology Association), 115–151.

Dong, S., Zhang, Y., Li, H., Shi, W., Xue, H., Li, J., et al. (2018). The Yanshan orogeny and late Mesozoic multi-plate convergence in East Asia—Commemorating 90th years of the "Yanshan Orogeny". *Sci. China Earth Sci.* 61, 1–22.

Ernst, W. G., Tsujimori, T., Zhang, R., and Liou, J. G. (2007). Permo–Triassic collision, subduction-zone metamorphism, and tectonic exhumation along the East Asian continental margin. *Ann. Rev. Earth Planet. Sci.* 35, 73–110. doi: 10.1146/annurev.earth.35.031306.140146

Faure, M., Fabbri, O., and Monie, P. (1988). The Miocene bending of southwest Japan: new 39Ar/40Ar and microtectonic constraints from the Nagasaki schist

(western Kyushu), an extension of the Sanbagawa high-pressure belt. *Earth Planet. Sci. Lett.* 91, 13–31.

Forster, H. J., Tischendorf, G., and Trumbull, R. B. (1997). An evaluation of the Rb vs. (Y + Nb) discrimination diagram to infer tectonic setting of silicic igneous rocks. *Lithos* 40, 261–293. doi: 10.1016/s0024-4937(97)00032-7

Frost, B. R., Barnes, C. G., Collins, W. J., Arculus, R. J., Ellis, D. J., and Frost, C. D. (2001). A geochemical classification for granitic rocks. *J. Petrol.* 42, 2033–2048. doi: 10.1093/petrology/42.11.2033

Fujii, M., Hayasaka, Y., and Horie, K. (2008). Metamorphism and timing of the nappe movement in the Asaji metamorphic area, eastern Kyusu. *J. Geol. Soc. Japan* 114, 127–140. doi: 10.5575/geosoc.114.127

Fukuyama, M., Ogasawara, M., Dunkley, D. J., Wang, K. L., Lee, D. C., Hokada, T., et al. (2014). The formation of rodingite in the Nagasaki metamorphic rocks at Nomo Peninsula, Kyushu, Japan – Zircon U–Pb and Hf isotopes and trace element evidence. *Island Arc* 23, 281–298. doi: 10.1111/iar.12086

Gualda, G. A. R., Ghiorso, M. S., Lemons, R. V., and Carley, T. L. (2012). Rhyolite-MELTS: a modified calibration of MELTS optimized for silica-rich, fluid-bearing magmatic systems. *J. Petrol.* 53, 875–890. doi: 10.1093/petrology/egr080

Hamamoto, T., Osanai, Y., and Kagami, H. (1999). Sm–Nd, Rb–Sr and K–Ar geochronology of the Higo metamorphic terrane, west-central Kyushu, Japan. *island Arc* 8, 323–334. doi: 10.1046/j.1440-1738.1999.00240.x

Hao, L. L., Wang, Q., Wyman, D. A., Qu, Q., Dan, W., Jiang, Z. Q., et al. (2016). Andesitic crustal growth via mélange partial melting: evidence from early cretaceous arc dioritic/andesitic rocks in southern Qiangtang, central Tibet. *Geochem. Geophys. Geosyst.* 17, 1641–1659. doi: 10.1002/2016gc006248

Harrison, T. M., and Watson, E. B. (1984). The behavior of apatite during crustal anatexis: equilibrium and kinetic considerations. *Geochim. Cosmochim. Acta.* 48, 1467–1477. doi: 10.1016/0016-7037(84)90403-4

Hattori, H., and Shibata, K. (1982). Radiometric dating of Pre-Neogene granitic and metamorphic rocks in northwest Kyushu, Japan – with emphasis on geotectonics of the Nishisonogi zone. *Bull. Geol. Surv. Japan* 33, 57–84.

Hou, M. L., Jiang, Y. H., Jiang, S. Y., Ling, H. F., and Zhao, K. D. (2007). Contrasting origins of late Mesozoic adakitic granitoids from the northwestern Jiaodong Peninsula, east China: implications for crustal thickening to delamination. *Geol. Mag.* 144, 619–631. doi: 10.1017/s0016756807003494

Imaoka, T., Nakajima, T., and Itaya, T. (1993). K – Ar ages of hornblendes in andesite and dacite from the Cretaceous Kanmon Group, southwest Japan. *J. Min. Petrol. Econ. Geol.* 88, 265–271. doi: 10.2465/ganko.88.265

Imaoka, T., Nakashima, K., Kamei, A., Itaya, T., Ohira, T., Nagashima, M., et al. (2014). Episodic magmatism at 105 Ma in the Kinki district, SW Japan: petrogenesis of Nb-rich lamprophyres and adakites, and geodynamic implications. *Lithos* 184–187, 105–131. doi: 10.1016/j.lithos.2013.10.014

Ishiwatari, A., and Tsujimori, T. (2003). Paleozoic ophiolites and blueschists in Japan and Russian Primorye in the tectonic framework of East Asia: a synthesis. *Island Arc* 12, 190–206. doi: 10.1046/j.1440-1738.2003.00390.x

Isozaki, Y., Aoki, K., Nakama, T., and Yanai, S. (2010). New insight into a subduction-related orogen: a reappraisal of the geotectonic framework and evolution of the Japanese Islands. *Gondwana Res.* 18, 82–105. doi: 10.1016/j.gr.2010.02.015

Kamei, A. (2002). Petrogenesisof cretaceous peraluminous granite suites with low initial Sr isotopic ratios, Kyushu Island, southwest Japan arc. *Gondwana Res.* 5, 813–822. doi: 10.1016/s1342-937x(05)70915-1

Kamei, A. (2004). An adakitic pluton on Kyushu Island, southwest Japan arc. *J. Asian Earth Sci.* 24, 43–58. doi: 10.1016/j.jseaes.2003.07.001

Kamei, A., Miyake, Y., Owada, M., and Kimura, J. (2009). A pseudo adakite derived from partial melting of tonalitic to granodioritic crust, Kyushu, southwest Japan arc. *Lithos* 112, 615–625. doi: 10.1016/j.lithos.2009.05.024

Kamei, A., Owada, M., Hamamoto, T., Osanai, Y., Yuhara, M., and Kagami, H. (2000). Isotopic equilibration ages for the Miyanohara tonalite from the Higo metamorphic belt in central Kyushu, Southwest Japan: implications for the tectonic setting during the Triassic. *Island Arc* 9, 97–112. doi: 10.1046/j.1440-1738.2000.00264.x

Kamei, A., Owada, M., Nagao, T., and Shiraki, K. (2004). High-Mg diorites derived from sanukitic HMA magmas, Kyushu Island, southwest Japan arc: evidence from clinopyroxene and whole rock compositions. *Lithos* 75, 359–371. doi: 10.1016/j.lithos.2004.03.006

Kamei, A., Owada, M., Osanai, Y., Hamamoto, T., and Kagami, H. (1997). Solidification and cooling ages for the Higo plutonic rocks in the Higo metamorphic terrane, central Kyushu. *J. Min. Petrol. Econ. Geol.* 92, 316–326. doi: 10.2465/ganko.92.316

Kim, S. W., Kwon, S., Park, S. I., Lee, C., Cho, D. L., Lee, H. J., et al. (2016). SHRIMP U–Pb dating and geochemistry of the Cretaceous plutonic rocks in the Korean Peninsula: a new tectonic model of the Cretaceous Korean Peninsula. *Lithos* 262, 88–106. doi: 10.1016/j.lithos.2016.06.027

Kiminami, K., and Imaoka, T. (2013). Spatiotemporal variations of Jurassic–Cretaceous magmatism in eastern Asia (Tan-Lu Fault to SW Japan): evidence for flat-slab subduction and slab rollback. *Terra Nova* 25, 414–422. doi: 10.1111/ter.12051

Kogiso, T., Tatsumi, Y., and Nakano, S. (1997). Trace element transport during dehydration processes in the subducted oceanic crust: 1. Experiments and implications for the origin of ocean island basalts. *Earth Planet. Sci. Lett.* 148, 193–205. doi: 10.1016/s0012-821x(97)00018-6

Kouchi, Y., Orihashi, Y., Obara, H., Miyata, K., Shimojo, M., Otoh, S., et al. (2011). Discovery of Shimanto high-P/T metamorphic rocks from the western margin of Kyushu, Japan. *J. Geogr.* 120, 30–39. doi: 10.5026/jgeography.120.30

Lan, T. G., Fan, H. R., Santosh, M., Hu, F. F., Yang, K. F., Yang, Y. H., et al. (2011). Geochemistry and Sr–Nd–Pb–Hf isotopes of the Mesozoic Dadian alkaline intrusive complex in the Sulu orogenic belt, eastern China: implications for crust–mantle interaction. *Chem. Geol.* 285, 97–114. doi: 10.1016/j.chemgeo.2011.03.013

Li, Z. X., and Li, X. H. (2007). Formation of the 1300-km wide intracontinental orogen and postorogenic magmatic province in Mesozoic South China: a flat-slab subduction model. *Geology* 35, 179–182.

Marschall, H. R., and Schumacher, J. C. (2012). Arc magmas sourced from mélange diapirs in subduction zones. *Nat. Geosci.* 5, 862–867. doi: 10.1038/ngeo1634

Maruyama, S., Isozaki, Y., Kimura, G., and Terabayashi, M. (1997). Paleogeographic maps of the Japanese Islands: plate tectonic synthesis from 750 Ma to the present. *Island Arc* 6, 121–142. doi: 10.1111/j.1440-1738.1997.tb00043.x

Matsuura, H. (1998). K–Ar ages of the Early Cretaceous Shimonoseki Subgroup and Kawara granodiorites, southwest Japan. *J. Min. Petrol. Econ. Geol.* 93, 307–312. doi: 10.2465/ganko.93.307

Miller, C. F., McDowell, S. M., and Mapes, R. W. (2003). Hot and cold granites? Implications of zircon saturation temperatures and preservation of inheritance. *Geology* 31, 529–532.

Miyazaki, K., Ikeda, T., Matsuura, H., Danhara, T., Iwano, H., and Hirata, T. (2018). Ascent of migmatites of a high-temperature metamorphic complex due to buoyancy beneath a volcanic arc: a mid-Cretaceous example from the eastern margin of Eurasia. *Int. Geol. Rev.* 61, 649–674. doi: 10.1080/00206814.2018.1443403

Miyazaki, K., Ozaki, M., Saito, M., and Toshimitsu, S. (2016). "The kyushu–ryukyu arc," in *The Geology of Japan*, eds, T. Moreno, S. Wallis, T. Kojima, and W. Gibbons (London: Geological Society of London), 139–174. doi: 10.1144/goj.6

Miyazaki, K., Suga, K., Mori, Y., Iwano, H., Yagi, K., Shigeno, M., et al. (2019). Kinetics and duration of metamorphic mineral growth in a subduction complex: zircon and phengite in the Nagasaki metamorphic complex, western Kyushu, Japan. *Contrib. Min. Petrol.* 174, 1–19.

Miyoshi, M., Yuguchi, T., Shinmura, T., Mori, Y., Arakawa, Y., and Toyohara, F. (2011). Petrological characteristics and K–Ar age of borehole core samples of basement rocks from the northwestern caldera floor of Aso, central Kyushu. *J. Geol. Soc. Japan* 117, 585–590. doi: 10.5575/geosoc.117.585

Mori, Y., Nishiyama, T., and Yanagi, T. (2007). Chemical mass balance in a reaction zone between serpentinite and metapelites in the Nishisonogi metamorphic rocks, Kyushu, Japan: implications for devolatilization. *Island Arc* 16, 28–39. doi: 10.1111/j.1440-1738.2007.00556.x

Mori, Y., Orihashi, Y., Miyamoto, T., Shimada, K., Shigeno, M., and Nishiyama, T. (2011). Origin of zircon in jadeitite from the Nishisonogi metamorphic rocks, Kyushu, Japan. *J. Metamorph. Geol.* 29, 673–684. doi: 10.1111/j.1525-1314.2011.00935.x

Mori, Y., Shigeno, M., and Nishiyama, T. (2014). Fluid-metapelite interaction in an ultramafic mélange: implications for mass transfer along the slab-mantle interface in subduction zones. *Earth Planets Space* 66, 1–8.

Nakajima, T., Nagakawa, K., Obata, M., and Uchiumi, S. (1995). Rb–Sr and K–Ar ages of the Higo metamorphic rocks and related granitic rocks, southwest Japan. *J. Geol. Soc. Jpn.* 101, 615–620. doi: 10.5575/geosoc.101.615

Nguyen, T. T. B., Satir, M., Siebel, W., and Chen, F. (2004). Granitoids in the Dalat zone, southern Vietnam: age constraints on magmatism and regional geological implications. *Int. J. Earth Sci.* 93, 329–340.

Nishimura, Y. (1998). Geotectonic subdivision and areal extent of the Sangun belt, inner zone of southwest Japan. *J. Metamorphic Geol.* 16, 129–140. doi: 10.1111/j.1525-1314.1998.00059.x

Nishimura, Y., Hirota, Y., Shiosaki, D., Nakahara, N., and Itaya, T. (2004). The Nagasaki metamorphic rocks and their geotectonics in Mogi area, Nagasaki Prefecture, southwest Japan –Juxtaposition of the Suo belt with the Sanbagawa belt–. *J. Geol. Soc. Jpn.* 110, 372–383. doi: 10.5575/geosoc.110.372

Nishiyama, T. (1978). Jadeitite from the Nishisonogi metamorphic region. *J. Geol. Soc. Jpn.* 84, 155–156.

Nishiyama, T. (1989). Petrological study of the Nagasaki metamorphic rocks in the Nishisonogi Peninsula –with special reference to the greenrock complex and the reaction-enhanced ductility–. *Mem. Geol. Soc. Jpn.* 33, 237–257.

Nishiyama, T. (1990). CO2-metasomatism of a metabasite block in a serpentine melange from the Nishisonogi metamorphic rocks, southwest Japan. *Contrib. Min. Petrol.* 104, 35–46. doi: 10.1007/bf00310644

Oh, C. W., and Kusky, T. (2007). The late permian to triassic hongseong–odesan collision belt in south Korea, and its tectonic correlation with China and Japan. *Int. Geol. Rev.* 49, 636–657. doi: 10.2747/0020-6814.49.7.636

Omori, S., and Isozaki, Y. (2011). Paleozoic Japan and the eastern extension of the collisional suture between the North and South China Cratons. *J. Geography* 120, 40–51. doi: 10.5026/jgeography.120.40

Osanai, Y., Hamamoto, T., Kagami, H., Suzuki, K., Owada, M., and Kamei, A. (1999). The Higo high-grade metamorphic rocks in Japan as a part of the collisional terrane between the Sino-Korean and Yangtze Cratons. *Gondwana Res.* 2, 599–601. doi: 10.1016/s1342-937x(05)70211-2

Osanai, Y., Masao, S., and Kagami, H. (1993). Rb – Sr whole rock isochron ages of granitic rocks from the central Kyushu, Japan. *Mem. Geol. Soc. Jpn.* 42, 135–150.

Osanai, Y., Owada, M., Kamei, A., Hamamoto, T., Kagami, H., Toyoshima, T., et al. (2006). The Higo metamorphic complex in Kyushu, Japan as the fragment of Permo–Triassic metamorphic complexes in East Asia. *Gondwana Res.* 9, 152–166. doi: 10.1016/j.gr.2005.06.008

Osborn, E. F. (1959). Role of oxygen partial pressure in the crystallization and differentiation of basaltic magma. *Am. J. Sci.* 257, 609–647. doi: 10.2475/ajs.257.9.609

Oshima, T. (1961). The Kitataku gabbro-complex, Taku City, Saga prefecture. *Fac. J. Saga Univ.* 10, 87–100.

Owada, M., Kamei, A., Yamamoto, K., Osanai, Y., and Kagami, H. (1999). Spatial-temporal variations and origin of granitic rocks from central to northern part of Kyushu. *Mem. Geol. Soc. Jpn.* 53, 349–363.

Pearce, J. A., Harris, N. B., and Tindle, A. G. (1984). Trace element discrimination diagrams for the tectonic interpretation of granitic rocks. *J. Petrol.* 25, 956–983. doi: 10.1093/petrology/25.4.956

Plank, T., Kelley, K. A., Zimmer, M. M., Hauri, E. H., and Wallace, P. J. (2013). Why do mafic arc magmas contain ˜4 wt% on average? *Earth Planet. Sci. Lett.* 364, 168–179. doi: 10.1016/j.epsl.2012.11.044

Sakashima, T., Terada, K., Takeshita, T., and Sano, Y. (2003). Large-scale displacement along the Median Tectonic Line, Japan: evidence from SHRIMP zircon U–Pb dating of granites and gneisses from the South Kitakami and paleo-Ryoke belts. *J. Asian Earth Sci.* 21, 1019–1039. doi: 10.1016/s1367-9120(02)00108-6

Sasada, M. (1987). Pre-Tertiary basement rocks of Hohi area, central Kyushu, Japan. *Bull. Geol. Surv. Jpn.* 38, 385–422.

Shellnutt, J. G., Lan, C.-Y., Long, T. V., Usuki, T., Yang, H.-J., Mertzman, S. A., et al. (2013). Formation of Cretaceous Cordilleran and post-orogenic granites and their microgranular enclaves from the Dalat zone, southern Vietnam: tectonic implications for the evolution of southeast Asia. *Lithos* 182-183, 229–241. doi: 10.1016/j.lithos.2013.09.016

Shigeno, M., Mori, Y., and Nishiyama, T. (2005). Reaction microtextures in jadeitites from the Nishisonogi metamorphic rocks, Kyushu, Japan. *J. Min. Petrol. Sci.* 100, 237–246. doi: 10.2465/jmps.100.237

Shigeno, M., Mori, Y., Shimada, K., and Nishiyama, T. (2012a). Jadeitites with metasomatic zoning from the Nishisonogi metamorphic rocks, western Japan: fluid–tectonic block interaction during exhumation. *Eur. J. Min.* 24, 289–311. doi: 10.1127/0935-1221/2012/0024-2195

Shigeno, M., Mori, Y., Shimada, K., and Nishiyama, T. (2012b). Origin of omphacitites from the Nishisonogi metamorphic rocks, western Kyushu, Japan: comparison with jadeitites. *Eur. J. Min.* 24, 247–262. doi: 10.1127/0935-1221/2012/0024-2198

Suga, K., Yui, T. F., Miyazaki, K., Sakata, S., Hirata, T., and Fukuyama, M. (2017). A revisit to the Higo terrane, Kyushu, Japan: the eastern extension of the North China–South China collision zone. *J. Asian Earth Sci.* 143, 218–235. doi: 10.1016/j.jseaes.2017.04.006

Sun, S. S., and McDonough, W. F. (1989). "Chemical and isotopic systematics of oceanic basalts: implications for mantle composition and processes," in *Magmatism in the Ocean Basins*, eds A. D. Saunders, and M. J. Norry (London: Geol. Soc. London Spec. Publ.), 313–435.

Takagi, H., Ishii, T., Tobe, E., Soda, Y., Suzuki, K., Iwano, H., et al. (2007). Petrology and radiogenic age of accidental clasts of granitic mylonite from the Aso-4 pyroclastic flow deposit and their correlation to the Nioki Granite. *J. Geol. Soc. Jpn.* 113, 1–14. doi: 10.5575/geosoc.113.1

Takagi, H., Soda, Y., and Yoshimura, J. (2000). K – Ar ages of the granitic clasts from the Onogawa Group, eastern Kyushu. *Mem. Geol. Soc. Jpn.* 56, 213–220.

Tiepolo, M., Langone, A., Morishita, T., and Yuhara, M. (2012). On the recycling of amphibole-rich ultramafic intrusive rocks in the arc crust: evidence from Shikanoshima Island (Kyushu, Japan). *J. Petrol.* 53, 1255–1285. doi: 10.1093/petrology/egs016

Whalen, J. B., and Hildebrand, R. S. (2019). Trace element discrimination of arc, slab failure, and A-type granitic rocks. *Lithos* 348–349:105179. doi: 10.1016/j.lithos.2019.105179

Wood, D. A., Gibson, I. L., and Thompson, R. N. (1976). Element mobility during zeolite facies metamorphism of the Tertiary basalts of eastern Iceland. *Contrib. Mineral. Petrol.* 55, 241–254. doi: 10.1007/bf00371335

Wu, G. (2005). The Yanshanian Orogeny and two kinds of Yanshanides in eastern-central China. *Acta Geol. Sin.* 79, 507–518. doi: 10.1111/j.1755-6724.2005.tb00917.x

Xu, J. F., Shinjo, R., Defant, M. J., Wang, Q., and Rapp, R. P. (2002). Origin of Mesozoic adakitic intrusive rocks in the Ningzhen area of east China: partial melting of delaminated lower continental crust? *Geology* 30, 1111–1114.

Yui, T. F., Maki, K., Wang, K. L., Lan, C. Y., Usuki, T., Iizuka, Y., et al. (2012). Hf isotope and REE compositions of zircon from jadeitite (Tone, Japan and north of the Motagua fault, Guatemala): implications on jadeitite genesis and possible protoliths. *Eur. J. Min.* 24, 263–275. doi: 10.1127/0935-1221/2011/0023-2127

Zheng, Y.-F., Xia, Q.-X., Chen, R.-X., and Gao, X.-Y. (2011). Partial melting, fluid supercriticality and element mobility in ultrahigh-pressure metamorphic rocks during continental collision. *Earth Sci. Rev.* 107, 342–374. doi: 10.1016/j.earscirev.2011.04.004

Zhou, X., Sun, T., Shen, W., Shu, L., and Niu, Y. (2006). Petrogenesis of Mesozoic granitoids and volcanic rocks in South China: a response to tectonic evolution. *Episodes* 29, 26–33. doi: 10.18814/epiiugs/2006/v29i1/004

Zhou, X. M., and Li, W. X. (2000). Origin of Late Mesozoic igneous rocks of south-eastern China: implications for lithosphere subduction and underplating of mafic magma. *Tectonophysics* 326, 269–287. doi: 10.1016/s0040-1951(00)00120-7

Conflict of Interest: The authors declare that the research was conducted in the absence of any commercial or financial relationships that could be construed as a potential conflict of interest.

frontiers in Earth Science

ORIGINAL RESEARCH
published: 30 June 2020
doi: 10.3389/feart.2020.00212

Petrogenesis of the Kanker Granites From the Bastar Craton: Implications for Crustal Growth and Evolution During the Archean-Proterozoic Transition

Ajay Dev Asokan[1], *R. Elangovan*[1], *Neeraj Vishwakarma*[2], *K. R. Hari*[3] *and M. Ram Mohan*[1]*

[1] CSIR-National Geophysical Research Institute, Hyderabad, India, [2] Department of Applied Geology, National Institute of Technology, Raipur, India, [3] Department of Geology and Water Resources Management, Pt. Ravishankar Shukla University, Raipur, India

Archean-Proterozoic boundary represents a significant transitional phase in the Earth's history. Bastar Craton is one of the major Archean cratons in the Indian subcontinent with voluminous granites, supracrustal rocks, and tectonic belts. Malanjkhand, Dongargarh, and Kanker are the three major granitic plutons emplaced during the Archean-Proterozoic transition in the Bastar Craton, and this study is confined to the granites of Kanker pluton. Based on geochemical systematics, the Kanker granites are classified into sanukitoids, biotite and two-mica granites, and hybrid granites. The compositional diversity of the Kanker granites is attributed to two end-member sources, i.e., the enriched mantle and an older felsic crust, and the interactions between them. The sanukitoids were derived from an enriched mantle source that was metasomatized by the subducted sediments. Heat supplied by the sanukitoid magmas induced the crustal melting to form the biotite and two-mica granites. The interaction between these two mutually end-member sources, i.e., the enriched mantle and an older felsic crust, resulted in the formation of hybrid granites. The evolution of the Kanker granites can be accounted for a transitional geodynamic environment, involving subduction, and collisional tectonics during the Archean-Proterozoic transition.

Keywords: sanukitoids, biotite and two-mica granites, Archean-Proterozoic transition, subduction and collisional tectonics, Bastar Craton

OPEN ACCESS

Edited by:
Steven W. Denyszyn, University of Western Australia, Australia

Reviewed by:
Marcos Garcia-Arias, University of Los Andes, Colombia
Xiaoping Xia, Chinese Academy of Sciences, China

***Correspondence:**
M. Ram Mohan
rammohan@ngri.res.in

Specialty section:
This article was submitted to Petrology, a section of the journal Frontiers in Earth Science

Received: *11 March 2020*
Accepted: *20 May 2020*
Published: *30 June 2020*

Citation:
Asokan AD, Elangovan R, Vishwakarma N, Hari KR and Ram Mohan M (2020) Petrogenesis of the Kanker Granites From the Bastar Craton: Implications for Crustal Growth and Evolution During the Archean-Proterozoic Transition. Front. Earth Sci. 8:212. doi: 10.3389/feart.2020.00212

INTRODUCTION

The Archean-Proterozoic boundary witnessed critical changes in the Earth's history, such as the increase in the crustal thickness, decrease in the rate of continental crustal growth, oxygenation of the atmosphere, widespread occurrences of plate tectonic indicators and the formation of supercontinental assemblages (Durrheim and Mooney, 1991; Condie and Kröner, 2008; Keller and Schoene, 2012; Cawood et al., 2013; Lee et al., 2016). Most of these changes are linked to the secular cooling of the Earth's mantle that has utmost implications on the geological processes and is related to the onset of present-day plate tectonics (Sizova et al., 2010; Keller and Schoene, 2012). Granitic magmatism has been recorded as early as Hadean, in the Acasta Gneissic Complex (Reimink et al., 2016) and continued into the Miocene (Hopkinson et al., 2017).

Granitic rocks, unique to the planet Earth, provide vital clues on the formation and evolution of the continental crust (Cawood et al., 2013). Formation of granitic rocks can occur by two different mechanisms, i.e., melting and differentiation of basaltic rock and/or by the melting of the pre-existing crustal rocks (Moyen et al., 2017). The transition from a stagnant lid tectonic regime to present-day plate tectonics is believed to have initiated by 3.0 Ga and became prominent by the end of the Archean (Dhuime et al., 2012; Keller and Schoene, 2012). The global transition in the nature and style of plate tectonic processes is well-reflected and resulted in the compositional diversification of the Neoarchean granitoids (Moyen et al., 2003; Laurent et al., 2014). Based on the source and petrogenetic mechanism, the Neoarchean granitoids have been classified into Tonalite Trondhjemite Granodiorites (TTGs), sanukitoids s.l., biotite and two-mica granites and hybrid granites (Laurent et al., 2014). The TTGs are sourced from the partial melting of metabasalts, sanukitoids are derived from an enriched mantle, and the biotite and two-mica granites are purely crustal-derived. The hybrid granites are formed by variable interaction between the three above-mentioned granitic melts (Laurent et al., 2014).

There has been widespread granitic magmatism in the Indian shield, as seen in the Aravalli, Bundelkhand, Dharwar, and Bastar cratons during the Archean-Proterozoic boundary (Jayananda et al., 2020). The Bastar Craton (**Figure 1**), with abundant Archean-Proterozoic supracrustals and granitoids, hold critical clues reflecting the significant changes that occurred during this period (Khanna et al., 2019; Mondal et al., 2019; Santosh et al., 2020). Malanjkhand, Dongargarh, and Kanker are the three major granitic plutons emplaced during the Archean-Proterozoic transition in the Bastar Craton. Based on the whole rock geochemistry, this study intends to characterize the granites of Kanker pluton and to provide new insights on the petrogenetic evolution of these granites. The results have implications on the crustal growth during the Archean-Proterozoic transition, vis-à-vis, the evolutionary history of the Bastar Craton.

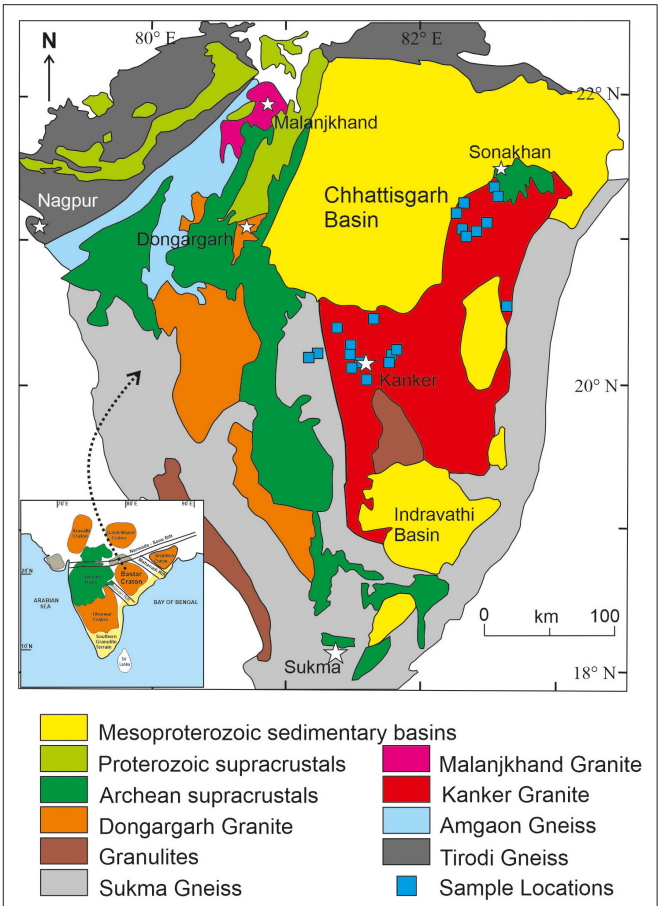

FIGURE 1 | Generalized geological map of the Bastar Craton, with the sample locations (modified after Mohanty, 2015). Inset map of Peninsular India, to show the major cratonic blocks.

GEOLOGY OF THE BASTAR CRATON

The Indian Shield is an amalgamation of cratonic blocks, namely Dharwar, Singhbhum, Bastar, Aravalli, and Bundelkhand cratons separated by Proterozoic mobile belts. The Bastar Craton of central India is bound by the Mahanadi Rift and the Eastern Ghats in the east, the Central Indian Tectonic Zone (CITZ) toward the west, and the Godavari rift in the southeast (**Figure 1**). The Eastern Ghats Mobile Belt forms the southeast boundary of this craton. The craton records evidence for crustal growth as early as Paleoarchean (Sarkar et al., 1993; Ghosh, 2004; Rajesh et al., 2009). The Sukma gneissic complex is considered as the basement of the Bastar Craton (Ramakrishnan, 1990). The basement gneisses are best exposed along the southern part of this craton. Tonalites forming the Sukma gneissic complex yielded a U-Pb zircon age of 3561 ± 11 Ma (Ghosh, 2004). The potassic granites associated with these TTGs were also emplaced during the Paleoarchean (Rajesh et al., 2009). The Sukma Group overlies the Paleoarchean basement gneisses and constitutes mafic-ultramafics, BIFs, para-amphibolites, and quartzites (Mohanty, 2015). The CITZ divides the Sukma gneissic complex into the southern Amgaon gneiss and the northern Tirodi gneiss. The ages of Amgaon gneiss ranges from 2378 to 3396 Ma (Sm-Nd ages, Ahmad et al., 2009). The Tirodi biotite gneisses yielded an emplacement age of 1618 ± 8 Ma (U-Pb zircon age, Bhowmik et al., 2011).

The Bengpal Group overlies the older Sukma Group with a basal unconformity. The major rock types of the Bengpal Group are quartzites, amphibolites, BIFs, and interlayered metabasalts with quartzites (Mohanty, 2015). Neoarchean boninite-like rocks and siliceous high magnesium basalts (SHMBs) were reported from the Bengpal Group (Srivastava et al., 2004) and the Neoarchean Sonakhan Greenstone Belt (SGB) (Manu Prasanth et al., 2018). The younger supracrustals of the craton comprise metavolcanics, metasedimentary sequences and BIFs that occur as enclaves, as well as linear belts. The Dongargarh, Sakoli and Sausar are the prominent supracrustal belts in this craton (Meert et al., 2010). The Dongargarh Supergroup, constituting the supracrustals and granites, is further divided into Nandgaon

and Khairagarh groups being separated by the Dongargarh granite (Deshpande et al., 1990). The Nandgaon Group consists of Bijli rhyolite and Pitapani basalts and andesites, whereas the Khairagarh Group consists of basalts interlayered with sandstone and arenites (Khanna et al., 2019). The volcanic rocks of the Dongargarh Supergroup, referred to as the Kotri-Dongargarh Mobile Belt (KDMB), are interpreted to have erupted by ∼2.5 Ga (Asthana et al., 2016; Manikyamba et al., 2016; Khanna et al., 2019), and are considered to have evolved in an arc setting (Asthana et al., 2018).

The Neoarchean orogenic events in the craton are marked by the formation of migmatites from the basement granitoids (Roy et al., 2006). The Neoarchean-early Paleoproterozoic granitic magmatism is reported in the form of three major plutons, namely, Dongargarh, Kanker, and Malanjkhand granites. The I-type Malanjkhand granite hosts a world-class copper-molybdenum deposit and was emplaced around 2478 Ma (Panigrahi et al., 2004). There is no consensus on the tectonic setting of the Malanjkhand granite and the origin of mineralization (Stein et al., 2004; Pandit and Panigrahi, 2012; Asthana et al., 2016). The Dongargarh granite is a composite pluton, with both I- and A-type affinity (Narayana et al., 2000) and is considered to have evolved in a continental rift setting (Pandit and Panigrahi, 2012; Manikyamba et al., 2016). Dongargarh granite has yielded a U-Pb zircon age of 2485 ± 6.5 Ma and is considered to be coeval with the 2.48 Ga Kanker granites (Sarkar et al., 1993; Bickford et al., 2014). In a recent study (Santosh et al., 2020), the Bastar Craton is divided into Western Bastar, and Eastern Bastar cratons, sutured by the N-S directed collisional Central Bastar Orogen. Several dyke swarms of the craton exhibit NW–SE trend, which is parallel to the Godavari Rift (Meert et al., 2010). French et al. (2008) has reported the U-Pb baddeleyite age of 1891.1 ± 0.9 Ma and U-Pb zircon age of 1883 ± 1.4 Ma for dolerite dykes from the southern part of this craton. Meso-Neoproterozoic Chhattisgarh, Khariar, and Indravathi basins overlie on the Kanker granite (Bickford et al., 2014).

FIELD RELATIONSHIPS AND PETROGRAPHY

We present the field, petrographic, and whole-rock geochemical studies for the unclassified granites representing the Kanker granitic pluton from the central part of the Bastar Craton. The Kanker granite is a composite granitic pluton with at least three phases of granites. Porphyritic feldspar megacrystic granites are the most common variety, varying from pink to gray in color (**Figures 2A,B**). Apart from the porphyritic granitoids, leucogranites and anatectic granites are also present (**Figures 2C,D**). Microgranular enclaves (MEs), and mafic synplutonic dykes were observed at several places (**Figure 2E**). The granite variants mostly display sharp contacts (**Figure 2F**). Elangovan et al. (2017, 2020), have found that the mafic and felsic magmatism were coeval. These granites are variably deformed at places and form granitic gneisses. Pegmatites, aplite, and epidote veins are found intruding into these granites. The pegmatite veins contain large alkali feldspar crystals (2–6 cm in length) with perfect twins and perthite exsolution along with tourmaline, titanite, and allanite. In general, these granites are oriented along NW-SE direction.

Based on the mineral assemblages, the Kanker granites can be divided into two, namely, biotite, and two-mica granite and hornblende biotite granite. The biotite and two-mica granites display inequigranular texture with twinned alkali feldspars showing the perthitic exsolution. The essential minerals that constitute biotite and two-mica granites are alkali feldspar, plagioclase, and quartz, with biotite and muscovite forming the accessory phases (**Figures 3A,B**). The alkali feldspars contain inclusions of plagioclase, quartz, and biotite. Perthite unmixing is common from both microcline and orthoclase. Mafic minerals such as hornblende, titanite, and opaques are nearly absent in these granites. Sericitization of plagioclase and chloritization of biotite are common (**Figure 3C**).

The Hornblende biotite granites exhibit hypidiomorphic texture with plagioclase, alkali feldspar, and quartz as the essential minerals. Titanite, epidote, opaques, apatite, zircon, and allanite forms the accessory phases (**Figure 3D**). The plagioclase feldspars are euhedral and display kink in their twins (**Figure 3D**). The alkali feldspars, which are subhedral to anhedral, exhibit perthitic exsolution. A few crystals of hornblende exhibit twinning, and most of them are chloritized, along with biotite. Apatites are mostly prismatic, though few acicular ones are also observed. Allanite crystals are well-zoned and elongated (**Figure 3E**). Primary epidotes are rarely seen, while the secondary epidotes are fairly common. Titanite grains are mostly associated with biotite and hornblende, and they vary from euhedral wedge to irregular in shape (**Figure 3F**).

ANALYTICAL TECHNIQUES

The granitoid samples weighing more than ∼3 kg were collected from fresh outcrops and working quarries. For geochemical analysis, the samples were crushed to fine powders of size <250 mesh sieve. The geochemical analysis was carried out using in-house facilities at CSIR-National Geophysical Research Institute, Hyderabad. The major elements of the studied samples are analyzed using XRF (Phillips Axios mAX4), following the pressed pellet sample preparation technique. USGS standard reference material G-2 was used as the standard. The details of instrument calibration, data acquisition, accuracy, and detection limits are provided in Krishna et al. (2016). The trace elements were analyzed using AttoM HR-ICP-MS (Nu Instruments, UK), following the closed digestion sample preparation technique. About 50 mg of finely powdered samples were taken in Savillex® vials to which 10 ml of the acid mixture containing HF and HNO_3 mixed in 7:3 ratio was added. After heating these vials for 48 h at 150°C to obtain a clear solution, 1 ml of perchloric acid was added, and the samples were heated to dryness. Twenty ml of a freshly prepared acid mixture containing HF and Millipore water in a 1:1 ratio was added to the vials and heated for nearly 1 h at 80°C. On cooling, the sample solution was transferred to 250 ml conical flasks, and 5 ml of 1 ppm Rh

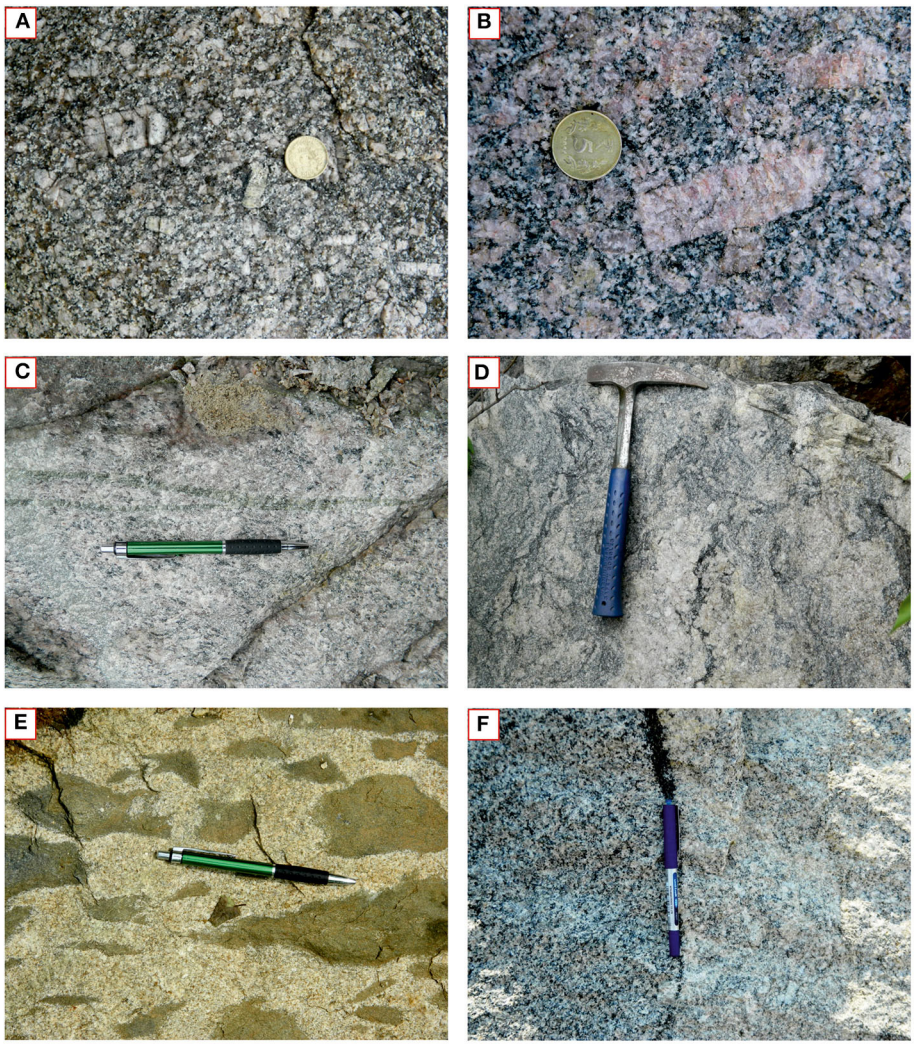

FIGURE 2 | Field photographs of different granite types from Kanker **(A)** Gray porphyritic granite with feldspar phenocryst. **(B)** Pink porphyritic granite with alkali feldspar phenocrysts. Both these granitoids are high in mafic minerals. **(C)** Medium- to coarse-grained leucogranite being intruded by an epidote vein. **(D)** Gray medium- to coarse-grained anatectic granite. **(E)** Medium to coarse- grained gray granite with abundant Magmatic Enclaves (MEs). **(F)** Two granitoid variants that differ in their mafic mineral contents, demarcated by a sharp boundary of biotite aggregates.

was added as an internal standard. The sample solution was initially diluted to 250 ml, followed by a 50 ml dilution, to achieve an optimal Total Dissolved Solid (TDS) level. Along with the samples, blank solutions and standards JG-1a and G-2 were also used. The data accuracy was monitored using certified reference materials (JG-1a and G-2), and the instrument sensitivity and stability was checked with Rh. The contamination was monitored using the blank solutions. The details of the sample digestion method, instrumental parameters, data acquisition, and quality are referred from Satyanarayanan et al. (2018).

RESULTS

Geochemistry

The whole-rock major and trace elemental data for 39 samples representing the Kanker granites are presented in **Table 1**. Based on the normative mineralogy, the Kanker granites are mostly granites with few granodiorites and quartz monzonite (**Figure 4A**). Considering the compositional variability of these granites, in conjunction with the variations in mineral assemblages, these granites are divided into sanukitoids, biotite and two-mica granites and hybrid granites (as dispositioned in **Figure 4B**). This classification scheme enables us to characterize these rocks for the petrogenetic evolution and sources, apart from being consistent with the global adaptability of Neoarchean granitoids (Laurent et al., 2014).

Sanukitoids

Based on the normative mineralogy, the sanukitoids of the Kanker are granites, granodiorites and quartz monzonites (**Figure 4A**) with a high content of ferromagnesian elements (Fe_2O_3, MgO, MnO and TiO_2, FMMT >5 wt.%) (**Figure 4B**).

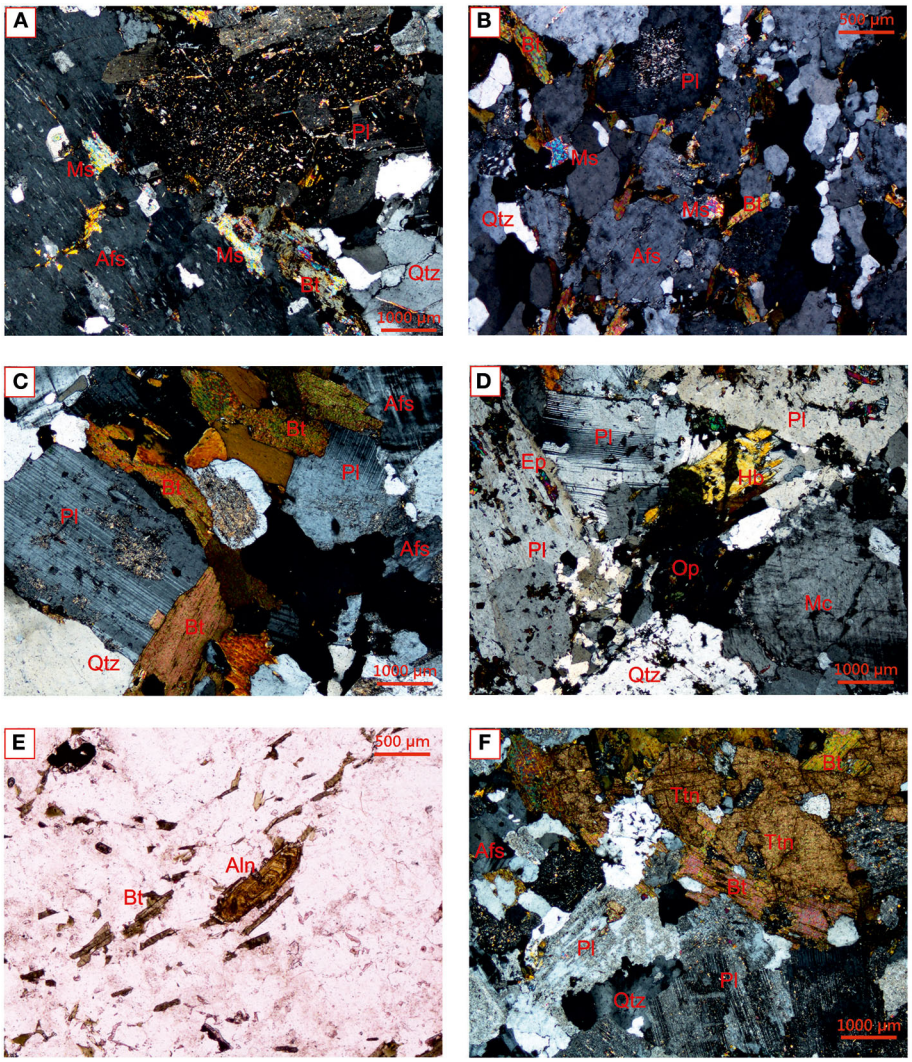

FIGURE 3 | Representative photomicrographs of Kanker granites **(A)** Biotite and two-mica granite with sericitized plagioclase, alkali feldspar with plagioclase and quartz inclusions, chloritized biotite, and muscovite. **(B)** Biotite and two-mica granite with plagioclase, alkali feldspar, quartz, biotite and muscovite. Quartz exhibits sub-grain formation. **(C)** Biotite granite with plagioclase, alkali feldspar, quartz and biotite. The alteration of plagioclase is limited to their cores and possess growth twins. **(D)** Hornblende biotite granite with hornblende, plagioclase, microcline, quartz and opaques. Plagioclase possesses deformational kinks. **(E)** An elongated zoned allanite grain observed in the biotite granite. **(F)** Biotite granite with large titanite grains associated with biotite, extensively sericitized plagioclase, alkali feldspar and recrystallized quartz. The mineral abbreviations in the figure are Ms, Muscovite; Afs, Alkali feldspar; Bt, Biotite; Pl, Plagioclase; Qtz, Quartz; Ep, Epidote; Op, Opaque; Mc, Microcline; Ttn, Titanite; Aln, Allanite.

Their silica and alumina compositions range between 63 and 69 wt.% and 12 to 16 wt.%, respectively (**Table 1**). These granites are essentially potassic (K_2O = 3.4–5.4 wt.%) with metaluminous affinity (A/CNK <1) and belongs to high-K calc-alkaline to shoshonitic series (**Figures 5A,B**). The sanukitoids have Mg number (Mg#) as high as 66 with an average of 46 (**Figure 5C**). On the Harker variation diagrams, these sanukitoids exhibit a negative trend against the major elements, with marked enrichment in the ferromagnesian elements (**Figures 5D–F**).

The sanukitoids have higher compositions of transition elements (**Table 1**). These rocks have low Rb (avg. 168 ppm) and high Sr (avg. 310 ppm) compositions, leading to extremely low Rb/Sr ratios (avg. Rb/Sr = 0.54). On the chondrite normalized rare earth element (REE) diagram, sanukitoids display a highly fractionated pattern [$(La/Yb)_N$ varying from 7.83 to 68.94, avg. = 29.8] with a negative Eu anomaly (Eu/Eu* varying from 0.96 to 0.20, avg. = 0.63) (**Figure 6A**). On the primitive mantle normalized multi-elemental variation diagram, the sanukitoids display prominent Large Ion Lithophile Elements (LILE) enrichment and High Field Strength Elements (HFSE) depletion (**Figure 6B**). These rocks exhibit negative anomalies of Nb,Ta, Sr, and Ti.

TABLE 1 | Major and trace elemental compositions of the Kanker granites.

	Biotite and two-mica granites							
Sample	B/5A	B/5B	B/6	BB14-1	S/240/3	S/230/4	S/237/3	S/239/1
SiO_2 (wt. %)	73.11	73.22	72.17	73.31	74.09	73.32	74.07	73.12
Al_2O_3	14.83	14.79	14.91	14.99	14.63	14.77	14.44	14.61
Fe_2O_3 (T)	1.50	1.63	1.74	1.38	1.41	1.47	1.30	1.45
MnO	0.02	0.02	0.03	0.01	0.03	0.02	0.02	0.02
MgO	0.20	0.22	0.22	0.16	0.14	0.12	0.19	0.18
CaO	1.03	1.10	1.07	1.23	0.96	0.81	0.90	1.05
Na_2O	3.96	3.63	3.76	3.89	3.59	3.72	3.83	3.78
K_2O	5.02	5.06	4.96	5.12	4.81	4.92	4.93	5.03
TiO_2	0.08	0.07	0.15	0.05	0.08	0.10	0.13	0.13
P_2O_5	0.03	0.03	0.05	0.01	0.01	0.01	0.02	0.04
LOI	0.44	0.63	0.54	0.35	0.42	0.51	0.35	0.35
Sum	100.22	100.39	99.60	100.50	100.15	99.78	100.18	99.78
Mg#	22.48	22.71	21.96	20.47	17.92	15.69	24.19	21.62
A/CNK	1.07	1.10	1.10	1.06	1.14	1.14	1.09	1.08
A/NK	1.24	1.29	1.29	1.25	1.32	1.29	1.24	1.25
Cr (ppm)	16.03	15.07	14.75	86.15	79.51	80.05	79.62	77.04
Co	1.92	1.89	2.44	1.83	2.14	1.82	2.14	2.52
Ni	2.75	3.94	2.80	6.01	6.42	6.23	5.54	5.58
Rb	296	270	263	287	270	332	207	209
Sr	35.61	59.46	68.89	39	34	34.8	75.9	79
Cs	1.99	1.75	2.42	1.18	1.13	0.679	0.528	0.22
Ba	180	267	242	115	73	89.9	140	201
Sc	1.92	1.49	1.59	2.18	4.22	1.53	1.32	1.26
V	0.56	0.64	1.10	8.42	4.46	4.49	6.09	8.05
Ta	2.85	2.08	3.06	1.62	0.89	1.34	1.01	0.31
Nb	19.9	14.8	20.7	13.23	35.31	31.91	23.81	20.35
Zr	60.91	77.01	123	137	213	274	191	140
Hf	2.85	3.07	4.70	4.57	7.44	10.5	6.37	4.19
Th	31.98	33.59	31.25	21.06	52.48	61.0	44.6	24.67
U	10.45	14.64	19.70	9.53	15.26	12.1	9.56	9.69
Y	28.34	23.49	21.82	16.19	45.15	43.5	24.8	26.11
La	134	210	149	101	106	202	206	120
Ce	101	148	109	69.63	79.38	137	139	87.22
Pr	60.36	91.61	73.07	56.54	74.87	112	108	76.06
Nd	39.45	57.71	49.43	33.47	50.22	65.07	58.90	46.69
Sm	24.03	30.44	28.24	21.35	41.83	40.85	30.02	31.31
Eu	3.69	4.85	5.52	3.23	3.80	4.89	6.38	5.81
Gd	13.36	15.46	14.84	11.10	24.83	21.38	14.98	16.57
Tb	14.80	14.89	13.83	11.94	32.64	24.89	15.51	19.12
Dy	16.22	14.18	13.91	8.69	27.25	20.08	11.66	15.04
Ho	13.60	11.33	10.89	6.67	21.73	16.57	9.17	11.65
Er	14.16	11.05	10.35	7.35	23.57	19.00	10.16	12.29
Tm	14.73	10.78	9.81	8.06	24.61	20.94	10.75	11.86
Yb	17.23	11.96	10.64	8.52	23.05	21.02	10.30	10.61
Lu	19.60	14.06	12.20	9.34	22.99	22.33	10.30	10.07
∑REE	485	647	510	357	556	727	641	475
(La/Yb)cn	8.02	18.15	14.44	12.28	4.74	9.92	20.68	11.73
(La/Sm)cn	5.74	7.12	5.43	4.89	2.61	5.10	7.09	3.97
(Gd/Yb)cn	0.78	1.29	1.39	1.30	1.08	1.02	1.45	1.56
(Eu/Eu*)	0.20	0.21	0.26	0.20	0.11	0.16	0.29	0.24
(Zr/Hf)	21.37	25.12	26.23	29.91	28.63	26.00	30.04	33.54
(Nb/Ta)	6.96	7.11	6.77	8.17	39.75	23.77	23.51	64.93
(Sr/Y)	1.26	2.53	3.16	2.39	0.76	0.80	3.06	3.01

	Sanukitoids											
Sample	B16/2	B16/5	B16/9	B16/13	B16/16	B16/36	B16/38	B16/40	S/236/2	S/236/5	S/227/4	S/239/5
SiO_2 (wt. %)	68.16	67.95	67.16	67.30	66.95	67.42	68.16	68.03	69.05	69.04	69.01	63.88
Al_2O_3	12.73	14.08	14.56	14.33	14.96	14.87	14.18	14.73	14.81	14.80	14.27	15.52
Fe_2O_3 (T)	4.22	3.55	3.80	3.69	4.43	4.24	4.12	3.97	3.66	3.55	3.78	5.50
MnO	0.05	0.04	0.04	0.04	0.03	0.06	0.05	0.04	0.03	0.03	0.05	0.04
MgO	1.71	1.32	1.46	1.47	1.96	1.56	1.32	1.29	1.29	1.25	1.19	3.11
CaO	3.03	2.99	2.87	2.76	3.37	2.87	2.94	2.75	2.72	2.83	2.75	3.53
Na_2O	3.77	3.84	3.86	4.01	3.61	3.25	4.02	3.59	3.13	3.72	2.73	3.31
K_2O	5.35	5.12	5.14	5.00	3.52	5.15	4.27	4.30	4.62	3.40	4.62	4.28
TiO_2	0.55	0.46	0.45	0.58	0.54	0.44	0.37	0.41	0.44	0.42	0.43	0.60
P_2O_5	0.42	0.23	0.26	0.26	0.52	0.13	0.19	0.19	0.17	0.27	0.36	0.23
LOI	0.42	0.35	0.46	0.52	0.39	0.43	0.51	0.58	0.41	0.40	0.54	0.47
Sum	100.42	99.95	100.06	99.97	100.28	100.43	100.11	99.88	100.33	99.71	99.73	100.47
Mg#	47.19	45.04	45.77	46.75	49.35	44.78	41.39	41.72	43.75	43.65	40.84	55.46
A/CNK	0.73	0.81	0.85	0.84	0.94	0.92	0.86	0.95	0.98	0.99	0.98	0.94
A/NK	1.06	1.19	1.22	1.19	1.54	1.36	1.26	1.39	1.46	1.51	1.50	1.54
Cr (ppm)	105	110	112	130	137	103	104	124	63.70	62.22	105	71.47
Co	10.63	3.70	8.16	7.64	12.79	3.76	5.37	4.99	3.21	5.64	8.12	13.27
Ni	9.14	8.42	12.26	11.00	9.07	8.26	7.53	9.30	6.04	5.44	6.75	6.89
Rb	140	243	269	324	107	116	107	104	200	100	149	163
Sr	254	158	186	145	485	251	329	306	241	465	453	450
Cs	0.30	1.04	3.04	1.99	1.03	0.69	0.60	0.88	0.93	0.84	0.31	0.69
Ba	1134	1025	774	809	1068	1399	1036	1257	1418	1235	1852	1388
Sc	8.73	4.79	9.50	7.90	7.37	6.86	8.92	10.27	3.14	4.56	8.97	9.78
V	35.55	16.10	39.07	33.13	62.68	16.94	26.17	24.32	12.34	31.48	42.47	62.1
Ta	0.94	0.76	1.74	0.28	0.80	0.09	0.09	0.07	1.37	0.70	0.84	1.49
Nb	34.04	17.95	30.88	47.48	22.74	7.89	10.38	7.17	20.65	17.57	20.44	18.54
Zr	690	482	463	1137	431	348	482	640	343	333	538	495
Hf	12.80	10.13	8.88	22.15	8.18	6.77	9.26	12.60	7.38	6.63	11.33	10.61
Th	43.89	74.58	53.80	143	3.49	11.71	14.99	14.80	20.19	15.15	23.88	21.38
U	8.03	11.21	11.58	36.65	2.43	1.83	1.65	2.07	8.50	2.73	8.37	3.86
Y	36.00	24.95	64.50	76.66	67.08	21.38	23.08	20.19	20.45	13.97	18.29	34.65
La	341	504	430	1086	138	198	256	224	319	279	381	349
Ce	235	347	289	762	107	131	165	145	202	171	249	241
Pr	207	278	226	614	104	107	134	117	158	132	197	204
Nd	134	161	129	349	74.26	63.57	79.35	70.91	89.25	74.87	114	130
Sm	77.39	81.47	71.47	184	67.77	34.54	41.91	36.68	39.34	32.77	48.33	68.27
Eu	27.28	21.07	20.14	26.78	29.25	21.18	22.85	23.19	19.32	22.75	29.18	36.53
Gd	36.61	35.68	37.76	85.21	46.86	16.37	20.22	18.33	17.32	14.93	20.16	31.94
Tb	35.33	31.67	44.88	81.97	53.95	16.65	19.42	18.27	15.81	12.67	15.64	30.20
Dy	22.87	18.47	34.71	52.91	42.19	11.79	13.88	12.55	11.25	8.48	9.94	21.13
Ho	16.17	11.43	27.89	36.11	30.89	9.00	10.59	9.20	8.77	6.28	7.50	15.61
Er	16.54	9.96	30.53	32.97	28.94	9.91	11.12	9.80	9.71	6.68	8.55	16.56
Tm	15.54	8.33	32.99	28.73	23.44	11.20	11.31	10.03	10.54	6.67	9.65	17.14
Yb	13.98	7.56	32.12	23.92	18.21	11.18	12.06	9.81	10.69	6.74	11.20	17.29
Lu	13.40	7.20	31.73	21.84	16.15	12.20	11.91	10.25	10.92	7.51	14.26	18.45
∑REE	1192	1523	1439	3385	781	654	810	716	922	782	1116	1197
(La/Yb)cn	25.22	68.94	13.83	46.93	7.83	18.34	21.96	23.60	30.84	42.72	35.12	20.87
(La/Sm)cn	4.55	6.39	6.21	6.09	2.10	5.93	6.31	6.31	8.37	8.78	8.13	5.28
(Gd/Yb)cn	2.62	4.72	1.17	3.56	2.57	1.46	1.68	1.87	1.62	2.21	1.80	1.85
(Eu/Eu*)	0.48	0.36	0.37	0.20	0.51	0.84	0.74	0.85	0.69	0.96	0.86	0.73
(Zr/Hf)	53.87	47.59	52.07	51.31	52.63	51.37	52.06	50.80	46.43	50.19	47.53	46.61
(Nb/Ta)	36.19	23.57	17.75	171	28.45	86.07	116	106	15.04	24.98	24.23	12.44
(Sr/Y)	7.04	6.34	2.88	1.90	7.24	11.75	14.26	15.13	11.78	33.26	24.78	12.99

	Hybrid granites																		
Sample	B16/1	B16/17	B16/22	B16/25	B16/29	B16/31	B16/33	B16/35	B/258/3	B/259/1	B/259/2	B/8A	B/8B	B/10	B/11	B/27	BB14-3	S/230/10	S/147/2
SiO_2 (wt. %)	71.90	71.29	70.27	69.31	71.45	71.21	69.94	71.49	70.27	71.50	71.93	70.70	69.83	71.01	69.93	69.81	71.30	71.29	73.38
Al_2O_3	14.28	14.87	15.76	14.69	14.62	14.91	14.41	14.56	14.60	14.48	13.85	14.96	15.02	14.81	14.87	15.10	14.57	13.77	13.80
Fe_2O_3 (T)	1.90	2.30	1.95	3.28	2.46	2.19	2.56	2.69	2.93	2.87	2.57	2.84	2.69	1.92	2.45	2.54	2.37	3.30	2.33
MnO	0.01	0.01	0.02	0.03	0.02	0.02	0.02	0.02	0.03	0.02	0.02	0.02	0.02	0.03	0.03	0.03	0.02	0.03	0.02
MgO	0.42	0.34	0.89	0.94	0.36	0.49	0.54	0.34	0.69	0.84	0.64	0.36	0.60	0.42	0.36	0.62	0.74	0.55	0.34
CaO	1.74	1.48	2.25	2.61	1.87	1.90	2.48	2.04	1.20	1.47	1.41	2.15	1.82	2.59	1.43	2.77	2.03	1.65	1.69
Na_2O	3.09	3.38	5.00	2.95	3.54	3.88	3.36	3.84	4.14	3.94	3.32	3.32	3.49	3.47	3.20	4.35	4.39	3.96	3.19
K_2O	5.38	4.97	2.79	4.91	4.46	4.15	5.29	4.52	4.36	4.12	4.20	4.90	4.58	4.81	5.59	3.97	3.43	3.90	4.97
TiO_2	0.17	0.25	0.28	0.40	0.23	0.22	0.25	0.23	0.27	0.32	0.24	0.26	0.31	0.17	0.19	0.28	0.27	0.43	0.10
P_2O_5	0.06	0.07	0.05	0.22	0.09	0.11	0.08	0.09	0.08	0.05	0.05	0.16	0.12	0.12	0.08	0.11	0.13	0.09	0.03
LOI	0.42	0.49	0.31	0.46	0.43	0.55	0.58	0.32	0.70	0.59	0.73	0.61	0.63	0.71	0.64	0.58	0.42	0.51	0.42
Sum	99.37	99.45	99.56	99.81	99.51	99.62	99.50	100.15	99.28	100.20	98.97	100.27	99.10	100.04	98.76	100.15	99.67	99.48	100.27
Mg#	32.59	24.65	50.18	38.76	24.41	32.87	31.54	22.00	34.02	39.03	35.22	21.74	32.76	32.31	24.20	34.97	40.78	26.65	24.44
A/CNK	1.02	1.09	1.03	0.99	1.04	1.04	0.91	0.97	1.06	1.06	1.10	1.02	1.07	0.95	1.07	0.92	1.00	1.00	1.01
A/NK	1.31	1.36	1.40	1.44	1.37	1.37	1.28	1.30	1.26	1.32	1.38	1.39	1.40	1.36	1.31	1.32	1.33	1.28	1.30
Cr (ppm)	125.32	105	113	108	96.25	110	144	103	13.73	13.25	14.57	11.83	11.58	13.45	15.35	9.99	83.78	83.44	82.14
Co	3.94	3.00	4.40	6.05	3.60	3.89	4.46	3.87	2.90	2.26	3.28	3.17	3.74	2.68	2.89	4.09	4.95	3.69	2.45
Ni	8.95	7.95	10.06	8.85	9.58	7.50	12.88	8.74	3.25	2.87	3.29	3.12	3.44	3.22	7.70	3.47	6.68	6.21	6.14
Rb	230	143	123	206	101	91	221	152	99	97	113	176	169	181	200	117	65	210	125
Sr	121	111	204	172	243	286	133	172	51	32	28	147	201	206	109	356	236	105	149
Cs	0.41	0.56	4.02	0.92	0.78	1.04	2.94	0.69	1.63	0.95	1.10	2.59	1.68	2.05	3.49	2.05	0.53	1.19	0.90
Ba	712	459	464	827	1295	983	445	958	1118	983	1025	800	836	925	664	695	875	498	952
Sc	6.03	5.16	6.71	6.26	5.75	6.70	10.49	7.82	3.73	3.42	3.55	2.71	2.68	2.59	2.17	3.07	3.63	3.77	2.20
V	11.60	11.26	31.92	35.07	14.16	14.49	19.05	15.05	1.09	0.91	0.79	1.29	1.54	0.89	0.94	1.94	14.84	11.83	8.67
Ta	2.11	0.57	0.84	0.41	0.34	0.32	0.11	0.07	1.60	2.10	2.54	1.11	0.67	2.17	1.73	0.91	0.29	1.21	0.28
Nb	32.42	11.31	14.99	24.03	10.74	7.44	10.55	9.25	26.59	29.16	33.77	16.34	12.81	20.28	16.16	8.67	11.81	27.15	4.08
Zr	382	304	571	461	443	239	343	364	207	212	293	218	260	167	171	135	406	578	219
Hf	8.59	6.63	11.66	9.20	8.60	5.02	7.67	7.67	6.95	7.35	9.89	6.63	7.67	5.92	6.05	4.02	8.30	13.53	5.79
Th	59.32	45.81	50.28	48.79	12.56	11.64	54.23	25.21	12.02	26.04	22.26	27.27	34.45	39.20	38.63	14.54	25.90	76.95	10.72
U	12.17	6.03	4.80	10.92	1.98	1.41	13.12	3.91	2.58	5.51	7.13	5.62	3.91	12.57	9.55	4.74	1.39	28.42	2.59
Y	27.95	9.06	19.67	31.25	13.52	7.11	23.06	17.08	42.55	51.76	66.46	19.50	10.31	21.18	12.83	8.52	11.50	40.91	6.68
La	335	482	381	384	189	159	307	271	211	254	382	300	382	265	256	125	309	1123	84.91
Ce	236	334	252	250	123	116	200	181	172	182	314	206	292	179	178	84.57	202	703	60.81
Pr	189	256	197	193	99.65	84.39	157	146	109	129	189	129	157	113	114	54.16	159	555	52.90
Nd	109	137	110	110	58.97	50.86	89.91	85.17	82.66	95.71	138	83.50	99.05	75.60	75.49	37.14	90.51	289.33	33.01
Sm	59.10	57.25	56.88	56.14	30.35	23.51	46.86	41.87	48.25	56.42	77.29	36.02	38.88	39.90	38.36	18.56	42.97	116.64	17.58
Eu	14.27	11.97	15.28	27.33	22.13	14.62	17.37	21.93	15.31	13.92	16.69	10.41	11.21	7.93	8.76	9.01	19.12	12.12	13.18
Gd	28.65	20.93	25.79	28.50	13.93	9.70	21.79	18.05	28.47	32.45	45.03	16.98	16.29	20.39	17.91	8.70	18.85	47.33	7.18
Tb	27.77	13.24	22.29	26.71	12.19	7.87	20.85	16.15	28.55	31.80	42.32	13.74	10.17	17.96	13.13	6.89	15.45	38.74	6.20
Dy	19.00	6.68	13.68	18.30	7.94	4.60	14.42	10.46	28.99	32.16	42.58	12.53	7.78	15.48	10.11	5.88	9.03	24.61	4.02
Ho	13.42	4.24	9.04	14.04	6.10	3.23	10.69	7.75	22.72	25.53	34.10	9.75	5.88	11.13	7.34	4.53	5.76	17.44	2.90
Er	12.39	4.04	8.50	15.34	6.33	3.26	11.04	7.84	20.88	24.27	33.34	8.84	5.38	9.65	6.51	4.25	5.03	18.53	3.10
Tm	11.75	3.84	7.78	16.11	6.47	3.41	11.43	8.68	19.05	23.02	32.57	7.93	4.88	8.17	5.68	3.97	4.14	19.13	3.38
Yb	11.26	3.82	7.46	16.60	6.34	3.25	11.11	8.69	19.90	24.94	36.41	8.08	5.08	7.96	5.75	4.12	3.64	19.45	3.69
Lu	12.33	3.89	8.51	17.01	7.83	3.47	11.98	10.03	22.19	28.39	42.05	9.28	6.03	8.91	7.00	5.39	3.88	20.69	4.46
∑REE	1080	1339	1115	1174	590	487	932	835	829	954	1426	851	1041	781	744	372	888	3005	297
(La/Yb)cn	30.75	130	52.82	23.94	30.84	50.64	28.52	32.20	10.94	10.52	10.84	38.33	77.71	34.44	46.02	31.34	87.65	59.70	23.78
(La/Sm)cn	5.85	8.70	6.92	7.07	6.44	7.00	6.76	6.68	4.51	4.65	5.10	8.59	10.13	6.87	6.89	6.95	7.43	9.94	4.99
(Gd/Yb)cn	2.54	5.47	3.46	1.72	2.19	2.98	1.96	2.08	1.43	1.30	1.24	2.10	3.21	2.56	3.11	2.11	5.17	2.43	1.94
(Eu/Eu*)	0.33	0.31	0.37	0.65	1.01	0.89	0.51	0.74	0.40	0.32	0.27	0.40	0.41	0.26	0.31	0.66	0.62	0.15	1.07
(Zr/Hf)	44.47	45.82	48.92	50.10	51.50	47.74	44.74	47.50	29.70	28.85	29.65	32.95	33.93	28.27	28.28	33.52	48.95	42.70	37.78
(Nb/Ta)	15.40	19.72	17.81	59.30	31.77	23.23	94.02	142	16.58	13.87	13.29	14.71	19.11	9.35	9.37	9.51	41.12	22.35	14.74
(Sr/Y)	4.32	12.23	10.36	5.51	17.97	40.21	5.76	10.09	1.21	0.62	0.43	7.52	19.50	9.75	8.50	41.75	20.56	2.57	22.32

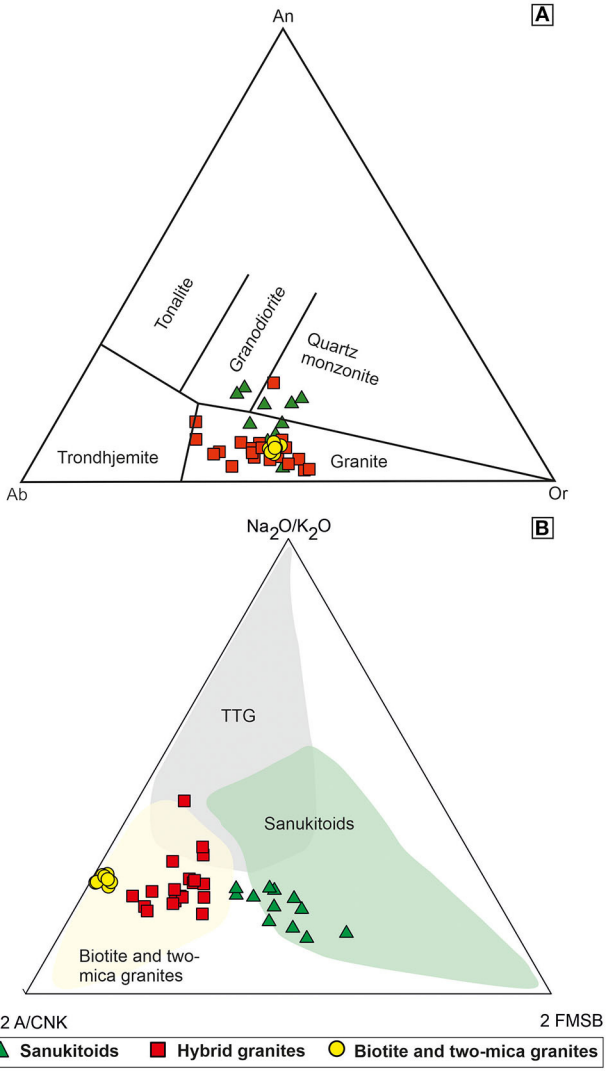

FIGURE 4 | (A) The distribution of Kanker granites on the normative An-Or-Ab triangle diagram (after O'Connor, 1965). **(B)** The disposition of the Kanker granites in the ternary classification diagram for Neoarchean granitoids (after Laurent et al., 2014), the fields correspond to that of well-studied suits from different cratons.

Biotite and Two-Mica Granites

Based on the normative mineralogy, the biotite and two-mica granites are essentially granites (**Figure 4A**). Their silica and alumina compositions vary in a narrow range, between 72 and 74 wt.% and 14–15 wt.%, respectively (**Table 1**). These granites are essentially potassic (K_2O = 4.9–5.1 wt.%) with peraluminous affinity (A/CNK >1) and belongs to high-K calc-alkaline series (**Figures 5A,B**). These rocks have lower compositions of ferromagnesian elements (Fe_2O_3+MnO+MgO+TiO_2 <2.2 wt.%) and are clustered toward the Alumina pole in the classification diagram for Archean granitoids (**Figure 4B** and **Table 1**). They have a low Mg number (Mg# <22) (**Figure 5C**). In Harker variation diagrams, these granites show negative correlation of CaO, MgO, TiO_2, and Fe_2O_3 (**Figure 5**). The biotite and two-mica granites have low transition elemental compositions (**Table 1**), have high Rb (avg. Rb = 267 ppm) and low Sr (avg. Sr = 53 ppm), resulting in high Rb/Sr ratios (avg. Rb/Sr = 5.9). Similarly, these granites have low Zr (avg. Zr = 152 ppm) and Hf (avg. Hf = 5.4 ppm), resulting in low Zr/Hf ratios (avg. Zr/Hf = 27.6).

On the chondrite normalized REE plot, the biotite and two-mica granites are less fractionated with $(La/Yb)_N$ varying from 4.74 to 20.68 (avg. $(La/Yb)_N$ = 12.5), but possess a strong negative Eu anomaly with Eu/Eu^* <0.3 (**Figure 6C**). On the multi-elemental variation diagram, biotite and two-mica granites display LILE enrichment and HFSE depletion with negative anomalies of Ba, Nb, Ta, Eu, Sr, and Ti (**Figure 6D**). The Nb-Ta depletion is not very prominent in the biotite and two-mica granites when compared to the sanukitoids.

Hybrid Granites

The hybrid granites of the Bastar Craton are compositionally diverse, with geochemical features intermediate between the sanukitoids and the biotite and two-mica granites. Based on normative mineralogy, they are granites (**Figure 4A**). Their silica and alumina compositions range between 69 and 73 and 13–16 wt.%, respectively (**Table 1**). On the Alumina Saturation Index diagram (Shand, 1943), the hybrid granites are distributed between metaluminous and peraluminous fields, with more affinity toward the latter (**Figure 5A**). These are potassic (K_2O = 2.8–5.6 wt.%), plotting in the fields of high-K calc-alkaline to shoshonitic series (**Figure 5B**). They have varied Mg number, ranging between 21 and 55 (avg. Mg# = 32) (**Figure 5C**). On Harker variation diagrams, the compositions of hybrid granites are distributed between the sanukitoids and biotite and two-mica granites (**Figures 5D–F**). These granites are low in ferromagnesian elements (1.8 ≤ FMMT ≤ 4.5 wt.%) (**Table 1**).

On the chondrite normalized REE plot, hybrid granites show incoherent REE abundances with a strongly fractionated elemental pattern [$(La/Yb)_N$ range from 10.5 to 130, avg. = 42] and variably negative Europium anomalies (between 0.15 and 1) (**Figure 6E**). On the primitive mantle normalized multi-elemental variation diagram, hybrid granites display LILE enrichment and HFSE depletion, with the trend intermediate between sanukitoids and biotite and two-mica granites (**Figure 6F**).

PETROGENESIS OF THE KANKER GRANITES

Source

Sanukitoids are considered to be derived from an incompatible element rich mantle source (Shirey and Hanson, 1984). Sanukitoids of the Kanker area are metaluminous, low in SiO_2, and high in ferromagnesian elements (**Figures 4B**, **5A**). They are also rich in transition metals and incompatible elements such as Ba and Sr (avg. Ba+Sr = 1510 ppm) (**Table 1**). Such compositional diversity (rich in compatible and incompatible elements) is suggestive of an enriched mantle source (**Figure 7**) (Shirey and Hanson, 1984; Heilimo et al., 2010). It has been

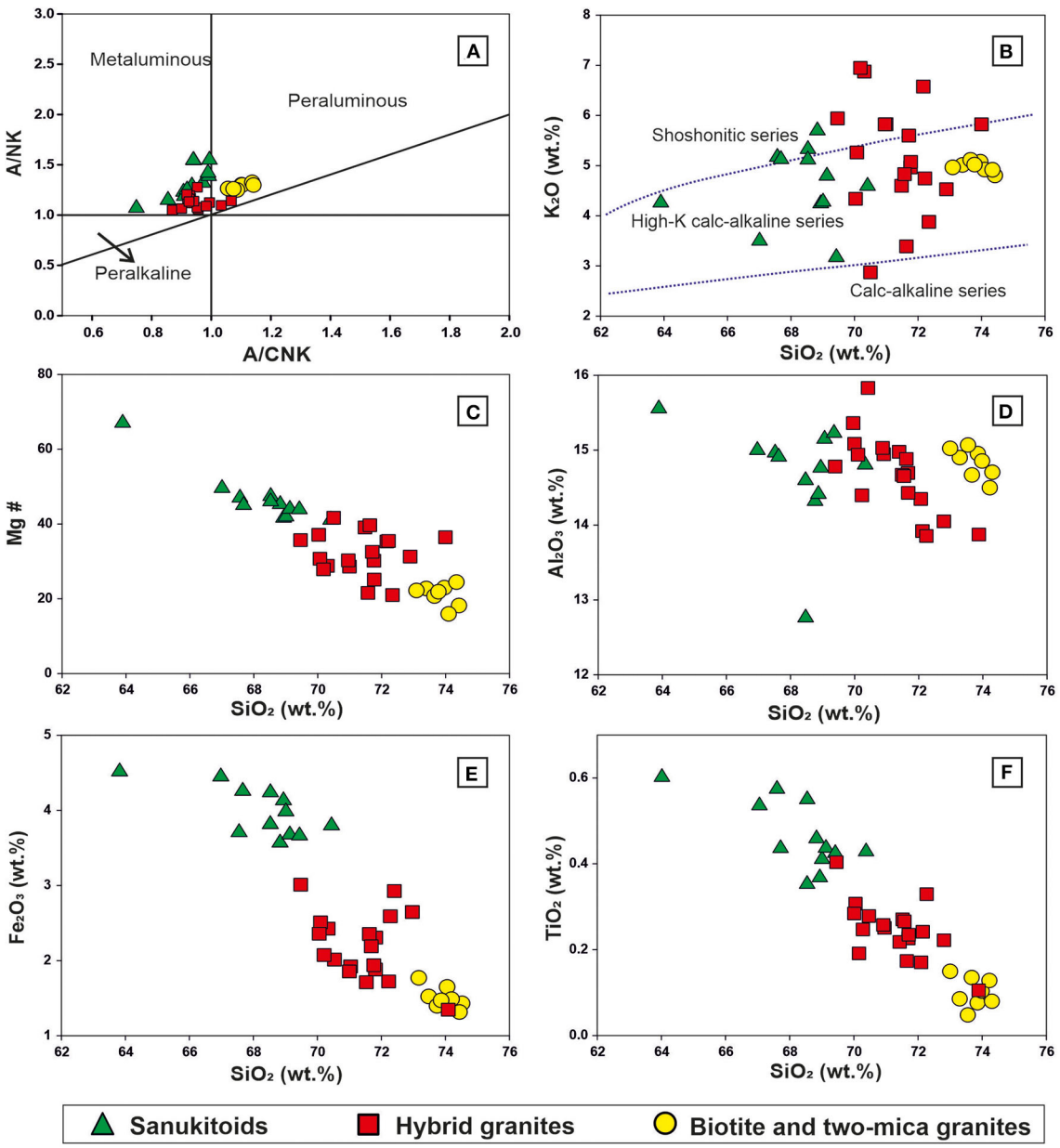

FIGURE 5 | (A) Alumina Saturation Index diagram (Shand, 1943), wherein the sanukitoids are confined to metaluminous field, biotite and two-mica granites are into peraluminous field. The hybrid granites are distributed among both fields. **(B)** SiO_2 vs. K_2O diagram (after Le Maitre, 1989) to show the variations in the melt affinity of different granite types of Kanker pluton. **(C)** SiO_2 vs. Mg# plot, wherein the sanukitoids with high Mg# suggest the mantle involvement (Rapp et al., 1999). **(D–F)** Harker variation diagrams depicting the major elemental compositional variations among the granite types of Kanker pluton. Note the compositional variability of hybrid granites and their distribution between the compositional range of sanukitoids and biotite and two-mica granites.

established that enrichment of the mantle can be caused by different metasomatic agents such as slab melts, carbonatite veins, fluids and/ or sediment melts (Smithies and Champion, 2000; Halla, 2005; Steenfelt et al., 2005; Martin et al., 2009; Laurent et al., 2011). In the slab melt model, petrogenesis of sanukitoids is explained by a two-stage process involving the interaction between slab melts and the mantle peridotite (Martin et al., 2009; Laurent et al., 2014). The sanukitoids from the Kanker are relatively poor in Sr (avg. Sr =310 ppm) when compared to the other well-studied sanukitoids, such as those from the Dharwar Craton (avg. Sr = 664 ppm; Mohan et al., 2019), Kapvaal Craton (avg. Sr = 553 ppm; Laurent et al., 2014) and Karelian and Kola cratons (avg. Sr = 729 ppm; Halla et al., 2009). The low Sr concentration could also be induced by plagioclase fractionation. The rocks have low Sr/Y values (Sr/Y $\leq$40), which rules out the role of slab melting in the metasomatisation of the mantle

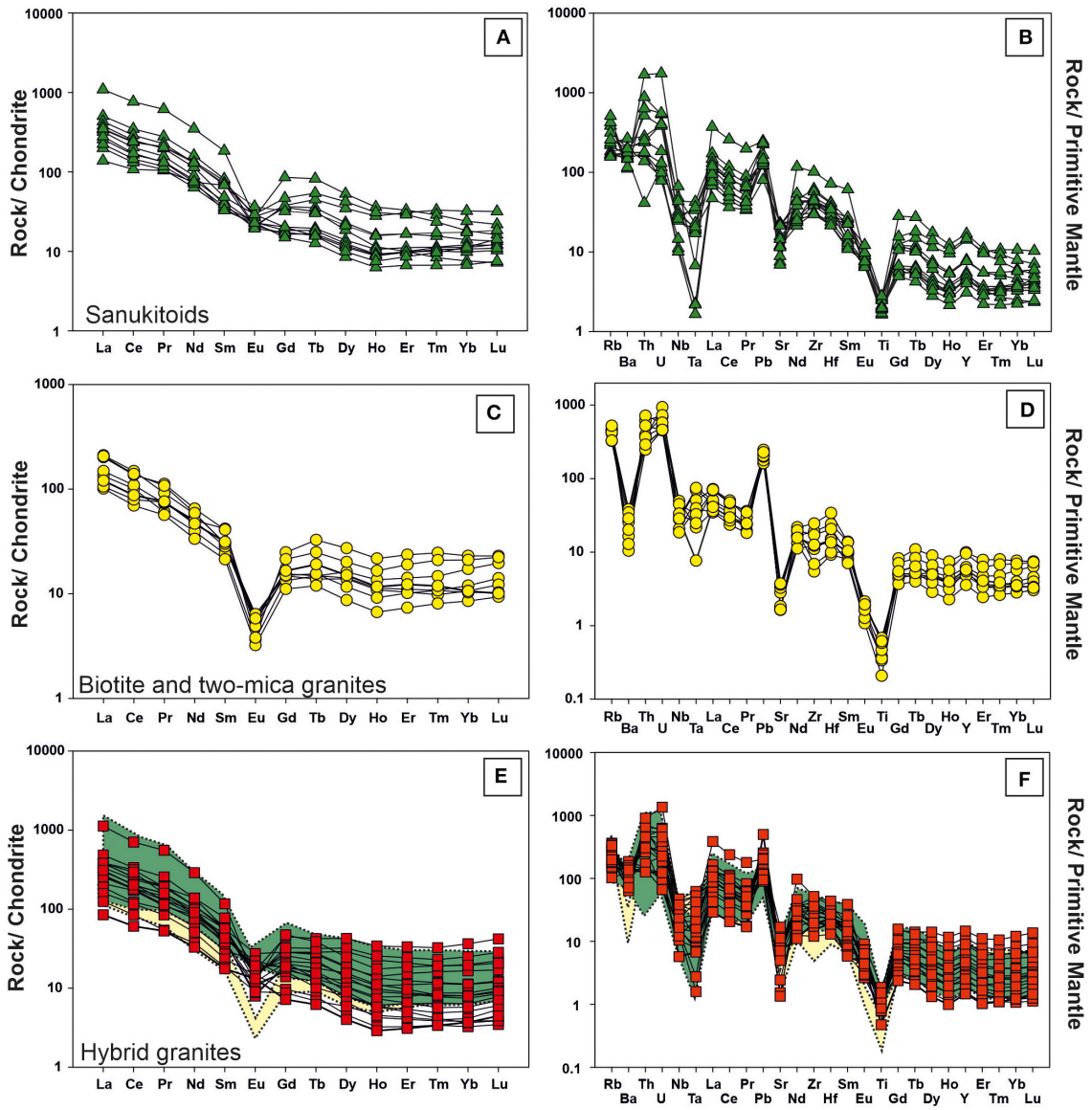

FIGURE 6 | Chondrite-normalized Rare earth element (REE) and primitive mantle-normalized multi-elemental variation diagram for the sanukitoids **(A,B)**, biotite and two-mica granites **(C,D)** and hybrid granites **(E,F)**. The compositional range of sanukitoids (green area) and biotite and two-mica granites (yellow area) are highlighted in the background **(E,F)** to show that hybrid granites are the mixtures of two primary granite types. Normalized values are from Sun and McDonough (1989).

(Martin et al., 2009). Also, Neoarchean TTG magmatism is yet to be reported from this craton. The lower Sr and Ca compositions, and corresponding enrichment of the HFSE (such as Nb, up to 47 ppm and Zr, up to 1,137 ppm) rules out the possibility of carbonate melt as a metasomatic agent in the genesis of these sanukitoids (Steenfelt et al., 2005). Also, there is no record of carbonatite magmatism in the vicinity of the study area.

Mantle enrichment can also be possible due to the involvement of subducting fluids (Elliott, 2004) and/ or due to sediment melting associated with the subducting oceanic crust (Woodhead et al., 2001). Trace elemental ratios such as Ba/La, U/Th, Th/Yb, Hf/Sm, and Ta/La can effectively differentiate between the fluid-related and sediment-melt related enrichments (Hawkesworth et al., 1997; La Flèche et al., 1998; Woodhead et al., 2001). The Bastar sanukitoids and a few hybrid granites follow the trend of sediment-melt related enrichment (**Figure 8A**). The above observation is also supported by the disposition of these samples in the Hf/Sm vs. Ta/La plot (**Figure 8B**). The available detrital zircon age data from the Bastar Craton indicates very older provenance, as old as extending from the Paleoproterozoic to Paleoarchean (1.75–3.67 Ga) (Khanna et al., 2019). Thus, the mantle enrichment, as evident in the case of Kanker sanukitoids, is possibly an outcome of sediment melting associated with earlier episode(s) of subduction.

The biotite and two-mica granites are considered to be the products of crustal reworking of older TTG with

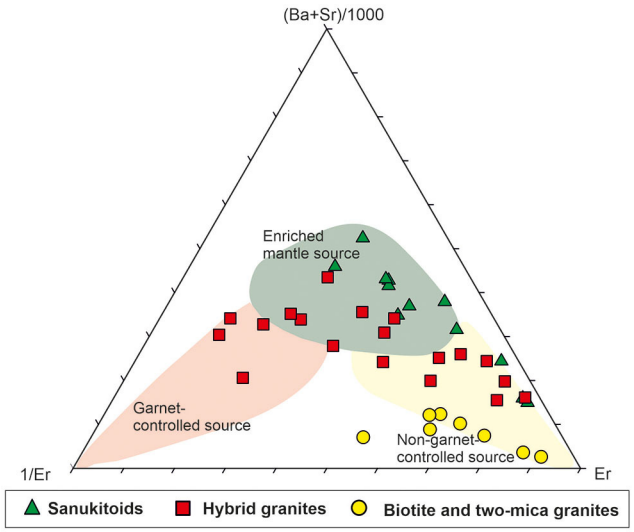

FIGURE 7 | Triangular plot using the discriminants Ba+Sr/1000, 1/Er and Er to differentiate the enriched mantle, garnet-controlled and non-garnet-controlled sources (after Heilimo et al., 2010).

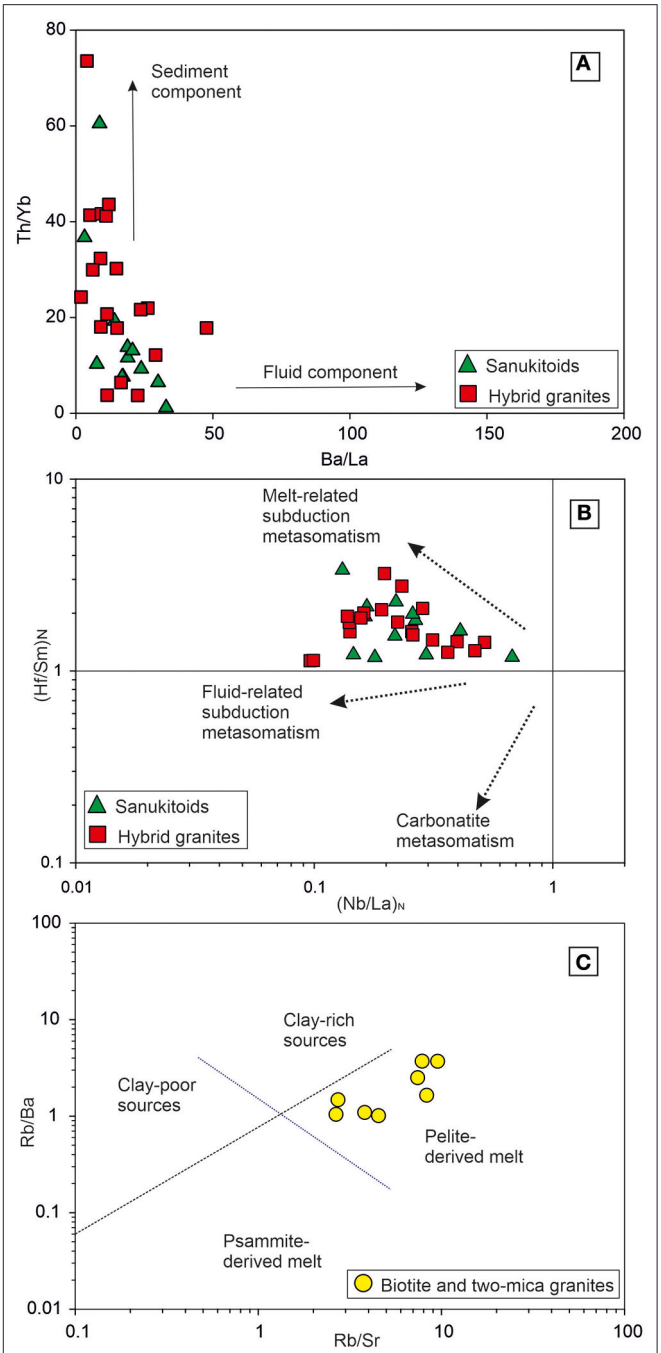

FIGURE 8 | (A) Th/Yb vs. Ba/La plot (Woodhead et al., 2001), to identify the role of sediment and fluid component. **(B)** $(Hf/Sm)_N$ vs. $(Nb/La)_N$ plot (La Flèche et al., 1998), to differentiate the metasomatic agent involved in the petrogenesis of Kanker granites **(C)** Rb/Ba vs. Rb/Sr plot (after Sylvester, 1998), to determine the nature of crustal sediments involved in the petrogenesis of strongly peraluminous biotite and two-mica granites.

sedimentary inputs (Laurent et al., 2014). These granites are SiO_2 rich, peraluminous, and poor in ferromagnesian elements. Paleoarchean basement rocks (TTG) are documented from the Bastar Craton (Sarkar et al., 1993; Ghosh, 2004; Rajesh et al., 2009). Possibly, the reworking of these older basement granitoids (TTG) is responsible for the origin of biotite and two-mica granites of Kanker. Besides, the role of sedimentary inputs in their genesis has been examined. The higher Rb, low Sr and Ba compositions of these strongly peraluminous rocks, and corresponding higher Rb/Ba and Rb/Sr ratios (**Figure 8C**) indicate their genesis from clay-rich sources (Sylvester, 1998). These elements are actively controlled by minerals of the feldspar and mica group (Harris and Inger, 1992). On the ternary source discrimination diagram (**Figure 7**), they are confined to non-garnet- controlled sources. This is further supported by strong negative europium anomaly, low Sr content (avg. 53 ppm) and flat HREE pattern (**Figure 6C**), to suggest the shallow depth of melting where plagioclase was in the source residue. Therefore, the biotite and two-mica granites could have been generated by the crustal melting with significant sediment input, or due to the reworking of older TTG. The availability of radiogenic isotopic data can resolve this preposition.

The hybrid granites are found in different Neoarchean cratons and are formed by variable interaction between the melts of TTG, biotite and two-mica granites and sanukitoids (Laurent et al., 2014; Mohan et al., 2019). The hybrid granites of Kanker possess geochemical compositions intermediate between the sanukitoids and biotite and two-mica granites. This observation is supported by geochemical signatures such as metaluminous to peraluminous affinity (**Figure 5A**), major elemental trends on Harker diagrams (**Figures 5C–F**) and incoherent REE patterns (**Figure 6E**). The large variability in incompatible elemental compositions such as Ba (445–1295 ppm, avg. Ba = 817 ppm), Rb (65–230 ppm, avg. Rb = 148 ppm), Sr (28–230 ppm, avg. Sr = 161 ppm) and REE (ΣREE varies from 83 ppm to 910

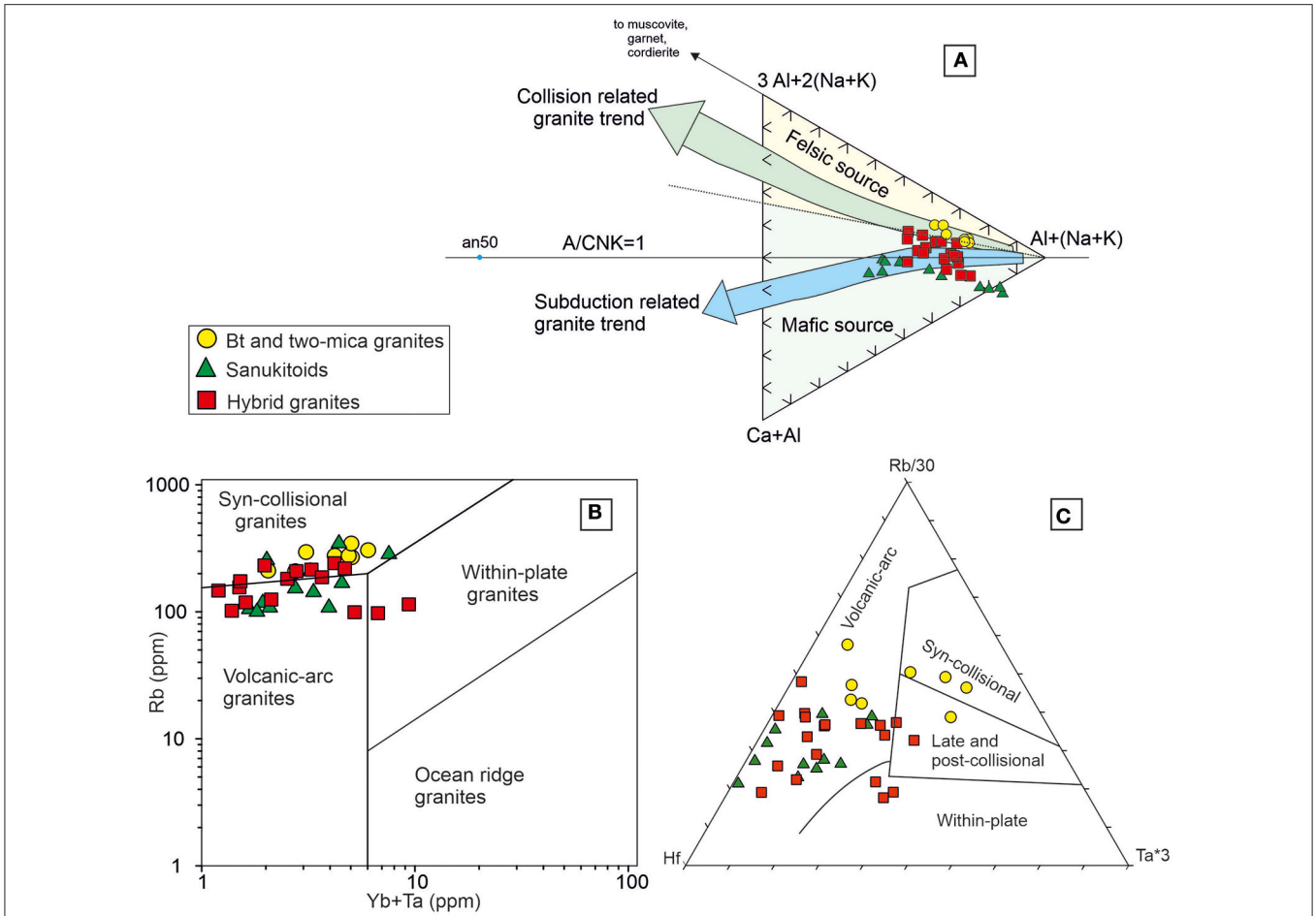

FIGURE 9 | (A) The Ca+Al - 3Al+2(Na+K) - Al+(Na+K) projection diagram to differentiate the sources and the tectonic setting trends in the evolution of granites (Moyen et al., 2017; Moyen and Laurent, 2018). The projection has been plotted using the GCDkit (Janoušek et al., 2016). **(B,C)** are tectonic discrimination diagrams for granites (Pearce et al., 1984; Harris et al., 1986) suggestive of an arc to collisional origin for the Kanker granites.

ppm, avg. ΣREE = 292 ppm), also reflect such heterogeneity. The large range of HFSEs in the hybrid granites could either reflect differentiation, melting depths and/or variable degree of interaction between the magma types. The presence of negative europium anomaly indicates shallow depth of melting or plagioclase fractionation. The geochemical anomalies displayed by these granites are similar to those granitoids that evolved in convergent margins (Pearce et al., 1984). Therefore, the hybrid granites of Kanker possibly had evolved from the melting of a heterogeneous source, formed by variable mixing of crustal and enriched mantle components.

Tectonic Setting

As outlined above, the Kanker granites with large compositional variability are derived from two mutually exclusive end-member sources, i.e., the enriched mantle and an older (felsic) crust. Diversity of these granites and their voluminous distribution within a restricted period during the Archean-Proterozoic transition can only be possible in a tectonic environment where these two distinct source reservoirs were spatially close, and could variably interact due to a heat source. Previous works on the Kanker granites are minimal and ascribe a tectonic setting variable between the subduction and syn-collision (Hussain et al., 2004; Mondal et al., 2006). Based on a compilation of experimental granitic melts, Moyen et al. (2017) devised Ca+Al - 3Al+2(Na+K) - Al+(Na+K) projection diagram to differentiate the mafic and felsic sources responsible for a variety of granitic rocks in arc and collisional systems during the Paleozoic, and further extended it to Archean granitoids (Moyen and Laurent, 2018). In the Ca+Al - 3Al+2(Na+K) - Al+(Na+K) projection diagram (**Figure 9A**), the sanukitoids from the Kanker are confined to the field of mafic source, and fall in the trend of subduction-related tectonic setting. In contrast, the biotite and two-mica granites of the Kanker are confined to the felsic source and fall in the trend of collision-related tectonic setting. The hybrid granites are distributed between the above two groups, indicating their heterogeneous nature, either in source or tectonic setting. Based on the above trend, it may be postulated that the Kanker granites were emplaced in a transitional tectonic setting, involving subduction and collision.

This inference is further supported by the distribution of these samples into the volcanic-arc and syn-collisional granite fields (**Figure 9B**) in the tectonic discrimination diagram (Pearce et al., 1984). A similar distribution is noted for the Kanker granites in the tectonic discrimination diagram of Harris et al. (1986) (**Figure 9C**). Neoarchean granites from many cratons exhibit such a transitional tectonic regime, involving subduction to collision (Laurent et al., 2014; Mohan et al., 2019). Such a transition in tectonic regime is attributed to the changes in geodynamo, and the nature and style of plate tectonics during the Archean-Proterozoic transition (Keller and Schoene, 2012).

In a subduction-collision regime, the subduction episode, prior to the collision results in the metasomatisation of the mantle. In most Archean cratons, sanukitoids represent the terminal event of subduction (Halla et al., 2009; Laurent et al., 2014). The arc magmas often show a transition from fluid fluxed melting to sediment melting with the maturation of subduction (Duggen et al., 2007). As outlined in the earlier section, the Kanker sanukitoids had been derived from the enriched mantle, possibly after the maturation of the arc or after the cessation of subduction. The mantle melts probably underwent differentiation and/or assimilation with the pre-existing older crustal rocks. The heat supplied by these melts resulted in low degree melting of crust with significant sedimentary input to form the peraluminous biotite and two-mica granites. Subsequent to the cessation of subduction, collision between the continental blocks leads to slab break-off, resulting in asthenospheric upwelling (Sylvester, 1998; Bonin, 2004; Halla et al., 2009). Thermal anomaly generated during the collision will induce partial melting of the previously enriched mantle, leading to the interaction between crust and mantle components resulting in the formation of a spectrum of granites (Bonin, 2004; Mikkola et al., 2011; Laurent et al., 2014; Moyen et al., 2017). The compositional heterogeneity of the hybrid granites suggests they could have formed at various stages, i.e., from subduction to collision, or could have resulted by the interaction between enriched mafic magmas with the pre-existing felsic crust. However, precise age and isotopic data will provide better clues on the sequence of emplacement of these granites, constraining the sources and extent of interactions between them. Based on field, geochemical evidences and with the aid of tectonic discrimination diagrams, the evolution of the Kanker granites can be best explained in an accretionary orogenic setting involving the subduction and subsequent collision.

IMPLICATIONS ON REGIONAL GEODYNAMICS

The Bastar Craton remains one of the prominent cratons in the Indian shield, mainly due to the mineralization, proximity to the CITZ and imprints of supercontinental cycles (Pandit and Panigrahi, 2012; Santosh et al., 2018; Liao et al., 2019). In addition to the Kanker, Dongargarh and Malanjkhand are the two other major Archean-Proterozoic granitic plutons. The available geochronological data indicate that these three plutons had emplaced at $\sim$ 2.48 Ga (Sarkar et al., 1993; Panigrahi et al., 2004; Bickford et al., 2014). Having established the subduction to collisional environment responsible for the evolution of the Kanker granites, it is essential to look for the coherence of the proposed tectonic environment with the existing tectonic models proposed for the Dongargarh and Malanjkhand granites.

Available geochemical studies indicate that Malanjkhand granites display I-type affinity (Pandit and Panigrahi, 2012). Also, it has been established that porphyry-type mineralization hosted by this granite was contemporaneous with its emplacement (Stein et al., 2004). The Malanjkhand granites are distributed into the fields of volcanic arc and syn-collisional granites in the tectonic discrimination diagram of Pearce et al. (1984) (refer to Figure 5 of Pandit and Panigrahi, 2012), Although porphyry copper deposits are generally related to convergent margin setting (Sillitoe, 2010), there are also evidences for their occurrences in the collisional environment such as Tibetan Orogen (Hou and Cook, 2009). In the collisional environment, the thermal anomaly associated with the collision could be the source for hydrothermal fluids responsible for the mineralization, as observed in the Malanjkhand granites.

The Dongargarh granite is a complex pluton, with both I- and A-type affinity (Narayana et al., 2000). Previous studies have attributed a continental rift setting for the evolution of the Dongargarh granite (Pandit and Panigrahi, 2012; Manikyamba et al., 2016). The available geochemical data on the intraplate Dongargarh granite, indicate that they are A_2 type granites. The A_2 type granites are considered to be post-orogenic, and are the product of crustal reworking (Eby, 1992; Bonin, 2007). The evolved hafnium isotopic signatures of the Dongargarh granite indicate the reworking of an older crust (Manikyamba et al., 2016). But the A_2 affinity of the Dongargarh granite negates the earlier postulated extensional back-arc or the continental rift environment (Pandit and Panigrahi, 2012; Manikyamba et al., 2016). Therefore, the Dongargarh granite can be related to the collapse of this collisional orogeny due to delamination and thermal relaxation.

To have a better understanding of the prevailing tectonic environment during the emplacement of the Kanker granites, it is imperative to know if any genetic relationship exists between the granites and adjacent supracrustal rocks. An island arc setting is proposed for the siliceous high Mg basalts (SHMB) from the 2.7 Ga Sonakhan Greenstone Belt (SGB), located on the eastern margin of the Kanker granite (Manu Prasanth et al., 2019). The field relationships indicate the intrusive nature of Kanker granites with the Sonakhan belt, suggesting that both lithologies are not contemporaneous (Manu Prasanth et al., 2018). Trace element signatures depict a depleted mantle source for the SGB basalts (Manu Prasanth et al., 2019), distinct from that of the Kanker granites. Geochemical and isotopic studies on the 2.5 Ga volcanic rocks of the Kotri Dongargarh Mobile Belt (KDMB) suggest that they were derived from a depleted mantle source and had evolved in an Andean type continental arc setting (Asthana et al., 2016; Khanna et al., 2019). Hence, it can be surmised that the supracrustals adjacent to the Kanker granites had a different source, and a convergent margin was active in the Bastar Craton during the Neoarchean and Early Proterozoic.

Hence, the granites of Kanker pluton evolved in a transitional geodynamic environment involving the subduction and collision during the Archean-Proterozoic transition. The proposed geodynamic environment can explain the origin of the Dongargarh and Malanjkhand granites, and also account for the mineralization associated with the latter. Compositional variations of the Kanker granites are attributed to variable crust-mantle interactions. Precise age and isotopic data will provide better clues on the sequence of emplacement of these granite types, constraining the sources and the extent of interactions between them. With these limitations, a craton scale geological model is beyond the scope of this contribution.

CONCLUSIONS

- Kanker granites are geochemically classified into sanukitoids, biotite and two-mica granites and hybrid granites.
- Two discrete end-member sources, i.e., the enriched mantle and an older felsic crust, and their variable interactions are responsible for the compositional diversity of the Kanker granites.
- The evolution of the Kanker granites can be accounted for a transitional geodynamic environment, involving subduction and collisional tectonics during the Archean-Proterozoic transition.
- The collisional tectonic regime can also be related to the porphyry mineralization in the Malanjkhand granite and the A_2 affinity of the Dongargarh granite.

DATA AVAILABILITY STATEMENT

All datasets generated for this study are included in the article/supplementary material.

AUTHOR CONTRIBUTIONS

AA: field work and initial draft preparation. RE: field work, petrography, geochemical analysis, and data processing. NV: field work and petrography. KH: field work and petrography. MR: conceptualisaion of problem, field work, data interpretation, and supervision. All authors have contributed equally to the data interpretation and writing of the paper.

FUNDING

INDEX project (CSIR-NGRI).

ACKNOWLEDGMENTS

The authors thank Director, CSIR-NGRI, for the permission to publish this work, which is an outcome of the INDEX project (NGRI/Lib/2020/Pub-31). This study forms part of the Ph.D. thesis of RE. We are grateful to Steven Denyszyn for efficient editorial handling. Critical reviews by two reviewers helped to significantly improve the earlier version. Drs. M. Satyanarayanan and A. Keshav Krishna are acknowledged for providing the whole-rock major and trace elemental data.

REFERENCES

Ahmad, T., Kaulina, T. V., Wanjari, N., Mishra, M. K., and Nitkina, E. A. (2009). "U–Pb zircon chronology and Sm–Nd isotopic characteristics of the Amgaon and Tirodi Gneissic Complex, Central Indian Shield: constraints on Precambrian crustal evolution," in *Precambrian Continental Growth And Tectonism*, eds V. K. Singh, and R. Chandra (New Delhi: Excel India Publishers), 137–138.

Asthana, D., Kumar, H., Balakrishnan, S., Xia, Q., and Feng, M. (2016). An early cretaceous analogue of the ∼2.5 Ga Malanjkhand porphyry Cu deposit, Central India. *Ore Geol. Rev*. 72, 1197–1212. doi: 10.1016/j.oregeorev.2015.10.015

Asthana, D., Kumar, S., Vind, A. K., Zehra, F., Kumar, H., and Pophare, A. M. (2018). Geochemical fingerprinting of ∼2.5 Ga forearc-arc-backarc related magmatic suites in the Bastar Craton, central India. *J. Asian Earth Sci*. 157, 218–234. doi: 10.1016/j.jseaes.2017.10.006

Bhowmik, S. K., Wilde, S. A., and Bhandari, A. (2011). Zircon U-Pb/Lu-Hf and monazite chemical dating of the Tirodi biotite gneiss: implication for latest Palaeoproterozoic to Early Mesoproterozoic orogenesis in the Central Indian Tectonic Zone. *Geol. J*. 46, 574–596. doi: 10.1002/gj.1299

Bickford, M. E., Basu, A., Kamenov, G. D., Mueller, P. A., Patranabis-Deb, S., and Mukherjee, A. (2014). Petrogenesis of 1000 Ma felsic tuffs, Chhattisgarh and Indravati basins, Bastar craton, India: geochemical and Hf isotope constraints. *J. Geol*. 122, 43–54. doi: 10.1086/674802

Bonin, B. (2004). Do coeval mafic and felsic magmas in post-collisional to within-plate regimes necessarily imply two contrasting, mantle and crustal, sources? a review. *Lithos* 78, 1–24. doi: 10.1016/j.lithos.2004.04.042

Bonin, B. (2007). A-type granites and related rocks: evolution of a concept, problems and prospects. *Lithos* 97, 1–29. doi: 10.1016/j.lithos.2006.12.007

Cawood, P. A., Hawkesworth, C. J., and Dhuime, B. (2013). The continental record and the generation of continental crust. *Bull. Geol. Soc. Am*. 125, 14–32. doi: 10.1130/B30722.1

Condie, K. C., and Kröner, A. (2008). When did plate tectonics begin? evidence from the geologic record. *Spec. Pap. Geol. Soc. Am*. 440, 281–294. doi: 10.1130/2008.2440(14)

Deshpande, G. G., Mohabey, N. K., and Deshpande, M. S. (1990). Petrography and tectonic setting of Dongargarh volcanics. *Visesa Prakasana-Bharatiya Bhuvaijñanika Sarveksana* 260–286.

Dhuime, B., Hawkesworth, C. J., Cawood, P. A., and Storey, C. D. (2012). A change in the geodynamics of continental growth 3 billion years ago. *Science* 335, 1334–1336. doi: 10.1126/science.1216066

Duggen, S., Portnyagin, M., Baker, J., Ulfbeck, D., Hoernle, K., Garbe-Schönberg, D., et al. (2007). Drastic shift in lava geochemistry in the volcanic-front to rear-arc region of the Southern Kamchatkan subduction zone: evidence for the transition from slab surface dehydration to sediment melting. *Geochim. Cosmochim. Acta* 71, 452–480. doi: 10.1016/j.gca.2006.09.018

Durrheim, R. J., and Mooney, W. D. (1991). Archean and Proterozoic crustal evolution: evidence from crustal seismology. *Geology* 19, 606–609. doi: 10.1130/0091-7613(1991)019<0606:AAPCEE>2.3.CO;2

Eby, G. N. (1992). Chemical subdivision of the A-type granitoids: petrogenetic and tectonic implications. *Geology* 20, 641–644. doi: 10.1130/0091-7613(1992)020<0641:CSOTAT>2.3.CO;2

Elangovan, R., Asokan, A. D., Pandit, D., and Ram Mohan, M. (2020). Magma chamber processes and geodynamic implications of the Pithora pluton, Bastar Craton, Central India. *Geol. J*. 55, 2738–2759. doi: 10.1002/gj.3534

Elangovan, R., Krishna, K., Vishwakarma, N., Hari, K. R., and Mohan, M. R. (2017). Interaction of coeval felsic and mafic magmas from the Kanker granite, Pithora region, Bastar Craton, Central India. *J. Earth Syst. Sci*. 126:92. doi: 10.1007/s12040-017-0886-z

Elliott, T. (2004). Tracers of the slab. *Geophys. Monogr. Ser*. 138, 23–45. doi: 10.1029/138GM03

French, J. E., Heaman, L. M., Chacko, T., and Srivastava, R. K. (2008). 1891–1883 Ma Southern Bastar–Cuddapah mafic igneous events, India: a newly recognized large igneous province. *Precambrian Res*. 160, 308–322. doi: 10.1016/j.precamres.2007.08.005

Ghosh, J. G. (2004). 3.56 Ga tonalite in the central part of the Bastar craton, India: oldest Indian date. *J. Asian Earth Sci*. 23, 359–364. doi: 10.1016/S1367-9120(03)00136-6

Halla, J. (2005). Late Archean high-Mg granitoids (sanukitoids) in the southern Karelian domain, eastern Finland: Pb and Nd isotopic constraints on crust-mantle interactions. *Lithos* 79, 161–178. doi: 10.1016/j.lithos.2004.05.007

Halla, J., van Hunen, J., Heilimo, E., and Hölttä, P. (2009). Geochemical and numerical constraints on Neoarchean plate tectonics. *Precambrian Res*. 174, 155–162. doi: 10.1016/j.precamres.2009.07.008

Harris, N. B. W., and Inger, S. (1992). Trace element modelling of pelite-derived granites. *Contrib. Mineral. Petrol*. 110, 46–56. doi: 10.1007/BF00310881

Harris, N. B. W., Pearce, J. A., and Tindle, A. G. (1986). Geochemical characteristics of collision-zone magmatism. *Geol. Soc. Spec. Publ*. 19, 67–81. doi: 10.1144/GSL.SP.1986.019.01.04

Hawkesworth, C. J., Turner, S. P., McDermott, F., Peate, D. W., and Van Calsteren, P. (1997). U-Th isotopes in arc magmas: implications for element transfer from the subducted crust. *Science* 276, 551–555. doi: 10.1126/science.276.5312.551

Heilimo, E., Halla, J., and Hölttä, P. (2010). Discrimination and origin of the sanukitoid series: geochemical constraints from the Neoarchean western Karelian Province (Finland). *Lithos* 115, 27–39. doi: 10.1016/j.lithos.2009.11.001

Hopkinson, T. N., Harris, N. B. W., Warren, C. J., Spencer, C. J., Roberts, N. M. W., Horstwood, M. S. A., et al. (2017). The identification and significance of pure sediment-derived granites. *Earth Planet. Sci. Lett*. 467, 57–63. doi: 10.1016/j.epsl.2017.03.018

Hou, Z., and Cook, N. J. (2009). Metallogenesis of the Tibetan collisional orogen: a review and introduction to the special issue. *Ore Geol. Rev*. 36, 2–24. doi: 10.1016/j.oregeorev.2009.05.001

Hussain, M. F., Mondal, M. E. A., and Ahmad, T. (2004). Petrological and geochemical characteristics of Archean gneisses and granitoids from Bastar Craton, Central India - Implication for subduction related magmatism. *Gondwana Res*. 7, 531–537. doi: 10.1016/S1342-937X(05)70803-0

Janoušek, V., Moyen, J.-F., Martin, H., Erban, V., and Farrow, C. (2016). *Geochemical Modelling of Igneous Processes–Principles and Recipes in R Language*. Berlin: Springer.

Jayananda, M., Dey, S., and Aadhiseshan, K. R. (2020). "Evolving early earth: Insights from peninsular India," in *Geodynamics of the Indian Plate: Evolutionary Perspectives*, eds. N. Gupta and S. K. Tandon (Cham: Springer International Publishing), 5–103. doi: 10.1007/978-3-030-15989-4_2

Keller, C. B., and Schoene, B. (2012). Statistical geochemistry reveals disruption in secular lithospheric evolution about 2.5Gyr ago. *Nature* 485, 490–493. doi: 10.1038/nature11024

Khanna, T. C., Bizimis, M., Barbeau, D. L., Keshav Krishna, A., and Sesha Sai, V. V. (2019). Evolution of ca. 2.5 Ga dongargarh volcano-sedimentary supergroup, Bastar craton, Central India: constraints from zircon U-Pb geochronology, bulk-rock geochemistry and Hf-Nd isotope systematics. *Earth Sci. Rev*. 190, 273–309. doi: 10.1016/j.earscirev.2018.11.014

Krishna, A. K., Khanna, T. C., and Mohan, K. R. (2016). Rapid quantitative determination of major and trace elements in silicate rocks and soils employing fused glass discs using wavelength dispersive X-ray fluorescence spectrometry. *Spectrochim. Acta B At. Spectrosc*. 122, 165–171. doi: 10.1016/j.sab.2016.07.004

La Flèche, M. R., Camire, G., and Jenner, G. A. (1998). Geochemistry of post-Acadian, Carboniferous continental intraplate basalts from the Maritimes Basin, Magdalen islands, Quebec, Canada. *Chem. Geol*. 148, 115–136. doi: 10.1016/S0009-2541(98)00002-3

Laurent, O., Martin, H., Doucelance, R., Moyen, J. F., and Paquette, J. L. (2011). Geochemistry and petrogenesis of high-K "sanukitoids" from the Bulai pluton, Central Limpopo Belt, South Africa: implications for geodynamic changes at the Archaean-Proterozoic boundary. *Lithos* 123, 73–91. doi: 10.1016/j.lithos.2010.12.009

Laurent, O., Martin, H., Moyen, J. F., and Doucelance, R. (2014). The diversity and evolution of late-Archean granitoids: evidence for the onset of "modern-style" plate tectonics between 3.0 and 2.5 Ga. *Lithos* 205, 208–235. doi: 10.1016/j.lithos.2014.06.012

Le Maitre, R. W (1989). *A Classification of Igneous Rocks and Glossary of Terms: Recommendations of the International Union of Geological Sciences and Submissions on the Systematics of Igneous Rocks*. Oxford: Blackwell Scientific Publications. p. 193.

Lee, C. T. A., Yeung, L. Y., McKenzie, N. R., Yokoyama, Y., Ozaki, K., and Lenardic, A. (2016). Two-step rise of atmospheric oxygen linked to the growth of continents. *Nat. Geosci*. 9, 417–424. doi: 10.1038/ngeo2707

Liao, A. C. Y., Shellnutt, J. G., Hari, K. R., Denyszyn, S. W., Vishwakarma, N., and Verma, C. B. (2019). A petrogenetic relationship between 2.37 Ga boninitic dyke swarms of the Indian Shield: evidence from the Central Bastar Craton and the NE Dharwar Craton. *Gondwana Res*. 69, 193–211. doi: 10.1016/j.gr.2018.12.007

Manikyamba, C., Santosh, M., Kumar, B. C., Rambabu, S., Tang, L., Saha, A., et al. (2016). Zircon U-Pb geochronology, Lu-Hf isotope systematics, and geochemistry of bimodal volcanic rocks and associated granitoids from Kotri Belt, Central India: implications for Neoarchean–Paleoproterozoic crustal growth. *Gondwana Res*. 38, 313–333. doi: 10.1016/j.gr.2015.12.008

Manu Prasanth, M. P., Hari, K. R., Chalapathi Rao, N. V., Hou, G., and Pandit, D. (2018). An island-arc tectonic setting for the Neoarchean Sonakhan Greenstone Belt, Bastar Craton, Central India: Insights from the chromite mineral chemistry and geochemistry of the siliceous high-Mg basalts (SHMB). *Geol. J*. 53, 1526–1542. doi: 10.1002/gj.2971

Manu Prasanth, M. P., Hari, K. R., Chalapathi Rao, N. V., Santosh, M., Hou, G., Tsunogae, T., et al. (2019). Neoarchean suprasubduction zone magmatism in the Sonakhan greenstone belt, Bastar Craton, India: implications for subduction initiation and melt extraction. *Geol. J*. 54, 3980–4000. doi: 10.1002/gj.3398

Martin, H., Moyen, J. F., and Rapp, R. (2009). The sanukitoid series: magmatism at the archaean-proterozoic transition. *Earth Environ. Sci. Trans. R. Soc. Edinburgh*. 100, 15–33. doi: 10.1017/S1755691009016120

Meert, J. G., Pandit, M. K., Pradhan, V. R., Banks, J., Sirianni, R., Stroud, M., et al. (2010). Precambrian crustal evolution of Peninsular India: a 3.0-billion-year odyssey. *J. Asian Earth Sci*. 39, 483–515. doi: 10.1016/j.jseaes.2010.04.026

Mikkola, P., Huhma, H., Heilimo, E., and Whitehouse, M. (2011). Archean crustal evolution of the Suomussalmi district as part of the Kianta Complex, Karelia: constraints from geochemistry and isotopes of granitoids. *Lithos* 125, 287–307. doi: 10.1016/j.lithos.2011.02.012

Mohan, M. R., Asokan, A. D., and Wilde, S. A. (2019). Crustal growth of the Eastern Dharwar Craton: a Neoarchean collisional orogeny? *Geol. Soc. London Spec. Publ*. SP489-2019–108. doi: 10.1144/SP489-2019-108

Mohanty, S. P. (2015). Palaeoproterozoic supracrustals of the Bastar Craton: dongargarh supergroup and sausar group. *Geol. Soc. Mem*. 43, 151–164. doi: 10.1144/M43.11

Mondal, M. E. A., Hussain, M. F., and Ahmad, T. (2006). Continental growth of Bastar craton, Central Indian shield during precambrian via multiphase subduction and lithospheric extension/rifting: evidence from geochemistry of gneisses, granitoids and mafic dykes. *J. Geosci*. 49, 137–151.

Mondal, M. E. A., Hussain, M. F., and Ahmad, T. (2019). Archean granitoids of the Bastar Craton, Central India. *Geol. Soc. London Spec. Publ*. SP489-2019–311. doi: 10.1144/SP489-2019-311

Moyen, J. F., and Laurent, O. (2018). Archaean tectonic systems: a view from igneous rocks. *Lithos* 302–303, 99–125. doi: 10.1016/j.lithos.2017.11.038

Moyen, J. F., Laurent, O., Chelle-Michou, C., Couzinié, S., Vanderhaeghe, O., Zeh, A., et al. (2017). Collision vs. subduction-related magmatism: two contrasting ways of granite formation and implications for crustal growth. *Lithos* 277, 154–177. doi: 10.1016/j.lithos.2016.09.018

Moyen, J. F., Martin, H., Jayananda, M., and Auvray, B. (2003). Late archaean granites: a typology based on the Dharwar Craton (India). *Precambrian Res*. 127, 103–123. doi: 10.1016/S0301-9268(03)00183-9

Narayana, B. L., Mallikharjuna Rao, J., Subba Rao, M. V., Murthy, N. N., and Divakara Rao, V. (2000). Geochemistry and origin of early proterozoic Dongargarh Rapakivi Granite Complex, Central India - an

example for magma mixing and differentiation. *Gondwana Res.* 3, 507–520. doi: 10.1016/S1342-937X(05)70757-7

O'Connor, J. T. (1965). A classification for quartz-rich igneous rocks. *Geol. Surv. Prof. Pap*. 525:79.

Pandit, D., and Panigrahi, M. K. (2012). Comparative petrogenesis and tectonics of Paleoproterozoic Malanjkhand and Dongargarh granitoids, Central India. *J. Asian Earth Sci*. 50, 14–26. doi: 10.1016/j.jseaes.2012.01.017

Panigrahi, M. K., Bream, B. R., Misra, K. C., and Naik, R. K. (2004). Age of granitic activity associated with copper–molybdenum mineralization at Malanjkhand, Central India. *Miner. Depos*. 39, 670–677. doi: 10.1007/s00126-004-0441-0

Pearce, J. A., Harris, N. B. W., and Tindle, A. G. (1984). Trace element discrimination diagrams for the tectonic interpretation of granitic rocks. *J. Petrol*. 25, 956–983. doi: 10.1093/petrology/25.4.956

Rajesh, H. M., Mukhopadhyay, J., Beukes, N. J., Gutzmer, J., Belyanin, G. A., and Armstrong, R. A. (2009). Evidence for an early Archaean granite from Bastar craton, India. *J. Geol. Soc. London*. 166, 193–196. doi: 10.1144/0016-76492008-089

Ramakrishnan, M. (1990). Crustal development in southern Bastar central Indian craton. *Visesa Prakasana-Bharatiya Bhuvaijñanika Sarveksana* 44–66.

Rapp, R. P., Shimizu, N., Norman, M. D., and Applegate, G. S. (1999). Reaction between slab-derived melts and peridotite in the mantle wedge: experimental constraints at 3.8 GPa. *Chem. Geol*. 160, 335–356. doi: 10.1016/S0009-2541(99)00106-0

Reimink, J. R., Chacko, T., Stern, R. A., and Heaman, L. M. (2016). The birth of a cratonic nucleus: lithogeochemical evolution of the 4.02-2.94 Ga Acasta Gneiss Complex. *Precambrian Res*. 281, 453–472. doi: 10.1016/j.precamres.2016.06.007

Roy, A., Kagami, H., Yoshida, M., Roy, A., Bandyopadhyay, B. K., and Chattopadhyay, A. (2006). Rb–Sr and Sm–Nd dating of different metamorphic events from the sausar mobile belt, central India: implications for proterozoic crustal evolution. *J. Asian Earth Sci*. 26, 61–76. doi: 10.1016/j.jseaes.2004.09.010

Santosh, M., Hari, K. R., He, X. F., Han, Y. S., and Manu Prasanth, M. P. (2018). Oldest lamproites from Peninsular India track the onset of Paleoproterozoic plume-induced rifting and the birth of Large Igneous Province. *Gondwana Res.* 55, 1–20. doi: 10.1016/j.gr.2017.11.005

Santosh, M., Tsunogae, T., Yang, C. X., Han, Y. S., Hari, K. R., Prasanth, M. P. M., et al. (2020). The Bastar craton, central India: a window to Archean – Paleoproterozoic crustal evolution. *Gondwana Res*. 79, 157–184. doi: 10.1016/j.gr.2019.09.012

Sarkar, G., Corfu, F., Paul, D. K., McNaughton, N. J., Gupta, S. N., and Bishui, P. K. (1993). Early Archean crust in Bastar Craton, Central India-a geochemical and isotopic study. *Precambrian Res*. 62, 127–137. doi: 10.1016/0301-9268(93)90097-L

Satyanarayanan, M., Balaram, V., Sawant, S. S., Subramanyam, K. S. V., Krishna, G. V., Dasaram, B., et al. (2018). Rapid determination of REEs, PGEs, and other trace elements in geological and environmental materials by high resolution inductively coupled plasma mass spectrometry. *At. Spectrosc*. 39, 1–15.

Shand, S. J. (1943). *The Eruptive Rocks*. New York, NY: John Wiley Publishers. p. 444.

Shirey, S. B., and Hanson, G. N. (1984). Mantle-derived Archaean monozodiorites and trachyandesites. *Nature* 310, 222–224. doi: 10.1038/310222a0

Sillitoe, R. H. (2010). Porphyry copper systems. *Econ. Geol*. 105, 3–41. doi: 10.2113/gsecongeo.105.1.3

Sizova, E., Gerya, T., Brown, M., and Perchuk, L. L. (2010). Subduction styles in the Precambrian: insight from numerical experiments. *Lithos* 116, 209–229. doi: 10.1016/j.lithos.2009.05.028

Smithies, R. H., and Champion, D. C. (2000). The Archaean high-Mg diorite suite: links to tonalite–trondhjemite–granodiorite magmatism and implications for early Archaean crustal growth. *J. Petrol*. 41, 1653–1671. doi: 10.1093/petrology/41.12.1653

Srivastava, R. K., Singh, R. K., and Verma, S. P. (2004). Neoarchaean mafic volcanic rocks from the southern Bastar greenstone belt, Central India: petrological and tectonic significance. *Precambrian Res*. 131, 305–322. doi: 10.1016/j.precamres.2003.12.013

Steenfelt, A., Garde, A. A., and Moyen, J. F. (2005). Mantle wedge involvement in the petrogenesis of Archaean gray gneisses in West Greenland. *Lithos* 79, 207–228. doi: 10.1016/j.lithos.2004.04.054

Stein, H. J., Hannah, J. L., Zimmerman, A., Markey, R. J., Sarkar, S. C., and Pal, A. B. (2004). A 2.5 Ga porphyry Cu-Mo-Au deposit at Malanjkhand, central India: Implications for Late Archean continental assembly. *Precambrian Res*.134,189–226. doi: 10.1016/j.precamres.2004.05.012

Sun, S.-S., and McDonough, W. F. (1989). Chemical and isotopic systematics of oceanic basalts: implications for mantle composition and processes. *Geol. Soc. London Spec. Publ*. 42, 313–345. doi: 10.1144/GSL.SP.1989.042.01.19

Sylvester, P. J. (1998). Post-collisional strongly peraluminous granites. *Lithos* 45, 29–44. doi: 10.1016/S0024-4937(98)00024-3

Woodhead, J. D., Hergt, J. M., Davidson, J. P., and Eggins, S. M. (2001). Hafnium isotope evidence for "conservative" element mobility during subduction zone processes. *Earth Planet. Sci. Lett*. 192, 331–346. doi: 10.1016/S0012-821X(01)00453-8

Conflict of Interest: The authors declare that the research was conducted in the absence of any commercial or financial relationships that could be construed as a potential conflict of interest.

The handling editor declared a past co-authorship with one of the authors NV.

frontiers in Earth Science

ORIGINAL RESEARCH
published: 09 July 2020
doi: 10.3389/feart.2020.00236

Early Evolution of Himalayan Orogenic Belt and Generation of Middle Eocene Magmatism: Constraint From Haweng Granodiorite Porphyry in the Tethyan Himalaya

Wei-Qiang Ji[1], Fu-Yuan Wu[1], Jia-Min Wang[1], Xiao-Chi Liu[1], Zhi-Chao Liu[2], Zhiyong Zhang[1], Wenrong Cao[3], Jian-Gang Wang[1] and Chang Zhang[1]*

[1] State Key Laboratory of Lithospheric Evolution, Institute of Geology and Geophysics, Chinese Academy of Sciences, Beijing, China, [2] School of Earth Sciences and Engineering, Sun Yat-sen University, Guangzhou, China, [3] Department of Geological Sciences and Engineering, University of Nevada, Reno, Reno, NV, United States

OPEN ACCESS

Edited by:
Steven W. Denyszyn, The University of Western Australia, Australia

Reviewed by:
Anders John McCarthy, University of Bristol, United Kingdom
Kezhang Qin, Chinese Academy of Sciences, China

***Correspondence:**
Wei-Qiang Ji
jiweiqiang@mail.iggcas.ac.cn

Specialty section:
This article was submitted to Petrology, a section of the journal Frontiers in Earth Science

Received: *14 March 2020*
Accepted: *03 June 2020*
Published: *09 July 2020*

Citation:
Ji W-Q, Wu F-Y, Wang J-M, Liu X-C, Liu Z-C, Zhang Z, Cao W, Wang J-G and Zhang C (2020) Early Evolution of Himalayan Orogenic Belt and Generation of Middle Eocene Magmatism: Constraint From Haweng Granodiorite Porphyry in the Tethyan Himalaya. Front. Earth Sci. 8:236. doi: 10.3389/feart.2020.00236

Although the Himalayan orogenic belt is dominant by Oligocene to Miocene leucogranites, it initiated magmatic activity from middle Eocene. However, the exact distribution and genesis of early magmatism are yet to be resolved. This study identified new outcrops of middle Eocene magmatism, Haweng granodiorite porphyries, from northwest Langkazi in the northern Tethyan Himalaya, southern Tibet. Identical zircon U–Pb ages were obtained by secondary ion mass spectrometry (17JT13: 45.3 ± 0.4 Ma; 17JT16: 44.5 ± 0.8 Ma) and laser ablation inductively coupled plasma mass spectrometry (LA-ICP-MS) (17JT15: 44.3 ± 0.8 Ma; 12FW75: 44.4 ± 0.6 Ma) methods for different outcrops there. Titanite LA-ICP-MS U–Pb analyses also gave consistent lower intercept ages for samples 17JT13 (45.3 ± 0.5 Ma) and 17JT15 (44.5 ± 0.6 Ma). Zircon metamorphic rims of sample 17JT15 recorded a younger thermal event of 29.9 ± 0.4 Ma. The analyzed samples possess high SiO_2 (69.98–73.53 wt.%), Al_2O_3 (15.07–16.15 wt.%), variable Na_2O (3.94–5.81 wt.%) with Na_2O/K_2O ratios of 1.57–7.88, and A/CNK values of 1.08–1.27 indicative of sodic peraluminous series. They show variable Sr (342–481 ppm) and Rb (37.9–133 ppm) concentrations and low Rb/Sr ratios (0.10–0.39), radiogenic Sr isotopes [$^{87}Sr/^{86}Sr_{(t)}$: 0.7190–0.7251], and unradiogenic Nd–Hf isotopes with $\varepsilon_{Nd}(t)$ values of −13.54 to −11.55 and $\varepsilon_{Hf}(t)$ values of −11.97 to −9.37, respectively. The variation of major and trace elements, such as increases in Na_2O and Sr and decreases in K_2O and Rb, resulted from cumulation of plagioclase and crystal fractionation of K-feldspar during magma evolution. The Haweng granodiorite porphyries were derived from partial melting of dominant amphibolites and variable metasedimentary rocks. The newly identified outcrops help conform the EW trending middle Eocene magmatic belt along the Yarlung Tsangpo suture zone, resulting from breakoff of the Neo-Tethyan slab at *ca.* 45 Ma.

Keywords: middle Eocene magmatism, granodiorite porphyry, Tethyan Himalaya, high Sr/Y, slab breakoff

INTRODUCTION

The Cenozoic Himalayan orogeny was accompanied by long-lasting magmatism. Deciphering the petrogenesis of these magmatic rocks is therefore a key issue to understand the formation and evolution of the orogenic belt. The Himalaya initiated crustal anatexis from middle Eocene after the India–Asia continental collision (Zeng et al., 2011; Hou et al., 2012; Carosi et al., 2015; and references therein), which lasted until late Miocene (*ca.* 44–7 Ma, Wu et al., 2015, 2020). Melt generation and granite emplacement are mainly related to the exhumation stage of the Greater Himalayan Sequence (GHS) during the late Oligocene to early Miocene (Harris and Massey, 1994; Hodges, 2000; Searle, 2013; Zeng and Gao, 2017).

With respect to this dominant magmatic stage, less attention has been paid to the magmatism during prograde metamorphism, especially initial stage of partial melting. The early partial melting includes two main styles: (1) anatexis during prograde/peak metamorphism of the GHS as reflected by anatectic melt inclusions within garnet (Carosi et al., 2015, 2019; Iaccarino et al., 2015) and (2) partial melting of thickened lower crust along the northern margin of Himalaya (Aikman et al., 2008; Zeng et al., 2011; Hou et al., 2012). Although evidence of early anatexis during prograde metamorphism was reported from frontal Himalaya, the ubiquitous existences of monazites of this stage preclude the possibility of widely partial melting, as the melting would consume monazites and erase their records of earlier metamorphism (Gibson et al., 2004; Kohn et al., 2005). The early magmatism, which is of relatively large scale and has been dated by zircon U–Pb method, is locally distributed and limited to the Yardoi dome and adjacent area from northeastern Himalaya (Aikman et al., 2008; Zeng et al., 2011; Hou et al., 2012). Furthermore, only some coeval granitic dikes were found in the Ramba dome (Liu et al., 2014).

Thus, more outcrops of Himalayan granites are necessary to reveal the distribution and generation of early Cenozoic magmatism, which is important to constrain the deep dynamic process of Himalayan orogenic evolution. And this study identified new exposure of middle Eocene granitic rocks from northwest of Langkazi county along the north margin of Himalaya. Zircon U–Pb age and Hf isotope, whole-rock element and Sr–Nd–Hf isotopes are invoked to reveal the petrogenesis and early evolution of the Himalayan orogenic belt.

GEOLOGICAL BACKGROUND AND SAMPLES

Geological Units of Southern Tibet

The Himalayan–Tibetan orogenic belt was generated by the India–Asia continental collision, which initiated at around 60 Ma along the Yarlung Tsangpo suture zone (YTSZ) (Wu et al., 2014; Hu et al., 2016; and references therein). It consists of several east–west trending geological blocks, namely, the Himalaya, Lhasa, Qiangtang, Songpan–Ganze, and Kunlun terranes from south to north. To the south of YTSZ, the Lhasa terrane was an active continental margin (the Gangdese arc) accompanying the northward Neo-Tethyan subduction (Searle et al., 1987). The arc magmatic activity in the southern margin of the Lhasa terrane lasted from middle Triassic to Eocene (cf. Wen et al., 2008; Ji et al., 2009; Wang et al., 2016) until the breakoff of the Neo-Tethyan oceanic slab at around 45 Ma (Ji et al., 2016 and references therein).

The Himalaya, to the south of YTSZ, can be divided into four tectonic belts including the Sub-Himalaya, the Lesser Himalayan Sequence (LHS), the GHS, and the Tethyan Himalayan Sequence (THS), separated by several faults and shear zones including the Main Boundary Thrust (MBT), the Main Central Thrust (MCT), and the South Tibetan Detachment System (STDS) (**Figure 1A**) (Hodges, 2000; Yin, 2006). The Sub-Himalaya, the southernmost and structurally lowest lithotectonic belt, is composed of the synorogenic sedimentary units of the Siwalik Group, bounded at the top by the MBT. In the hanging wall of the MBT, the LHS encompasses Paleoproterozoic to early Mesoproterozoic metasedimentary rocks, and Paleoproterozoic granites. Bound by the MCT at the base and STDS at the top, the GHS is the metamorphic core of the Himalaya comprising high-grade metasedimentary and meta-igneous rocks with age ranging from Neoproterozoic to Ordovician. The GHS was intruded by leucogranitic rocks of various scales varying from sills and dikes to plutons, especially in its upper part blew the brittle strand of the STDS (Debon et al., 1986; Searle et al., 2010). Above the STDS, the THS consists of continuous sedimentary sequence from Paleozoic to Eocene, which belongs to a passive continental margin during the northward Neo-Tethyan subduction. The THS has been deformed during the Cenozoic India–Asia collision, but the metamorphic grade is very low with the highest of greenschist facies.

Early Cenozoic Evolution of Southern Tibet

After the initial India–Asia continental collision, the Indian continent began to underthrust beneath the southern margin of Asia continent (i.e., the Lhasa terrane) because of drag of the attached Neo-Tethyan oceanic slab. The shallow crust of Indian continent was decoupled and stayed at the top, forming the THS, whereas the deep crust was dragged to various depths, parts of which exhumed later in the form of (ultra) high-pressure rocks, such as the eclogites in the Kagan Valley and Tso Morori in the northwest Himalaya (e.g., de Sigoyer et al., 2000; Kaneko et al., 2003), and the GHS extruded southward between the MCT and the STDS (Burchfiel et al., 1992; Le Fort, 1996). The YTSZ and adjacent regions underwent fast crustal thickening after initial collision as indicated by crustal deformation, development of fold and thrust belt, and magmatism. These N-S contractional structures were intruded by undeformed middle Eocene granitic rocks (45–44 Ma) in several locations along the YTSZ (Ding et al., 2005; Pullen et al., 2011). As the leading edge of collision belt, regions adjacent to the YTSZ were prone to obtain thickened crust first, and they already had thickened crust by middle Eocene suggested by the widespread development of adakitic rocks along strike (e.g., Guan et al., 2012; Ji et al., 2012; Liu et al., 2014; Ma et al., 2014; Shellnutt et al., 2014). They should have maintained

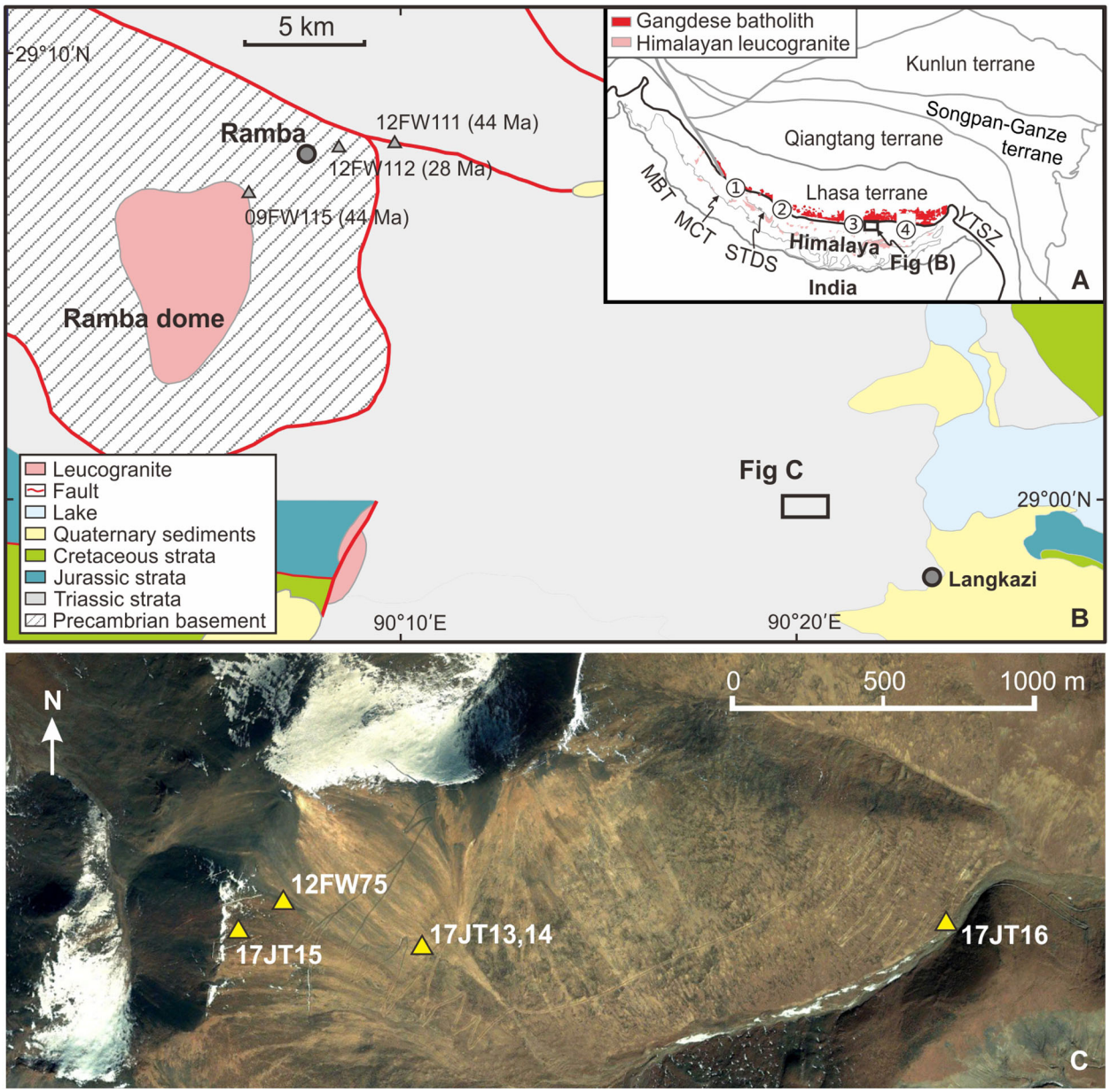

FIGURE 1 | Geological map of the study area and sample location. **(A)** Geological background of study area and distribution of identified middle Eocene magmatic rocks along the suture zone. **(B)** Simplified geological map of the study area. **(C)** Outcrops and distribution of samples (base map from Google Earth). Abbreviations: MBT, Main Boundary Thrust; MCT, Main Central Thrust; STDS, South Tibetan Detachment System; YTSZ, Yarlung Tsang suture zone. Middle Eocene magmatic rocks: ① Xiao Gurla Range (Pullen et al., 2011); ② Niuku (Ding et al., 2005); ③ Langshan OIB (Oceanic island basalt)–type gabbro (Ji et al., 2016); ④ Yardoi area (Aikman et al., 2008; Zeng et al., 2011; Hou et al., 2012).

the thickest crust of the Tibet with a present thickness greater than 70 km on the basis of geophysical observation (cf. Zhao et al., 2001; Nábělek et al., 2009).

The early process of crustal thickening was not limited to the suture zone but propagated southward quickly. The THS, the structurally highest units of the Himalayan orogenic belt, developed horizontal shortening and regional fold and thrust belt during early–middle Eocene (*ca.* 50–45 Ma: Ratschbacher et al., 1994; Wiesmayr and Grasemann, 2002), and the main stage of shortening and crustal thickening for the shallow crust could have completed prior to middle Eocene (44.1 ± 1.2 Ma, Aikman et al., 2008 and references therein). The crustal thickening was documented by early Eocene growth of garnet in the middle crust in the Mabja (54–52 Ma) and Kangmar (51–49 Ma) domes from central Himalaya (Smit et al., 2014). In the eastern Himalaya, the schists from Yardoi dome underwent Eocene (48–36 Ma) prograde metamorphism (Ding et al., 2016a,b). The authors regarded these upper crust rocks as part of the upper

level of the GHS, which were buried to 20–30 km due to shallow subduction of the Indian continent beneath the Lhasa terrane. The garnet amphibolite and granitic gneiss recorded high amphibolite and granulite facies metamorphism in the Yardoi dome at 45.0 ± 1.0 and 47.6 ± 1.8 Ma, respectively, followed by anatexis at 43.5 ± 1.3 Ma (Zeng et al., 2011; Gao et al., 2012). The middle Eocene granitic rocks (46–42 Ma) from Yardoi dome and adjacent areas show adakitic affinities indicating thickened crust already occurred at that time (Zeng et al., 2011; Hou et al., 2012). Thus, southern Tibet was located in an N-S compressional setting in the early Cenozoic, accompanied with continental subduction, structural shortening, crustal thickening, and prograde metamorphism.

The study area is located in the north margin of the THS (**Figure 1A**). Grandiorite porphyry outcrops were identified from the Haweng deposit, northwest of the Langkazi County (**Figure 1B**). The granodiorite porphyry intruded into the late Triassic Nieru Formation, consisting of slate, siltstone, meta-sandstone, and crystalline limestone, as dikes or stocks of different scale from the mountainside to the mountain ridge/peak (**Figures 1C**, **2**). Samples 17JT13 and 17JT14 were collected from the same outcrop in the mountainside (**Figure 1C**). The granodiorite porphyry here intruded into the sandstone of Nieru Formation and developed sandstone enclave (**Figure 2**). Sample 12FW75 was collected in a higher location close to the mountain ridge, whereas sample 17JT15 was from the mountain ridge, namely, a small peak. The outcrop of sample 17JT15 was of large scale with severely cracked intrusive rocks at the top (**Figure 2A**). Sample 17JT16 was a rolling stone collected in the valley, which has least mafic minerals and is different from the investigated outcrop samples. It is used to reveal the potential magmatic evolution. All the intrusive rocks show porphyritic texture (**Figures 2C,D**), and the phenocrysts are mainly plagioclase, quartz, K-feldspar, small biotite, and a some muscovite (**Figures 2E,F**), whereas the accessory minerals include zircon, apatite, and titanite.

ANALYTICAL METHODS

Zircon secondary ion mass spectrometry (SIMS) U–Pb dating for samples 17JT13 and 17JT16 and laser ablation inductively coupled plasma mass spectrometry (LA-ICP-MS) U–Pb and Hf isotopic analysis for sample 12FW75 were performed at the Institute of Geology and Geophysics, Chinese Academy of Sciences (IGGCAS), Beijing, China. Cathodoluminescence (CL) images were used for selection of zircon grain and dating position. Zircon SIMS U–Pb dating was conducted using a Cameca IMS-1280, following the analytical procedures described by Li et al. (2009). The ellipsoidal spot is approximately 10 × 15 μm in size. Calibration of Pb/U ratios is relative to the standard zircon Plešovice. Zircon LA-ICP-MS U–Pb analysis for sample 12FW75 was performed on an Agilent 7500a Q-ICP-MS equipped with a 193-nm Excimer ArF laser ablation system (Geolas plus), using zircon 91500 as external standard with circle spot of 30 μm in diameter. The detailed analytical procedures for zircon U–Pb age can be found in Xie et al. (2008). Zircon Hf isotopic analyses were conducted on the dated spots by the MC-ICPMS method (Wu et al., 2006) using a Thermo-Finnigan Neptune multicollector connected to the same laser ablation system. Data reduction was carried out using Isoplot/Ex v 3.0 program (Ludwig, 2003). The in-house zircon U–Pb age standard for SIMS analysis, Qinghu, yielded $^{206}Pb/^{238}U$ age of 160.8 ± 1.7 Ma [Mean Square of Weighted Deviates (MSWD), = 0.34, n = 8], whereas the zircon standards for LA-ICP-MS analyses gave a mean age of 604.6 ± 6.4 Ma (MSWD = 0.13, n = 13) for GJ1. These obtained standard ages are consistent with the recommended values (Elhlou et al., 2006; Li et al., 2009). The $^{176}Hf/^{177}Hf$ ratios for zircons GJ1 and Mud Tank are 0.282010 ± 9 (MSWD = 4.2, n = 24) and 0.282506 ± 6 (MSWD = 3.1, n = 21), respectively, agreeing well with the recommended values (Woodhead and Hergt, 2005; Elhlou et al., 2006).

Zircon (17JT15) and titanite (17JT13 and 17JT15) U–Pb analyses were performed at the Beijing Quick-Thermo Science & Technology Co., Ltd., using an ESI New Wave NWR 193^{UC} (TwoVol2) laser ablation system connected to an Agilent 8900 ICP–QQQ. Individual zircon/titanite grains (mounted and polished in epoxy) were ablated in a constant stream of He that is mixed downstream with N_2 and Ar before entering the torch region of the ICP–QQQ. After warm-up of the ICP–QQQ and connection with the laser ablation system, the ICPMS is first tuned for robust plasma conditions by optimizing laser and ICP–QQQ setting and monitoring $^{232}Th^{16}O^+/^{232}Th^+$ ratios (always ≤ 0.2%) and $^{238}U^+/^{232}Th^+$ ratios (always between 0.95 and 1.05), while ablating NIST SRM 612 in line scan mode. 91500 zircon and Plešovice zircon were used as primary and secondary reference materials, respectively, for zircon U–Pb age determination. OLT-1 titanite and Fish Canyon Tuff titanite were used as primary and secondary reference materials, respectively, during titanite U–Pb age determination. Background subtraction and correction for laser downhole elemental fractionation were performed using the Iolite data reduction package within the Wavemetrics Igor Pro data analysis software (Paton et al., 2010). The analytical spots for zircon and titanite are 15 and 40 μm in diameter, respectively. Plešovice zircon gave mean ages of 337.7 ± 2.4 Ma (MSWD = 0.1, n = 31), whereas the titanite standard (Fish Canyon Tuff) had a lower intercept of 29.2 ± 1.0 Ma (MSWD = 2.6; n = 44). These dating results for LA-ICP-MS analyses are consistent with the recommended values within errors (Schmitz and Bowring, 2001; Sláma et al., 2008).

Whole-rock major and trace elements were measured by PANalytical Axios XRF and Agilent 7700x ICP-MS, respectively, at ALS Chemex Company (Guangzhou, China). The analytical precision and accuracy for major elements are better than 5 and 2%, respectively, and for trace elements are better than 10 and 10%, respectively. Whole-rock Sr–Nd–Hf isotopes of Sample 12FW75 were separated in a combined procedure from a single sample digestion according to the procedure of Yang et al. (2010), and then $^{87}Sr/^{86}Sr$, $^{143}Nd/^{144}Nd$, and $^{176}Hf/^{177}Hf$ were analyzed by multicollector inductively coupled plasma mass spectrometry (MC-ICP-MS) at IGGCAS following the methods of Yang et al. (2010, 2011a,b), respectively. The total procedural blanks measured for Lu, Hf, Rb, Sr, Sm, and Nd were less than 10, 50,

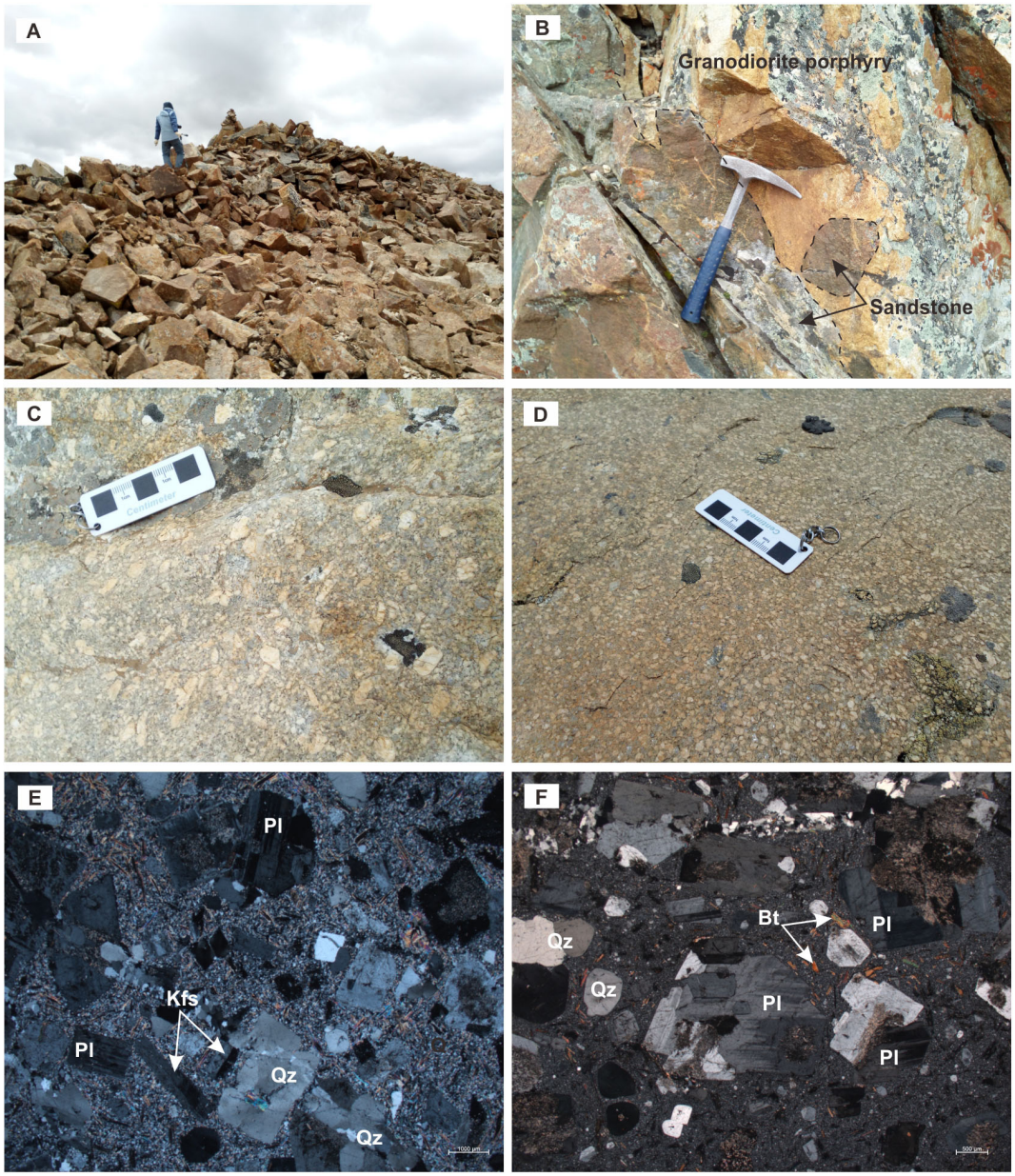

FIGURE 2 | Field pictures and micrographs for Haweng granodiorite porphyries. **(A,C,E)** Are for sample 17JT15, whereas **(B,D,F)** are for sample 17JT13. Abbreviations: Bt, biotite; Kfs, K-feldspar; Pl, plagioclase; Qz, quartz.

50, 100, 50, and 50 pg, respectively. The $^{87}Sr/^{86}Sr$, $^{143}Nd/^{144}Nd$, and $^{176}Hf/^{177}Hf$ ratios were normalized to $^{87}Sr/^{86}Sr = 0.1194$, $^{143}Nd/^{144}Nd = 0.7219$, and $^{176}Hf/^{177}Hf = 0.7325$ by exponential law, respectively. During the period of data acquisition, standards yielded results of $^{87}Sr/^{86}Sr = 0.710248 \pm 0.000007$ (2 SD, $n = 6$) for NBS987, $^{143}Nd/^{144}Nd = 0.512108 \pm 5$ (2 SD, $n = 6$) for Jndi-1, and $^{176}Hf/^{177}Hf = 0.282184 \pm 4$ (2 SD, $n = 7$) for Alfa Hf 14374. In addition, USGS reference materials AGV-2 was also processed for Sr–Nd–Hf isotopes and yielded ratios of 0.703991 ± 11 for $^{87}Sr/^{86}Sr$, 0.512784 ± 14 for $^{143}Nd/^{144}Nd$, and 0.282965 ± 10 for $^{176}Hf/^{177}Hf$, respectively, which are identical within error, to the recommended values (Weis et al., 2006, 2007). Sr–Nd–Hf isotopic analyses for samples 17JT13–17JT16 were carried out at Nanjing FocuMS Technology Co. Ltd., following a similar method. Geochemical reference materials of USGS BCR-2, BHVO-2, AVG-2, and RGM-2 were treated as quality control. Their isotopic results (BCR-2: $^{87}Sr/^{86}Sr = 0.705001 \pm 4$, $^{143}Nd/^{144}Nd = 512633 \pm 2$, $^{176}Hf/^{177}Hf = 0.282873 \pm 2$; BHVO-2: $^{87}Sr/^{86}Sr = 0.703516 \pm 5$, $^{143}Nd/^{144}Nd = 512976 \pm 2$, $^{176}Hf/^{177}Hf = 0.283087 \pm 2$; RGM-2: $^{87}Sr/^{86}Sr = 0.704373 \pm 3$, $^{143}Nd/^{144}Nd = 512791 \pm 2$, $^{176}Hf/^{177}Hf = 0.283008 \pm 1$; STM-2: $^{87}Sr/^{86}Sr = 0.703700 \pm 4$, $^{143}Nd/^{144}Nd = 512909 \pm 2$,

$^{176}Hf/^{177}Hf$ = 0.283025 ± 2) agree with previous publication within analytical uncertainty (Weis et al., 2006, 2007). The initial Sr–Nd–Hf isotopes in **Table 1** were corrected by t = 45 Ma.

RESULTS

Zircon and Titanite U–Pb Ages and Zircon Hf Isotope

The zircon U–Pb SIMS (17JT13 and 17JT16) and LA-ICP-MS (12FW75 and 17JT15) dating results are listed in **Supplementary Tables 1**, **2**, respectively. Most of the separated zircons have core–rim textures. The cores are irregular, whereas most rims developed oscillatory zonings (**Figure 3A**). We mainly selected dating positions on the rims with enough sizes, but some are in the center for zircons without core–rim textures (**Figure 3B**). Some zircons from sample 17JT15 developed additional narrow rims, which are black in the CL images without oscillatory zoning. This results in core–mantle–rim textures that the mantles developed oscillatory zonings similar to rims of other zircons.

Eighteen zircons from sample 17JT13 were dated by SIMS method, but only 14 of them are available, whereas the others did not give valid data. All the dating spots have high contents of U (1,664–11,349 ppm) and Th (245–1,549 ppm) and relatively low Th/U ratios (0.05–0.18). The dating spots yield $^{206}Pb/^{238}U$ age of 42.8 to 50.8 Ma. Except for two younger dates (43.0 ± 0.7 and 42.8 ± 0.6 Ma) and two older dates (48.3 ± 0.8 and 50.8 ± 0.8 Ma), the other 10 dating results are clustered (44.1 to 46.1 Ma) and weighted as 45.3 ± 0.4 Ma (n = 10; MSWD = 0.57) (**Figure 4A**). The two younger ones were not consistent with the majority within error and may undergo lead loss. With regard to sample 17JT16, eight dating spots out of 18 ones gave useful dates. They also show high concentrations of U (3,176–12,345 ppm) and Th (150–746 ppm) and relatively low Th/U ratios (0.02–0.17). Except spot 17JT16@09-r (48.4 ± 0.7 Ma), the other seven dates give identical $^{206}Pb/^{238}U$ age (43.5–46.0 Ma), yielding a weight mean of 44.5 ± 0.8 Ma (n = 7; MSWD = 1.5) (**Figure 4B**) identical to that of sample 17JT13.

Samples 17JT15 and 12FW75 were dated by zircon LA-ICP-MS U–Pb method. Zircons from sample 17JT15 show various textures (**Figure 3B**); for example, uniform, core–rim or core–mantle–rim, and the zircon mantles and rims have enough sizes and were dated by dating spot of 15 μm. Most dating spots yield Eocene $^{206}Pb/^{238}U$ ages from 43.3 to 45.9 Ma and give a weight mean of 44.3 ± 0.8 Ma (n = 13; MSWD = 0.29) (**Figure 4C**), identical to the other dated samples. Some dates from the narrow dark rims yield Oligocene $^{206}Pb/^{238}U$ ages of 29.2 to 30.9 Ma weighted at 29.9 ± 0.4 Ma (n = 7; MSWD = 0.59). These younger population displays evidently higher contents of Th (593–5,180 ppm) and U (13,670–36,100 ppm) than the Eocene group (Th = 159–2,920 ppm; U = 1,120–6,030 ppm). The Th/U ratios of the Oligocene dates (0.02–0.14) are much lower than the Eocene ones (0.03–1.04). Sixteen dating results were obtained for sample 12FW75 using analytical spot of 30 μm (**Figure 3D**). The dating spots gave high contents of U (878–10,261 ppm) and Th (132–1,207 ppm) with Th/U ratios from 0.03 to 0.34. The $^{206}Pb/^{238}U$ ages range from 43.0 to 51.9 Ma. With the exception of three elder spots (49.0, 50.0, and 51.9 Ma), the others yield a weight mean of 44.4 ± 0.6 Ma (n = 12; MSWD = 0.70) (**Figure 4D**), similar to the other dating results within error.

Titanites were separated from two samples (17JT13 and 17JT15) of Haweng granodiorite porphyries and were subjected to LA-ICP-MS U–Pb dating, and the dating results are listed in **Supplementary Table 3**. Except spot 17JT13#25, the other 29 analyses of sample 17JT13 are plotted on the discordia line with a lower intercept of 45.3 ± 0.5 Ma (MSWD = 1.2) (**Figure 4E**). The weighted mean of ^{207}Pb-corrected $^{206}Pb/^{238}U$ ages for sample 17JT13 shows an identical age of 45.5 ± 0.3 Ma (n = 29; MSWD = 1.10). All the analyses of sample 17JT15 are plotted on the discordia line, intercepting the concordia curve at 44.5 ± 0.6 Ma (MSWD = 1.7, n = 30) (**Figure 4F**). Their ^{207}Pb-corrected ages gave a weighted mean of 44.7 ± 0.4 Ma (MSWD = 1.5; n = 30).

We conducted zircon *in situ* Hf isotopic analysis for sample 12FW75, which are mostly on the dating spots or adjacent realm with consistent CL characteristics with spot size of 40 μm. The analytical results are listed in **Supplementary Table 4**. All the dated zircons show similar Hf isotopic compositions with $^{176}Hf/^{177}Hf$ of 0.282389 to 0.282545. The corresponding $\varepsilon_{Hf}(t)$ values range from −12.58 to −7.04 with crustal model ages mainly of Paleoproterozoic (1,570–1,921 Ma).

Whole-Rock Geochemistry

Whole-rock major element, trace element, and Sr–Nd–Hf isotope analytical results are listed in **Table 1** and presented in **Figures 5–7**. The analyzed samples show low LOI (loss on ignition) values (1.09–2.60 wt.%), suggesting they are fresh. They exhibit high SiO_2 (69.98–73.53 wt.%), Al_2O_3 (15.07–16.15 wt.%), and Na_2O (3.94–5.81 wt.%); moderate CaO (1.83–2.85 wt.%); and high Na_2O/K_2O ratios (1.57–7.88) (**Figure 5**). They have A/CNK values of 1.08 to 1.27, indicative of peraluminous series (A/CNK > 1). Some samples possess evidently high Na_2O/K_2O ratios due to much lower K_2O contents (0.72–0.79 wt.%).

These samples have rare earth elements (REE) contents of 93–134 ppm, large REE fractionation with La_N/Sm_N = 3.9–4.3 and La_N/Yb_N = 37.7–45.7 (N denotes chondrite normalized value), and weak Eu anomalies [$Eu/Eu^* = 2Eu_N/(Sm + Gd)_N$] from 0.82 to 0.88. They are relatively enriched in large ion lithophile elements (LILE, e.g., Rb, Ba, Th, and U) and light REEs (LREE, e.g., La and Ce) and relatively depleted in high field strong elements (e.g., Nb, Ta, and Ti) and heavy REEs (HREEs) in the primitive-mantle normalized spidergrams (**Figure 6**). All samples display spikes of Pb in spidergrams and depletions of Ba relative to other LILE. Furthermore, these granodiorite porphyry samples show high Sr concentrations (342–481 ppm), high Sr/Y ratios (63–86 ppm), and low Rb/Sr ratios (0.10–0.39) (**Figures 5G,H**).

The analyzed samples display similar Sr–Nd–Hf isotopic compositions (**Figure 7**). They have low $^{87}Rb/^{86}Sr$ ratios (0.2898–1.1252), and their measured $^{87}Sr/^{86}Sr$ ratios range from 0.719206 to 0.725827 with initial $^{87}Sr/^{86}Sr$ ratios [$^{87}Sr/^{86}Sr_{(t)}$] of 0.7190 to 0.7251. They have unradiogenic Nd and Hf isotopic compositions with $^{143}Nd/^{144}Nd$ of 0.511920–0.512024 and $^{176}Hf/^{177}Hf$ of

TABLE 1 | Whole-rock geochemical compositions for Haweng granodiorite porphyries.

Sample	12FW75	17JT13	17JT14	17JT15	17JT16	Sample	12FW75	17JT13	17JT14	17JT15	17JT16
wt.%						Dy	1.18	1.11	1.01	1.13	1.26
SiO_2	69.98	71.37	72.19	73.53	71.48	Ho	0.19	0.19	0.17	0.19	0.22
TiO_2	0.21	0.20	0.20	0.20	0.20	Er	0.44	0.45	0.43	0.45	0.52
Al_2O_3	15.96	15.70	15.35	15.07	16.15	Tm	0.07	0.06	0.06	0.07	0.07
TFe_2O_3	1.32	1.35	1.37	1.33	1.29	Yb	0.38	0.38	0.37	0.44	0.38
MnO	0.02	0.02	0.02	0.02	0.02	Lu	0.06	0.06	0.06	0.06	0.05
MgO	0.78	0.78	0.79	0.79	0.67	Hf	5.46	3.5	3.6	3.8	3.9
CaO	2.14	2.28	2.03	1.83	2.85	Ta	0.88	0.6	0.7	0.8	0.6
Na_2O	3.94	5.81	5.67	4.16	5.30	Pb	122	52.4	48.2	91.7	40.9
K_2O	2.51	0.76	0.72	1.60	0.79	Th	12.77	10.60	10.15	12.20	11.10
P_2O_5	0.09	0.05	0.04	0.08	0.07	U	4.75	4.84	4.21	5.58	4.43
LOI	2.60	1.09	1.55	1.45	1.24	Na_2O/K_2O	1.57	7.64	7.88	2.60	6.71
Total	99.55	99.49	99.99	100.14	100.14	A/CNK	1.22	1.08	1.11	1.27	1.09
ppm						ΣREE	102	94	93	103	107
Li	14.5	13.3	18.7	26.5	17.6	Eu/*Eu	0.82	0.84	0.86	0.88	0.85
Sc	2.7	3.1	2.9	3.0	3.3	Sr/Y	63	77	86	63	82
V	20	15	20	18	12	$(La/Yb)_N$	42	37	38	35	43
Cr	8	8	10	7	2	Rb/Sr	0.39	0.10	0.11	0.29	0.12
Co	1.8	2.8	2.1	2.3	1.6	$^{87}Rb/^{86}Sr$	1.1252	0.2898	0.2964	0.8643	0.3158
Ni	6.6	8.0	7.6	7.4	2.8	$^{87}Sr/^{86}Sr$	0.725827	0.719206	0.720111	0.724641	0.722206
Cu	1.1	1.2	0.6	0.8	0.8	2SE	0.000022	0.000006	0.000006	0.000006	0.000006
Zn	36	35	36	34	34	$^{87}Sr/^{86}Sr(t)$	0.7251	0.7190	0.7199	0.7241	0.7220
Ga	21.0	20.6	21.0	23.0	21.7	$^{147}Sm/^{144}Nd$	0.1225	0.1252	0.1223	0.1205	0.1161
Rb	133	37.9	46.8	100	56.8	$^{143}Nd/^{144}Nd$	0.511992	0.512019	0.512024	0.511986	0.511920
Sr	342	379	412	349	481	2SE	0.000010	0.000004	0.000004	0.000004	0.000004
Y	5.4	4.9	4.8	5.5	5.9	$\varepsilon_{Nd}(0)$	−12.61	−12.07	−11.98	−12.72	−14.00
Zr	128	106	113	116	114	$\varepsilon_{Nd}(t)$	−12.18	−11.66	−11.55	−12.29	−13.54
Nb	6.1	4.1	4.6	5.8	5.2	$f_{Sm/Nd}$	−0.38	−0.36	−0.38	−0.39	−0.41
Cs	12.81	4.29	4.87	6.44	4.84	$T_{DM1}Nd$	1,929	1,941	1,872	1,898	1,914
Ba	460	324	278	417	325	$T_{DM2}Nd$	1,841	1,799	1,790	1,850	1,952
La	23.8	20.9	21.1	23.1	24.2	$^{176}Lu/^{177}Hf$	0.0016	0.0024	0.0024	0.0022	0.0018
Ce	43.9	42.6	42.2	46.7	48.6	$^{176}Hf/^{177}Hf$	0.282407	0.282481	0.282435	0.282467	0.282407
Pr	5.23	4.70	4.66	5.03	5.18	2SE	0.000007	0.000007	0.000007	0.000007	0.000007
Nd	19.4	16.6	16.2	18.2	19.1	$\varepsilon_{Hf}(0)$	−12.90	−10.28	−11.94	−10.77	−12.90
Sm	3.93	3.44	3.28	3.63	3.67	$\varepsilon_{Hf}(t)$	−11.96	−9.37	−11.02	−9.85	−11.97
Eu	0.90	0.81	0.80	0.91	0.92	$T_{DM1}Hf$	1,211	1,133	1,199	1,147	1,220
Gd	2.45	2.22	2.15	2.47	2.70	$T_{DM}{}^{C}Hf$	1,874	1,710	1,814	1,740	1,874
Tb	0.26	0.24	0.23	0.24	0.28	$f_{Lu/Hf}$	−0.95	−0.93	−0.93	−0.93	−0.95

0.282407–0.282481. The corresponding $\varepsilon_{Nd}(t)$ and $\varepsilon_{Hf}(t)$ values are −13.54 to −11.55 and −11.97 to −9.37, respectively. The two-stage Nd-depleted mantle model ages (1,790–1,952 Ma) and the crustal model age of Hf isotope (1,710–1,874 Ma) are similar and both of Paleoproterozoic.

DISCUSSION

Geochronology of Haweng Granodiorite Porphyry and Coeval Himalayan Magmatism

Zircon and titanite have high closure temperatures for the U–Pb system as indicated by previous studies, such as >800°C for zircon (Cherniak and Watson, 2001) and 660–700°C for titanite (Scott and St-Onge, 1995). The Haweng granodiorite porphyries intruded the Triassic sedimentary rocks and were exposed in a shallow level of crust, implying fast cooling and crystallization; thus, both zircon and titanite U–Pb ages can constrain the magma crystallization time. Based on zircon U–Pb dating for samples collected from different outcrops in the Haweng area, four identical $^{206}Pb/^{238}U$ ages were obtained from 44.3 ± 0.8 to 45.3 ± 0.4 Ma. The titanite U–Pb dating results for samples 17JT13 and 17JT15 gave consistent middle Eocene ages (*ca.* 45 Ma). It is interesting that sample 17JT15 shows two age groups, that is, 44.3 ± 0.8 and 29.9 ± 0.4 Ma. As the older zircon population is identical to titanite U–Pb dating results, it should represent the magma crystallization age. The younger age group from the black zircon rims reflects a later event of zircon overgrowth or recrystallization, possibly under low temperature

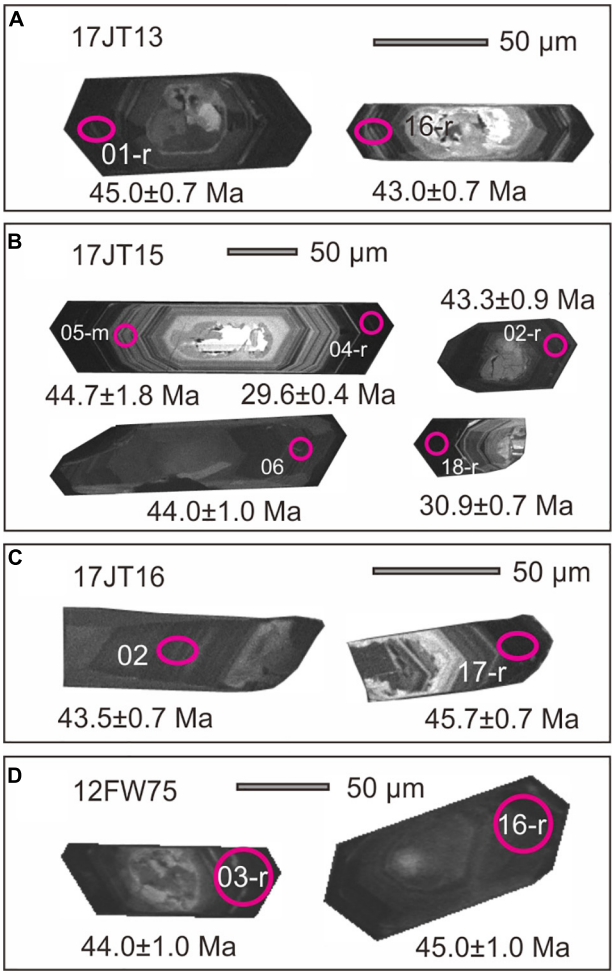

FIGURE 3 | Representative cathodoluminescence (CL) images for zircons from Haweng granodiorite porphyries. The analytical spots for SIMS method **(A,C)** are elliptic of 10 × 15 μm in size, whereas the LA-ICP-MS spots are circular, 15 μm for 17JT15 **(B)** and 30 μm for 12FW75 **(D)**.

and fluid-assisted condition because the granodiorite porphyries have no obvious metamorphism or deformation. Furthermore, five older spots were obtained from the dated zircon rims from 48.3 to 51.9 Ma including samples 17JT13, 17JT16, and 12FW75. There are two possible explanations for these early Eocene ages. First, they are antecrysts, growing earlier at prograde metamorphic conditions. Second, these analytical results are contaminated by older inherited core, as the dated rims are narrow and thin.

In the east of Ramba dome, Liu et al. (2014) obtained similar U–Pb ages for the porphyritic two-mica granite gneiss (dikes) with 09FW115 of 44.3 ± 0.5 Ma and 12FW111 of 44.1 ± 0.8 Ma (**Figure 1B**). Another sample (12FW112) from different dike with similar lithology there yielded Oligocene U–Pb age (28.2 ± 5.2 Ma, n = 2). If the three younger dates (27.8–32.8 Ma) of this sample are included for average calculation, they would give a mean of 29.5 ± 6.2 Ma, which resembles the younger rim age of sample 17JT15 (29.9 ± 0.4 Ma) within error. These similar radiometric ages document the existence of early Oligocene thermal event (*ca.* 30 Ma) in the study area, which has been reported along the YTSZ (e.g., Chen et al., 2015).

It is noteworthy that middle Eocene magmatism represents the earliest magmatic activity in the Himalayan orogenic belt after initial continental collision. Previously reported middle Eocene granite plutons are limited to Yardoi dome and adjacent areas, such as Dala and Quedang, in the northeastern Himalaya (number 4 in **Figure 1A**; Aikman et al., 2008; Zeng et al., 2011, 2015; Hou et al., 2012). This study identified new outcrops of middle Eocene magmatism in the Haweng area. Together with the coeval granitic dikes in Ramba dome (Liu et al., 2014), Langkazi–Ramba area is another important region for middle Eocene granitic magmatism, and there may exist intrusion of larger scale but has not been exposed on the basis of field characters. If the suture belt area is taken into account, some small plutons intruded the mélange of YTSZ, such as granite in Xiao Gurla Range (43.9 ± 0.9 Ma, number 1 in **Figure 1A**; Pullen et al., 2011) and Niuku leucogranite (44.8 ± 2.6 Ma, number 2 in **Figure 1A**; Ding et al., 2005). Evidence of this magmatic activity is also documented by abundant middle Eocene inherited zircons in the Miocene dikes intruding northern Tethyan Himalaya and YTSZ in the Xigaze area (Ji et al., 2020). The overall spatial distribution of middle Eocene magmatic activities is located in an east–west trending belt along the northern Himalayan margin.

Magma Nature and Source Characters

Haweng granodiorite porphyries display variable phenocryst contents on outcrops and micrographs, indicative of magma evolution. SiO_2 and Al_2O_3 have a negative correlation, suggesting fractional crystallization of Al-bearing minerals, such as plagioclase, K-feldspar, and biotite. Large variations occur in some major and trace elements, such as Na_2O, Na_2O/K_2O, Rb, and Sr (**Figure 5**). K_2O, Rb, and Ba show close correlations, and they are all compatible in K-feldspar, whereas Na_2O is dominated by plagioclase. Sample 17JT13 with lower K_2O contents (0.76 wt.%) has less K-feldspar phenocrysts, whereas sample 17JT15 has higher K_2O contents (1.60 wt.%) and more K-feldspar phenocrysts (**Figure 2E**). The samples enriched in Sr possess high Na_2O contents (**Figure 5F**), probably indicating cumulation of plagioclase. The three high-Sr samples show negative correlation between Sr and Na_2O may suggest crystal fractionation of K-feldspar, which are also enriched in Sr.

Sample 12FW75 has the lowest SiO_2 and Na_2O and highest K_2O, and it may represent the least evolutional melt of Haweng granodiorite porphyries. As the Haweng granodiorite porphyries and Ramba Eocene porphyritic two-mica granitic dikes (09FW115 and 12FW111) were coeval and spatially adjacent, they may have close generic link and were considered together for study of magma nature. Sample 12FW111 has the lowest SiO_2 (67.62 wt.%) of middle Eocene rocks (**Figure 5**); thus, it may represent primitive component. The Ramba Eocene dikes possess higher Rb and lower Sr contents and weaker depletion of Nb and Ta than other Eocene granitic rocks (**Figure 6**). If the relatively primitive magma was characterized by high Rb and low Sr, the enrichment of Sr was related to cumulation of plagioclase as the samples enriched in Sr have high Na_2O

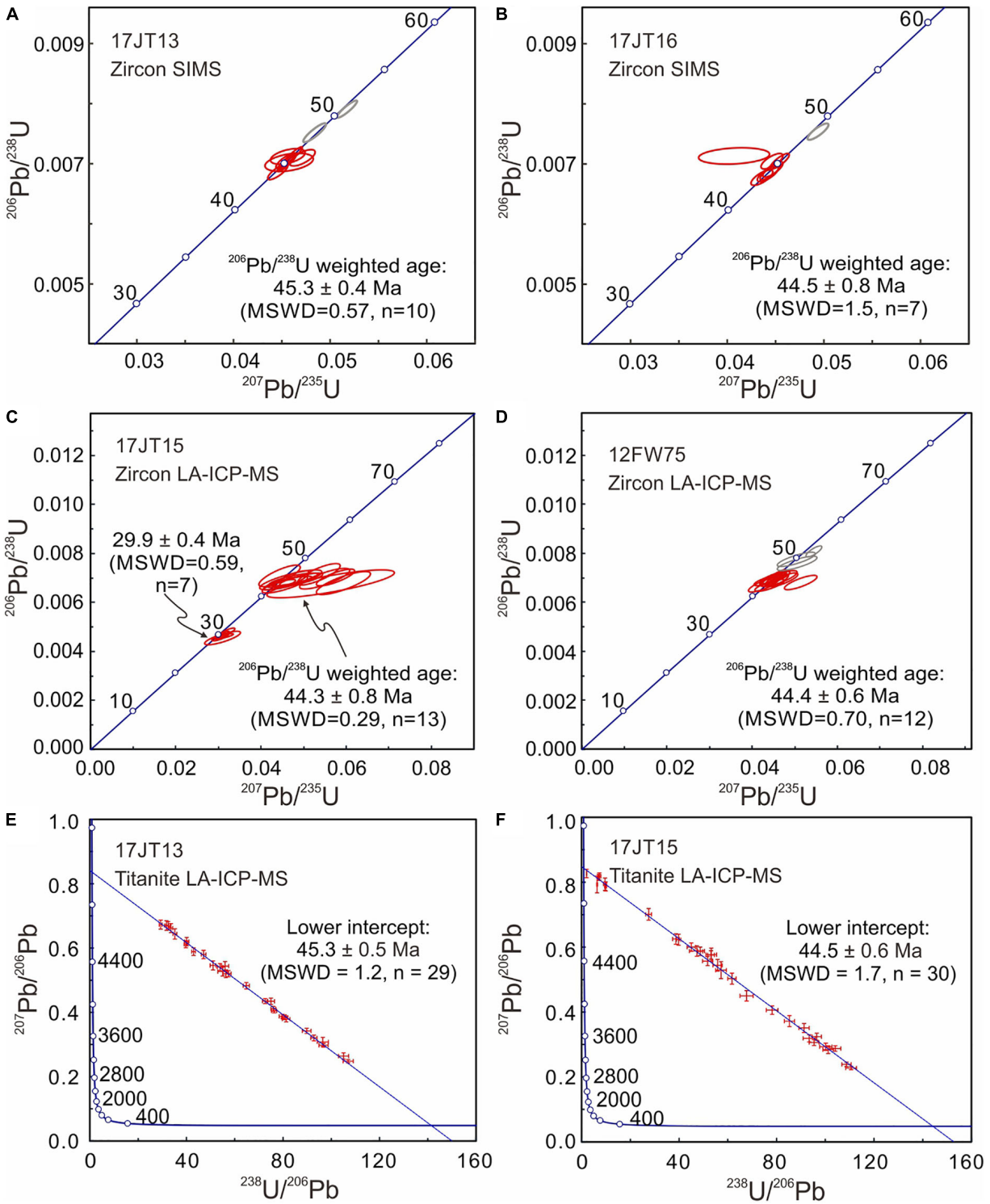

FIGURE 4 | Zircon U–Pb conventional Wetherill concordia **(A–D)** and titanite Tera–Wasserburg concordia **(E,F)** diagrams for Haweng granodiorite porphyries. Data-point error ellipses and error crosses are 2σ. MSWD, Mean Square of Weighted Deviates.

(**Figure 5F**). The modeling calculation based on Ba and Rb suggests that fractional crystallization of K-feldspar can account for their decreasing trend for Haweng granodiorite porphyries (**Figure 5H**). This process would lead to evident decrease in Sr and Eu contents, as well as Eu/Eu* values; however, this is not the case for the middle Eocene granites. A potential

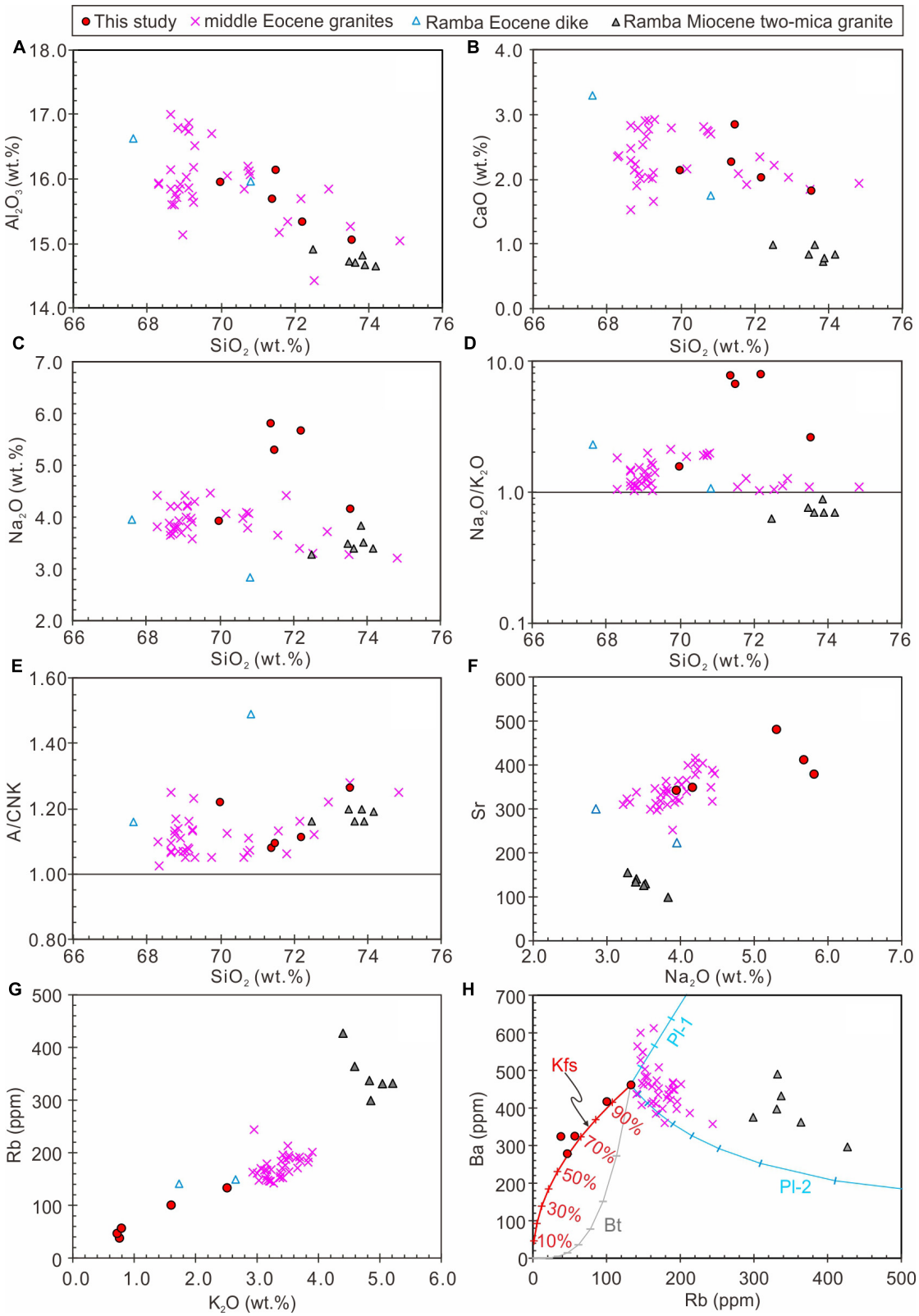

FIGURE 5 | Variation diagrams for selected major and trace elements. Variations of **(A)** Al_2O_3, **(B)** CaO, **(C)** Na_2O, **(D)** Na_2O/K_2O, **(E)** A/CNK vs. SiO_2. Variations of **(F)** Sr vs. Na_2O, **(G)** Rb vs. K_2O, and **(H)** Ba vs. Rb. The numbers in percent of (H) denote melt fractions. The partition coefficients of Rb and Ba for K-feldspar (Kfs) (Rb: 3; Ba: 2), plagioclase (Pl) (Pl-1: Rb = 0.03, Ba = 0.1; Pl-2: Rb = 0.3, Ba = 1.5), and biotite (Bt) (Rb: 2.5; Ba: 6) are from Laurent et al. (2013). Data sources: middle Eocene granites: Zeng et al. (2011) and Hou et al. (2012); Ramba Eocene dike and Miocene two-mica granite: Liu et al. (2014).

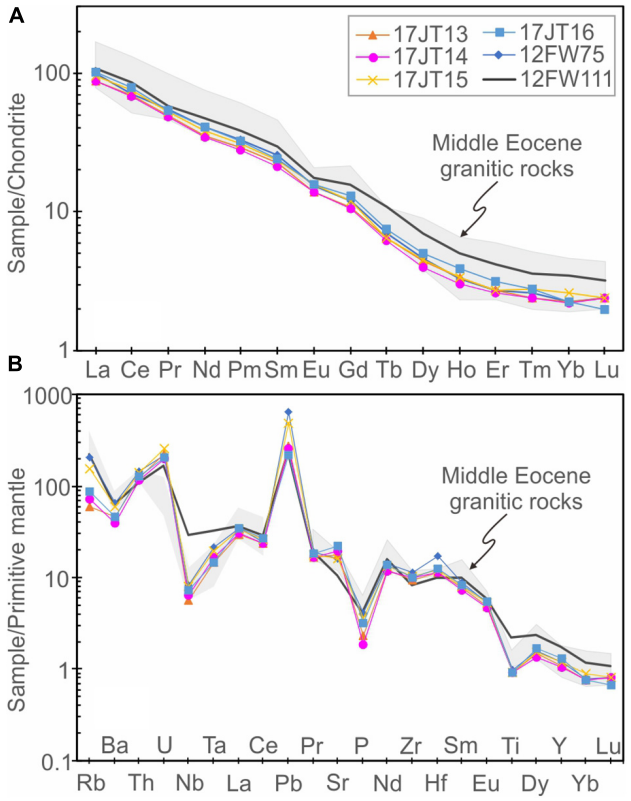

FIGURE 6 | Chondrite-normalized REE variation diagram **(A)** and primitive mantle-normalized spider diagrams **(B)** for samples of this study. The normalization data are from Sun and McDonough (1989). Data sources: middle Eocene granitic rocks: Zeng et al. (2011) and Hou et al. (2012); Ramba Eocene dike (12FW111): Liu et al. (2014).

explanation is that the decreases in Sr and Eu due to fractionation of K-feldspar were balanced by other process enriching them, most likely by the cumulation of plagioclases. This is evidenced by the widespread existence of plagioclase phenocrysts. The plagioclase has larger partition coefficients of Ba in more felsic magma (0.5–1.5 for SiO_2 > 70 wt.%) than intermediate melts (0.1–0.5 for 60 < SiO_2 < 70 wt.%) (Laurent et al., 2013). The fractional crystallization of plagioclase would lead to increase in Ba during early magma evolution (Pl-1 in **Figure 5H**), whereas it results in decrease in Ba in more felsic magma (Pl-2 in **Figure 5H**). The middle Eocene granites and Ramba Miocene granites show evolutional trend controlled by fractionation of plagioclase in contrast with the Haweng granodiorite porphyries dominated by K-feldspar (**Figure 5H**). The variation of major and trace elements for Haweng granodiorite porphyries would involve multiple processes of magma evolution, including earlier cumulation of plagioclase and later fractionation of K-feldspar. The more complicated process of Haweng granodiorite porphyry implies there existed a much larger scale of magma than that exposed on the outcrops.

The Haweng granodiorite porphyries were plotted in the scope of amphibolites in the Sr-Nd diagram; thus, they can result from partial melting of mixing component of different amphibolites (orange lines in **Figure 7A**). They can also be generated by mixing source (blue lines in **Figure 7A**) between amphibolite and metapelite (end-member F) with the contribution of amphibolites of 50% to 70% (blue lines in **Figure 7A**). In **Figure 7B**, the analyzed samples are all located above the crustal array line (Vervoort et al., 1999), in consistence with potential involvement of mature crustal materials in the magma source. Based on the CL images, most of the zircons developed core–rim textures, and the existence of ancient zircon cores (Liu et al., 2014) suggests important contribution of ancient Himalayan metasedimentary rocks. The Haweng granodiorite porphyries were plotted between middle Eocene granites and Himalayan leucogranites in the Sr–Nd–Hf diagrams (**Figure 7**); thus, they have more involvement of metasedimentary components than other middle Eocene granites, which were attributed to partial melting of amphibolite-dominated source under thickened crustal conditions based on high Sr concentration and Sr/Y ratios (Zeng et al., 2011). However, the high Sr and Sr/Y ratios of Haweng granodiorite porphyries may be related to cumulation of plagioclase, and the relative primitive sample shows lower Sr and Sr/Y ratios.

Petrogenesis of Haweng Granodiorite Porphyry

Partial Melting During Prograde Metamorphism in the Himalaya

Many studies suggested that the GHS underwent partial melting as early as the stage of prograde metamorphism (see review in Zhang et al., 2017); however, anataxis records are much less and later than that for the prograde metamorphism. Records of early to middle Eocene prograde metamorphism were reported in several Himalayan domes, such as Mabja (54–52 Ma) and Kangmar (51–49 Ma) domes from central Himalaya (Smit et al., 2014), and Yardoi dome (48–36 Ma) from eastern Himalaya (Ding et al., 2016a,b). Furthermore, Eocene prograde metamorphic records have been widely identified in the GHS along the Himalayan front. In the Pakistan and Garhwal Himalayas, prograde metamorphism was accompanied by growth of monazite (45–36 Ma) and garnet (44–38 Ma) (Foster et al., 2000; Stübner et al., 2014). In the Nepal Himalaya, pervasive prograde metamorphism has initiated as early as early–middle Eocene, such as Karnali Klippe (41–38 Ma, Soucy La Roche et al., 2018), Jajarkot klipe (44–33 Ma, Soucy La Roche et al., 2019), Jumla region (43–33 Ma, Carosi et al., 2010; 41–38 Ma, Gibson et al., 2016; 48–30 Ma, Braden et al., 2017), Annapurna region (38–30, Corrie and Kohn, 2011; 43–36 Ma, Iaccarino et al., 2015; 48–30 Ma, Larson and Cottle, 2015; 48–45, Carosi et al., 2016; 43–30 Ma for the western part, Gibson et al., 2016), and Everest region (*ca.* 45 Ma, Catlos et al., 2002; 40–27 Ma, Cottle et al., 2009). Besides the aforementioned prograde metamorphism, the mineral chemistry of monazite can record the process of anatexis (Gibson et al., 2004; Kohn et al., 2005). Based on the trace elements of analyzed monazites, Braden et al. (2017) speculated the lower GHS in the Jumla region, western Nepal, underwent partial melting as early as *ca.* 40 Ma, as indicated by increase in Y and HREEs of monazite related to

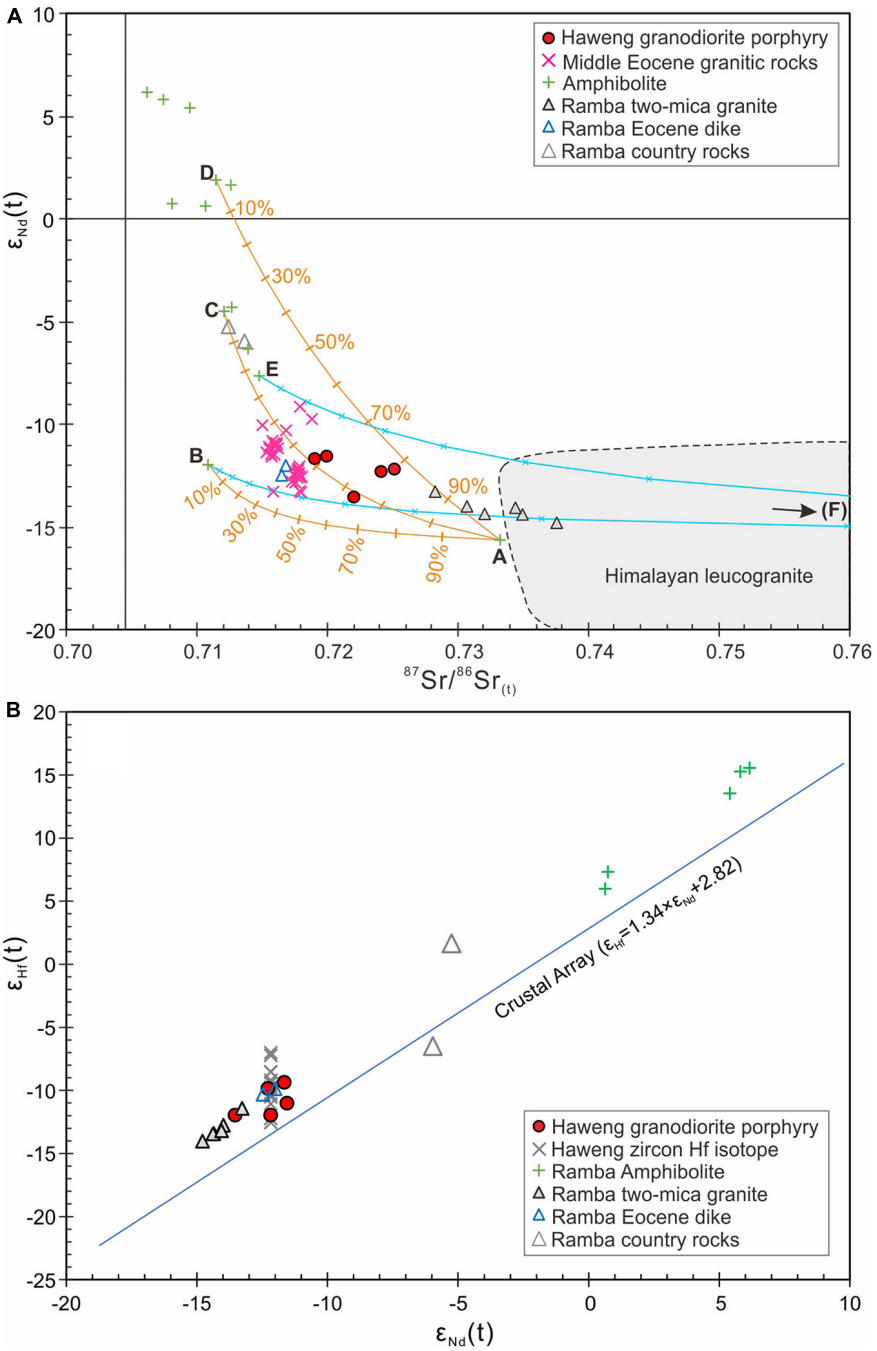

FIGURE 7 | (A) Sr–Nd and **(B)** Nd–Hf isotope systematics of Haweng granodiorite porphyries and related rocks. The end-member components for amphiolites (A: T0389-17; B: T0394-6; C: T0321-08; D: T0394-21; E: T0394-8) and metapelite (F: T0321-12) are from Zeng et al. (2009) and Zeng et al. (2011). Data sources: amphibolite: Zeng et al. (2011) and Liu et al. (2014); middle Eocene granitic rocks: Zeng et al. (2011); Aikman et al. (2012), and Hou et al. (2012); Ramba Eocene dikes, country rocks and two-mica granite: Liu et al. (2014); Himalayan leucogranite: Zhang et al. (2004); King et al. (2011), and Guo and Wilson (2012) and references therein.

garnet breakdown during partial melting. However, no direct evidence for anatexis or presence of melt was identified there. Some scholars documented that partial melting occurred during the peak stage of prograde metamorphism. For example, Carosi et al. (2015) reported Eocene partial melting (41–36 Ma; monazite U-Th-Pb age) in the form of nanotonalite inclusions from garnets at the base of the GHS in the Kali Gandaki valley (central Nepal) and attributed it to underthrusting of the GHS. As partial melting would dissolve monazite and greatly affect the preservation of early monazite (Rubatto et al., 2001; Kelsey et al., 2008;

Yakymchuk and Brown, 2014; Wang et al., 2017), the melting would consume monazites and erase their records of earlier metamorphism (Gibson et al., 2004; Kohn et al., 2005; Larson et al., 2011). Therefore, the presence of abundant early–middle Eocene monazites generated by prograde metamorphism of the GHS implies the frontal Himalaya should not have undergone large-scale or widespread partial melting.

It is noteworthy that Wang et al. (2013) discovered middle-late Eocene zircon outgrowth (*ca.* 40–34 Ma) from sillimanite migmatite in Nyalam (central GHS), which was ascribed to muscovite dehydration melting during prograde metamorphism. Recently, Singh (2019) reported zircon rim dating results (46–20 Ma) for tourmaline-bearing leucogranite in west Garhwal and interpreted the ages representing coeval fluid-fluxed partial melting due to exhumation of migmatite zone. The protracted growth of zircon indicates equilibrium partial melt of its source before the final extraction and emplacement (Singh, 2019). The melt remained trapped within a depth of midcrust when there was episodic liberation of fluids and melts resulting in protracted episodic growth of zircon, garnet, and monazite (Foster et al., 2000). However, because of limit flux of aqueous fluids, the fluid-present melting is difficult for generating large volume of granitic rocks, especially for the segregation of melts from source region in deep crust (Prince et al., 2001). Only under suitable pressure and/or temperature conditions could the melts rise through crust and emplace at high-structural level (Singh, 2019). In the Eastern Himalayan Syntaxis, the Namche Barwa complex underwent long-lived (44–7 Ma) high-temperature granulite facies metamorphism and dehydration melting of muscovite and biotite in buried Indian continent (Zhang et al., 2015). Whether these lines of evidence for migmatization and zircon overgrowth indicate large-scale partial melting and granite formation is yet to be resolved, as the leucosomes in migmatite are distinct from the leucogranites in various aspects, and it is difficult to build their genetic relationship (Yang et al., 2019; Wu et al., 2020).

Genetic Mechanism of Haweng Granodiorite Porphyry and Coeval Magmatism

Based on the review of tectonomagmatic records in the early evolution of southern Tibet, it is indicated that there was a north–south compressional setting, and the early prograde metamorphism was difficult to result in large-scale crustal anatexis. Thus, additional mechanism is necessary for the development of Himalayan magmatism, such as heating, decompression, and addition of water. Generally, continental subduction does not directly trigger decompression, and it is not efficient for water supply; thus, heating is a potential mechanism for the magma generation. According to the distribution of middle Eocene magmatic rocks (**Figure 1**), the heat source should be focused beneath this narrow belt along the YTSZ. Zeng et al. (2011) first used slab breakoff model to account for the origin of middle Eocene (44–42 Ma) granitic rocks in Yardoi dome and adjacent areas, which was attributed to partial melting of amphibolite dominated source under high pressure due to juvenile heat induced by slab breakoff.

Although problems arose in the application of breakoff model in orogenic evolution (cf. Garzanti et al., 2018), this model is by far the most plausible explanation for evolution of southern Tibet. There are various lines of evidence for slab breakoff of Neo-Tethyan slab at around 45 Ma after India–Asia continental collision. Based on tomographic imaging of the mantle under Tibet, Van der Voo et al. (1999) found several high-velocity anomalies, and one of the southern zones was interpreted as remnants of oceanic lithospheric slab. Later, Negredo et al. (2007) estimated the slab breakoff occurred at *ca.* 44–48 Ma according to paleomagnetic reconstructions and tomographical characters. Kohn and Parkinson (2002) also got breakoff time of *ca.* 45 Ma on the basis of ages of ultrahigh-pressure (UHP) rocks from the western Himalaya and related records. The UHP eclogite in the Kaghan Valley recorded very rapid exhumation rate from ∼100 to ∼35 km during *ca.* 46 to 44 Ma (Parrish et al., 2006), agreeing with breakoff model. Ji et al. (2016) identified OIB (oceanic island basalt)–type gabbro of 45 Ma, derived from partial melting of asthenosphere, which was used to constrain the breakoff time of Neo-Tethyan slab for the middle–east part of the orogenic belt. In combination with coeval geological records, it is proposed that the Neo-Tethyan slab underwent a full-scale detachment (Ji et al., 2016). The breakoff resulted in the cessation of Gangdese arc magmatism (45–40 Ma) to the north of the YTSZ because the subducted continental lithosphere rotated upward to come against the base of the overriding plate (Chemenda et al., 2000) and shielded the active continental margin (the Lhasa terrane) from the convective heat provided previously by corner flow in the mantle wedge during oceanic slab subduction. The breakoff model is also consistent with the clear deceleration of convergence between India and Asia from 8 to 10 to 4 to 6 cm per year at *ca.* 45 Ma (cf. Patriat and Achache, 1984; van Hinsbergen et al., 2011), possibly due to loss of slab pull after slab breakoff. This study identified new outcrops for middle Eocene magmatism in Langkazi area along the northern Himalayan margin. The variable geochemical compositions of Haweng granodiorite porphyries indicated complicated process of magmatic evolution at depth, implying that the magma scale in the study area should be much larger than that exposed on the outcrops.

CONCLUSION

Based on review of the early to middle Eocene tectonic, metamorphic, and magmatic evolution of the Himalayan orogen, we conducted zircon and titanite U–Pb dating, zircon Hf isotope analyses, whole-rock element, and Sr–Nd–Hf isotope analyses for the newly found Haweng granodiorite porphyries and came to the following conclusions.

(1) The Haweng granodiorite porphyries were generated at *ca.* 45 Ma, supporting the existence of middle Eocene magmatic belt along the YTSZ. Furthermore, the Langkazi–Ramba area developed a younger thermal event of *ca.* 30 Ma.

(2) The Haweng granodiorite porphyries display variable element and isotopic compositions, such as Na_2O, K_2O, Rb, Sr, and Ba contents and Rb/Sr and $^{87}Sr/^{86}Sr_{(t)}$ ratios, which indicated magma evolution process involving cumulation of plagioclase and crystal fractionation of K-feldspar. The complicated magma evolution process implies that a much larger scale of magma may occur beneath the less exposed outcrops.

(3) Although early to middle Eocene prograde metamorphism was widespread in the Himalayan orogenic belt, the evidence for accompanied anatexis was sparse. The Haweng granodiorite porphyries and the east–west trending magmatic belt of middle Eocene were attributed to breakoff of the Neo-Tethyan slab at around 45 Ma.

DATA AVAILABILITY STATEMENT

All datasets generated for this study are included in the article/**Supplementary Material**.

AUTHOR CONTRIBUTIONS

W-QJ and F-YW designed the study. W-QJ, F-YW, WC, Z-CL, J-GW, and CZ conducted the fieldwork. W-QJ, X-CL, and ZZ performed the experiments. W-QJ, X-CL, and J-MW wrote the manuscript. All the authors participated in discussion of the study.

FUNDING

This work was funded by the National Key R&D Program of China (2016YFC0600407), the National Natural Science Foundation of China (Grants 41888101, 41572055, and 41772058), the State Key Laboratory of Lithospheric Evolution grant (SKL-Z201706), and the second comprehensive scientific investigation into Qinghai-Tibet Plateau (2019QZKK0803).

ACKNOWLEDGMENTS

We are grateful to AM and KQ for their constructive comments and to SD for manuscript handling. We thank the staff of the Cameca-1280 SIMS lab at Institute of Geology and Geophysics, Chinese Academy of Sciences (IGGCAS) for help with zircon U–Pb analyses, the staff of MC–ICPMS lab (IGGCAS) for help with zircon U–Pb age and Hf isotope and whole-rock Sr–Nd–Hf isotope analyses, the Beijing Quick-Thermo Science & Technology Co., Ltd for zircon and titanite U-Pb analyses, the ALS Chemex Company (Guangzhou, China), and the Nanjing FocuMS Technology Co., Ltd. for whole-rock element and isotope analyses. Thanks to B. Wan for experiment on thin section.

SUPPLEMENTARY MATERIAL

The Supplementary Material for this article can be found online at: https://www.frontiersin.org/articles/10.3389/feart.2020.00236/full#supplementary-material

REFERENCES

Aikman, A. B., Harrison, T. M., and Hermann, J. (2012). The origin of Eo-and Neo-himalayan granitoids, Eastern Tibet. *J. Asian Earth Sci.* 58, 143–157. doi: 10.1016/j.jseaes.2012.05.018

Aikman, A. B., Harrison, T. M., and Lin, D. (2008). Evidence for early (> 44 Ma) Himalayan crustal thickening, Tethyan Himalaya, southeastern Tibet. *Earth Planet. Sci. Lett.* 274, 14–23. doi: 10.1016/j.epsl.2008.06.038 doi: 10.1016/j.chemgeo.2004.01.003

Braden, Z., Godin, L., and Cottle, J. M. (2017). Segmentation and rejuvenation of the Greater Himalayan sequence in western Nepal revealed by *in situ* U–Th/Pb monazite petrochronology. *Lithos* 284, 751–765. doi: 10.1016/j.lithos.2017.04.023

Burchfiel, B. C., Zhiliang, C., Hodges, K. V., Yuping, L., Royden, L. H., and Changrong, D. (1992). The south tibetan detachment system, himalayan orogen: extension contemporaneous with and parallel to shortening in a collisional mountain belt. *Geol. Soc. Am. Spec. Pap.* 269, 1–41. doi: 10.1130/spe269-p1

Carosi, R., Montomoli, C., Iaccarino, S., Massonne, H.-J., Rubatto, D., Langone, A., et al. (2016). Middle to late Eocene exhumation of the Greater Himalayan Sequence in the Central Himalayas: progressive accretion from the Indian plate. *Geol. Soc. Am. Bull.* 128, 1571–1592. doi: 10.1130/b31471.1

Carosi, R., Montomoli, C., Iaccarino, S., and Visonà, D. (2019). "Structural evolution, metamorphism and melting in the Greater Himalayan Sequence in central-western Nepal," in *Himalayan Tectonics: A Modern Synthesis*, eds P. J. Treloar, and M. P. Searle (Berkeley, CA: Geological Society of London Special Publication), 305–323. doi: 10.1144/sp483.3

Carosi, R., Montomoli, C., Langone, A., Turina, A., Cesare, B., Iaccarino, S., et al. (2015). "Eocene partial melting recorded in peritectic garnets from kyanite-gneiss, Greater Himalayan Sequence, central Nepal," in *Proceedings of the 29th Himalaya-Karakoram-Tibet Workshop*, Lucca, 111–129. doi: 10.1144/sp412.1

Carosi, R., Montomoli, C., Rubatto, D., and Visonà, D. (2010). Late Oligocene high-temperature shear zones in the core of the Higher Himalayan Crystallines (Lower Dolpo, western Nepal). *Tectonics* 29:TC4029. doi: 10.1029/2008TC002400

Catlos, E. J., Harrison, T. M., Manning, C. E., Grove, M., Rai, S. M., Hubbard, M. S., et al. (2002). Records of the evolution of the Himalayan orogen from *in situ* Th–Pb ion microprobe dating of monazite: eastern Nepal and western Garhwal. *J. Asian Earth Sci.* 20, 459–479. doi: 10.1016/s1367-9120(01)00039-6

Chemenda, A. I., Burg, J.-P., and Mattauer, M. (2000). Evolutionary model of the Himalaya–Tibet system: geopoem: based on new modelling, geological and geophysical data. *Earth Planet. Sci. Lett.* 174, 397–409. doi: 10.1016/s0012-821x(99)00277-0

Chen, L., Qin, K.-Z., Li, G.-M., Li, J.-X., Xiao, B., Zhao, J.-X., et al. (2015). Zircon U–Pb ages, geochemistry, and Sr–Nd–Pb–Hf isotopes of the Nuri intrusive rocks in the Gangdese area, southern Tibet: Constraints on timing, petrogenesis, and tectonic transformation. *Lithos* 212, 379–396. doi: 10.1016/j.lithos.2014.11.014

Cherniak, D. J., and Watson, E. B. (2001). Pb diffusion in zircon. *Chem. Geol.* 172, 5–24. doi: 10.1016/s0009-2541(00)00233-3

Corrie, S. L., and Kohn, M. J. (2011). Metamorphic history of the central Himalaya, Annapurna region, Nepal, and implications for tectonic models. *Geol. Soc. Am. Bull.* 123, 1863–1879. doi: 10.1130/b30376.1

Cottle, J. M., Searle, M. P., Horstwood, M. S., and Waters, D. J. (2009). Timing of midcrustal metamorphism, melting, and deformation in the Mount Everest region of southern Tibet revealed by U (-Th)-Pb geochronology. *J. Geol.* 117, 643–664. doi: 10.1086/605994

Debon, F., Le Fort, P., Sheppard, S. M., and Sonet, J. (1986). The four plutonic belts of the Transhimalaya-Himalaya: A chemical, mineralogical, isotopic, and chronological synthesis along a Tibet-Nepal section. *J. Petrol.* 27, 219–250. doi: 10.1093/petrology/27.1.219

de Sigoyer, J., Chavagnac, V., Blichert-Toft, J., Villa, I. M., Luais, B., Guillot, S., et al. (2000). Dating the Indian continental subduction and collisional thickening in

the northwest Himalaya: multichronology of the Tso Morari eclogites. *Geology* 28, 487–490. doi: 10.1130/0091-7613(2000)028<0487:dticsa>2.3.co;2

Ding, H., Zhang, Z., Dong, X., Tian, Z., Xiang, H., Mu, H., et al. (2016a). Early Eocene (c. 50 Ma) collision of the Indian and Asian continents: constraints from the North Himalayan metamorphic rocks, southeastern Tibet. *Earth Planet. Sci. Lett.* 435, 64–73. doi: 10.1016/j.epsl.2015.12.006

Ding, H., Zhang, Z., Hu, K., Dong, X., Xiang, H., and Mu, H. (2016b). P–T–t–D paths of the North Himalayan metamorphic rocks: implications for the Himalayan orogeny. *Tectonophysics* 683, 393–404. doi: 10.1016/j.tecto.2016.06.035

Ding, L., Kapp, P., and Wan, X. Q. (2005). Paleocene–Eocene record of ophiolite obduction and initial India-Asia collision, south central Tibet. *Tectonics* 24:TC3001. doi: 10.1029/2004tc001729

Elhlou, S., Belousova, E., Griffin, W. L., Pearson, N. J., and O'reilly, S. Y. (2006). Trace element and isotopic composition of GJ red zircon standard by laser ablation. *Geochim. Cosmochim. Acta* 70:A158.

Foster, G., Kinny, P., Vance, D., Prince, C., and Harris, N. (2000). The significance of monazite U–Th–Pb age data in metamorphic assemblages; a combined study of monazite and garnet chronometry. *Earth Planet. Sci. Lett.* 181, 327–340. doi: 10.1016/s0012-821x(00)00212-0

Gao, L., Zeng, L., and Xie, K. (2012). Eocene high grade metamorphism and crustal anatexis in the North Himalaya Gneiss Domes, Southern Tibet. *Chin. Sci. Bull.* 57, 639–650. doi: 10.1007/s11434-011-4805-4

Garzanti, E., Radeff, G., and Malusà, M. G. (2018). Slab breakoff: a critical appraisal of a geological theory as applied in space and time. *Earth Sci. Rev.* 177, 303–319. doi: 10.1016/j.earscirev.2017.11.012

Gibson, H. D., Carr, S. D., Brown, R. L., and Hamilton, M. A. (2004). Correlations between chemical and age domains in monazite, and metamorphic reactions involving major pelitic phases: an integration of ID-TIMS and SHRIMP geochronology with Y–Th–U X-ray mapping. *Chem. Geol.* 211, 237–260. doi: 10.1016/j.chemgeo.2004.06.028

Gibson, R., Godin, L., Kellett, D. A., Cottle, J. M., and Archibald, D. (2016). Diachronous deformation along the base of the Himalayan metamorphic core, west–central Nepal. *Geol. Soc. Am. Bull.* 128, 860–878. doi: 10.1130/b31328.1

Guan, Q., Zhu, D.-C., Zhao, Z.-D., Dong, G.-C., Zhang, L.-L., Li, X.-W., et al. (2012). Crustal thickening prior to 38 Ma in southern Tibet: evidence from lower crust-derived adakitic magmatism in the Gangdese Batholith. *Gondwana Res.* 21, 88–99. doi: 10.1016/j.gr.2011.07.004

Guo, Z., and Wilson, M. (2012). The Himalayan leucogranites: constraints on the nature of their crustal source region and geodynamic setting. *Gondwana Res.* 22, 360–376. doi: 10.1016/j.gr.2011.07.027

Harris, N., and Massey, J. (1994). Decompression and anatexis of Himalayan metapelites. *Tectonics* 13, 1537–1546. doi: 10.1029/94tc01611

Hodges, K. V. (2000). Tectonics of the Himalaya and southern Tibet from two perspectives. *Geol. Soc. Am. Bull.* 112, 324–350. doi: 10.1130/0016-7606(2000)112<324:tothas>2.0.co;2

Hou, Z.-Q., Zheng, Y.-C., Zeng, L.-S., Gao, L.-E., Huang, K.-X., Li, W., et al. (2012). Eocene-Oligocene granitoids in southern Tibet: constraints on crustal anatexis and tectonic evolution of the Himalayan orogen. *Earth Planet. Sci. Lett.* 349, 38–52. doi: 10.1016/j.epsl.2012.06.030

Hu, X., Garzanti, E., Wang, J., Huang, W., An, W., and Webb, A. (2016). The timing of India-Asia collision onset – Facts, theories, controversies. *Earth Sci. Rev.* 160, 264–299. doi: 10.1016/j.earscirev.2016.07.014

Iaccarino, S., Montomoli, C., Carosi, R., Massonne, H.-J., Langone, A., and Visonà, D. (2015). Pressure–temperature–time–deformation path of kyanite-bearing migmatitic paragneiss in the Kali Gandaki valley (Central Nepal): investigation of Late Eocene–Early Oligocene melting processes. *Lithos* 231, 103–121. doi: 10.1016/j.lithos.2015.06.005

Ji, W.-Q., Wu, F.-Y., Chung, S.-L., Li, J.-X., and Liu, C.-Z. (2009). Zircon U–Pb geochronology and Hf isotopic constraints on petrogenesis of the Gangdese batholith, southern Tibet. *Chem. Geol.* 262, 229–245. doi: 10.1016/j.chemgeo.2009.01.020

Ji, W.-Q., Wu, F.-Y., Chung, S.-L., Wang, X.-C., Liu, C.-Z., Li, Q.-L., et al. (2016). Eocene Neo-Tethyan slab breakoff constrained by 45 Ma oceanic island basalt–type magmatism in southern Tibet. *Geology* 44, 283–286. doi: 10.1130/g37612.1

Ji, W.-Q., Wu, F.-Y., Liu, C.-Z., and Chung, S.-L. (2012). Early Eocene crustal thickening in southern Tibet: new age and geochemical constraints from the Gangdese batholith. *J. Asian Earth Sci.* 53, 82–95. doi: 10.1016/j.jseaes.2011.08.020

Ji, W.-Q., Wu, F.-Y., Liu, X.-C., Liu, Z.-C., Zhang, C., Liu, T., et al. (2020). Pervasive Miocene melting of thickened crust from the Lhasa terrane to Himalaya, southern Tibet and its constraint on generation of Himalayan leucogranite. *Geochim. Cosmochim. Acta* 278, 137–156. doi: 10.1016/j.gca.2019.07.048

Kaneko, Y., Katayama, I., Yamamoto, H., Misawa, K., Ishikawa, M., Rehman, H., et al. (2003). Timing of Himalayan ultrahigh-pressure metamorphism: sinking rate and subduction angle of the Indian continental crust beneath Asia. *J. Metamorphic Geol.* 21, 589–599. doi: 10.1046/j.1525-1314.2003.00466.x

Kelsey, D., Clark, C., and Hand, M. (2008). Thermobarometric modelling of zircon and monazite growth in melt-bearing systems: examples using model metapelitic and metapsammitic granulites. *J. Metamorphic Geol.* 26, 199–212. doi: 10.1111/j.1525-1314.2007.00757.x

King, J., Harris, N., Argles, T., Parrish, R., and Zhang, H. (2011). Contribution of crustal anatexis to the tectonic evolution of Indian crust beneath southern Tibet. *Geol. Soc. Am. Bull.* 123, 218–239. doi: 10.1130/b30085.1

Kohn, M., Wieland, M., Parkinson, C., and Upreti, B. (2005). Five generations of monazite in Langtang gneisses: implications for chronology of the Himalayan metamorphic core. *J. Metamorphic Geol.* 23, 399–406. doi: 10.1111/j.1525-1314.2005.00584.x

Kohn, M. J., and Parkinson, C. D. (2002). Petrologic case for Eocene slab breakoff during the Indo-Asian collision. *Geology* 30, 591–594. doi: 10.1130/0091-7613(2002)030<0591:PCFESB>2.0.CO;2

Larson, K. P., and Cottle, J. M. (2015). Initiation of crustal shortening in the Himalaya. *Terra Nova* 27, 169–174. doi: 10.1111/ter.12145

Larson, K. P., Cottle, J. M., and Godin, L. (2011). Petrochronologic record of metamorphism and melting in the upper Greater Himalayan sequence, Manaslu–Himal Chuli Himalaya, west–central Nepal. *Lithosphere* 3, 379–392. doi: 10.1130/l149.1

Laurent, O., Doucelance, R., Martin, H., and Moyen, J.-F. (2013). Differentiation of the late-Archaean sanukitoid series and some implications for crustal growth: insights from geochemical modelling on the Bulai pluton, Central Limpopo Belt, South Africa. *Precambrian Res.* 227, 186–203. doi: 10.1016/j.precamres.2012.07.004

Le Fort, P. (1996). "Evolution of the Himalaya," in *The Tectonic Evolution of Asia*, eds A. Yin and T. M. Harrison (Cambridge: Cambridge University Press), 95–109.

Li, X. H., Liu, Y., Li, Q. L., Guo, C. H., and Chamberlain, K. R. (2009). Precise determination of Phanerozoic zircon Pb/Pb age by multicollector SIMS without external standardization. *Geochem. Geophys. Geosyst.* 10:Q04010. doi: 10.1029/2009GC002400

Liu, Z. C., Wu, F. Y., Ji, W. Q., Wang, J. G., and Liu, C. Z. (2014). Petrogenesis of the Ramba leucogranite in the Tethyan Himalaya and constraints on the channel flow model. *Lithos* 208, 118–136. doi: 10.1016/j.lithos.2014.08.022

Ludwig, K. R. (2003). *User's Manual for Isoplot 3.00, a Geochronlogical Toolkit for Microsoft Excel*. Berkeley, CA: Geological Society of London, 25–32.

Ma, L., Wang, B.-D., Jiang, Z.-Q., Wang, Q., Li, Z.-X., Wyman, D. A., et al. (2014). Petrogenesis of the early Eocene adakitic rocks in the Napuri area, southern Lhasa: partial melting of thickened lower crust during slab break-off and implications for crustal thickening in southern Tibet. *Lithos* 196, 321–338. doi: 10.1016/j.lithos.2014.02.011

Nábělek, J., Hetényi, G., Vergne, J., Sapkota, S., Kafle, B., Jiang, M., et al. (2009). Underplating in the Himalaya-Tibet collision zone revealed by the Hi-CLIMB experiment. *Science* 325, 1371–1374. doi: 10.1126/science.1167719

Negredo, A. M., Replumaz, A., Villaseñor, A., and Guillot, S. (2007). Modeling the evolution of continental subduction processes in the Pamir–Hindu Kush region. *Earth Planet. Sci. Lett.* 259, 212–225. doi: 10.1016/j.epsl.2007.04.043

Parrish, R. R., Gough, S. J., Searle, M. P., and Waters, D. J. (2006). Plate velocity exhumation of ultrahigh-pressure eclogites in the Pakistan Himalaya. *Geology* 34, 989–992.

Paton, C., Woodhead, J. D., Hellstrom, J. C., Hergt, J. M., Greig, A., and Maas, R. (2010). Improved laser ablation U-Pb zircon geochronology through robust downhole fractionation correction. *Geochem. Geophys. Geosyst.* 11:Q0AA06. doi: 10.1029/2009GC002618

Patriat, P., and Achache, J. (1984). India–Eurasia collision chronology has implications for crustal shortening and driving mechanism of plates. *Nature* 311, 615–621. doi: 10.1038/311615a0

Prince, C., Harris, N., and Vance, D. (2001). Fluid-enhanced melting during prograde metamorphism. *Geochem. Geophys. Geosyst.* 158, 233–241. doi: 10.1144/jgs.158.2.233

Pullen, A., Kapp, P., DeCelles, P. G., Gehrels, G. E., and Ding, L. (2011). Cenozoic anatexis and exhumation of Tethyan Sequence rocks in the Xiao Curia Range, Southwest Tibet. *Tectonophysics* 501, 28–40. doi: 10.1016/j.tecto.2011.01.008

Ratschbacher, L., Frisch, W., Liu, G., and Chen, C. (1994). Distributed deformation in southern and western Tibet during and after the India-Asia collision. *J. Geophys. Res.* 99, 19917–19945. doi: 10.1029/94jb00932

Rubatto, D., Williams, I. S., and Buick, I. S. (2001). Zircon and monazite response to prograde metamorphism in the Reynolds Range, central Australia. *Contrib. Mineral. Petrol.* 140, 458–468. doi: 10.1007/pl00007673

Schmitz, M. D., and Bowring, S. A. (2001). U-Pb zircon and titanite systematics of the Fish Canyon Tuff: an assessment of high-precision U-Pb geochronology and its application to young volcanic rocks. *Geochim. Cosmochim. Acta* 65, 2571–2587. doi: 10.1016/s0016-7037(01)00616-0

Scott, D. J., and St-Onge, M. R. (1995). Constrains on Pb closure temperature in titanite based on rocks from the Ungava orogen, Canada: implication for U-Pb geochronology and P-T-t path determination. *Geology* 23, 1123–1126.

Searle, M. (2013). Crustal melting, ductile flow, and deformation in mountain belts: cause and effect relationships. *Lithosphere* 5, 547–554. doi: 10.1130/rf.l006.1

Searle, M., Cottle, J., Streule, M., and Waters, D. (2010). Crustal melt granites and migmatites along the Himalaya: melt source, segregation, transport and granite emplacement mechanisms. *Earth Environ. Sci. Trans. R. Soc. Edinb.* 100, 219–233. doi: 10.1017/s175569100901617x

Searle, M., Windley, B., Coward, M., Cooper, D., Rex, A., Rex, D., et al. (1987). The closing of Tethys and the tectonics of the Himalaya. *Geol. Soc. Am. Bull.* 98, 678–701.

Shellnutt, J. G., Lee, T.-Y., Brookfield, M. E., and Chung, S.-L. (2014). Correlation between magmatism of the Ladakh Batholith and plate convergence rates during the India–Eurasia collision. *Gondwana Res.* 26, 1051–1059. doi: 10.1016/j.gr.2013.09.006

Singh, S. (2019). Protracted zircon growth in migmatites and *in situ* melt of Higher Himalayan Crystallines: U–Pb ages from Bhagirathi Valley, NW Himalaya, India. *Geosci. Front.* 10, 793–809. doi: 10.1016/j.gsf.2017.12.014

Sláma, J., Košler, J., Condon, D. J., Crowley, J. L., Gerdes, A., Hanchar, J. M., et al. (2008). Plešovice zircon—a new natural reference material for U–Pb and Hf isotopic microanalysis. *Chem. Geol.* 249, 1–35. doi: 10.1016/j.chemgeo.2007.11.005

Smit, M. A., Hacker, B. R., and Lee, J. (2014). Tibetan garnet records early Eocene initiation of thickening in the Himalaya. *Geology* 42, 591–594. doi: 10.1130/g35524.1

Soucy La Roche, R., Godin, L., Cottle, J. M., and Kellett, D. A. (2018). Preservation of the early evolution of the Himalayan middle crust in foreland klippen: insights from the Karnali klippe, west Nepal. *Tectonics* 37, 1161–1193. doi: 10.1002/2017tc004847

Soucy La Roche, R., Godin, L., Cottle, J. M., and Kellett, D. A. (2019). Tectonometamorphic evolution of the tip of the Himalayan metamorphic core in the Jajarkot klippe, west Nepal. *J. Metamorphic Geol.* 37, 239–269. doi: 10.1111/jmg.12459

Stübner, K., Grujic, D., Parrish, R. R., Roberts, N. M., Kronz, A., Wooden, J., et al. (2014). Monazite geochronology unravels the timing of crustal thickening in NW Himalaya. *Lithos* 210, 111–128. doi: 10.1016/j.lithos.2014.09.024

Sun, S.-S., and McDonough, W. F. (1989). "Chemical and isotopic systematics of oceanic basalts: implications for mantle composition and processes," in *Magmatism in the Ocean Basins*, Vol. 42, eds A. D. Saunders, and M. J. Norry (Berkeley, CA: Geological Society of London Special Publication), 313–345. doi: 10.1144/gsl.sp.1989.042.01.19

Van der Voo, R., Spakman, W., and Bijwaard, H. (1999). Tethyan subducted slabs under India. *Earth Planet. Sci. Lett.* 171, 7–20. doi: 10.1016/S0012-821X(99)00131-4

van Hinsbergen, D. J., Steinberger, B., Doubrovine, P. V., and Gassmöller, R. (2011). Acceleration and deceleration of India–ŘAsia convergence since the Cretaceous: Roles of mantle plumes and continental collision. *J. Geophys. Res. Solid Earth* 116, B06101. doi: 10.1029/2010JB008051

Vervoort, J. D., Patchett, P. J., Blichert-Toft, J., and Albarède, F. (1999). Relationships between Lu–Hf and Sm–Nd isotopic systems in the global sedimentary system. *Earth Planet. Sci. Lett.* 168, 79–99. doi: 10.1016/s0012-821x(99)00047-3

Wang, C., Ding, L., Zhang, L.-Y., Kapp, P., Pullen, A., and Yue, Y.-H. (2016). Petrogenesis of Middle–Late Triassic volcanic rocks from the Gangdese belt, southern Lhasa terrane: implications for early subduction of Neo-Tethyan oceanic lithosphere. *Lithos* 262, 320–333. doi: 10.1016/j.lithos.2016.07.021

Wang, J., Zhang, J., and Wang, X. (2013). Structural kinematics, metamorphic P–T profiles and zircon geochronology across the Greater H imalayan Crystalline Complex in south-central T ibet: implication for a revised channel flow. *J. Metamorphic Geol.* 31, 607–628. doi: 10.1111/jmg.12036

Wang, J.-M., Wu, F.-Y., Rubatto, D., Liu, S.-R., Zhang, J.-J., Liu, X.-C., et al. (2017). Monazite behaviour during isothermal decompression in pelitic granulites: a case study from Dinggye, Tibetan Himalaya. *Contrib. Mineral. Petrol.* 172:81.

Weis, D., Kieffer, B., Hanano, D., Nobre Silva, I., Barling, J., Pretorius, W., et al. (2007). Hf isotope compositions of US Geological Survey reference materials. *Geochem. Geophys. Geosyst.* 8:Q06006. doi: 10.1029/2006GC001473

Weis, D., Kieffer, B., Maerschalk, C., Barling, J., de Jong, J., Williams, G. A., et al. (2006). High-precision isotopic characterization of USGS reference materials by TIMS and MC-ICP-MS. *Geochem. Geophys. Geosyst.* 7:Q08006. doi: 10.1029/2006GC001283

Wen, D.-R., Liu, D., Chung, S.-L., Chu, M.-F., Ji, J., and Zhang, Q. (2008). Zircon SHRIMP U–Pb ages of the Gangdese Batholith and implications for Neotethyan subduction in southern Tibet. *Chem. Geol.* 252, 191–201. doi: 10.1016/j.chemgeo.2008.03.003

Wiesmayr, G., and Grasemann, B. (2002). Eohimalayan fold and thrust belt: implications for the geodynamic evolution of the NW-Himalaya (India). *Tectonics* 21:1058. doi: 10.1029/2002TC001363

Woodhead, J. D., and Hergt, J. M. (2005). Preliminary appraisal of seven natural zircon reference materials for *in situ* Hf isotope determination. *Geostand. Geoanal. Res.* 29, 183–195. doi: 10.1111/j.1751-908x.2005.tb00891.x

Wu, F. Y., Ji, W. Q., Wang, J. G., Liu, C. Z., Chung, S. L., and Clift, P. D. (2014). Zircon U–Pb and Hf isotopic constraints on the onset time of India-Asia collision. *Am. J. Sci.* 314, 548–579. doi: 10.2475/02.2014.04

Wu, F.-Y., Liu, X.-C., Liu, Z.-C., Wang, R.-C., Xie, L., Wang, J.-M., et al. (2020). Highly fractionated Himalayan leucogranites and associated rare-metal mineralization. *Lithos* 35:105319. doi: 10.1016/j.lithos.2019.105319

Wu, F. Y., Liu, Z. C., Liu, Z. C., and Ji, W. Q. (2015). Himalayan leucogranite: petrogenesis and implications to orogenesis and plateau uplift. *Acta Petrol. Sin.* 31, 1–36.

Wu, F.-Y., Yang, Y.-H., Xie, L.-W., Yang, J.-H., and Xu, P. (2006). Hf isotopic compositions of the standard zircons and baddeleyites used in U–Pb geochronology. *Chem. Geol.* 234, 105–126. doi: 10.1016/j.chemgeo.2006.05.003

Xie, L., Zhang, Y., Zhang, H., Sun, J., and Wu, F. (2008). *In situ* simultaneous determination of trace elements, U–Pb and Lu–Hf isotopes in zircon and baddeleyite. *Chin. Sci. Bull.* 53, 1565–1573. doi: 10.1007/s11434-008-0086-y

Yakymchuk, C., and Brown, M. (2014). Consequences of open-system melting in tectonics. *Geochem. Geophys. Geosyst.* 171, 21–40. doi: 10.1144/jgs2013-039

Yang, L., Liu, X.-C., Wang, J.-M., and Wu, F.-Y. (2019). Is Himalayan leucogranite a product by *in situ* partial melting of the Greater Himalayan Crystalline? A comparative study of leucosome and leucogranite from Nyalam, southern Tibet. *Lithos* 342, 542–556. doi: 10.1016/j.lithos.2019.06.007

Yang, Y.-H., Chu, Z.-Y., Wu, F.-Y., Xie, L.-W., and Yang, J.-H. (2011a). Precise and accurate determination of Sm, Nd concentrations and Nd isotopic compositions in geological samples by MC-ICP-MS. *J. Anal. Atomic Spectrom.* 26, 1237–1244.

Yang, Y.-H., Wu, F.-Y., Xie, L.-W., Yang, J.-H., and Zhang, Y.-B. (2011b). High-precision direct determination of the 87Sr/86Sr isotope ratio of bottled Sr-rich natural mineral drinking water using multiple collector inductively coupled plasma mass spectrometry. *Spectrochim. Acta Part B Atomic Spectrosc.* 66, 656–660. doi: 10.1016/j.sab.2011.07.004

Yang, Y.-H., Zhang, H.-F., Chu, Z.-Y., Xie, L.-W., and Wu, F.-Y. (2010). Combined chemical separation of Lu, Hf, Rb, Sr, Sm and Nd from a single rock digest and precise and accurate isotope determinations of Lu–Hf, Rb–Sr and Sm–Nd isotope systems using Multi-Collector ICP-MS and TIMS. *Int. J. Mass Spectrom.* 290, 120–126. doi: 10.1016/j.ijms.2009.12.011

Yin, A. (2006). Cenozoic tectonic evolution of the Himalayan orogen as constrained by along-strike variation of structural geometry, exhumation history, and foreland sedimentation. *Earth Sci. Rev.* 76, 1–131. doi: 10.1016/j.earscirev.2005.05.004

Zeng, L., and Gao, L. (2017). Cenozoic crustal anatexis and the leucogranites in the Himalayan collisional orogenic belt. *Acta Petrol. Sin.* 33, 1420–1444.

Zeng, L., Gao, L.-E., Tang, S., Hou, K., Guo, C., and Hu, G. (2015). "Eocene magmatism in the Tethyan Himalaya, southern Tibet," in *Tectonics of the Himalaya*, eds S. Mukherjee, R. Carosi, P. A. Van der Beek, B. K. Mukherjee, and D. M. Robinson (Berkeley, CA: Geological Society of London Special Publication), 287–316. doi: 10.1144/sp412.8

Zeng, L., Liu, J., Gao, L., Xie, K., and Wen, L. (2009). Early Oligocene anatexis in the Yardoi gneiss dome, southern Tibet and geological implications. *Chinese Sci. Bull.* 54, 104–112. doi: 10.1007/s11434-008-0362-x

Zeng, L. S., Gao, L. E., Xie, K. J., and Jing, L. Z. (2011). Mid-Eocene high Sr/Y granites in the Northern Himalayan Gneiss Domes: melting thickened lower continental crust. *Earth Planet. Sci. Lett.* 303, 251–266. doi: 10.1016/j.epsl.2011.01.005

Zhang, H., Harris, N., Parrish, R., Kelley, S., Zhang, L., Rogers, N., et al. (2004). Causes and consequences of protracted melting of the mid-crust exposed in the North Himalayan antiform. *Earth Planet. Sci. Lett.* 228, 195–212. doi: 10.1016/j.epsl.2004.09.031

Zhang, Z., Dong, X., Ding, H., Tian, Z., and Xiang, H. (2017). Metamorphism and partial melting of the Himalayan orogen. *Acta Petrol. Sin.* 33, 2313–2341.

Zhang, Z., Xiang, H., Dong, X., Ding, H., and He, Z. (2015). Long-lived high-temperature granulite-facies metamorphism in the Eastern Himalayan orogen, south Tibet. *Lithos* 212-215, 1–15. doi: 10.1016/j.lithos.2014.10.009

Zhao, W., Mechie, J., Brown, L., Guo, J., Haines, S., Hearn, T., et al. (2001). Crustal structure of central Tibet as derived from project INDEPTH wide-angle seismic data. *Geophys. J. Int.* 145, 486–498. doi: 10.1046/j.0956-540x.2001.01402.x

Conflict of Interest: The authors declare that the research was conducted in the absence of any commercial or financial relationships that could be construed as a potential conflict of interest.

The reviewer KQ declared a shared affiliation, with no collaboration, with several of the authors, F-YW, J-MW, X-CL, ZZ, J-GW, CZ, to the handling Editor at the time of review.

frontiers in Earth Science

ORIGINAL RESEARCH
published: 24 July 2020
doi: 10.3389/feart.2020.00190

Schlieren-Bound Magmatic Structures Record Crystal Flow-Sorting in Dynamic Upper-Crustal Magma-Mush Chambers

Katie E. Ardill[1]†, Scott R. Paterson[1], Jonathan Stanback[1], Pablo H. Alasino[2,3], James J. King[4,5] and Simon E. Crosbie[4]*

[1] Department of Earth Sciences, University of Southern California, Los Angeles, CA, United States, [2] Centro Regional de Investigaciones Científicas y Transferencia Tecnológica de LaRioja (Prov. de LaRioja–UNLaR–SEGEMAR–UNCa–CONICET), Anillaco, Argentina, [3] Instituto de Geología y Recursos Naturales, Centro de Investigación e Innovación Tecnológica, Universidad Nacional de LaRioja (INGeReN-CENIIT-UNLaR), La Rioja, Argentina, [4] Department of Earth Sciences, Durham University, Durham, United Kingdom, [5] Department of Earth Sciences, University of Oxford, Oxford, United Kingdom

OPEN ACCESS

Edited by:
J. Gregory Shellnutt, National Taiwan Normal University, Taiwan

Reviewed by:
Saskia Erdmann, UMR 7327 Institut des Sciences de la Terre d'Orléans (ISTO), France
George Bergantz, University of Washington, United States

***Correspondence:**
Katie E. Ardill
ardill@csus.edu

†Present address:
Katie E. Ardill
California State University, Sacramento, CA, United States

Specialty section:
This article was submitted to Petrology, a section of the journal Frontiers in Earth Science

Received: *03 March 2020*
Accepted: *12 May 2020*
Published: *24 July 2020*

Citation:
Ardill KE, Paterson SR, Stanback J, Alasino PH, King JJ and Crosbie SE (2020) Schlieren-Bound Magmatic Structures Record Crystal Flow-Sorting in Dynamic Upper-Crustal Magma-Mush Chambers. Front. Earth Sci. 8:190. doi: 10.3389/feart.2020.00190

The size, longevity, and mobility of upper-crustal magma mushes, and thus their ability to mix and interact with newly arriving magma batches, are key factors determining the evolution of magma reservoirs. Magmatic structures in plutons represent local sites of structural and compositional diversity and provide an opportunity to test the extent of physical and chemical processes that operated through time. Regional compilation of compositionally defined magmatic structures, specifically those involving schlieren, in the Tuolumne Intrusive Complex (TIC), yields a synthesis of ∼1500 schlieren-bound structure measurements. Field observations, petrography, and whole-rock geochemistry were integrated to test schlieren formation mechanisms. At a local scale (1 mm–1 m), we find that schlieren-bound structures formed from the surrounding host magma during dynamic magmatic processes such as crystal flow-sorting, magmatic faulting, and folding. Fluidization of the magma mush, interpreted from 1 m to 1 km wide domains of clustered schlieren-bound structures, appears to have operated within a hydrogranular medium, or "crystal slurry" (Bergantz et al., 2017). At the regional scale (10's km), outward younging patterns of troughs, migrating tubes, and plumes indicate that the mush convected, driven by intrusion of new pulses. Troughs and planar schlieren are weakly oriented parallel to nearby major unit contacts, which could be related to internal mush convection or effects of high thermochemical gradients at internal unit boundaries. We hypothesize that these younging patterns and orientations have the potential to constrain the size of mobile magma mixing regions, that in the TIC extended to a minimum of 150 km^2 (∼1500 km^3) and were long-lived (>1 m.y). These require the generation of extensive melt-present reservoirs that could flow magmatically,

formed from the amalgamation of intruding magma pulses, and precludes dike, sill, or laccolith emplacement models. We conclude that schlieren-bound structures are faithful recorders of the multi-scale, hypersolidus evolution of upper-crustal magma bodies, and represent useful tools for studying plutonic systems.

Keywords: magmatic structures, schlieren, flow sorting, crystal mush, magmatic fabric, Tuolumne Intrusive Complex, Sierra Nevada

INTRODUCTION

On the path to solidification, magma reservoirs reside in the crust as a crystal-rich mush (Marsh, 1981). Current debates relate to the size and longevity of magma mushes, and the extent to which they can be mobilized by internal (magmatic) and external (tectonic) forces (e.g., Annen et al., 2015; Bachmann and Huber, 2016; Paterson et al., 2016; Bartley et al., 2018; Holness, 2018; Jackson et al., 2018). Each of these factors controls the importance, and spatiotemporal extent, of physical and chemical magmatic processes that drive differentiation within magma reservoirs (e.g., Spera and Bohrson, 2018). Thus, these factors have implications for understanding transcrustal magmatic plumbing systems, and how material is transported and differentiated vertically in the crust (e.g., Lipman, 2007; Cashman et al., 2017). Additionally, the size, longevity, and mobility of magma mushes in the upper-crust is closely coupled with eruptive behavior at volcanic centers (e.g., Bachmann and Bergantz, 2004).

Investigating the evolving behavior of magma reservoirs is a multi-faceted issue due to the multiphase nature of magmas as well as the effects of incremental emplacement, magma–host rock interactions, and local and regional stresses on the magmatic plumbing system. In addition, magma experiences a substantial transition in effective viscosity during crystallization, between 10 and 20 orders of magnitude, emphasizing that a wide range of behaviors are possible (e.g., Petford, 2003; Sparks et al., 2019). Early studies suggested that magma composition and crystallinity were primary indicators of magma viscosity, as well as whether the magma could erupt, or "lock up" (e.g., Van der Molen and Paterson, 1979; Rosenberg and Handy, 2005; Petford, 2009). More recently, the primary focus has been on describing magmatic systems from the mechanical perspective of hydrogranular, dense, crystal-rich slurries, with or without exsolved volatiles (e.g., Schleicher et al., 2016; Bergantz et al., 2017; Degruyter et al., 2019; McIntire et al., 2019; Petford et al., 2020). This perspective is particularly relevant for magma mushes as it incorporates the effects of particle-particle interactions and deformation on the state of the mush, which are both well-documented in field-based studies of magmatic structures in plutons (e.g., Paterson et al., 2018).

The Late Cretaceous Tuolumne Intrusive Complex (TIC), in the central Sierra Nevada, California is one exceptionally exposed example of a long-lived, composite, upper-crustal pluton, incrementally emplaced over ∼10 m.y. at 6–10 km depth (Ague and Brimhall, 1988; Bateman, 1992; Coleman et al., 2004; Memeti et al., 2010; Paterson et al., 2016). The emplacement history and evolution of the TIC continues to be intensely studied and debated (e.g., Memeti et al., 2014; Paterson et al., 2016; Bartley et al., 2018). On one hand, the TIC has been proposed to consist of sheets with ephemeral mush systems that have little interaction with each other during or after emplacement (e.g., Coleman et al., 2012; Bartley et al., 2018). In contrast, other studies have proposed that the TIC formed several long-lived (i.e., 0.5–2 m.y.) magma chambers, regions of interconnected magma mush that experienced convection and return flow (e.g., Bateman, 1992; Burgess and Miller, 2008; Solgadi and Sawyer, 2008; Memeti et al., 2010; Paterson et al., 2011, 2016). Each model has distinct implications for the origin of diverse magma compositions, the thermal history of the complex, the expected volume of eruptible magma, as well as magma rheology and the structural evolution of the complex.

The TIC contains an unusually wide range of magmatic structures; studying them can start to address issues surrounding the magmatic history of the complex. Compositionally defined magmatic structures, and specifically schlieren-bound structures, are the focus of this study (Cloos, 1936; Bateman, 1992; Reid et al., 1993; Žák et al., 2007; Solgadi and Sawyer, 2008; Paterson, 2009; Memeti et al., 2014; Paterson et al., 2018). In plutonic systems generally, the processes driving compositionally defined magmatic structure formation and consequent implications for magma rheology remain controversial, with contrasting models that rely on either physical (active) or chemical (static) mechanisms (e.g., McBirney and Noyes, 1979; Weinberg et al., 2001; Paterson, 2009; Boudreau, 2011; Hodge et al., 2012). Thus, understanding the formation and significance of magmatic structures is an important step towards understanding the physical and chemical evolution of upper-crustal magma reservoirs.

This article examines compositionally defined magmatic structures in the TIC from field, structural, and geochemical perspectives to investigate the evolution and dynamics of an upper crustal magma storage region at scales ranging from individual structures to pluton-wide dimensions. We find that schlieren-bound structures formed by physical flow-sorting in an active crystal-mush environment, triggered by local flow instabilities. Dense minerals were selectively accumulated, to varying degrees, along both steeply and gently dipping boundaries. Schlieren-bound structures may form highly intricate and disorganized patterns at the outcrop scale, reflecting the complexity of crystal-melt and crystal-crystal interactions in a hydrogranular medium (e.g., Bergantz et al., 2017). Within mappable domains, the clustering of structures reflects the spatial and temporal heterogeneity of the magma mush, where fluidized (more mobile crystal mush) regions promote structure formation, and less dynamic zones are devoid of schlieren-bound structures. Preservation of structures occurs within a

"window" of favorable magmatic conditions (e.g., crystallinity, density, viscosity), which moves through time as the magmatic system cools. At the regional scale, schlieren-bound structures show weak to moderate alignment with internal unit contacts and outward younging directions that we propose are the result of internal return flow and convection of the mush. We use these patterns to estimate the maximum and minimum sizes of active magma chambers.

BACKGROUND

Compositionally Defined Magmatic Structure Models

Magmatic structures may be broadly grouped by the preferred alignment of objects (e.g., fabrics), deformation related structures (e.g., folds and faults), structures of growth, younging, or kinematics (e.g., cross-cutting boundaries, S-C structures), and structures involving internal contacts and layering (e.g., dikes and hybrid zones; Paterson et al., 2018). A fifth group includes compositionally defined magmatic structures. For example, the heterogeneous clustering of mineral populations, such as K-feldspar megacryst clusters (Vernon and Paterson, 2006; Memeti et al., 2014; Rocher et al., 2018), plagioclase clusters (Oppenheim et al., in review), and schlieren (Barrière, 1981; Reid et al., 1993).

The formation of compositionally defined magmatic structures in mafic magmatic systems has been the focus of studies for decades (e.g., reviews by Namur et al., 2015; Holness et al., 2017; O'Driscoll and VanTongeren, 2017). For example, the Skaergaard intrusion preserves spectacular rhythmic layering as well as channel-shaped trough structures (e.g., Wager and Brown, 1968; Irvine et al., 1998; Vukmanovic et al., 2018). Fewer studies in silicic magmatic systems, the focus of this study, are of great interest as they demonstrate that compositionally defined magmatic structures may form over a wide compositional and rheological range (e.g., Wiebe and Collins, 1998; Weinberg et al., 2001; Paterson, 2009; Clemens et al., 2020).

One subset of compositionally defined magmatic structures involves the formation of schlieren. Schlieren are igneous modally defined layers that may contain abundant hornblende, biotite, magnetite, apatite, titanite, and zircon, amongst other accessory minerals. They may be modally- or grain-size-graded. While observed in granitoid plutons worldwide, a few localities are noted for their rich abundance, and variety, of schlieren-bound magmatic structures: the Ploumanac'h massif, Brittany (Barrière, 1981), the Tavares pluton, Brazil (Weinberg et al., 2001), the Halifax pluton, Nova Scotia (Smith, 1974; Clarke, 2003; Clarke et al., 2013), the Vinalhaven granite, Maine (Wiebe and Collins, 1998; Wiebe et al., 2007), and the TIC, California (e.g., Cloos, 1936; Bateman, 1992; Reid et al., 1993; Paterson, 2009).

Schlieren are commonly found in planar form (e.g., Bateman, 1992; Žák and Klomínský, 2007; Burgess and Miller, 2008; Pinotti et al., 2016), but also delineate curved boundaries of structures such as: channel-shaped magmatic troughs (e.g., Wahrhaftig, 1979; Barrière, 1981; Solgadi and Sawyer, 2008; Žák and Paterson, 2010; Alasino et al., 2019; see also Wager and Brown, 1968; Vukmanovic et al., 2018 for mafic systems), stationary and migrating tubes, also called ladder dikes (e.g., Reid et al., 1993; Weinberg et al., 2001; Wiebe et al., 2007; Dietl et al., 2010; Clarke et al., 2013), meter-scale diapirs and plume heads (e.g., Weinberg et al., 2001; Paterson, 2009), and mafic ellipsoids (e.g., Memeti et al., 2014).

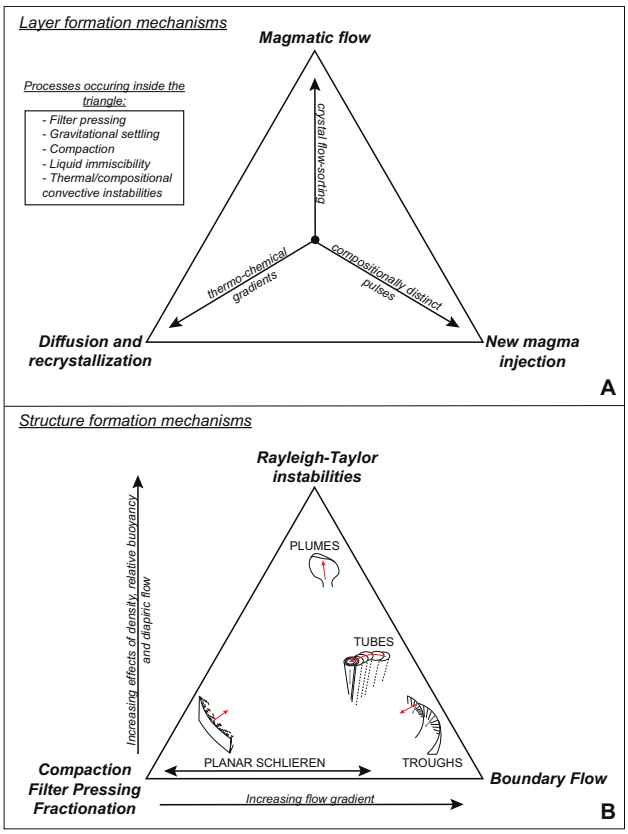

FIGURE 1 | Summary of formation mechanisms for schlieren and different magmatic structures. **(A)** Layer formation mechanisms. Processes listed in the box can occur in the field inside the triangle and represent combinations of end-member processes (bold). **(B)** Structure formation mechanisms. A summary of proposed formation mechanisms and how different schlieren-bound structures have been interpreted. Schematic diagrams show the approximate 3D geometries of each structure. Gray arrows represent interpreted motion/flow directions. Red arrows represent younging or migration directions.

In general, studies of schlieren-bound magmatic structures aim to address two related questions: (1) under what magmatic conditions and by which process(es) do schlieren form (**Figure 1A**) and (2) how do these processes influence, or contribute to, the variety of schlieren-bound structures of different geometries and characteristics (**Figure 1B**)?

Models describing schlieren formation generally fall within the range of three end-member processes, or "schools of thought" (**Figure 1A**; see also Solgadi and Sawyer, 2008; Barbey, 2009). The first considers schlieren as a product of incomplete mixing of new (mafic) magma injections. One example of this process

would be the disaggregation of mafic magmatic enclaves into layers (e.g., Barbey et al., 2008; Farner et al., 2018). Related models propose that schlieren are a product of contamination and assimilation of host rock fragments (e.g., Beard et al., 2005), however, these schlieren are not considered here further in the TIC due to the rarity of host rock fragments associated with the schlieren-bound structures. The second school of thought calls upon *in-situ* thermochemical diffusion and recrystallization as principal mechanisms to generate modal layering in schlieren. Processes such as oscillatory nucleation and Ostwald ripening are important in these models (lower left **Figure 1A**; e.g., McBirney and Noyes, 1979; Glazner, 2014). The third school of thought views schlieren as resulting from magmatic flow against a more rigid boundary, in its most dynamic form by magmatic currents or avalanching, to sort crystals by size and/or density (e.g., Irvine et al., 1998; Solgadi and Sawyer, 2008; Alasino et al., 2019; **Figure 1A**).

Under this framework, a range of schlieren-forming processes have been proposed that involve different combinations of these three end-members (**Figure 1A**). These processes include thermal and compositional convective instabilities that could result from intrusion of new magma pulses or thermochemical gradients within a solidification front (Griffiths, 1986; Weinberg et al., 2001; Pons et al., 2006; Wiebe et al., 2007; Paterson, 2009; Rocher et al., 2018; Alasino et al., 2019), shear/hydrodynamic flow sorting (Cloos, 1936; Bhattacharji and Smith, 1964; Barrière, 1981; Pitcher, 1997; Clarke et al., 2013) together with compaction and filter pressing at rheologic boundaries to extract melts (Weinberg et al., 2001; Žák et al., 2007; Paterson, 2009), gravitational settling (e.g., Coats, 1936; Wager and Deer, 1939), and liquid immiscibility (e.g., Glazner et al., 2012).

Physical processes have been proposed to create the wide variety of schlieren-bound structures; structure types have been distinguished and explained by variations in magma flow geometry and intensity, magma rheology, and the importance of thermal and compositional gradients (**Figure 1B**) (e.g., Weinberg et al., 2001; Paterson, 2009; Wiebe et al., 2017). These variations suggest that planar schlieren could form horizontally in a largely static environment, with repeated filter pressing and/or compaction. Compaction would produce a distinct microstructural record of viscous deformation (Holness et al., 2017). However, this is not observed in Skaergaard troughs (Vukmanovic et al., 2018). Where layers are steeply dipping, graded, and deformed, magmatic flow conditions are considered to be more dynamic (**Figure 1B**; Paterson, 2009). For example, in this model, troughs represent magmatic erosion and boundary flow processes within a channel-shaped, basal mushy surface where minerals are deposited and flow is channelized, as shown by magmatic hornblende lineations plunging down-axis in trough basal surfaces (Solgadi and Sawyer, 2008; Paterson, 2009; Vukmanovic et al., 2018). Where relative buoyancy and density effects are significant in the magma chamber, structures such as tubes and plumes may be favored (**Figure 1B**; e.g., Wiebe et al., 2007; Paterson, 2009; Clarke et al., 2013). Models to describe tube formation suggest that they represent vertical magma (or volatile) pathways (e.g., Weinberg et al., 2001; Paterson, 2009; Dietl et al., 2010; Clarke et al., 2013), are a record of sinking objects (e.g., Wiebe et al., 2007; Clarke et al., 2013) or are a package of stacked trough channels (e.g., Wiebe et al., 2017). Plume heads represent examples of (now variably oriented) Rayleigh-Taylor instabilities in their dome-like heads, detached from the surrounding host (Griffiths, 1986; Paterson, 2009). The rheology of the surrounding host magma must play a role in forming and deforming structures (e.g., Wiebe and Collins, 1998; Vernon and Paterson, 2006; Hodge et al., 2012), but it is unclear if it controls the types of structures that can form.

The Tuolumne Intrusive Complex

The TIC is a ∼1100 km^2 partially nested, composite intrusive complex, emplaced over ∼10 m.y. (Calkins, 1930; Bateman and Chappell, 1979; Bateman, 1992; Coleman et al., 2004; Memeti et al., 2010; Paterson et al., 2016). From oldest to youngest, major units are: the 95–92 Ma Kuna Crest granodiorite (KC; **Figure 2**), the 92–90 Ma equigranular Half Dome Granodiorite (eHD; **Figure 2**), the 90–88 Ma porphyritic Half Dome Granodiorite (pHD; **Figure 2**), the 88–85 Ma Cathedral Peak Granodiorite (CP; **Figure 2**). Sheet-like to irregularly shaped leucogranite bodies are found throughout all units, and the largest known is the Johnson Granite Porphyry (JP; **Figure 2**; Kistler and Fleck, 1994; Coleman et al., 2004; Bracciali et al., 2008; Memeti et al., 2010, 2014; Paterson et al., 2016). Memeti et al. (2014) published a zircon isochron map of the TIC, using chemical abrasion-isotope dilution-thermal ionization mass spectrometry (CA-ID-TIMS) U-Pb in zircon ages and structural observations, that illustrates the spatial relationships in zircon crystallization ages. Minor modification to this model is shown in red contours, drawn by eye following age interpretations of Memeti et al. (2010) and Paterson et al. (2016). Regions of steep age gradients, representing large age ranges over a short distance, include the western TIC margin, and the Kuna Crest lobe (Figure 4-3 in Memeti et al., 2014; **Figure 2**). These regions are associated with internal contacts, involving magmatic erosion and recycling along boundaries (Paterson et al., 2016). In contrast, the inner portion of the CP unit contains larger regions of similar zircon ages, depicted by shallow gradients, and indicates a general younging towards the north (Memeti et al., 2010; Figure 4-3 in Memeti et al., 2014; **Figure 2**).

Major and minor boundaries within the TIC are defined by a range of internal contact types (Memeti et al., 2010, 2014; Paterson et al., 2016). These include sharp and gradational contacts, and contacts defined by a change in composition and/or microstructure (Memeti et al., 2014; Paterson et al., 2016). Contacts are variable both along and across strike; for example, at Glen Aulin (GA in **Figure 2**), the boundary between eHD and pHD is characteristically gradational over 10–25 m, while the younger pHD-CP contact alternates between a gradational and sharp contact along strike at the 100 m scale (Paterson et al., 2016). Contacts in some cases are defined by compositionally defined magmatic structures and may have approximately contact-parallel magmatic or solid-state fabrics (Žák et al., 2007, 2009; Paterson et al., 2008). These zones are interpreted to record information about magma mingling and mixing, erosion, recycling, and preserve information about thermal or rheological magmatic conditions (Memeti et al., 2010; Paterson et al., 2016).

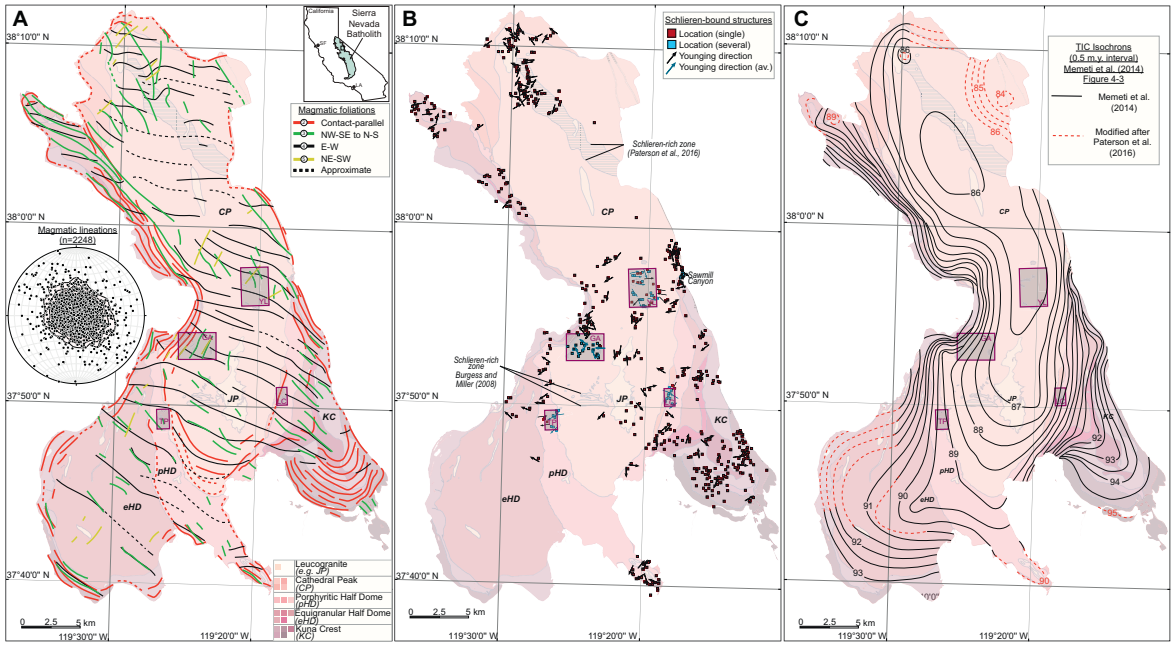

FIGURE 2 | Synthesis of magmatic structures in the Tuolumne Intrusive Complex. **(A)** Magmatic fabric summary. Foliation data are summarized by trend lines. Lineations are summarized on the stereonet inset. Inset map shows the location of the Tuolumne Intrusive Complex (outlined in box). **(B)** Map summary of schlieren-bound structural data. Points represent the locations of schlieren-bound structures. Zones of concentrated structures are highlighted in blue, and observations of younging/migration are labeled with arrows. **(C)** Map summary of U-Pb zircon geochronology after Figure 4-3 in Memeti et al. (2014). Isochrons shown in 0.5 m.y. intervals. Black lines represent contours on the isochron map of Memeti et al. (2014). Red dashed lines denote interpreted modified contours drawn by eye, following ages published in Memeti et al. (2010) and Paterson et al. (2016). Unit abbreviations as follows: KC, Kuna Crest granodiorite; eHD, equigranular Half Dome granodiorite; pHD, porphyritic Half Dome granodiorite; CP, Cathedral Peak granodiorite; JP, Johnson Granite Porphyry. The locations of the four mapped domains are labeled. GA = Glen Aulin; YL, Young Lakes; TP, Tenaya Peak; LC, Lyell Canyon. Data sources for map and structural data: Chesterman (1975), Bateman et al. (1988), Loetterle (2004), Burgess and Miller (2008), Paterson et al. (2008), Solgadi and Sawyer (2008), Žák et al. (2009), Memeti et al. (2010, 2014), Paterson et al. (2016), and Oppenheim et al. (in review). We acknowledge Vali Memeti, Bob Miller, and Jiri Žák for sharing field data for this synthesis.

The complex is generally more mafic in older units and more felsic in younger units; however, every unit is highly composite, and a variety of rock types occur in each unit (Bateman, 1992; Memeti et al., 2014; Paterson et al., 2016). Four lobes at the margins of the TIC are each normally zoned (Memeti et al., 2010). Kuna Crest granodiorite rocks are both the most mafic and most varied in composition, from generally equigranular, minor gabbro and diorite to tonalite, granodiorite, granite, and leucogranite. The eHD and pHD are granodiorite units containing euhedral cm-size hornblende and biotite, with the addition of <3 cm K-feldspar phenocrysts in the pHD (Bateman and Chappell, 1979; Bateman, 1992; Memeti et al., 2014). Cathedral Peak granodiorite rocks are dominantly granodiorite to granite with K-feldspar megacrysts 2–12 cm forming the porphyritic texture (Bateman, 1992; Memeti et al., 2014). The most evolved, peraluminous rocks in the TIC are found in the youngest, NE corner of the CP unit (Memeti et al., 2010).

TIC rocks are metaluminous to locally peraluminous, calc-alkaline compositions, spanning a wide range of SiO_2 contents (48–79 wt.%) (Bateman and Chappell, 1979; Bateman, 1992; Memeti et al., 2014). Hornblende analyses indicate that all units experienced crystal accumulation and/or melt loss to varying degrees, contributing to the wide variation in rock type (Barnes et al., 2016; Werts et al., 2020). The considerable compositional overlap between units in major and trace elements, as well as isotopes, has been attributed to a combination of fractionation and mixing processes involving multiple magma sources; the depth that these processes occur is debated (e.g., Kistler et al., 1986; Bateman, 1992; Gray et al., 2008; Coleman et al., 2012; Memeti et al., 2014; Barnes et al., 2016).

Mapping by Cloos (1936), Bateman et al. (1983), Žák and Paterson (2005), and Žák et al. (2007) revealed multiple, time-transgressive magmatic fabrics within the TIC, defined by the alignment of hornblende, biotite, plagioclase, and quartz and K-feldspar to a lesser extent. Four magmatic fabrics were distinguished: Type 1 fabric is associated with local compositionally defined structures (e.g., schlieren) and is generally discordant to, or overprinted by, additional regionally extensive fabrics. Type 2 foliations, approximately margin parallel, but in detail at an angle to internal contacts, are typically the earliest formed (Žák et al., 2007). While type 3 (NW–SE-striking) and 4 (E–W-striking) fabrics may show contradictory or ambiguous overprinting relationships to each other at a single outcrop, Žák et al. (2007) concluded that the type 4 fabric

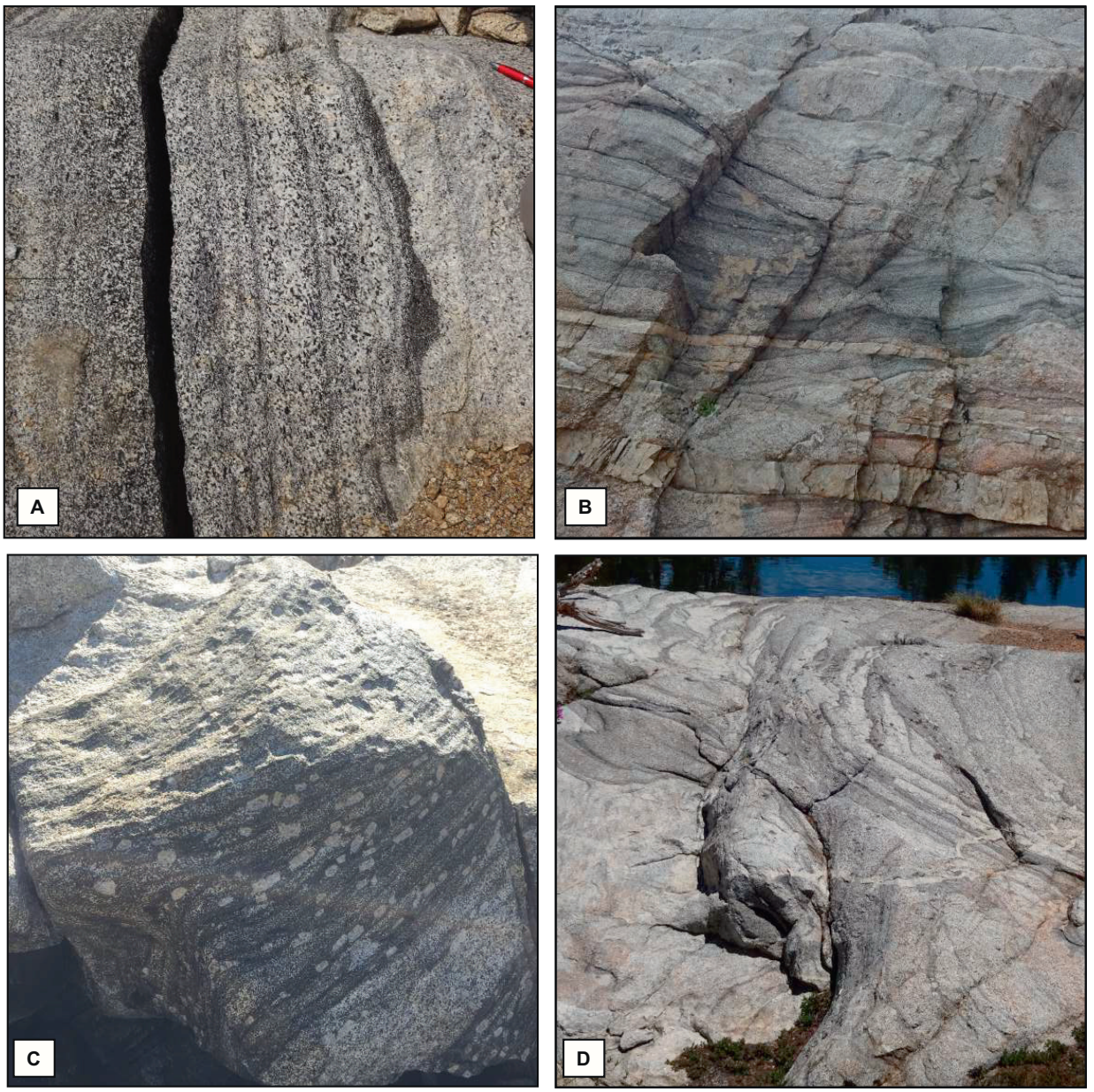

FIGURE 3 | Field photos of planar schlieren and trough structures. **(A)** Modally and grain-size graded schlieren layering in eHD, Sawmill Canyon area. Layers have a sharp, fine-grained base, and increase in grain size while reducing the amount of hornblende and biotite towards the right of the photo before the next layer forms. Pen for scale. **(B)** Erosion and redeposition of schlieren trough packages in CP at Sawmill Canyon. The package is upward-younging, and locally contains K-feldspar megacrysts. Leucogranite dikes cut the entire section. **(C)** Megacryst-bearing schlieren troughs showing low-angle truncation. Photo courtesy of J. McColl. **(D)** Complex schlieren trough packages with interlayered felsic material that is distinct from the surrounding host. Sawmill Canyon area.

is generally younger than type 3. Magmatic lineation plunges steeply in all cases (Žák et al., 2007).

Schlieren-Bound Magmatic Structures in the Tuolumne Intrusive Complex

The earliest studies of schlieren-bound magmatic structures in the TIC by Cloos (1936), Bateman (1992), and Reid et al. (1993) documented field characteristics of planar schlieren, troughs, and tubes (referred to as ladder dikes). These included planar to concave upward schlieren geometries with horizonal to sub-vertical dips, reverse (size) graded layering, and cross-bedding. Schlieren were proposed to form by either gravitational settling of crystals (e.g., Coats, 1936) or crystal flow-sorting (e.g., Cloos, 1936; Bhattacharji and Smith, 1964). Reid et al. (1993) suggested that the schlieren bounding tubes "settled from crystal slushes flowing through narrow vertical channels." Repeated events of schlieren deposition and erosion, and

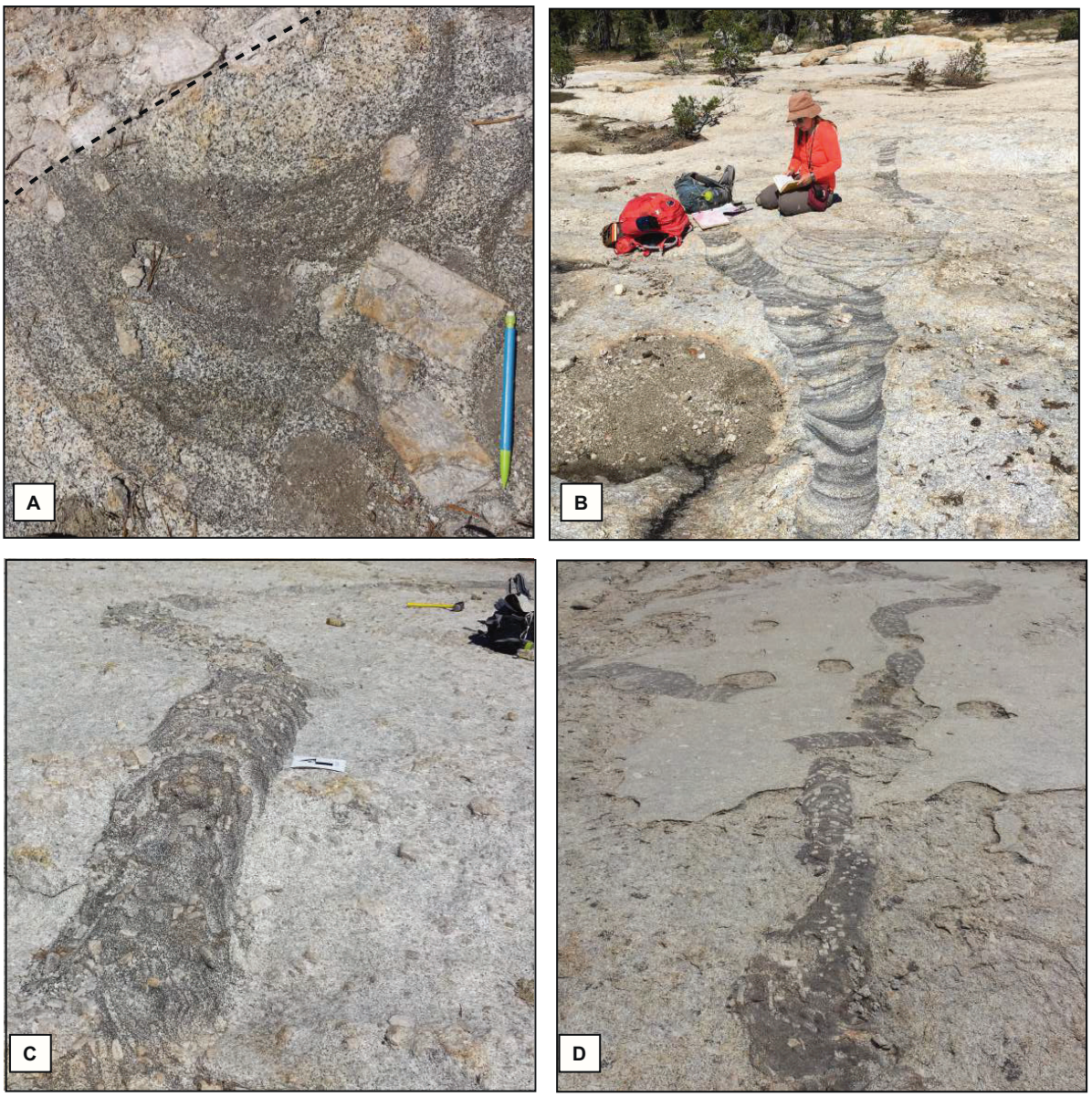

FIGURE 4 | Field photos of magmatic tubes. **(A)** Stationary tube truncated by host CP in the Glen Aulin area. Dashed line shows the contact where the tube is truncated by megacrystic CP. This tube contains at least 6 rings and unusually, the K-feldspar megacrysts within the structure are larger than the surrounding host megacrysts and also oriented at high angle to the schlieren rings. **(B)** Bifurcated migrating tube in the Glen Aulin area. This steeply dipping tube is ∼10 m in length, younging towards the field mapper. The diameter of the tube varies in size as it migrates, and in places is re-intruded by host CP. Photo from Paterson et al. (2018). **(C)** 6 m long migrating tube, migrating towards the bottom of the photo. These densely concentrated rings contain K-feldspar megacrysts. **(D)** 11 m migrating tube and 3 m migrating tube, Glen Aulin area. Segments of the longer tube have been re-intruded by host CP magma and rotated. The K-feldspar megacrysts align with the mafic minerals in the schlieren rings. Migration direction is towards the bottom of the photo (see also Hodge et al., 2012 for more information on this structure).

gradients in magma flow intensity were proposed to explain field observations of the layers (Bateman, 1992; Reid et al., 1993). Bateman (1992) first observed the map-scale pattern of outward-dipping planar schlieren towards older, outer units and interpreted this pattern to result from magma tilting and shearing on the partly solid margins of the magma chamber, driven by emplacement of new magma at the core of the complex.

Reid et al. (1993) noted that migrating tubes in the TIC are spatially clustered, and that the minerals in schlieren defining tubes, while highly concentrated, matched the assemblage of the surrounding host. Whole-rock major and trace element data supported interpretations that schlieren are cumulate rocks derived from main-sequence TIC magmas, with some derived from more mafic magmas. Notably, schlieren are depleted in Al_2O_3, and other elements necessary to form plagioclase,

relative to the main-sequence TIC rocks (Reid et al., 1993). Because of this, crystal accumulation associated with schlieren formation was not considered a viable mechanism to generate the compositional variety of main-sequence TIC rocks.

Subsequent studies investigated the interaction between structure formation and local- to regional-scale magmatic deformation. Loetterle and Bergantz (2003) interpreted deformation-related structures such as schlieren slumping to represent loading of a crystal mush at low melt fractions between 20 and 50%. Žák and Paterson (2005) mapped sheeted zones in the TIC and found outward younging planar schlieren, troughs, and tubes that formed during and after assembly of the sheets. These structures were subsequently deformed by magmatic faults and folds and overprinted by magmatic fabrics (Žák and Paterson, 2005). Domains with the most complex structural and petrologic relationships were found at irregularly shaped contacts, such as corners (Žák and Paterson, 2005).

Paterson et al. (2008) interpreted magmatic structures within the Sawmill Canyon sheeted zone as local thermal-mechanical instabilities in crystal-rich magmas. Schlieren are enriched by 3–4-fold in the high-field-strength elements (HFSE) relative to the surrounding host, but K, Na, Sr, and Rb remain constant, consistent with the enrichment and depletion trends identified by Reid et al. (1993). Least-squares modeling of whole-rock data (Albarède, 1996) required ∼30% accumulation of the constituent minerals to form schlieren. Leveraging zircon saturation temperatures calculated for TIC magmas (Miller et al., 2007), the authors proposed schlieren formation to occur between ∼760°C and the solidus. The structures are locally intensely magmatically deformed, but also record the regional strain by overprinted magmatic fabric, which likely became effective when the local magma flow field waned (Paterson et al., 2008). The authors emphasized the importance of rheologic flow and stress gradients over gravitational forces alone in forming steeply dipping schlieren.

The Sawmill Canyon structures were also studied from a microstructural and chemical perspective by Solgadi and Sawyer (2008). Within planar schlieren and trough structures, they identified multiple hornblende populations corresponding to the major host rock units in the area (KC, HD, and CP units), and thus interpreted schlieren to represent crystal mixtures. Hornblende did not show intra-layer compositional gradients, and thus did not form from a gradually evolving melt composition or in-situ fractionation (Solgadi and Sawyer, 2008). All minerals within schlieren gradually were rotated away from basal, layer-parallel orientations towards the top of the layer. These observations together with field observations of erosional features led to the interpretation that dense minerals were mobilized and segregated into schlieren by high-energy "hyper-concentrated (magmatic) sedimentary gravity flows." As the flow waned, crystals were deposited, and as crystal separation became less efficient, graded layers formed. Changing flow intensities or conditions could explain different types of schlieren layers and structures.

Burgess and Miller (2008) identified a densely concentrated, heterogeneously distributed 1–2 km wide zone of planar schlieren and tubes near Tenaya Lake. The majority of planar schlieren are oriented at low-angles to the adjacent contact between pHD and CP. They viewed schlieren forming in areas of strong rheological contrasts (along boundaries), and disrupted schlieren (faulted, folded, and re-intruded) as evidence for a destabilized crystal mush. In addition to whole-rock elemental trends comparable with earlier schlieren studies (Reid et al., 1993; Paterson et al., 2008; Solgadi and Sawyer, 2008), whole-rock Sm-Nd and Rb-Sr isotope compositions between a schlieren sample and host sample were indistinguishable in εNd_i, but the schlieren had slightly lower $^{87}Sr/^{86}Sr_i$ values than the host CP. Their interpretations focused on the mixing processes that generated the relatively narrow range of isotope compositions in the CP unit.

Paterson (2009) described the key characteristics of several TIC schlieren-bound structures, including the addition of plume heads, diapirs, and pipes, and outlined their structure-specific dynamic features. Paterson (2009) noted that structures were clustered in space across each unit of the TIC, with certain patterns: Troughs young outwards, potentially favoring low-stress sites, and tube structures are statistically vertically plunging, and thus may be useful paleo-vertical indicators. The implications of this study were that this group of structures together preserve a time-transgressive history of magma mobility in a crystal-rich, already-constructed magma chamber. Future, open questions concerned the spatial clustering of structures, and whether schlieren-bound structures might record tectonic information.

Žák et al. (2009) modeled whole-rock schlieren compositions in the Mammoth Peak sheeted zone to show that schlieren were enriched in major and trace elements from ∼150% (large-ion-lithophile elements, or LILE) to >500% [middle rare earth elements (MREE), Fe, Mg, Mn] over the adjacent host granitoids. Some minerals in schlieren form glomerocrysts (e.g., magnetite), separated by interstitial quartz and K-feldspar. The clots (if formed prior to structure formation) have a greater density than the individual minerals and thus may enhance the effects of gravitational settling and flow-sorting processes (Žák et al., 2009). Žák and Paterson (2010) further explored the dynamic interplay between regional tectonics and magmatic processes at magmatic internal contacts, showing that the magmatic tubes were statistically elongated parallel to the regional NW–SE magmatic foliation, indicating that the local-flow structures were experiencing the regional stress when they formed.

Hodge et al. (2012) explored the spatial clustering of tube structures at Glen Aulin, finding regular spacing between clusters of tubes of 1–10 m. In this area, tubes were statistically oriented perpendicular to the nearby CP-pHD contact. Using detailed maps and structural measurements, they proposed that tube structures were buoyant magma plumes that were oriented and deformed by rheological contrasts between the buoyant plume and the host magma. They defined regimes in which structures were most likely to be deformed (ponding or tension) and estimated a yield strength of the magma on the order of 10^3 Pa.

In contrast to previous studies that view schlieren-bound structures originating from physical, flow-dominated processes, Glazner et al. (2012) and Bartley et al. (2013) proposed

a chemically driven mechanism for schlieren formation in migrating tube structures. In this model, the felsic inner core represents a conduit for late, Si-rich immiscible liquids, while the dense, Fe-rich liquid is deposited at the tube base, forming schlieren. These studies do not address the field observations of concentric magmatic fabrics in the schlieren walls of the tube, as well as processes that could produce the migrating pattern.

Memeti et al. (2014) reviewed the wide array of TIC magmatic structures in the context of regional geochronology and petrology of the main-sequence rocks. They mapped a regionally extensive planar schlieren zone in the north of the CP unit (**Figure 2**). U-Pb in zircon CA-ID-TIMS dates from zircons in schlieren and surrounding host overlapped, and thus were interpreted to be locally derived. Paterson et al. (2016) expanded these datasets and outlined several lines of evidence for magmatic erosion and recycling in the TIC main sequence rocks, that included schlieren-bound structures. Extrapolating from the known occurrence and approximate density of structures, they estimated that the TIC contains >9000 schlieren-bound magmatic structures with local erosional features.

Wiebe et al. (2017) proposed a model for the formation of migrating tube structures involving progressive downward flow and stacking of schlieren-bounded channels (akin to trough channels). They suggest that tubes migrate outwards (towards older units) when new magma pulses are intruded in the center of the complex (e.g., Bateman, 1992).

Bartley et al. (2018) interpreted schlieren layers at Tenaya Lake, which grade towards older units in the west, as one part of "kilometer-scale lithologic cycles" where regional E-W extension makes space for the emplacement of N-S striking dikes. In this model, the schlieren (representing early crystallizing components) concentrate in the lower part of the dike to form modal, graded layers. This study does not address the spatially variable orientations of schlieren, deformation of schlieren, more complex geometries observed in the same area as planar, graded schlieren (e.g., tubes-Burgess and Miller, 2008), as well as the lack of graded layering in other parts of the Tenaya Lake area (e.g., the host equigranular Half Dome unit).

Building on previous studies of schlieren-bound magmatic structures in the TIC, this study will focus on characterizing and quantifying observations of planar schlieren, troughs, tubes, and plumes at multiple spatial scales.

MATERIALS AND METHODS

Field Data

Regional Compilations

Ongoing regional compilations of TIC datasets are summarized here in order to provide context to schlieren-bound structure data. Existing regional mapping (>1:24,000 scale) and new 1:10,000 scale maps of the TIC, including information about the nature of contacts from previous studies (Žák and Paterson, 2005; Paterson et al., 2008, 2016; Žák et al., 2009; Memeti et al., 2010, 2014), were compiled and digitized using ESRI ArcGIS 10.6.1 (for a list of map sources, see **Figure 2**). The compilation of TIC fabric data is the result of ∼50 years of field mapping by the USGS (Chesterman, 1975; Bateman et al., 1983) and others (Žák and Paterson, 2005; Žák et al., 2007, 2009; Burgess and Miller, 2008; Paterson et al., 2008; Memeti et al., 2010; Aldiss, 2017; McColl, 2017; this study). Fabric data from the USGS quadrangle maps (Chesterman, 1975; Bateman et al., 1983) were digitized by Graham (2012) as part of the Geologic Resources Inventory Project for Yosemite National Park and Devils Postpile National Monument. (2006–2012) compositionally defined magmatic structures, such as K-feldspar megacryst clusters, are reported widely in the TIC, however, they do not form part of the digital database. Schlieren-bound magmatic structure data were digitized from the same sources as the fabric data, and assigned locations, orientations and defining characteristics (e.g., structure type), where available. In legacy data (pre-2009), the schlieren-structure type was not always specified (e.g., planar schlieren, trough, tube, plume). In these cases, strike and dip measurements were assigned as planar schlieren by default.

Mapping Domains

Mapping in four domains at 1:5,000 to 1:10,000 scale was performed over four field seasons (see **Figure 2** for domain locations). Domains were selected in a symmetrical pattern around the center of the southern CP region in locations that were variably proximal to contacts with the older pHD unit (e.g., domains are adjacent to, traversed across, or distanced from, the major unit contact) to encompass a range of magmatic conditions. Domains were mapped in order to provide information on the distribution of magmatic structures across areas 2–12 km^2 in size. Mapping focused on characterizing the location, type, and orientation of schlieren-bound structures within each domain, and documenting their relationships to lithology, magmatic fabrics, and contacts. Structures studied include planar schlieren, troughs, tubes (stationary and migrating) and plumes in each domain. Less emphasis was placed on mafic ellipsoids, K-feldspar clusters and K-feldspar pipes; the location of these structures was noted in the field.

Grid Mapping

Individual structures or outcrops were selected for grid mapping at 1:10–1:100 scale to highlight key field relationships and as a tool to unravel complicated structure. Each grid square was drawn out with a tape measure and string. Measurements were taken of magmatic fabrics and all schlieren-bound structures in each square. Photographs aided in digitizing the map.

Taking Structural Measurements and Determining Younging/Migration Directions

Measurements of the strike, dip and intensity of the magmatic fabric(s) were made at approximately regular intervals across domains. When recording information about schlieren-bound structures specifically, a protocol was implemented as follows: (1) record structure type and approximate dimensions; (2) measure strike and dip of planar features (e.g., planar schlieren strike and dip); (3) measure trend and plunge of linear features in the structure (e.g., trough or tube axis); (4) measure

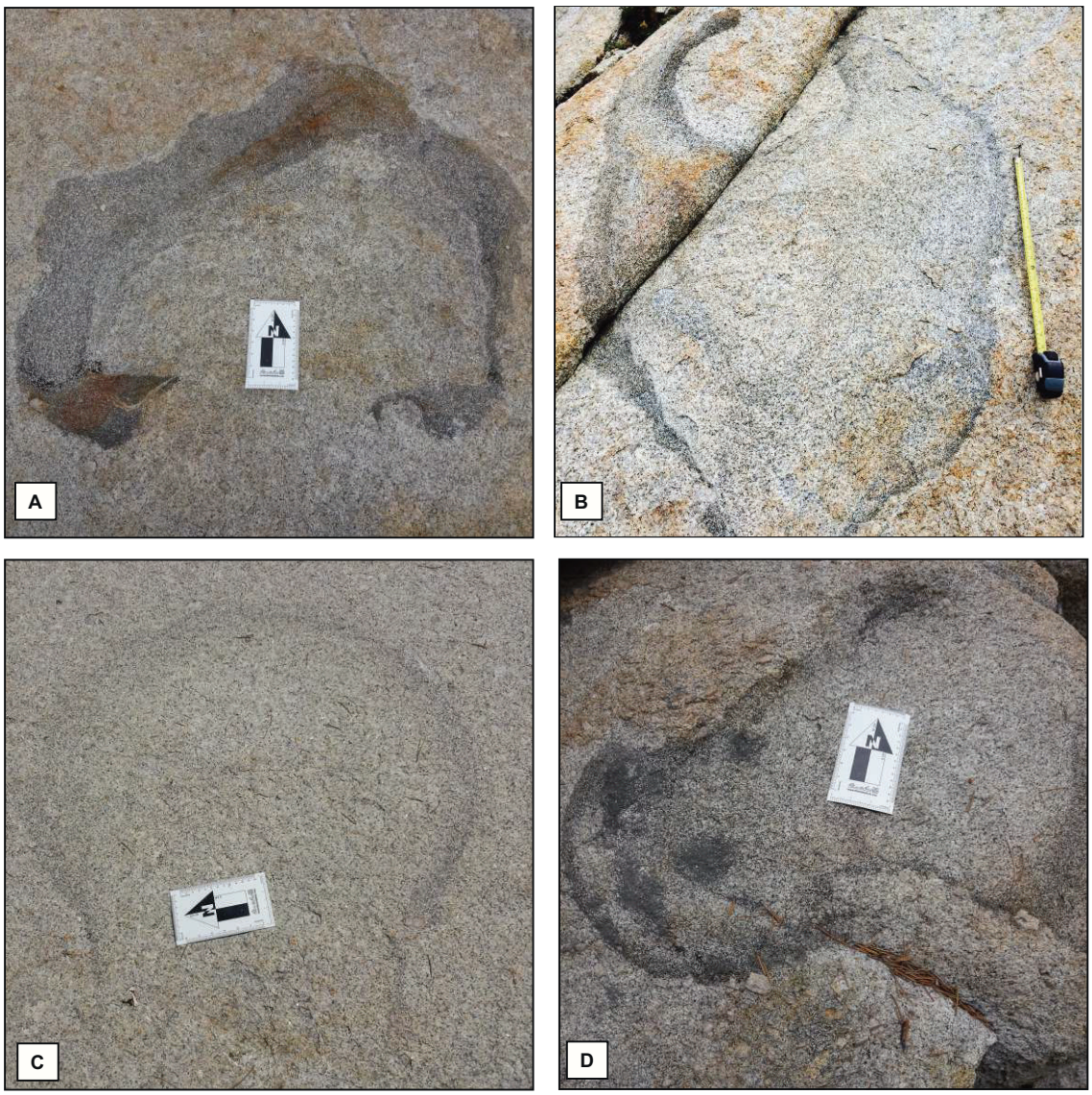

FIGURE 5 | Field photos of plumes. **(A)** Plume with a ∼0.5 m diameter and thick schlieren head, Glen Aulin area. The thickness of the schlieren varies around the margins of the plume, is sharpest at the contact with host CP, and more diffuse towards the interior. **(B)** ∼1 m wide plume head, Young Lakes area. As in panel **(A)**, the schlieren is sharpest at the contact with host CP and is diffuse towards the interior. The plume is re-intruded by host CP. **(C)** Diffuse plume with tail preserved, Lyell Canyon area. This diffuse type of schlieren is common in the central regions of the CP unit (see also Pothole Dome area; Paterson, 2009). **(D)** Plume with well-defined head and elongate tail. The interior of this plume has a clear compositional difference with the surrounding host CP.

younging or migration directions (see below and **Figure 1B**); and (5) note additional relative timing indicators if observed, such as overprinting relationships of fabrics, or relationships between structures.

Planar schlieren younging directions are measured if they are reverse graded; the younging azimuth is towards coarser grained, less modally concentrated compositions, perpendicular to the strike of the layer (**Figures 1B**, **3A**). Troughs show evidence of layer erosion and truncation of older troughs. These cross-cutting relationships define a relative younging direction that is measured perpendicular to the trough axis (**Figures 1B**, **3B–D**). A strike and dip measurement can also be taken at this point to constrain 3D geometry. In stationary tubes, usually the younging is inward, and so a migration direction is not measured (**Figure 4A**). Sharp erosional contacts between crescent-shaped schlieren rings define the migration direction of a (migrating) tube structure (**Figures 1B**, **4B–D**). To measure plume head migration, azimuthal younging is measured in the direction perpendicular, and towards the convex side of the plume head (**Figures 1B**, **5A–D**). Measurements are made in 3D where possible, but working on glacially polished surfaces resulted in some measurements in 2D (e.g., azimuthal younging/migration directions).

Statistical Analysis of Structural Measurements From Domains

Statistical analysis of structural measurements (strike, dip, younging, or migration directions) was performed for each type of structure (foliation, planar schlieren and troughs, tubes, and plumes) in each domain. Structural data was separated by unit before analysis. Stereonets and rose diagrams were created using Stereonet 10 software (Cardozo and Allmendinger, 2013), and mean vectors and cylindrical best fits of the data within the program were used to estimate average orientations.

Angular difference was calculated as [foliation strike – schlieren strike] (planar schlieren and troughs only) at each field station. The angular difference was converted to a 0°–90° scale (i.e., ignoring dip direction). In cases where no fabric measurement was taken, the fabric strike from the adjacent station was used. For stations with two or more fabrics, the angular difference was calculated for each foliation measurement at that station. The same applies for multiple schlieren strike measurements at one station. Foliation measurements were assigned to a Type (2, 3, or 4) based on their orientation, and following the protocol used in the regional scale map.

Sample Collection and Analysis

Samples were collected from each of the main TIC units, from a range of schlieren-bound structure types (sample locations provided in **Supplementary Material**). The largest group consists of planar schlieren and troughs, with a smaller subset of tube and plume samples. In many cases, multiple samples were collected from a single structure, or outcrop, and divided into "schlieren," "felsic," and "adjacent host" components. Samples were used for petrographic analysis and whole-rock geochemistry.

Petrography

Seven representative samples were selected for petrographic description and mineral mode estimation: two samples each from the pHD and KC units, and three samples from the CP unit (samples listed in **Table 1**). In each unit, one schlieren sample from a trough and an adjacent host sample were studied. In the CP unit, one additional schlieren sample was studied from a migrating tube structure adjacent to the sampled trough. Thin section images were traced and scanned into ImageJ software (Schindelin et al., 2012) where they were subsequently processed using the Color Threshold tool to isolate individual phases. We then used ImageJ to calculate the proportion of mineral phases in each sample. Quartz and feldspar proportions were estimated by difference (subtracted the mafic phases) and then estimated under an optical microscope.

Whole Rock Geochemistry

A subset of 19 samples, consisting of 9 schlieren, 5 felsic components, and 5 host samples, were analyzed by ICP-MS at Activation Laboratories, or by XRF and ICP-MS at the University of Washington, GeoAnalytical Laboratory for major, trace, and rare-earth element (REE) concentrations (samples are labeled by method in **Table 2**). Kuna Crest granodiorite major, trace, and REE sample data and materials were provided by V. Memeti. Six of these samples of a trough and adjacent host, each from the CP,

TABLE 1 | Mineral proportions of representative schlieren-host pairs from TIC units.

Sample Number:	Rock Type	UTM Easting	UTM Northing	Whole-rock SiO_2 (wt.%)	Modal proportion (%)							
					Hbl	Bt	Mag	Ttn	Ap	Fsp	Qtz	Accessory
KCL384-1	KC host	301292	4183347	61.97	10	10	–	–	–	60*	20*	Ap > Mag > Zrn > Ttn
KCL384-2	KC schlieren	301292	4183347	51.82	45	11	–	–	–	24*	20*	Ap > Mag > Zrn > Ttn
TI16-2b	pHD host	284027	4190256	64.80	2	5	1	1	–	61–66	25–30	Mag > Tit > Ap > Zrn
TL16-2a	pHD schlieren	284027	4190256	55.73	11	14	5	2	–	48–50	20–22	Mag > Tit > Ap > Zrn
GA223-3	CP host	288764	4197674	66.43	4	3	2	1	–	60*	30*	Ap > Zrn
GA223-A3	CP schlieren	288764	4197674	39.44	15	20	16	6	–	29–34	11–15	Ap > Zrn
GA64-1C	CP schlieren	288769	4197670	53.33	9	15	17	7	2	32*	18*	Ap > Zrn

*–Indicates mineral abundance <1%, notes provided in accessory column. Accessory: qualitative estimates given where abundance is too low to measure quantitatively. Relative abundance shown. Ap, apatite; Ttn, titanite; Zrn, Zircon; Mag, magnetite. *Qtz v. Pl/Ksp proportions estimated by difference and by thin section observation. Co-ordinate system: UTM NAD27, Zone 11S.*

TABLE 2 | Whole-rock geochemistry for representative schlieren, host, and felsic samples.

	Kuna Crest granodiorite			Porphyritic Half Dome granodiorite		Cathedral Peak granodiorite			
Sample number	KCL384-1*	KCL384-2*	KCL-386*	TL16-2b	TL16-2a	GA223-3	GA223-A3	GA64-1c	GA64-2
Sample type	host	Schlieren	Felsic layer	Host	Schlieren	Host	Schlieren	Schlieren	Felsic layer
UTM easting	0301292	0301292	0301409	0283945	0283945	0288682	0288682	0288687	0288687
UTM northing	4183347	4183347	4183151	4190456	4190456	4E+06	4197874	4197870	4197870
Major oxides (wt %)									
SiO_2	61.97	51.82	68.53	64.80	55.73	66.43	39.44	53.33	69.26
TiO_2	0.78	1.18	0.30	0.67	1.59	0.62	3.68	1.95	0.37
Al_2O_3	16.28	9.54	17.38	15.67	13.68	16.33	10.32	13.66	15.75
FeO_t	5.72	11.38	1.56	4.83	12.57	4.32	24.84	16.33	2.71
Fe_2O_3	–	–	–	–	–	–	–	–	–
MnO	0.10	0.35	0.02	0.08	0.20	0.08	0.37	0.22	0.06
MgO	2.63	9.45	0.63	1.43	2.61	1.15	5.13	2.37	0.71
CaO	5.34	8.86	4.16	3.67	4.04	3.95	5.97	4.18	3.09
Na_2O	3.44	1.70	3.91	3.97	2.67	4.76	2.03	3.56	4.44
K_2O	2.78	2.30	3.35	3.04	5.20	2.39	2.81	2.65	2.71
P_2O_5	0.19	0.71	0.10	0.21	0.53	0.23	1.12	0.54	0.18
Total	99.22	97.30	99.94	98.83	99.41	100.56	96.07	98.82	99.72
Trace elements (ppm)									
Cs	6.0	8.3	4.5	7.5	4.3	3.3	10.8	5.6	3.0
Rb	114	94	104	174	118	90	205	136	99
Sr	522	113	570	452	583	712	248	543	729
Ba	654	256	844	1918	436	381	363	644	594
La	40.3	44.5	19.1	115.0	37.9	39.8	204.0	109.0	23.0
Ce	72.3	105.2	35.3	205.0	65.6	78.0	454.0	231.0	41.4
Pr	7.4	14.7	3.9	22.1	6.8	8.5	52.4	26.4	4.5
Nd	26.6	68.6	14.5	82.2	25.2	29.8	192.0	96.7	16.5
Sm	5.0	20.3	2.9	13.4	4.2	5.0	31.3	15.5	2.3
Eu	1.3	2.2	0.8	2.9	1.0	1.2	6.5	3.3	0.6
Gd	3.9	20.9	2.2	8.7	2.9	3.4	20.1	9.9	1.5
Tb	0.6	3.6	0.3	1.2	0.4	0.4	2.6	1.2	0.2
Dy	3.1	22.5	1.8	5.9	1.8	2.1	13.2	6.3	0.9
Ho	0.6	4.5	0.3	1.0	0.3	0.4	2.3	1.1	0.2
Er	1.6	12.7	0.9	2.8	0.9	1.1	6.5	3.1	0.5
Tm	0.2	1.8	0.1	0.4	0.1	0.2	0.9	0.4	0.1
Yb	1.6	10.9	0.8	2.7	0.8	1.0	6.2	2.9	0.5
Lu	0.3	1.6	0.1	0.4	0.1	0.1	1.0	0.5	0.1
U	7.4	6.3	4.4	16.1	6.2	3.5	15.8	9.0	1.8
Th	29.8	25.4	9.4	85.5	23.3	15.4	42.1	29.7	5.9
Y	17	128	10	32	10	12	72	34	5
Nb	9	18	5	21	6	11	60	31	6
Zr	131	266	94	556	157	212	1313	941	116
Hf	4.0	8.5	2.9	14.2	3.9	5.6	17.6	23.2	3.3
Ta	0.9	1.3	0.7	2.3	0.7	1.1	5.1	2.6	0.6
Co	N.A.	N.A.	N.A.	18	9	7	36	21	5
Cr	13	62	5	B.D.L	20	B.D.L	20	B.D.L.	B.D.L.
Pb	13	7	18	18	17	15	8	12	16
V	130	304	35	237	78	72	517	358	43
Zn	77	158	28	190	80	90	440	280	70
Isotope ratios									
$^{87}Sr/^{86}Sr_i$	0.705991	0.706224	N.A.	0.706517	0.706656	0.706639	N.A.	0.706607	N.A.
std error (%)	0.0007	0.0012	N.A.	0.0011	0.0011	0.0011	N.A.	0.0008	N.A.
εNd_i	–2.21	–0.63	N.A.	–4.58	–4.48	–5.42	N.A.	–5.58	N.A.
std error (%)	0.0016	0.0009	N.A.	0.0012	0.0006	0.001	N.A.	0.0006	N.A.

UTM projection is NAD27 Zone 11S. N.A., not analyzed; B.D.L., below detection limit. Full dataset (n = 19) included in the ***Supplementary Material****. *Major, trace, and rare earth elements for KCL samples from Memeti (2009). Isotopic data from this study.*

pHD, and KC units (the same samples analyzed for mineralogy), were selected for isotope analysis. Four additional samples were selected from the Pothole Dome area of schlieren and host (not paired). Samples selected for Sr, and Nd isotope analyses were analyzed at the University of Arizona. Full laboratory conditions and methods for isotope analyses are described in Otamendi et al. (2009). Element and isotope data from schlieren, felsic components, and nearby host samples in the TIC were compiled from the literature to supplement our dataset (Data sources: Loetterle, 2004; Burgess and Miller, 2008; Paterson et al., 2008; Solgadi and Sawyer, 2008; Memeti, 2009; Žák et al., 2009; Memeti et al., 2014).

RESULTS

Regional Syntheses

Magmatic Foliations and Lineations

The 6485 magmatic foliation measurements and 1933 lineation measurements, covering >70% of the intrusive complex, are summarized in **Figure 2A**. Building on the findings of Žák et al. (2007), we mapped the distribution of Type 2–4 foliations and identified one additional N-NE striking foliation (Type 5; **Figure 2A**). Many domains contain multiple magmatic foliations. Magmatic lineations are steeply plunging; 80% of measurements plunge ≥ 60° (**Figure 2A**).

Compositionally Defined Magmatic Structures

Compositionally defined magmatic structures, specifically heterogeneous crystal clusters, are found in all TIC units (Paterson, 2009). K-feldspar megacryst clusters are especially common in the CP unit, even in regions of sparse to absent schlieren (e.g., Paterson et al., 2005; Vernon and Paterson, 2006). K-feldspar megacryst clusters are found both inside and outside mapped domains, in zones of concentrated schlieren-bound structures as well as in zones with sparse schlieren-bound structures (see below). They form a wide range of shapes from irregular, to pipes and sheets (Paterson, 2009; Memeti et al., 2014).

Schlieren-Bound Magmatic Structures

The compilation identified >1500 schlieren-bound magmatic structures (planar schlieren, troughs, tubes, and plumes). Schlieren-bound structures are also widely distributed and appear to be either sparsely or densely clustered (Paterson, 2009; **Figure 2B**). In addition, the types of structures vary between units. Planar schlieren and troughs, tubes, and plumes are found in all major TIC units, are less common in the KC unit and rare in late leucogranites. Tubes (both stationary and migrating) and plumes are abundant in the CP unit, and found less commonly in the pHD, eHD, and KC units (Paterson, 2009).

Younging indicators suggest that schlieren orientations largely young or migrate outwards, towards older contacts (∼70% of the younging dataset; $n = 470$) (see also Bateman, 1992; Burgess and Miller, 2008; Paterson et al., 2008; Solgadi and Sawyer, 2008; Paterson, 2009; Žák et al., 2009). They often migrate or young at high angles to nearby contacts (Hodge et al., 2012; Wiebe et al., 2017). However, a smaller population (∼30% of the dataset; $n = 202$) show inward younging or contact-parallel orientations, in part reflecting some of the heterogeneity found across smaller spatial scales (see section "Outcrop-Scale Patterns").

Summary

Compositionally defined magmatic structures, including schlieren-bound magmatic structures, are widespread in the TIC and found in all units spanning the entire duration of the complex (i.e., they are times transgressive). Schlieren-bound structures are not evenly distributed in the TIC; instead they are broadly clustered in packages on the order of 5–15 km^2 in size, irrespective of unit type, distance to nearest contacts, or contact orientation. They are found across both sharp and gradational contact zones. Relative younging directions of tubes and troughs are generally outward towards contacts. Fabric type spatially varies throughout the TIC, defining several domains with multiple, different fabrics preserved. Schlieren-bound magmatic structures are not associated with any particular regional fabric configuration at the regional scale.

Domain-Scale Structure Patterns

In each of the four study areas, schlieren-bound magmatic structures are abundant (**Figure 2B**, blue squares). Planar schlieren and troughs represent ∼60% of the structures reported in the four domains. Stationary and migrating tubes represent 22% of the structures in the four study regions and plumes make up 18% of the dataset. For each domain, we describe: (1) rock types, ages, and contact relationships; (2) magmatic foliation and lineation patterns; (3) planar schlieren and trough orientations and their relationship to fabrics; (4) tube and plume structure patterns; and (5) structure clustering.

Glen Aulin Domain

The Glen Aulin domain is situated at the western margin of the CP unit, crossing the contacts with pHD and eHD units (**Figures 2**, **6**). The CP unit at Glen Aulin is characterized by hornblende biotite granodiorite in the west and becomes increasingly granitic eastwards towards Pothole Dome, as hornblende and biotite decrease in abundance. Hornblende in the eastern part of the domain is replaced by biotite, except in schlieren where it is sometimes preserved. K-feldspar megacrysts range in size from 3 to 10 cm and generally increase in size to the east. K-feldspar clusters and leucogranite dikes are widely found. Contacts between the CP and pHD units, and pHD and eHD units both strike NE-SW (azimuth: 033) in the north, and bend to an E-W (azimuth: 090) orientation at the western margin of the study area. The contact between the CP and pHD transitions from a sharp to gradational contact southwards along strike. The nearest U-Pb in zircon ages range from 88.1 ± 0.2 Ma in the CP unit to 89.79 ± 0.15 Ma in the pHD (Coleman et al., 2004; Paterson et al., 2016). There are steep age gradients across the contacts in the isochron map (Memeti et al., 2014; **Figure 2C**).

Regional E–W striking (Type 4) and local NE–SW striking (Type 2) approximately margin-parallel magmatic foliations are dominant, and the regional NW–SE fabric (Type 3) is locally and weakly expressed in the north of the domain

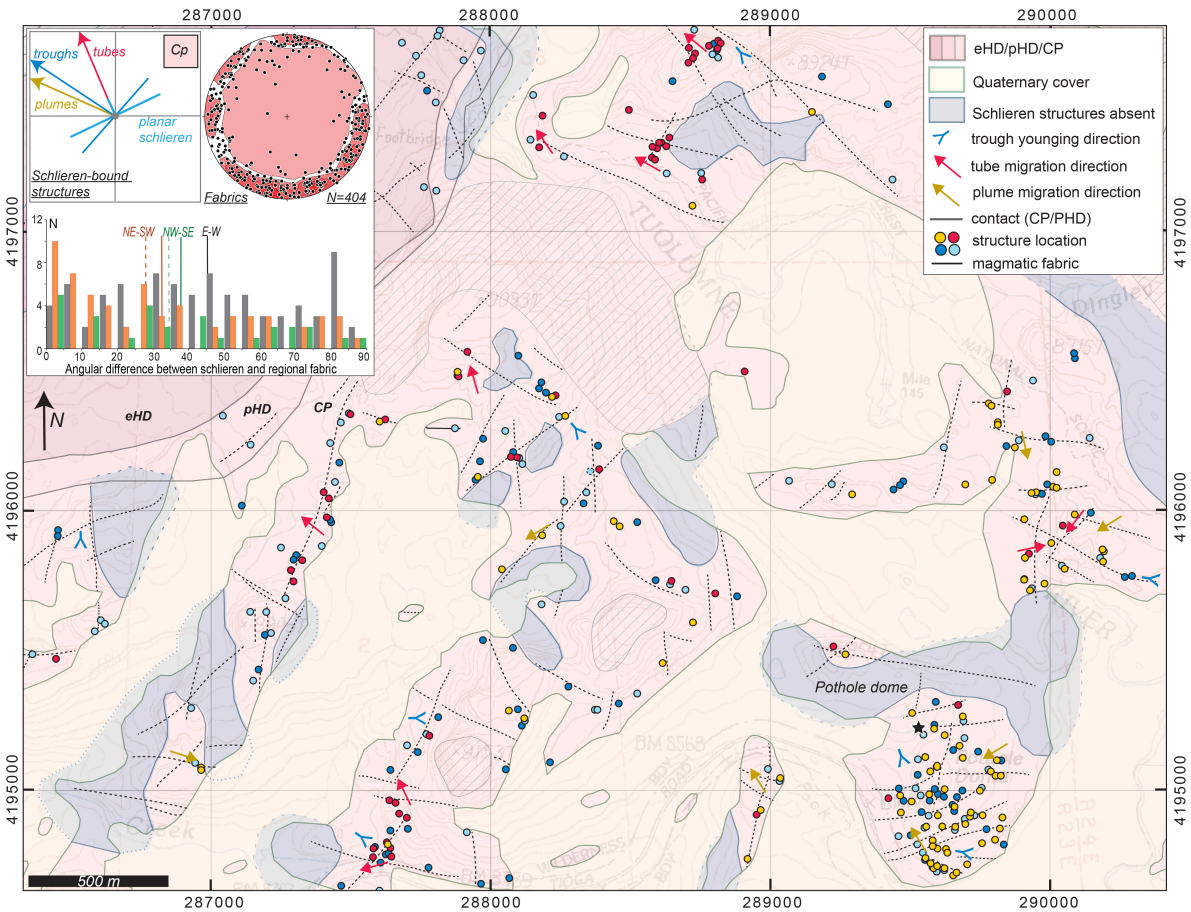

FIGURE 6 | Magmatic structures field data summary of the Glen Aulin area, NW quadrant. Bold lines mark major unit contacts. Hatching indicates unmapped areas. The trend of steeply dipping (70°–90°) magmatic foliations is shown by dashed lines. Magmatic lineations are steeply plunging, regardless of the strike of the foliation. The locations of different schlieren-bound structures are shown by colored dots (light blue-planar schlieren; dark blue-trough; red; tube; yellow; plume). Y or arrow symbols are oriented in the direction of measured migration/younging. Inset box shows the domain-scale magmatic foliation summary on a stereonet, and a summary of average younging/migration orientations shown with arrows. For Glen Aulin and Young Lakes domains, angular difference measurements between the foliations and schlieren are shown as a histogram in the inset box, color-coded by fabric type. eHD-Equigranular Half Dome granodiorite. pHD-Porphyritic Half Dome granodiorite; CP-Cathedral Peak granodiorite; Co-ordinate system used: UTM NAD27 zone 11S.

(**Figure 6**). Lineations plunge steeply, with a best fit of 83→235 (plunge→trend; $n = 18$).

Planar schlieren and troughs are observed in all orientations and range from shallow to sub-vertical dips. In the CP unit, the cylindrical best fit orientation is 212/78 ($n = 87$) for planar schlieren and 221/76 ($n = 75$) for troughs, although there is a wide scatter. Trough younging (perpendicular to trough strike), similarly is varied in orientation. The largest population of troughs in the CP unit young toward the NW, perpendicular to, and towards, the CP-pHD contact at an average azimuth of 304 ± 24° (**Figure 6**; 2σ uncertainty). Troughs in the southwestern part of the CP unit, where the contact strikes E–W, have a younging direction to the north, perpendicular to the adjacent contact. pHD and eHD planar schlieren ($n = 38$) and troughs ($n = 8$) trend N–S to NE–SW, dip to the west, and young on average towards 333, perpendicular and towards older contacts of eHD and KC, respectively. There is no clear pattern between the orientations of the regional Type 3 and 4 foliations and schlieren orientations (**Figure 6** histogram). However, schlieren orientations and the contact-parallel foliations (Type 2) are more similar, as shown by the number of schlieren with a low angular difference to the foliation.

The average azimuthal orientation of tube migration in the CP unit is 339 ± 23° ($n = 113$), perpendicular and towards the contact with the pHD, a result consistent with previous studies of TIC tubes in this area (**Figure 6**) (e.g., Hodge et al., 2012; Wiebe et al., 2017). pHD or eHD tubes are less commonly found north of Glen Aulin. Plume heads are abundant in the central and eastern parts of the study area, within the CP unit ($n = 131$). Most observations of plumes are on horizontal to shallowly dipping planes, and in 2D they have variable migration directions, with a mean azimuth towards 293 ± 17° (**Figure 6**). No plumes were identified in the pHD or eHD.

Consistent with regional patterns, schlieren-bound structures at Glen Aulin are non-uniformly distributed throughout the map area (**Figure 6**). Schlieren-bound structures are concentrated

in zones that range in size between 0.3 and 1.1 km^2. These clusters are separated by zones where schlieren-bound structures are rare to absent, ranging in size from 0.02 to 0.2 km^2. Both zones contain magmatic fabrics, and other compositionally defined structures such as K-feldspar megacryst clusters. To a first order, structures are weakly clustered by type, with plumes most abundant in the eastern part of the domain (e.g., Pothole Dome), and tubes most abundant in the western part. Planar schlieren and troughs are, in contrast, evenly distributed within structure-rich zones.

Young Lakes Domain

The Young Lakes domain is situated in the east-central part of the CP unit (**Figures 2**, **7**). The dominant rock type is biotite granodiorite, with rare hornblende (pseudomorphed by biotite). K-feldspar megacrysts are between 3 and 6 cm in size. Mafic enclaves and K-feldspar clusters are common, and rare leucogranite dikes are observed. Young Lakes is located 2–3 km west of the nearest contact, which is the gradational internal contact of the CP unit with the pHD and eHD units at Sawmill Canyon, striking NW–SE (azimuth: 300). This contact transitions to a sharp contact with the eHD southwards along strike (Paterson et al., 2008). The nearest U-Pb in zircon age is 88.53 ± 0.12 Ma from Sawmill Canyon (Paterson et al., 2016). On the isochron map of Memeti et al. (2014), the domain is characterized by a shallow age gradient of broadly similar ages (**Figure 2C**).

Both Type 3 and 4 foliations are found at Young Lakes and appear to be equally dominant (**Figure 7**). A weaker NE–SW striking foliation (Type 5) is also identified locally. Lineations are steeply plunging (see **Figure 3** in Paterson et al., 2008).

Planar schlieren (n = 13) and troughs (n = 117) have a strong preferred orientation, striking NE–SW and dipping SE, with cylindrical best fit orientations of 009/50 and 013/41 for planar schlieren and troughs, respectively. Troughs young predominantly towards the ESE (mean azimuth: 102 ± 17°), and broadly perpendicular to, the CP-pHD contact at Sawmill Canyon (**Figure 7**). A smaller population (∼27%) young in other orientations. The angular difference between the Type 3 and 4 foliations and schlieren orientations is high (median between 45° and 60°) and each foliation type has a distinct angular difference distribution (**Figure 7** histogram). Migrating and stationary tubes (n = 2) as well as plumes (n = 4) are rare at Young Lakes and do not show any preferred orientation.

Structural diversity is relatively low at Young Lakes, making it difficult to estimate clustering by structure type. However, planar schlieren and troughs are clustered in space. Zones where schlieren are rare to absent range in size from 0.07 to 0.6 km^2. These domains are smaller than the extent of zones where schlieren-bound structures are abundant (0.6–1 km^2). Within the structure-rich clusters, structures appear more sparsely distributed than in Glen Aulin.

Tenaya Peak Domain

The Tenaya Peak domain is situated in a narrow N-S trending belt of the pHD unit (**Figures 2**, **8A**). The pHD unit is a biotite-hornblende granodiorite with hornblende phenocrysts and biotite books 3–8 mm in size. K-feldspar megacrysts are 2–3 cm in size, increasing in size towards the CP unit (see also Bateman, 1992; Memeti et al., 2014). The mapped domain crosses the N–S trending sharp contact of the CP-pHD in the east (azimuth: 350-000; **Figure 8A**) and is ∼200 m from the N-S trending gradational contact of the pHD-eHD in the west. The eastern part of the domain, in the CP unit, was previously mapped and studied by Burgess and Miller (2008). Ages range from 87.3 ± 0.7 Ma to 89.79 ± 0.15 across the contact (Burgess and Miller, 2008; Paterson et al., 2016), represented by a smoothly varying age gradient on the zircon isochron map (Memeti et al., 2014; **Figure 2C**).

The E-W Type 4 foliation is dominant over the NW–SE Type 3 foliation (**Figure 8A**). A N–S to NE–SW striking foliation (Type 2) is locally well-defined in the pHD unit, but weak-to-absent in other areas. Burgess and Miller (2008) report steeply plunging lineations between 70° and 90°.

Planar schlieren and troughs in the pHD unit, on average, strike parallel to the contact (165/40; n = 26 schlieren, 147/44; n = 35 troughs; **Figure 8A**), although there is a wide range in orientation, with strikes between 021 and 358. Trough younging orientation is variable, with a weak preference towards the west (mean vector: 245 ± 50°). Including measurements by Burgess and Miller (2008), troughs in the CP unit (n = 7) vary in orientation between NW–SE striking to E–W striking. Two troughs measured in the adjacent CP unit young westward, and one trough youngs towards the east. The small number of foliation and planar schlieren/trough measurements from this domain precludes statistical analysis of angular difference. Qualitatively, the cylindrical best fit orientations for planar schlieren and troughs aligns with the orientations for Type 2 and Type 3 foliations.

Migrating tubes in the pHD are concentrated at the eastern margin of the pHD, adjacent to the contact with the CP. A small number of measurements (n = 13) show a preference for westward migration (mean vector: 266 ± 26°; **Figure 8A**), perpendicular to the nearby eHD contact. In the CP unit, including measurements by Burgess and Miller (2008), tubes are also westward-younging (n = 9; not shown). Thirteen plumes mapped across the pHD have a widely variable orientation, with a mean vector of 284 ± 99° (**Figure 8A**). Plumes were not found at the western margin of the CP unit.

Within this domain, the structures are not strongly clustered by type. However, tubes seem to be most abundant close to the pHD-CP contact. Areas ranging in size from 0.1 to 0.4 km^2 do not contain schlieren-bound structures. Domains that contain abundant structures are ∼0.5–1 km^2 in area.

Lyell Canyon Domain

The Lyell Canyon domain is situated in a wide gradational zone at the southeastern margin of the CP unit, bordering the pHD unit to the east (**Figures 2**, **8B**) (Oppenheim et al., in review). The pHD unit here is a porphyritic granodiorite with biotite > hornblende, and locally contains biotite books and K-feldspar megacrysts (2–3 cm in size). In the transitional CP unit, the K-feldspar megacrysts increase in size and number. The gradational contact strikes NE-SW (azimuth: 015). The

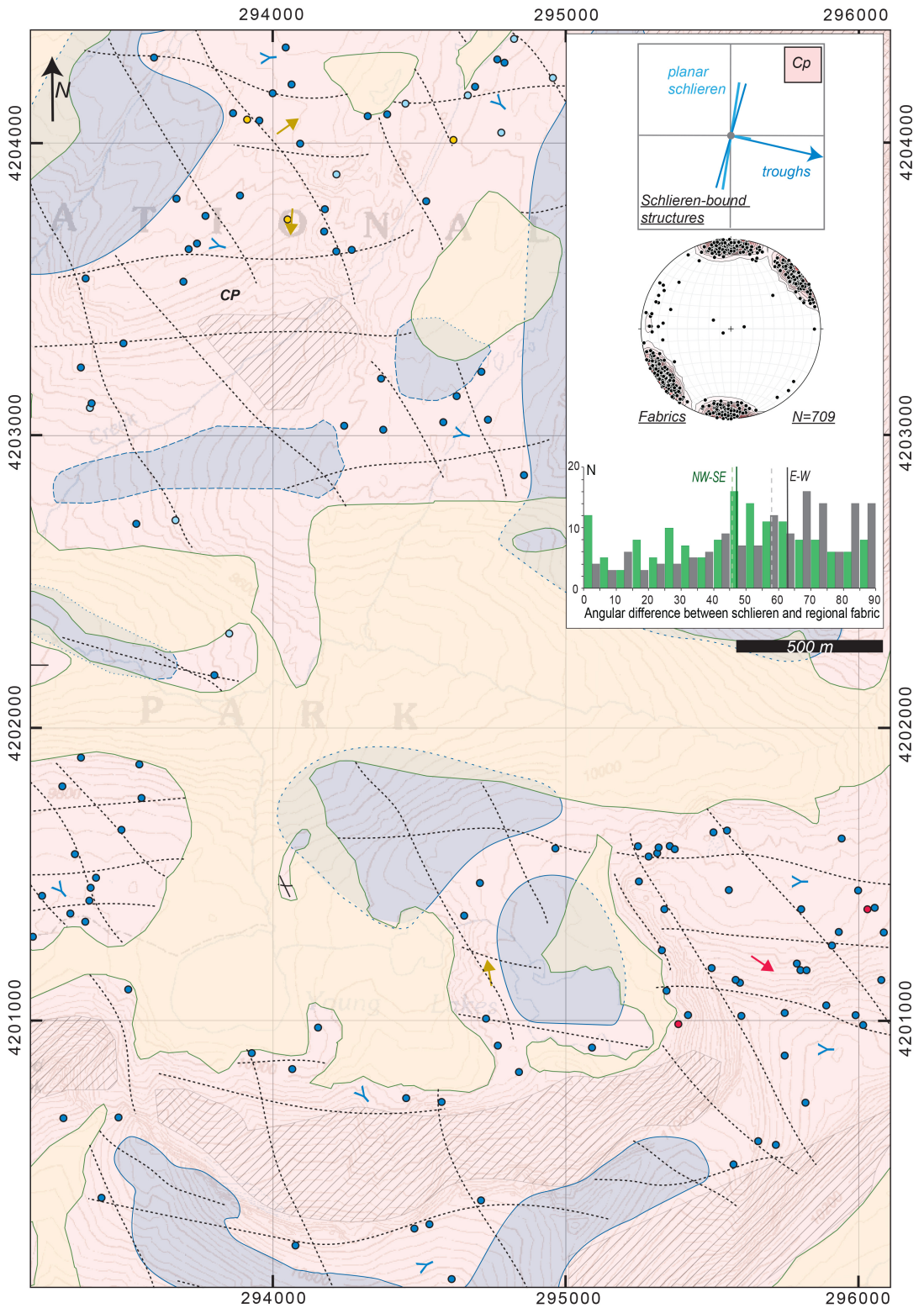

FIGURE 7 | Magmatic structures field data summary of the Young Lakes area, NE quadrant. Bold lines mark major unit contacts. Hatching indicates unmapped areas. The trend of steeply dipping (70°–90°) magmatic foliations is shown by dashed lines. Magmatic lineations are steeply plunging, regardless of the strike of the foliation. The locations of different schlieren-bound structures are shown by colored dots (see key in **Figure 6**). Y or arrow symbols are oriented in the direction of measured migration/younging. Inset box shows the domain-scale magmatic foliation summary on a stereonet, and a summary of average younging/migration orientations shown with arrows. For Glen Aulin and Young Lakes domains, angular difference measurements between the foliations and schlieren are shown as a histogram in the inset box, color-coded by fabric type. CP-Cathedral Peak granodiorite. Co-ordinate system used: UTM NAD27 zone 11S.

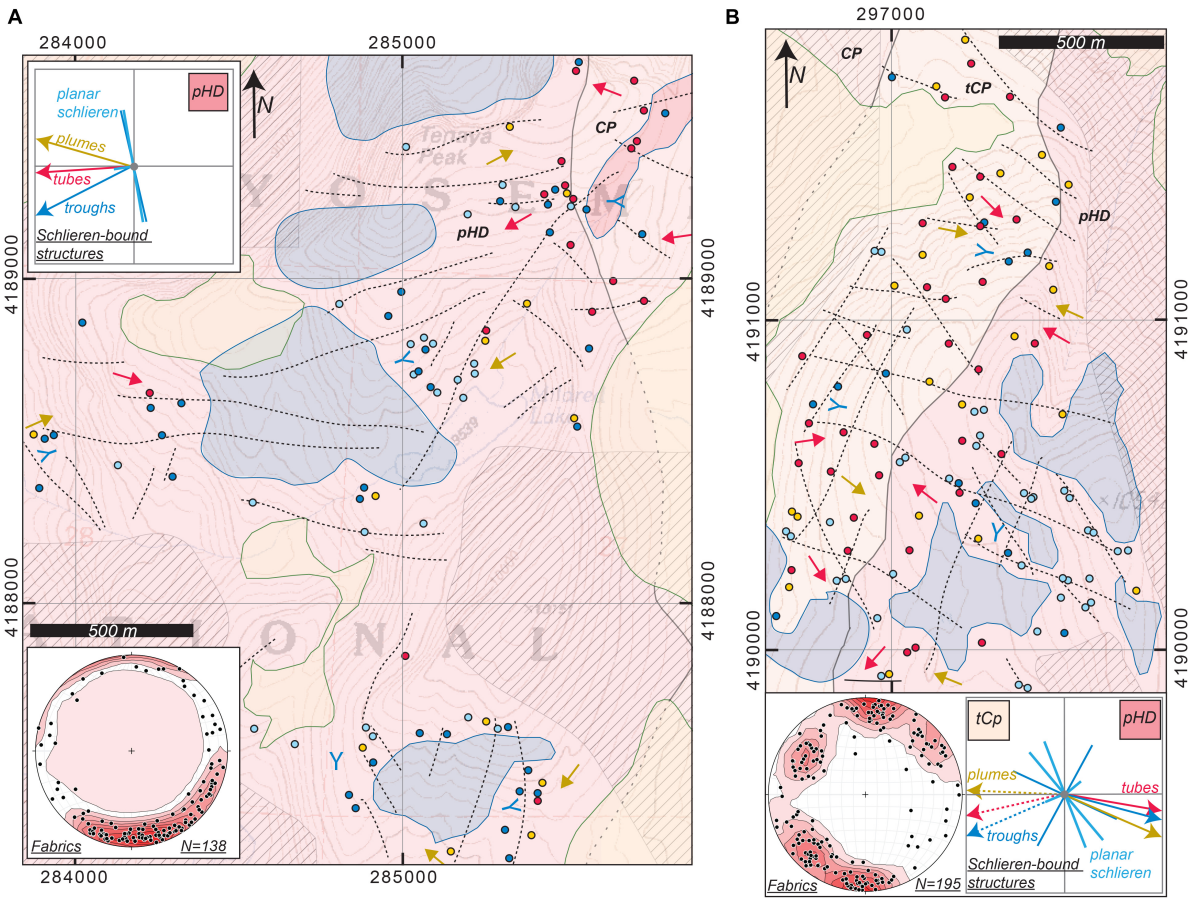

FIGURE 8 | Magmatic structures field data summary of the Tenaya Peak and Lyell Canyon areas. Bold lines mark major unit contacts. Hatching indicates unmapped areas. The trend of steeply dipping (70°–90°) magmatic foliations is shown by dashed lines. Magmatic lineations are steeply plunging, regardless of the strike of the foliation. The locations of different schlieren-bound structures are shown by colored dots (see key in **Figure 6**). Y or arrow symbols are oriented in the direction of measured migration/younging. Inset box shows the domain-scale magmatic foliation summary on a stereonet, and a summary of average younging/migration orientations shown with arrows. pHD-Porphyritic Half Dome granodiorite; CP-Cathedral Peak granodiorite; tCP-Transitional Cathedral Peak granodiorite. **(A)** Tenaya Peak, SW quadrant (after Aldiss, 2017). **(B)** Lyell Canyon, SE quadrant (after McColl, 2017). Co-ordinate system used: UTM NAD27 zone 11S.

gradational contact between the transitional CP and main CP unit is found at the western edge of the mapped domain and also strikes NE-SW. There are no age estimates for this section of the CP unit. The interpolation on the isochron map of Memeti et al. (2014) suggests that this region has broadly similar ages (a shallow age gradient) of about 87 Ma (**Figure 2C**).

Regional Type 3 and 4 foliations are observed in equal intensity and cross-cut the CP-pHD contact (**Figure 8B**). A broadly contact-parallel, NE–SW striking foliation (Type 2) is also found in both units. Lineations were not recorded in this domain.

The Lyell Canyon domain is the smallest of the four mapped domains, and the number of structures observed is also the smallest. Thus, less emphasis is placed on statistically average orientations (for comparison to other domains, average orientations are given in inset summary diagram **Figure 8B**). A small number of planar schlieren and troughs in the CP unit (n = 16) vary widely in orientation, but the largest group are NW to NE striking. A small number of graded schlieren measurements (n = 5) indicate younging eastwards towards the pHD unit and troughs also young towards the contact, between 060 and 160. In the pHD unit, planar schlieren and troughs are both striking NW (n = 37): 337/61 (n = 30) and 294/79 (n = 7), respectively. Planar schlieren grading in the pHD unit indicates younging westwards (n = 9), with a smaller number younging to the NE (n = 2). Trough azimuthal younging directions are between 180 and 330, opposite to structures in the CP unit. Angular relationships between foliations and schlieren orientations were not calculated due to the limited size of the dataset.

Tubes and plumes are found across the contact in both units. In the CP unit, tubes (n = 24) and plumes (n = 11) migrate eastwards, with plumes showing a wider scatter in orientation. In the pHD unit, migration directions are reversed, as tubes (n = 12) and plumes (n = 10) migrate westwards (**Figure 8B**).

Domains where structures are rare to absent are 0.1–0.3 km^2 in area, similar to the other study areas, but spatially restricted to the southern parts of the domain. The rest of the domain

has abundant structures, approximately evenly spaced. With a larger dataset covering a broader area, clustering by type could be evaluated.

Summary

Domain-scale mapping revealed structure clustering on the order of 0.3–1 km^2 in size, separated by zones of sparse to absent schlieren-bound structures. Both zones are characterized by magmatic fabrics and K-feldspar megacryst clusters. Structure-rich and structure-poor domains form highly irregular shapes, with no apparent preferred orientation in map view. The clusters show no clear spatial relationship to nearby contacts or magmatic fabric orientations. In a subset of domains (Glen Aulin and Tenaya Peak) plume and tube structures are weakly grouped by type. In contrast, planar schlieren and troughs appear in all clusters of the four domains. Planar schlieren and troughs are weakly aligned with contact-parallel magmatic fabrics at Glen Aulin, and younging or migration directions of all schlieren-bound structure types in the CP unit is, on average, outward younging, perpendicular to contact orientations (with overall a wide range in orientations). There is additional complexity to resolve in the pHD unit.

Outcrop-Scale Patterns

Magmatic Structure Patterns

Grid mapping of several outcrops illustrates several features of schlieren-bound structures: (1) Schlieren-bound structures include a component of schlieren, but also include components that are more felsic, or slightly different composition, than the surrounding host (e.g., layers between schlieren bases of troughs, tube centers, **Figures 3B**, **4A**; herein called "felsic components"); (2) Schlieren-bound structures may be deformed, evidenced by magmatic faulting and folding (**Figures 3A,D**, **4D**, **9A**), and structures broken and re-intruded by the surrounding host pluton (**Figures 4B–D**, **9A–C**, see also Hodge et al., 2012); (3) While structures are typically classified as tubes, troughs, and plumes (or others, not part of this study), outcrops less commonly show structures that represent transitions, or combinations, of structures (**Figure 9B**); (4) K-feldspar megacrysts, where observed in schlieren-bound structures, are often strongly aligned with local schlieren-parallel foliation or sorted by size (**Figures 9A–C**). This is not common in the surrounding host, where K-feldspar megacrysts are clustered or weakly aligned in a magmatic fabric (e.g., Paterson, 2009).

Local schlieren-parallel foliations (Type 1) in schlieren-bound structures are discordant to magmatic foliations in the surrounding host (Type 2–5). The schlieren-parallel foliation in the mafic (schlieren) component of structures is rarely overprinted by other magmatic foliations. However, minerals defining fabrics in the felsic components of schlieren-bound structures (e.g., hornblende and biotite) are discordant to schlieren-parallel foliations, and rotated to Type 2, 3, 4, or 5 orientations. In addition, the presence of schlieren-bound structures at an outcrop does not modify the orientation of the magmatic foliations in the host (**Figures 9A,B**).

Effects of Magmatic Deformation and Rotation

Field evidence described above in each of the mapped domains indicates that some structures were magmatically deformed (i.e., translated, rotated, and distorted), and no longer record their original orientations. This deformation can also produce multiple younging directions within a single outcrop (**Figure 9A**). Even in outcrops where structures appear undeformed, there may be multiple schlieren-bound structures with varying orientations and several, opposing younging indicators (**Figures 4B**, **9B**). Thus, the effects of rotation are not easily quantified and generate scatter in the structural data.

However, even with this scatter, the observation that multiple types of structures show similar outward-younging trends at regional and domain-scales indicates that the most prominent younging direction, or orientation, measured in the outcrop is meaningful. There is no systematic rotation of the structures in the dataset in space (e.g., changing strikes and dips towards contact zones). In addition, schlieren foliations (type 1) are discordant to, and thus not rotated by, strain producing the host magmatic fabric (types 2–5), suggesting they are in a primary orientation (see above). The possibility of rotated structures underscores the importance of using large datasets at the domain- or regional-scales when interpreting patterns in orientation or younging.

Schlieren Petrography

Schlieren in the TIC contain between 2 and 8 times more hornblende, biotite, magnetite, apatite, titanite, and zircon than the surrounding plutonic material (e.g., Wahrhaftig, 1979; Reid et al., 1993; **Table 1**). The relative modal proportions of these minerals in the schlieren structures varies with the mineralogy of the host unit. Within the TIC, the ratio of biotite to hornblende increases towards the interior of the complex (e.g., Bateman and Chappell, 1979; Memeti et al., 2014). This trend is mirrored in the schlieren found in different TIC units (**Table 1**). The proportion of quartz to feldspar also increases from the KC to the CP in both schlieren and host samples.

The abundance of magnetite, titanite and apatite increases from the outer KC unit to the interior CP unit in both host and schlieren samples, yet the relative proportions of these minerals are highly unit-dependent (**Table 1**). For example, both the Kuna Crest host and schlieren are generally titanite-poor, relative to younger units. In contrast, the Cathedral Peak unit is richer in titanite (∼1%; **Table 1**), which is also pronounced in the schlieren (∼7%; **Table 1**). Magnetite forms crystal clusters in all schlieren samples, which also includes titanite clusters in the CP schlieren. Zircon is sometimes observed in thin section but is generally too small to measure quantitatively. Previous workers have also identified allanite in select samples (e.g., Reid et al., 1993; Paterson, 2009). These changes towards the TIC interior coincide with an increase in the grain size of the accessory minerals, and in all studied samples, the grain size of accessory minerals is, on average, larger in the schlieren than in the host.

In thin section, schlieren-bound magmatic structures record the same type of microstructures found in the surrounding host and are dominantly magmatic in origin. For example,

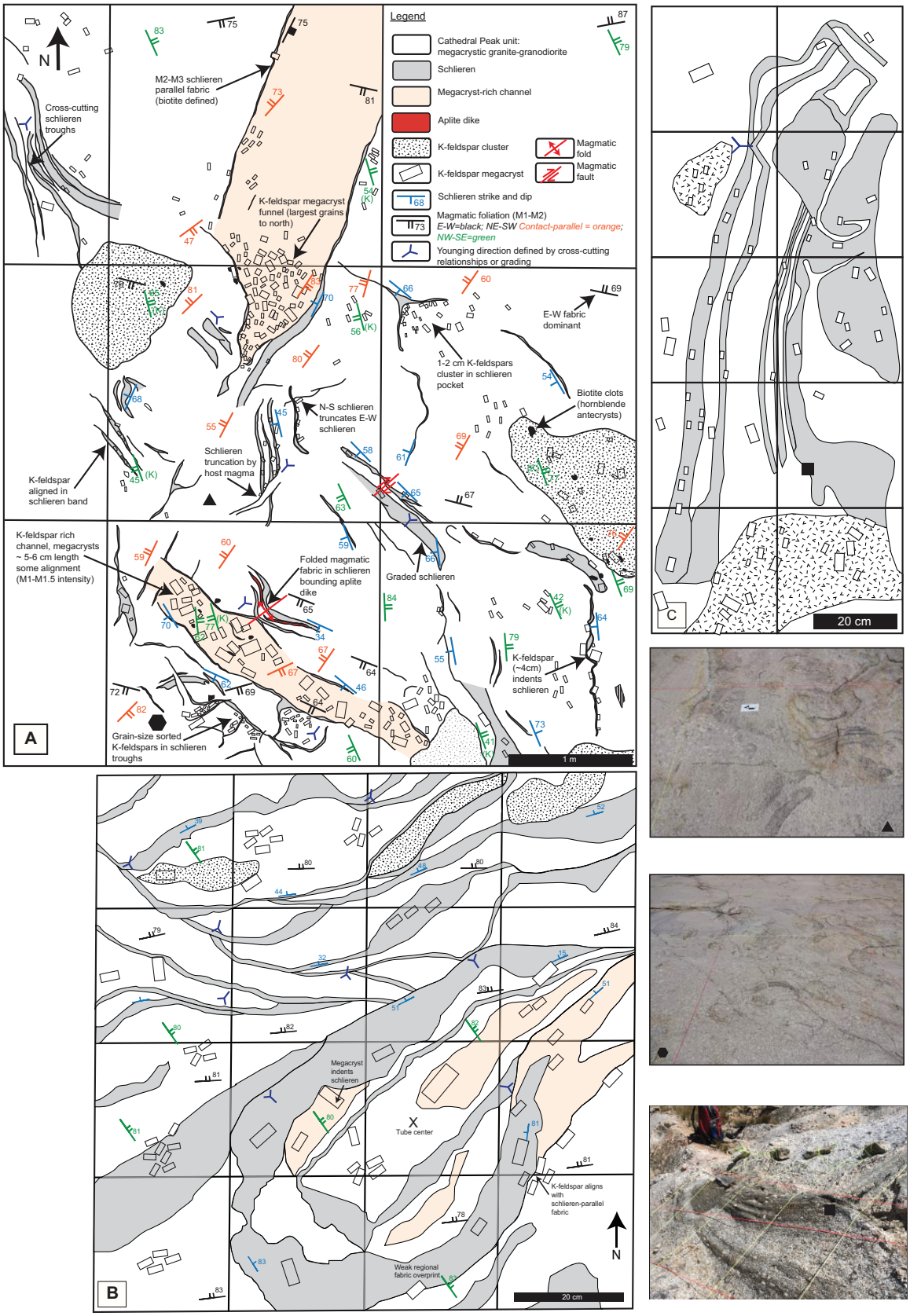

FIGURE 9 | Continued

FIGURE 9 | Outcrop-scale grid maps showing complex schlieren-bound structures. **(A)** Pothole Dome, Glen Aulin area (NW quadrant). Schlieren are sharply truncated, or re-intruded, by Cathedral Peak magma, and are locally folded. The Cathedral Peak unit contains K-feldspar megacrysts from ∼4 to 6 cm in size at Pothole Dome. At this outcrop, K-feldspar megacrysts are densely clustered (stippled pattern) and are sorted by grain size into funnel- or channel-shaped structures bounded by schlieren. K-feldspars are included in schlieren, and where observed, they are aligned with schlieren-parallel fabric defined by hornblende and biotite. This is an example where there are multiple younging directions preserved at one outcrop. The regional fabric is locally distorted into-schlieren-parallel orientations, although a clear regional E–W orientation and contact-parallel NE–SW orientation is still dominant. **(B)** Young Lakes area (NE quadrant). The northern section of the map shows a package of cm wide schlieren troughs, with a consistent younging direction to the NNE. K-feldspar megacrysts (3–8 cm) are abundant within schlieren layers and align in a schlieren-parallel orientation. Within some layers (yellow) the schlieren are generally more megacryst-rich. The trough package is truncated by an elliptical-shaped tube structure which is stationary (youngest rings are in the center of the tube). K-feldspar megacrysts in the tube are aligned parallel to schlieren. K-feldspar defined fabric within the CP is weakly defined, except in and around schlieren-bound magmatic structures. **(C)** Young Lakes area (NE quadrant). Folded schlieren troughs with 3D relief younging to the east. The northern portion of the structure has slumped with a small ∼10 cm displacement to create an apparent sinistral offset. Schlieren include K-feldspar megacrysts that are variably aligned. The most well defined foliation in thin elongate layers, and weak foliation in irregularly shaped schlieren.

interstitial quartz is pinned by phenocrystic feldspar, biotite, and hornblende. Crystal clots of feldspar, magnetite, and titanite are common in all studied examples. Crystal-plastic deformation is limited to undulose extinction in quartz, and rare cases of deformation twinning in feldspar.

Whole-Rock Geochemistry

Major, minor, and trace elements

TIC schlieren have a wide range in SiO_2 contents (40–70 wt.%; **Figures 10A–D**), encompassing much of the variation in SiO_2 found in the main TIC units (48–79 wt.% SiO_2), except at the high-silica end >70 wt.% SiO_2. As described in earlier studies (Reid et al., 1993; Paterson et al., 2008; Solgadi and Sawyer, 2008; Žák et al., 2009), for many elements TIC schlieren samples plot at a high angle to the main TIC trend in SiO_2-element space. Schlieren are enriched in TiO_2, MnO, and P_2O_5, relative to the host TIC for a given SiO_2 contents and have a variable FeO_t contents at SiO_2 <62 wt.% (**Figure 10B**). Schlieren are depleted in Al_2O_3 (**Figure 10A**) and CaO relative to the surrounding host, and Na_2O ranges from depleted to overlapping with the host at higher SiO_2 content. K_2O is enriched in schlieren relative to the host at low SiO_2 and then compositionally overlaps with the host at SiO_2 >60 wt.%. Felsic components of schlieren-bound structures compositionally overlap with the surrounding TIC rocks. SiO_2 contents of the felsic component are between 57 and 78 wt.%, falling at the felsic end of schlieren compositions and in some cases matching compositions of TIC leucogranite samples (**Figure 10**). The intersection of linear trends formed by the schlieren samples and felsic or host samples is consistently between 65 and 70 wt.% SiO_2.

Some large-ion-lithophile-elements such as Rb, Cs, and Eu are enriched in the schlieren relative to the host for a given SiO_2 content, while Sr (**Figure 10C**) and Ba are depleted (**Table 2**). Most high-field-strength-elements, such as Y, Nb, and Zr (**Figure 10D**) are enriched relative to the host (**Table 2**). Pb and Sc contents in both schlieren and host are approximately equal (**Table 2**), forming one trend line.

Rare earth elements

The main TIC units have classic arc-type REE slopes, with La_N/Yb_N values between 2 and 44. The REE patterns vary between units, with the CP samples showing the most fractionated patterns. TIC schlieren generally have REE patterns parallel to the host unit they are situated in, with the exception of schlieren samples in the Kuna Crest granodiorite (**Figure 11A**). A key feature that distinguishes schlieren from the main TIC units is that the schlieren have REE abundances up to 10 times greater than the surrounding host. Felsic components also have REE patterns parallel to those of the host but display lower REE contents (as much as 10 times lower than the host) (**Figures 11A–C**). A felsic component sample from the Half Dome units shows a slight positive Eu anomaly, which is not found in the sample of the adjacent host (**Figure 11B**).

Sr and Nd isotopes

The TIC has a large range initial $^{143}Nd/^{144}Nd$ (εNd_i notation used) between −2.0 and −9.5 and initial $^{87}Sr/^{86}Sr$ values (Sr_i notation used), between 0.7055 and 0.7077, with the CP unit and late leucogranite samples producing the most evolved compositions (Kistler et al., 1986; Memeti et al., 2014; **Figure 11D**). Within one unit, the isotopes vary up to 5 epsilon units (εNd_i), with smaller variations in Sr_i (**Figure 11D**; Memeti et al., 2014). Schlieren and host pairs are isotopically similar, corresponding well with the isotopic composition of the unit they are found in. However, the schlieren and host pairs are not identical. Differences in εNd_i between paired schlieren and host samples are <1 epsilon unit, and in pHD and CP samples this difference is minimized to within 0.2 epsilon units. The schlieren samples in all but one example have higher Sr_i ratios than their adjacent host (**Figure 11D**). These differences are greater than the 2σ analytical uncertainty (0.0006–0.0025%, smaller than the size of the symbols in **Figure 11D**).

Relative Timing Indicators

The zircon isochron map of Memeti et al. (2014) provides the only absolute timing constraint on schlieren-bound structure formation; notably, schlieren-bound structures span the entire 10 m.y. history of the complex (**Figure 2C**). At the scale of a single schlieren trough, Memeti et al. (2014) also found identical ages between zircons contained in the schlieren and zircons in the surrounding host.

Several examples have been found where intrusive contacts sharply truncate schlieren-bound structures (e.g., **Figure 4A**) indicating that these schlieren-bound structures formed prior to arrival of a new magma pulse. Examples have also been found where materials of one unit slumped off a contact into the adjacent unit to form a compositionally defined magmatic structure, requiring that they formed immediately

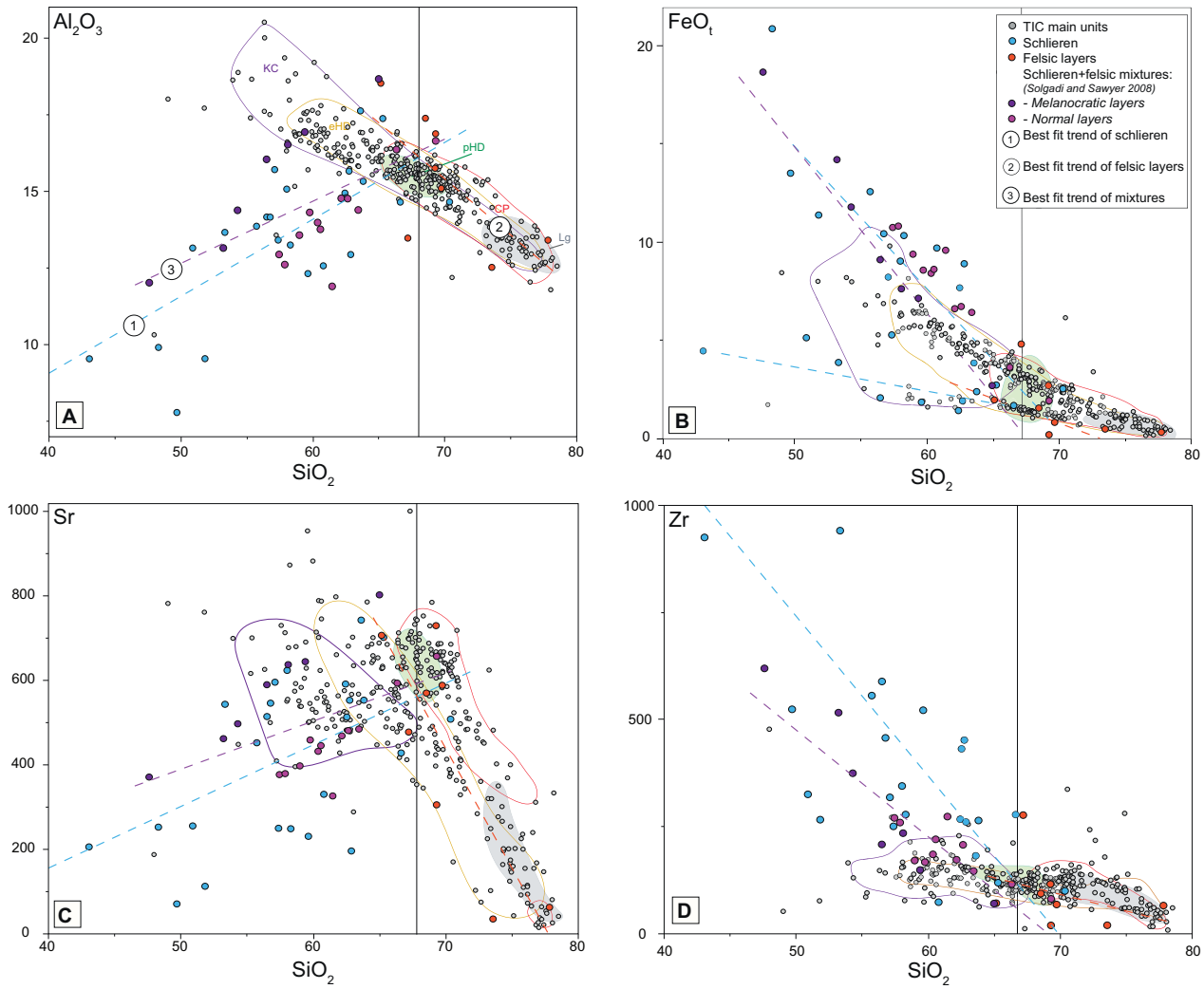

FIGURE 10 | Major and trace element data from schlieren, felsic components, and host TIC samples. **(A)** Al_2O_3 v. SiO_2; **(B)** FeO_t v. SiO_2; **(C)** Sr v. SiO_2; **(D)** Zr v. SiO_2. Data sources: Bateman and Chappell (1979), Peck and Van Kooten (1983), Kistler et al. (1986), Bateman et al. (1988), Loetterle (2004), Burgess and Miller (2008), Gray et al. (2008), Paterson et al. (2008), Solgadi and Sawyer (2008), Economos et al. (2009), Memeti (2009), Žák et al. (2009), Coleman et al. (2012), and new data (**Table 2**).

after juxtaposition of two magma pulses (Paterson et al., 2008). Elsewhere, schlieren-bound structures seem to cluster along internal contacts indicating the contact already existed (e.g., Žák and Paterson, 2005). Together with the temporal history established from zircon ages, these observations indicate that compositionally defined magmatic structures formed from many repeated events both prior to, during, and after juxtaposition of magma pulses, over the entire 10 m.y. history of the TIC.

The relative timing between different types of schlieren-bound structures (i.e., planar schlieren, troughs, tubes, and plumes) is not clear. This is because different schlieren-bound structures are generally spaced ∼1–10 m apart and do not cross-cut each other (see also Hodge et al., 2012), except in rare cases (**Figure 9B**). Often, transitional-type structures are observed, for example, trough structures that grade into tubes, or bifurcating tubes (**Figure 4B**), where a local relative timing relationship can be determined (e.g., Paterson, 2009). Overprinting relationships between type 1 magmatic fabrics in schlieren-bound structures and fabric types 2–5, described above, suggest that schlieren-bound structures and magmatic fabric types 2–5 formed synchronously.

In addition, schlieren major and trace element compositions consistently intersect TIC host compositions between 65 and 70 wt.% SiO_2. We used these intersections to estimate the bulk composition of a TIC magma that we could model under fixed pressure and varying temperature conditions. Werts et al. (2020) and Barnes et al. (2020), using the thermometer of Putirka (2016), calculated hornblende crystallization temperatures ranging from >800 to ∼650°C across all TIC units. As hornblende is abundant in all schlieren studied, the temperature range 800–700°C was considered relevant to schlieren formation to a first order. Further, a study of apatite in TIC rocks (also abundant in

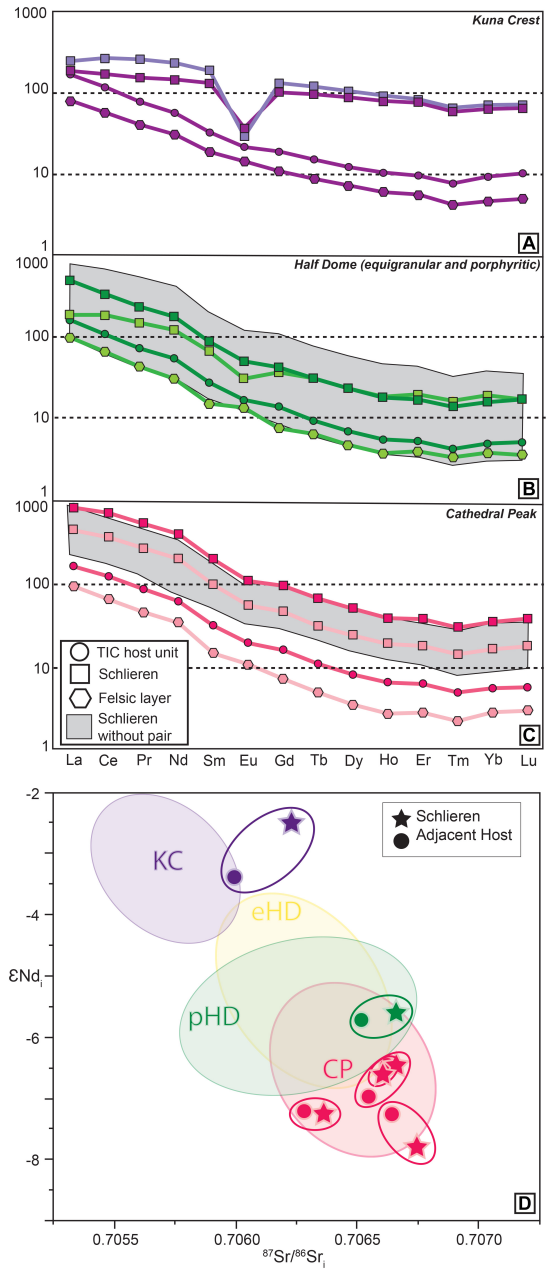

FIGURE 11 | (A–C) Rare Earth Element patterns in TIC host, schlieren and felsic components. Plots are divided up by major unit. **(A)** Kuna Crest granodiorite [sample data from Memeti (2009)]. **(B)** Half Dome granodiorite units. eHD and pHD have been combined to maximize data coverage. **(C)** Cathedral Peak granodiorite. Matching colors indicate that the samples were collected from the same outcrop, at adjacent layers. Normalized after Sun and McDonough (1989). **(D)** Whole rock isotopes $^{87}Sr/^{86}Sr_i$ v.εNd_i. TIC samples are color-coded by unit. They define a broad isotopic range. Schlieren-host pairs collected at the same outcrop are circled. Fields defined by host rock samples as shown in Memeti et al. (2014). Standard errors are smaller than the size of the symbols and provided in **Table 2**. Data sources: Bateman and Chappell (1979), Peck and Van Kooten (1983), Kistler et al. (1986), Bateman et al. (1988), Loetterle (2004), Burgess and Miller (2008), Gray et al. (2008), Paterson et al. (2008), Solgadi and Sawyer (2008), Economos et al. (2009), Memeti (2009), Žák et al. (2009), Coleman et al. (2012), and new data (**Table 2**).

schlieren) suggested that at apatite saturation (~900°C) magma crystallinity was 9% (Piccoli and Candela, 1994), which we use as a minimum crystallinity here. The modeled compositions included 4 wt.% H_2O in the melt due to the presence of hornblende (Naney, 1983; Fox and Miller, 1990). This represents a minimum estimate on water contents in the system. The presence of miarolitic cavities and vugs in the TIC indicate that volatiles were exsolved during magma crystallization and cooling, however the relative timing of volatile exsolution and schlieren-formation is not yet clear and is a target for future study (Bateman, 1992; Memeti et al., 2014). At higher H_2O contents, effective viscosity decreases. Thus, the effective viscosity estimates below can be considered broadly as maximum values for each modeled composition.

Using the estimated bulk composition from schlieren-host TIC intersections (**Table 3**), with 4 wt.% H_2O and 65 wt.% SiO_2, we calculated effective viscosities of the bulk composition containing between 10% and 90% crystals from 800 to 700°C using the method of Murase et al. (1985; equation 3). This method incorporates the major element composition, H_2O contents, and the volume fraction and mean size of spherical crystals. Although a simplification of the natural system, it provides an initial estimate of effective viscosity that provides a basis for future study. At this bulk composition at 800°C, effective viscosity increases from $10^{6.9}$ to $10^{9.3}$ Pa s with increasing crystal contents

TABLE 3 | Viscosity summary.

	Starting compositions			
Model number	**1**	**2**		
Model type	**Bulk**	**Hornblende**	**Amphibole uncertainties from Zhang et al. (2017)**	
Major oxides (wt %)				
SiO_2	65.00	76.97	3.7	
TiO_2	0.50	0.20	0.62	
Al_2O_3	16.00	13.62	0.93	
FeO_t	3.00	0.99	1.67	
MnO	0.50	–	–	
MgO	2.00	0.22	0.96	
CaO	3.00	1.82	1.31	
Na_2O	3.80	3.50	–	
K_2O	4.00	3.12	0.57	
P_2O_5	0.15	–	–	
H_2O	4.00	4.00	–	
Total	101.95	104.44	–	
	Log effective viscosity (Pa s)			
Temperature (°C)	800	700	800	700
Crystal contents (%)				
10	6.87	7.90	8.14	9.34
25	7.66	8.69	8.93	10.1
50	8.43	9.47	9.71	10.90
75	8.98	10	10.26	11.5
90	9.25	10.3	10.53	11.7

and reaches a maximum of $10^{10.3}$ at 700°C (**Table 3**). Werts et al. (2020) demonstrated that the bulk composition of many TIC samples is generally more mafic than the composition of melts in equilibrium with hornblende due to crystal accumulation. We compared our bulk-rock results to a model using a calculated melt composition in equilibrium with CP hornblende, containing 4 wt.% H_2O and 76 wt.% SiO_2 (equations 3, 5, 7, 9, 11, 13, and 14 and associated uncertainties from Zhang et al., 2017). This model resulted in calculated effective viscosities ranging between $10^{8.2}$ and $10^{10.5}$ Pa s at 800°C, with a maximum of $10^{11.8}$ Pa s at 700°C.

DISCUSSION

Our field and geochemical results allow us to analyze schlieren-bound magmatic structure formation across several spatial scales. First, outcrop-scale observations and sample compositions are discussed, forming the basis for physical and chemical models of schlieren formation. Kilometer-scale domainal clustering and 10's km scale regional patterns are then discussed to characterize the scale and mobility of the magma mush system(s).

Outcrop Scale

Evaluating Models to Form Schlieren

New (mafic) magma injection

Models concluding that schlieren form from distinct, mafic magma batches (e.g., from a similar source as mafic magmatic enclaves) cannot describe the origin of most TIC schlieren (**Figure 1A**). The varied geometries and field patterns of schlieren from outcrop to regional scales are difficult to explain by injection of mafic magma batches alone. In addition, mineralogy and whole-rock geochemistry suggests that schlieren are sourced from the surrounding host magma, rather than an "exotic" mafic magma. Schlieren mineral assemblages reflect, to a first order, the assemblage of the surrounding host, with different modal abundances (**Table 1**, see also Reid et al., 1993; Alasino et al., 2019). Parallel REE patterns further suggest that the mixture of REE-bearing minerals in schlieren is matched in the host and indicates a common magma source, distinct from enclaves (Reid et al., 1993), which is supported by the similarity in host and schlieren isotope compositions (**Figure 11D**). The unique bulk-rock compositions of schlieren, together with modal assemblages, indicate that they are cumulates (**Figure 10** and **Table 1**, see below). Thus, their present bulk compositions are not representative of the more evolved parental magma from which they were derived. One interpretation of this parental magma composition is that it falls between 65 and 70 wt.% SiO_2, where the best fit line of schlieren compositions intersects the main TIC trend. Another, determined from calculated melts in equilibrium with TIC hornblende compositions, suggests a range from 67 to 79 wt.% SiO_2 (Werts et al., 2020).

Diffusion and re-crystallization

Thermochemical diffusion and recrystallization end-member models are also not supported by our combined structural and geochemical datasets (**Figure 1A**). Field patterns of schlieren, including cross-cutting relationships, are not explained by this model. Solgadi and Sawyer (2008) demonstrated, using hornblende Mg-number, that schlieren lacked any compositional gradients from base to top, which either a thermal or chemical gradient should impose. *In-situ* mineral analyses of samples across all TIC units reveal complex zoning patterns, which suggests that thermochemical diffusion did not re-equilibrate the mineral compositions (Memeti et al., 2014; Barnes et al., 2016; Werts et al., 2020). In a liquid immiscibility model, a form of chemical diffusion (e.g., Glazner et al., 2012; Bartley et al., 2019), isotope compositions should be identical between schlieren and host, and the felsic component to the mafic schlieren should be enriched in alkalis, Rb, Cs, Sr, and Ba (Ryerson and Hess, 1978; Hurai et al., 1998), neither of which are observed in TIC samples. Instead, the felsic component has a similar composition to the host. Mixing schlieren and felsic components together as demonstrated by analyses of Solgadi and Sawyer (2008) and shown on **Figure 10** produces a compositional array parallel to schlieren trends, distinct from the host. Furthermore, if mafic schlieren represented the Fe-rich liquid of an immiscible pair, the density of the schlieren should be considerably greater than the host and would be expected to separate from felsic components and the host, rather than be interlayered with them.

Magmatic flow

Our proposed model to explain field and geochemical datasets involves hydrodynamic flow-sorting of crystals in a mush to produce schlieren layering (**Figure 12C**). TIC schlieren contain dense minerals and reduced abundance of low-density feldspar. An exception includes schlieren containing K-feldspar megacrysts, which are a part of some (but not all) schlieren-bound structures (e.g., **Figures 3C**, **4A,C,D**). Their considerably greater size compared to other minerals may contribute to their inclusion. Together with evidence of common mode and size grading of schlieren layers, these observations are consistent with mineral accumulation that depends on the density, size, and shape of individual crystals (e.g., Bhattacharji and Smith, 1964; Kawabata et al., 2013). Further, outcrop scale cross-cutting relationships, truncation of structures by the host magma, and consistent patterns of outward-younging orientations within and across domains that span a range of crystallization ages requires physical, magmatic erosion and flow processes to operate synchronously and repeatedly. Schlieren form an array of major and trace element compositions at high-angle to the main TIC trend, which are interpreted here to represent the varying degrees of crystal accumulation of hornblende, biotite, apatite, titanite and zircon that dominate schlieren compositions. As a suitable complementary felsic fractionate is not observed (see above), we interpret that any melts resulting from schlieren accumulation were mixed back in with surrounding host magma, to form the felsic components of schlieren-bound structures (see also Alasino et al., 2019).

Small shifts towards radiogenic Sr_i in schlieren, and variable differences in εNd_i between schlieren and host are also compatible with a flow-sorting crystal accumulation model. Measurable isotopic shifts at the scale of the schlieren and adjacent host could be caused by: (1) crystal-melt fractionation from an isotopically hybrid magma (e.g., Beard, 2008);

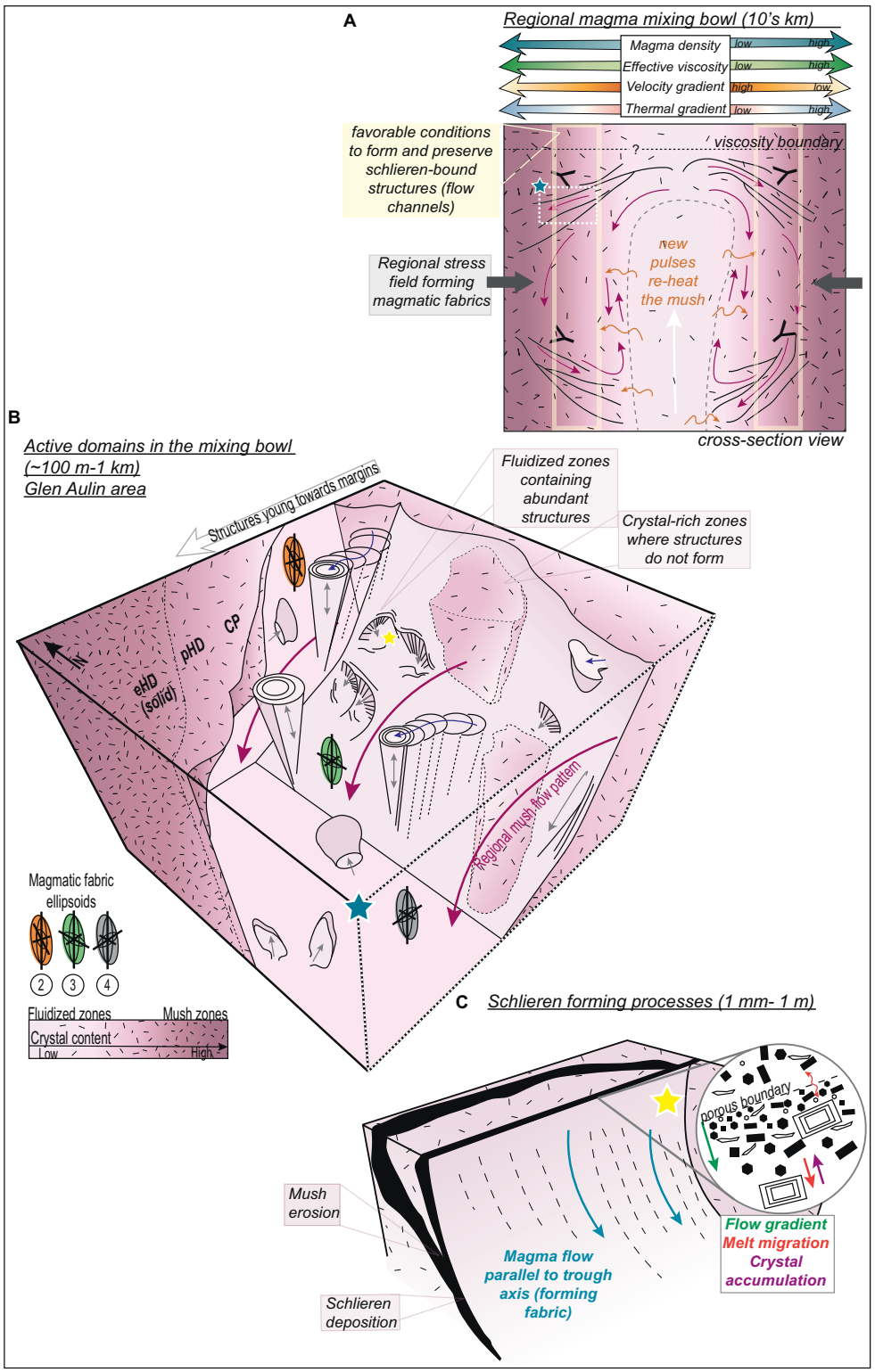

FIGURE 12 | Summary of multi-scale dynamic processes operating in mobile magma mushes. **(A)** Mixing bowl scale. Return flow of the mush is triggered by intruding pulses in the center of the complex. Thermal/mechanical gradients aid convection. **(B)** Domain scale activity summarized as a 3D diagram. Structures form in fluidized zones that are more melt-rich due to local changes in pore-pressure, viscosity, and stress, while crystal rich zones represent zones that are absent of schlieren-bound structures. They still contain melt as they contain magmatic fabrics, dikes and other structure. **(C)** Structure-scale processes demonstrated for a magmatic trough. Flow sorting, filter pressing, crystal accumulation and melt escape are all important processes at the mm-cm scale. Flow along the trough channel produces a lineation in hornblende.

(2) selective crystal accumulation of Rb-bearing minerals, or Sm-bearing minerals; or (3) alteration of minerals by late magmatic fluids (e.g., Li et al., 2018; Alasino et al., 2019). Diffusion or metasomatism by late magmatic fluids should leach mobile elements, such as Rb, from samples, leading to low Rb/Sr. However, the relationship between pairs of related samples is not the same for all samples studied or compiled; in most cases (five samples out of six), Sr_i is more radiogenic in schlieren, but εNd_i is variable. In addition, the preservation of textural and compositional zoning in Rb-bearing phases such as K-feldspar, and Sm and Nd-bearing phases such as hornblende (and apatite) demonstrates that diffusion of fast- and slow-diffusing elements was limited in the TIC (Memeti et al., 2014; Barnes et al., 2016; Werts et al., 2020). Thus, isotopic differences between schlieren and host are interpreted as primary magmatic features of the samples resulting from processes (1) and (2), rather than secondary features (3).

As the TIC is isotopically heterogeneous (Kistler et al., 1986; Gray et al., 2008; Memeti et al., 2014), models that fractionate crystals from a hybrid magma and create further heterogeneity, as illustrated by Beard (2008) are considered likely to explain schlieren-host isotopes in combination with field data and mineral assemblages. Furthermore, selective fractionation and accumulation of minerals could amplify the difference in isotope composition between schlieren and the surrounding host (e.g., Kendall et al., 1995; Blum and Erel, 1997). Rubidium-bearing minerals such as biotite, abundant in the CP schlieren, could result in high Sr_i ratios, while accumulation of Sm-bearing minerals such as apatite and hornblende could result in high $^{143}Nd/^{144}Nd_i$ and thus more primitive εNd_i values. An example of the latter is the KC schlieren sample, which contains ∼40% hornblende.

The Significance of Forming Schlieren Between 65 and 79 wt.% SiO_2

TIC host magmas were already mixed before schlieren formation based on whole-rock isotope trends (Memeti et al., 2014). The flow-sorting model requires that most, if not all, of the highly concentrated minerals (biotite, hornblende, magnetite, titanite, apatite, and zircon) were saturated in the host magma before schlieren minerals were separated and requires sharp rheological boundaries to exist in the mush. Melt presence is required to deform schlieren-bound structures by magmatic faulting and folding, for the felsic component of schlieren accumulation to mix back in with the host magma, and also to form magmatic fabrics (discussed below). The structure must have formed in a sufficiently strong magma to erode and sometimes break structures without losing definition in individual layers and also to form sub-vertically dipping schlieren (e.g., Bergantz, 2000; Weinberg et al., 2001; Paterson, 2009; Alasino et al., 2019). Each of these observations suggest that the magma was chemically evolved and crystal-rich during schlieren formation.

The intersection of major and trace element best-fit trends of schlieren with TIC host and felsic component samples lies consistently between 65 and 70 wt.% SiO_2. One possibility is that this represents the bulk composition of the parental magma when the schlieren and felsic components were formed. However calculated melt compositions from hornblende, using the Zhang et al. (2017) chemometer range between 67 and 79 wt.% SiO_2 within the TIC, highlighting the effects of crystal accumulation (Barnes et al., 2020; Werts et al., 2020). In the CP unit, with the calibrated uncertainties on the amphibole calculations (listed in **Table 3**), these melts are rhyolitic (Werts et al., 2020). Further, these two independent approaches to estimate melt compositions overlap within the smaller range of 67–70 wt.% SiO_2. In both examples we can place initial constraints on magmatic conditions during schlieren formation, specifically the magma viscosity. Given the rhyolite composition of the melt, the largest effects can be expected from changing temperature (800–700°C), crystal content, and H_2O content, which here is considered a minimum. During the temperature interval of 800–700°C, when schlieren likely formed, calculated effective viscosities increased from $\sim 10^7$ to 10^{11} Pa s as crystal content increased in both starting compositions, with considerable overlap between models, and the calculated melt compositions providing the highest values.

Although these values appear on the high end to facilitate magmatic flow, previous studies have demonstrated that small variations in pore pressure or strain rate may manifest as large variations in magma viscosity, without substantially reducing temperature or crystallinity of the magma to generate local rheologic boundaries (e.g., Weinberg et al., 2001; Bergantz et al., 2017; Sparks et al., 2019). Numerical modeling of hydrogranular crystal networks suggest that, at the crystal scale, particle-particle-melt interactions and forces such as melt lubrication, crystal clustering, jamming, and the migration of particle force chains all can aid or inhibit movement of crystals and fluids under magmatic conditions and thus instantaneously and dramatically modify mush rheology to promote or inhibit magmatic flow (Bergantz et al., 2017; Carrara et al., 2019; McIntire et al., 2019). Thus, bulk or effective viscosity does not fully describe the mobility or the dynamics of the system. Future studies exploring parameters such as volatile content (including separate fluid phases), estimating strain rates, crystal properties (e.g., size, shape, density), and the porosity and pore pressure of the system could help to constrain the dynamics of the system during schlieren formation. These processes that locally and transiently reduce viscosity may also enhance melt migration out of the schlieren and into the surrounding host mush; potential mechanisms include filter-pressing or porous flow (e.g., Weinberg et al., 2001). Similar magmatic flow models were previously proposed in granitoid systems by Weinberg et al. (2001), Paterson (2009), and Alasino et al. (2019), who invoked deformation-assisted mineral-melt separation to form schlieren structures in the Tavares pluton, the TIC, and the Sonora Pass Intrusive Suite, respectively.

Evaluating Models to Form Different Schlieren-Bound Structures

The results of this study support a range of physical processes to form different schlieren-bound structures, as described by Weinberg et al. (2001) and Paterson (2009). These include boundary flow, filter pressing, and Rayleigh-Taylor instabilities. Combinations of these processes might operate to create transitional-type structures described in section "Relative Timing

Indicators" (e.g., troughs grading into tubes). Instabilities triggering fluidization of the mush and structure formation may be driven by sinking of dense objects or magma mushes (e.g., Wiebe et al., 2007), or the rise of buoyant objects (e.g., exsolved volatiles, extracted melts: Clarke, 2003; Dietl et al., 2010), both of which have been proposed to form individual tube structures. In addition, the intrusion of new magma pulses into the chamber may promote thermal, chemical and mechanical instability (e.g., Pons et al., 2006). This behavior has been suggested to drive crystal avalanches (forming troughs; Solgadi and Sawyer, 2008; Alasino et al., 2019), as well as local rising of magmas (forming tubes or plumes; Paterson, 2009).

The diversity in the types of observed magmatic structures within most map domains (GA, TP, and LC) indicates that at a single outcrop (∼10–20 m scale), local flow fields were complex enough to form geometrically distinct troughs, tubes and plumes. For example, at several localities at Glen Aulin there may be both vertical magma flow through tube structures, and moderately down-dipping flow in troughs. This raises the question if different structures may require or favor different magmatic conditions, or driving mechanisms, to form (e.g., **Figure 1B**). In contrast, within the Young Lakes area, tubes and plumes are sparse and planar schlieren and troughs are dominant, which could suggest the magmatic flow field was distinct, and perhaps more uniform.

There is a weak spatial control on the types of structures that form. At Glen Aulin, plumes are generally concentrated in the east, and tubes are concentrated in the west. The eastern edge of the domain is the youngest edge of the domain, formed across a steep age gradient (Memeti et al., 2014 isochron plot), which suggests that this could result from a temporal shift in physical flow mechanisms, in addition to a spatial shift.

Domain Scale

Magma Chamber Domains Are Spatially Heterogeneous as a Result of Flow Instabilities

TIC schlieren-bound structures are spatially clustered between large (∼0.1–0.5 km^2) zones where structures are sparse to absent. As described above (section "The Significance of Forming Schlieren Between 65 and 79 wt.% SiO_2"), schlieren are likely recording events within an evolved, crystal-rich mush, at temperatures between 800 and 700°C, thus they represent a view into later stage magma flow and evolution within a chamber. The difference between the structure-rich and structure-poor zones could reflect: (1) zones which were "fluidized," more melt-rich and therefore more mobile mush, producing abundant structures, separated by mushy zones that were unable to flow as dynamically and therefore lack schlieren-bound structures (a form of partitioning); (2) structures were uniformly present throughout the chamber and were subsequently erased by later mixing and homogenization; and (3) structure rich domains represent zones of sharp flow velocity gradients that could have increased mobility due to positive feedbacks as structures started forming; or 4) structure rich zones represent channels of porous flow. All scenarios imply that magma dynamics were spatially heterogeneous at the 1–10 km scale. It appears more difficult to completely erase the evidence of schlieren-bound structures, because that would require thorough mixing at high crystal contents. Field observations show that schlieren-bound structures can deform semi-rigidly (by faulting and folding and re-intrusion) or mingle with the host magma, suggesting it may be mechanically challenging to fully erase the schlieren once they form. This is supported by the weak to absent overprinting of local type 1 fabrics by regional type 2–5 fabrics in schlieren, but more pervasive overprinting in the felsic parts of the structures.

Spatial clustering of schlieren-bound structures is documented in other plutons. In the Vinalhaven intrusive complex, schlieren-bound structures (mostly tubes) "occur widely but sparsely," wherever sinking enclaves could sufficiently shear the surrounding crystal mush (Wiebe et al., 2007). The pluton was strongly vertically stratified, controlling the path of the enclave (Wiebe et al., 2007). Clarke et al. (2013) suggested that tube structures were preferentially found near the pluton margins in the Halifax pluton, Nova Scotia, a result also found in K-feldspar pipes associated with schlieren by Rocher et al. (2018) in the San Blas intrusive complex, Argentina. Clarke et al. (2013) further posited that the cause of structures clustering within the contact zone could be attributed to "restricted zones of permeability," which could represent the fluidized zones described here.

Processes triggering domain-scale flow instabilities

The occurrence of domain-scale magmatic structure patterns suggests that broader-scale dynamic instabilities were present in TIC mushes, and not restricted to the outcrop-scale where individual structures formed. Several processes may have operated in the TIC. The intrusion of new pulses, or upwards migration of volatiles, could lead to mobilization and convection of the mush (e.g., Bachmann and Bergantz, 2006; Burgisser and Bergantz, 2011; Pinotti et al., 2016; **Figure 12A**). In computational models, the heterogeneous distribution of particle force chains maps transient high and low stress zones in the mush, that has implications for pore-pressure variability, and overall mush porosity (e.g., Estep and Dufek, 2012; Bergantz et al., 2017). Focused porous flow could also create zones of increased permeability that promote flow instability (Kelemen et al., 1995; Paterson et al., 2012). In other cases (e.g., Sawmill Canyon) structure-rich domains may be spatially restricted to magma sheets or cracks (e.g., Clarke and Clarke, 1998; Paterson et al., 2008). Pluton roofs and internal contacts may generate vertical domain-scale instabilities. Roof instability can lead to sinking of crystalline mush, which could then be further segregated by density (e.g., "crystal-rich drips"; Bergantz and Ni, 1999; Rocher et al., 2018; Carrara et al., 2019). We infer that the present-day exposed levels of the TIC are representative of the upper levels of the magma body, close to the roof. Evidence includes local exposures of roof flaps and an approximately uniform elevation plane of highest (plutonic) peaks across the TIC (e.g., Bateman, 1992; Cruden et al., 2017). Sub-vertical, internal contacts are ideal locations for solidification fronts, leading to mush collapse and avalanching along steeply dipping walls (e.g., Marsh, 1996; Bergantz, 2000; Rocher et al., 2018; Alasino et al., 2019).

Domain-scale solidification fronts may play a larger role in the Glen Aulin area, relative to the Young Lakes or Lyell Canyon areas, as major unit contacts are closely spaced, with potentially greater thermal, chemical, and rheologic gradients across them. While all of these processes likely were active during the evolution of the TIC, the lack of similarity in domain size, shape and orientation, together with our outcrop- and regional-scale structural patterns favor forming domains by spatial heterogeneity in particle-particle interactions, driven by new pulses.

Planar Schlieren and Troughs Weakly Align With Nearby Contacts Due to Boundary Conditions

In the Glen Aulin domain, there is a weak preference for planar schlieren and trough orientations in a NE–SW direction that aligns with the well-defined Type 2 foliation, and with the adjacent contacts of the Cathedral Peak unit with the older Half Dome units. This is also qualitatively suggested in N–S striking contact-parallel schlieren at Tenaya Peak, although this interpretation is complicated by a similarly oriented Type 3 foliation. In contrast, this relationship is not apparent in the Young Lakes domain, where the nearest contact (2–3 km away) is NW-SE striking, yet planar schlieren and troughs are oriented at high angle to the NW-SE foliation, and instead show a preference for NE–SW striking orientations.

The relationship between schlieren orientations and the contact is ambiguous at Lyell Canyon, potentially because the contact is a wide, gradational zone between units that hybridized (Žák and Paterson, 2005; Paterson et al., 2011, 2016; Oppenheim et al., in review). At Glen Aulin, the contacts between eHD (probably near-solidus) and the pHD and CP (active magma mushes of varying crystallinity, **Figure 12B**) are proximal across a 100–200 m wide zone. Thermal and chemical gradients could be significant in driving flow gradients, and perhaps play a larger role in defining the orientations of the structures at Glen Aulin than in the other domains (**Figure 12B**). As domains devoid of structures are interspersed with domains concentrated in structures across zones both near and far from contacts, we suggest that nearby contacts are not controlling the formation of schlieren, but potentially play an indirect role in their orientation at the schlieren-bound structure scale.

Crystal Clustering Is Widespread and Independent of Domains

The observation that K-feldspar megacryst clusters are found widely in the TIC, even in areas of sparse to absent schlieren complicates the story of heterogeneous, isolated, schlieren-rich domains (e.g., Paterson et al., 2005). In some cases they are associated with schlieren, but they also represent a similarly local (meter-scale), selective mineral sorting and accumulation process that does not seem to be as spatially restricted. The K-feldspar megacryst clusters could be mechanically sorted (Paterson et al., 2005; Vernon and Paterson, 2006; Paterson, 2009), possibly representing "logjams" in a less-dynamic flow field, brought together in a cluster due to their large size (Weinberg et al., 2001).

Regional Scale

Outward-Younging Patterns Reflect Re-mobilization of the Mush by New Pulses

At the regional scale, the TIC is defined by four compositionally distinct units, which are bounded by a wide variety of external and internal contacts. Multiple magmatic fabrics are found in each of the units, and cross several of these internal contacts. Compositionally defined magmatic structures occur across all TIC units. Schlieren-bound structures are clustered, with a dominant pattern of structure migration or younging outwards, towards internal contacts with older units. The regional patterns listed above may provide insight into viable emplacement models for the TIC, including dike emplacement, sill/laccolith emplacement, or a combination of sheet and diapir emplacement. Emplacement models are described below, specifically focusing on what these models predict for schlieren-bound structure patterns at regional scales and how our regional-scale results (contacts, fabrics, schlieren-bound structures) compare. A broader overview of TIC emplacement is provided in section "Implications for Emplacement Models and the Minimum Sizes of Magma Chambers."

Incremental growth models for the TIC

Some studies have proposed that the TIC was emplaced by a series of stacked sills, or laccoliths that were subsequently folded and eroded to produce the nested map pattern of major units (Bartley et al., 2006; Coleman et al., 2012). Individual sills freeze before younger sheets or sills are intruded, and so deeper source regions are responsible for observed compositional/textural heterogeneity in a closed system. In this model, outward-younging patterns of schlieren-bound magmatic structures represent an artifact of the folding of individual sills, assuming that the structures were initially horizontal (layer-parallel) and upward younging, as suggested by Bartley et al. (2018). The model also predicts that schlieren-bound structure dips should systematically shift from the center of the TIC to the margin, with initially vertical and upward-younging orientations in the center, towards rotated, horizontal, and outward-younging orientations at the margins. This model cannot explain why schlieren-bound structures are clustered. We have found no evidence for systematically changing structural dip across transects of the TIC, in any of the mapped structures. Further, magmatic fabrics show no evidence for being axial planar to a TIC-scale fold, nor is there a systematic change in dip, as magmatic lineations are largely sub-vertical throughout the TIC. The observation that fabrics can overprint unit contacts (e.g., Žák et al., 2007), and that mixing occurred between units (Chambers et al., 2020) precludes the idea that older units were completely solidified before emplacement of new batches.

A similar model proposes that the pulses are vertical dikes instead of sills, which also freeze before subsequent dikes are emplaced (Bartley et al., 2018). In this case, older dikes are displaced outwards by younger, producing a strict temporal sequence. This model is also problematic for the TIC, as it shares several of the same issues as the sill model above, with some additions: Firstly, sheeted contacts are restricted to locally mapped zones (Paterson et al., 2008; Žák et al., 2009;

Memeti et al., 2010). Secondly, the schlieren-bound structures have a wide range of types, and do not show any preferential orientations that would be consistent with flow along dike walls. The observations of magmatic deformation, erosion, and flow of crystals with mixed mineral populations is also inconsistent with a dike model (e.g., Solgadi and Sawyer, 2008).

A third model suggests that the TIC grew initially by sheets, which amalgamated into larger magma bodies and facilitated the emplacement of diapirs (e.g., Memeti et al., 2010; Paterson et al., 2011). In this model, schlieren-bound structures form from magmatic flow as a response, at the regional scale, to the intrusion of new magma batches. Older and younger batches can interact within the magma chamber to generate emplacement-level, open system magma mixing. This model explains observations of internal contacts that vary along and across strike as regions of differential magmatic erosion and recycling, and the regional extents of multiple magmatic fabrics as a record of regionally extensive melt-present regions (Paterson et al., 2016). Below we discuss our schlieren-bound structure results in the context of this model:

Return flow model

Outward younging directions in the Cathedral Peak unit are consistent with a model where new pulses, intruded at the center of the complex, drives displacement of the mush and causes it to flow outwards and downwards (see also Bateman, 1992; Paterson et al., 2016; Wiebe et al., 2017; **Figure 12A**). Physical gradients (e.g., flow velocity, viscosity, density) and thermal gradients help drive convection of the mush, as well as define the regions in which structure formation and preservation are favorable (**Figure 12A**). At the margins of the mush, cooler, more crystalline portions sink, and flow downwards. The intruding hotter pulses re-heat the mush to create melt-rich regions, as well as draw lower levels of the mush pile to higher levels of the chamber (**Figure 12A**). This region of mobile mush is referred to as the mixing bowl, after Bergantz et al. (2015, 2017). We propose that movement of the mush occurred within a vertically extensive magma mush body, accommodated by downward flow that creates space for new magma batches (**Figure 12A**). This is supported by sub-vertical external and internal contacts, a steep magmatic lineation, moderate to steeply dipping schlieren and vertical tube axes (Oliver, 1977; Paterson, 2009; Paterson et al., 2011). The return flow model implies that towards the base of the magma body, the structures should start to young inwards, influenced by the downward flow of the mush and the intruding pulses (**Figure 12A**). Inward younging structural patterns are reported in other plutons in the central Sierra Nevada (e.g., Alasino et al., 2019), however, this model would optimally be tested in a tilted pluton, where multiple levels are exposed.

Alternative models

There are likely multiple causes of younging, or migration directions measured in schlieren-bound structures. Flow in magma sheets related to cracking of the magma mush is one mechanism that could create a broader-scale younging direction (Paterson et al., 2008; Žák et al., 2009). This process is likely to have dominated where sheeted zones are documented.

Other scenarios that could cause structures to migrate and young outwards, such as regional extension, a thin, laterally spreading mush, or a static, inwardly cooling mush, are not supported by our datasets. In the former, the regional dextral-transpressive tectonic setting recorded in the surrounding host rock, as well as rapid crustal thickening, regional inward magmatic focusing patterns, and steep magmatic lineations in the TIC, all preclude any extensional emplacement model (e.g., Žák and Paterson, 2005; Cao et al., 2015, 2016b; Ardill et al., 2018; Hartman et al., 2018). We note that extension could occur locally in the return flow model. In a static, cooling mush, where cooling at the margins outpaces intrusion by new pulses, the structures are predicted to young inwards, not outwards, due to collapse of the newly solidifying mush at the margins.

Significance of return flow: mapping mixing bowls

As the outward younging pattern is found in each of the TIC units, this process occurred repeatedly over the 10 m.y. lifespan of the TIC. In addition, the outward-younging structures across four mapped domains of the CP unit are consistent with the possibility that it was as a single large mixing bowl (see below section "Implications for Emplacement Models and the Minimum Sizes of Magma Chambers"; **Figure 12**). In contrast, inward-younging structures in the eastern porphyritic Half Dome unit observed in the Lyell Canyon area represent an exception to the outward-younging pattern found elsewhere in the CP and pHD. Although the dataset is limited in size, one possibility is that the pHD mixing bowls were smaller than the CP mixing bowl, and that the Lyell Canyon structures and the Tenaya Peak structures record events from two different pHD mixing bowls. Although much of the pHD unit has been removed by the CP, mapping larger areas containing pHD structures can test this hypothesis.

External Processes Are Not a Significant Control on Schlieren-Bound Structure Orientation

Tectonism has been proposed to cause magma mush instability on the timescales of seconds to minutes (e.g., earthquakes; Davis et al., 2007), and at the m.y. time-scale can form fabrics and extract melts (e.g, Paterson et al., 1998; Garibaldi et al., 2018; Bachmann and Huber, 2019). Regional tectonism during emplacement of the TIC was dextral transpressive, with metavolcanic and metasedimentary host-rock fabric orientations consistent with the regional NW–SE magmatic foliation found in TIC domains (e.g., Žák et al., 2007; Cao et al., 2015; Hartman et al., 2018). At the scale of the intrusive complex, regional E–W magmatic foliations and vertical lineation are pervasive. Schlieren do not show a clear angular relationship to either regional foliation orientations within any of the mapped domains. This supports the conclusion that strain caused by local magmatic flow, forming schlieren-bound structures, dominated over regional-scale strains that formed fabrics, and suggest this is due to higher strain rates in structures formed by magmatic flow (Žák et al., 2007; Paterson et al., 2008). Magmatic fabrics are time-transgressive throughout the 10 m.y. lifespan of the TIC, indicating that the regional strain fields were long-lived

(Žák et al., 2007). Schlieren-bound structures, found in all TIC units, are thus also a time transgressive record of internal magmatic processes.

Timing of Schlieren-Bound Structure Formation

Examination of the field and geochemical datasets indicate that schlieren-bound structure formation occurred in a crystal-rich mush, where crystal frameworks were important to form, deform, and also preserve schlieren-bound structures. In the broader context of the TIC, schlieren-bound structures formed pre, syn, and post formation of major unit contacts, and after crystallization of minerals contained in abundance in the schlieren-bound structure (e.g., zircon; Memeti et al., 2014; hornblende, biotite). Schlieren formation was widespread, occurring repeatedly over the 10 m.y. lifespan of the TIC.

Magmatic erosion, re-deposition and deformation occurred in a magma that had a yield strength (see also Hodge et al., 2012). Since these processes occurred in quick succession at a single outcrop, it suggests that there were complex interactions between crystallinity and effective viscosity, particle-particle interactions, pore-pressure, and crystal lubrication effects (Weinberg et al., 2001; Paterson, 2009; Bergantz et al., 2017; Carrara et al., 2019). Discordance between local schlieren-defined fabric and the regional fabrics and the overprinting relationships within felsic components indicates that the strain fields forming regional fabrics and local schlieren fabrics were active at the same time, but at different rates. The schlieren fabric likely formed at faster strain rates than the regional fabrics, producing discordance. When the rate of magmatic flow and deposition slowed, the regional fabric was able to re-orient minerals in melt-rich felsic components, producing the overprinting relationships (e.g., Paterson et al., 2008).

Mineralogically, quartz abundance varies little in abundance between schlieren and host samples, which, together with petrographic textures, suggests that it was the main mineral to crystallize late in the magmatic history (after schlieren formation) from trapped, interstitial melts that were evolved. The bulk rock compositions and equilibrium melt compositions suggest that schlieren formed from an evolved magma mush, containing 65–79 wt.% SiO_2.

Implications for Emplacement Models and the Minimum Sizes of Magma Chambers

The TIC is a composite magmatic complex, containing gabbro to leucogranite with granodiorite and granite the most abundant rock types. The complex spans a 10 m.y. zircon crystallization history, with four major units bounded by sharp to gradational contacts that internally range from homogenous (at outcrop scale) plutons to sheeted zones (Žák et al., 2009; Memeti et al., 2010). To explain these observations, different incremental emplacement models have been proposed, and are outlined above (section "Incremental growth models for the TIC"). Regionally extensive magmatic fabrics (e.g., **Figure 1A**), recycling of older units into younger, compositional evidence for widespread magma mixing and recycling in bulk rocks and in minerals, geochronologic studies, and thermal models all suggest that TIC magma chambers (interconnected melt regions) in the Cathedral Peak unit, and in each of the older units, were volumetrically extensive (∼1000 km^3) and long-lived (up to 1.5 m.y.) (e.g., Matzel et al., 2005, 2006; Žák et al., 2007; Solgadi and Sawyer, 2008; Memeti et al., 2010, 2014; Paterson et al., 2011, 2016; Barnes et al., 2016). Together with the above-listed evidence, outcrop-scale flow features, domain-scale clustering and regional-scale outward-younging schlieren-bound structure patterns presented here require a magma emplacement model where incrementally emplaced new magma pulses can interact with older pulses dynamically by magmatic flow, transferring mass and energy to the larger-scale interconnected-melt region, or magma mush. This has been proposed to occur by the interaction of dike- or diapir-shaped pulses that amalgamate in time and space to form long-lived, dynamic magma bodies (e.g., Miller and Paterson, 2001; Memeti et al., 2010; Cao et al., 2016a).

The multi-scale observations of magmatic structures also allow us to place additional constraints on the minimum sizes of likely magma chambers that existed in the Cathedral Peak unit. As the younging patterns in each study area of the CP unit are all consistently outward (**Figure 12A**), then the southern portion of the CP unit, encompassing all four domains, represents the minimum size of one mixing bowl, or magma chamber, in the return flow model described earlier. This results in an area of about 150–175 km^2, or a volume between 750 and 1750 km^3 (using the vertical extents estimated by Karlstrom et al., 2017). The zircon isochron map of Memeti et al. (2014) suggests that this mixing bowl formed across ∼1.5 m.y. At shorter timescales, the domainal fluidized zones could each represent their own active magma chambers, capable of magma mixing, mingling and fractionation. Their sizes, between approximately 0.5–2 km^2 in area (vertical extents unknown), suggest they could be locally important for producing structural and compositional diversity in plutons, but are unlikely to explain the outcrop-scale to map-scale homogeneous appearance of the well-mixed CP unit.

Implications for the Behavior of Magma Mush Systems

The above observations indicate crystal-rich mushes, even in upper crustal magma chambers, can be highly dynamic environments. Numerical modeling of mushy plutonic systems has demonstrated the potential for complex crystal-melt and crystal-crystal interactions that schlieren may represent just one (visible) example of (e.g., Bergantz et al., 2017). The "mixing bowl" model of Bergantz et al. (2015) and Schleicher et al. (2016) displays a number of features that match field-based structural observations in the TIC. These include magmatic faulting, slumping, and folding of schlieren, and erosion of earlier formed layers. In addition, the spatial heterogeneity of the deforming mush, with locally "active" and "static" areas in the model is consistent with our interpretation of the spatial clustering of magmatic structures. Finally, the outward younging patterns predicted by the upper parts of the model concur with our field dataset. The widespread distribution of the

structures across the TIC suggest that dynamic hypersolidus conditions, as exemplified by the "mixing bowl" model, existed in different units and areas of the TIC repeatedly throughout its entire ∼10 m.y. lifespan. The schlieren-bound structures represent sites of compositional differentiation occurring at the emplacement level, and sites of local magmatic recycling (e.g., Paterson et al., 2016).

No clear relationship yet exists between the orientation of regional magmatic fabrics (Types 3–5) and schlieren-bound structure orientations (Type 1). This suggests that internal magmatic processes dominate in the formation and orientation of schlieren-bound structures. Garibaldi et al. (2018) proposed that magmatic fabrics and magmatic structures (e.g., miarolitic cavities) in the Huemul pluton record evidence for a crystal-rich mush mobilizing interstitial rhyolitic melts by tectonic filter pressing. Other studies have also considered tectonism as a mechanism to mobilize crystal-mushes and re-orient earlier-formed magmatic structures, including fabrics (e.g., Žák and Paterson, 2010; Alasino et al., 2019). To reconcile these findings in the context of schlieren-bound structures in the TIC, we suggest that the strain rates producing regional fabrics (of which some may be tectonic) are slower, but longer-lived than strain rates producing local schlieren-bound structure fabrics.

Despite large variations in composition, size and emplacement depth, schlieren-bound structures are ubiquitous in plutons, although less well developed in many. Some notable localities include the Tavares pluton, Brazil (Weinberg et al., 2001), the Skaergaard intrusion, Greenland (Wager and Brown, 1968; Holness et al., 2017), and the Coastal Maine batholith (Wiebe and Collins, 1998), which, in addition to the TIC, contain a high abundance and diversity of schlieren-bound structures. It suggests that the physical flow-sorting mechanisms proposed here are an intrinsic feature of magma mushes, and are not primarily dependent on magma compositions, pressure, or temperature.

Future Directions

Further quantifying the physical and chemical magma properties at the time schlieren-bound structures formed is an important step in reconstructing magma mush dynamics. In addition, exploring why some plutons are rich in schlieren-bound structures, while others are poorer, may provide definition on the most important magma properties or mechanisms to form schlieren-bound structures. Ongoing and future studies must explore these themes at multiple scales.

At the mineral scale, this includes determining which minerals grew in-situ within a structure, and which were physically sorted into schlieren. Studies have proposed that some structures may represent volatile pathways (Paterson, 2009; Clarke et al., 2013). The role of any exsolved fluid or gas that aids or impedes the formation and preservation of structures remains unclear and would benefit from quantitative structural and compositional analysis. Recent studies indicate that magmatic deformation of mushes leaves a microstructural signature (Holness et al., 2017; Holness, 2018), which could be illuminating in terms of schlieren formation. For example, do the minerals in schlieren show evidence of crystal-plastic deformation indicating that they were compacted (e.g., Holness, 2018), or is crystal-repacking a suitable alternative (Bachmann and Huber, 2019)? What was the porosity of the schlieren cumulate when melts were extracted, and did they experience secondary grain-boundary adjustments (e.g., Holness, 2018)? Is there a microstructural record of regional-scale deformation in schlieren-bound structures, and can we quantify the strain rates forming schlieren fabrics and regional fabrics?

At the outcrop scale, the diversity of structures in the TIC suggests that different magmatic conditions and/or mechanisms operate within a magma mush at any one time or place. Future directions could investigate the mechanical and fluid-dynamical relationships between different types of structures, as well as quantitatively considering the role of the surrounding magma and its physical and chemical properties in determining which type of structure forms.

Across the entire TIC, constraining the different mechanisms of fabric formation is needed to place a regional context to the internal magmatic schlieren-forming process. Additional statistical analysis of the regional compilation could resolve why schlieren-bound structures are clustered at this scale, and whether certain structures dominate certain clusters (e.g., by comparing the structures that are the target structures nearest neighbor), and resolve the distinction between the distribution of compositionally defined magmatic structures like K-feldspar megacryst structures, and schlieren-bound structures.

CONCLUSION

Schlieren layers are locally sourced from nearby magmas and provide evidence for local magma flow, mineral-melt separation, and compositional differentiation. Although the diversity of schlieren-bound structures in the TIC suggests there are multiple mechanisms of formation, schlieren are a common link between them. Thus, schlieren-forming processes such as hydrogranular flow-sorting, melt migration and crystal accumulation are considered both widespread and significant in magma mush systems.

Analysis of magmatic structure orientations from outcrop, domainal, and regional scales suggests that magma mushes are highly dynamic environments across multiple length scales, and field observations are remarkably similar to hydrogranular behavior described by the "mixing bowl" models (Bergantz et al., 2015, 2017; Schleicher et al., 2016). Domainal clustering of structures indicates that mush fluidization is spatially and temporally heterogeneous.

Outward-younging patterns are likely driven by regional-scale convection and return flow of the magma mush, driven by the intrusion of new pulses at the center of the magma mush chamber. This pattern, recorded in all types of schlieren-bound structures studied here, can provide clues to the extent of magma mixing bowls, and the sizes of active domains within them. Schlieren-bound structure orientations are sensitive to some boundary types, such as local rheological boundaries and nearby internal contacts, but not to regional stress fields. Thus,

the interplay of internal and external forces operating within magma chambers remains an exciting avenue of future research.

DATA AVAILABILITY STATEMENT

The datasets generated for this study are available on request to the corresponding author.

AUTHOR CONTRIBUTIONS

KA and SP designed the research. KA compiled data and wrote the first draft of the manuscript. KA, SP, JS, and PA analyzed the data. KA, SP, and PA wrote sections of the manuscript. KA, JS, JK, and SC drafted the figures. All authors performed the research in the field and lab to collect the data. All authors have contributed to the article and approved all submitted versions.

FUNDING

We acknowledge support from National Science Foundation grants EAR-1624847 and EAR-1019636 awarded to SP, and a GSA Graduate Student Research Grant Lipman Research Award to KA that funded valuable fieldwork and bulk-rock geochemical analyses.

ACKNOWLEDGMENTS

We thank V. Memeti for providing samples of the KC schlieren and host and for providing field data from the Tuolumne Intrusive Complex with contributions from R. Miller and J. Žák. We also thank G. Aldiss, L. Ardill, M. Cuevas, J. McColl, K. O' Rourke, and L. Teruya for assistance in fieldwork, and Yosemite National Park rangers for their continued support. D. De La Cruz is thanked for assistance in organizing the TIC field data. We thank C. Barnes for the helpful comments during manuscript preparation. We also thank S. Erdmann and G. Bergantz for their constructive reviews that improved the manuscript, as well as G. Shellnutt for editorial handling.

SUPPLEMENTARY MATERIAL

The Supplementary Material for this article can be found online at: https://www.frontiersin.org/articles/10.3389/feart.2020.00190/full#supplementary-material

REFERENCES

Ague, J. J., and Brimhall, G. H. (1988). Magmatic arc asymmetry and distribution of anomalous plutonic belts in the batholiths of California: effects of assimilation, crustal thickness, and depth of crystallization. *Geol. Soc. Am. Bull.* 100, 912–927. doi: 10.1130/0016-76061988100<0912:MAAADO<2.3.CO;2

Alasino, P. H., Ardill, K., Stanback, J., Paterson, S. R., Galindo, C., and Leopold, M. (2019). Magmatically folded and faulted schlieren zones formed by magma avalanching in the Sonora Pass Intrusive Suite. Sierra Nevada, California. *Geosphere* 15, 1677–1702. doi: 10.1130/GES02070.1

Albarède, F. (1996). *Introduction to Geochemical Modeling*. Cambridge: Cambridge University Press.

Aldiss, G. P. F. B. (2017). *The geology of Iron Mountain and Tenaya Peak areas, Sierra National Forest and Yosemite National Park, Sierra Nevada, California*. Durham: Durham University.

Annen, C., Blundy, J. D., Leuthold, J., and Sparks, R. S. J. (2015). Construction and evolution of igneous bodies: towards an integrated perspective of crustal magmatism. *Lithos* 230, 206–221. doi: 10.1016/j.lithos.2015.05.008

Ardill, K., Paterson, S., and Memeti, V. (2018). Spatiotemporal magmatic focusing in upper-mid crustal plutons of the Sierra Nevada arc. *Earth Planet. Sci. Lett.* 498, 88–100. doi: 10.1016/j.epsl.2018.06.023

Bachmann, O., and Bergantz, G. W. (2004). On the origin of crystal-poor rhyolites: extracted from batholithic crystal mushes. *J. Petrol.* 45, 1565–1582. doi: 10.1093/petrology/egh019

Bachmann, O., and Bergantz, G. W. (2006). Gas percolation in upper-crustal silicic crystal mushes as a mechanism for upward heat advection and rejuvenation of near-solidus magma bodies. *J. Volcanol. Geother. Res.* 149, 85–102. doi: 10.1016/j.jvolgeores.2005.06.002

Bachmann, O., and Huber, C. (2016). Silicic magma reservoirs in the Earth's crust. *Am. Mineral.* 101, 2377–2404. doi: 10.2138/am-2016-5675

Bachmann, O., and Huber, C. (2019). The inner workings of crustal distillation columns; the physical mechanisms and rates controlling phase separation in silicic magma reservoirs. *J. Petrol.* 60, 3–18. doi: 10.1093/petrology/egy103

Barbey, P. (2009). Layering and schlieren in granitoids: a record of interactions between magma emplacement, crystallization and deformation in growing plutons (The André Dumont medallist lecture). *Geol. Bel.* 12, 109–133.

Barbey, P., Gasquet, D., Pin, C., and Bourgeix, A. L. (2008). Igneous banding, schlieren and mafic enclaves in calc-alkaline granites: the Budduso pluton (Sardinia). *Lithos* 104, 147–163. doi: 10.1016/j.lithos.2007.12.004

Barnes, C. G., Memeti, V., and Coint, N. (2016). Deciphering magmatic processes in calc-alkaline plutons using trace element zoning in hornblende. *Am. Mineral.* 101, 328–342. doi: 10.2138/am-2016-5383

Barnes, C. G., Werts, K., Memeti, V., and Ardill, K. (2020). Most granitoid rocks are cumulates: deductions from hornblende compositions and zircon saturation. *J. Petrol.* 60, 2227–2240. doi: 10.1093/petrology/egaa008

Barrière, M. (1981). On curved laminae, graded layers, convection currents and dynamic crystal sorting in the Ploumanac'h (Brittany) subalkaline granite. *Contribut. Mineral. Petrol.* 77, 214–224. doi: 10.1007/BF00373537

Bartley, J. M., Coleman, D. S., and Glazner, A. F. (2006). Incremental pluton emplacement by magmatic crack-seal. *Earth Environ. Sci. Trans. R. Soc. Edinburgh* 97, 383–396. doi: 10.1017/S0263593300001528

Bartley, J. M., Glazner, A. F., and Coleman, D. S. (2018). Dike intrusion and deformation during growth of the Half Dome pluton, Yosemite National Park, California. *Geosphere* 14, 1283–1297. doi: 10.1130/GES01458.1

Bartley, J. M., Glazner, A. F., Coleman, D. S., and Law, B. (2013). Geometry and emplacement of ladder dikes in the Cathedral Peak granodiorite, Yosemite National Park. *Geol. Soc. Am. Abst. Progr.* 45:13.

Bartley, J. M., Glazner, A. F., and Law, B. (2019). Ladder structures in the Cathedral Peak granodiorite, Yosemite: two-phase flow in fingered dikes? *Geol. Soc. Am. Abst. Progr.* 51, doi: 10.1130/abs/2019AM-338571

Bateman, P. C. (1992). "Plutonism in the central part of the Sierra Nevada batholith, California," in *USGS Professional Paper 1483*, (Reston, VI: USGS), doi: 10.3133/pp1483

Bateman, P. C., and Chappell, B. W. (1979). Crystallization, fractionation, and solidification of the Tuolumne intrusive series, Yosemite National Park, California. *Geol. Soc. Am. Bull.* 90, 465–482.

Bateman, P. C., Chappell, B. W., Kistler, R. W., Peck, D. L., and Busacca, A. (1988). Tuolumne Meadows quadrangle, California - analytic data. *US Geol. Surv. Bull.* 1819:43. doi: 10.3133/b1819

Bateman, P. C., Kistler, R. W., Peck, D. L., and Busacca, A. (1983). *Geologic map of the Tuolumne Meadows quadrangle, Yosemite National Park, California (No. 1570)*. California: Yosemite National Park, doi: 10.3133/gq1570

Beard, J. S. (2008). Crystal–melt separation and the development of isotopic heterogeneities in hybrid magmas. *J. Petrol.* 49, 1027–1041. doi: 10.1093/petrology/egn015

Beard, J. S., Ragland, P. C., and Crawford, M. L. (2005). Reactive bulk assimilation: a model for crust-mantle mixing in silicic magmas. *Geology* 33, 681–684. doi: 10.1130/G21470AR.1

Bergantz, G. W. (2000). On the dynamics of magma mixing by reintrusion: implications for pluton assembly processes. *J. Struct. Geol.* 22, 1297–1309. doi: 10.1016/S0191-8141(00)00053-5

Bergantz, G. W., and Ni, J. (1999). A numerical study of sedimentation by dripping instabilities in viscous fluids. *Int. J. Multiphase Flow* 25, 307–320. doi: 10.1016/S0301-9322(98)00050-0

Bergantz, G. W., Schleicher, J. M., and Burgisser, A. (2015). Open-system dynamics and mixing in magma mushes. *Nat. Geosci.* 8, 793–796. doi: 10.1038/ngeo2534

Bergantz, G. W., Schleicher, J. M., and Burgisser, A. (2017). On the kinematics and dynamics of crystal-rich systems. *J. Geophys. Res.* 122, 6131–6159. doi: 10.1002/2017JB014218

Bhattacharji, S., and Smith, C. H. (1964). Flowage differentiation. *Science* 145, 150–153. doi: 10.1126/science.145.3628.150

Blum, J. D., and Erel, Y. (1997). Rb-Sr isotope systematics of a granitic soil chronosequence: the importance of biotite weathering. *Geochim. Cosmochim. Acta* 61, 3193–3204. doi: 10.1016/S0016-7037(97)00148-8

Boudreau, A. (2011). The evolution of texture and layering in layered intrusions. *Int. Geol. Rev.* 53, 330–353. doi: 10.1080/00206814.2010.496163

Bracciali, L., Paterson, S. R., Memeti, V., Rocchi, S., Matzel, J., and Mundil, R. (2008). "Build-up of the Tuolumne Batholith, California: the Johnson Granite Porphyry," in *Proceedings of the LASI III Conference Abstracts*, Malaysia, 17–18.

Burgess, S. D., and Miller, J. S. (2008). Construction, solidification and internal differentiation of a large felsic arc pluton: Cathedral Peak granodiorite, Sierra Nevada Batholith. *Geol. Soc. Lond. Spec. Publ.* 304, 203–233. doi: 10.1144/SP304.11

Burgisser, A., and Bergantz, G. W. (2011). A rapid mechanism to remobilize and homogenize highly crystalline magma bodies. *Nature* 471, 212–215. doi: 10.1038/nature09799

Calkins, F. C. (1930). "The granitic rocks of the Yosemite region, in Matthes," in *Geologic history of the Yosemite Valley: USGS Professional Paper 160*, ed. E. Francois (Reston, VI: USGS), 120–129. doi: 10.3133/pp160

Cao, W., Kaus, B. J., and Paterson, S. (2016a). Intrusion of granitic magma into the continental crust facilitated by magma pulsing and dike-diapir interactions: numerical simulations. *Tectonics* 35, 1575–1594. doi: 10.1002/2015TC004076

Cao, W., Paterson, S., Saleeby, J., and Zalunardo, S. (2016b). Bulk arc strain, crustal thickening, magma emplacement, and mass balances in the Mesozoic Sierra Nevada arc. *J. Struct. Geol.* 84, 14–30. doi: 10.1016/j.jsg.2015.11.002

Cao, W., Paterson, S., Memeti, V., Mundil, R., Anderson, J. L., and Schmidt, K. (2015). Tracking paleodeformation fields in the Mesozoic central Sierra Nevada arc: implications for intra-arc cyclic deformation and arc tempos. *Lithosphere* 7, 296–320. doi: 10.1130/L389.1

Cardozo, N., and Allmendinger, R. W. (2013). Spherical projections with OSXStereonet. *Comput. Geosci.* 51, 193–205. doi: 10.1016/j.cageo.2012.07.021

Carrara, A., Burgisser, A., and Bergantz, G. W. (2019). Lubrication effects on magmatic mush dynamics. *J. Volcanol. Geother. Res.* 380, 19–30. doi: 10.1016/j.jvolgeores.2019.05.008

Cashman, K. V., Sparks, R. S. J., and Blundy, J. D. (2017). Vertically extensive and unstable magmatic systems: a unified view of igneous processes. *Science* 355:eaag3055. doi: 10.1126/science.aag3055

Chambers, M., Memeti, V., Eddy, M. P., and Schoene, B. (2020). Half a million years of magmatic history recorded in a K-feldspar megacryst of the Tuolumne Intrusive Complex. California, USA. *Geology* 48, 400–404. doi: 10.1130/G46873.1

Chesterman, C. W. (1975). Geology of the Matterhorn Peak 15-minute Quadrangle, Mono and Tuolumne Counties, California. *California Division of Mines and Geology*, Map Sheet 22, scale 1:48,000.

Clarke, D. B. (2003). *Exploded Xenoliths, layered Granodiorites, and Chaotic Schlieren associated with the eastern contact of the South Mountain Batholith*. Wolfville: Atlantic Geoscience Society.

Clarke, D. B., and Clarke, G. K. C. (1998). Layered granodiorites at Chebutco Head, South Mountain batholith, Nova Scotia. *J. Struct. Geol.* 20, 1305–1324. doi: 10.1016/s0191-8141(98)00067-4

Clarke, D. B., Grujic, D., McCuish, K. L., Sykes, J. C., and Tweedale, F. M. (2013). Ring schlieren: description and interpretation of field relations in the Halifax Pluton, South Mountain Batholith, Nova Scotia. *J. Struct. Geol.* 51, 193–205. doi: 10.1016/j.jsg.2013.01.009

Clemens, J. D., Stevens, G., le Roux, S., and Wallis, G. L. (2020). Mafic schlieren, crystal accumulation and differentiation in granitic magmas: an integrated case study. *Contrib. Mineral Petrol.* 175:51. doi: 10.1007/s00410-020-01689-x

Cloos, E. (1936). Der Sierra Nevada Pluton in Californien. Neues Jahrbuch für Mineralogie. *Geol. Paleontol.* 76, 355–450.

Coats, R. R. (1936). Primary banding in basic plutonic rocks. *J. Geol.* 44, 407–419. doi: 10.1086/624432

Coleman, D. S., Bartley, J. M., Glazner, A. F., and Pardue, M. J. (2012). Is chemical zonation in plutonic rocks driven by changes in source magma composition or shallow-crustal differentiation? *Geosphere* 8, 1568–1587. doi: 10.1130/GES00798.1

Coleman, D. S., Gray, W., and Glazner, A. F. (2004). Rethinking the emplacement and evolution of zoned plutons: geochronologic evidence for incremental assembly of the Tuolumne Intrusive Suite. California. *Geology* 32, 433–436. doi: 10.1130/G20220.1

Cruden, A. R., McCaffrey, K. J. W., and Bunger, A. P. (2017). "Geometric Scaling of Tabular Igneous Intrusions: Implications for Emplacement and Growth," in *Physical Geology of Shallow Magmatic Systems. Advances in Volcanology (An Official Book Series of the International Association of Volcanology and Chemistry of the Earth's Interior)*, eds C. Breitkreuz and S. Rocchi (Cham: Springer).

Davis, M., Koenders, M. A., and Petford, N. (2007). Vibro-agitation of chambered magma. *J. Volcanol. Geother. Res.* 167, 24–36. doi: 10.1016/j.jvolgeores.2007.07.012

Degruyter, W., Parmigiani, A., Huber, C., and Bachmann, O. (2019). How do volatiles escape their shallow magmatic hearth?. *Philos. Trans. R. Soc. A* 377:20180017. doi: 10.1098/rsta.2018.0017

Dietl, C., De Wall, H., and Finger, F. (2010). Tube-like schlieren structures in the Fürstenstein Intrusive Complex (Bavarian Forest, Germany): evidence for melt segregation and magma flow at intraplutonic contacts. *Lithos* 116, 321–339. doi: 10.1016/j.lithos.2009.11.011

Economos, R. C., Memeti, V., Paterson, S. R., Miller, J. S., Erdmann, S., and Žák, J. (2009). Causes of compositional diversity in a lobe of the Half Dome granodiorite, Tuolumne Batholith, Central Sierra Nevada, California. *Earth Environ. Sci. Trans. R. Soc. Edinburgh* 100, 173–183. doi: 10.1017/S1755691009016065

Estep, J., and Dufek, J. (2012). Substrate effects from force chain dynamics in dense granular flows. *J. Geophys. Res.* 117:F01028. doi: 10.1029/2011JF002125

Farner, M. J., Lee, C. T. A., and Mikus, M. L. (2018). Geochemical signals of mafic-felsic mixing: case study of enclave swarms in the Bernasconi Hills pluton, California. *GSA Bull.* 130, 649–660. doi: 10.1130/B31760.1

Fox, L. K., and Miller, D. M. (1990). "Jurassic granitoids and related rocks of the southern Bristol Mountains, southern Providence Moutnains, and Colton Hills, Mojave Desert, California," in *The Nature and Origin of Cordilleran Magmatism*, Vol. 174, ed. J. L. Anderson (Washington, DC: GSA Memoirs), 111. doi: 10.1130/MEM174-p111

Garibaldi, N., Tikoff, B., Schaen, A. J., and Singer, B. S. (2018). Interpreting granitic fabrics in terms of rhyolitic melt segregation, accumulation, and escape via tectonic filter pressing in the Huemul pluton. Chile. *J. Geophys. Res.* 123, 8548–8567. doi: 10.1029/2018JB016282

Glazner, A. F. (2014). Magmatic life at low Reynolds number. *Geology* 42, 935–938. doi: 10.1130/G36078.1

Glazner, A. F., Bartley, J. M., Law, B., and Coleman, D. S. (2012). Ladder dikes, crazy geochemistry, and liquid immiscibility (?) in otherwise sane granites. *Geol. Soc. Am. Abst. Progr.* 44:21.

Graham, J. (2012). *Yosemite National Park: Geologic resources inventory report. Natural Resource Report NPS/NRSS/GRD/NRR—2012/560*. Fort Collins, CL: National Park Service.

Gray, W., Glazner, A. F., Coleman, D. S., and Bartley, J. M. (2008). Long-term geochemical variability of the Late Cretaceous Tuolumne intrusive suite, central Sierra Nevada, California. *Geol. Soc. Lond. Spec. Publ.* 304, 183–201. doi: 10.1144/SP304.10

Griffiths, R. W. (1986). Thermals in extremely viscous fluids, including the effects of temperature-dependent viscosity. *J. Fluid Mech.* 166, 115–138. doi: 10.1017/S002211208600006X

Hartman, S. M., Paterson, S. R., Holk, G. J., and Kirkpatrick, J. D. (2018). Structural and hydrothermal evolution of a strike-slip shear zone during a ductile-brittle transition, Sierra Nevada, CA. *J. Struct. Geol.* 113, 134–154. doi: 10.1016/j.jsg.2018.05.010

Hodge, K. F., Carazzo, G., Montague, X., and Jellinek, A. M. (2012). Magmatic structures in the Tuolumne Intrusive Suite, California: a new model for the formation and deformation of ladder dikes. *Contribut. Mineral. Petrol.* 164, 587–600. doi: 10.1007/s00410-012-0760-6

Holness, M. B. (2018). Melt segregation from silicic crystal mushes: a critical appraisal of possible mechanisms and their microstructural record. *Contribut. Mineral. Petrol.* 173:48. doi: 10.1007/s00410-018-1465-2

Holness, M. B., Vukmanovic, Z., and Mariani, E. (2017). Assessing the role of compaction in the formation of adcumulates: a microstructural perspective. *J. Petrol.* 58, 643–673. doi: 10.1093/petrology/egx037

Hurai, V., Simon, K., Wiechert, U., Hoefs, J., Konečný, P., Huraiová, M., et al. (1998). Immiscible separation of metalliferous Fe/Ti-oxide melts from fractionating alkali basalt: P-T-f O2 conditions and two-liquid elemental partitioning. *Contribut. Mineral. Petrol.* 133, 12–29. doi: 10.1007/s004100050433

Irvine, T. N., Andersen, J. C. Ø, and Brooks, C. K. (1998). Included blocks (and blocks within blocks) in the Skaergaard intrusion: geologic relations and the origins of rhythmic modally graded layers. *Geol. Soc. Am. Bull.* 110, 1398–1447. doi: 10.1130/0016-76061998110<1398:IBABWB<2.3.CO;2

Jackson, M. D., Blundy, J., and Sparks, R. S. J. (2018). Chemical differentiation, cold storage and remobilization of magma in the Earth's crust. *Nature* 564, 405–409. doi: 10.1038/s41586-018-0746-2

Karlstrom, L., Paterson, S. R., and Jellinek, A. M. (2017). A reverse energy cascade for crustal magma transport. *Nat. Geosci.* 10, 604–608. doi: 10.1038/ngeo2982

Kawabata, H., Nishiura, D., Sakaguchi, H., and Tatsumi, Y. (2013). Self-organized domain microstructures in a plate-like particle suspension subjected to rapid simple shear. *Rheol. Acta* 52, 1–21. doi: 10.1007/s00397-012-0657-3

Kelemen, P. B., Whitehead, J. A., Aharonov, E., and Jordahl, K. A. (1995). Experiments on flow focusing in soluble porous media, with applications to melt extraction from the mantle. *J. Geophys. Res.* 100, 475–496. doi: 10.1029/94JB02544

Kendall, C., Sklash, M. G., and Bullen, T. D. (1995). "Isotope tracers of water and solute sources in catchments," in *Solute Modelling in Catchment Systems*, Ed. S. Trudgill (New York, NY: John Wiley and Sons), 261–303.

Kistler, R. W., Chappell, B. W., Peck, D. L., and Bateman, P. C. (1986). Isotopic variation in the Tuolumne intrusive suite, central Sierra Nevada, California. *Contribut. Mineral. Petrol.* 94, 205–220. doi: 10.1007/BF00592937

Kistler, R. W., and Fleck, R. J. (1994). Field guide for a transect of the central Sierra Nevada. California. *Geochronol. Isotope Geol.* 94, 267. doi: 10.3133/ofr94267

Li, X. C., Zhou, M. F., Yang, Y. H., Zhao, X. F., and Gao, J. F. (2018). Disturbance of the Sm-Nd isotopic system by metasomatic alteration: A case study of fluorapatite from the Sin Quyen Cu-LREE-Au deposit, Vietnam. *Am. Mineral.* 103, 1487–1496. doi: 10.2138/am-2018-6501

Lipman, P. W. (2007). Incremental assembly and prolonged consolidation of Cordilleran magma chambers: Evidence from the Southern Rocky Mountain volcanic field. *Geosphere* 3, 42–70. doi: 10.1130/GES00061.1

Loetterle, J. (2004). *Sedimentary Structures in a Layered Granodiorite: A Window Into Physical Conditions Present During the Development of the Tuolumne Intrusive Suite, Sierra Nevada, California*. MSc thesis, University of Washington, Washington, DC.

Loetterle, J., and Bergantz, G. W. (2003). Sedimentary structures in a layered granodiorite: an example of magma multiphase dynamics from the Tuolumne Intrusive Suite, Sierra Nevada, California. *Geol. Soc. Am. Abst. Progr.* 35:555.

Marsh, B. D. (1981). On the crystallinity, probability of occurrence, and rheology of lava and magma. *Contribut. Mineral. Petrol.* 78, 85–98. doi: 10.1007/BF00371146

Marsh, B. D. (1996). Solidification fronts and magmatic evolution. *Mineral. Magaz.* 60, 5–40. doi: 10.1180/minmag.1996.060.398.03

Matzel, J., Miller, J. S., Mundil, R., and Paterson, S. R. (2006). Zircon saturation and the growth of the Cathedral Peak pluton. CA. *Geochim. Cosmochim. Acta* 70:403. doi: 10.1016/j.gca.2006.06.813

Matzel, J., Mundil, R., Paterson, S., Renne, P., and Nomade, S. (2005). Evaluating pluton growth models using high resolution geochronology: Tuolumne intrusive suite, Sierra Nevada, CA. *Geol. Soc. Am. Abst. Progr.* 37:131.

McBirney, A. R., and Noyes, R. M. (1979). Crystallization and layering of the Skaergaard intrusion. *J. Petrol.* 20, 487–554. doi: 10.1093/petrology/20.3.487

McColl, J. A. R. (2017). *Geological mapping in Yosemite National Park, Sierra Nevada, California: Geologic history of the Mount Dana area and magmatic structure kinematics in the Tuolumne Intrusive Suite*. Durham: Durham University.

McIntire, M. Z., Bergantz, G. W., and Schleicher, J. M. (2019). On the hydrodynamics of crystal clustering. *Philos. Trans. R. Soc. A* 377:20180015. doi: 10.1098/rsta.2018.0015

Memeti, V. (2009). *Growth of the Cretaceous Tuolumne Batholith and Synchronous Regional Tectonics, Sierra Nevada, CA: A Coupled System in a Continental Margin Arc Setting*. Ph.D. thesis, University of Southern California, California.

Memeti, V., Paterson, S., Matzel, J., Mundil, R., and Okaya, D. (2010). Magmatic lobes as "snapshots" of magma chamber growth and evolution in large, composite batholiths: an example from the Tuolumne intrusion. Sierra Nevada, California. *Geol. Soc. Am. Bull.* 122, 1912–1931. doi: 10.1130/B30004.1

Memeti, V., Paterson, S., Mundil, R., Paterson, S. R., and Putirka, K. D. (2014). "Day 4: magmatic evolution of the tuolumne intrusive complex," in *Formation of the Sierra Nevada Batholith: Magmatic and Tectonic Processes and Their Tempos*, Vol. 34, eds V. Memeti, S. R. Paterson, and K. D. Putirka (Boulder, CL: Geological Society of America Field Guide), 43–74. doi: 10.1130/2014.0034(04)

Miller, J. S., Matzel, J. E., Miller, C. F., Burgess, S. D., and Miller, R. B. (2007). Zircon growth and recycling during the assembly of large, composite arc plutons. *J. Volcanol. Geother. Res.* 167, 282–299. doi: 10.1016/j.jvolgeores.2007.04.019

Miller, R. B., and Paterson, S. R. (2001). Construction of mid-crustal sheeted plutons: examples from the North Cascades, Washington. *Geol. Soc. Am. Bull.* 113, 1423–1442. doi: 10.1130/0016-76062001113<1423:COMCSP<2.0.CO;2

Murase, T., McBirney, A. R., and Melson, W. G. (1985). Viscosity of the dome of Mount St. Helens. *J. Volcanol. Geother. Res.* 24, 193–204. doi: 10.1016/0377-0273(85)90033-2

Namur, O., Abily, B., Boudreau, A. E., Blanchette, F., Bush, J. W., Ceuleneer, G., et al. (2015). "Igneous layering in basaltic magma chambers," in *Layered Intrusions*, eds R. Latypov, O. Namur, B. Charlier, and C. Tegner (Dordrecht: Springer), 75–152. doi: 10.1007/978-94-017-9652-1_2

Naney, M. T. (1983). Phase equilibria of rock-forming ferromagnesian silicates in granitic systems. *Am. J. Sci.* 283, 993–1033. doi: 10.2475/ajs.283.10.993

O'Driscoll, B., and VanTongeren, J. A. (2017). Layered intrusions: from petrological paradigms to precious metal repositories. *Elements* 13, 383–389. doi: 10.2138/gselements.13.6.383

Oliver, H. W. (1977). Gravity and magnetic investigations of the Sierra Nevada batholith, California. *Geol. Soc. Am. Bull.* 88, 445–461. doi: 10.1130/0016-7606197788<445:GAMIOT<2.0.CO;2

Oppenheim, L. F., Memeti, V., Barnes, C. G., Chambers, M., Werts, K., and Esposito, R. (in review). Feldspar recycling across magma mush bodies during the voluminous Half Dome and Cathedral Peak stages of the Tuolumne Intrusive Complex, Yosemite National Park, California. *Geosphere*.

Otamendi, J. E., Ducea, M. N., Tibaldi, A. M., Bergantz, G. W., Jesús, D., and Vujovich, G. I. (2009). Generation of tonalitic and dioritic magmas by coupled partial melting of gabbroic and metasedimentary rocks within the deep crust of the Famatinian magmatic arc, Argentina. *J. Petrol.* 50, 841–873. doi: 10.1093/petrology/egp022

Paterson, S., Memeti, V., Mundil, R., and Žák, J. (2016). Repeated, multiscale, magmatic erosion and recycling in an upper-crustal pluton: implications for magma chamber dynamics and magma volume estimates. *Am. Mineral.* 101, 2176–2198. doi: 10.2138/am-2016-5576

Paterson, S. R. (2009). Magmatic tubes, pipes, troughs, diapirs, and plumes: late-stage convective instabilities resulting in compositional diversity and permeable networks in crystal-rich magmas of the Tuolumne batholith. Sierra Nevada, California. *Geosphere* 5, 496–527. doi: 10.1130/GES00214.1

Paterson, S. R., Ardill, K., Vernon, R., and Žák, J. (2018). A review of mesoscopic magmatic structures and their potential for evaluating the hypersolidus evolution of intrusive complexes. *J. Struct. Geol.* 125, 134–147. doi: 10.1016/j.jsg.2018.04.022

Paterson, S. R., Fowler, T. K. Jr., Schmidt, K. L., Yoshinobu, A. S., Yuan, E. S., and Miller, R. B. (1998). Interpreting magmatic fabric patterns in plutons. *Lithos* 44, 53–82. doi: 10.1016/S0024-4937(98)00022-X

Paterson, S. R., Memeti, V., Pignotta, G., Erdmann, S., Žák, J., Chambers, J., et al. (2012). Formation and transfer of stoped blocks into magma chambers: The high-temperature interplay between focused porous flow, cracking, channel flow, host-rock anisotropy, and regional deformation. *Geosphere* 8, 443–469. doi: 10.1130/GES00680.1

Paterson, S. R., Okaya, D., Memeti, V., Economos, R., and Miller, R. B. (2011). Magma addition and flux calculations of incrementally constructed magma chambers in continental margin arcs: combined field, geochronologic, and thermal modeling studies. *Geosphere* 7, 1439–1468. doi: 10.1130/GES00696.1

Paterson, S. R., Vernon, R. H., and Žák, J. (2005). Mechanical instabilities and physical accumulation of K-feldspar megacrysts in granitic magma, Tuolumne Batholith, California, USA. *J. Virt. Expl.* 18, 1–18. doi: 10.3809/jvirtex.2005.00114

Paterson, S. R., Žák, J., and Janoušek, V. (2008). Growth of complex sheeted zones during recycling of older magmatic units into younger: Sawmill Canyon area, Tuolumne batholith, Sierra Nevada, California. *J. Volcanol. Geother. Res.* 177, 457–484. doi: 10.1016/j.jvolgeores.2008.06.024

Peck, D. L., and Van Kooten, G. K. (1983). *Merced Peak Quadrangle, Central Sierra Nevada, California: Analytic Data, No. 1170, US Geological Survey*. Reston, VI: USGS.

Petford, N. (2003). Rheology of granitic magmas during ascent and emplacement. *Ann. Rev. Earth Planet. Sci.* 31, 399–427. doi: 10.1146/annurev.earth.31.100901.141352

Petford, N. (2009). Which effective viscosity? *Mineral. Magaz.* 73, 167–191. doi: 10.1180/minmag.2009.073.2.167

Petford, N., Koenders, M. A., and Clemens, J. D. (2020). Igneous differentiation by deformation. *Contribut. Mineral. Petrol.* 175, 1–21. doi: 10.1007/s00410-020-1674-3

Piccoli, P., and Candela, P. (1994). Apatite in felsic rocks; a model for the estimation of initial halogen concentrations in the Bishop Tuff (Long Valley) and Tuolumne Intrusive Suite (Sierra Nevada Batholith) magmas. *Am. J. Sci.* 294, 92–135. doi: 10.2475/ajs.294.1.92

Pinotti, L. P., D'Eramo, F. J., Weinberg, R. F., Demartis, M., Tubía, J. M., Coniglio, J. E., et al. (2016). Contrasting magmatic structures between small plutons and batholiths emplaced at shallow crustal level (Sierras de Córdoba. Argentina). *J. Struct. Geol.* 92, 46–58. doi: 10.1016/j.jsg.2016.09.009

Pitcher, W. S. (1997). *The Nature and Origin of Granite*. Berlin: Springer Science & Business Media.

Pons, J., Barbey, P., Nachit, H., and Burg, J. P. (2006). Development of igneous layering during growth of pluton: the Tarcouate Laccolith (Morocco). *Tectonophysics* 413, 271–286. doi: 10.1016/j.tecto.2005.11.005

Putirka, K. (2016). Amphibole thermometers and barometers for igneous systems and some implications for eruption mechanisms of felsic magmas at arc volcanoes. *Am. Mineral.* 101, 841–858. doi: 10.2138/am-2016-5506

Reid, J. B. Jr., Murray, D. P., Hermes, O. D., and Steig, E. J. (1993). Fractional crystallization in granites of the Sierra Nevada: how important is it? *Geology* 21, 587–590. doi: 10.1130/0091-76131993021<0587:FCIGOT<2.3.CO;2

Rocher, S., Alasino, P. H., Grande, M. M., Larrovere, M. A., and Paterson, S. R. (2018). K-feldspar megacryst accumulations formed by mechanical instabilities in magma chamber margins, Asha pluton, NW Argentina. *J. Struct. Geol.* 112, 154–173. doi: 10.1016/j.jsg.2018.04.017

Rosenberg, C. L., and Handy, M. R. (2005). Experimental deformation of partially melted granite revisited: implications for the continental crust. *J. Metamorphic Geol.* 23, 19–28. doi: 10.1111/j.1525-1314.2005.00555

Ryerson, F. J., and Hess, P. C. (1978). Implications of liquid-liquid distribution coefficients to mineral-liquid partitioning. *Geochim. Cosmochim. Acta* 42, 921–932. doi: 10.1016/0016-7037(78)90103-5

Schindelin, J., Arganda-Carreras, I., Frise, E., Kaynig, V., Longair, M., Pietzsch, T., et al. (2012). Fiji: an open-source platform for biological-image analysis. *Nat. Methods* 9, 676–682. doi: 10.1038/nmeth.2019

Schleicher, J. M., Bergantz, G. W., Breidenthal, R. E., and Burgisser, A. (2016). Time scales of crystal mixing in magma mushes. *Geophys. Res. Lett.* 43, 1543–1550. doi: 10.1002/2015GL067372

Smith, T. E. (1974). The geochemistry of the granitic rocks of Halifax County, Nova Scotia. *Can. J. Earth Sci.* 11, 650–657. doi: 10.1139/e74-062

Solgadi, F., and Sawyer, E. W. (2008). Formation of igneous layering in granodiorite by gravity flow: a field, microstructure and geochemical study of the Tuolumne Intrusive Suite at Sawmill Canyon, California. *J. Petrol.* 49, 2009–2042. doi: 10.1093/petrology/egn056

Sparks, R. S. J., Annen, C., Blundy, J. D., Cashman, K. V., Rust, A. C., and Jackson, M. D. (2019). Formation and dynamics of magma reservoirs. *Philos. Trans. R. Soc. A* 377:20180019. doi: 10.1098/rsta.2018.0019

Spera, F. J., and Bohrson, W. A. (2018). Rejuvenation of crustal magma mush: a tale of multiply nested processes and timescales. *Am. J. Sci.* 318, 90–140. doi: 10.2475/01.2018.05

Sun, S. S., and McDonough, W. F. (1989). Chemical and isotopic systematics of oceanic basalts: implications for mantle composition and processes. *Geol. Soc. Lond. Spec. Publ.* 42, 313–345. doi: 10.1144/gsl.sp.1989.042.01.19

Van der Molen, I., and Paterson, M. S. (1979). Experimental deformation of partially-melted granite. *Contribut. Mineral. Petrol.* 70, 299–318. doi: 10.1007/BF00375359

Vernon, R. H., and Paterson, S. R. (2006). Mesoscopic structures resulting from crystal accumulation and melt movement in granites. *Earth Environ. Sci. Trans. R. Soc. Edinburgh* 97, 369–381. doi: 10.1017/S0263593300001516

Vukmanovic, Z., Holness, M. B., Monks, K., and Andersen, J. Ø (2018). The Skaergaard trough layering: sedimentation in a convecting magma chamber. *Contribut. Mineral. Petrol.* 173:43. doi: 10.1007/s00410-018-1466-1

Wager, L. R., and Brown, G. M. (1968). *Layered igneous rocks*. San Francisco: Freeman, 588. doi: 10.1180/minmag.1968.036.284.25

Wager, L. R., and Deer, W. A. (1939). Geological investigations in East Greenland. Part III. The petrology of the Skaergaard intrusion, Kangerdlussuaq, East Greenland. *Meddelelser Grønland* 105, 352.

Wahrhaftig, C. (1979). Significance of asymmetric schlieren for crystallization of granites in the Sierra Nevada batholith, California. *Geol. Soc. Am. Abst. Progr.* 11:133.

Weinberg, R. F., Sial, A. N., and Pessoa, R. R. (2001). Magma flow within the Tavares pluton, northeastern Brazil: compositional and thermal convection. *Geol. Soc. Am. Bull.* 113, 508–520. doi: 10.1130/0016-76062001113<0508:MFWTTP<2.0.CO;2

Werts, K., Barnes, C. G., Memeti, V., Ratschbacher, B., Williams, D., and Paterson, S. R. (2020). Hornblende as a tool for assessing mineral-melt equilibrium and recognition of crystal accumulation. *Am. Mineral.* 105, 77–91. doi: 10.2138/am-2020-6972

Wiebe, R. A., and Collins, W. J. (1998). Depositional features and stratigraphic sections in granitic plutons: implications for the emplacement and crystallization of granitic magma. *J. Struct. Geol.* 20, 1273–1289. doi: 10.1016/S0191-8141(98)00059-5

Wiebe, R. A., Jellinek, A. M., and Hodge, K. F. (2017). New insights into the origin of ladder dikes: implications for punctuated growth and crystal accumulation in the Cathedral Peak granodiorite. *Lithos* 277, 241–258. doi: 10.1016/j.lithos.2016.09.015

Wiebe, R. A., Jellinek, M., Markley, M. J., Hawkins, D. P., and Snyder, D. (2007). Steep schlieren and associated enclaves in the Vinalhaven granite, Maine: possible indicators for granite rheology. *Contribut. Mineral. Petrol.* 153:121. doi: 10.1007/s00410-006-0142-z

Žák, J., and Klomínský, J. (2007). Magmatic structures in the Krkonoše–Jizera Plutonic Complex, Bohemian Massif: evidence for localized multiphase flow and small-scale thermal–mechanical instabilities in a granitic magma chamber. *J. Volcanol. Geother. Res.* 164, 254–267. doi: 10.1016/j.jvolgeores.2007.05.006

Žák, J., and Paterson, S. R. (2005). Characteristics of internal contacts in the Tuolumne Batholith, central Sierra Nevada, California (USA): implications for episodic emplacement and physical processes in a continental arc magma chamber. *Geol. Soc. Am. Bull.* 117, 1242–1255. doi: 10.1130/B25558.1

Žák, J., and Paterson, S. R. (2010). Magmatic erosion of the solidification front during reintrusion: the eastern margin of the Tuolumne batholith, Sierra Nevada, California. *Int. J. Earth Sci.* 99, 801–812. doi: 10.1007/s00531-009-0423-7

Žák, J., Paterson, S. R., Janoušek, V., and Kabele, P. (2009). The Mammoth Peak sheeted complex, Tuolumne batholith, Sierra Nevada, California: a record of initial growth or late thermal contraction in a magma

chamber? *Contribut. Mineral. Petrol.* 158:447. doi: 10.1007/s00410-009-0391-8

Žák, J., Paterson, S. R., and Memeti, V. (2007). Four magmatic fabrics in the Tuolumne batholith, central Sierra Nevada, California (USA): implications for interpreting fabric patterns in plutons and evolution of magma chambers in the upper crust. *Geol. Soc. Am. Bull.* 119, 184–201. doi: 10.1130/B25773.1

Zhang, J., Humphreys, M. C., Cooper, G. F., Davidson, J. P., and Macpherson, C. G. (2017). Magma mush chemistry at subduction zones, revealed by new melt major element inversion from calcic amphiboles. *Am. Mineral.* 102, 1353–1367. doi: 10.2138/am-2017-5928

Conflict of Interest: The authors declare that the research was conducted in the absence of any commercial or financial relationships that could be construed as a potential conflict of interest.

frontiers in Earth Science

ORIGINAL RESEARCH
published: 28 July 2020
doi: 10.3389/feart.2020.00311

Late Jurassic Leucogranites of Macau (SE China): A Record of Crustal Recycling During the Early Yanshanian Orogeny

J. Gregory Shellnutt[1], Matthew W. Vaughan[2], Hao-Yang Lee[3] and Yoshiyuki Iizuka[3]*

[1] Department of Earth Sciences, National Taiwan Normal University, Taipei, Taiwan, [2] Siletzia Resources, Lake Oswego, OR, United States, [3] Institute of Earth Sciences, Academia Sinica, Taipei, Taiwan

OPEN ACCESS

Edited by:
Patrizia Fiannacca, University of Catania, Italy

Reviewed by:
Mei-Fu Zhou, The University of Hong Kong, Hong Kong
Veronique Gardien, Université Claude Bernard Lyon 1, France
Federico Farina, Université de Genève, Switzerland

***Correspondence:**
J. Gregory Shellnutt
jgshelln@ntnu.edu.tw

Specialty section:
This article was submitted to Petrology, a section of the journal Frontiers in Earth Science

Received: *09 March 2020*
Accepted: *30 June 2020*
Published: *28 July 2020*

Citation:
Shellnutt JG, Vaughan MW, Lee H-Y and Iizuka Y (2020) Late Jurassic Leucogranites of Macau (SE China): A Record of Crustal Recycling During the Early Yanshanian Orogeny. Front. Earth Sci. 8:311. doi: 10.3389/feart.2020.00311

The Yanshanian Orogeny consists of Jurassic to Cretaceous compressional-extensional cycles related to the subduction of the Paleo-Pacific Ocean beneath East Asia. Numerous granitic plutons were emplaced across southeast China at distinct intervals over a period of ∼100 million years that migrate from the interior to the coast. A key region to help constrain the secular evolution of granitic magmatism related to the Yanshanian Orogeny is the Peal River estuary as three distinct Mesozoic magmatic belts congregate. The islands of Taipa and Coloane, Macau Special Administrative Region, are located along the western bank of the Pearl River estuary and are composed of spessartine-bearing biotite leucogranite. *In situ* zircon geochronology yielded Late Jurassic weighted-mean $^{206}Pb/^{238}U$ ages of 160.0 ± 2.0 and 161.5 ± 2.0 Ma that correlate to the late Early Yanshanian Orogeny. Inherited zircons of Middle Triassic to Middle Jurassic age were also identified. The rocks are peraluminous, ferroan, calc-alkalic to calcic and classify as post-collisional granite. Geochemical modeling indicates that the chemical variability of the rocks is related to hydrous fractional crystallization under reducing conditions (ΔFMQ −1) at ∼7 km depth. The Sr-Nd isotopes [I_{Sr} = 0.71156 to 0.72477; $\varepsilon_{Nd}(t)$ = −7.9 to –8.6], zircon Hf isotopes [$\varepsilon_{Hf}(t)$ = −3.8 to −8.8], incompatible trace element ratios, and whole rock composition indicate that the parental magma was derived primarily from a sedimentary source. It is likely that the islands of Taipa and Coloane form a coherent plutonic complex that may be a member of larger batholith that extends across the Pearl River estuary to Hong Kong. The emplacement of the leucogranites is attributed to decompressional melting associated with a period of crustal relaxation or tensional plate stress that occurred during the transition from low angle subduction to high angle subduction of the Paleo-Pacific plate.

Keywords: Early Yanshanian Orogeny, SE China, post-collisional granite, S-type granite, Cathaysia block

INTRODUCTION

The Mesozoic Era was a critical time in the lithotectonic development of East and Southeast Asia (Zhou and Li, 2000; Wu, 2005; Metcalfe, 2006; Zhou et al., 2006; Li et al., 2013; Shellnutt et al., 2013; Wang et al., 2013; Xu et al., 2016; Dong et al., 2018; Rossignol et al., 2018). Three major orogenic events centered around the South China Block (SCB), an amalgam of the Yangtze and Cathaysia blocks, occurred. The Early Triassic Indosinian Orogeny marks the collision between the rifted terranes of Tethyan Gondwana (e.g., Indochina, Simao) and the southern SCB (Metcalfe, 2006; Wang et al., 2013; Liu et al., 2018; Rossignol et al., 2018); in the northern SCB, the Early to Middle Triassic Qinling-Dabie orogenic belt marks the initial stages of the collision between the SCB and the North China Block (NCB) (Wu and Zheng, 2013; Dong and Santosh, 2016); and, in the east, the Early Jurassic to Late Cretaceous Yanshanian Orogeny is related to compressional-extensional cycles caused by the westward subduction of the Paleo-Pacific Ocean (Wu, 2005; Zhou et al., 2006; Li and Li, 2007; Shu et al., 2009; Dong et al., 2018). In all cases, orogenic activity was accompanied and/or followed by the emplacement of granitic plutons. However, granitic magmatism related to the Yanshanian Orogeny is unique as it lasted ∼100 million years, occurred at distinct intervals, migrated eastward, and their compositions became less aluminous over time (Zhou and Li, 2000; Zhou et al., 2006; Li et al., 2013, 2014; Shellnutt et al., 2013).

The southeastern margin of the Cathaysia Block preserves the distinct secular evolution of primarily silicic (rhyolitic and granitic), Jurassic to Cretaceous magmatic rocks associated with the Yanshanian Orogeny (**Figure 1A**). From the interior to the coast there are sub-parallel magmatic belts that decrease in age from 180−160 Ma, 160−140 Ma, to 140−90 Ma (Zhou and Li, 2000; Zhou et al., 2006; Li et al., 2013). The origin and formation of the magmatic belts is debated but, the secular evolution and the changing composition of the silicic rocks is likely related to the shift in the regional tectonic regime from the Triassic, Tethyan-controlled, Indosinian Orogeny to episodes of extension-related Early Yanshanian (180 to 142 Ma) magmatism and predominantly compression-related (142 to 67 Ma) Late Yanshanian magmatism (Zhou et al., 2006; Dong et al., 2018). Furthermore, the eastward migration of magmatism may also be related to an increase in dip angle of the westward subducting Paleo-Pacific Ocean over time (Zhou and Li, 2000; Li and Li, 2007; Jiang et al., 2009; Li et al., 2012; Zhu et al., 2014; Zuo et al., 2017).

A key region for constraining the Mesozoic tectonic evolution of SE China is the Pearl River estuary as it appears to have been the focal point of the transition from Indosinian-related orogenesis to Yanshanian-related orogenesis (**Figure 1**; Zhou et al., 2006). Thus, it is possible that periods of Yanshanian-related magmatism spatially overlap with Indosinian-related magmatism and can elucidate the importance of crustal recycling in the development and stabilization of the Cathaysia Block until the latest Cretaceous. Granitic rocks are well exposed around the coastal regions of the Pearl River estuary and there are a number of granitic islands and islets between Hong Kong and Macau that extend southward into the South China Sea (**Figures 1B,C**). The territory of Macau, located on the western bank of the Pearl River estuary is composed primarily of biotite leucogranite (Ribeiro et al., 1992; Dias et al., 2018). The leucogranites are relatively understudied but zircon U-Pb geochronology has demonstrated that they were emplaced in two separate pulses during the Jurassic (164.6 ± 0.2 to 159.3 ± 0.3 Ma, and 146.6 ± 0.2 to 140.4 ± 0.2 Ma) and contemporaneous with the late period of the Early Yanshanian Orogeny (Quelhas et al., 2020).

In this paper, we present *in situ* zircon U-Pb geochronology and Hf isotopes, mineral chemistry, whole rock geochemistry, and whole rock Sr-Nd isotopes on a collection of rocks from the Mesozoic granitic islands of Taipa and Coloane, Macau Special Administrative Region. The results of this study are used to constrain the timing, petrogenesis, and tectonomagmatic evolution of the leucogranites from southern Macau and offer new insight of the role that crustal recycling plays in the genesis of Early Yanshanian granitic magmatism within the southeastern margin of the Cathaysia Block.

GEOLOGICAL BACKGROUND

The South China Block (SCB) is one of the largest cratons of East Asia (Wang et al., 2013). It is comprised of the Archean to Paleoproterozoic Yangtze Block in the northwest and Cathaysia Block in the southeast that were sutured together during the Neoproterozoic (900 Ma to 800 Ma), or possibly younger, Jiangnan Orogeny (Li et al., 2009; Zhao, 2015; Sun et al., 2018). The SCB is constrained by the Mesozoic Qinling-Dabie-Sulu Orogen to the north, the Indochina Block along the Ailaoshan-Song Ma suture to the south, and the Songpan-Ganzi terrane along the Longmenshan fault to the west (Wang et al., 2013).

The Cathaysia Block is separated from the Yangtze Block by the Jiangshan-Shaoxing suture and consists of Precambrian basement rocks (Neoarchean to Neoproterozoic), Sinian (∼600 Ma) to Mesozoic sedimentary and volcanic cover rocks, and extensive granitic plutons (Chen and Jahn, 1998; Xu et al., 2007; Charvet, 2013; Sun et al., 2018). During the Phanerozoic there were three regionally extensive tectonothermal events that are referred to as the "Kwangsian," "Indosinian," and "Yanshanian" (Wang et al., 2013). The Kwangsian tectonism occurred during the middle Paleozoic (Ordovician to Devonian) and largely affected the western and southern margin of the Cathaysia Block. The nature of the Kwangsian event is uncertain but is considered to be either an intracontinental deformation or a subduction-related event that led to the closure of an ocean (Wang et al., 2011). The Indosinian Orogeny occurred during the Late Permian to Late Triassic (255 Ma to 202 Ma) and is related to the collision between the Indochina block and the southern margin of SCB after the closure of the Paleotethys Ocean (Liu et al., 2018; Rossignol et al., 2018). Numerous I- and S-type granitic plutons were emplaced during this period (Chen and Jahn, 1998; Wang et al., 2013; Gao et al., 2017; Liu et al., 2018). The Yanshanian Orogeny occurred in two main stages during the Jurassic and Cretaceous and was related to subduction of the Paleo-Pacific Ocean beneath the eastern margin of Eurasia (Zhou and Li, 2000; Zhou et al., 2006; Li et al., 2013).

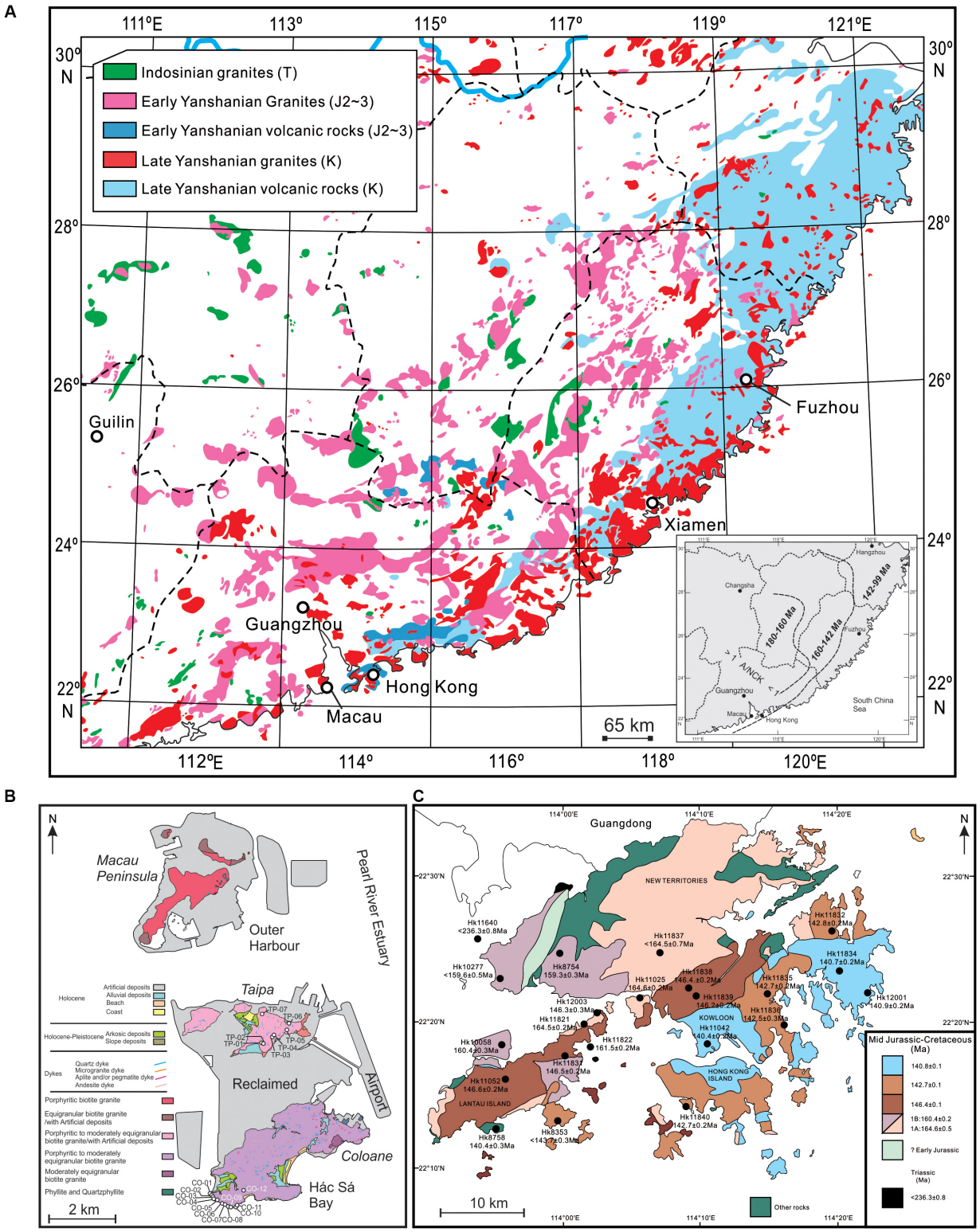

FIGURE 1 | (A) Regional geological map of the South China Block showing the spatial-temporal migration of Mesozoic magmatism from the interior to the coast. Inset map is of the age and compositional trend of Mesozoic volcanic and plutonic rocks of SE China. The alumina saturation index (A/NCK = Al/Na + Ca + K) of Mesozoic volcanic and plutonic rocks increases from NW to SE whereas the age decreases (Zhou et al., 2006). **(B)** Geological map of Macau Special Administrative Region showing the sample locations of this study (modified from Quelhas et al., 2020). **(C)** Geological map of Hong Kong Special Administrative Region showing locations of samples dated using high precision zircon U-Pb methods (modified from Davis et al., 1997).

The territory of Macau is located ∼65 km west of Hong Kong Island and covers an area of ∼30.5 km^2 (**Figures 1A,B**). It is comprised of the densely populated and urbanized Macau peninsula, and lightly populated islands of Taipa and Coloane that are connected by reclaimed land. Granite exposures on peninsular Macau are primarily exposed as small hills within city parks (Jardim Luís Camões, Parque Municipal Mong-Há, Parque Municipal do Monte Guia) or along road cuts (Estrada da Penha) at or near the southern peninsula (Ribeiro et al., 1992; Dias et al., 2018; Quelhas et al., 2020). The bedrock geology of Taipa Island is exposed primarily within forested hills of Taipa Grande and Taipa Pequena. The current and former coastal areas as well as hiking trails of Coloane are the best exposures of the bedrock in the territory of Macau. The granites observed throughout the territory are light gray to cream color, coarse grained, and granular. Microgranular and mafic enclaves as well as aplite veins were observed at many locations but may be more abundant on Coloane.

The studied samples were collected from Taipa and Coloane along two transects. Seven samples from Taipa were collected from the largest and least altered exposures along a hiking trail that encircles Parque Natural de Taipa Grande (**Figure 1B**). The exposures are mostly structureless but joints and fractures, quartz veins, and aplite dykes were observed. The rocks from Coloane were collected along the southwestern to southern coastal exposure starting at Tam Kung Temple (CO-01) and ending at Praia de Hác Sá (CO-12) along Estrada da Aldeia (**Figure 1B**). A total of fourteen samples were collected including one microgranular enclave (CO-08ME) and an aplite vein (CO-09A).

PETROGRAPHY

The granites from Taipa and Coloane are texturally and mineralogically similar and therefore described together (**Figure 2**). The rocks are granular, coarse grained, and primarily composed of alkali feldspar (40−50 vol%), quartz (30−40 vol%), and plagioclase (10−20 vol%). Biotite (∼5 vol%) is the most common mafic mineral but there is subordinate secondary (<5 vol%) amphibole (hornblende), chlorite, and epidote. The alkali feldspar is subhedral to anhedral, and is identified by microcline twinning. Crystal boundaries tend to be irregular or serrated suggesting that it was an early formed mineral and reacted with a liquid. Quartz is typically round or sub-round and of similar size (2−3 mm) to the alkali feldspar but some crystals are smaller. Plagioclase is identified by polysynthetic twinning. It is medium to coarse grained (≤3 mm), euhedral to subhedral and has blocky to lath-like shapes with straight edge boundaries. The plagioclase and alkali feldspars are, in some cases, altered to saussurite. Biotite is medium to fine grained, interstitial to the primary minerals, has light green to light brown pleochroism, and is commonly tabular in shape with serrated crystal boundaries. Typically, biotite form clusters that have crystals of various sizes. Within or marginal to the biotite clusters is fine to medium grained garnet (<1 vol%) and xenotime (<1 vol%). Many biotite crystals have small metamict zircon. There are a few crystals of secondary hornblende but it is not a significant mineral. There is some mineral variability in abundance within and between the two islands as the rocks from Coloane tend to have very little, if any, amphibole whereas the Taipa granites tend to have accessory amounts. Apatite is present (<1 vol%) as small hexagonal crystals that are commonly associated with the biotite clusters. Subhedral to anhedral titanite (<1 vol%) and euhedral to subhedral tourmaline (<1 vol%) were identified but are relatively uncommon. There are few opaque minerals (≤1 vol%) but they are nearly always associated with altered biotite and hornblende. The opaque minerals were identified by scanning electron microscopy (SEM) as Ti-rich magnetite.

MATERIALS AND METHODS

Electron Probe Microanalyzer

Mineralogical investigations were executed using a field emission electron microprobe (JEOL EPMA JXA-8500F) equipped with five wave-length dispersive spectrometers (WDS). Rock specimens were sliced out within a 1-inch diameter size and mounted into epoxy resin, and then polished. Secondary- and back-scattered electron images were used to guide the analysis on target positions of minerals. A 2 μm defocused beam was operated for quantitative analysis at an acceleration voltage of 12 kV with a beam current of 6 nA. The measured X-ray intensities were corrected by ZAF-oxide method using the standard calibration of synthetic and natural chemical-known standards with various diffracting crystals, as follows: wollastonite for Si-*K*α, with TAP crystal, rutile for Ti-*K*α with PET crystal, corundum for Al-*K*α (TAP), chromium oxide for Cr-*K*α (PET), hematite for Fe-*K*α with LiF crystal, Mangum oxide for Mn-*K*α (PET), periclase for Mg-*K*α (TAP), Nickel oxide for Ni-*K*α (LiF), Zinc oxide for Zn-*K*α (LiF), wollastonite for Ca-*K*α (PET), albite for Na-*K*α (TAP), sanidine for K-*K*α (PET), fluorite for F-*K*α (TAP), and apatite for P-*K*α (PET). Peak counting times for F was 20 s, and others were 10 s, respectively. Accuracy of all standard calibrations were less than 1% and the data can be found in **Supplementary Table S1**.

Laser Ablation ICP-MS Zircon U-Pb Dating

Samples TP-03 and CO-06 were selected for zircon separation and sent to Yu-Neng Rock and Mineral Separation Company (Lanfang, Hebei, China). Cathodoluminescence (CL) images were taken at the Institute of Earth Sciences, Academia Sinica, Taipei for examining the internal structures of individual zircon grains and selecting suitable positions for U-Pb analyses. Zircon U-Pb isotopic analyses were performed by laser ablation-inductively coupled plasma mass spectrometry (LA-ICPMS) using an Agilent 7500cx ICP-MS and a New Wave UP213 laser ablation system set up at the Department of Geosciences, National Taiwan University, Taipei, following the analytical procedure of Chiu et al. (2009). A spot size of 40 μm with laser repetition rate of 5 Hz was used and the laser energy density was ∼10 J/cm^2. Calibration was performed by using the zircon standard GJ-1 (608.5 ± 0.4 Ma; Jackson et al., 2004), and Plešovice (337.1 ± 0.4 Ma; Sláma et al., 2008)

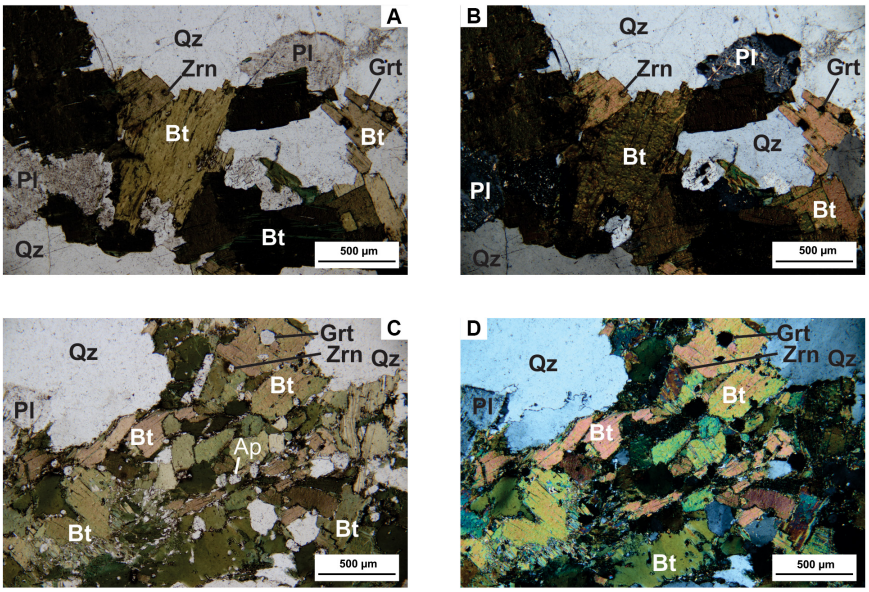

FIGURE 2 | Photomicrograph of the Taipa granite (TP-01) in panel **(A)** plane polarized light and **(B)** cross-polars. Photomicrograph of the Coloane granite (CO-03) in panel **(C)** plane polarized light and **(D)** cross-polars. Pl, plagioclase; Qz, quartz; Bt, biotite; Grt, garnet; Zrn, zircon; and Ap, apatite.

and 91500 (1065 Ma; Wiedenbeck et al., 1995) were used as secondary standards. Measured U-Th-Pb isotope ratios were calculated using the GLITTER 4.4 software (Griffin et al., 2008) and the relative standard deviations of reference values for GJ-1 were set at 2%. The common lead was directly corrected using the common lead correction function proposed by Andersen (2002, 2008).

The majority of the data, before common lead correction, from both samples are discordant suggesting many of the zircons, in particular the older zircons (>170 Ma) experienced Pb loss (**Supplementary Tables S2, S3**). However, the zircon $^{206}Pb/^{238}U$ ratio has nearly all of the chronometric information for Phanerozoic rocks and we interpret the emplacement age of the samples based on the weighted-mean value (Ludwig, 1998). The weighted mean U-Pb ages and Concordia plots were carried out using Isoplot v. 4.1 (Ludwig, 2011).

Laser Ablation MC-ICP-MS Hf Isotopes

In situ zircon Hf isotope analyses were carried out on the same zircon spots for dating by using a Photon Machines Analyte G2 laser-ablation microprobe (193 nm, 4 ns excimer), attached to a Nu Plasma HR multi-collector ICP-MS, at the Institute of Earth Sciences, Academia Sinica in Taipei. Most analyses were carried out with a beam diameter of 50 µm, 8 Hz repetition rate, and energy of ~8–9 J/cm^2. This resulted in total Hf signals of up to ~10 V, depending on the precise conditions and Hf contents. Analyzing times were ~2 min including 30 s of the background noise and ~80 s of the sample intensity after laser ablation. The He carrier gas of ~0.9 L/min (MFC1 = ~0.7 L/min and MFC2 = ~0.2 L/min) transported the ablated sample from the laser-ablation cell via a mixing chamber where it was mixed with Ar of ~0.7 L/min prior to entering the ICP-MS torch. The He gas could substantially reduce the deposition of ablated material onto the sample surface and greatly improve transport efficiency, and thus increase the signal intensities. Typical within-run precision (1σ) on the analysis of $^{176}Hf/^{177}Hf$ is better than ± 0.000030, equivalent to an uncertainty of ~1 epsilon unit. International zircon standards of Mud Tank served as the primary external reference material to monitor the condition facilities, and Plešovice, 91500, and TEMORA also served as the secondary external reference materials for data quality control. They have long-term average $^{176}Hf/^{177}Hf$ values of 0.282494 ± 28 (2σ, n = 395), 0.282485 ± 28 (2σ, n = 45), 0.282314 ± 23 (2σ, n = 40) and 0.282689 ± 30 (2σ, n = 42), respectively, all in accordance with those of 0.282504 ± 44, 0.282482 ± 13, 0.282307 ± 31 and 0.282680 ± 31 reported in Woodhead and Hergt (2005), Wu et al. (2006), and Sláma et al. (2008). All calculated data were considered for isobaric interferences and normalized to $^{179}Hf/^{177}Hf$ = 0.7325, using an exponential correction for mass bias. The Hf isotope results of the samples are presented in the online supplementary material (**Supplementary Table S4**).

Wave-Length Dispersive X-Ray Fluorescence

For each sample, three grams (3.0000 ± 0.0005 g) was added to a ceramic crucible of known mass (+lid) and placed in an oven for 3 h at 105°C. After heating, the samples were cooled inside a desiccator for ~15 min before they were weighed. All samples were then heated in a furnace to peak temperature of 900°C and held for 10 min before cooling. After the samples were sufficiently cooled (<200°C) they were removed from the furnace and placed in a desiccator until reaching ambient temperature. Each sample was weighed again and the loss on ignition was determined from the masses obtained

from the low and high temperature cycles. Lithium metaborate (6.0000 ± 0.0005 g) was added to the samples (0.6000 ± 0.0005 g) at a ratio of 10:1 and fused to produce a glass disc using a Claisse M4 fluxer. The major elements were measured by Panalytical Axios^{mAX} WDXRF at XRF Laboratory, Department of Earth Sciences, National Taiwan Normal University. Standard reference material sample BIR-1a was measured after every five samples to track the accuracy and stability of the machine. The measured accuracy for BIR-1a is better than 5% for all elements.

Inductively Coupled Plasma Mass Spectrometry

The glass bead used for XRF analysis for each sample (40 ± 5 mg) was decomposed in screw-top Savillex Teflon beakers containing 30 to 25 drop mixture of 1:1 nitric acid (HNO_3) and fluoric acid (HF). The beakers were placed on a hot plate at 140°C for 12 h. After drying of the solution, 1.5 ml HNO_3 was added to the dried residua. The beakers were then placed on a hot plate at 140°C for 12 h. The solution was diluted to 1500 times. The samples solution was initially diluted 500 times with 2% HNO_3 into 50ml bottles. The solutions were then diluted 3 times with 2% HNO_3 and internal standard 10 ppb (Rh + Bi) into 12ml tubes. The solutions were measured at the Institute of Earth Sciences, Academia Sinica using an Agilent 7500cx mass spectrometer. Measured standard reference materials for this study (BCR-2, BHVO-2, AGV-2, and DNC-1) and their recommended values are found in **Table 1**.

Thermal Ionization Mass Spectrometry

Five samples (TP-02, TP-05, TP-07, CO-05, and CO-12) were measured for Sr isotopes using a Finnigan MAT-262 TIMS at the Mass Spectrometry Lab, Institute of Earth Sciences, Academia Sinica, Taipei. Approximately 100 mg of each sample powder was added to a Teflon beaker with 50 drops of concentrated HNO_3 and HF. The mixture was heated to 100°C for 2 days and then dried. 2 ml of 6N HCl was added to the residua and dried. After repeating this step twice, 2 ml of 1N HCl was added to the residua and then centrifuged for 10 min to congregate the supernatant. Chromatographic/column separation was used to isolate Sr from all other elements. The first column isolated the Sr and REEs using a polyethylene column (23 mm length × 5 mm in diameter) with 2.5 ml of cation exchange resin (sulfonated polystyrene resin, BioRad AG 50W-X8, Analytical Grade, 100−200 mesh). Strontium was further purified by passing through a cation exchange resin bed polyethylene column (23 mm length × 5 mm in diameter) filled with 1 ml of AG50W-X8. For the Sr isotopic measurement, the samples were loaded with H_3PO_4 on treated single rhenium filament. $^{87}Sr/^{86}Sr$ ratios were normalized to $^{86}Sr/^{88}Sr = 0.1194$. The 2σ external precision ($2\sigma_m$) for all samples is ≤0.000013 (**Table 2**). The certified standard NBS987 was used to ensure quality both as an internal standard and as a check for instrumental functionality. Analyses of NBS987 during the study period yielded $^{87}Sr/^{86}Sr$ ratio of 0.710248 ± 21.

Additional samples were measured for Sr (TP-04, CO-08, and CO-11) and Nd (TP-02, TP-04, TP-07, CO-05, CO-08, and CO-11) isotopes at Activation Laboratories, Ancaster, Ontario. The Sr isotopic compositions were measured in static mode by multicollector inductively coupled plasma mass spectrometry (MC-ICP-MS), and are normalized for variable mass fractionation to a value of 0.1194 for $^{86}Sr/^{88}Sr$ using the exponential law. All analyses reported here are presented relative to an $^{87}Sr/^{86}Sr$ value of 0.710245 for the NIST SRM987 international Sr isotope standard. The rock powders were accurately weighed and dissolved in mixed 24N HF + 16N HNO3 media in sealed PFA Teflon vessels at 160°C for 6 days. The fluoride residue is converted to chloride with HCl, and Nd and Sm are separated by conventional cation and HDEHP-based chromatography (Creaser et al., 1997; Unterschutz et al., 2002). The isotopic composition of Nd is determined in static mode by MC-ICP-MS (Schmidberger et al., 2007). All isotope ratios are normalized for variable mass fractionation to a value of $^{146}Nd/^{144}Nd = 0.7219$ using the exponential fractionation law. Using the same isotopic analysis and normalization procedures above, the Geological Survey of Japan Nd isotope standard "Shin Etsu: J-Ndi-1" was measured for this study (Tanaka et al., 2000) and has a $^{143}Nd/^{144}Nd$ value of 0.512107 ± 7 relative to a LaJolla $^{143}Nd/^{144}Nd$ value of 0.511850, when normalized to $^{146}Nd/^{144}Nd = 0.7219$.

RESULTS

Mineral Chemistry

The composition of biotite was calculated into cation proportions using the method of Tindle and Webb (1990). Following the cation calculation, the total Fe was recalculated into Fe^{2+} and Fe^{3+} using charge balance (Nenova, 1997). The biotite crystals from both islands are siderophyllite but only five analyses classify as primary magmatic whereas the other analyses fall within the domain of re-equilibrated biotite (Nachit et al., 2005). The Fe/(Fe + Mg) ratios are high and range from 0.72 to 0.78 but the TiO_2 tends to be higher in the biotite from Taipa whereas the Al_2O_3 (14.26 wt% to 16.88 wt%) tends to be lower (Al_2O_3 = 16.57 wt% to 17.71 wt%) compared to the biotite from Coloane (**Supplementary Table S1**).

Garnet is present as an accessory mineral within some samples. The cations and garnet end-member compositions were calculated using the method of Locock (2008). Analysis of three crystals shows that the garnet is spessartine (**Supplementary Table S1**). The spessartine component of the garnet ranges from 45.5 to 51.4 with the almandine component ranging from 19.5 to 23.5, and the grossular component ranges from 23.4 to 27.5. The andradite (3.0 to 3.8) and pyrope (0.1 to 0.2) components are minor.

In situ Zircon U-Pb Ages

Individual zircon grains from the Taipa (TP-03) leucogranite (22°9′22.12″N, 113°33′59.85″E) are ∼100 μm × ∼300 μm (**Supplementary Figure S1**). The majority (22 of 28) of the zircons have euhedral prismatic shapes that are similar to the

TABLE 1 | Whole-rock chemical composition of the leucogranites from Taipa and Coloane.

Sample	**TP-01**	**TP-02**	**TP-03**	**TP-04**	**TP-05**	**TP-06**	**TP-07**	**CO-01**	**CO-02**
Island	**Taipa**	**Taipa**	**Taipa**	**Taipa**	**Taipa**	**Taipa**	**Taipa**	**Coloane**	**Coloane**
Lat. (N)	**22.1545**	**22.1543**	**22.1561**	**22.1563**	**22.1580**	**22.1600**	**22.1609**	**22.1122**	**22.1130**
Lon. (E)	**113.5638**	**113.5640**	**113.5666**	**113.5669**	**113.5688**	**113.5686**	**113.5637**	**113.5494**	**113.5499**
SiO_2 (%)	76.43	75.66	76.59	76.47	75.15	75.40	76.31	78.29	79.08
TiO_2	0.12	0.07	0.10	0.06	0.07	0.15	0.09	0.15	0.20
Al_2O_3	12.85	12.88	13.18	12.71	13.71	13.08	12.79	11.85	10.87
Fe_2O_3	1.55	1.29	1.33	0.97	1.05	1.58	1.01	1.57	1.99
MnO	0.07	0.10	0.05	0.07	0.04	0.06	0.05	0.08	0.06
MgO	0.19	0.11	0.17	0.09	0.11	0.24	0.10	0.25	0.36
CaO	1.03	0.80	1.04	0.75	0.75	1.22	0.77	1.09	1.13
Na_2O	3.37	3.67	3.33	3.66	3.68	3.33	4.33	3.15	2.75
K_2O	4.27	4.39	4.70	4.30	5.05	4.30	3.50	3.03	2.91
P_2O_5	0.02	0.01	0.02	0.01	0.01	0.03	0.01	0.04	0.04
LOI	0.40	0.53	0.42	0.87	0.57	0.57	0.66	0.85	0.84
TOTAL	100.31	99.50	100.93	99.95	100.18	99.97	99.62	100.36	100.22
Mg#	19.6	14.2	19.9	14.9	16.8	23.2	16.5	24.3	26.2
Sc (ppm)	15.9	10.9	14.3	16.7	21.8	17.3	22.8	22.1	25.3
V	7.4	2.0	5.0	1.4	3.1	8.8	0.9	7.2	12.3
Cr			1.4	1.2	0.1	0.8		1.1	
Co	1.2	0.7	1.0	0.5	0.7	1.5	0.4	1.7	2.0
Ni	3.1	2.4	0.5	1.5	7.7	1.0	2.0	5.1	1.1
Cu	3.8	3.7	3.0	3.9	2.9	2.3	2.6	5.4	2.6
Zn	38.5	37.9	43.0	27.9	24.4	23.2	18.7	37.9	48.5
Ga	16.8	18.9	16.1	18.4	17.7	17.3	18.0	16.1	15.5
Rb	276	412	255	383	357	277	297	221	229
Sr	76.0	28.5	80.8	34.2	76.7	110	56.6	110	102
Y	49.9	124	23.7	123	51.1	51.8	103	26.2	65.2
Zr	116	110	88	71	81	116	93	113	145
Nb	20.6	34.6	14.1	26.8	11.9	20.8	44.2	18.4	20.3
Cs	10.2	23.5	7.7	9.1	9.9	13.4	7.4	8.4	10.1
Ba	148	43	205	37	195	233	37	142	188
La	30.1	11.3	19.3	10.8	14.1	33.6	12.6	27.7	35.3
Ce	64.3	26.4	43.6	27.0	31.8	66.9	37.3	59.6	58.4
Pr	7.83	3.85	5.15	3.90	4.11	8.13	4.40	7.14	8.42
Nd	29.4	16.9	19.36	17.4	16.7	29.7	19.0	26.2	30.8
Sm	7.03	7.43	4.75	8.04	5.50	6.70	8.35	5.83	7.40
Eu	0.45	0.22	0.49	0.18	0.44	0.64	0.23	0.56	0.60
Gd	7.03	11.91	4.17	12.28	6.08	6.97	12.18	4.95	7.92
Tb	1.17	2.39	0.67	2.40	1.21	1.18	2.40	0.78	1.38
Dy	7.22	16.81	3.87	16.14	7.72	7.32	16.25	4.44	8.86
Ho	1.54	3.74	0.78	3.48	1.60	1.58	3.45	0.88	1.92
Er	4.57	11.42	2.28	10.34	4.71	4.80	10.12	2.56	5.79
Tm	0.73	1.89	0.38	1.67	0.76	0.76	1.60	0.43	0.94
Yb	4.65	12.74	2.50	11.07	5.02	4.92	10.21	2.88	6.20
Lu	0.70	1.90	0.39	1.61	0.75	0.74	1.44	0.43	0.95
Hf	4.16	5.51	3.20	3.57	3.21	4.22	4.44	3.90	5.08
Ta	2.20	6.23	1.76	5.28	2.43	3.30	7.24	2.56	3.14
Th	43.0	35.8	32.9	27.7	26.4	32.9	39.0	37.5	40.8
U	13.7	22.9	6.5	13.7	8.3	10.6	12.7	5.3	8.9
Eu/Eu*	0.19	0.07	0.33	0.06	0.22	0.28	0.07	0.31	0.24
$(La/Sm)_N$	2.8	1.0	2.6	0.9	1.7	3.2	1.0	3.1	3.1
$(La/Yb)_N$	4.6	0.6	5.5	0.7	2.0	4.9	0.9	6.9	4.1

(Continued)

TABLE 1 | Continued

Sample	**CO-03**	**CO-04**	**CO-05**	**CO-06**	**CO-07**	**CO-08**	**CO-08ME**	**CO-09A**	**CO-09**
Rock	**Coloane**	**Coloane**	**Coloane**	**Coloane**	**Coloane**	**Coloane**	**Coloane**	**Coloane**	**Coloane**
Lat.	**22.1127**	**22.1119**	**22.1119**	**22.1114**	**22.1109**	**22.1104**	**22.1104**	**22.1103**	**22.1103**
Lon.	**113.5500**	**113.5505**	**113.5512**	**113.5525**	**113.5531**	**113.5539**	**113.5539**	**113.5539**	**113.5539**
SiO_2 (%)	76.59	74.23	73.71	74.96	75.33	71.28	74.02	76.55	76.02
TiO_2	0.19	0.14	0.19	0.22	0.13	0.09	0.17	0.03	0.15
Al_2O_3	12.27	13.58	12.69	12.02	13.26	14.30	13.52	12.83	13.10
Fe_2O_3	1.98	1.51	2.03	2.27	1.51	1.20	1.94	0.98	1.70
MnO	0.08	0.06	0.08	0.08	0.05	0.04	0.08	0.03	0.09
MgO	0.31	0.23	0.33	0.37	0.22	0.14	0.26	0.04	0.22
CaO	1.50	1.17	1.36	1.39	1.06	0.97	1.24	0.73	1.45
Na_2O	3.23	3.28	3.23	3.18	3.10	3.37	3.31	4.30	3.64
K_2O	3.34	5.04	4.02	3.46	5.14	6.40	4.67	3.80	3.35
P_2O_5	0.05	0.03	0.04	0.05	0.03	0.02	0.04		0.03
LOI	0.63	0.55	0.61	0.59	0.51	0.39	0.56	0.50	0.37
TOTAL	100.16	99.81	98.31	98.59	100.33	98.21	99.80	99.77	100.12
Mg#	23.7	23.1	24.3	24.2	22.0	19.0	20.9	7.3	20.5
Sc (ppm)	19.9	15.2	22.7	15.3	24.9	15.7	21.3	21.0	19.7
V	12.4	9.2	11.8	15.6	6.8	5.4	8.0	1.0	6.0
Cr	0.9	1.1	3.2	4.0	1.9	3.6	3.3	4.0	2.8
Co	2.1	1.6	2.2	2.6	1.3	1.0	1.7	0.2	1.4
Ni	2.0	0.9	3.6	6.9	0.6	1.6	0.7	0.8	0.6
Cu	4.3	2.2	2.5	3.5	1.9	79.7	1.9	2.4	2.2
Zn	39.2	38.5	48.2	44.2	28.7	32.8	37.7	9.8	32.0
Ga	16.9	16.9	17.9	17.7	16.5	17.3	17.3	20.8	18.0
Rb	225	278	268	259	248	283	231	293	243
Sr	115	122	119	114	111	116	112	12.5	113
Y	39.8	44.5	54.2	53.0	35.6	36.2	35.8	118.2	49.3
Zr	142	110	138	165	138	105	152	99	138
Nb	19.0	15.3	22.4	24.0	15.3	10.3	18.1	78.6	23.7
Cs	10.7	7.6	16.2	11.2	5.2	6.4	5.1	8.5	13.7
Ba	204	330	260	212	460	436	296	12	186
La	27.4	21.0	31.0	27.7	42.7	41.0	33.5	6.8	41.6
Ce	58.1	44.7	65.8	59.4	88.2	84.4	69.5	17.6	85.7
Pr	6.94	5.40	7.87	7.22	10.10	9.74	8.13	2.58	9.98
Nd	25.9	20.4	29.2	27.3	35.8	34.7	29.5	11.1	35.9
Sm	6.24	5.46	7.30	7.04	7.39	7.31	6.57	5.68	8.13
Eu	0.58	0.66	0.62	0.58	0.75	0.81	0.71	0.09	0.65
Gd	6.11	6.09	7.57	7.58	6.31	6.35	6.09	8.96	7.63
Tb	1.01	1.09	1.31	1.30	0.99	1.02	1.00	1.93	1.27
Dy	6.09	6.97	8.12	8.16	5.77	5.85	5.82	14.25	7.59
Ho	1.25	1.45	1.69	1.71	1.17	1.17	1.20	3.28	1.56
Er	3.70	4.21	5.00	4.99	3.41	3.42	3.46	10.53	4.57
Tm	0.60	0.65	0.82	0.80	0.54	0.54	0.55	1.86	0.75
Yb	3.89	4.22	5.44	5.01	3.52	3.56	3.54	12.99	5.07
Lu	0.59	0.62	0.80	0.74	0.53	0.54	0.53	1.97	0.77
Hf	4.75	3.82	4.83	5.64	4.57	3.45	4.84	6.30	4.68
Ta	2.44	1.75	3.34	2.85	1.58	1.42	1.55	9.83	2.85
Th	36.5	26.5	24.7	39.6	40.2	34.4	29.7	39.3	35.9
U	8.8	9.2	10.1	10.7	8.6	6.5	8.0	39.9	12.1
Eu/Eu*	0.28	0.35	0.25	0.24	0.33	0.35	0.34	0.04	0.25
$(La/Sm)_N$	2.8	2.5	2.7	2.5	3.7	3.6	3.3	0.80	3.30
$(La/Yb)_N$	5.1	3.6	4.1	4.0	8.7	8.3	6.8	0.40	5.9

(Continued)

TABLE 1 | Continued

Sample	**CO-10**	**CO-11**	**CO-12**	**BIR-1a**	**BIR-1a**	**BCR-2**	**BCR-2**	**BHVO-2**	**BHVO-2**
Rock	**Coloane**	**Coloane**	**Coloane**	**m.v.**	**r.v.**	**m.v.**	**r.v.**	**m.v.**	**r.v.**
Lat. (N)	**22.1101**	**22.1100**	**22.1137**	**(4)**		**(2)**		**(2)**	
Lon. (E)	**113.556**	**113.556**	**113.5579**						
SiO_2 (%)	78.27	75.07	75.81	47.34	47.96				
TiO_2	0.15	0.19	0.10	0.96	0.96				
Al_2O_3	11.64	13.05	13.08	15.31	15.5				
Fe_2O_3	1.64	2.10	1.14	11.11	11.3				
MnO	0.06	0.08	0.04	0.17	0.175				
MgO	0.23	0.28	0.16	9.55	9.7				
CaO	1.18	1.41	0.94	13.18	13.3				
Na_2O	2.99	3.29	3.10	1.74	1.82				
K_2O	3.57	4.11	5.26	0.03	0.03				
P_2O_5	0.03	0.04	0.02	0.02	0.021				
LOI	0.43	0.48	0.33						
TOTAL	100.20	100.10	99.97						
Mg#	21.9	21.2	21.8						
Sc (ppm)	22.6	15.5	16.9			33	33.5	31	31.8
V	6.6	10.0	5.2			425	418	309	318
Cr	3.1	2.9	4.0			16	15.9	292	287
Co	1.3	1.7	1.0			37	37.3	44	44.9
Ni	1.3	0.6	0.4			14	12.6	119	120
Cu	1.8	2.9	2.0			22	19.7	128	129
Zn	32.4	44.9	22.5			132	130	105	104
Ga	15.3	17.7	15.5			22.1	22.1	21.4	21.4
Rb	219	237	246			46	46	9.5	9.3
Sr	88.6	111	102			337	337	388	394
Y	41.1	38.5	26.0			36	36.1	26.1	25.9
Zr	131	165	87			183	187	169	171
Nb	18.9	19.6	11.7			12.3	12.4	18.1	18.1
Cs	7.2	7.8	4.1			1.2	1.16	0.1	0.1
Ba	207	249	261			698	684	135	131
La	26.2	52.2	21.3			24.8	25.1	14.9	15.2
Ce	56.4	107.1	44.6			52.6	53.1	36.7	37.5
Pr	6.64	12.18	5.28			6.8	6.83	5.22	5.34
Nd	24.3	42.7	19.2			28.4	28.3	23.8	24.3
Sm	5.86	8.59	4.43			6.52	6.55	5.99	6.02
Eu	0.54	0.67	0.63			1.98	1.99	1.97	2.04
Gd	5.91	7.19	4.25			6.81	6.81	6.20	6.21
Tb	1.00	1.12	0.70			1.07	1.08	0.94	0.94
Dy	6.25	6.20	4.14			6.43	6.42	5.27	5.28
Ho	1.30	1.24	0.86			1.32	1.31	0.99	0.99
Er	3.89	3.56	2.49			3.64	3.67	2.52	2.51
Tm	0.64	0.57	0.39			0.54	0.534	0.34	0.335
Yb	4.29	3.93	2.65			3.39	3.39	1.98	1.99
Lu	0.65	0.61	0.39			0.51	0.505	0.28	0.275
Hf	4.64	5.63	2.96			4.91	4.97	4.39	4.47
Ta	2.61	3.13	1.51			0.78	0.79	1.17	1.15
Th	30.7	41.5	20.7			5.88	5.83	1.20	1.22
U	7.4	7.6	6.1			1.69	1.68	0.42	0.41
Eu/Eu*	0.28	0.25	0.44						
$(La/Sm)_N$	2.9	3.9	3.1						
$(La/Yb)_N$	4.4	9.5	5.8						

(Continued)

TABLE 1 | Continued

Sample	AGV-2a	AGV-2a	DNC-1	DNC-1
Rock	m.v.	r.v.	m.v.	r.v.
Lat. (N)	(3)		(2)	
Lon. (E)				
SiO_2 (%)				
TiO_2				
Al_2O_3				
Fe_2O_3				
MnO				
MgO				
CaO				
Na_2O				
K_2O				
P_2O_5				
LOI				
TOTAL				
Mg#				
Sc (ppm)	19	13.1	21	31.4
V	119	119	148	147.5
Cr	16	16.2	281	270
Co	16	15.5	55	56.8
Ni	17	18.9	247	247
Cu	53	51.5	97	99.7
Zn	87	86.7	60	70.1
Ga	21.0	20.4	13.7	14.7
Rb	67	67.8	3.6	4.7
Sr	658	660	152	144
Y	20.1	19.1	17.1	18.5
Zr	235	232	34.6	38.5
Nb	14.2	14.1	1.45	3.19
Cs	1.2	1.17	0.2	0.44
Ba	1127	1134	104	118
La	37.4	38.2	3.57	3.58
Ce	68.4	69.4	7.89	9.14
Pr	8.08	8.17	1.07	
Nd	30.0	30.5	4.75	5.2
Sm	5.45	5.51	1.37	1.41
Eu	1.64	1.55	0.58	0.59
Gd	4.57	4.68	2.09	2.2
Tb	0.66	0.65	0.38	0.42
Dy	3.50	3.55	2.72	3.0
Ho	0.68	0.68	0.63	0.44
Er	1.82	1.83	1.92	1.7
Tm	0.26	0.262	0.30	0.33
Yb	1.64	1.65	1.97	1.98
Lu	0.25	0.251	0.30	0.32
Hf	5.21	5.14	0.99	1.01
Ta	0.85	0.87	0.08	0.10
Th	6.20	6.15	0.23	0.22
U	1.91	1.89	0.06	
Eu/Eu*				
$(La/Sm)_N$				
$(La/Yb)_N$				

*Mg# = {MgO (mol)/[MgO (mol) + FeOt (mol)]}*100. FeOt = Fe_2O_3t* 0.8998. Eu/Eu* = 2*Eu_N/(Sm_N + Gd_N). N, chondrite normalized to Sun and McDonough (1989). m.v., measured value; r.v., recommended value. Number in parentheses for standards is averaged number of analyses.*

P1, P2, P3, P4, S5, and S10 types of Pupin (1980) whereas the others are equant (AB3, AB4 types). Twelve of the twenty-eight zircons do not show internal structures in the CL images. Of the remaining zircons, some (8) have bright cores with darker rims, some (3) have bright rims and darker cores, some (3) have clear oscillatory zoning, and the remaining two zircons are unique (Corfu et al., 2003). One is equant with an off-center bright ring around a dark core and the other has an irregular dark core surrounded by a brighter oscillatory zoned rim. The size, morphology, and zonation of the zircons do not appear to show systematic age distribution. Analyses of 28 zircons yielded a total range of $^{206}Pb/^{238}U$ ages from 140 ± 5 Ma to 234 ± 5 Ma (1σ) and have Th/U ratios that range from 0.11 to 1.27. Twenty-four spot measurements of the standard reference materials (GJ-1 = 14, 91500 = 7; PLS = 3) yielded results within their certifiable $^{206}Pb/^{238}U$ ages (**Supplementary Table S2**). One zircon was analyzed in the core and two rim locations to evaluate temporal growth. Five age populations are identified based on the clustering of the ages (**Supplementary Table S2**). There are two distinct Triassic groups and two Jurassic groups (**Figure 3A**). The oldest Triassic age group is comprised of two zircons with ages of 234 ± 5 Ma (1σ). The younger Triassic ages are 207 ± 5 Ma (core analysis), 208 ± 5 Ma, and 217 ± 5 Ma (1σ). The oldest Jurassic ages are 172 ± 4 Ma, 173 ± 5 Ma (rim), 169 ± 4 Ma, and 169 ± 4 Ma (1σ). The largest age group ranges from 166 ± 4 Ma to 156 ± 4 Ma (1σ) and has a weighted-mean $^{206}Pb/^{238}U$ age of 160.0 ± 2.0 Ma (2σ, n = 16). The weighted-mean age is within uncertainty of the Concordia intercept age of 159.5 ± 2.4 Ma. Four zircons yielded Late Jurassic to Early Cretaceous ages (153 ± 5 Ma, 140 ± 5 Ma, 144 ± 4 Ma, 145 ± 4 Ma, 1σ) but they are more discordant than the Oxfordian zircons suggesting they experienced lead loss. One zircon yielded a $^{206}Pb/^{238}U$ age of 168 ± 6 Ma (1σ) Ma but has a comparatively large measured uncertainty in the $^{207}Pb/^{235}U$ ratio.

Individual zircon grains of the Coloane (CO-06) leucogranite (22°6′40.27″N, 113°33′8.82″E) are similar in size and shape of those from TP-03 (**Supplementary Figure S2**). Twenty-five of thirty zircons from CO-06 are euhedral to subhedral, prismatic, and similar to the P1, P2, P3, P4, S5, and S10 types of Pupin (1980). The remaining five zircons are sub-round to equant in shape and resemble the AB3, AB4, and G2 types of Pupin (1980). Eight of the thirty zircons do not show internal structures in the CL images. Of the remaining zircons, some have bright cores with darker rims, one has a bright rim and darker core, and some have obvious oscillatory zoning (Corfu et al., 2003). Similar to the zircons from TP-03, the size, morphology, and zonation of the zircons do not appear to show an age correlation. Analyses of 30 zircons yielded a total range of $^{206}Pb/^{238}U$ ages from 141 ± 5 Ma to 234 ± 6 Ma (1σ) and have Th/U ratios that range from 0.12 to 0.67. Seventeen spot measurements of the standard reference materials (GJ-1 = 11, 91500 = 5; PLS = 1) yielded results within their certifiable $^{206}Pb/^{238}U$ ages (**Supplementary Table S3**). Four population clusters are identified in this sample but they are similar to TP-03 (**Supplementary Table S3**). There is one Triassic group and two Jurassic groups, and one Cretaceous group (**Figure 3B**). The Triassic group is comprised of two zircons with ages of 222 ± 12 Ma and 234 ± 6 Ma (1σ). The older Jurassic zircons range in age from 168 ± 4 Ma to

TABLE 2 | Sr and Nd isotopes of the leucogranites from Taipa and Coloane.

Sample	Rb (ppm)	Sr (ppm)	$(^{87}Rb/^{86}Sr)_m$	$(^{87}Sr/^{86}Sr)_m$	2σ	I_{Sr}	Sm (ppm)	Nd (ppm)	$(^{147}Sm/^{144}Nd)_m$	$(^{143}Nd/^{144}Nd)_m$	2σ	$\varepsilon_{Nd}(t)$	T_{DM} (Ma)
TP-02	412	28.5	42.293	0.82217	9	0.72477	7.4	16.9	0.2658	0.512306	8	−7.9	
TP-04	383	34.2	32.675	0.79412	5	0.71887	8.0	17.4	0.2793	0.512291	7	−8.5	
TP-05	357	76.7	15.518	0.74696	7	0.71583							
TP-07	297	56.6	15.249	0.75284	13	0.71772	8.4	19.0	0.2657	0.512272	6	−8.6	
CO-05	268	119	6.529	0.72838	6	0.71334	7.3	29.2	0.1511	0.512152	8	−8.5	2420
CO-08	283	116	7.074	0.73003	3	0.71374	7.3	34.7	0.1274	0.512139	7	−8.3	1780
CO-11	237	111	6.188	0.72581	2	0.71156	8.6	42.7	0.1216	0.512131	6	−8.3	1683
CO-12	246	102	6.992	0.72901	11	0.71291							

m, measured. Rb, Sr, Sm, and Nd concentrations were obtained by ICP-MS and the precisions are better than ± 2%. T_{DM}*-1 = (1/λ)*ln[1 + (($^{143}Nd/^{144}Nd)_m$-0.51315)/(($^{147}Sm/^{144}Nd)_m$-0.2137)]; λ = 0.00654 Ga^{-1}.*

187 ± 7 Ma (1σ) and have a weighted-mean $^{206}Pb/^{238}U$ age of 174.7 ± 2.7 Ma (2σ, *n* = 11). The largest group has ages ranging from 167 ± 4 Ma to 155 ± 4 Ma (1σ) with a weighted-mean $^{206}Pb/^{238}U$ age of 161.5 ± 2.0 Ma (2σ, *n* = 15). The Concordia intercept age (162.2 ± 2.5 Ma) is within uncertainty of the weighted-mean age. One zircon has an Early Cretaceous age (141 ± 5, 1σ) and another yielded a $^{206}Pb/^{238}U$ age of 161 ± 7 Ma (1σ) Ma but has a comparatively large measured uncertainty in the $^{207}Pb/^{235}U$ ratio.

In situ Zircon Hf Isotopes

Zircon Hf isotopes were measured on the same spots as the crystals for U-Pb geochronology of samples TP-03 and CO-06. Not all zircons were able to yield results as some crystals were almost entirely ablated during the U-Pb measurement. The entire dataset can be found in the **Supplementary Table S4** of the online supplementary material. The Lu-Hf isotope system is more stable than the U-Pb isotope system due to the higher retentivity of Hf, Lu and U than Pb in zircon. Consequently, this may cause the zircons with ancient ages and/or those that experienced metamorphism to have suffered Pb loss (Zeh et al., 2007; Guitreau et al., 2012). For the older zircons, the calculated initial Hf isotopic values would be incorrect if using underdetermined ages. Here, we used the individual zircon $^{206}Pb/^{238}U$ ages presented above to calculate the initial $\varepsilon_{Hf}(t)$ values.

Eleven of the 30 zircons analyzed for U-Pb dating from Taipa (TP-03) yielded results. The zircons range in age from 173 ± 5 Ma (1σ) to 156 ± 4 Ma (1σ) and the time integrated ratios were calculated to the age reported for each individual zircon. The $^{176}Hf/^{177}Hf(t)$ ratios range from 0.282479 to 0.282579 and correspond to $\varepsilon_{Hf}(t)$ values from −3.0 to −7.4. The T_{DM1} ages range from 985 Ma to 1109 Ma whereas the T_{DM2} ages range from 1411 Ma to 1678 Ma (**Supplementary Table S2**).

Half (15 of 30) of the zircons from Coloane analyzed for U-Pb dating were measured for Hf isotopes. The zircons range in age from 176 ± 5 Ma (1σ) to 156 ± 4 Ma (1σ) and the time integrated ratios were calculated to the age reported for each individual zircon. The time integrated $^{176}Hf/^{177}Hf(t)$ ratios range from 0.282428 to 0.282533 with corresponding $\varepsilon_{Hf}(t)$ values from −5.1 to −8.2. The T_{DM1} ages range from 1043 Ma to 1196 Ma with the T_{DM2} ages range from 1535 Ma to 1770 Ma (**Supplementary Table S3**).

Major and Trace Elemental Geochemistry

The major and trace elemental results are summarized in **Table 1**. The SiO_2 contents of the rocks range from ∼71.3 wt% to ∼79.1 wt%. The rocks are chemically ferroan (Fe* = 0.83 to 0.96), peraluminous (A/CNK = 1.0 to 1.1), and calc-alkalic to calcic (**Figure 4**; Frost et al., 2001). The rocks from Taipa and Coloane are broadly similar in composition. The rocks are more potassic than sodic as their K_2O/Na_2O ratios tend to be >1 but there are six samples that have a ratio close to or below 1. The Mg# of the rocks is generally between ∼15 and ∼26 but there are two samples with low values (∼14 and ∼7). The TiO_2, MnO, and P_2O_5 are all <0.25 wt%. All rocks have normative

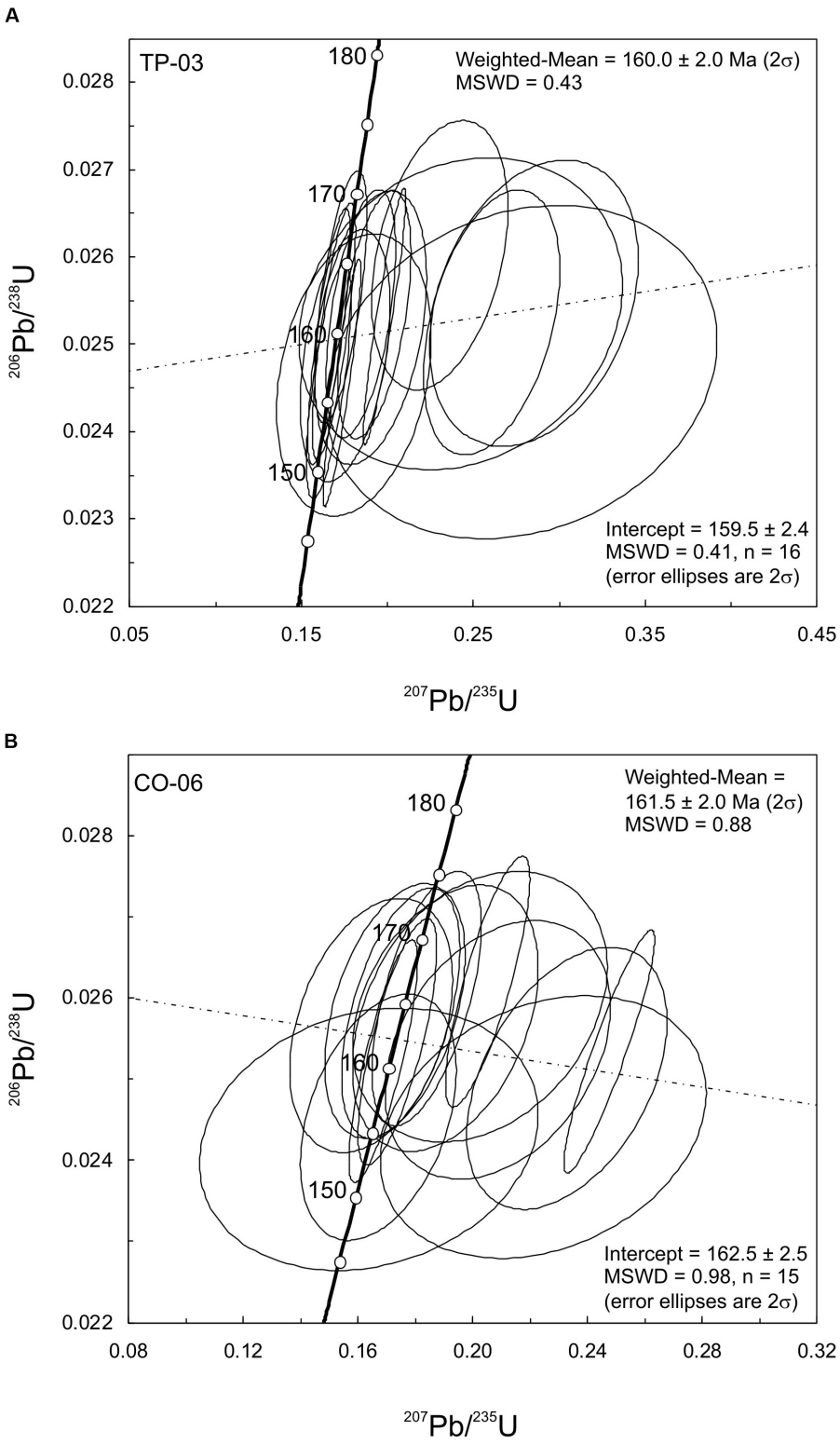

FIGURE 3 | (A) Concordia diagram with the weighted-mean age of zircon U-Pb data from TP-03. **(B)** Concordia diagram with the weighted-mean age of zircon U-Pb data from CO-06.

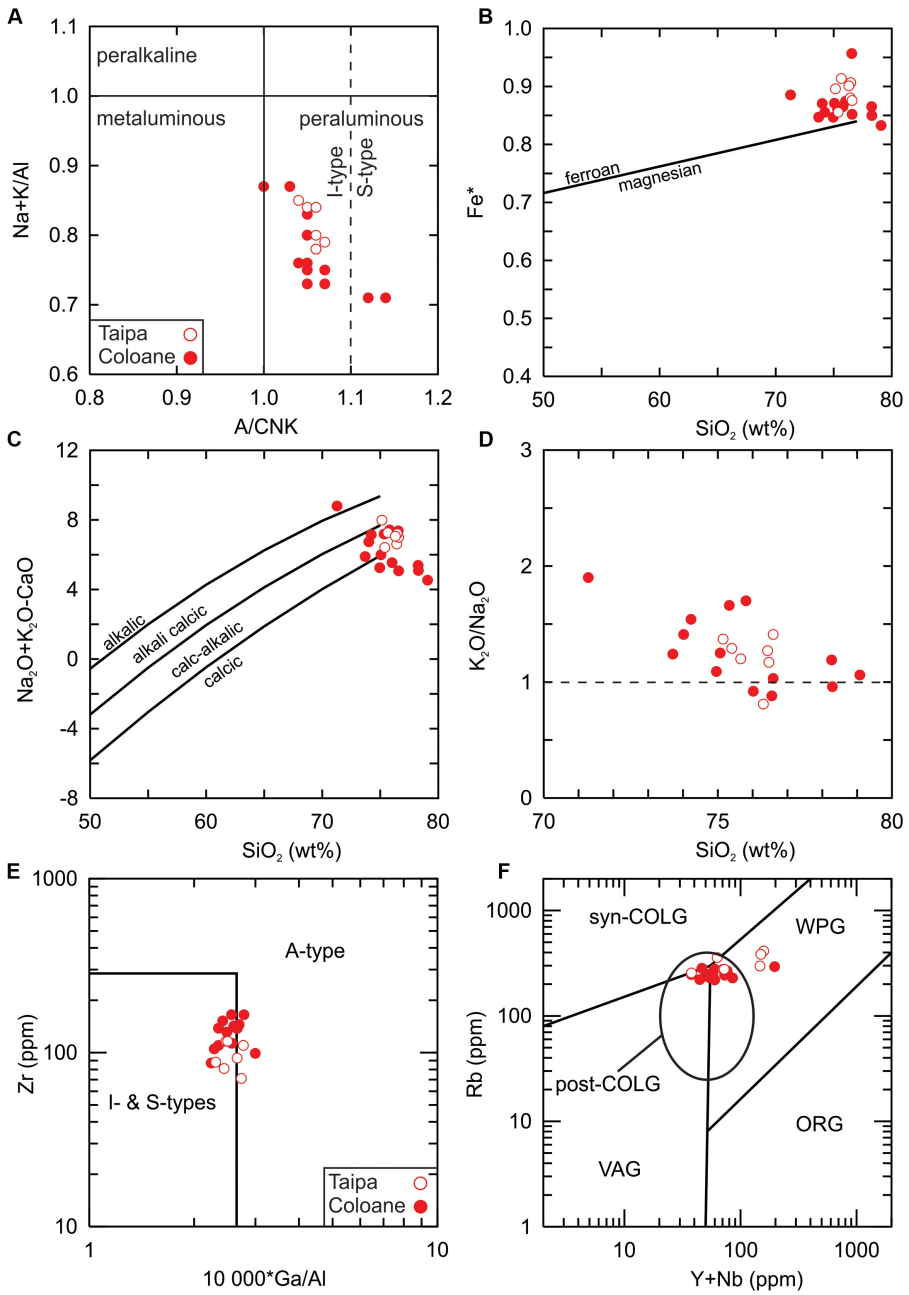

FIGURE 4 | Major element classification plots of the leucogranites from Taipa and Coloane. **(A)** Alkali index (Na + K/Al) vs. aluminum saturation index (ASI = Al/Ca + Na + K). Classification of the granites according to scheme of Frost et al. (2001) using **(B)** the Fe* [FeOt/(FeOt + MgO)] value and **(C)** the modified alkali-lime index ($Na_2O + K_2O$-CaO) vs. SiO_2 (wt%). **(D)** K_2O/Na_2O vs. SiO_2 showing the potassic nature of the rocks. **(E)** Tectonomagmatic discrimination of granitic rocks using the criteria of Whalen et al. (1987). **(F)** Classification of granitic rocks using Rb (ppm) vs. Y + Nb (ppm) of Pearce (1996). Syn-COLG, syn-collisional granite; WPG, within-plate granite; VAG, volcanic-arc granite; ORG, ocean-ridge granite; post-COLG, post-collisional granite.

quartz, plagioclase, orthoclase, corundum, hypersthene, ilmenite, magnetite, and apatite. The normative corundum is between ∼0.1 and ∼1.5 vol% which straddles the divide between the classification of I-type and S-type granite (Chappell and White, 1974). The low loss on ignition values (<0.9%) suggests the rocks did not experience significant post-emplacement hydrothermal alteration. Tectonomagmatic discrimination diagrams indicate the rocks straddle the boundary between within-plate (A-type) and volcanic-arc (I-type) granites suggesting they may be similar to post-collisional granites (**Figures 4E,F**; Whalen et al., 1987; Pearce, 1996).

The trace element compositions of Taipa and Coloane are characterized by low concentrations of transition metals with Sc (∼10 to ∼25 ppm), V (≤16 ppm), Cr (≤4 ppm), Co

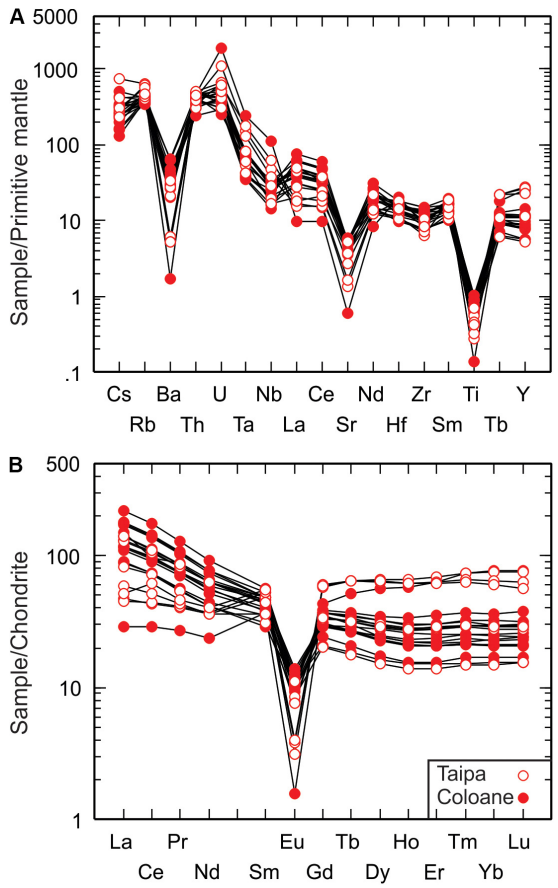

FIGURE 5 | (A) Primitive-mantle normalized incompatible element and **(B)** chondrite normalized rare earth element diagrams of the leucogranites from Taipa and Coloane. Rocks are normalized to values of Sun and McDonough (1989).

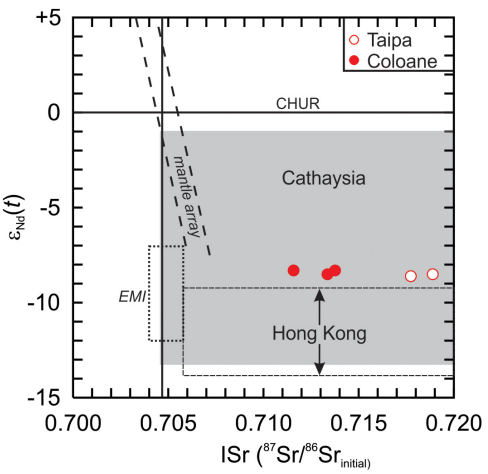

FIGURE 6 | Age corrected Sr-Nd isotopes of the leucogranites from Taipa and Coloane. Range of granitic rocks from the Cathaysia Block in gray (Chen and Jahn, 1998). The Sr-Nd range of Jurassic granitic rocks from Hong Kong (HK) from Darbyshire and Sewell (1997). EMI = enriched mantle I (Zindler and Hart, 1986); CHUR = chondrite uniform reservoir.

(≤3 ppm), and Ni (≤7 ppm) all less than 30 ppm. The contents of Rb (219 to 412 ppm), Zr (71 to 165 ppm), Sr (28 to 122 ppm), and Ba (43 to 460 ppm) are high and somewhat variable. The Th (20 to 43 ppm) and U (5 to 40 ppm) contents are relatively high compared to average upper crust values (Th = 10.5 ppm; *U* = 2.7 ppm; Rudnick and Gao, 2003). The primitive mantle normalized incompatible patterns of all rocks are similar with negative anomalies of Ba, Nb, Sr and Ti (**Figure 5A**). The chondrite normalized rare earth element (REE) patterns (**Figure 5B**) are more variable with depleted to enriched La_N/Sm_N (0.8-3.9) ratios and flat to enriched heavy REE patterns (Gd_N/Yb_N = 0.6−1.5). All samples have negative Eu-anomalies (Eu/Eu^* = 0.07 to 0.44).

Sr-Nd Isotope Geochemistry

A total of eight samples were selected for Sr isotopic analysis whereas six were selected for Nd isotopic analysis (**Table 2**). The initial Sr (I_{Sr}) and Nd isotope ratios were calculated to the emplacement age of 162 Ma. The I_{Sr} of the granites shows a wide range from 0.71156 to 0.72477. The large range is likely due to error propagation related to some samples having high (>10) $^{87}Rb/^{86}Sr$ ratios (Jahn, 2004). In fact, the rocks from Taipa have the highest $^{87}Rb/^{86}Sr$ ratios (13.518 to 42.293) and the widest I_{Sr} range (0.009) whereas the rocks from Coloane have lower and more restricted $^{87}Rb/^{86}Sr$ ratios (6.188 to 7.074) and a narrower I_{Sr} range (0.002). Consequently, the Sr isotopic values from Coloane are probably more indicative of the magma source (**Figure 6**). The initial $^{143}Nd/^{144}Nd$ ratios have a relatively narrow range (0.511990 to 0.512024) across all samples. The corresponding $\varepsilon_{Nd}(t)$ values range from −7.9 to −8.6 assuming a $^{147}Sm/^{144}Nd$ ratio of 0.1967 and $CHUR_{today}$ value of 0.512638. There is no significant difference between the rocks from Taipa and Coloane. The T_{DM} ages range from 2420 Ma to 1683 Ma for the samples with $^{147}Sm/^{144}Nd$ ratios < 0.165.

DISCUSSION

Emplacement Age and Inheritance Within the Pearl River Estuary Granites

The rocks of Macau, Taipa and Coloane were dated by isotope dilution (ID) TIMS and laser ablation multi-collector ICP-MS (Quelhas et al., 2020). The ages cluster into two distinct populations. The older rocks from Taipa and Coloane are Oxfordian (164.5 ± 0.6 Ma to 162.9 ± 0.7 Ma) whereas the younger rocks from peninsular Macau are Kimmeridgian (156.6 ± 0.2 Ma to 155.5 ± 0.8 Ma). Two dykes that intrude Taipa (~150 Ma) and Coloane (<119.7 ± 0.1 Ma) yielded the youngest ages. The zircon geochronology results from this study yielded ages within uncertainty of the TIMS ages for Taipa and Coloane. Sample TP-03 yielded a weighted-mean $^{206}Pb/^{238}U$ age of 160.0 ± 2.0 Ma whereas CO-06 yielded an age of 161.5 ± 2.0 Ma. All of the reported ages indicate that magmatism in Macau corresponds to the early period of the Yanshanian

Orogeny although the Kimmeridgian rocks probably indicate the waning stages of magmatism.

Across the Pearl River estuary, detailed geochronology and geochemical investigations of the silicic rocks of Hong Kong show that the majority of granites and rhyolites were emplaced during two periods: (1) 164.6 ± 0.2 Ma to 159.3 ± 0.3 Ma, and (2) 146.6 ± 0.2 Ma to 140.4 ± 0.2 Ma with two minor intrusions emplaced at 151.9 ± 0.2 Ma to 148.1 ± 0.2 Ma (Davis et al., 1997; Sewell et al., 2012). Moreover, the rocks show a compositional evolution from calc-alkaline, through high-K calc-alkaline, to transitional shoshonite that is thought to be related to a change in the tectonic regime from subduction-related to extension-related (Sewell and Campbell, 1997). The Oxfordian ages of Taipa and Coloane are within the uncertainty of ages reported from the period 1 (164.6 ± 0.2 Ma to 159.3 ± 0.3 Ma) granites of Hong Kong suggesting there could be a voluminous, contiguous batholith comprised of a number of individual plutons that extends across the Pearl River estuary (Davis et al., 1997; Sewell et al., 2012). The younger ages (Tai Lam < 159.6 ± 0.5 Ma; Tsing Shan = 159.3 ± 0.3 Ma) are still ∼3 Ma older than peninsular Macau indicating there are at least three distinct Late Jurassic pulses. The relative quiescence of magmatism between the Kimmeridgian rocks and the Tithonian to Berriasian (146.6 ± 0.2 Ma to 140.4 ± 0.3 Ma) granites of Hong Kong marks the transition from the Early Yanshanian to the Late Yanshanian Orogeny and may be related to change from a flat slab collisional regime to one of back-arc extension and high angle subduction (Zhu et al., 2014).

The leucogranites from this study revealed three (2 Triassic, 1 Jurassic) distinct populations of inherited zircons. The oldest population is Carnian. The combined four zircons (2 from Taipa and 2 from Coloane) yield $^{206}Pb/^{238}U$ ages from 222 ± 12 Ma to 234 ± 6 Ma (1σ). The middle population is the smallest (3 zircons), exclusively derived from Taipa, and Norian in age. The individual ages range from 207 ± 5 Ma (2σ) to 217 ± 5 (1σ). The largest population of inherited (15) zircons are Toarcian and found in both intrusions but are more abundant in Coloane (11) relative to Taipa (4). The weighted-mean $^{206}Pb/^{238}U$ age for all Toarcian zircons is 173.4 ± 2.3Ma (2σ). One zircon included in the Toarcian age from Coloane is 187 ± 14 (1σ) and statistically anomalous. Consequently, it is likely that there is a major Middle Triassic to Early Jurassic component in the crust around the Pearl River estuary.

The three groups of inherited zircons identified in our study overlap with single ID-TIMS analysis reported from Hong Kong (192.4 ± 0.5 Ma, 181.5 ± 0.7 Ma, 176.9 ± 0.5 Ma), Taipa (172.6 ± 3.6 Ma), and Coloane (204.2 ± 0.2 Ma). Moreover, a single Middle Triassic age of <236.3 ± 0.8 Ma was reported for the two-mica Deep Bay pluton located between Hong Kong and Shenzhen (**Figure 1C**). Inherited zircons measured by *in situ* methods reported by Quelhas et al. (2020) shows there are single zircons of Toarcian, Pliensbachian, and Norian ages but also there are Devonian, Silurian, Neoproterozoic (∼900 Ma to ∼700 Ma), Mesoproterozoic (∼1100 Ma), Paleoproterozoic (∼2400 Ma) and Archean (∼3300 Ma) zircons. Thus, the formation of the granitic rocks in Hong Kong and Macau involved recycling of Early Yanshanian rocks and crustal material dating to the formation of the Cathaysia Block until their emplacement during the Oxfordian (Xu et al., 2007; Zhu et al., 2014).

Petrogenesis of the Taipa and Coloane Granites

Tectonomagmatic Classification

The granites from Taipa and Coloane are somewhat unusual as they tend to defy numerous granite classification schemes (**Figures 4E,F**, **7**). For example, their ASI values are mostly weakly peraluminous (A/NCK < 1.1) but there are two samples with higher values (>1.1). The division between I-type and S-type granite according to Chappell and White (2001) is ∼1.1. Moreover, all rocks have normative corundum <1%, hornblende is uncommon, Na_2O tends to be but not always <3.2 wt% in rocks with ∼5 wt% K_2O, the rocks straddle the boundary between A-type and I- and S-type in the classification of Whalen et al. (1987), and fall along the boundary between syn-collisional, post-collisional, and within-plate granite of the Rb-Y + Nb diagram of Pearce (1996).

According to the classification scheme of Frost et al. (2001), the rocks from Taipa and Coloane are ferroan, and calc-alkalic to calcic. Rocks of this composition are considered to be generated by low pressure partial melting of the crust (Frost and Frost, 2011). A crustal origin is very likely as the isotopes, trace element ratios, and inherited zircons are all consistent with an enriched source (**Figure 6**). The petrogenesis will be discussed in more detail below but a crustal origin does not help to constrain the likely tectonic environment (i.e., compression vs. extension) during emplacement. The discrimination of granites by Maniar and Piccoli (1989) categorizes rocks into seven tectonic environments using major element data. The granites from Taipa and Coloane consistently fall within the post-orogenic granite (POG) field and the CaO/Na_2O and Al_2O_3/TiO_2 ratios indicate the rocks are strongly peraluminous post-collisional granites (**Figures 7A–C**; Sylvester, 1998). Furthermore, the rocks are broadly similar to the high-K calc-alkaline granites (KCG) of Barbarin (1999). The KCG are described as being present in various geodynamic environments but mainly associated with the transition from compressional regimes to tensional regimes. The broad consistency between of the classification schemes of Maniar and Piccoli (1989), Pearce (1996), Sylvester (1998), Barbarin (1999) suggest the rocks were likely emplaced during a period of crustal relaxation and are best described as post-collisional granites.

Magmatic Conditions

Common minerals (biotite, hornblende) and mineral pairs (ilmenite, magnetite) of granitic rocks can be used to estimate the thermodynamic conditions (temperature, relative oxidation state, pressure) of their crystallization (Hammarstrom and Zen, 1986; Frost et al., 1988; Shabani et al., 2003; Uchida et al., 2007; Mutch et al., 2016). The estimates can then provide constraints on the formation and evolution of their parental magma. The granitic rocks from Taipa and Coloane do not contain significant quantities of amphibole or Fe-Ti oxide minerals. However, the crystallization temperature (Luhr et al., 1984), pressure (Uchida

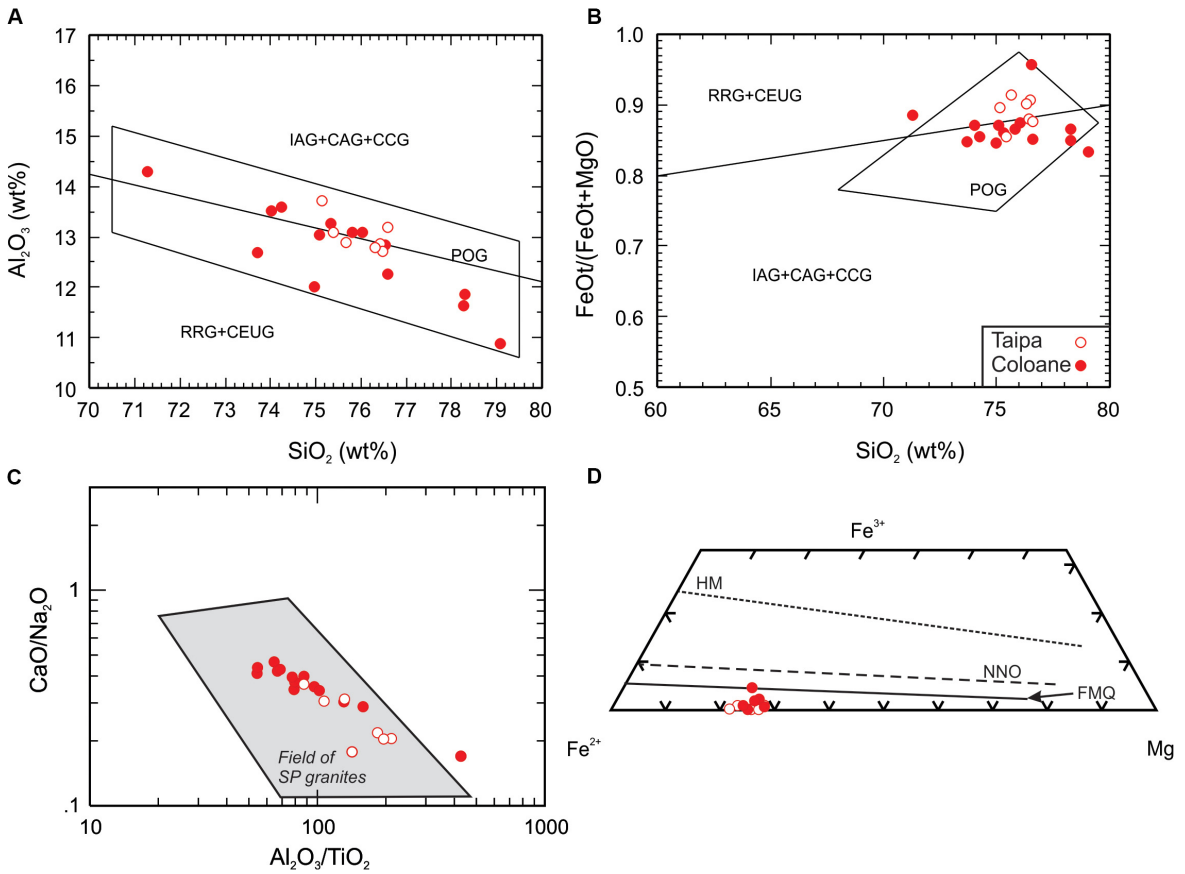

FIGURE 7 | Tectonomagmatic discrimination of granitic rocks and biotite composition redox estimates. **(A)** Distinction between collisional (IAG + CAG + CCG) and non-collisional (RRG + CEUG) granites using Al_2O_3 (wt%) vs. SiO_2 (wt%). **(B)** Distinction between collisional (IAG + CAG + CCG) and non-collisional (RRG + CEUG) granites of Maniar and Piccoli (1989) using FeOt/(FeOt + MgO) vs. SiO_2 (wt%). FeOt, total Fe expressed as Fe_2O_3 wt% * 0.8998. RRG, rift-related granitoids; CEUG, continental epeirogenic uplift granitoids; POG, post-orogenic granitoids; IAG, island arc granitoids; CAG, continental arc granitoids; CCG, continental collision granitoids. **(C)** CaO/Na_2O vs. Al_2O_3/TiO_2 classification of strongly peraluminous granitic rocks. **(D)** Composition of biotite from the Taipa and Coloane leucogranites express in the Fe^{2+}-Fe^{3+}-Mg diagram from Wones and Eugster (1965). FMQ, fayalite-magnetite-quartz buffer; NNO, Ni-NiO buffer; HM, hematite-magnetite-buffer.

et al., 2007), and redox state (Wones and Eugster, 1965; Shabani et al., 2003) can be estimated based on the composition of biotite.

The crystallization temperature of biotite may be estimated in granitic rocks using the equation (1) of Luhr et al. (1984):

$$T\,(K) = \frac{838}{1.0337 - \frac{Ti}{Fe2+}} \quad (1)$$

The magmatic biotite thermometry estimates, as calculated by the equation reported, ranges from ~930 K to ~890 K (~650°C to ~610°C). The temperatures are relatively low as it is thought that granitic solidification should occur around 650°C to 700°C (Freiberg et al., 2001) but it is possible that solidification can extend to lower (<650°C) temperatures. Glazner and Johnson (2013), Challener and Glazner (2017) suggest that repeated cycles of heating and fluxing by water-rich fluids may allow the crystallization of many minerals in calc-alkalic granites to be lower than 650°C and thus consolidation temperatures may also be lower. Regardless, we think the highest biotite crystallization temperature (~650°C) is probably representative of the crystallization temperature of biotite in this system. The highest temperature (~650°C) is within the uncertainty (±40°C) of the zircon saturation temperatures (T_{Zr}°C = 751°C to 681°C) estimated from the whole rock data but is generally lower (Boehnke et al., 2013). The different temperature estimates between the two methods is not surprising as the crystallization temperature of zircon is variable but tends to be higher than for biotite (Harrison et al., 2007). Moreover, the inheritance-rich nature of the granites from Taipa and Coloane is consistent with the generally lower T_{Zr}°C values but also that it probably required fluid fluxing for melting initiation (Miller et al., 2003). Therefore it is likely that the initial magmatic temperature was generally low (e.g., ≤850°C) but closer to the highest zircon saturation temperature estimates and that biotite crystallized relatively late.

The Al-in-hornblende geobarometer is one of the few methods that can estimate crystallization pressure within granitic systems but in the absence of hornblende there are few minerals or mineral pairs that could constrain the depth of crystallization (Hammarstrom and Zen, 1986; Mutch et al., 2016). Uchida et al.

(2007) demonstrated that Al-in-biotite appears to be sensitive to pressure in a manner similar to Al-in-hornblende and is a potentially more robust geobarometer due to its ubiquity with granitic rocks (equation 2).

$$P\ (kbar) = 3.33Al^{T} - 6.53\ (\pm 0.33) \quad (2)$$

Using the equation of Uchida et al. (2007), we calculated the crystallization pressure of the magmatic biotite from this study. The pressure estimates range from 1.48 kbar to 3.28 kbar. The variability in the pressure estimates could be an artifact related to redistribution of biotite that crystallized at different pressure within the magma system during emplacement. Nevertheless, the results suggest the granites of Taipa and Coloane were emplaced between ∼5.5 km and ∼12.1 km depth.

The relative oxidation state of biotite can be estimated using the Fe^{2+}-Fe^{3+}-Mg components (Wones and Eugster, 1965; Shabani et al., 2003). The Fe^{3+} content of the magmatic biotite from this study was not directly measured but was estimated using charge balance (Nenova, 1997). The results show that the biotite from Taipa and Coloane are close to the fayalite-magnetite-quartz (FMQ) buffer (**Figure 7D**). If we convert the biotite chemistry results to log fO_2 values using the pressure estimates then they range from −19.01 to −20.17 that is equivalent to ΔFMQ −1 (ΔFMQ = −0.96 to −1.00) and reducing conditions.

Fractional Crystallization Modeling

The granites from Taipa and Coloane are compositionally similar and highly silicic (SiO_2 > 72 wt%) but there is chemical variability between the least (CO-08) silicic sample and the most (CO-02) silicic sample. However, in comparison, most (TiO_2, Fe_2O_3t, MgO, CaO, P_2O_5) major elements do not show clear evolutionary trends with respect to SiO_2 but, Al_2O_3, Na_2O, and K_2O clearly decrease with increasing SiO_2. Given that the feldspars and quartz are the main constituents of the rocks it is likely that the negative trends of alumina and alkalis are a consequence of their crystallization. Therefore, in order to test this hypothesis we apply fractional crystallization modeling using the program MELTS (Smith and Asimow, 2005).

We use the least "evolved" composition (CO-08) as the parental magma, the redox condition and pressure estimates from the biotite mineral chemistry, and the two-feldspar mineralogy to constrain the water content. Based on the biotite composition, the redox condition used for the model is ΔFMQ -1. The pressure estimates from the biotite cover a wide range from ∼0.15 GPa to ∼0.33 GPa (∼5.5 to ∼12.1 km depth) suggesting that the plutons may have crystallized over a depth of ∼7 km. Therefore, we selected a pressure of 0.2 GPa for the model. The water content is difficult to estimate as biotite is the primary volatile-rich mineral but due to the presence of two feldspars we suggest the magma was originally water-rich and thus select near water-saturation (H_2O = 4.0 wt%) conditions.

The evolution of the liquid composition is shown in **Figure 8** at 10°C intervals and the fractionation assemblage and modal proportions are summarized in **Table 3**. The entire results are in **Supplementary Table S5**. The liquidus temperature is 870°C as alkali feldspar ($An_1Ab_{24}Or_{76}$) is the first mineral to crystallize and is followed by plagioclase ($An_{22}Ab_{70}Or_8$) at 770°C, clinoamphibole (anthophyllite) at 760°C, ilmenite at 750°C, and olivine (Fo_8) at 730°C. As the model reaches the terminal temperature (650°C), quartz (710°C), and aluminous minerals (garnet at 670°C, cordierite at 660°C, and sillimanite at 650°C) begin to crystallize. The chemical variability of the granites is reproduced across all elements by 740°C after ∼42% fractionation composed of sodic plagioclase (∼6.1%), alkali feldspar (∼35.1%), ilmenite (∼0.04%) and clinoamphibole (∼0.8%). The modeling results indicate that the chemical variability in the granites is principally controlled by alkali feldspar and plagioclase. This is consistent with the whole rock trace element compositions as Ba, Sr, and Eu/Eu* decrease with increasing SiO_2. Furthermore, the results are applicable for both groups of granites (Taipa and Coloane) suggesting it is possible that they are members of the same intrusive body rather than separate plutons or magma batches.

Magma Source

The geochemical and isotopic evidence indicates that the leucogranites are derived from the crust with limited or no input from the mantle. As discussed earlier, peraluminous, ferroan, and calc-alkalic to calcic granitoids are interpreted to be products of partial melting of quartzofeldspathic crust (Frost and Frost, 2011). The enriched whole rock Nd isotopes are consistent with a crustal source for the parental magmas of Taipa and Coloane as they overlap with the basement rocks of the Cathaysia Craton (**Figure 6**). The zircon Hf isotopes indicate there is no significant difference between the two islands although the Oxfordian zircons tend to have slighter higher $\varepsilon_{Hf}(t)$ values from Taipa (weighted-mean = −5.6 ± 0.7, 2σ) than Coloane (weighted-mean = −6.5 ± 0.6, 2σ) but the weighted-mean values are within uncertainty. The Toarcian inherited zircons from each island cannot be readily distinguished from their main Oxfordian populations suggesting the source of the two magmatic pulses was either similar or the same. Moreover, the zircon Hf crustal evolution model ages (∼1730 Ma to ∼1410 Ma) and whole rock Nd model ages (∼2420 Ma to ∼1680 Ma) are contemporaneous with a major crustal event in Cathaysia during the Paleoproterozoic (Chen and Jahn, 1998).

The primitive mantle normalized incompatible element patterns have depletions of Nb-Ta, and enrichment of Th-U that are associated with continental crust (Rudnick and Gao, 2003). Consequently, the trace element ratios such as Th/Nb, Nb/U, and Th/Yb are very high and extend beyond average upper crust values of Wedepohl (1995); Rudnick and Gao (2003) (**Figure 9**). The biotite chemistry is consistent with granitic rocks that are strongly contaminated and reduced and also within the range of S-type granites (**Figure 9**; Abdel-Rahman, 1994; Shabani et al., 2003). A crustal origin is also consistent with high Rb/Sr (2 to 46) ratios as it is similar to peraluminous low-Sr, leucogranites that are derived from melting of a metasedimentary source (**Figure 10A**; Patiño Douce, 1999; Altherr et al., 2000; Kemp and Hawkesworth, 2003). A comparison between the whole rock composition of the Taipa and Coloane leucogranites and melt compositions generated from metasedimentary and metabasaltic rocks show an affinity for a metagraywacke or a clay-rich source (**Figures 10B,C**). Furthermore, the wide age range of inherited

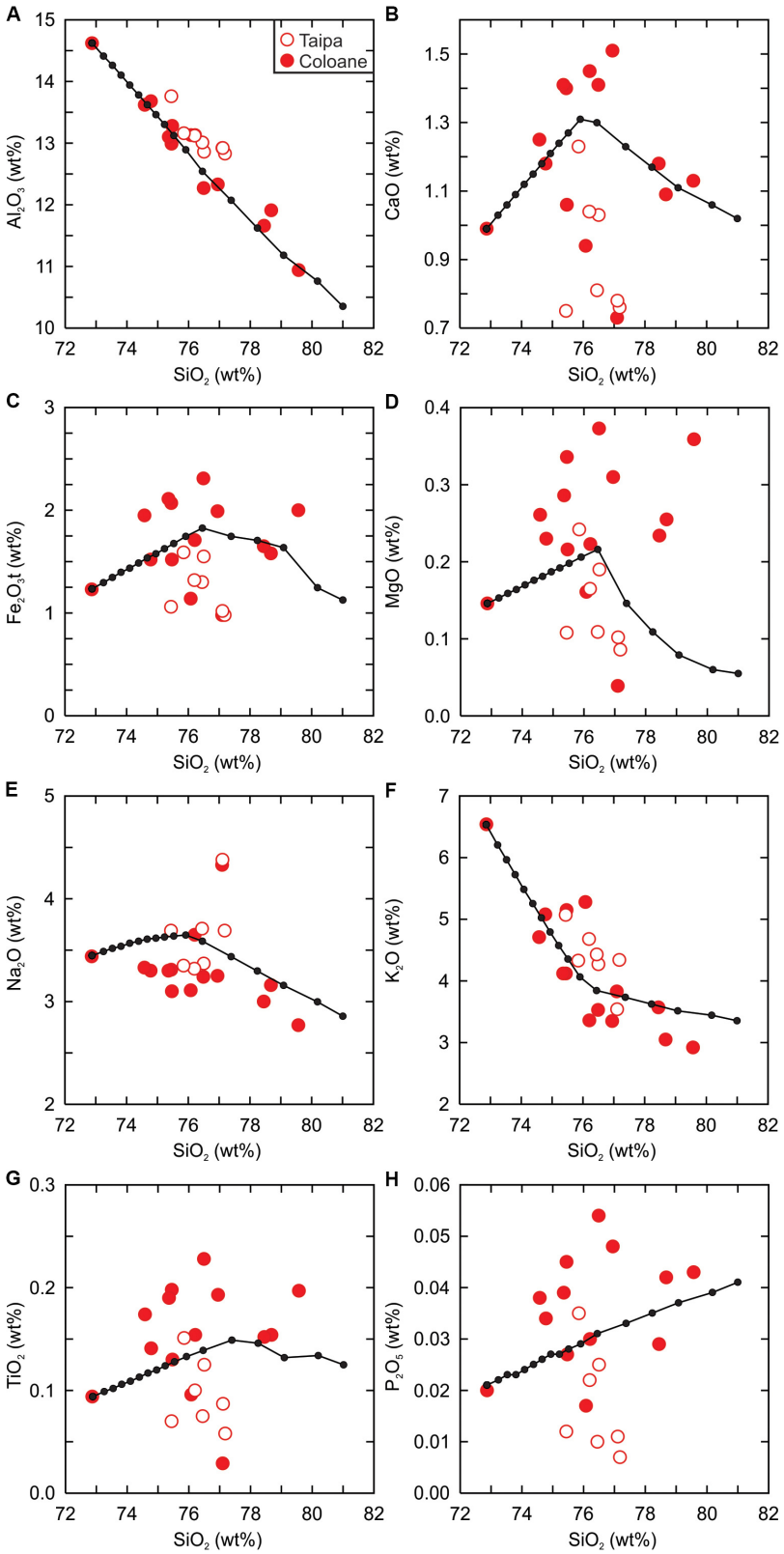

FIGURE 8 | MELTS fractional crystallization modeling of the leucogranites showing the major element liquid composition evolution curves. **(A)** Al_2O_3 (wt.%) vs. SiO_2 (wt%), **(B)** CaO (wt.%) vs. SiO_2 (wt%), **(C)** Fe_2O_3t (wt.%) vs. SiO_2 (wt%), **(D)** MgO (wt.%) vs. SiO_2 (wt%), **(E)** Na_2O (wt.%) vs. SiO_2 (wt%), **(F)** K_2O (wt.%) vs. SiO_2 (wt%), **(G)** TiO_2 (wt.%) vs. SiO_2 (wt%), and **(H)** P_2O_5 (wt.%) vs. SiO_2 (wt%). The model shows the liquid compositions at 10°C intervals (solid black dots). All data recalculated on an anhydrous basis.

TABLE 3 | Summary of mineral fractionation and modes of the MELTS models.

	FMQ−1		
Mineral	**Temp. (°C)**	**Composition**	**Modal %**
Afs	870–650	$An_1Ab_{24-22}Or_{76-78}$	50.2
Pl	770–650	$An_{22-29}Ab_{70-67}Or_{8-4}$	19.9
Il	750–650		0.2
Cam	760–750, 680		0.8
Ol	730–680	Fo_{8-10}	1.1
Qz	710–650		23.7
Grt	670–650	$Py_{13-16}Al_{80-77}Gr_{7-6}$	0.02
Crd	660–650		0.003
Sil	650		0.03

Afs, alkali feldspar; Pl, plagioclase; Il, ilmenite; Cam, clinoamphibole (anthophyllite); Ol, olivine; Qz, quartz; Grt, garnet; Crd, cordierite; Sil, sillimanite. Mineral abbreviations from Whitney and Evans (2010). An, anorthite component; Ab, albite component; Or, orthoclase; Fo, forstertite component; Py, pyrope component; Al, almandine component Gr, grossular component.

zircons favors a sedimentary source as Mesozoic sedimentary rocks deposited near the margin of Cathaysia could conceivably contain Archean (∼3300) to Phanerozoic (∼174 Ma) zircons.

Additional supporting evidence of a sedimentary source origin of the leucogranites is the presence of garnet. Garnet is a common accessory mineral within S-type granites due to excess Al in the source rocks (Sylvester, 1998; Chappell and White, 2001). The spessartines of this study are compositionally similar to magmatic garnet from silicic plutonic rocks (Miller and Stoddard, 1981). Due to the decomposition reaction of chlorite-chloritoid, almandine garnet is more common in metapelitic/metapsammitic rocks and thus is more likely to exert influence on the magma composition by increasing maficity (Mg + Fe mol/100g) and heavy rare earth element concentrations, and decreasing Si content (Stevens et al., 2007). Thus, whole rock correlations between maficity, Si (mol/100g), Ca (mol/100g), and heavy are earth elements (HREE) can indicate the influence of peritectic garnet in the magma system (Stevens et al., 2007; Villaros et al., 2009). In the case of Taipa and Coloane, it appears that peritectic garnet was not an influence in the magma system as maficity does not significantly increase with decreasing Si, or increasing Ca and HREE (**Figure 11**). The implication is that the source rocks did not likely contain garnet and that they were no deeper than ∼10 km depth (≤0.3 GPa) and experienced a maximum metamorphic facies of hornfels before

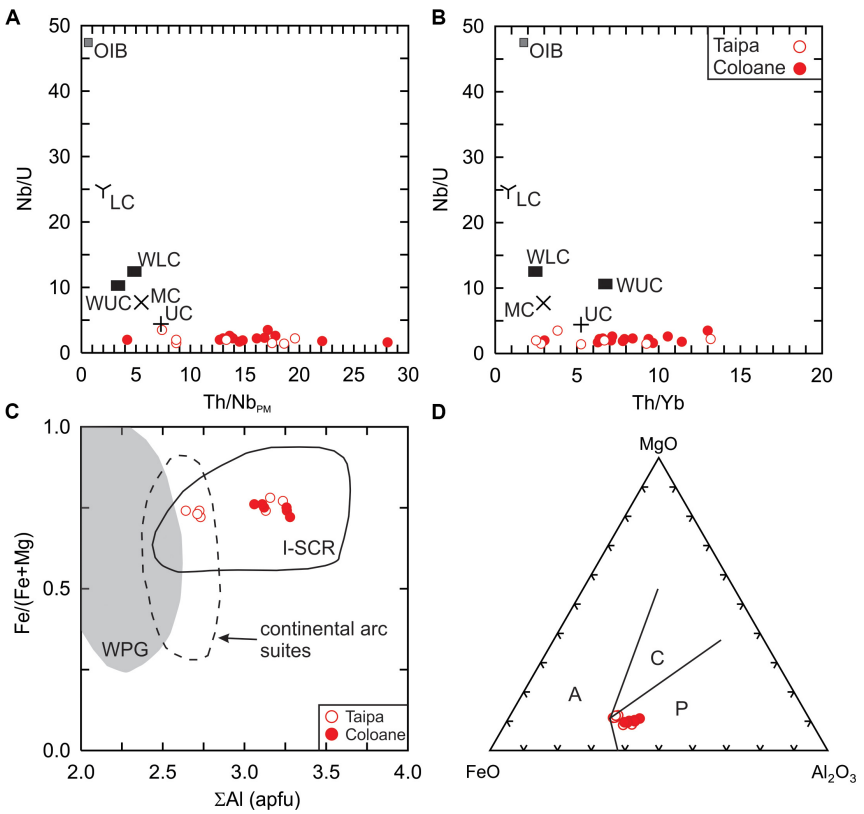

FIGURE 9 | (A) Nb/U vs. Th/NbPM and **(B)** Nb/U vs. Th/Yb of the Taipa and Coloane leucogranites. PM = primitive mantle normalized. UC = upper crust, MC = middle crust, LC = lower crust of Rudnick and Gao (2003). WUC = upper crust of Wedepohl (1995), WLC = lower crust of Wedepohl (1995). OIB = ocean-island basalt of Sun and McDonough (1989). **(C)** Composition of biotite from the Taipa and Coloane leucogranites expressed as Fe/(Fe+Mg) vs. total (S) Al (apfu) with respected to biotite from within-plate (A-type) granites, continental arc suites, and strongly contaminated and reduced I-type (I-SCR) granites (Shabani et al., 2003). **(D)** FeO_{total}-MgO-Al_2O_3 discrimination diagram for biotite from anorogenic alkaline suites (A), in peraluminous (including S-type) suites (P), and calc-alkaline orogenic suites (C) from Abdel-Rahman (1994).

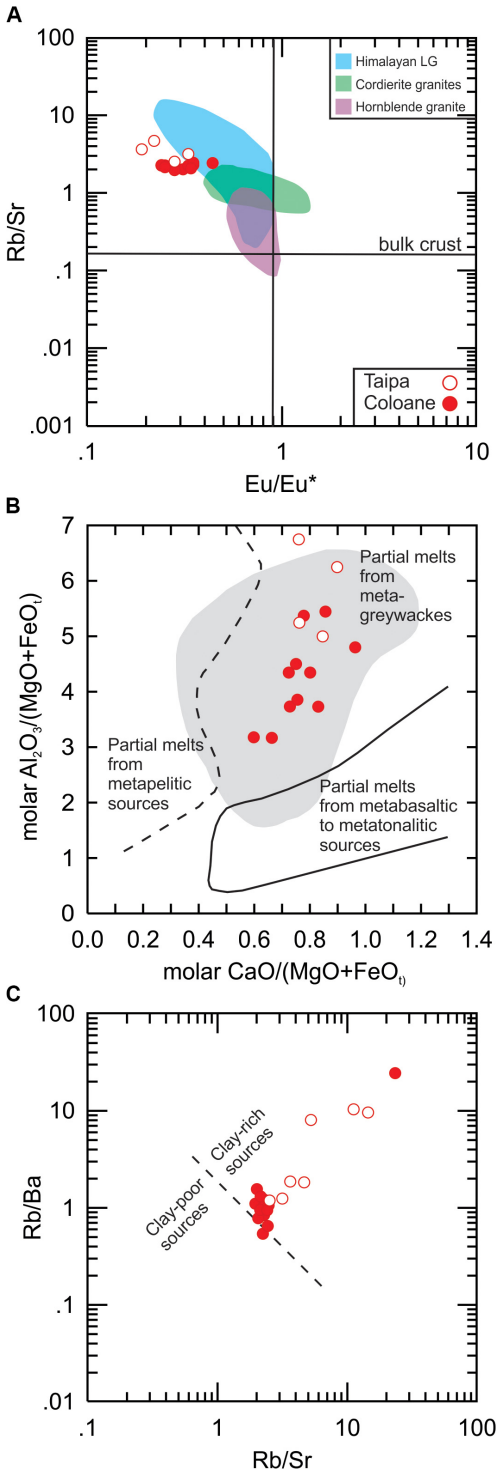

FIGURE 10 | (A) Logarithmic Sr/Rb vs. Eu/Eu* plot of the Taipa and Coloane leucogranites with ranges of hornblende granites, Himalayan leucogranites, and cordierite granites from Kemp and Hawkesworth (2003). **(B)** Molar Al_2O_3/(MgO + FeOt) vs. molar CaO/(MgO + FeOt) with the fields outlining compositions of melts derived by dehydration melting of different bulk compositions (Altherr et al., 2000). **(C)** Post-collisional strongly peraluminous granites divided into clay-poor and clay-rich sources on the basis of Rb/Ba and Rb/Sr (Sylvester, 1998).

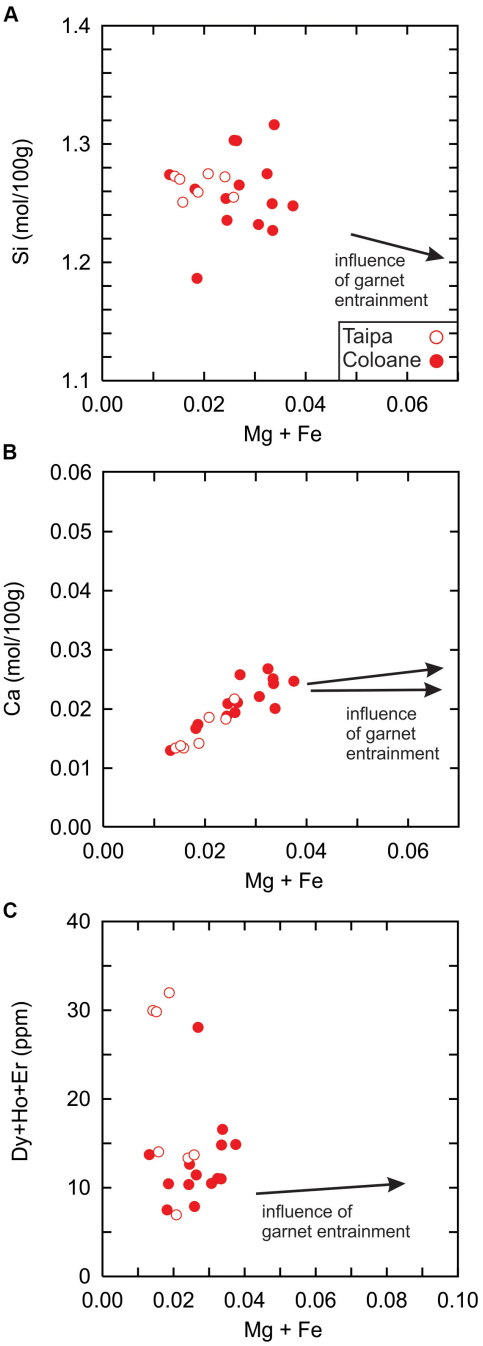

FIGURE 11 | (A) Si (molar) vs. maficity (Mg + Fe molar) of the Taipa and Coloane leucogranites. **(B)** Ca (molar) vs. K (molar) of the Taipa and Coloane granites. **(C)** Dy + Ho + Er vs. maficity (Mg + Fe molar) of the Taipa and Coloane leucogranites. The direction of garnet entrainment from Stevens et al. (2007).

melting. The flat chondrite normalized heavy rare earth element patterns (Gd_N/Yb_N = 0.6–1.5) of the rocks is also consistent with the absence of residual garnet in the source (**Figure 5B**). The precise source rock of the leucogranites is uncertain but is likely to be similar to greywacke or metagreywacke. One possible

candidate for the magma source is the Middle Jurassic Tai O Formation, a fine grained sandstone alternating with siltstone and sandy siltstone, in Hong Kong that may be correlative with the Qiaoyuan Formation in Guangdong (Sewell et al., 2000; Wang et al., 2014).

Implications for the Early Yanshanian Orogeny

The Callovian-Oxfordian stage of the Early Yanshanian Orogeny is markedly different from the Toarcian-Bajocian stage as the nature of the magmatism changes from bimodal to predominately silicic (Li et al., 2007a,b). Moreover, ∼80% or more of the dated Jurassic igneous rocks in the eastern SCB were emplaced during the Callovian-Oxfordian (Li et al., 2007b). The cause of the magmatic flare-up is uncertain but Li and Li (2007); Zhu et al. (2014) suggest that the Callovian-Oxfordian magmatism was related to flat-slab subduction and foundering of the Paleo-Pacific plate followed by mantle up-welling that increased the geotherm and led to volumetrically significant melting of Cathaysia crust. Alternatively, other models suggest that magmatism was related to subduction and slab roll-back of the Paleo-Pacific plate (Jiang et al., 2006, 2009; Wang and Shu, 2012; Zuo et al., 2017).

The leucogranites from Taipa and Coloane based on the distribution of inherited zircons, bulk rock composition, and Sr-Nd-Hf isotopes were primarily derived by partial melting of sedimentary or metasedimentary rocks. The inherited zircons suggest that the source was probably Sinemurian-Pliensbachian in age as it must have accumulated both young and old detritus from the Cathaysia Block. Moreover, the modeling results, temperature and pressure estimates, and bulk rock composition are similar to the genesis of leucogranites that are derived by decompressional melting after the collapse of thickened crust (Sylvester, 1998; Castro et al., 2000; Clemens, 2003; Collins and Richards, 2008). Such a scenario is sufficient to induce melting at lower pressure and is applicable to the rocks of Taipa and Coloane as there is little evidence (e.g., mafic dykes) that indicates a high thermal regime occurred during the Oxfordian (Castro et al., 2000; Li et al., 2004, 2007a,b; Deng et al., 2019).

Whether flat-slab subduction and foundering or subduction and roll-back of the Paleo-Pacific plate was the reason, it is clear there was a major period of magmatism throughout the interior and margin of the eastern SCB from ∼170 Ma to ∼150 Ma and that mafic magmatism was volumetrically minor. The likely scenario for the genesis of the Taipa and Coloane leucogranites is decompression and dehydration melting of the lower upper crust to upper middle crust during a period of extension. The thermal regime associated with the emplacement of the leucogranites is consistent with the limited amount or absence of mafic magmatism during the Callovian-Oxfordian in the region. The location of Taipa and Coloane seems to favor a lithotectonic process that is related to subduction and roll-back as this could not only affect a large area extending from the interior to the margin of Cathaysia but could also induce crustal thinning.

CONCLUSION

The spessartine-bearing biotite leucogranites from Taipa and Coloane were emplaced during the Late Jurassic (Oxfordian) period of the Yanshanian Orogeny. The biotite chemistry and petrological modeling indicates that the chemical variability within the leucogranites can be attributed to hydrous fractional crystallization at upper to middle crust depth (∼5 to ∼12 km) under reducing conditions (ΔFMQ −1). The Sr-Nd-Hf isotopes [I_{Sr} = 0.71156 to 0.72477; $\varepsilon_{Nd}(t)$ = −7.9 to −8.6; $\varepsilon_{Hf}(t)$ = −3.8 to −8.8], incompatible trace element ratios, and whole rock composition indicates that the leucogranites were derived by partial melting of a sedimentary or metasedimentary source that was comprised of detritus from the Cathaysia Block. Tectonomagmatic discrimination diagrams are consistent with emplacement at a post-collisional tectonic setting. The islands of Taipa and Coloane are very likely the same intrusion and it is possible that they may be members of a larger batholith that extends across the Pearl River estuary to Hong Kong. The formation of the Taipa and Coloane S-type leucogranites is attributed to decompressional melting associated with a period of crustal relaxation or tensional plate stress that may have occurred during the transition from low angle subduction to high angle subduction of the Paleo-Pacific plate.

DATA AVAILABILITY STATEMENT

All datasets generated for this study are included in the article/ **Supplementary Material**.

AUTHOR CONTRIBUTIONS

JS conceived the study, collected the samples, and wrote the manuscript. MV assisted in fieldwork and contributed to the ideas expressed. H-YL and YI contributed to the zircon Hf isotope and mineral chemistry measurements. All authors contributed to the manuscript, read, and approved the submitted version.

FUNDING

This project received support from the Ministry of Science and Technology (Taiwan) through grant 107-2628-M-003-003-MY3.

ACKNOWLEDGMENTS

PF is thanked for editorial handling. We also appreciate the instrumental influence of Mick, Keith, Charlie, and Ron during field work.

SUPPLEMENTARY MATERIAL

The Supplementary Material for this article can be found online at: https://www.frontiersin.org/articles/10.3389/feart.2020.00311/full#supplementary-material

REFERENCES

Abdel-Rahman, A.-F. M. (1994). Nature of biotites from alkaline, calc-alkaline, and peraluminous magmas. *J. Petrol.* 35, 525–541. doi: 10.1093/petrology/35.2.525

Altherr, R., Holl, A., Hegner, E., Langer, C., and Kreuzer, H. (2000). High-potassium, calc-alkaline I-type plutonism in the european variscides: northern Vosges (France) and northern Schwarzwald (Germany). *Lithos* 50, 51–73. doi: 10.1016/s0024-4937(99)00052-3

Andersen, T. (2002). Correction of common lead in U-Pb analyses that do not report 204Pb. *Chem. Geol.* 192, 59–79. doi: 10.1016/s0009-2541(02)00195-x

Andersen, T. (2008). "ComPbCorr-software for common lead correction of U-Th-Pb analyses that do not report 204Pb," in *Laser Ablation-ICP-MS in the Earth Sciences: Current Practices and Outstanding Issues*, ed. P. Sylvester (Quebéc City, QC: Mineralogical Association of Canada), 312–314.

Barbarin, B. (1999). A review of the relationships between granitoids types, their origins and their geodynamic environments. *Lithos* 46, 605–626. doi: 10.1016/s0024-4937(98)00085-1

Blichert-Toft, J., Chauvel, C., and Albarède, F. (1997). The Lu-Hf geochemistry of chondrites and the evolution of the mantle- crust system. *Earth Planet. Sci. Lett.* 148, 243–258. doi: 10.1016/s0012-821x(97)00040-x

Boehnke, P., Watson, E. B., Trail, D., Harrison, T. M., and Schmitt, A. K. (2013). Zircon saturation re-revisited. *Chem. Geol.* 351, 324–334. doi: 10.1016/j.chemgeo.2013.05.028

Castro, A., Corretgé, L. G., El-Biad, M., El-Hmidi, H., Fernández, C., and Patiño Douce, A. E. (2000). Experimental constraints on *Hercynian anataxis* in the Iberian Massif, Spain. *J. Petrol.* 41, 1471–1488. doi: 10.1093/petrology/41.10.1471

Challener, S. C., and Glazner, A. F. (2017). Igneous or metamorphic? hornblende phenocrysts as greenschist facies reaction cells in the half dome granodiorite, California. *Am. Mineral.* 102, 436–444. doi: 10.2138/am-2017-5864

Chappell, B. W., and White, A. J. R. (1974). Two contrasting granite types. *Pacif. Geol.* 8, 173–174.

Chappell, B. W., and White, A. J. R. (2001). Two constrasting granite types: 25 years later. *Aust. J. Earth Sci.* 48, 489–499. doi: 10.1046/j.1440-0952.2001.00882.x

Charvet, J. (2013). The neoproterozoic-early paleozoic tectonic evolution of the South china block: an overview. *J. Asian Earth Sci.* 74, 198–209. doi: 10.1016/j.jseaes.2013.02.015

Chen, J., and Jahn, B.-M. (1998). Crustal evolution of southeastern China: Nd and Sr isotopic evidence. *Tectonophysics* 284, 101–133. doi: 10.1016/s0040-1951(97)00186-8

Chiu, H.-Y., Chung, S.-L., Wu, F.-Y., Liu, D., Liang, Y.-H., Lin, I. J., et al. (2009). Zircon U-Pb and Hf isotopic constraints from eastern transhimalayan batholiths on the precollisional magmatic and tectonic evolution in southern Tibet. *Tectonophysics* 477, 3–19. doi: 10.1016/j.tecto.2009.02.034

Clemens, J. D. (2003). S-type granitic magmas - petrogenetic issues, models and evidence. *Earth Sci. Rev.* 61, 1–18. doi: 10.1016/s0012-8252(02)00107-1

Collins, W. J., and Richards, S. W. (2008). Geodynamic significance of S-type granites in circum-Pacific orogens. *Geology* 36, 559–562.

Corfu, F., Hanchar, J. M., Hoskin, P. W. O., and Kinny, P. (2003). Atlas of zircon textures. *Rev. Mineral. Geochem.* 53, 469–500. doi: 10.2113/0530469

Creaser, R. A., Erdmer, P., Stevens, R. A., and Grant, S. L. (1997). Tectonic affinity of Nisutlin and Anvil assemblage strata from the Teslin tectonic zone, northern Canadian Cordillera: constraints from neodymium isotope and geochemical evidence. *Tectonics* 16, 107–121. doi: 10.1029/96tc03317

Darbyshire, D. P. F., and Sewell, R. J. (1997). Nd and Sr isotope geochemistry of plutonic rocks from Hong Kong: implications for granite petrogenesis, regional structure and crustal evolution. *Chem. Geol.* 143, 81–93. doi: 10.1016/s0009-2541(97)00101-0

Davis, D. W., Sewell, R. J., and Campbell, S. D. G. (1997). U-Pb dating of mesozoic igneous rocks from Hong Kong. *J. Geol. Soc. Lond.* 154, 1067–1076. doi: 10.1144/gsjgs.154.6.1067

Deng, Y., Li, J., Peng, T., Ma, Q., Song, X., Sun, X., et al. (2019). Lithospheric structure in the cathaysia block (South China) and its implication for the Late Mesozoic magmatism. *Phys. Earth Planet. Int.* 291, 24–34. doi: 10.1016/j.pepi.2019.04.003

Dias, A., Quelhas, P., Mata, J., Borges, R., and Lou, V. (2018). *Geologic Map of Macao, Institute of Science and Environment*. Hartford: University of Saint Joseph.

Dong, S., Zhang, Y., Li, H., Shi, W., Xue, H., Li, J., et al. (2018). The yanshan orogeny and the late Mesozoic multi-plate convergence in East Asia - Commemorating 90th years of the "Yanshan Orogeny". *Sci. China Earth Sci.* 61, 1888–1909. doi: 10.1007/s11430-017-9297-y

Dong, Y., and Santosh, M. (2016). Tectonic architecture and multiple orogeny of the qinling orogenic belt, Central China. *Gondwana Res.* 29, 1–40. doi: 10.1016/j.gr.2015.06.009

Freiberg, R., Hecht, L., Cuney, M., and Morteani, G. (2001). Secondary Ca-Al silicates in plutonic rocks and implications for their cooling history. *Contrib. Mineral. Petrol.* 141, 415–429. doi: 10.1007/s004100100241

Frost, B. R., Barnes, C. G., Collins, W. J., Arculus, R. J., Ellis, D. J., and Frost, C. D. (2001). A geochemical classification for granitic rocks. *J. Petrol.* 42, 2033–2048. doi: 10.1093/petrology/42.11.2033

Frost, B. R., Lindsley, D. H., and Andersen, D. J. (1988). Fe-Ti oxide-silicate equilibria: assemblages with fayalitic olivine. *Am. Mineral.* 73, 727–740.

Frost, C. D., and Frost, B. R. (2011). On the ferroan (A-type) granitoids: their compositional variability and modes of origin. *J. Petrol.* 52, 39–53. doi: 10.1093/petrology/egq070

Gao, P., Zheng, Y.-F., and Zhao, Z.-F. (2017). Triassic granites in South China: a geochemical perspective on their characteristics, petrogenesis, and tectonic significance. *Earth Sci. Rev.* 173, 266–294. doi: 10.1016/j.earscirev.2017.07.016

Glazner, A. F., and Johnson, B. R. (2013). Late crystallization of K-feldspar and the paradox of megacrystic granites. *Contrib. Mineral. Petrol.* 166, 777–779.

Griffin, W. L., Pearson, N. J., Belousova, E., Jackson, S. E., van Achterbergh, E., O'Reilly, S. Y., et al. (2000). The Hf isotope composition of cratonic mantle: LAM-MC-ICPMS analysis of zircon megacrysts in kimberlites. *Geochim. Cosmochim. Acta* 64, 133–147. doi: 10.1016/s0016-7037(99)00343-9

Griffin, W. L., Powell, W. J., Pearson, N. J., and O'Reilly, S. Y. (2008). "GLITTER: data reduction software for laser ablation ICP-MS," in *Laser Ablation-ICP-MS in the Earth Sciences: Current Practices and Outstanding Issues*, ed. P. Sylvester (Quebéc City, QC: Mineralogical Association of Canada), 308–311.

Griffin, W. L., Wang, X., Jackson, S. E., Pearson, N. J., O'Reilly, S. Y., Xu, X., et al. (2002). Zircon chemistry and magma mixing, SE China: in-situ analysis of Hf isotopes, Tonglu and Pingtan igneous complexes. *Lithos* 61, 237–269. doi: 10.1016/s0024-4937(02)00082-8

Guitreau, M., Blichert-Toft, J., Martin, H., Mojzsis, S. J., and Albarède, F. (2012). Hafnium isotope evidence from archean granitic rocks for deep-mantle origin of continental crust. *Earth Planet. Sci. Lett.* 337-338, 211–223. doi: 10.1016/j.epsl.2012.05.029

Hammarstrom, J. M., and Zen, E. (1986). Aluminum in hornblende: An empirical igneous geo-barometer. *Am. Mineral.* 71, 1297–1313.

Harrison, T. M., Watson, E. B., and Aikman, A. B. (2007). Temperature spectra of zircon crystallization in plutonic rocks. *Geology* 35, 635–638.

Jackson, S. E., Pearson, N. J., Griffin, W. L., and Belousova, E. A. (2004). The application of laser ablation-inductively coupled plasma-mass spectrometry to in situ U-Pb zircon geochronology. *Chem. Geol.* 211, 47–69. doi: 10.1016/j.chemgeo.2004.06.017

Jahn, B.-M. (2004). "The central Asian orogenic belt and growth of the continental crust in the Phanerozoic," in *Aspects of the Tectonic Evolution of China*, eds J. Malpas, C. J. N. Fletcher, J. R. Ali, and J. C. Aitchison (Bath: Geological Society of London Special Publication), 73–100. doi: 10.1144/gsl.sp.2004.226.01.05

Jiang, Y.-H., Jiang, S.-Y., Dai, B.-Z., Liao, S.-Y., Zhao, K.-D., and Ling, H.-F. (2009). Middle to late Jurassic felsic and mafic magmatism in southern hunan province, southeast China: implications for a continental arc to rifting. *Lithos* 107, 185–204. doi: 10.1016/j.lithos.2008.10.006

Jiang, Y.-H., Jiang, S.-Y., Zhao, K.-D., and Ling, H.-F. (2006). Petrogenesis of Late Jurassic Qianlishan granites and mafic dykes, southeast China: implications for a back-arc extension setting. *Geol. Mag.* 143, 457–474. doi: 10.1017/s0016756805001652

Kemp, A. I. S., and Hawkesworth, C. J. (2003). Granitic perspectives on the generation and secular evolution of the continental crust. *Treatise Geochem.* 3, 349–410. doi: 10.1016/b0-08-043751-6/03027-9

Li, P., Yu, X., Li, H., Qiu, J., and Zhou, X. (2013). Jurassic-cretaceous tectonic evolution of southeast China: geochronological and geochemical constrains of *Yanshanian granitoids*. *Int. Geol. Rev.* 55, 1202–1219. doi: 10.1080/00206814.2013.771952

Li, X.-H., Chung, S.-L., Zhou, H., Lo, C.-H., Liu, Y., and Chen, C.-H. (2004). "Jurassic intraplate magmatism in southern Hunan-eastern Guangxi: 40Ar/39Ar dating, geochemistry, Sr-Nd isotopes and implications for the tectonic evolution of SE China," in *Aspects of the Tectonic Evolution of China*, eds J. Malpas, C. J. N. Fletcher, J. R. Ali, and J. C. Aitchison (Bath: Geological Society of London Special Publication), 193–215. doi: 10.1144/gsl.sp.2004.226.01.11

Li, X.-H., Li, W.-X., and Li, Z.-X. (2007a). On the genetic classification and tectonic implications of the Early Yanshanian granitoids in the Nanling Range, South China. *Chinese Sci. Bull.* 52, 1873–1885. doi: 10.1007/s11434-007-0259-0

Li, X.-H., Li, Z.-X., Li, W.-X., Liu, Y., Yuan, C., Wei, G., et al. (2007b). U-Pb zircon, geochemical and Sr-Nd-Hf isotopic constraints on age and origin of Jurassic I- and A-type granites from central Guangdong, SE China: a major igneous event in response to foundering of a subducted flat slab? *Lithos* 96, 186–204. doi: 10.1016/j.lithos.2006.09.018

Li, X.-H., Li, W.-X., Wang, X.-C., Li, Q.-L., Liu, Y., and Tang, G.-Q. (2009). Role of mantle-derived magma in genesis of early yanshanian granites in the Nanling Range, South China: in situ zircon Hf-O isotopic constraints. *Sci. China Earth Sci.* 52, 1262–1278. doi: 10.1007/s11430-009-0117-9

Li, Z., Qiu, J.-S., and Yang, X.-M. (2014). A review of the geochronology and geochemistry of Late Yanshanian (Cretaceous) plutons along the Fujian coastal area of southeastern China: implications for magma evolution related to slab break-off and rollback in the Cretaceous. *Earth Sci. Rev.* 128, 232–248. doi: 10.1016/j.earscirev.2013.09.007

Li, Z.-X., and Li, X.-H. (2007). Formation of the 1300-km-wide intracontinental orogeny and post-orogenic magmatic province in Mesozoic South China: a flat slab subduction model. *Geology* 35, 179–182.

Li, Z.-X., Li, X.-H., Chung, S.-L., Lo, C.-H., Xu, X., and Li, W.-X. (2012). Magmatic switch-on and switch-off along the South China continental margin since the Permian: transition from an Andean-type to a Western Pacific-type plate boundary. *Tectonophysics* 532–535, 271–290. doi: 10.1016/j.tecto.2012.02.011

Liu, H., Wang, Y., Li, Z., Zi, J.-W., and Huangfu, P. (2018). Geodynamics of the Indosinian orogeny between the South China and Indochina blocks: insights from latest Permian-Triassic granitoids and numerical modeling. *Geol. Soc. Am. Bull.* 130, 1289–1306. doi: 10.1130/b31904.1

Locock, A. J. (2008). An Excel spreadsheet to recast analyses of garnet into end-member components, and a synopsis of the crystal chemistry of natural silicate garnets. *Comput. Geosci.* 34, 1769–1780. doi: 10.1016/j.cageo.2007.12.013

Ludwig, K. R. (1998). On the treatment of concordant uranium-lead ages. *Geochim. Cosmochim. Ac.* 62, 665–676. doi: 10.1016/s0016-7037(98)00059-3

Ludwig, K. R. (2011). Isoplot v. 4.15: a geochronological toolkit for microsoft excel. *Berkel. Geochronol. Center Spec. Public.* 4:70.

Luhr, J. F., Carmichael, I. S. E., and Varekamp, J. C. (1984). The 1982 eruptions of El Chichón volcano, Chiapas, Mexico: mineralogy and petrology of the anhydrite-bearing pumices. *J. Volcanol. Geoth. Res.* 23, 69–108. doi: 10.1016/0377-0273(84)90057-x

Maniar, P. D., and Piccoli, P. M. (1989). Tectonic discrimination of granitoids. *Geol. Soc. Am. Bull.* 101, 635–643. doi: 10.1130/0016-7606(1989)101<0635:tdog>2.3.co;2

Metcalfe, I. (2006). Palaeozoic and mesozoic tectonic evolution and palaeogeography of East Asian crustal fragments: the Korean Peninsula in context. *Gondwana Res.* 9, 24–46. doi: 10.1016/j.gr.2005.04.002

Miller, C. F., McDowell, S. M., and Mapes, R. W. (2003). Hot and cold granites? Implications of zircon saturation temperatures and preservation of inheritance. *Geology* 31, 529–532.

Miller, C. F., and Stoddard, E. F. (1981). The role of manganese in the paragenesis of magmatic garnet: an example from the Old Woman-Piute range, California. *J. Geol.* 89, 233–246. doi: 10.1086/628582

Mutch, E. J. F., Blundy, J. D., Tattitch, B. C., Cooper, F. J., and Brooker, R. A. (2016). An experimental study of amphibole stability in low-pressure granitic magmas and a revised Al-in-hornblende geobarometer. *Contrib. Mineral. Petrol.* 171:85. doi: 10.1007/s00410-016-1298-1299

Nachit, H., Ibhi, A., Abia, E. H., and Ohoud, M. B. (2005). Discrimination between primary magmatic biotites, reequilibrated biotites and neoformed biotites. *C.R. Geosci.* 337, 1415–1420. doi: 10.1016/j.crte.2005.09.002

Nenova, P. I. (1997). Fe23: a computer program for calculating the number of Fe2+ and Fe3+ ions in minerals. *Comput. Geosci.* 23, 215–219. doi: 10.1016/s0098-3004(97)85445-3

Nowell, G. M., Kempton, P. D., Noble, S. R., Fitton, J. G., Saunders, A. D., Mahoney, J. J., et al. (1998). High precision Hf isotope measurements of MORB and OIB by thermal ionization mass spectrometry: insight into the depleted mantle. *Chem. Geol.* 149, 211–233. doi: 10.1016/s0009-2541(98)00036-9

Patiño Douce, A. E. (1999). "What do experiments tell us about the relative contributions of crust and mantle to the origin of granitic magmas?," in *Understanding Granites: Integrating New and Classical Techniques*, eds A. Castro, C. Fernández, and J. L. Vigneresse (Bath: Geological Society of London Special Publication), 55–75. doi: 10.1144/gsl.sp.1999.168.01.05

Pearce, J. A. (1996). Sources and settings of granitic rocks. *Episodes* 19, 120–125. doi: 10.18814/epiiugs/1996/v19i4/005

Pupin, J. P. (1980). Zircon and granite petrology. *Contrib. Mineral. Petrol.* 73, 207–220. doi: 10.1007/bf00381441

Quelhas, P., Dias, A. A., Mata, J., Davis, D. W., and Ribeiro, M. L. (2020). High-precision geochronology of mesozoic magmatism in Macao, southeast China: evidence for multistage granite emplacement. *Geosci. Front.* 11, 243–263. doi: 10.1016/j.gsf.2019.04.011

Ribeiro, M. L., Ramos, J. M. F., Pereira, E., and Dias, R. P. (1992). *Noticia Explicativa da Carta Geologica de Macau na Escala 1/5000*. Lisboa: Servicos Geologicos.

Rossignol, C., Bourquin, S., Hallot, E., Poujol, M., Dabard, M.-P., Martini, R., et al. (2018). The Indosinian orogeny: a perspective from sedimentary archive of north Vietnam. *J. Asian Earth Sci.* 158, 352–380. doi: 10.1016/j.jseaes.2018.03.009

Rudnick, R. L., and Gao, S. (2003). Composition of the continental crust. *Treatise Geochem.* 3, 1–64. doi: 10.1016/b0-08-043751-6/03016-4

Schmidberger, S. S., Heaman, L. M., Simonetti, A., Creaser, R. A., and Whiteford, S. (2007). Lu-Hf, in-situ Sr and Pb isotope and trace element systematics for mantle eclogites from the Diavik diamond mine: evidence for paleoproterozoic subduction beneath the *Slave craton*, Canada. *Earth Planet. Sci. Lett.* 254, 55–68. doi: 10.1016/j.epsl.2006.11.020

Sewell, R. J., and Campbell, S. D. G. (1997). Geochemistry of coeval mesozoic plutonic and volcanic suites in Hong Kong. *J. Geol. Soc. Lond.* 154, 1053–1066. doi: 10.1144/gsjgs.154.6.1053

Sewell, R. J., Campbell, S. D. G., Fletcher, C. J. N., Lai, K. W., and Kirk, P. A. (2000). *The Pre-Quaternary Geology of Hong Kong*. Hong Kong: Geotechincal Engineering Office.

Sewell, R. J., Davis, D. W., and Campbell, S. D. G. (2012). High precision U-Pb zircon ages for mesozoic igneous rocks from Hong Kong. *J. Asian Earth Sci.* 43, 164–175. doi: 10.1016/j.jseaes.2011.09.007

Shabani, A. A. T., Lalonde, A., and Whalen, J. B. (2003). Composition of biotite from granitic rocks of the canadian appalachian orogen: a potential tectonomagmatic indicator. *Can. Mineral.* 41, 1381–1396. doi: 10.2113/gscanmin.41.6.1381

Shellnutt, J. G., Lan, C.-Y., Long, T. V., Ususki, T., Yang, H.-J., Mertzman, S. A., et al. (2013). Formation of cretaceous cordilleran and post-orogenic granites and their microgranular enclaves from the Dalat zone, southern Vietnam: tectonic implications for the evolution of Southeast Asia. *Lithos* 182–183, 229–241. doi: 10.1016/j.lithos.2013.09.016

Shu, L. S., Zhou, X. M., Deng, P., Wang, B., Jiang, S. Y., Yu, J. H., et al. (2009). Mesozoic tectonic evolution of the southeast China block: new insights from basin analysis. *J. Asian Earth Sci.* 34, 376–391. doi: 10.1016/j.jseaes.2008.06.004

Sláma, J., Košler, J., Condon, D. J., Crowley, J. L., Gerdes, A., Hanchar, J. M., et al. (2008). Plešovice zircon - A new natural reference material for U-Pb and Hf isotopic microanalysis. *Chem. Geol.* 249, 1–35. doi: 10.1016/j.chemgeo.2007.11.005

Smith, P. M., and Asimow, P. D. (2005). Adiabat_1ph: a new public front-end to the MELTS, pMELTS, and pHMELTS models. *Geochem. Geophys. Geosyst.* 6:Q02004. doi: 10.1029/2004GC000816

Söderlund, U., Patchett, P. J., Vervoort, J. D., and Isachsen, C. E. (2004). The 176Lu decay constant determined by Lu-Hf and U-Pb isotope systematics of Precambrian mafic intrusions. *Earth Planet. Sci. Lett.* 219, 311–324. doi: 10.1016/s0012-821x(04)00012-3

Stevens, G., Villaros, A., and Moyen, J.-F. (2007). Selective peritectic garnet entertainment as the origin of geochemical diversity in S-type granites. *Geology* 35, 9–12.

Sun, J., Shu, L., Santosh, M., and Wang, L. (2018). Precambrian crustal evolution of the central Jiangnan orogen (South China): evidence from detrital zircon U-Pb

ages and Hf isotopic compositions of neoproterozoic metasedimentary rocks. *Precambrian Res.* 318, 1–24. doi: 10.1016/j.precamres.2018.09.008

Sun, S. S., and McDonough, W. F. (1989). "Chemical and isotopic systematics of oceanic basalts: implications for mantle composition and processes," in *Magmatism in the Ocean Basins*, eds A. D. Saunders and M. J. Norry (Bath: Geological Society of London Special Publication), 313–435.

Sylvester, P. J. (1998). Post-collisional strongly peraluminous granites. *Lithos* 45, 29–44. doi: 10.1016/s0024-4937(98)00024-3

Tanaka, T., Togashi, S., Kamioka, H., Amakawa, H., Kagami, H., Hamamoto, T., et al. (2000). JNdi-1: a neodymium isotopic reference in consistency with LaJolla neodymium. *Chem. Geol.* 168, 279–281. doi: 10.1016/s0009-2541(00)00198-4

Tindle, A. G., and Webb, P. C. (1990). Estimation of lithium contents in trioctahedral micas using microprobe data: application to micas from granitic rocks. *Eur. J. Mineral.* 2, 595–610. doi: 10.1127/ejm/2/5/0595

Uchida, E., Endo, S., and Makino, M. (2007). Relationship between solidification depth of granitic rocks and formation of hydrothermal ore deposits. *Resource Geol.* 57, 47–56. doi: 10.1111/j.1751-3928.2006.00004.x

Unterschutz, J. E., Creaser, R. A., Erdmer, P., Thompson, R. I, and Daughtry, K. L. (2002). North American margin origin of Quesnel terrane strata in the southern Canadian Cordillera: Inferences from geochemical and Nd isotopic characteristics of triassic metasedimentary rocks. *Geol. Soc. Am. Bull.* 114, 462–475. doi: 10.1130/0016-7606(2002)114<0462:namooq>2.0.co;2

Villaros, A., Stevens, G., and Buick, I. S. (2009). Tracking S-type granite from source to emplacement: clues from garnet in the Cape Granite suite. *Lithos* 112, 217–235. doi: 10.1016/j.lithos.2009.02.011

Wang, D., and Shu, L. (2012). Late Mesozoic basin and range tectonics and related magmatism in southeast China. *Geosci. Front.* 3, 109–124. doi: 10.1016/j.gsf.2011.11.007

Wang, Y., Fan, W., Zhang, G., and Zhang, Y. (2013). Phanerozoic tectonics of the South China block: key observations and controversies. *Gondwana Res.* 23, 1273–1305. doi: 10.1016/j.gr.2012.02.019

Wang, Y., Wu, X., Duan, W., and Li, L. (2014). The discovery of Jurassic plants in Shenzhen and Guangdong, southern China and related significance. *Chin. Sci. Bull.* 59, 3630–3637. doi: 10.1007/s11434-014-0449-5

Wang, Y., Zhang, A., Fan, W., Zhao, G., Zhang, G., Zhang, Y., et al. (2011). Kwangsian crustal anataxis within the eastern South China Block: geochemical, zircon U-Pb geochronological and Hf isotopic fingerprints from the gneissoid granites of Wugong and Wuyi-Yunkai domains. *Lithos* 127, 239–260. doi: 10.1016/j.lithos.2011.07.027

Wedepohl, K. H. (1995). The composition of the continental crust. *Geochim. Cosmochim. Acta* 59, 1217–1232.

Whalen, J. B., Currie, K. L., and Chappell, B. W. (1987). A-type granites: geochemical characteristics, discrimination and petrogenesis. *Contrib. Mineral. Petrol.* 95, 407–419. doi: 10.1007/bf00402202

Whitney, D. L., and Evans, B. (2010). Abbreviations for names of rock-forming minerals. *Am. Mineral.* 95, 185–187. doi: 10.2138/am.2010.3371

Wiedenbeck, M., Allé, P., Corfu, F., Griffin, W. L., Meier, M., Oberli, F., et al. (1995). Three natural zircon standards for U-Th-Pb, Lu-Hf, trace element and REE analyses. *Geostandard. Newslett.* 19, 1–23. doi: 10.1111/j.1751-908x.1995.tb00147.x

Wones, D. R., and Eugster, H. P. (1965). Stability of biotite: experiment, theory, and application. *Am. Mineral.* 50, 1228–1272.

Woodhead, J. D., and Hergt, J. M. (2005). A preliminary appraisal of seven natural zircon reference materials for in situ Hf isotope determination. *Geostand. Geoanal. Res.* 29, 183–195. doi: 10.1111/j.1751-908x.2005.tb00891.x

Wu, F.-Y., Yang, Y.-H., Xie, L.-W., Yang, J.-H., and Xu, P. (2006). Hf isotopic compositions of the standard zircons and baddeleyites used in U-Pb geochronology. *Chem. Geol.* 234, 105–126. doi: 10.1016/j.chemgeo.2006.05.003

Wu, G. (2005). The yanshanian orogeny and two kinds of yanshanides in eastern-central China. *Ac. Geol. Sinica* 79, 507–518. doi: 10.1111/j.1755-6724.2005.tb00917.x

Wu, Y.-B., and Zheng, Y.-F. (2013). Tectonic evolution of a composite collision orogeny: an overview on the Qinling-Tongbai-Hong'an-Dabie-Sulu orogenic belt in central China. *Gondwana Res.* 23, 1402–1428. doi: 10.1016/j.gr.2012.09.007

Xu, C., Shi, H., Barnes, C. G., and Zhou, Z. (2016). Tracing a late Mesozoic magmatic arc along the Southeast Asian margin from the granitoids drill from the northern South China Sea. *Int. Geol. Rev.* 58, 71–94. doi: 10.1080/00206814.2015.1056256

Xu, X., O'Reilly, S. Y., Griffin, W. L., Wang, X., Pearson, N. J., and He, Z. (2007). The crust of Cathaysia: age, assembly and reworking of two terranes. *Precambrian Res.* 158, 51–78. doi: 10.1016/j.precamres.2007.04.010

Zeh, A., Gerdes, A., Klemd, R., and Barton, J. M. (2007). Archaean to Proterozoic Crustal evolution in the Central Zone of the Limpopo Belt (South Africa-Botswana): constraints from combined U-Pb and Lu-Hf isotope analyses of zircon. *J. Petrol.* 48, 1605–1639. doi: 10.1093/petrology/egm032

Zhao, G. (2015). Jiangnan Orogen in South China: developing from divergent double subduction. *Gondwana Res.* 27, 1173–1180. doi: 10.1016/j.gr.2014.09.004

Zhou, X., Sun, T., Shen, W., Shu, L., and Niu, Y. (2006). Petrogenesis of mesozoic granitoids and volcanic rocks in south China: a response to tectonic evolution. *Episodes* 29, 26–33. doi: 10.18814/epiiugs/2006/v29i1/004

Zhou, X. M., and Li, W. X. (2000). Origin of Late Mesozoic igneous rocks in southeastern China: implications for lithospheric subduction and underplating of mafic magmas. *Tectonophysics* 326, 269–267.

Zhu, K.-Y., Li, Z.-X., Xu, X.-S., and Wilde, S. A. (2014). A Mesozoic Andean-type orogenic cycle in southeastern China as recorded by granitoid evolution. *Am. J. Sci.* 314, 187–234. doi: 10.2475/01.2014.06

Zindler, A., and Hart, S. (1986). Chemical geodynamics. *Annu. Rev. Earth Planet. Sci.* 14, 493–571.

Zuo, X., Chan, L. S., and Gao, J.-F. (2017). Compression-extension transition of continental crust in a subduction zone: a parametric numerical modeling study with implications on Mesozoic-Cenozoic tectonic evolution of the Cathaysia block. *PLoS One* 12:e0171536. doi: 10.1371/journal.pone.0171536

Conflict of Interest: MV was employed by the company Siletzia Resources LLC.

The remaining authors declare that the research was conducted in the absence of any commercial or financial relationships that could be construed as a potential conflict of interest.

frontiers in Earth Science

ORIGINAL RESEARCH
published: 04 August 2020
doi: 10.3389/feart.2020.00330

Structural Evolution of Extended Continental Crust Deciphered From the Cretaceous Batholith in SE China, a Kinmen Island Perspective

*Tsung-Han Huang[1] and Meng Wan Yeh[2]**

[1] Department of Geosciences, National Taiwan University, Taipei, Taiwan, [2] Department of Earth Sciences, National Taiwan Normal University, Taipei, Taiwan

The continental crust of southeast Asia underwent from thickening, thinning to almost rifting during the Mesozoic era as the active continental margin transformed into a passive one. Such crustal thinning history is well-preserved in the Kinmen Island, as the lower crustal granitoids retrograded and rapidly exhumed to surface that were crosscutted by mafic dike swarm. Kinmen Island is situated on the SE coast of Asia, featured by the widespread Cretaceous magmatism as the Paleo-Pacific plate subducted and rollbacked underneath the South China block. Although these complex magmatism are well reported and studied, their associated structural evolution and plate kinematics have not been clearly deciphered. Detailed field mapping, structural measurement, and petrographic analysis of the Kinmen Island were conducted. Up to five deformation events accompanied with five relevant magmatic episodes as well as their corresponding kinematic setting are reconstructed. The ∼129 Ma Chenggong Tonalite (G_1) preserved all deformation events identified in this study, which marks the lower bound timing of all reported events. D_1 formed a gneiss dome with the Taiwushan Granite (∼139 Ma) at the core bounded by moderately dipping gneissic foliation (S_1) as crust extended. D_2 formed subhorizontal S-tectonite (S_2) with further exhumation of D_1 gneiss dome due to middle-to-lower crustal flow associated with further crustal thinning. D_3 formed a sinistral ENE-WSW striking steeply S dipping shear belts with well-developed S/C/C' fabrics. The moderately E-plunging lineation on C surface indicates its transtensional nature. Widespread garnet-bearing leucogranite (G_2) associated with decompressional melting showed long lasting intrusion prior to D_2 until post D_3. D_4 was the intrusion of biotite-bearing Tienpu Granite (∼100 Ma; G_3) that truncated G_1, G_2, and all fabrics, which was followed by the intrusion of E-W striking, steeply dipping biotite-bearing pegmatite (G_4) as the crust further extended. The youngest deformation event (D_5) was NE-SW striking subvertical mafic dike swarm (G_5; 90–76 Ma) due to mantle upwelling through significantly thinned crust. By integrating the structural evolution and the previously reported strain pattern, we delineate the slab rollback direction of the Paleo-pacific plate, which changed from northeastward (129∼114 Ma) to southeastward (107∼76 Ma). This plate kinematic movement switched during 114–107 Ma.

Keywords: Cretaceous magmatism, structural evolution, Paleo-Pacific plate, extended continental crust, slab rollback

OPEN ACCESS

Edited by:
Kwan-Nang Pang, Academia Sinica, Taiwan

Reviewed by:
Kong-Yang Zhu, Zhejiang University, China
Wei Lin, Chinese Academy of Sciences (CAS), China

****Correspondence:***
Meng Wan Yeh
marywyeh@ntnu.edu.tw

Specialty section:
This article was submitted to Petrology, a section of the journal Frontiers in Earth Science

Received: *28 March 2020*
Accepted: *15 July 2020*
Published: *04 August 2020*

Citation:
Huang T-H and Yeh MW (2020) Structural Evolution of Extended Continental Crust Deciphered From the Cretaceous Batholith in SE China, a Kinmen Island Perspective. Front. Earth Sci. 8:330. doi: 10.3389/feart.2020.00330

INTRODUCTION

The most profound tectono-structural features along the continental margin of southeast Asia are the hundreds-kilometer scale spreading of the Cretaceous magmatism along with the development of hundreds-kilometer long NE-SW trending metamorphic belt (e.g., Pingtan-Dongshan metamorphic belt; PDMB) and shear zone (e.g., Changle-Nanao Shear Zone; CNSZ; **Figure 1**). The geodynamic origin of these widespread Mesozoic tectono-magmatic events and associated metamorphism and structural evolution had aroused large interests and controversies over the past decades (e.g., Li and Li, 2007; Li J. et al., 2014; Dong et al., 2018; Mai et al., 2018; Huang et al., 2019). Numerous tectonic models were proposed for the generation of these magmatic events: (1) subduction and rollback/retreat of the Paleo-Pacific plate beneath the Cathaysia block (e.g., John et al., 1990; Zhou and Li, 2000; Zhou et al., 2006; Li and Li, 2007; Sun et al., 2007; Wong et al., 2009; Wang et al., 2011, 2013; Liu et al., 2012; Li J. et al., 2014; Mao et al., 2014; Yang et al., 2018); (2) collision between the Huanan and Dongnanya continental block (Hsü et al., 1990); (3) mantle plume activities (Xie et al., 2001). Despite the diverse tectonic models, the Cretaceous magmatic events are generally accepted as their association to the crustal thinning during the tectonic interaction between the Paleo-Pacific plate and the Eurasian plate. This Mesozoic tectonic event is extremely influential as it not only shapes the present geological framework of the East Asia from Japan to Vietnam, but also layouts the foundation for the development and evolution of basins along the marginal seas (e.g., Mai et al., 2018).

Based on abundant geochemistry data, the alternated crustal shortening (∼170–136 Ma) followed by extension (∼135–90 Ma) related to subduction, back-arc extension to slab break off and mantle flare up were recognized for the Cretaceous tectono-magmatic events (e.g., Li, 2000; Zhou et al., 2006; Wong et al., 2009; Li Z. et al., 2014; Dong et al., 2018; Yang et al., 2018). Two episodes of A-type granite intrusions were noted: 140–120 Ma mainly in the Zhejiang Province and 100–90 Ma along the coastal region of the Fujian Province (**Figure 1B**; Li, 2000; Yang et al., 2012; Li et al., 2013; Li Z. et al., 2014; Zhao et al., 2018). Based on the temporal and spatial correlation of the Jurassic and Cretaceous magmatic bodies, three general evolution patterns were recognized and proposed. One is that the magmatic activity migrated toward southeast during 180–80 Ma due to the steepening of subduction angle of the Paleo-Pacific plate (e.g., Zhou and Li, 2000). The second is the northeastward younging trend of igneous rocks from 180 to 125 Ma owing to northeastward slab rollback of the southwestward obliquely subducted Pacific plate (e.g., Wang et al., 2011). The third is the west to east younging trend of the igneous rocks from 190 to 100 Ma due to slab rollback and/or break-off of the Paleo-Pacific plate (e.g., Wong et al., 2009). Due to the complexity and inconsistency of previously recognized temporal and spatial patterns, Dong et al. (2018) and Mao et al. (2014) suggested the presence of multi-plate convergence with multidirectional extrusion and extension tectonism should be considered. Although the distribution and geochemistry signatures of magmatic rocks are good proxies to decipher the tectonic setting and crustal evolution, the strain setting and the kinematic evolution would be more clearly revealed via detailed structural pattern mapping along the margin of continental crust. Nonetheless, such studies were absent previously. In this study, we depicted the Kinmen Island (**Figure 2**), which is situated on the SE edge of the Eurasian continental margin, as a window to delineate the structural and plate kinematic evolution since Cretaceous time.

GEOLOGICAL BACKGROUND

The continental lithosphere within the southeast region of the Eurasian plate is comprised of the South China block and the Indochina block. The South China block is composed of the Yangtze Block to the northwest, and the Cathaysia Block to the southeast (**Figure 1A**). The southeast region of the Cathaysia Block is characterized by extensive distribution of Jurassic to Cretaceous plutonics, volcanics, NE-trending sinistral CNSZ, and the PDMB along the coast (**Figure 1**; Wang et al., 2013; Li J. et al., 2014). Three major magmatic periods of: ∼187 Ma, 147–130 Ma, and 125–90 Ma were noted, but the Cretaceous magmatism mostly affected areas along the southeast coast (e.g., Liu et al., 2016 and references within). The Cretaceous geological features resulted from the tectono-magmatic events induced by the subduction and retreat of the Paleo-Pacific plate beneath the South China Block (Liu et al., 2012; Zhang et al., 2012; Wang et al., 2013; Li J. et al., 2014; Li Z. et al., 2014; Li et al., 2015; Mao et al., 2014). These Cretaceous rocks consist of high-K calc-alkaline I-type granites with minor A-type granites and gabbros as well as acidic to basaltic volcanic rocks (Li, 2000; Zhou et al., 2006; Li Z. et al., 2014). Extensional setting associated to their generation were delineated from the intimate temporal-spatial characteristics of the 115–95 Ma gabbro with the surrounding I-type granitoids, and the 100–90 Ma A-type granites in the Fujian Province (Li Z. et al., 2014). The bimodal signatures of the 115–95 Ma gabbro and I-type granitoids (Li Z. et al., 2014), and the 94–81 Ma bimodal volcanism further support such interpretation (Chen et al., 2004). These Cretaceous magmatic rocks were later intruded by NE-trending mafic dykes (Lee, 1994; Zhao et al., 2007).

Similar lithology was also noted from the Kinmen Island offshore the Fujian Province, on the leading edge of the continental margin of the South China Block. Four Cretaceous granitoid bodies were mapped out (**Figure 2A**): the Taiwushan Granite (139 Ma, Yui et al., 1996), the Chenggong Tonalite (129 Ma, Lin et al., 2011), the Doumen Granite (120 Ma, Lin et al., 2011), and the Tienpu Granite (100 Ma, Yui et al., 1996), all of which were intruded by the 90–76 Ma mafic dike swarms (Lee, 1994; Lan et al., 1995; Lin et al., 2011). These Cretaceous granitoids were inferred to evolve from the same parental magma under separate stages of fractional crystallization from post-orogenic to continental extension (Lan et al., 1997). The later mafic dike swarms intruded along the NE-trending fractures (Lee, 1994; Lin, 1994; Lan et al., 1997; Lin et al., 2011). The intrusion depth of the Taiwushan Granite was considered to be 28–30 km according to the Al-hornblende

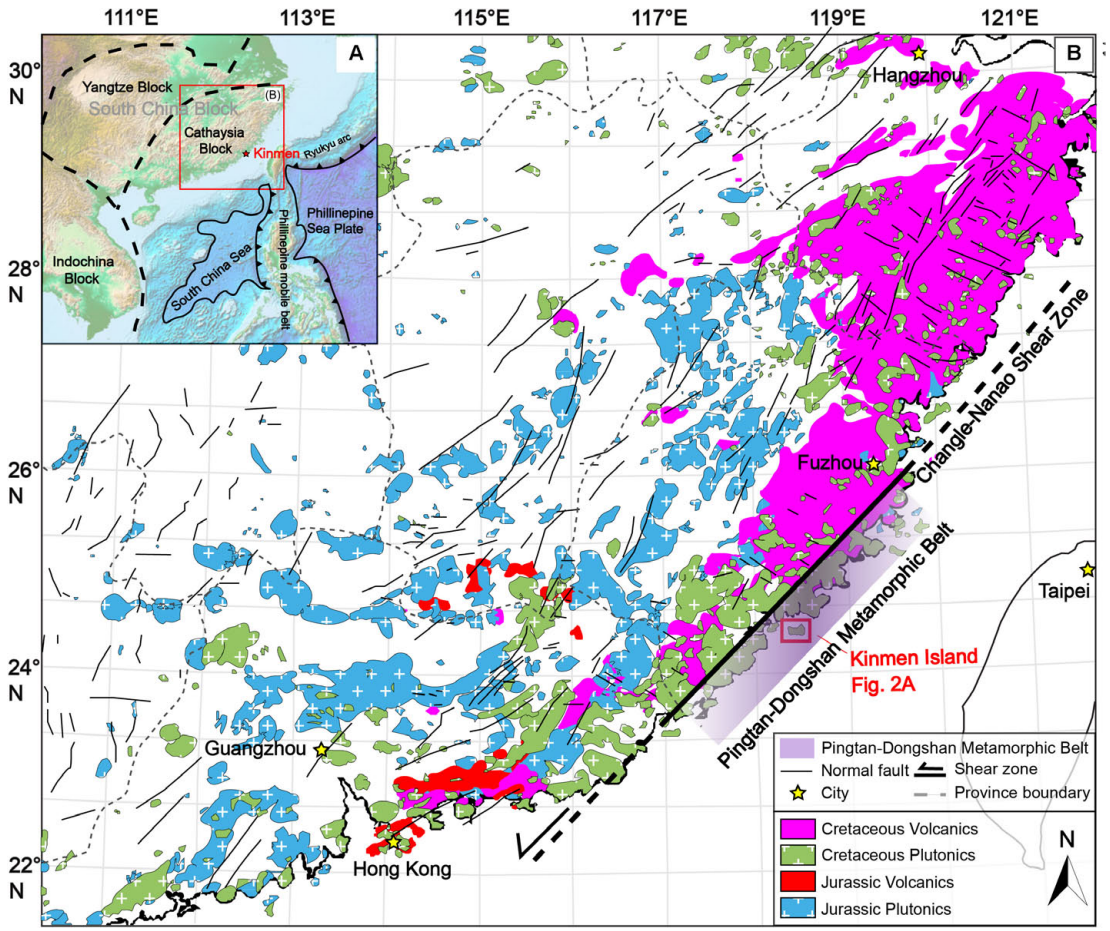

FIGURE 1 | Simplified tectonic and geological map of southeast Asia. **(A)** Topography map showing tectonic components of southeast Asia under present-day configuration. The black dashed lines mark the boundaries of the tectonic blocks while the black solid lines mark the boundaries between continental crust and oceanic crust. Solid black lines with triangles indicate the subduction zones. **(B)** Geological map modified and compiled from Li J. et al. (2014) and Zhou et al. (2006) illustrating the distribution of the Jurassic and Cretaceous plutonics and volcanics, Mesozoic normal faults, Changle-Nanao Shear Zone (CNSZ), and the Pingtan-Dongshan Metamorphic Belt (PDMB). The red rectangle indicates the study site in this study.

geobarometer (Lo et al., 1993). Combined with the upper crustal intrusion of the mafic dike swarms, Lin (1994) concluded the continental crust of the Kinmen Island underwent thinning and the exhumation of the lower crustal granitoids. To decipher more detailed history of crustal extension as well as the plate interactions, it is crucial to understand the structural evolution of the metamorphosed and highly deformed units, which has been omitted from previous studies. Hence, detailed outcrop mapping, structural measurements and petrographic analysis in the Kinmen Island were conducted.

RESULTS AND INTERPRETATION

Field and oriented thin section analysis were conducted from 14 sites, which are divided into two groups according to their exhumed batholiths (**Figures 2**, **3**). One belongs to the Taiwushan Granite, including Fu Guo Duen (FGD), Dong Cun (DC), Nan Shih Hu (NSH), Liang Jin Farm (LJF), Tai Hu Road (THR), Gung Yan Road (GYR), Kinmen Botanical Garden (KBG), Huan Jung Road (HJR), Ma Shan (MS), Han She Hua (HSH), and Zhain Shan (ZS). The other falls into the Chenggong Tonalite, encompassing Hou Bian (HB), Tien Pu (TP), and Cheng Gong (CG) (**Figure 2**). A total of 568 structural measurements were taken (**Figure 3** and **Supplementary Table S1**) with three oriented samples analyzed for petrography. There are two newly identified rock units in this study: the amphibolite schist and garnet-bearing leucogranite (**Figure 4**). The amphibolite schist is only confined within the Chenggong Tonalite as abundant xenoliths, which records the same deformation history as the country rocks (**Figure 4B**). The garnet-bearing leucogranite was previously considered to be the differentiates of the Tienpu Granite (Lin et al., 2011); however, we now considered it to be an independent rock unit because it not merely was deformed during D_2 and D_3 but also intruded by the Tienpu Granite (**Figure 4F**).

Based on the crosscutting relationships of fabrics and lithology units in the field and oriented thin sections, we recognized

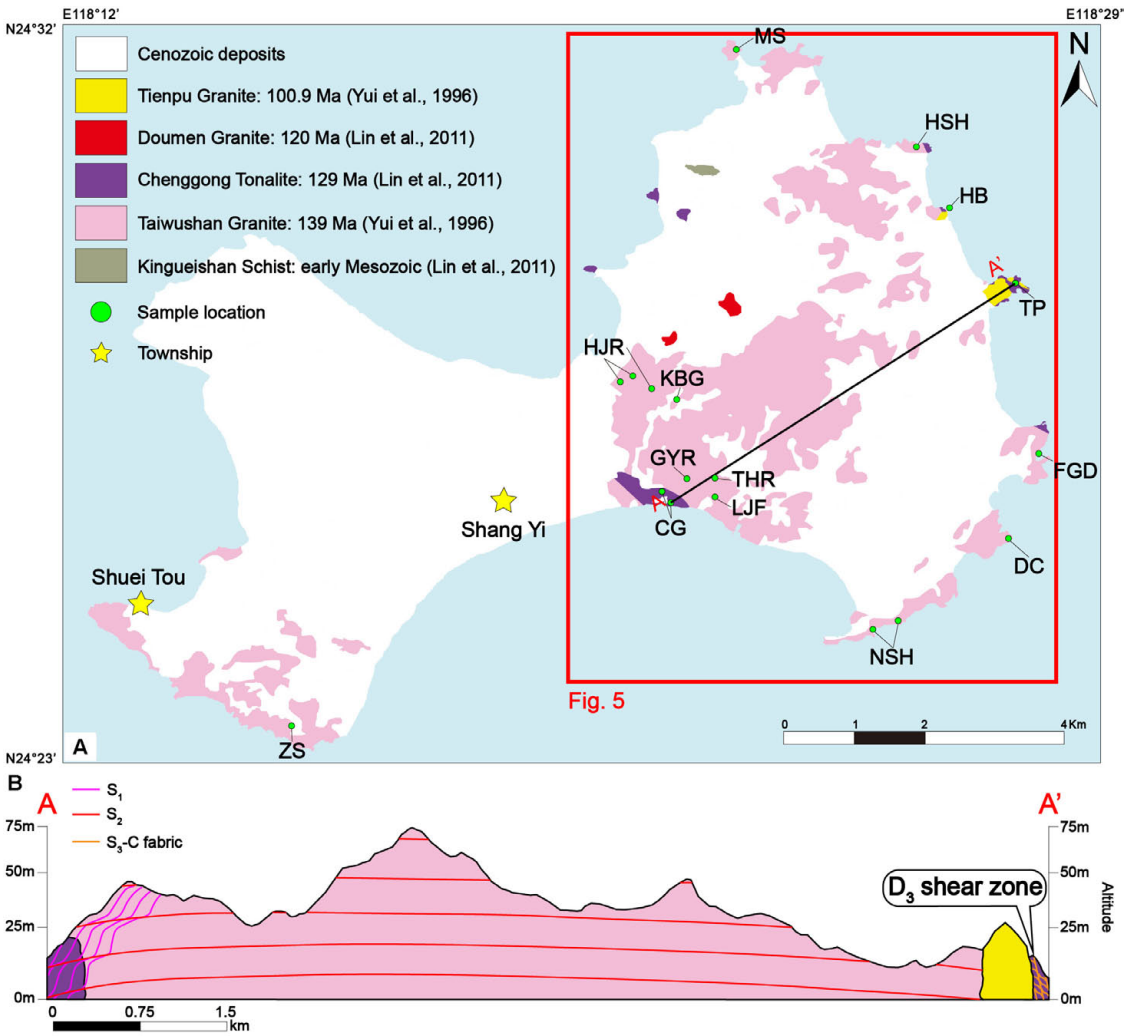

FIGURE 2 | Geological map of the Kinmen Island showing the distribution of Cretaceous magmatism and sample locations. **(A)** Geological map modified from Lin et al. (2011). **(B)** Schematic diagram of reconstructed A-A' cross section. The pink line indicates the gneissic foliation (S_1) defining the D_1 doming event. The red line indicates the subhorizontal S-tectonite (S_2) of D_2. The orange line indicates the locally developed D_3 shear belts (S/C fabric).

five deformation events and five magmatic events combining all study sites. The Taiwushan Granite, Chenggong Tonalite, and amphibolite schist xenoliths record all the deformation events (D_1–D_5; **Figures 2–8**). The magmatism of garnet-bearing leucogranite (G_2) persisted from pre-D_2 to post-D_3 (**Figures 4C,F**, **6E**, **7D,E,I**). The undeformed Tienpu Granite (G_3) crosscuts the Chenggong Tonalite and garnet-bearing leucogranite, which marks the end of all the ductile deformation events (D_1–D_3) at 100.9 Ma (age from Yui et al., 1996; **Figures 2B**, **4D,F**). With the age of 129 Ma reported for the Chenggong Tonalite by Lin et al. (2011), we constrain the D_1–D_3 ductile deformation events between 129 and 100.9 Ma. Both G_2 and G_3 have close spatial relationship to the distribution of D_3 shear belts. The D_4 and D_5 are K-feldspar-quartz ± biotite pegmatitic dykes (G_4) and mafic dykes (G_5) following brittle factures (**Figures 4G,H**, **8**). Our petrography analysis and field observation indicate that the metamorphic condition retrograded from the granulite facies (D_1), to the upper- to middle-amphibolite facies (D_2–D_3), and finally into the greenschist facies (D_4–D_5). The results of reconstructed evolution are described below.

D_1

D_1 is a kilometer scale gneiss-dome structure with the Chenggong Tonalite skirting the central Taiwushan Granite at the southwest and northeast margin (at CG, FGU, TP, HB, and HSH locality of **Figures 2**, **5**). Moderately to shallowly dipping gneissic foliation (S_1) were formed around the margin of Taiwushan Granite and within the Chenggong Tonalite, all of which dip away from the core of Taiwushan Granite (**Figures 2B**, **3**, **5**). The moderately to shallowly down-dipping mineral stretching lineation was mainly developed at the southwest, south and southeast side of the Taiwushan Granite at CG, NSH, and DC, respectively (**Figure 5**). The south

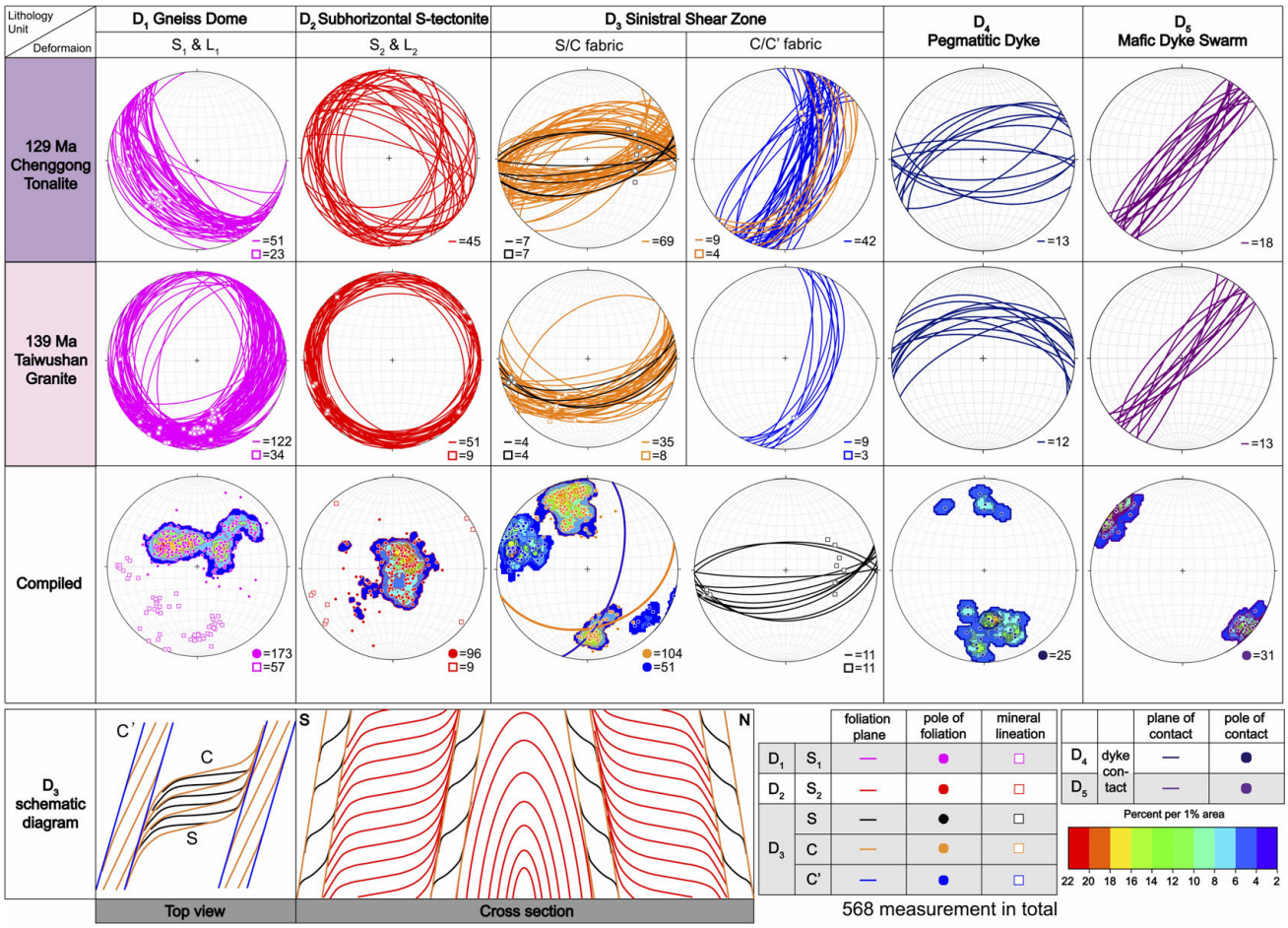

FIGURE 3 | Equal-area southern hemisphere stereographic projections of structure measurement data from 139 Ma Taiwushan Granite and 129 Ma Chenggong Tonalite with D_3 schematic diagrams showing the structural relationships of D_2 and D_3 as well as S/C/C' fabrics. Different colors represent different deformation fabrics. The pole of foliation is used to show the compiled structure data. The mean plane of the D_3 fabric (C and C' surface) is plotted. The measurement data can be found in **Supplementary Table S1**.

limb of the dome is characterized by L-S tectonite with W-, SW- to S-plunging lineation indicative of non-coaxial strain, while S-tectonite is the feature of the east and west side of the dome at FGD and HJR locality suggestive of the flattening strain (**Figures 3**, **5**). It is implied that the strain state was mainly non-coaxial at the southwest, south and maybe northeast side of the Taiwushan Granite. This idea is further supported by the intrusion location of the Chenggong Tonalite and the development of the D_3 shear belt at the northeast side of the dome.

In the field at CG, the S_1 foliation is accompanied with *in situ* partial melting of the Chenggong Tonalite, which sets the peak metamorphic condition of D_1 as the granulite-facies (**Figure 6A**). The S_2-folded leucocratic melt further constrains this migmatitic condition only during D_1 event (**Figure 6B**). Petrographically, S_1 is defined by the alignment of subhedral biotite at the cleavage domain, whereas elongated quartz, aligned feldspar and anhedral hornblende within the microlithon domain (sample 1118CG01; **Figure 9**). Other than foliation-defining biotite, randomly oriented anhedral biotite and euhedral epidote can also be observed within the microlithon domain. The random orientation of anhedral biotite and hornblende within microlithon domain suggests they are igneous relicts. The foliation-defining biotite are often in contact with hornblende indicating these coarser subhedral biotite grains are new metamorphic minerals grown by fluid-and-deformation-facilitated metamorphic reaction under the amphibolite facies condition (Berger and Stünitz, 1996). Apart from hornblende to biotite and epidote reaction, grain boundary migration (GBM) with dynamic inter-fingering growth, chessboard extinction of quartz can be observed indicating deformation temperature for D_1 should be above 630°C (Stipp et al., 2002). The feldspars are deformed mainly by sub-grain rotation recrystallization (SGR) and bulging (BLG). The presence of myrmekite between the grain boundaries of plagioclase and K-feldspar indicates the occurrence of K-metasomatism during deformation (**Figure 9B**). These mineral assemblages and crystallographic deformation conditions suggest D_1 persisted from the granulite facies to the

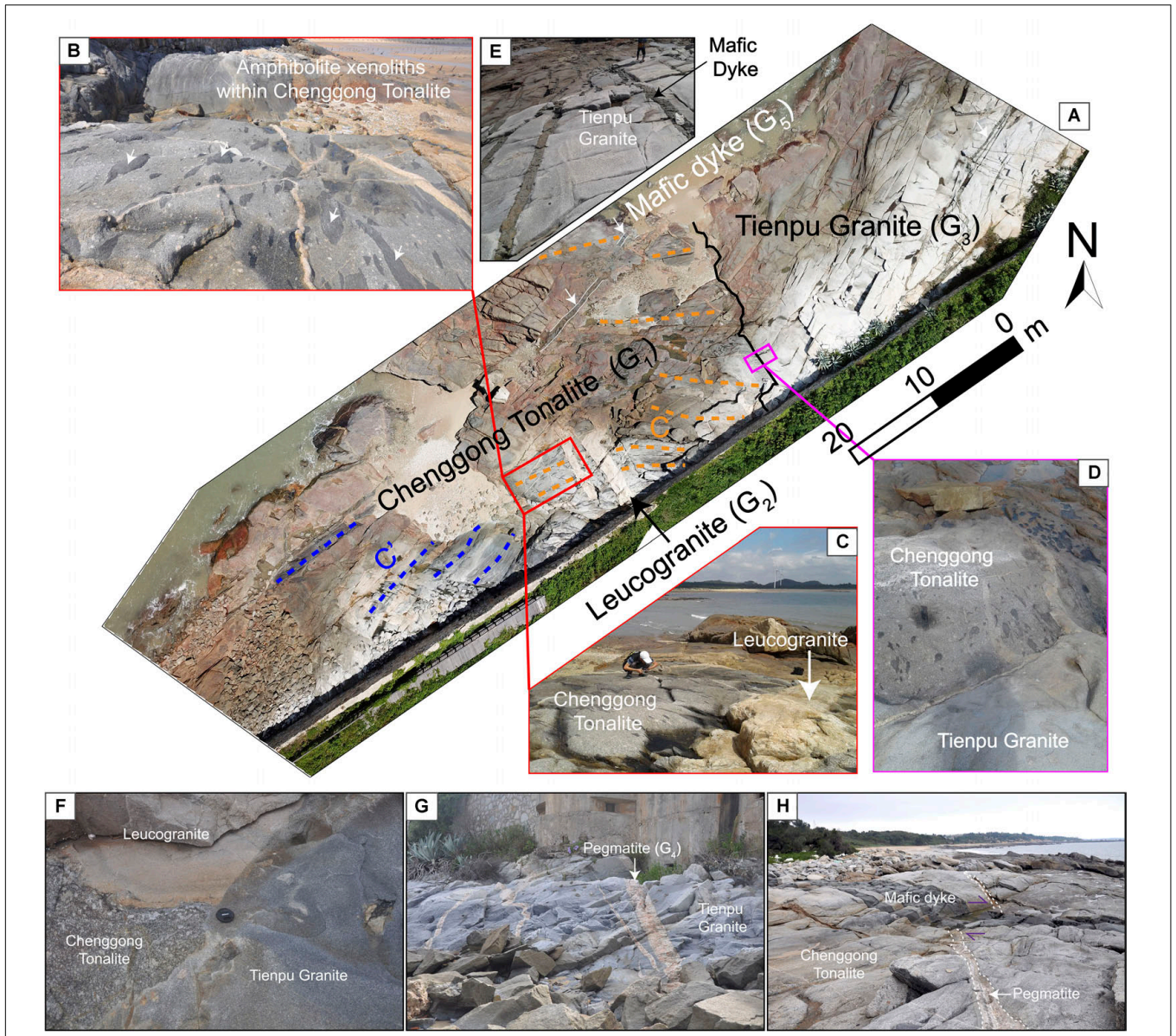

FIGURE 4 | Aerial and outcrop photos of Tien Pu (TP) region showing the crosscutting relationships of different lithology units (G_1–G_5). **(A)** Aerial photo of part of the TP region with sketched D_3 C/C' fabrics and labeled lithology units of Chenggong Tonalite (G_1), leucogranite (G_2), Tienpu Granite (G_3), and mafic dykes (G_5). **(B)** Deformed Chenggong Tonalite with aligned amphibolite schist xenoliths that are heterogeneously deformed and sheared. **(C)** Deformed Chenggong Tonalite intruded by post-D_3 leucogranite. **(D)** Deformed Chenggong Tonalite intruded by undeformed Tienpu Granite. **(E)** Undeformed Tienpu Granite truncated by the mafic dike. **(F)** Chenggong Tonalite intruded by leucogranite, both of which are truncated by Tienpu Granite. **(G)** Tienpu Granite intruded by pegmatites (G_4). **(H)** Pegmatites crosscutted and dextrally displaced by the mafic dike.

upper amphibolite facies. Post D_1 retrograde chlorite replacing hornblende and biotite can also be observed.

D_2

D_2 formed subhorizontal S-tectonite with little to none mineral lineation as the D_1 gneiss dome further exhumed (**Figures 3**, **6F**). The S_2 gneissic foliation distorted the S_1 doming fabrics into wavy foliations indicative of crustal extrusion from the core of Taiwushan Granite to the margin (**Figures 5B**, **6C,D**). The vertical shortening stress is suggested by the flattening strain of the subhorizontal S-tectonite. The S_2 foliation was well-developed at the northeast side of the dome with S_1 doming fabrics all transposed and unobservable within both the Taiwushan Granite and Chenggong Tonalite (e.g., HSH and TP; **Figures 7D,I**). In contrast, the S_2 fabric is confined to a discrete, centimeter-scale zone with wavy S_1 doming foliations preserved at the other parts of the dome margin (e.g., CG and FGD; **Figures 5B**, **6C,D**). The stronger and more penetrative S_2 fabric development at the northeast side of the dome reveals the strain partitioning and strain concentration

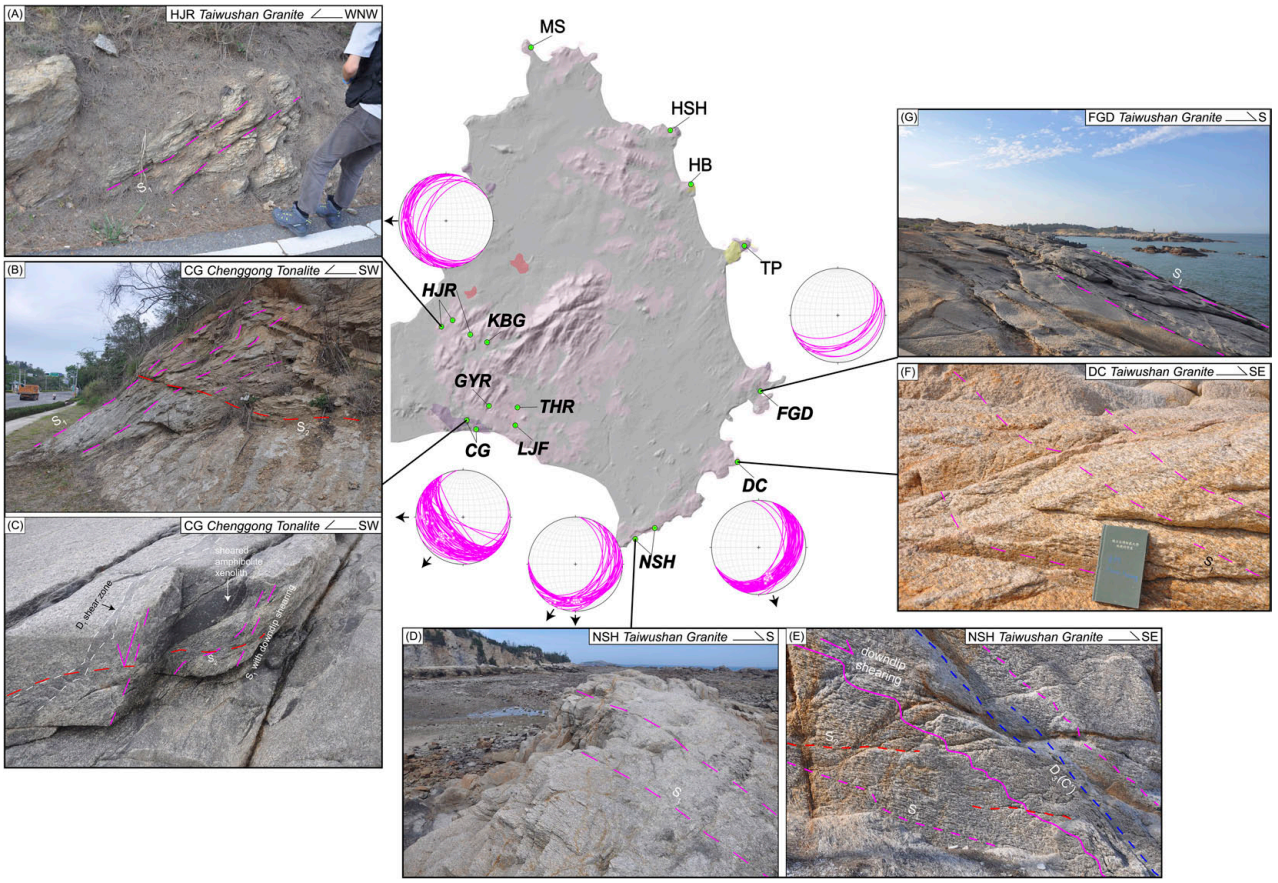

FIGURE 5 | Topographic map overlaid by the geological map showing outcrop photos with measured S_1 gneissic foliation and mineral lineation plotted with equal area southern hemisphere stereonet projection to demonstrate D_1 gneiss dome. The bold italic words indicate the sample locations with S_1 fabrics preserved. **(A)** The N-S striking and shallowly W-dipping gneissic foliation with poorly to none mineral lineation developed at HJR. **(B,C)** The NW-SE striking, shallowly to moderately SW-dipping gneissic foliation (S_1) with well-developed W and SW plunging lineation at CG. The S_1 fabric is deformed into a wavy form due to the subhorizontal S_2 foliation. The sheared amphibolite xenolith indicates the down-dip shearing along the S_1 foliation. **(D,E)** The NE-SW striking, shallowly to moderately SE-dipping gneissic foliation (S_1) with well-developed SW and S plunging lineation at NSH. The kinking of S_1 foliation is owing to the weak development of the subhorizontal S_2 foliation, both of which are crosscutted by D_3 shear zone (C' fabric). **(F)** The NE-SW striking, moderately SE-dipping gneissic foliation (S_1) with well-developed SSE plunging lineation at DC. **(G)** The ENE-WSW striking, moderately SE-dipping gneissic foliation (S_1) with none lineation developed at FGD.

at the northeast side of the gneiss dome. In addition, the subhorizontal foliation can be traced continuously at the same height level with the core of meter-scale thickness and the margin of centimeter-scale (**Figures 6C,D,F**). It's suggested that the vertical shortening stress was more concentrated in the core of Taiwushan Granite in the hint of the vertical movement of the gneiss dome as evidenced by the kink fold of S_1 fabric at the NSH locality (**Figure 5E**).

The S_2 folded leucocratic melt and lack of migmatite in the D_2 domain imply the peak deformation condition of D_2 was below granulite facies condition (**Figure 6B**). Similar to D_1, the S_2 foliation is defined by elongated quartz, feldspar ribbons, euhedral to subhedral biotite and subhedral to anhedral hornblende folia (**Figure 10**). The deformation mechanism of quartz is mainly of GBM and even chessboard extinction suggestive of peak deformation temperature >630°C (**Figures 10A,B**; Stipp et al., 2002). Both K-feldspar and plagioclase augens were deformed by SGR. The peak deformation condition of D_2 can be constrained to the upper amphibolite facies.

D_3

D_3 is a ENE-WSW striking subvertical sinistral shear zone forming S/C/C' fabrics and shear folds with regional heterogeneous strain partitioning ranging from centimeter-scale to a-hundred-meter scale (**Figure 7A**). The centimeter-scale mylonite belt are observed at the core (e.g., THR; **Figure 7B**), and along the margin of the Taiwushan Granite (e.g., NSH and FGD; **Figure 7C**). At the northeast limb of the dome (HSH, HB, and TP), D_3 is characterized by a-hundred-meter scale mylonite belt with locally preserved S_2 fabric and folded pre-D_3 leucogranitic dike (**Figures 7D,I**). The S/C/C' fabric, σ-type feldspar augens, shear folding along the S fabric indicate the sinistral shear sense of the shear zone (**Figures 7F–H**). The S/C/C' fabric can be noted from the amphibolite schist xenolith, Chenggong Tonalite, and Taiwushan Granite (**Figures 7F,H, 11A,D**).

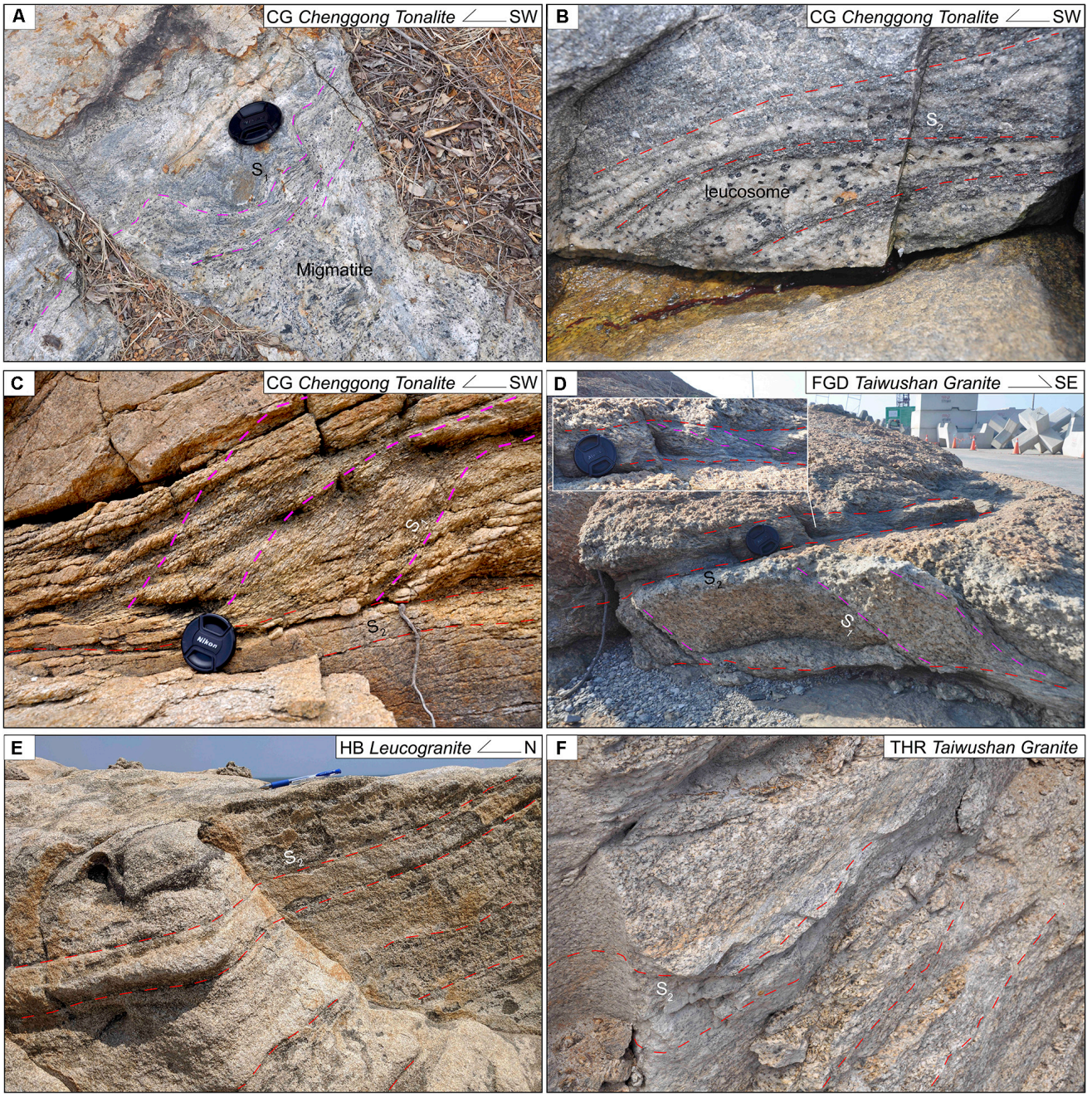

FIGURE 6 | Outcrop photos and sketches showing interpreted structures of D_1 and D_2. **(A)** *In situ* migmatite developed along the S_1 gneissic foliation within Chenggong Tonalite at CG. **(B)** S_2-folded leucosome in Chenggong Tonalite indicates that the migmatitic condition is confined in D_1 domain at CG. **(C)** Wavy S_1 foliation due to the development of subhorizontal S_2 foliation at CG. **(D)** Subhorizontal S_2 foliation crosscuts the S_1 doming fabric in Taiwushan Granite at FGD. **(E)** Subhorizontal S_2 foliation developed within the leucogranite showing the pre-D_2 magmatic intrusion at HB. **(F)** Subhorizontal S_2 foliation (S-tectonite) developed in Taiwushan Granite at THR.

The mineral stretching lineation and the D_3 fold axis show two dominant orientations: one plunges toward the north to east quadrant, while the other plunges toward west to south quadrant (**Figures 3**, **7A**). Combining with the sinistral sense of shear, the N- to E-plunging lineation reveals a transtensional nature for the shear belt. Although the W- to S-plunging lineation reveals transpressional nature, it was possibly due to heterogeneous strain localization effect. Of all outcrops other than HB and NSH indicate transtentional deformation environment of D_3.

The foliations observed from the Chenggong Tonalite are defined by the alignment of subhedral to anhedral hornblende,

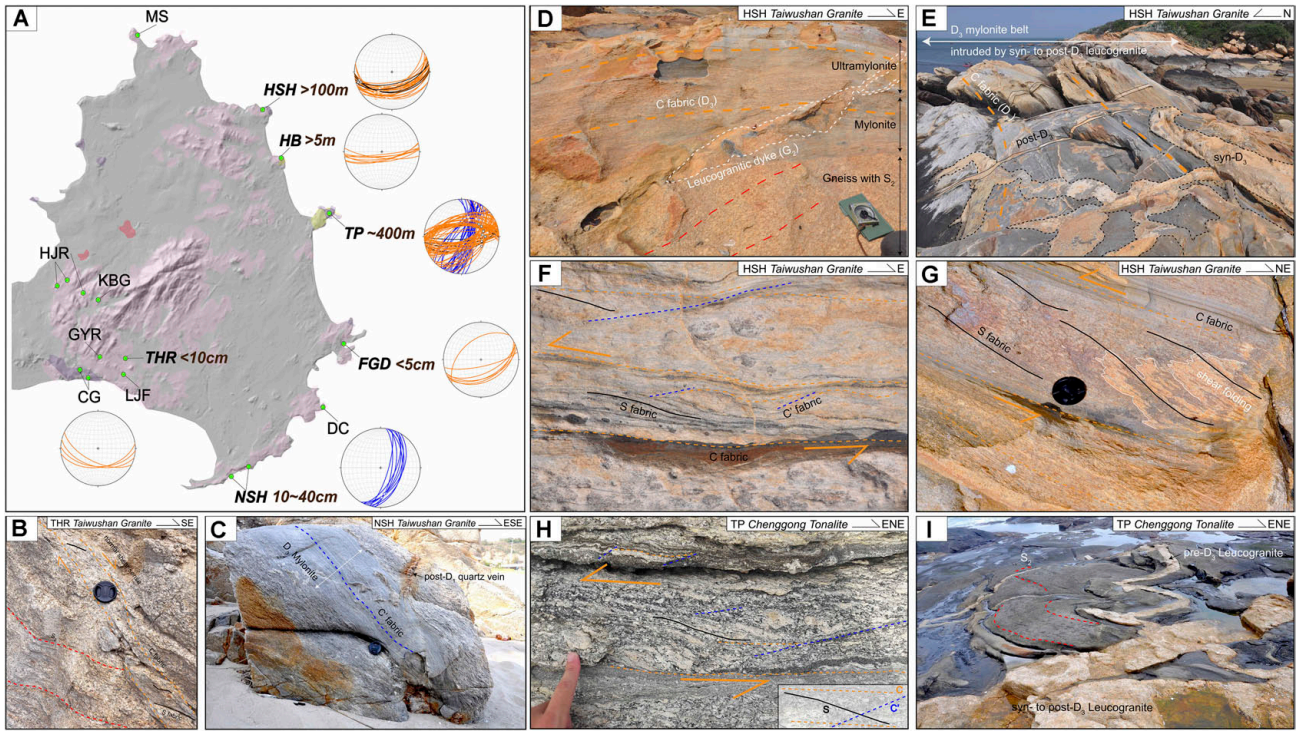

FIGURE 7 | Topographic map overlaid by the geological map showing outcrop photos with measured D_3 shear fabrics and mineral lineation plotted with equal area southern hemisphere stereonet projection. The bold italic words indicate the sample locations with D_3 shear fabrics identified. **(A)** Topographic map with geological map showing the sample locations with D_3 shear zone developement. The brown numbers show the width of the shear zone. **(B)** S/C fabric with normal shear sense crosscuts the subhorizontal S_2 foliation within Taiwushan Granite at THR. **(C)** D_3 mylonite (C' surface) crosscuts the post-D_1 quartz vein within Taiwushan Granite at NSH. **(D)** D_3 shear zone (C fabric) development from mylonite to ultramylonite crosscutting the S_2 fabric, both of which are intruded by leucogranitic dike (G_2) within Taiwushan Granite at HSH. **(E)** D_3 mylonite belt intruded by syn- to post- D_3 leucogranite (G_2) within Taiwushan Granite at HSH. **(F)** S/C/C' fabric showing sinistral shear sense within Taiwushan Granite at HSH. **(G)** S/C fabric indicating sinistral shear sense with shear folding along the S fabric within Taiwushan Granite at HSH. **(H)** S/C/C' fabric showing sinistral shear sense within Chenggong Tonalite at TP. **(I)** Subhorizontal S_2 fabric and pre-D_3 leucogranite (G_2) folded during D_3, both of which are intruded by syn- to post-D_3 leucogranite (G_2) at TP.

elongated quartz ribbons, and biotite folia (**Figures 10C**, **11D**). The deformation mechanisms observed from quartz are mainly GBM without chessboard extinction, which indicates the deformation temperature during shearing should range between 550 and 630°C. This is further supported as the observed K-feldspar and plagioclase was deformed mainly by SGR, and the precipitation of myrmekite along the K-feldspar grain boundaries (**Figure 11E**). The S/C/C' fabrics are better preserved within the amphibolite xenolith as the grain size are much finer than that of the Chenggong Tonalite. Two generations of hornblende can be noted, as one is the igneous relict (anhedral with green color, Hb1) and the other is the syn-D_3 metamorphism (euhedral to subhedral with yellow color, Hb2; **Figures 11A,B**). The new growth of metamorphic amphibole indicates the D_3 shearing event occurred under middle to lower amphibolite facies condition. Aside from the high-temperature deformation features, most quartz and feldspar have granoblastic polygonal texture showing annealing effect after the shearing event (**Figure 11C**). Based on that, we suggest the metamorphic temperature was still $\geq$400°C post D_3 shearing event. Greenschist-facies retrograde mineral assemblage of chlorite and epidote overprinted the biotite and hornblende, indicating that retrograde metamorphism occurred post D_3 (**Figures 11C,F**).

D_4 and D_5

D_4 is defined by the intrusion of the Tienpu Granite (G_3) followed by E-W striking, both N and S steeply dipping pegmatites (G_4; **Figures 4G,H**, **8A**). After the intrusion of the Tienpu Granite (G_3), no ductile deformation is noted. The pegmatite intrusion (G_4) is accompanied by sinistral displacement as they truncate and sinistrally offset the D_3 mylonite belts (**Figure 8A**). Greenschist facies mineral assemblages of chlorite, epidote and sericite are noted under thin section (**Figures 11C,F**). The retrograde replacement of biotite and hornblende to chlorite and epidote (**Figure 11**) further supports the lower temperature condition should be reached post D_3. The youngest deformation event (D_5) was NE-SW striking subvertical mafic dike swarms (G_5), which crosscuts all the magmatic rock units (G_1–G_4) and D_1–D_3 fabrics (**Figures 3**, **4A,E,H**). The mafic dike intrusion is accompanied by dextral displacement shown by the displaced D_4 pegmatite and the dextral fault displacing the aplitic dykes (**Figures 4H**, **8B**). The brittle nature of the basaltic dike intrusion indicate the temperature condition for D_5 should

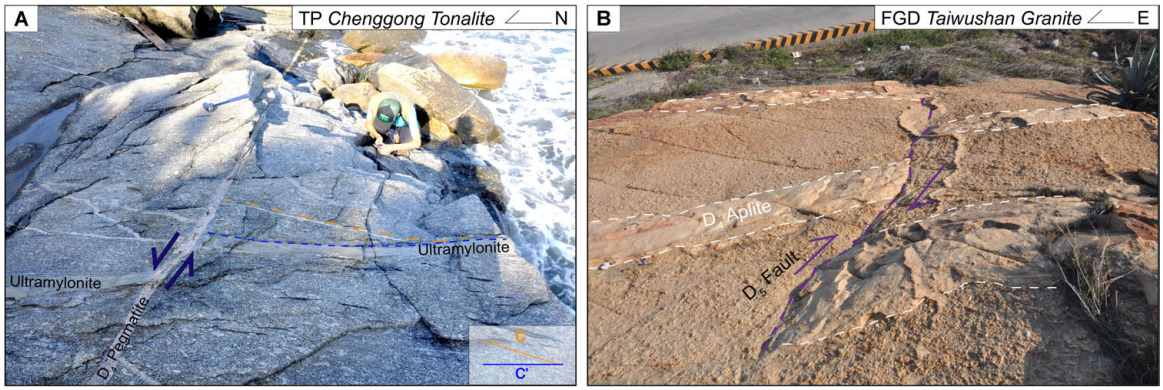

FIGURE 8 | Outcrop photos and sketches showing interpreted structures of D_4 and D_5. **(A)** D_4 pegmatite sinistrally displaced the Chenggong Tonalite with C/C' fabric, suggested by the displaced ultramylonite. **(B)** D_5 fault dextrally displaced the D_4 aplite.

also be under the lower greenschist facies, and was close to the ground surface.

DISCUSSION

Thermochronological Constraints on the Reconstructed Structural Evolution

Based on the crosscutting relationship observed in the field and oriented thin sections, three ductile deformation events (D_1, D_2, D_3) are reconstructed from both the Taiwushan Granite and the Chenggong Tonalite. These ductile events were followed by three magma intrusion under brittle condition (D_4/G_3, G_4, and D_5/G_5). The timing of D_4 and D_5 can be readily allocated to the crystallization ages of the magmatism, which are ca. 100 Ma (Yui et al., 1996) and between 90 and 76 Ma (Lee, 1994), respectively. Among these structural and magmatic intrusion events, the crystallization ages of the deformed Taiwushan Granite (139 Ma, Yui et al., 1996), the Chenggong Tonalite (129 Ma, Lin et al., 2011), and the undeformed Tienpu Granite (100 Ma, Yui et al., 1996), provide a rough time constraint for the three ductile deformation events to at 129–100 Ma. However, to establish the detailed timing of each deformation event, further work of $^{40}Ar/^{39}Ar$ geochronology, petrography and P-T estimates of these rocks are required.

$^{40}Ar/^{39}Ar$ thermochronology has been widely utilized to investigate the timing, rates and durations of deformation events (e.g., Wang and Lu, 2000; Chen et al., 2002; Chiu et al., 2018). Such study was uncommonly applied for the structural evolution of Cretaceous batholiths along the coast of SE Asia (Wang and Lu, 2000; Chen et al., 2002). One major reason is that the deformation events were interpreted as syn-magmatism, hence zircon U-Pb geochronology was dominantly employed to decipher the structural evolution (Tong and Tobisch, 1996; Shi, 2011; Li et al., 2015). To better constrain the timing of our reconstructed deformation events of the Kinmen Island, the available $^{40}Ar/^{39}Ar$ geochronology data are compiled and discussed below (**Figure 12**).

Lo et al. (1993) conducted $^{40}Ar/^{39}Ar$ geochronology for the Taiwushan Granite and reported plateau ages of 100.2 ± 0.9 Ma for hornblende separates (green square within **Figure 12A**) with estimated closure temperature of 557 ± 7°C, and 97.4 ± 0.9, 97.2 ± 0.9 Ma for biotite separates with estimated closure temperature of 333 ± 4°C and 292 ± 3°C (brown squares within **Figure 12A**). Complex age spectrum with a minimum age of 80 Ma in low-temperature steps that become older to a maximum of 90 Ma in high-temperature steps were reported for K-feldspar separates with closure temperature being estimated to 292 ± 3°C (Figure 2C within Lo et al., 1993). In addition, Lin (1994) analyzed the K-Ar ages of biotite and K-feldspar separates from both the Taiwushan Granite and Chenggong Tonalite. The acquired ages for biotite were 93.0 ± 2.0 and 94.1 ± 2.0 Ma and for K-feldspars are 90.9 ± 2.0 and 84.5 ± 1.8 Ma.

By plotting reported $^{40}Ar/^{39}Ar$ ages according to their estimated closure temperature, two cooling paths can be constructed. One is for the ductile deformed Taiwushan Granite and Chenggong Tonalite from 129 Ma (pink dash line in **Figure 12A**), while the other is for the undeformed Tienpu Granite since 100 Ma (yellow dash line within **Figure 12A**). Our petrological and microstructural analyses indicate upper amphibolite facies (≥630°C) metamorphic condition for D_1 and D_2. As we correlate the reconstructed cooling curve to 630°C, 107 Ma marks the boundary between D_2 and D_3 (**Figure 12A**). Similarly, as we correlate the temperature range of granulite facies (≥700°C) of D_1, a range between 129 and 114 Ma can be inferred (**Figure 12A**). The D_4 Tienpu Granite (100 Ma) crosscutting all foliations marks the termination of D_3, and the initiation of D_4. The brittle nature of D_4 and D_5 indicate the metamorphic condition are at shallow crustal level close to the surface. The low temperature condition (150–400°C) of the reconstructed cooling path and the presence of retrograde mineral assemblages further support the reconstructed temperature evolution.

The deformed Taiwushan Granite and Chenggong Tonalite underwent a rapid cooling from 550 to 300°C around 100 Ma. Similar rapid cooling rate is noted for the Tienpu Granite since 100–90 Ma (200°C). It's indicated that the crystalline rock was uplifted by about 12 km during that time (average

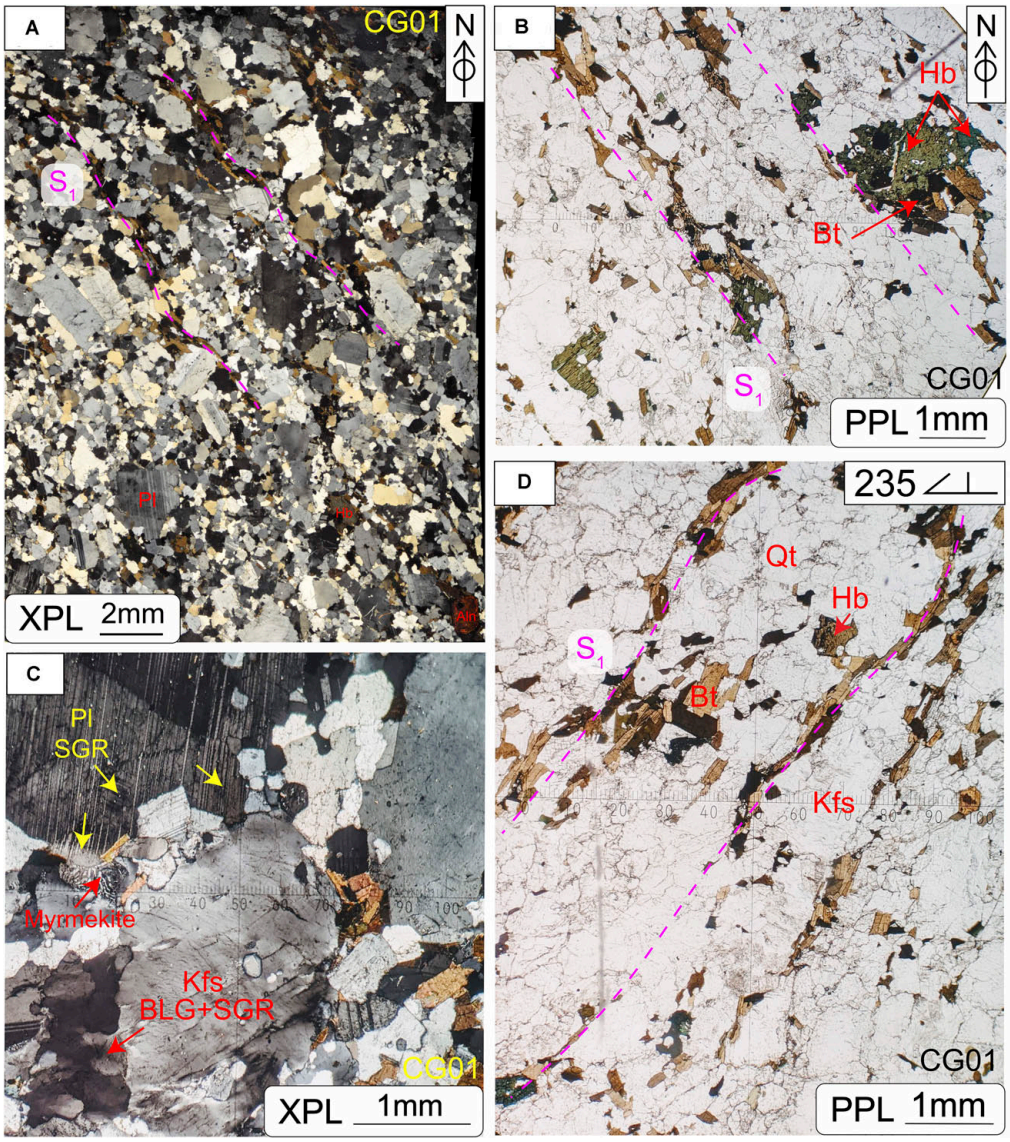

FIGURE 9 | Microphotographs showing microstructures and petrographic relationship of D_1. **(A)** S_1 foliation defined by alignment of biotite, elongated quartz, and plagioclase. The weak development of foliation is due to the low percentage of biotite in the sample and the granoblastic interlobate texture developed in the granulite facies condition. **(B)** Myrmekite precipitated between the K-feldspar and plagioclase, which is post the granoblastic interlobate matrix of quartz and feldspar aggregates. The deformation mechanism is SGR and BLG for K-feldspar, and SGR for plagioclase. **(C,D)** Gneissic layering suggested by the biotite cleavage domain and the quartzofeldspathic microlithon domain. Hb-hornblende; Bt-biotite; Pl-plagioclase; Aln-allanite; SGR-subgrain rotation recrystallization; BLG-bulging.

crustal geothermal gradient 25°C/km) revealing an average uplifting rate of 12 mm/a. Such rapid cooling rate can not be explained by the magma cooling alone. Blythe (1998) examined the surface uplift rates under different tectonic settings utilizing isotopic and fission track analysis, and revealed a surface uplift rate of 5–10 mm/a for active contraction region such as the Himalaya and Southern Alps in New Zealand. A much less surface uplift rate of ∼7 mm/a was obtained for the active extension region, such as for the D'Entrecasteaux Islands and Papua New Guinea. An even smaller uplift rate of 1–5 mm/a was obtained along the restraining bends of San Andreas strike slip fault systems. According to our reconstruction, this rapid cooling resulted from D_3 transtensional shearing. If we combine the uplift rate for the extension and strike-slip region, an 8–12 mm/a uplift rate is inferred, which is similar to what the cooling path suggests. The transtensional shearing can not only produce free space for later magma emplacement (Tienpu Granite), but also trigger larger vertical displacement. Taking the transtensional shearing and the denudation of the brittle upper crust induced by crustal extension into combination, such a rapid cooling rate is acquired around 100 Ma. This idea is further supported by the $^{40}Ar/^{39}Ar$ ages of the rocks within the PDMB [the sample of FJ07, FJ08, FJ12, and FJ17 in Chen et al. (2002); **Figure 12B**]. It's shown that the rapid cooling from the

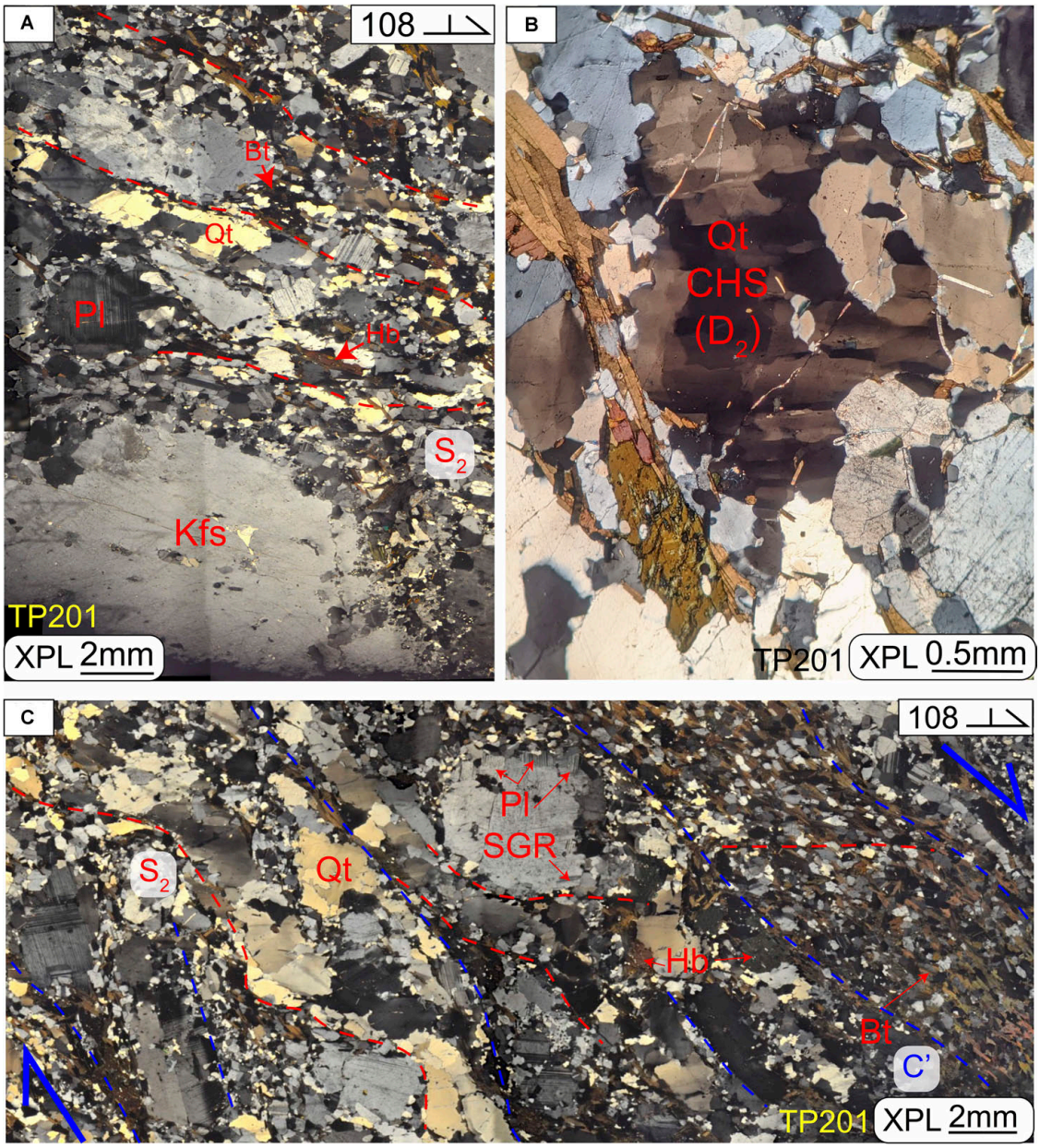

FIGURE 10 | Microphotographs showing microstructures and petrographic relationship of D_2 and D_3. **(A)** S_2 foliation defined by alignment of biotite, elongated quartz, feldspar, and hornblende. The K-feldspar porphyroclasts are mainly deformed by SGR and BLG with myrmekite along the margin. The plagioclases are recrystallized with granoblastic polygonal texture and SGR within the microlithon domain. The quartzs are deformed mainly by grain boundary migration (GBM). The deformation mechanisms of these quartz-feldspar aggregates suggest upper amphibolite facies condition. **(B)** Chessboard extinction of quartz illustrating the deformation temperature is >630°C. **(C)** S_2 foliation sheared by C' fabric with normal sense of shear. D_2-domain is defined by the coarser grain-sizes of quartz-feldspar aggregates with granoblastic interlobate texture and preserved chessboard extinction within quartzs. D_3-domain (C' fabric) is defined by the finer recrystallized quartz-feldspar aggregates and biotite folia due to the shearing-induced grain size reduction.

hornblende to biotite closure temperature ranges from 109 to 90 Ma overlapping the timing of D_3 transtensional shearing and D_4 brittle fracturing, especially the clusters within D_3 events. Accordingly, the D_3 transtensional shearing along with the later brittle fracturing and accompanied denudation of upper crust could contribute to the rapid cooling during 109–90 Ma along the coast of SE Asia.

Correlation to the Structural Evolution of the Changle-Nanao Shear Zone

Other than the diachronous distribution of Cretaceous magmatism, the NE-SW striking CNSZ is another major structural feature along the coastal region of SE Asia (Chen et al., 2002; Li et al., 2015; Wei et al., 2015). By integrating data and observations in previous studies (Wang and Lu, 2000;

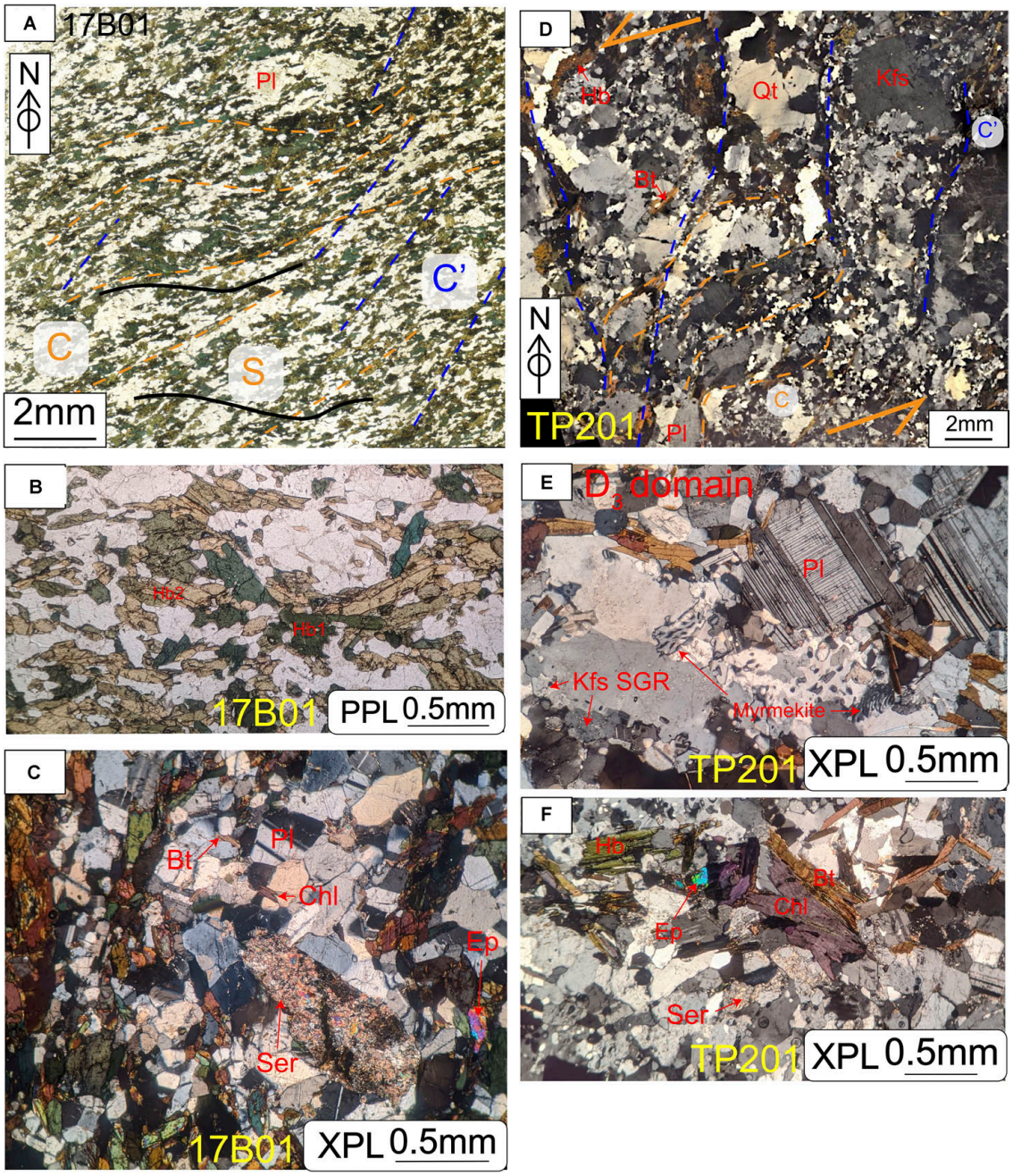

FIGURE 11 | Microphotographs showing microstructures and petrographic relationship of D_3. **(A)** S/C/C' fabric in amphibolite xenolith showing sinistral sense of shear. All fabrics are defined by the alignment of hornblende suggestive of amphibolite facies condition. **(B)** Detailed microphotograph under open nicol showing igneous hornblende (green) altered and replaced by secondary metamorphic hornblende (yellow) with granoblastic polygonal plagioclase matrix. **(C)** Granoblastic polygonal texture of plagioclase showing post-D_3 annealing with biotite growth along the plagioclase grain boundary. The retrograde overprint of the greenschist facies is shown by the chlorite, epidote and sericite. **(D)** C/C' fabric in the Chenggong Tonalite showing sinistral sense of shear. The D_3-domain is defined by the recrystallized finer-grained quartz-feldspar aggregates. The plasticity of feldspar indicated by fish structure and SGR shows amphibolite facies condition in agreement with the condition observed within amphibolite xenoliths. **(E)** Myrmekite precipitates between plagioclase and K-feldspar illustrating metasomatic process accompanying D_3 shearing. The K-feldspar is deformed by BLG and SGR. **(F)** Mineral assemblages of epidote, chlorite and sericite showing the greenschist facies post-D_3.

Shi, 2011; Wei et al., 2015), six deformation events were identified within the CNSZ based on their structural styles, metamorphic conditions and proposed relative timing. During 178–165 Ma, NE-trending foliation were developed with the amphibolite facies metamorphism (Wang and Lu, 2000). Between 149.2 and 145.4 Ma, a dextral-thrusting from NWW to SEE at lower

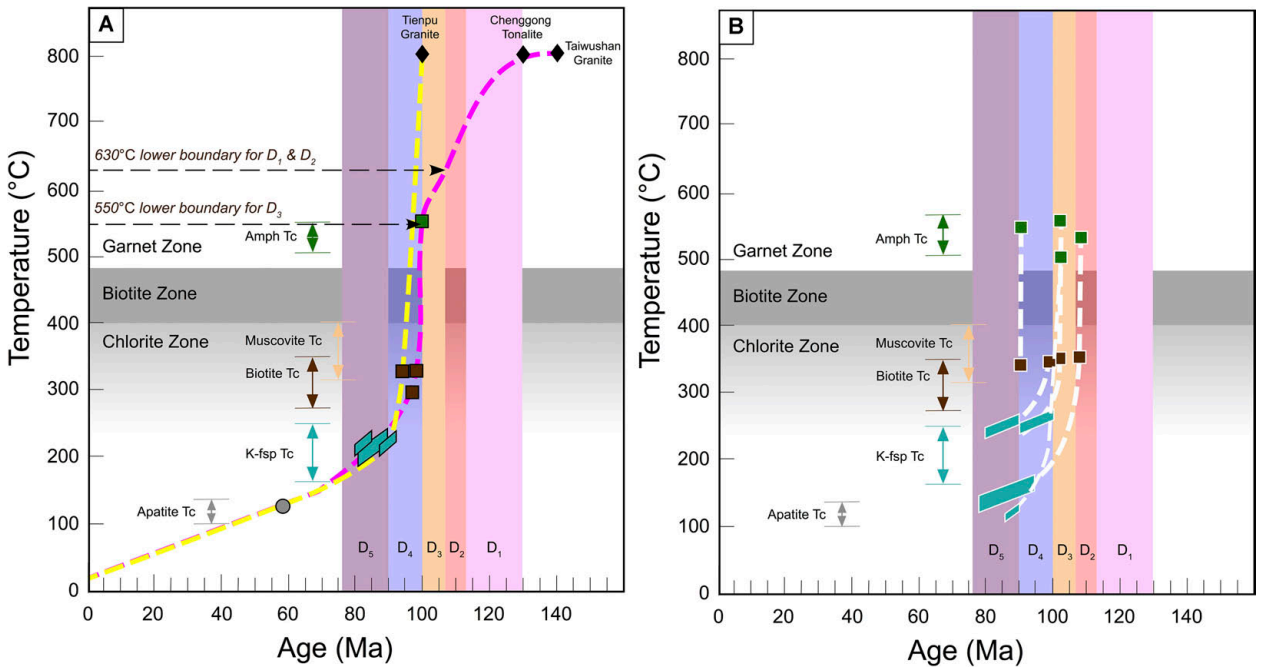

FIGURE 12 | Reconstructed cooling path of the Cretaceous magmatism of **(A)** Kinmen Island and **(B)** nearby regions based on previously published geochronological results (Lo et al., 1993; Lin, 1994; Yui et al., 1996; Chen et al., 2002; Lin et al., 2011). **(A)** The dashed pink line describes the cooling path for the 139 Ma Taiwushan Granite and the 129 Ma Chenggong Tonalite, while the dashed yellow line delineates the cooling path of the 100 Ma Tienpu Granite. **(B)** The cooling path of the gneiss within the PDMB from samples FJ07, FJ08, FJ12, and FJ17 in Chen et al. (2002). The closure temperature ranges for different mineral systems are as followed: U-Pb zircon (>800–900°C; solid black diamond Lee et al., 1997), Ar-Ar amphibole (Amph; solid green square 500–550°C; Harrison, 1982), Ar-Ar muscovite (350 ± 50°C; McDougall and Harrison, 1999), Ar-Ar biotite (275–350°C; solid brown square Döpke, 2017), Ar-Ar K-feldspar (K-fsp; solid green parallelogram 250–150°C; Harrison and McDougall, 1982), apatite fission track (110 ± 10°C; solid gray circle Gleadow and Duddy, 1981). The timing for the five deformation events (D_1–D_5) are distinguished by correlating the metamorphic conditions proposed in this study to the reconstructed cooling path.

amphibolite facies was recognized, which was followed by a sinistral-thrusting from NNW to SSE at upper-greenschist facies during 145.4–137 Ma (Shi, 2011). From 130 to 105 Ma, Wei et al. (2015) reported a northwest-directed ductile thrust with a top-to-the-NW shear sense followed by a later NE-SW folding event under amphibolite facies condition (their E1 event). During this period, Wang and Lu (2000) further separated an 118–107 Ma NE-SW trending mylonitic foliation under greenschist facies condition. Finally, a dextral strike-slip faulting with normal component at lower greenschist facies was around 100 Ma (Shi, 2011).

Compared to CNSZ, similar structural evolution of 130–105 Ma subhorizontal foliation (our D_2) followed by 118–107 Ma NE-SW mylonite belt (our D_3) and ca. 100 Ma dextral displacement (D_5) are also recognized in our study area. The structural evolution within the CNSZ from 129 Ma toward 100 Ma was generally considered to be formed under collisional setting (Li et al., 2015; Wei et al., 2015). Our data from the Kinmen Island reveals the opposite. The D_1 gneiss dome structure has never been reported previously within neither Kinmen nor CNSZ. The down-dip shearing strain pattern along the northeast and southwest limbs of this gneiss dome (**Figures 2B**, **3**), and the retrograde metamorphic conditions from granulite facies to upper amphibolite facies (**Figure 12A**) indicate extensional setting for this previously unrecognized doming event. Furthermore, despite similar subhorizontal foliations identified throughout CNSZ and Kinmen, previous researchers interpreted the origin of this subhorizontal foliation as thrust folding. Yet, according to our observation in the Kinmen island, these intervally developed subhorizontal foliations are likely generated owing to collapsing of the gneiss dome as crust further thinned (**Figure 13**). The NE-SW mylonitic foliation is also noted in the Kinmen, but it's delineated as the C' fabric of our D_3 transtensional shear belt shown by the normal shear sense (**Figure 10C**). At last, the dextral faulting can be correlated to our D_5 mafic dike swarm accompanied with dextral displacement at upper crustal level. To sum up, although similar structural evolution of D_2, D_3, and D_5 can be correlated between CNSZ and the Kinmen island, different kinematics are proposed in this study. All deformation events of Kinmen Island might have formed under extensional environment during crustal thinning. This crustal thinning event was recognized in not only the SE Asia but also the NE Asia (Sheldrick et al., 2020), which suggests the continental crust of East Asia had been thinned during the Cretaceous. Though the crustal thinning mechanism might be different among NE Asia to SE Asia, the regional structural orientations/patterns are fundamentally controlled by the regional tectonic settings. Thus, the deformation events/styles must reflect regional tectonic setting. Despite the diverse lithologies and different metamorphic condition, if East Asia had

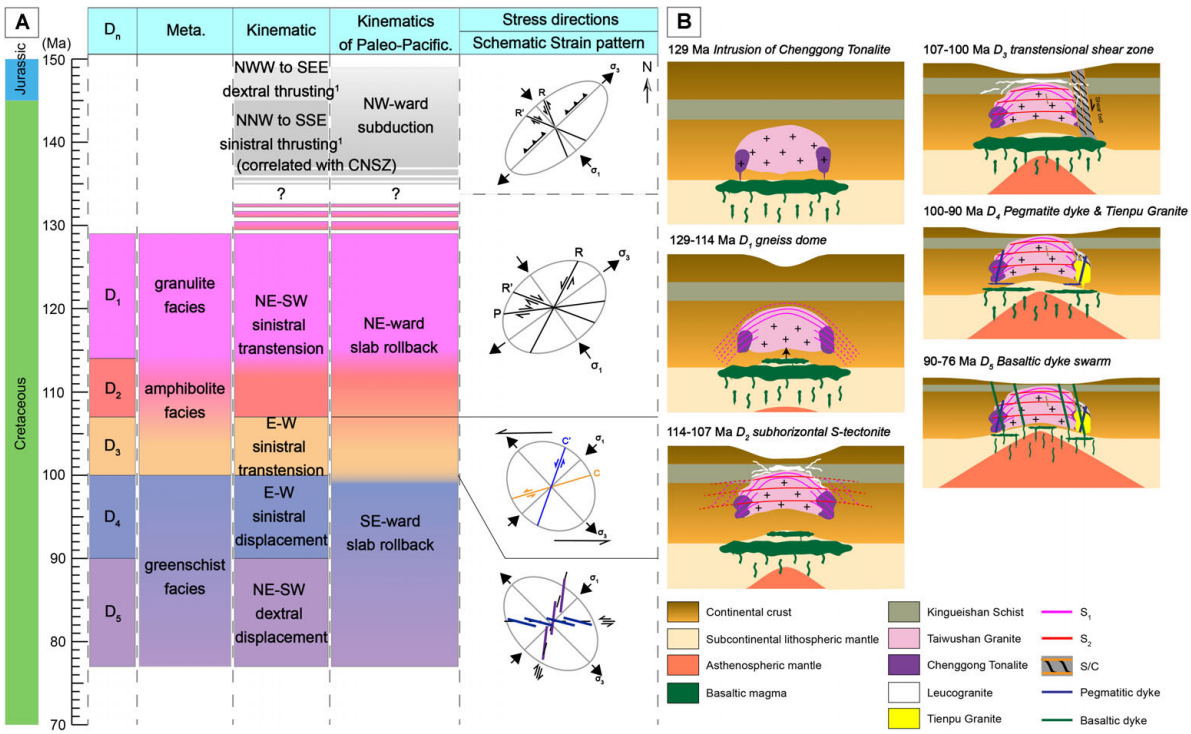

FIGURE 13 | A compiled diagram showing the structural and tectonic evolution of the Kinmen Island. **(A)** Composite diagram showing the reconstructed structural evolution and the associated plate kinematics and the schematic strain pattern. The structural evolution of Kinmen is correlated to the regional-scale Changle-Nanao Shear Zone (superscript 1; Shi, 2011). Besides, the normal fault systems of the extensional basins within the Cathaysia Block (Li J. et al., 2014) is compiled to constrain the stress field during D_1–D_2. **(B)** Schematic diagram of the tectonic evolution of the Kinmen Island between 129 and 76 Ma. Both horizontal and vertical dimensions are not to scale.

undergone extensive crustal thinning, extensional stress should be a more reasonable explanation for the development of these reported Early Cretaceous structures.

Correlation to the Stress Evolution of Cretaceous Extensional Basins Within SE Asia

Numerous early Cretaceous (145–100 Ma) NE-trending and WNW-ESE trending intracontinental extensional basins are bounded by high-angle normal faults within the Cathaysia Block (e.g., Shu et al., 2009; Li J. et al., 2014). The development of these sedimentary basins and their boundary normal fault systems reflected the stress setting during their formation. These boundary normal fault systems indicated general stress pattern of NW-SE extension around 136–118 Ma, and NW-SE transpression around 118–107 Ma. The extension direction switched to NWW-SEE during 107–85 Ma, WNW-ESE transpression around 85 Ma, and to N-S extension during 80–65 Ma. The schematic strain pattern derived from our reconstructed structural evolution reveals similar yet more detailed stress evolution along the coast of SE Asia (**Figure 13A**). From 150 to 137 Ma, the continental crust was under NW-SE compression (σ_1) with NE-SW extension (σ_3) due to the forward subduction of the Paleo-Pacific plate. The stress pattern switched to NE-SW extension (σ_3) with NW-SE compression (σ_1) during ~129–107 Ma (our D_1 and D_2) as the crust extended due to the northeastward rollback of the Paleo-Pacific plate. Owing to the changing rollback direction into southeastward, the stress setting shifted to NW-SE extension (σ_3) and NE-SW compression (σ_1) during 107–76 Ma (our D_3–D_5). Most of the previous studies interpreted the NE-striking mylonitic foliation as the main structure (S/C fabric) of the CNSZ (Tong and Tobisch, 1996; Wang and Lu, 2000; Chen et al., 2002; Wei et al., 2015). In this study, well-developed S/C/C' fabrics (**Figures 3**, **7A,F,H**, **13A**) are noted. The S/C/C' fabrics allow us to decipher the non-coaxial sinistral shearing setting under NW-SE extension (σ_3) and NE-SW compression (σ_1) stress pattern for the D_3 event (**Figure 13A**). Likewise, rather than WNW-ESE transpression and N-S extension, if we consider our D_4 pegmatites and D_5 basalt dykes to form along the shear fractures under the same stress setting as D_3, NW-SE extension with NE-SW compression is adequate to produce such structural pattern.

Changing Direction of the Paleo-Pacific Plate Rollback

According to our reconstructed structural evolution in the Kinmen Island, two stress fields of NW-SE compression (σ_1) with NE-SW extension (σ_3) for D_1 to D_2, and NE-SW compression (σ_1) with NW-SE extension (σ_3) from D_3 till D_5 are delineated. Our reconstructed stress field evolution could be linked to

the changing direction of slab rollback of the Paleo-Pacific plate as indicated by the maximum extension direction (σ_3). The northeastward slab rollback correlates nicely with the northeastward younging trend of the 180–125 Ma igneous rocks within the Cathaysia Block as Wang et al. (2011) proposed. The oblique subduction might have triggered the strike-slip deformation within the overriding plates (Holdsworth et al., 1998) while the slab rollback might have induced the back-arc extension of the continental lithosphere, as demonstrated by the geodynamic modeling (Chen et al., 2016). It's suggested that the northeastward slab rollback satisfies the oblique divergence setting and could have initiated the sinistral shear zone (e.g., CNSZ) and numerous NE-SW and WNW-ESE normal fault systems (**Figure 13A**). In light of the 149–137 Ma NW-SE thrusting of CNSZ (Shi, 2011), we prefer a northwestward forward subduction of the Paleo-Pacific plate during this period but not southwestward oblique subduction. Accordingly, the crustal extension along the coast of SE Asia was initiated during 137–129 Ma, consistent with the previous studies of 135–90 Ma crustal extension (Dong et al., 2018). The stress field changed to NE-SW compression (σ_1) with NW-SE extension (σ_3) during 114–107 Ma as the direction of slab rollback shifted to southeastward when the Cathaysia Block is characterized by the magmatic quiescence (118–107 Ma, Li J. et al., 2014). The alternation of σ_1 and σ_3 between $D_{1\sim2}$ then to $D_{3\sim5}$ demonstrates that all observed structures of this study are mainly developed or reactivated along two weak zones that reflect the slab rollback direction.

Tectonic and Crustal Evolution of the Kinmen Island

During early Cretaceous time, numerous granitoid batholiths intruded along the coast of SE Asia, including PDMB (Li et al., 2015) and the Kinmen Island (e.g., Taiwushan Granite and Chenggong Tonalite). The northeastward rollback of the Paleo-Pacific plate initiated the continental crust extension and post-orogenic magmatism (e.g., Taiwushan Granite in Kinmen; Lan et al., 1997). This NE-ward slab rollback imposed the NE-SW extension on the crust, which generated the kilometer-scale gneiss dome (D_1; 129–114 Ma) in the Kinmen Island and NE-SW extensional folding within the PDMB. The slab-rollback-induced extension thinned the continental crust by opening of the extensional basins, denudation of the upper brittle crust and exhumation of ductile lower-to-middle crust. The crustal thinning resulted from the bulk extension triggered the middle to lower crustal flow (Teyssier and Whitney, 2002) along with the exhumation of the gneiss dome to form the subhorizontal S-tectonite (D_2; 114–107 Ma). The further crustal thinning and vertical displacement of the gneiss dome due to the sustained slab rollback and the density-inversion diapiric flow triggered the ENE-WSW striking sinistral transtensional shear zone (D_3; 107–100 Ma). The exhumation of the gneiss dome into the middle crust during D_2–D_3 produced the longstanding magmatism of leucogranite from pre-D_2 to post-D_3 and related amphibolite facies metamorphism owing to the decompression melting. Under the same stress setting of southeastward slab rollback as D_3, the continental crust was continually uplifted into upper crust in D_4 (100–90 Ma) with intrusion of Tienpu Granite and later pegmatites along E-W striking extensional shear fractures marking the end of ductile deformation. The final D_5 (90–76 Ma) was NE-SW striking mafic dike swarms sourced from the upwelling asthenosphere, representing the almost rifting stage of continental crust (**Figure 13B**).

CONCLUSION

The granitic batholiths within the Kinmen Island record the crustal thinning history of the southeast coast of China during the Cretaceous period, induced by the longstanding slab rollback of the Paleo-Pacific plate from 139 to 76 Ma. Based on our reconstructed structural evolution and petrographic analysis, five deformation events accompanied with the exhumation of deep-seated granitoids and the associated stress field was revealed. The kilometer-scale gneiss dome (D_1; 129∼114 Ma) was formed at lower continental crust under granulite facies condition post the intrusion of the Chenggong Tonalite (G_1). Further crustal thinning and exhumation of the gneiss dome generated subhorizontal S-tectonite (D_2; 114∼107 Ma) under upper amphibolite facies. The stress field of D_1 and D_2 was both under NW-SE compression with NE-SW extension due to the northeastward slab rollback of the Paleo-Pacific plate. The local development of ENE-WSW striking sinistral transtensional shear zones under amphibolite facies condition (D_3; 107∼100 Ma) were initiated under NW-SE extension as the slab rollback direction of Paleo-Pacific plate shifted to southeast. This strongly developed transtensional shear zones facilitated not only the exhumation of the gneiss dome to the upper continental crust, but also decompressional melting to form the G_2 leucogranite. With further slab rollback and the crustal thinning, the 100 Ma Tienpu Granite (G_3) intruded both the Chenggong Tonalite (G_1) and the leucogranite (G_2) on account of decompression melting of the upwelling asthenosphere. Under the same stress setting of NW-SE extension, the E-W striking pegmatitic dykes (D_4/G_4; 100∼90 Ma) were emplaced, and were followed by the intrusion of NE-SW striking mafic dike swarms (D_5/G_5; 90∼76 Ma) as the continental crust was almost rifted as a consequence of the prolonged crustal extension caused by continual slab rollback of the Paleo-Pacific plate.

DATA AVAILABILITY STATEMENT

All datasets presented in this study are included in the article/**Supplementary Material**.

AUTHOR CONTRIBUTIONS

Both authors contributed to the design, field, sample collection, conception of this study, the interpretation of data, manuscript writing, revision, and read and approved the submitted version. T-HH was responsible to the data compilation and thin section making and petrography analysis.

FUNDING

This research received funding support from the Ministry of Science and Technology of Taiwan under project ID: 105WFA0350331 and 107-2813-C-002-113-M. The funding supports the field work and analytical instruments.

ACKNOWLEDGMENTS

Dr. M. F. Chu is thanked for her input on the discussion about the igneous petrogenesis in our study area. Besides, we appreciate the aerial photos provided by Mr. C. H. Tsao to clearly identify the crosscutting relationships between the different lithologies. The Kinmen Weather Station is thanked for providing the accommodation. Finally, MOST of Taiwan is appreciated for their funding support under project IDs: 105WFA0350331 and 107-2813-C-002-113-M.

SUPPLEMENTARY MATERIAL

The Supplementary Material for this article can be found online at: https://www.frontiersin.org/articles/10.3389/feart.2020.00330/full#supplementary-material

TABLE S1 | Measured structural data in the form of dip direction and dip for planar structures, and as trend and plunge for linear structures.

REFERENCES

Berger, A., and Stünitz, H. (1996). Deformation mechanisms and reaction of hornblende: examples from the Bergell tonalite (Central Alps). *Tectonophysics* 257, 149–174. doi: 10.1016/0040-1951(95)00125-5

Blythe, A. E. (1998). "Active tectonics and ultrahigh-pressure rocks," in *When Continents Collide: Geodynamics and Geochemistry of Ultrahigh-Pressure Rocks*, eds B. Hacker and J.G. Liou (Dordrecht: Springer), 141–160. doi: 10.1007/978-94-015-9050-1_6

Chen, C. H., Lin, W., Lan, C. Y., and Lee, C. Y. (2004). Geochemical, Sr and Nd isotopic characteristics and tectonic implications for three stages of igneous rock in the Late Yanshanian (Cretaceous) orogeny, SE China. *Earth Environ. Sci. Trans. R. Soc. Edinburgh* 95, 237–248. doi: 10.1017/s0263593300001048

Chen, W. S., Yang, H. C., Wang, X., and Huang, H. (2002). Tectonic setting and exhumation history of the Pingtan–Dongshan metamorphic belt along the coastal area, Fujian Province, Southeast China. *J. Asian Earth Sci.* 20, 829–840. doi: 10.1016/s1367-9120(01)00066-9

Chen, Z., Schellart, W. P., Strak, V., and Duarte, J. C. (2016). Does subduction-induced mantle flow drive backarc extension? *Earth Planet. Sci. Lett.* 441, 200–210. doi: 10.1016/j.epsl.2016.02.027

Chiu, Y. P., Yeh, M. W., Wu, K. H., Lee, T. Y., Lo, C. H., Chung, S. L., et al. (2018). Transition from extrusion to flow tectonism around the Eastern Himalaya syntaxis. *GSA Bull.* 130, 1675–1696. doi: 10.1130/b31811.1

Dong, S., Zhang, Y., Li, H., Shi, W., Xue, H., Li, J., et al. (2018). The Yanshan orogeny and late Mesozoic multi-plate convergence in East Asia—Commemorating 90th years of the "Yanshan Orogeny". *Sci. China Earth Sci.* 61, 1888–1909. doi: 10.1007/s11430-017-9297-y

Döpke, D. (2017). *Modelling the Thermal History of Onshore Ireland, Britain and Its Offshore Basins Using Low-temperature Thermochronology*. Doctoral dissertation, Trinity College Dublin, Ireland.

Gleadow, A. J. W., and Duddy, I. R. (1981). A natural long-term track annealing experiment for apatite. *Nuclear Tracks* 5, 169–174. doi: 10.1016/0191-278x(81)90039-1

Harrison, T. M. (1982). Diffusion of 40Ar in hornblende. *Contrib. Mineral. Petrol.* 78, 324–331. doi: 10.1007/bf00398927

Harrison, T. M., and McDougall, I. (1982). The thermal significance of potassium feldspar K-Ar ages inferred from 40Ar39Ar age spectrum results. *Geochim. Cosmochim. Acta* 46, 1811–1820. doi: 10.1016/0016-7037(82)90120-x

Holdsworth, R. E., Strachan, R. A., and Dewey, J. F. (eds) (1998). *Continental Transpressional and Transtensional Tectonics*. London: Geological Society.

Hsü, K. J., Li, J., Chen, H., Wang, Q., Sun, S., and Şengör, A. M. C. (1990). Tectonics of South China: key to understanding West Pacific geology. *Tectonophysics* 183, 9–39. doi: 10.1016/0040-1951(90)90186-c

Huang, L., Wang, L., Fan, H. R., Lin, M., and Zhang, W. (2019). Late early-cretaceous magma mixing in the langqi island, fujian province, china: evidences from petrology, geochemistry and zircon geochronology. *J. Earth Sci.* 31, 468–480. doi: 10.1007/s12583-019-1022-7

John, B. M., Zhou, X. H., and Li, J. L. (1990). Formation and tectonic evolution of southeastern China and Taiwan: isotopic and geochemical constraints. *Tectonophysics* 183, 145–160. doi: 10.1016/0040-1951(90)90413-3

Lan, C. Y., Chung, S. L., and Mertzman, S. A. (1997). Mineralogy and geochemistry of granitic rocks from Chinmen, Liehyu and Dadan Islands, Fujian. *J. Geol. Soc. China* 40, 527–558.

Lan, C. Y., Chung, S. L., Mertzman, S. A., and Chen, C. H. (1995). Mafic dykes from Chinmen and Liehyu Islands, off Southeast China: petrochemical characteristics and tectonic implications. *J. Geol. Soc. China* 38, 183–213.

Lee, C. Y. (1994). *Chronology and Geochemistry of Basaltic Rocks from Penghu Islands and Mafic Dykes from East Fujian: Implications for The Mantle Evolution of SE China Since Late Mesozoic*. Doctoral dissertation, National Taiwan University, Taipei.

Lee, J. K., Williams, I. S., and Ellis, D. J. (1997). Pb, U and Th diffusion in natural zircon. *Nature* 390, 159–162. doi: 10.1038/36554

Li, J., Zhang, Y., Dong, S., and Johnston, S. T. (2014). Cretaceous tectonic evolution of South China: a preliminary synthesis. *Earth Sci. Rev.* 134, 98–136. doi: 10.1016/j.earscirev.2014.03.008

Li, X. H. (2000). Cretaceous magmatism and lithospheric extension in Southeast China. *J. Asian Earth Sci.* 18, 293–305. doi: 10.1016/s1367-9120(99)00060-7

Li, Y., Ma, C. Q., Xing, G. F., and Zhou, H. W. (2015). The early cretaceous evolution of SE China: insights from the changle–nan'ao metamorphic belt. *Lithos* 230, 94–104. doi: 10.1016/j.lithos.2015.05.014

Li, Z., Qiu, J. S., and Yang, X. M. (2014). A review of the geochronology and geochemistry of Late Yanshanian (Cretaceous) plutons along the Fujian coastal area of southeastern China: implications for magma evolution related to slab break-off and rollback in the Cretaceous. *Earth Sci. Rev.* 128, 232–248. doi: 10.1016/j.earscirev.2013.09.007

Li, Z., Zhou, J., Mao, J., Santosh, M., Yu, M., Li, Y., et al. (2013). Zircon U–Pb geochronology and geochemistry of two episodes of granitoids from the northwestern Zhejiang Province, SE China: implication for magmatic evolution and tectonic transition. *Lithos* 179, 334–352. doi: 10.1016/j.lithos.2013.07.014

Li, Z. X., and Li, X. H. (2007). Formation of the 1300-km-wide intracontinental orogen and postorogenic magmatic province in Mesozoic South China: a flat-slab subduction model. *Geology* 35, 179–182.

Lin, W. (1994). *Geochemistry and Thermal History of Late Yanshanian Granites from Chinmen Area*. Master thesis, National Taiwan University, Taipei.

Lin, W., Lee, C. Y., Yang, H. C., and Chen, C. H. (2011). *Geological Map of Taiwan scale 1:50000, Kinmen Area*. Kolkata: Central Geological Survey.

Liu, L., Xu, X., and Xia, Y. (2016). Asynchronizing paleo-Pacific slab rollback beneath SE China: insights from the episodic Late Mesozoic volcanism. *Gondwana Res.* 37, 397–407. doi: 10.1016/j.gr.2015.09.009

Liu, Q., Yu, J. H., Wang, Q., Su, B., Zhou, M. F., Xu, H., et al. (2012). Ages and geochemistry of granites in the Pingtan–Dongshan Metamorphic Belt, Coastal South China: new constraints on Late Mesozoic magmatic evolution. *Lithos* 150, 268–286. doi: 10.1016/j.lithos.2012.06.031

Lo, L. C. H., Onstott, T. C., and Lee, W. L. C. W. (1993). 40Ar/39Ar dating of plutonic/metamorphic rocks from Chinmen Island off Southeast China and its tectonic implications. *J. Geol. Soc. China* 36, 35–55.

Mai, H. A., Chan, Y. L., Yeh, M. W., and Lee, T. Y. (2018). Tectonic implications of Mesozoic magmatism to initiation of Cenozoic basin development within

the passive South China Sea margin. *Int. J. Earth Sci.* 107, 1153–1174. doi: 10.1007/s00531-017-1537-y

Mao, J., Li, Z., and Ye, H. (2014). Mesozoic tectono-magmatic activities in South China: retrospect and prospect. *Sci. China Earth Sci.* 57, 2853–2877. doi: 10.1007/s11430-014-5006-1

McDougall, I., and Harrison, T. M. (1999). *Geochronology and Thermochronology by the 40Ar/39Ar Method*. Oxford: Oxford University Press.

Sheldrick, T. C., Barry, T. L., Dash, B., Gan, C., Millar, I. L., Barfod, D. N., et al. (2020). Simultaneous and extensive removal of the East Asian lithospheric root. *Sci. Rep.* 10, 1–6.

Shi, J. J. (2011). Dividing of deformation and metamorphic stages and determination of its ages in Changle-Nanao tectonic zone. *Geol. Fujian* 3, 189–199.

Shu, L. S., Zhou, X. M., Deng, P., Wang, B., Jiang, S. Y., Yu, J. H., et al. (2009). Mesozoic tectonic evolution of the Southeast China Block: new insights from basin analysis. *J. Asian Earth Sci.* 34, 376–391. doi: 10.1016/j.jseaes.2008.06.004

Stipp, M., StuÈnitz, H., Heilbronner, R., and Schmid, S. M. (2002). The eastern Tonale fault zone: a 'natural laboratory'for crystal plastic deformation of quartz over a temperature range from 250 to 700 C. *J. Struct. Geol.* 24, 1861–1884. doi: 10.1016/s0191-8141(02)00035-4

Sun, W., Ding, X., Hu, Y. H., and Li, X. H. (2007). The golden transformation of the Cretaceous plate subduction in the west Pacific. *Earth Planet. Sci. Lett.* 262, 533–542. doi: 10.1016/j.epsl.2007.08.021

Teyssier, C., and Whitney, D. L. (2002). Gneiss domes and orogeny. *Geology* 30, 1139–1142.

Tong, W. X., and Tobisch, O. T. (1996). Deformation of granitoid plutons in the Dongshan area, southeast China: constraints on the physical conditions and timing of movement along the Changle-Nanao shear zone. *Tectonophysics* 267, 303–316. doi: 10.1016/s0040-1951(96)00107-2

Wang, F. Y., Ling, M. X., Ding, X., Hu, Y. H., Zhou, J. B., Yang, X. Y., et al. (2011). Mesozoic large magmatic events and mineralization in SE China: oblique subduction of the Pacific plate. *Int. Geol. Rev.* 53, 704–726. doi: 10.1080/00206814.2010.503736

Wang, Y., Fan, W., Zhang, G., and Zhang, Y. (2013). Phanerozoic tectonics of the South China Block: key observations and controversies. *Gondwana Res.* 23, 1273–1305. doi: 10.1016/j.gr.2012.02.019

Wang, Z. H., and Lu, H. F. (2000). Ductile deformation and 40Ar/39Ar dating of the Changle–Nanao ductile shear zone, southeastern China. *J. Struct. Geol.* 22, 561–570. doi: 10.1016/s0191-8141(99)00179-0

Wei, W., Faure, M., Chen, Y., Ji, W., Lin, W., Wang, Q., et al. (2015). Back-thrusting response of continental collision: early cretaceous NW-directed thrusting in the Changle-Nan'ao belt (Southeast China). *J. Asian Earth Sci.* 100, 98–114. doi: 10.1016/j.jseaes.2015.01.005

Wong, J., Sun, M., Xing, G., Li, X. H., Zhao, G., Wong, K., et al. (2009). Geochemical and zircon U–Pb and Hf isotopic study of the Baijuhuajian metaluminous A-type granite: extension at 125–100 Ma and its tectonic significance for South China. *Lithos* 112, 289–305. doi: 10.1016/j.lithos.2009.03.009

Xie, G. Q., Hu, R. Z., Zhao, J. H., and Jiang, G. H. (2001). Mantle plume and the relationship between it and Mesozoic large-scale metallogenesis in southeastern China: a preliminary discussion. *Geotectonica Metallogenia* 25, 179–186.

Yang, J., Zhao, Z., Hou, Q., Niu, Y., Mo, X., Sheng, D., et al. (2018). Petrogenesis of Cretaceous (133–84 Ma) intermediate dykes and host granites in southeastern China: implications for lithospheric extension, continental crustal growth, and geodynamics of Palaeo-Pacific subduction. *Lithos* 296, 195–211. doi: 10.1016/j.lithos.2017.10.022

Yang, S. Y., Jiang, S. Y., Zhao, K. D., Jiang, Y. H., Ling, H. F., and Luo, L. (2012). Geochronology, geochemistry and tectonic significance of two Early Cretaceous A-type granites in the Gan-Hang Belt, Southeast China. *Lithos* 150, 155–170. doi: 10.1016/j.lithos.2012.01.028

Yui, T. F., Heaman, L., and Lan, C. Y. (1996). U-Pb and Sr isotopic studies on granitoids from Taiwan and Chinmen-Lieyu and tectonic implications. *Tectonophysics* 263, 61–76. doi: 10.1016/s0040-1951(96)00023-6

Zhang, Y. Q., Dong, S. W., Li, J. H., Cui, J. J., Shi, W., Su, J. B., et al. (2012). The new progress in the study of Mesozoic tectonics of South China. *Diqiu Xuebao* 33, 257–279.

Zhao, J. H., Hu, R., Zhou, M. F., and Liu, S. (2007). Elemental and Sr–Nd–Pb isotopic geochemistry of Mesozoic mafic intrusions in southern Fujian Province, SE China: implications for lithospheric mantle evolution. *Geol. Magaz.* 144, 937–952. doi: 10.1017/s0016756807003834

Zhao, X., Jiang, Y., Xing, G., Chen, Z., Liu, K., Yu, M., et al. (2018). A geochemical and geochronological study of the Early Cretaceous, extension-related Honggong ferroan (A-type) granite in southwestern Zhejiang Province, southeast China. *Geol. Magaz.* 155, 549–567. doi: 10.1017/s0016756816000790

Zhou, B. X., Sun, T., Shen, W., Shu, L., and Niu, Y. (2006). Petrogenesis of Mesozoic granitoids and volcanic rocks in South China: a response to tectonic evolution. *Episodes* 29:26. doi: 10.18814/epiiugs/2006/v29i1/004

Zhou, X. M., and Li, W. X. (2000). Origin of Late Mesozoic igneous rocks in Southeastern China: implications for lithosphere subduction and underplating of mafic magmas. *Tectonophysics* 326, 269–287. doi: 10.1016/s0040-1951(00)00120-7

Conflict of Interest: The authors declare that the research was conducted in the absence of any commercial or financial relationships that could be construed as a potential conflict of interest.

frontiers in Earth Science

ORIGINAL RESEARCH
published: 04 August 2020
doi: 10.3389/feart.2020.00318

An Assessment of the Magmatic Conditions of Late Neoproterozoic Collisional and Post-collisional Granites From the Guéra Massif, South-Central Chad

Chi Thi Pham[1], J. Gregory Shellnutt[1], Meng-Wan Yeh[1] and Yoshiyuki Iizuka[2]*

[1] Department of Earth Sciences, National Taiwan Normal University, Taipei, Taiwan, [2] Institute of Earth Sciences, Academia Sinica, Taipei, Taiwan

The Guéra Massif, in South-Central Chad hosts granitic rocks that were emplaced during distinct intervals (595–590; ∼570; ∼560 Ma) of the Late Ediacaran Central African Orogenic Belt. To the northwest of the Guéra Massif, younger post-collisional granites (554–545 Ma) are found near Lake Fitri. The older (≥590 Ma) rocks have geochemical characteristics of collisional granites whereas the younger (≤570 Ma) rocks are similar to post-collisional granites. Biotite and amphibole were analyzed to constrain the magmatic conditions of the granites. The biotite from the collisional granites tends to have higher Al and Ti and lower Fe# ($Fe\#_{average} \approx 0.67$) than the post-collisional granites ($Fe\#_{average} \approx 0.88$). The average crystallization temperatures range from 696 ± 37 to 612 ± 8°C, with the average pressure of crystallization from 0.25 ± 0.09 to 0.13 ± 0.02 GPa, and redox conditions between the nickel-nickel oxide (NNO) and quartz-fayalite-magnetite (QFM) buffers. The biotite crystallization temperatures of the post-collisional rocks are generally lower than the collisional rocks (570 Ma = 630 ± 26 to 619 ± 30°C, 560 Ma = 626 ± 20 to 607 ± 4°C, 550 Ma = 639 ± 18 to 612 ± 13°C), but the crystallization pressures are similar (0.27 ± 0.05 to 0.14 ± 0.04 GPa). The redox conditions transition from the QFM buffer to the wüstite-magnetite (WM) buffer. In contrast, the biotite from the Lake Fitri post-collisional granites crystallized at higher pressure (0.39 ± 0.08 to 0.35 ± 0.03 GPa) but similar redox conditions. The amphiboles in the younger (∼590 Ma) collisional granites and the post-collisional granites yielded crystallization pressure estimates that are generally higher (∼0.6 to 0.1 GPa) than the biotite estimates but there is overlap. The difference in pressure may be due to the timing of crystallization and/or crystal redistribution. Overall, there appears to be a secular change from high to low temperature and pressure whereas the redox conditions appear to be spatially related. The biotite crystallization pressure of the Lake Fitri granites suggests they were likely emplaced into a different domain/terrane of the Saharan Metacraton than the Guéra Massif.

Keywords: Saharan Metacraton, biotite chemistry, Guéra Massif, collisional granites, post-collisional granite, Central African Orogenic Belt

OPEN ACCESS

Edited by:
Scott Andrew Whattam, King Fahd University of Petroleum and Minerals, Saudi Arabia

Reviewed by:
Kenneth Johnson, University of Houston–Downtown, United States
Marcos Garcia-Arias, University of Los Andes, Colombia

****Correspondence:***
J. Gregory Shellnutt
jgshelln@ntnu.edu.tw

Specialty section:
This article was submitted to Petrology, a section of the journal Frontiers in Earth Science

Received: *14 February 2020*
Accepted: *06 July 2020*
Published: *04 August 2020*

Citation:
Pham CT, Shellnutt JG, Yeh M-W and Iizuka Y (2020) An Assessment of the Magmatic Conditions of Late Neoproterozoic Collisional and Post-collisional Granites From the Guéra Massif, South-Central Chad. Front. Earth Sci. 8:318. doi: 10.3389/feart.2020.00318

INTRODUCTION

The Saharan Metacraton occupies the North-Central part of Africa and covers an area of ∼5 million km^2 (Abdelsalam et al., 2002; Liégeois et al., 2013). It is surrounded by the Tuareg Shield to the west, the Arabian-Nubian Shield (ANS) to the east, the Congo Craton to the south, and the African continental margin to the north (**Figure 1A**). The boundaries of the Saharan Metacraton are the result of lithospheric-scale suturing processes caused by Neoproterozoic (∼750–550 Ma) collisional events. The eastern boundary is considered to be the north-trending Keraf–Kabus–Sekerr Shear Zone which is an arc-continental suture that separates the Saharan Metacraton from the ANS (Abdelsalam and Dawoud, 1991; Stern, 1994; Abdelsalam and Stern, 1996). The western boundary is the north-trending Raghane Shear Zone which marks the collision zone between the Saharan Metacraton and the Tuareg Shield (Liégeois et al., 1994, 2003; Henry et al., 2009). The southern boundary is not well-defined but is considered to be the northern border of the Central African Orogenic Belt (CAOB) in the southwest and the Aswa Shear Zone farther east. The east-west trending CAOB separates the Saharan Metacraton from the Congo Craton to the south (Pin and Poidevin, 1987; Poidevin, 1994; Toteu et al., 2006). The northern boundary of the Saharan Metacraton is unconstrained but is likely located in southern Egypt and Libya and covered by thick Phanerozoic sediments (Abdelsalam et al., 2002).

The Saharan Metacraton comprises medium to high-grade metamorphic rocks including gneiss, metasedimentary rocks, migmatites and granulites as well as low-grade volcano-sedimentary sequences that are intruded by Neoproterozoic granitic rocks (Klerkx and Deutsch, 1977; Stern et al., 1994; Sultan et al., 1994; Abdelsalam et al., 2002; Shang et al., 2010). Isotope model ages and U-Pb geochronology of basement rocks vary from ∼3100 to 500 Ma suggesting there is an Archean ancestry within the Saharan Metacraton (Abdelsalam et al., 2002). Nevertheless, the principal magmatic phases of the Saharan Metacraton occurred from ∼750 to 550 Ma (Abdelsalam et al., 2002; Suayah et al., 2006; Shellnutt et al., 2017, 2018).

Mesoproterozoic to Neoproterozoic rocks of the Saharan Metacraton are exposed in Chad within the Tibesti, Ouaddaï, and Gueìra massifs (**Figure 1B**). The Guéra Massif is located in South-Central Chad and is primarily comprised of granitic rocks many of which are cross-cut by dolerite dykes (Isseini et al., 2013; Nkouandou et al., 2017). The main lithologic and structural characteristics are described by Isseini et al. (2013), and the geochronology and geochemistry are documented by Pham (2018). Granitic intrusions were emplaced during and after the collision between the Congo-São Francisco Craton and the Saharan Metacraton. Pham (2018) proposed that there are two types of granites: (1) the older (595–590 Ma), collision-related granites that formed by subduction and syn-collisional processes, and (2) the younger (570–560 Ma), post-collisional granites. Furthermore, even younger (554–545 Ma) post-collisional granites are located ∼150 to 350 km to the NW of the Guéra Massif near Lake Fitri and are compositionally similar to the Guéra post-collisional granites. Consequently, the Lake Fitri granites could be representative of a third post-collisional period in south-central Chad, and/or represent a northwestward extension of the Guéra Massif (**Figures 1C,D**; Shellnutt et al., 2017, 2018).

Mafic minerals (e.g., amphibole, biotite) are fundamental components of many granitic rocks. For example, the compositions of amphibole and biotite reflect the magmatic conditions and the nature of the parental magma from which they crystallized (Zen, 1988; Abdel-Rahman, 1994; Shabani et al., 2003). In general, biotite composition can be used to: (1) track the oxidation state of the melt from which it crystallized (Wones and Eugster, 1965; Burkhard, 1991, 1993), (2) discriminate geotectonic settings (Nachit et al., 1985; Abdel-Rahman, 1994; Hecht, 1994; Shabani et al., 2003), (3) estimate crystallization temperature (Luhr et al., 1984), and (4) constrain the depth of crystallization (Uchida et al., 2007). Similarly, amphibole can also provide constraints on the crystallization conditions of granitic magma (c.f., Wones, 1981; Hammarstrom and Zen, 1986).

In this study, we present the chemistry of biotite and amphibole from the collision-related and post-collisional granites of the Guéra Massif with the aim to: (1) describe the mineral-chemical evolution of the mafic minerals from the granites of the Guéra Massif; (2) estimate magmatic conditions (pressure and temperature of crystallization, and oxygen fugacity) that prevailed during the crystallization of biotite; (3) characterize the geochemical differences in biotite between the collisional and the post-collisional granites, and (4) discuss the tectonomagmatic implications. The new data are used to constrain the secular evolution of magmatism as it changes from a collisional setting to a post-collisional setting. Moreover, the results provide additional constraints on the nature of crustal building processes within the Saharan Metacraton.

GEOLOGICAL BACKGROUND

The bedrock geology of Chad is characterized by the exposure of Late Ediacaran basement rocks within the Tibesti Massif in the north, Ouaddaï Massif in the east, Guéra Massif in the south-central part, and the Mayo Kebbi and Yadé massifs in the south (**Figure 1B**). The massifs are surrounded by younger sedimentary rocks, which include Lower Paleozoic sandstone sequences, Lower Cretaceous continental clastic rocks and Upper Cretaceous marine sediments in the north and northeast, Paleogene continental sediments in the south, and the Neogene lacustrine sediments (known as Chad Formation) of the Chad basin.

The Guéra Massif, also known as Massif Central tchadien (**Figure 2**), comprises magmatic and metamorphic rocks that developed during the Late Ediacaran collision between the Congo-São Francisco Craton and the Saharan Metacraton (Black, 1992; Kusnir and Schneider, 1995; Kusnir and Moutaye, 1997; Schlüter, 2008; Shellnutt et al., 2017, 2019b). Biotite granites are mainly exposed in the northern region near Mongo, which is intruded by gabbro whereas hornblende-biotite granites and hornblende granites and its fine grained equivalent are located in the east and south of the massif (**Figure 2**). A geochronological investigation of the granitic plutons shows that they are

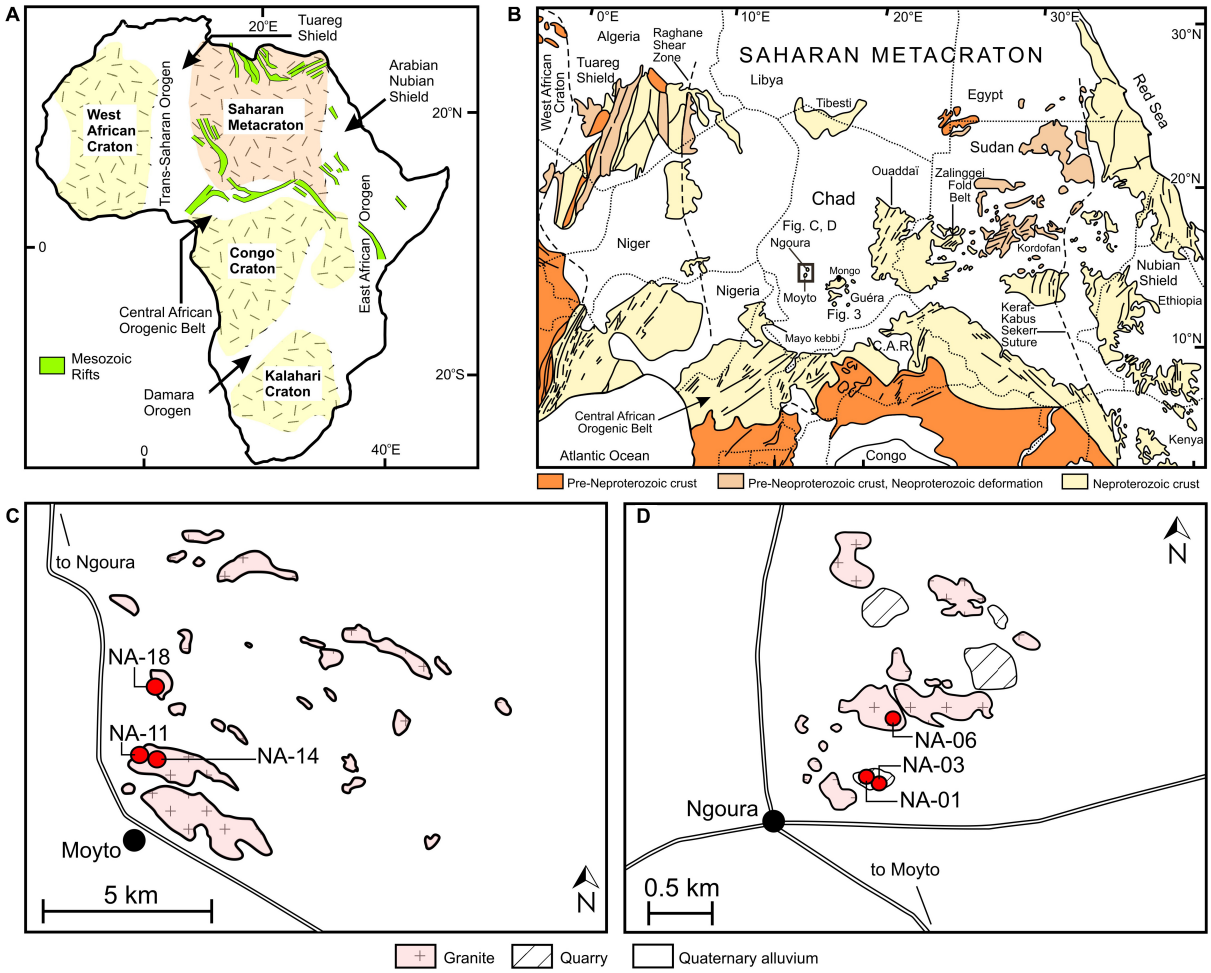

FIGURE 1 | (A) Major cratons of continental Africa and locations of Mesozoic rifts. **(B)** Simplified geological map of the Saharan Metacraton, showing the location of the study areas (modified from Abdelsalam et al., 2002). The sample localities of the Lake Fitri inliers near **(C)** Moyto and **(D)** Ngoura (after Shellnutt et al., 2018).

Neoproterozoic (595–560 Ma) in age and were subsequently buried under a sedimentary cover dominated by Quaternary alluvium (Kusnir and Schneider, 1995; Shellnutt et al., 2017; Pham, 2018). Cross-cutting the older (595–590 Ma) granites in the Mongo area are dolerite dykes that are oriented along/parallel to NNE–SSW, NE–SW, and ENE–WSW faults. They are described as vertical to sub-vertical dykes and extend over several kilometers. The Mongo doleritic dyke swarm intruded pre-existing fractures and may record the final stage of lithotectonic stabilization of the Guéra Massif (Nkouandou et al., 2017).

The ancient basement of the Guéra Massif is probably Meso- to Paleoproterozoic as inherited zircons of that age were identified within the collision-related granites (Shellnutt et al., 2017, 2019a). The collision-related granites are mostly biotite-granite, metaluminous to peraluminous, alkali calcic to calc-alkalic and magnesian to ferroan in composition, where the magnesian (∼595 Ma) granites are similar to volcanic-arc granite and were emplaced before the ferroan (∼590 Ma) syn-collisional granites (**Supplementary Table S1**; Frost et al., 2001; Pham, 2018; Shellnutt et al., 2019a). In contrast, the post-collisional granites include biotite-granite and hornblende-biotite-granite, and are peraluminous to metaluminous, alkali calcic to calc-alkalic, and ferroan in composition. The compositionally similar ferroan rocks were emplaced at two distinct periods of ∼570 and ∼560 Ma (**Supplementary Table S1**; Pham, 2018). The whole rock compositions and zircon 206Pb/238U weighted-mean ages of the rocks in this study are summarized in **Supplementary Table S1**.

Sampling Locations of the Collision-Related Granites

Samples 14ZA02 (595 ± 8 Ma), 14ZA06, 14ZA25C are collected from three different locations of the same magnesian biotite-bearing granitic pluton surrounding Mongo (**Figure 2**). Each sample is about 50 km from each other. Sample 14ZA02 is located at the western part of the pluton (**Figure 2**). Sample 14ZA06 is located to the north whereas sample 14ZA25C is an amphibolite melanosome within gneissose granitoid located to the east (**Figure 3A**). The eastern outcrop was intruded by

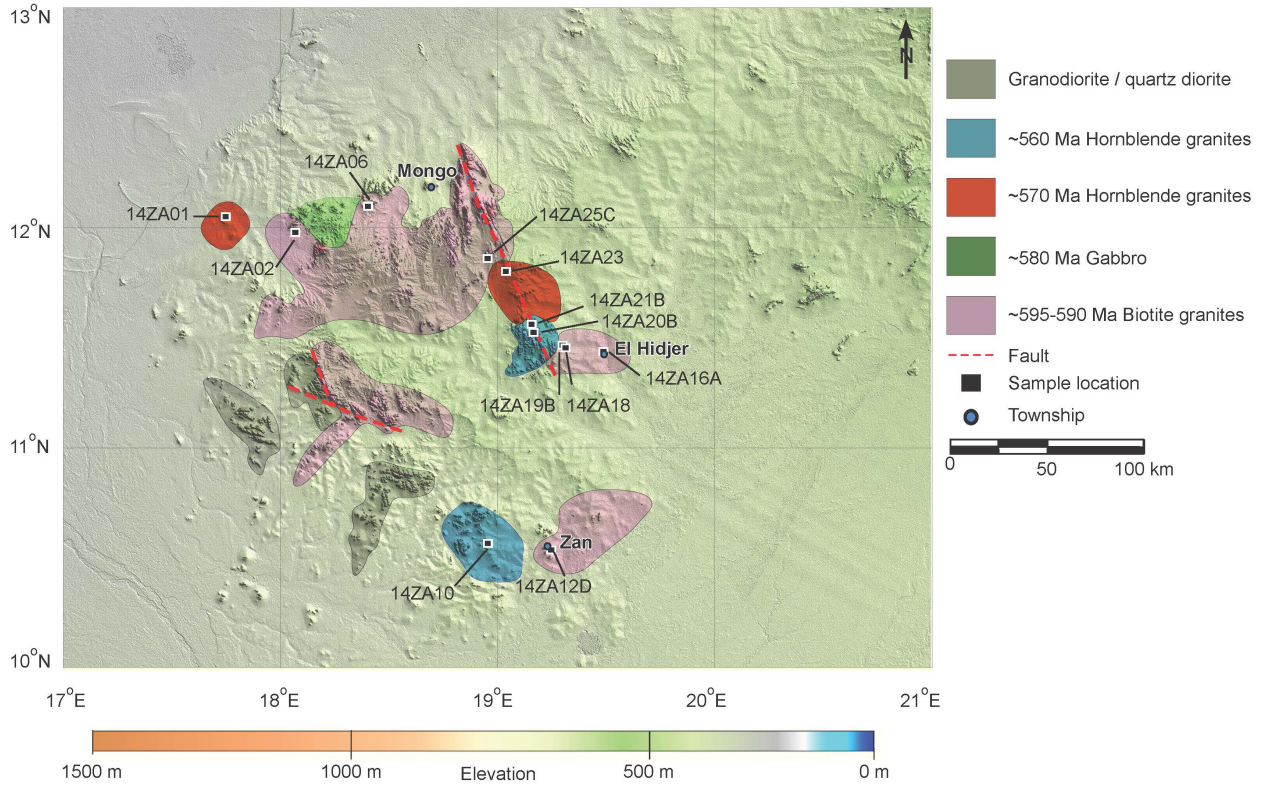

FIGURE 2 | Sample location map of the granitoids selected for this study. The distribution of Guéra Massif granites draped onto Shuttle Rader Topography Mission (SRTM) Digital Elevation Model (DEM).

younger granite that has not been dated. Sample 14ZA16A (593 ± 7 Ma) is a pink, ferroan granite that was intruded by a fine grained quartzofeldspathic dyke ∼3 km east of El Hidjer (**Figures 2**, **3B**). Sample 14ZA12D (589 ± 6 Ma) was collected from a granite outcrop about 20 km north of Zan. The textural, mineralogical, and age similarities of 14ZA16A and 14ZA12D suggests that they may be the same pluton.

Sampling Locations of the Post-collisional Granites

Sample 14ZA01 (568 ± 7 Ma) is a biotite-bearing gneissic granitoid collected ∼100 km west of Mongo between Bakoro and Bitkin villages (**Figure 2**). This sample belongs to the westernmost pluton of the study and is texturally and minerallogically different from the older Mongo granite (**Figures 2**, **4A**). Sample 14ZA23 (568 ± 6 Ma) was collected ∼50 km to the southeast of Mongo, halfway between Mongo and El Hidjer (**Figure 2**).

Samples 14ZA20B and −21B were collected about 50 km west of El Hidjer (**Figure 2**). The outcrop exposes multiple magmatic rocks ranging from biotite-hornblende gneissose enclave to NW-SE striking steep dipping foliated gneissic granite (14ZA20B) truncated by younger mafic intrusions, and quartzofeldspathic veins (**Figures 4B,C**). Sample 14ZA21B is coarse grained granite that contains darker microgranular enclaves. Pink granite samples 14ZA18 and ZA1419B (561 ± 6 Ma) were collected from a pluton with an exfoliation dome-like structure ∼30 km west of El Hidjer that is texturally different from the pluton in which samples 14ZA20B and 14ZA21B were collected (**Figure 2**). The granite is composed of coarse grained K-feldspar, plagioclase, biotite, hornblende with concentrated patches of amphibolite xenoliths. Sample 14ZA10 (556 ± 7 Ma) is biotite-bearing granite with centimeter size feldspar phenocrysts collected from one of the southernmost plutons ∼30 km west of Zan. The granites are slightly deformed as there is an alignment of biotite (**Figure 4D**).

The Lake Fitri inliers are located to the northwest of the Guéra Massif and comprise fresh and coarse-grained biotite-bearing granites (**Figures 1C,D**). They are exposed as lenticular to ellipsoidal granitic hills up to several kilometers in length and less than 1 km wide near or between the communities of Ngoura and Moyto. Generally, the Lake Fitri granites have similar texture, mineralogy (biotite, quartz, K-feldspar), whole-rock chemistry (peraluminous to metaluminous, alkali calcic to calc-alkalic, high potassium and ferroan) and Nd isotopic compositions (Shellnutt et al., 2018). Moreover, they are somewhat compositionally similar to the post-collisional granites of the Guéra Massif but are slightly younger (554 ± 8 and 546 ± 8 Ma) and have moderately depleted Nd isotopic compositions [$\varepsilon_{Nd}(t)$ = +1.3 to +2.9] as opposed to the enriched Nd isotopes [$\varepsilon_{Nd}(t)$ = −13.1 to +0.2] of the rocks from the Guéra Massif (Pham, 2018; Shellnutt et al., 2018). Biotite compositions from the granitic rocks at Ngoura

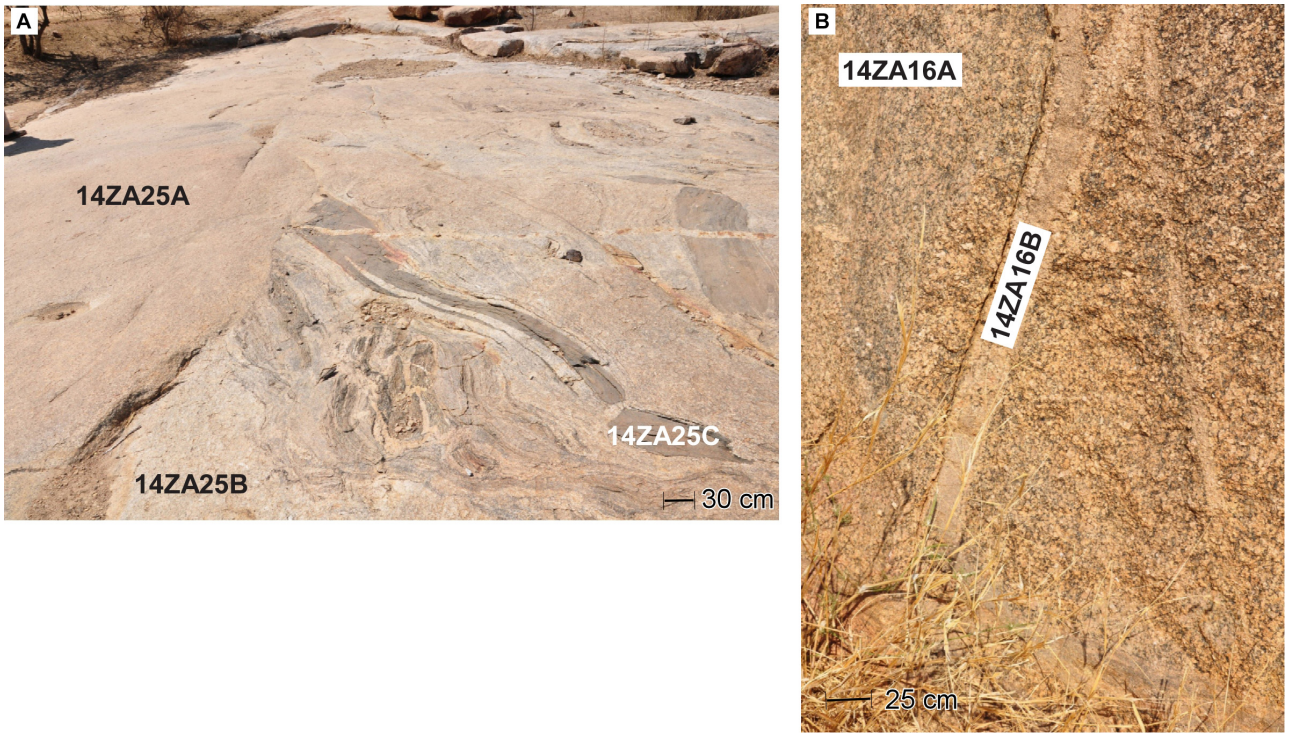

FIGURE 3 | Field photographs of the **(A)** magnesian collision-related granites near Mongo and the **(B)** ferroan collision-related granite near El Hidjer.

and Moyto were presented by Shellnutt et al. (2018) and are discussed in this paper.

PETROGRAPHY

Collision-Related Granitic Rocks

The collisional granites include both hornblende-biotite granite (590 Ma group) and biotite granite (595 Ma group) that vary from coarse-grained and granular to fine grained. Exsolution textures, such as perthite and myrmekite, are common in both groups. The 590 Ma collisional granites (**Figures 5A,B**) are primarily composed of plagioclase (10–20 vol.%), K-feldspar (35–45 vol.%), biotite (8–10 vol.%), and quartz (20–30 vol.%) with accessory amounts of amphibole (1–2 vol.%), opaques (Fe-Ti oxide and sulfide minerals), zircon, and apatite. The plagioclase crystals display albite twinning. The K-feldspar crystals are medium- to coarse grained (0.5–1 mm or larger), and commonly have subsolidus exsolution (cross-hatched twinning perthite) and lamellar exsolution. Some of the K-feldspar is altered to clay minerals and secondary muscovite. The biotite crystals are coarse-grained and $\leq$2 mm in length, have greenish brown to brown pleochroism, and contain inclusions of apatite and zircon (metamict halo). The quartz crystals are fine- to coarse-grained (0.75–1 cm), fractured, and have undulose extinction. In comparison, the 595 Ma granites (**Figures 5C,D**) have the same mineral assemblage of plagioclase (10–20 vol.%), K-feldspar (25–50 vol.%), biotite (15–17 vol.%), and quartz (20–30 vol.%) with opaque accessory (Fe-Ti oxide and sulfide minerals), zircon, secondary muscovite, and apatite but amphibole was not observed. The rocks have similar mineral textures as ∼590 Ma rocks but the biotite crystals were generally more abundant and have green to greenish brown pleochroism.

Post-collisional Granitic Rocks

The post-collisional granites are mostly hornblende-biotite granites and are coarse-grained and granular (**Figure 6**). The most distinguishing feature between younger (∼560 Ma) and older (∼570 Ma) post-collisional granites is the abundance of amphibole (hornblende) that can be up to 15–20 vol.% (sample 14ZA20B). These rocks are generally fresh, but some crystals of quartz and K-feldspar are cloudy. Exsolution textures such as perthite and myrmekite are common (**Figure 6A**). The 560 Ma group has a mineral assemblage of amphibole (∼2–20 vol.%), plagioclase (8–10 vol.%), biotite (2–10 vol.%), K-feldspar (30–50 vol.%), quartz (20–40 vol.%), and accessory (1–3 vol.%) minerals (**Figures 6B–D**). Most of the amphibole crystals are hornblende that are identified by deep-green to light-green pleochroism. In some cases the hornblende is altered to a mixture of reddish-brown oxyhornblende and oxide (hematite, rutile) minerals (**Figure 6D**). The plagioclase phenocrysts (0.5–2.25 mm) have albite and polysynthetic twinning. The biotite crystals are observed as both phenocrysts and inclusions within K-feldspar but the phenocrysts are commonly interstitial to other minerals and have pale yellow-brown to pale brown pleochroism. The K-feldspar crystals are medium to coarse-grained and regularly

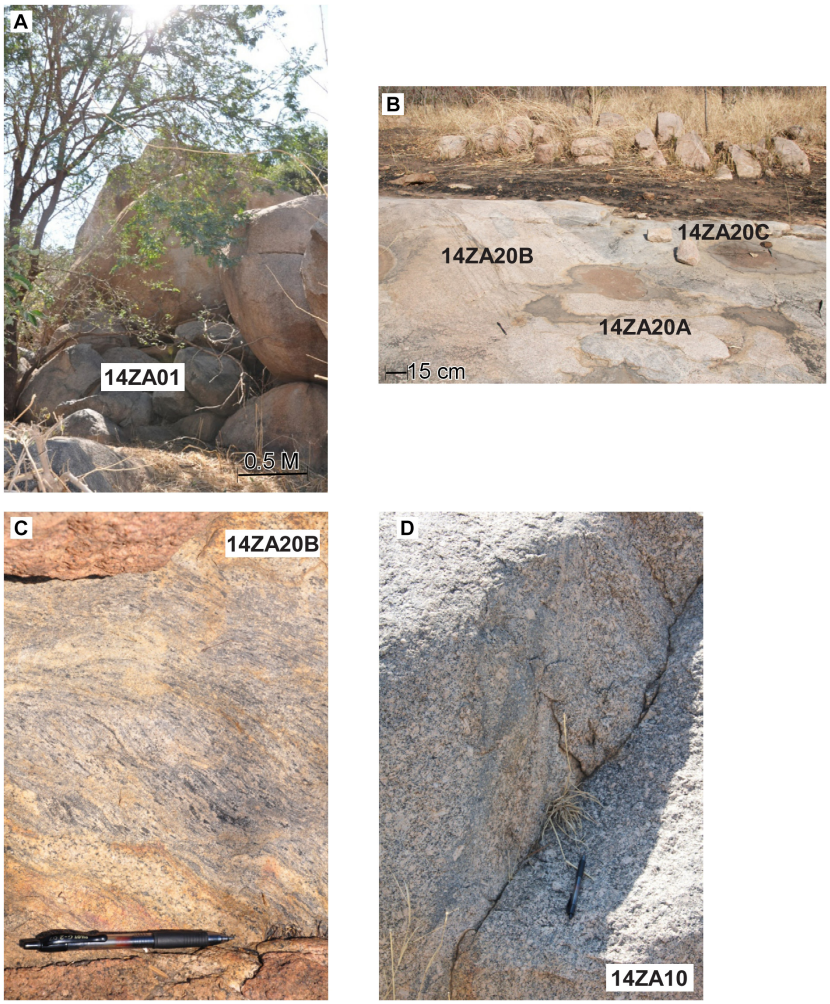

FIGURE 4 | (A) Field photograph of the ~570 Ma post-collisional granites west of Mongo. Field photographs of ~560 Ma post-collisional granites west of El Hidjer **(B,C)** and near Zan **(D)**.

exhibit Carlsbad or microcline twinning. There are some alkali feldspar crystals with perthite exsolution lamellae. The quartz crystals are fractured, randomly oriented, and have variable grain sizes. Accessory minerals include: zircon, muscovite, chlorite and opaques. The 570 Ma granites have a similar mineral assemblage of plagioclase (15–20 vol.%), K-feldspar (35–40 vol.%), biotite (8–10 vol.%), quartz (20–25%) with similar accessory minerals (<3 vol.% of chlorite, zircon and opaques), but tend to have less amphibole (3–4 vol.%) as compared to the 560 Ma granites (**Figures 6E,F**).

MATERIALS AND METHODS

To investigate the mineralogical composition of the Gueìra Massif granites a total of twelve samples of biotite-granite and hornblende-biotite-granite were selected for analysis by electron probe micro-analyzer (EPMA). The EPMA used for this study is a JEOL JXA-8500F, equipped with five WDSs at EPMA laboratory in the Institute of Earth Sciences, Academia Sinica, Taipei. The equipment operated at 16 kV voltage and 6 nA current beam with a 2 mm diameter electron beam. The ZAF method using the standard calibration of synthetic chemical-known standard minerals with diverse diffracting crystals used to correct the X-ray intensities, are as follows: wollastonite for Si with TAP crystal, rutile for Ti (PETJ), corundum for Al (TAP), Cr-oxide for Cr (PET), hematite for Fe (LiF)l, Mn-oxide for Mn (PET), periclase for Mg (TAP), Ni-oxide for Ni (LiF), Co-oxide for Co (LiF), wollastonite for Ca (PET), albite for Na (TAP), orthoclase for K (PET), Zn-oxide for Zn (LiF), apatite for P (PET), fluorite for F (TAP), tugtupite for Cl (PET) and anhydrite for S (PET). The relative standard deviations (RSD) for F, Cl, S, and P were less than 2%, for Si, Na, and K were less than 1%, and other elements were less than 0.5%. The detection limits for F, Cl, S, and P were less than 0.5 wt%. The analysis results are shown in **Supplementary Table S1**.

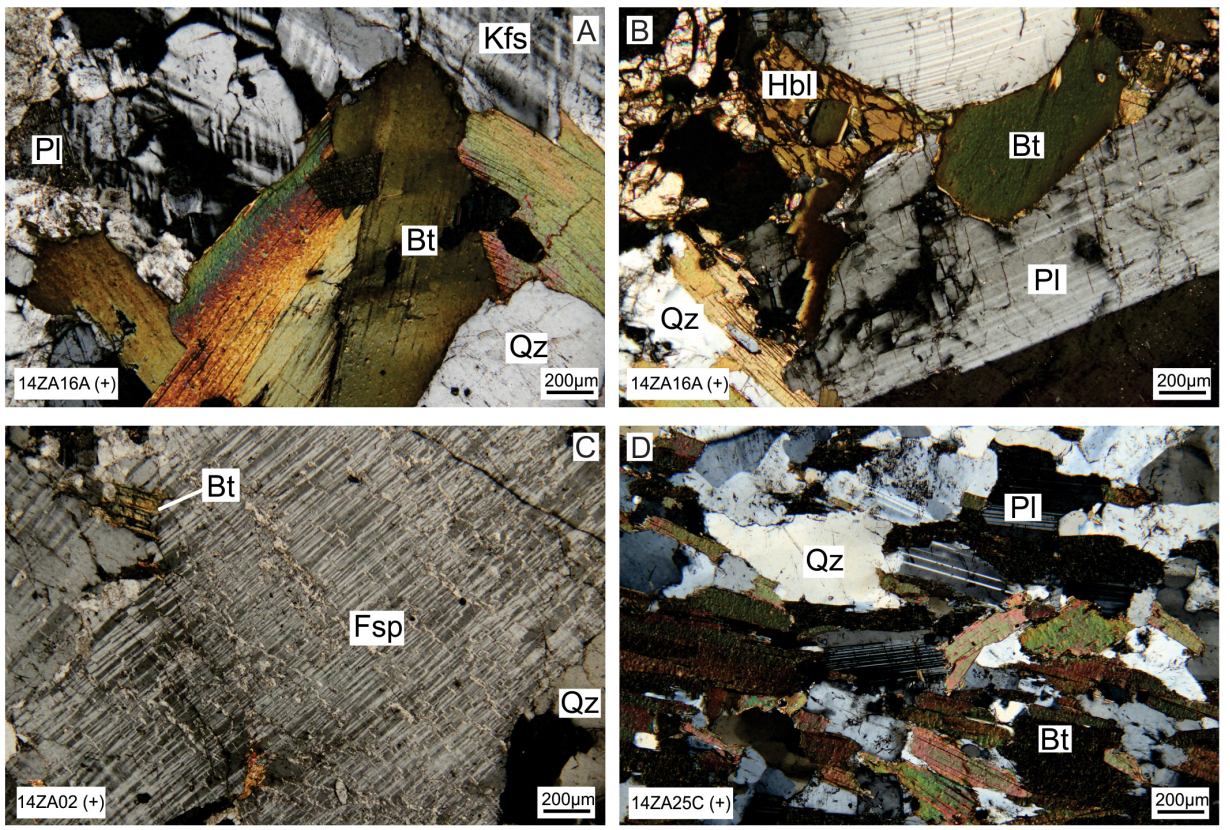

FIGURE 5 | Photomicrographs of the Guéra Massif collisional granites under crossed polarizers. Panels **(A,B)** are from 14ZA16A of the 590 Ma granites, and **(C)** 14ZA02, and **(D)** 14ZA25C of the 595 Ma granites. Qz, quartz; Pl, plagioclase; Bt, biotite; Kfs, potassium feldspar; Fsp, perthitic feldspar, Hbl, hornblende.

The structural formulae of biotite were calculated on the basis of 22 oxygen equivalents without H_2O^+ and 13 cations by using the Excel spreadsheet program designed by Tindle and Webb (1990). For this study, only the biotite results that classify as "primary magmatic biotite" are considered (Nachit et al., 2005). The partitioning of Fe^{3+} and Fe^{2+} from the total iron (FeO^t) was calculated by charge balance using the program "Fe23" (Nenova, 1997). It is reported that the calculated Fe^{2+} and Fe^{3+} deviate from the experimental derived contents by less than 1%. The chemical formulae of amphibole are recalculated on the basis of 23 oxygens equivalents with Fe^{2+}/Fe^{3+} estimation, without H_2O^+, and 13 cations using the program Probe-AMPH (Tindle and Webb, 1994). The chemical formula, geochemical features of amphibole and biotite, and their computed stoichiometry are summarized and listed in **Supplementary Table S1**. Biotite chemistry from the Lake Fitri granites, reported by Shellnutt et al. (2018), will also be discussed in relation to the Guéra Massif granites.

RESULTS

Collisional-Related Granites

There are distinct compositional differences between the biotite crystals from the 590 Ma (14ZA12D, −16A) and 595 Ma (14ZA02, −06, −25C) collision-related intrusions. The 590 Ma granites samples tend to have similar Al_2O_3 (13.23–16.21 wt.%) and TiO_2 (1.32–3.84 wt.%) but lower MgO (0.64–6.66 wt.%), and higher FeO^t (26.43–34.46 wt.%), and Fe# (0.70–0.98) than the biotite crystals of 595 Ma granites (Al_2O_3 = 13.94–17.53 wt.%; TiO_2 = 1.12–4.05 wt.%; MgO = 7.48–13.68 wt.%; FeO^t = 13.07–23.33 wt.%; Fe# = 0.46–0.62). Furthermore, the biotite from the 590 Ma rocks classify as siderophyllite whereas the biotite from the 595 Ma rocks classify as Fe-biotite (Foster, 1960).

The calcic amphibole (ferro-edenite to ferro-pargasite) crystals from the 590 Ma collision-related granites (14ZA12D, −16A) are fairly homogeneous within each sample but between samples there is significant variability of the major elements. The amphibole from sample 14ZA12D has higher SiO_2 (>41 wt%) and MnO (>0.7 wt%) but lower TiO_2 (<1 wt%), Al_2O_3 (<8.7 wt%), Na_2O (<1.7 wt%), and K_2O (≤1 wt%) compared to 14ZA16A (SiO_2 < 40 wt%; TiO_2 > 0.8 wt%, Al_2O_3 > 10.4 wt%; MnO < 0.7 wt%; Na_2O > 1.3 wt%; K_2O > 1.6 wt%).

Post-collisional Granites

The compositions of the biotite crystals from the 560 Ma granites (14ZA01, −10, −18, −19B, −20B, −21B, 23) are similar (Al_2O_3 = 12.35–17.17 wt%; TiO_2 = 2.48–4.02 wt%; MgO = 0.30–5.13 wt%; FeO^t = 26.50–35.35 wt%) to the biotite crystals from

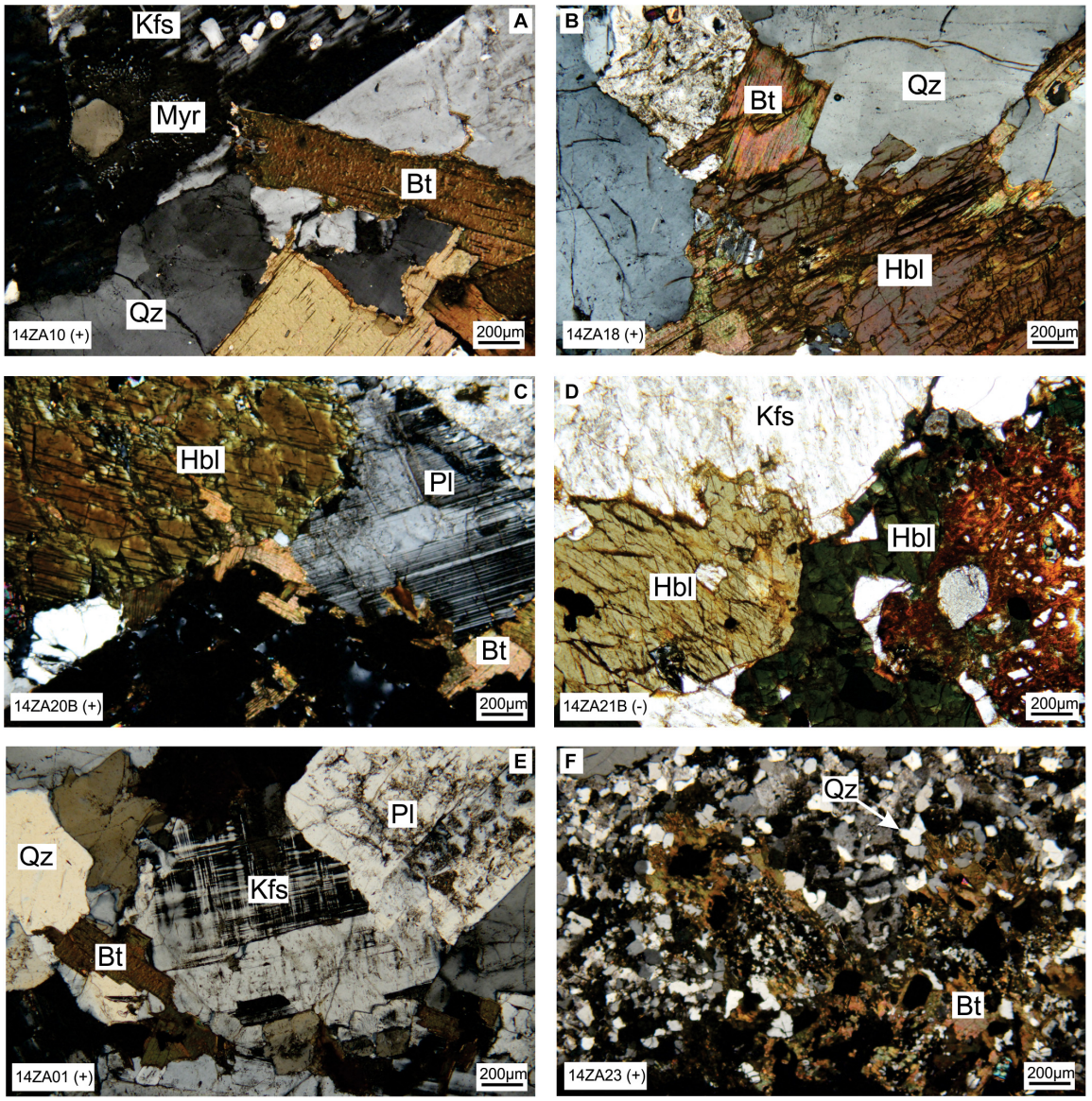

FIGURE 6 | Photomicrographs of the Guéra Massif post-collisional granites under crossed polarizers. **(A)** 14ZA10, **(B)** 14ZA18, **(C)** 14ZA20B, and **(D)** 14ZA21B of the 560 Ma granites. **(E)** 14ZA01, and **(F)** 14ZA23 of the 570 Ma granites. Qz, quartz; Pl, plagioclase; Bt, biotite; Kfs, potassium feldspar; Myr, myrmerkite, Hbl, hornblende.

570 Ma (14ZA01, −23) granites (Al_2O_3 = 10.94–15.26 wt%; TiO_2 = 2.35–4.88 wt%; MgO = 0.68–5.46 wt%; FeO^t = 24.70–35.35 wt%). All biotite are Fe-rich (siderophyllite) and have similar Fe# values (0.73–0.98).

The amphibole crystals from the post-collisional (560 Ma = 14ZA18, −19B, −20B, 21B; 570 Ma = 14ZA01, −23) intrusions are calcic (ferro-edenite to ferro-pargasite). The compositions of the amphibole from the 560 Ma rocks are generally similar to each other (SiO_2 = 45.2–36.2 wt%,TiO_2 = 2.3–0.3 wt%, Al_2O_3 = 9.6–5.0 wt%, MnO = 0.9–0.2 wt%, CaO = 11.0–8.4 wt%, Na_2O = 2.0–0.5 wt%, K_2O = 2.9–0.7 wt%, Fe# = 0.80–0.74) but slightly different from those analyzed from the 570 Ma rocks (SiO_2 = 41.2–40.6 wt%,TiO_2 = 2.0–0.9 wt%, Al_2O_3 = 9.1–8.2 wt%, MnO = 0.9–0.6 wt%, CaO = 10.9–10.3 wt%, Na_2O = 2.2–1.5 wt%, K_2O = 1.3–1.1 wt%, Fe# = 0.81–0.78). Only two analysis were obtained from sample 14ZA23.

DISCUSSION

Biotite Crystallization Temperature Estimates

The presence of ilmenite and magnetite in granitic rocks is a common mineral pairing used to estimate magmatic temperature of silicic igneous rocks (Buddington and Lindsley, 1964; Ghiorso and Sack, 1991; Anderson et al., 1993). However, the temperature

sensitivity of Ti and Ti/Fe^{2+} in biotite can also be used to obtain reliable temperature estimations in igneous and metamorphic rocks (Luhr et al., 1984). The granitic rocks from the Guéra Massif are primarily composed of plagioclase, K-feldspar, and quartz but have significant amounts (5–15 vol.%) of hornblende and biotite with accessory (<5 vol.%) amounts of apatite, Fe-Ti oxide minerals (ilmenite, magnetite), and sulfide minerals are also present. Consequently, we are able to use the equation of Luhr et al. (1984) to calculate the biotite crystallization temperatures based on the coupled exchange of Ti and Fe^{2+} in biotite. The temperatures are calculated from Eq. (1).

$$T\,(K) = \frac{838}{1.0337 - \frac{Ti}{Fe^{2+}}} \quad (1)$$

The maximum, minimum, and average crystallization temperatures of the biotite from the Guéra Massif and Lake Fitri inliers are listed in **Table 1** with the entire data set presented in **Supplementary Table S1**. Overall, the biotites from the collisional granites tend to have higher average crystallization temperatures than the post-collisional granites from Guéra Massif and the Lake Fitri region (**Figures 7A,B**). Specifically, the results from sample 14ZA02 (595 Ma) have the highest temperature (723°C) and average temperature (696 ± 37°C). The other two remaining 595 Ma rocks have the second (14ZA25 = 666 ± 42°C) and the fifth highest average temperatures (14ZA06 = 633 ± 21°C). In comparison, the 590 Ma rocks have lower average temperatures (14ZA16A = 619 ± 22°C; 14ZA12D = 612 ± 8°C). The post-collisional granites have lower average temperatures overall but overlap with 590 Ma collisional rocks (630 ± 26–607 ± 7°C). The Lake Fitri post-collisional rocks are somewhat different from the Guéra Massif rocks. The biotite from the Ngoura rocks yields higher average temperatures (634 ± 21, 639 ± 18, 625 ± 20°C) than the biotite from the younger Moyto granites (612 ± 13°C).

TABLE 1 | The range of crystallization temperature estimates of biotite from the granites of the Gueìra Massif and Lake Fitri region.

Pluton	Sample	Temperature (°C)		
		Max	Min	Average
595 Ma	14ZA02	723	648	696 ± 37
595 Ma	14ZA06	658	615	633 ± 21
595 Ma	14ZA25C	708	624	666 ± 42
590 Ma-N	14ZA16A	650	606	619 ± 22
590 Ma-S	14ZA12D	623	606	612 ± 8
570 Ma-W	14ZA01	659	606	630 ± 26
570 Ma-E	14ZA23	663	603	619 ± 30
560 Ma-S	14ZA10	644	604	626 ± 20
560 Ma-N	14ZA18	614	601	607 ± 7
560 Ma-N	14ZA19B	634	601	619 ± 16
560 Ma-N	14ZA20B	628	602	614 ± 13
560 Ma-N	14ZA21B	633	602	614 ± 15
550 Ma Ngoura	NA01	656	614	634 ± 21
550 Ma Ngoura	NA03	659	624	639 ± 18
550 Ma Ngoura	NA06	645	605	625 ± 20
550 Ma Moyto 2	NA18	631	604	612 ± 13

Average = average value of the temperature in Celsius including the uncertainty in the average.

Amphibole Pressure Estimates

Emplacement pressure estimates of granitic rocks can be calculated based on the Al content of hornblende providing the host rocks contain the requisite mineral assemblages (Hammarstrom and Zen, 1986; Hollister et al., 1987; Johnson and Rutherford, 1989; Schmidt, 1992). There are concerns regarding the constraints for an accurate geobarometer estimate using amphibole given all of the parameters that could potentially affect the results (Hollister et al., 1987; Ghent et al., 1991). Although, the computed pressure may display the depth at which the hornblende crystallizes, it may not indicate the pressure at which the granite reached neutral buoyancy (i.e., emplacement depth) in the crust because it is likely that the majority of minerals crystallize after hornblende (Ghent et al., 1991).

We find that the hornblende geobarometers of Hammarstrom and Zen (1986) and Johnson and Rutherford (1989) are better suited for our samples as the mineral assemblages are ideal and our results are closest to their calibration curves. However, we prefer the geobarometer of Johnson and Rutherford (1989) due to better constraints on the pressure uncertainty (i.e., ±0.5 kbar). The amphibole crystallization pressure of the Guéra Massif granitic rocks is calculated using Eq. (2).

$$P\left(\pm 0.5\,\text{kbar}\right) = 3 - 3.46\ (\pm\ 0.24) + 4.23\ (\pm\ 0.13)\ (Al^{T}) \quad (2)$$

Where Al^{t} designates the total number of Al atoms in amphibole based on 23 oxygen equivalents. The calibration is based on the relation between Al^{t} in hornblende and pressure for calc-alkalic granitic rocks that are made of up of an igneous mineral assemblage consisting of hornblende, plagioclase, biotite, K-feldspar, quartz, titanite, and magnetite or ilmenite. The results indicate that the crystallization of hornblende occurred between ∼0.1 and 0.6 GPa across all samples but the ∼590 Ma collisional rocks have the greatest variability (**Table 2** and **Supplementary Table S1**; **Figure 7C**). Amphibole is not present in all of the studied samples. Thus, there is a limited application of this method across all granitic rocks from the Guéra Massif granites.

Biotite Pressure Estimates

The concentration of TiO_2 and Al^{VI} in biotite is linked to the emplacement depth of its host pluton. In particular, granites with biotite that have low TiO_2 and high Al^{VI} content are typical for an abyssal depth of formation. Furthermore, granites that crystallize at deeper depth are characterized by high TiO_2 and Al^{VI} content (Machev et al., 2004; Bora and Kumar, 2015). In this study, the TiO_2 and Al^{VI} contents in biotite of collisional granite are TiO_2 = 2.19–4.05 wt%, Al^{VI} = 0.05–0.9 apfu. The values of the post-collisional granites are as follows: TiO_2 = 2.35–4.88 wt%, Al^{VI} = 0.07–0.48 apfu, for 570 Ma granite; TiO_2 = 2.48–4.02 wt%, Al^{VI} = 0.10–0.74 apfu, for 560 Ma granite; TiO_2 = 1.3–4.0 wt%, Al^{VI} = 0.46–1.15 apfu, for Lake Fitri granite. The Lake Fitri post-collisional granites have relatively high Al^{VI} contents and low TiO_2 content, potentially indicating the highest pressure

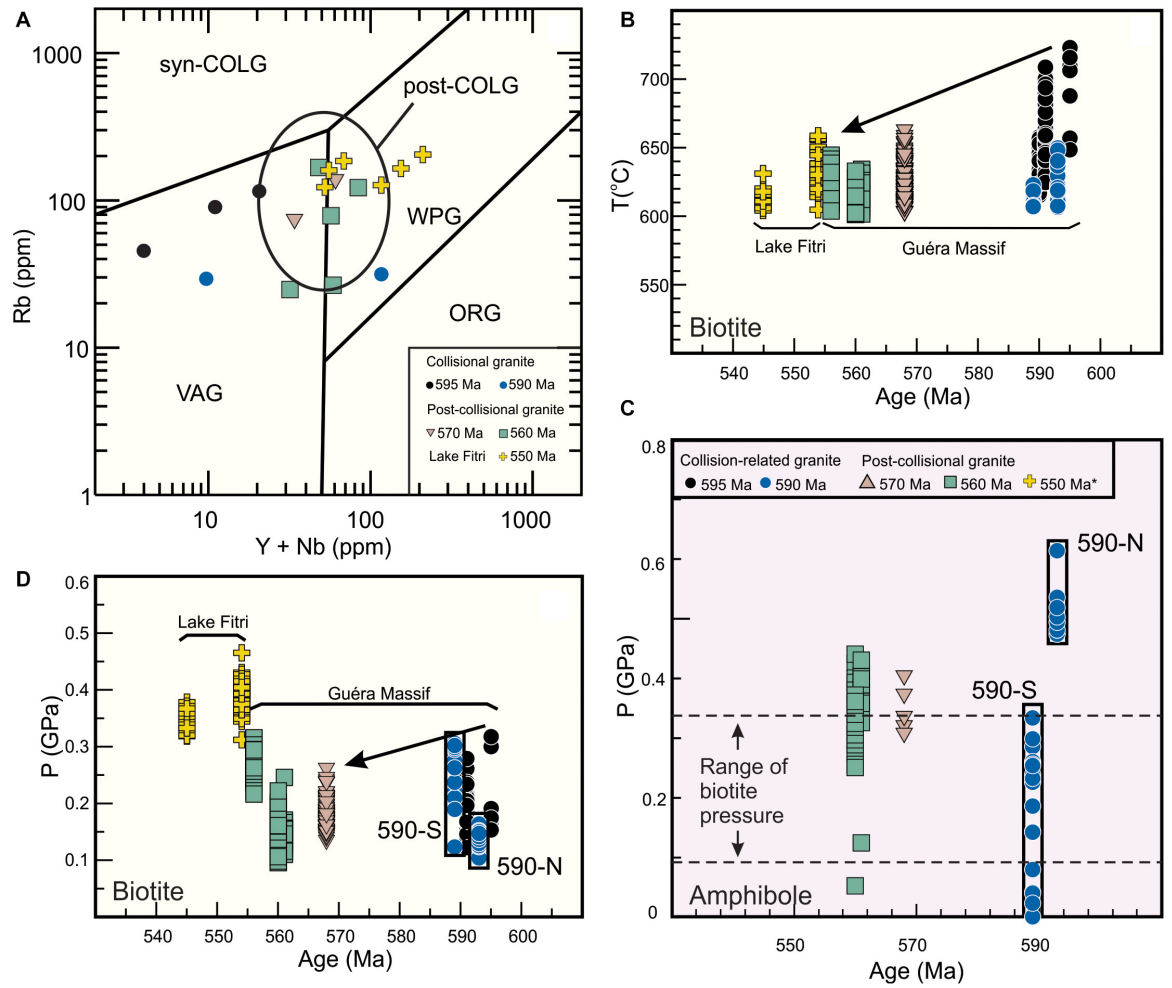

FIGURE 7 | (A) Classification of granitic rocks using Rb (ppm) vs Y + Nb (ppm) of Pearce (1996). Syn-COLG = syn-collisional granite, WPG = within-plate granite, VAG = volcanic-arc granite, ORG = ocean-ridge granite, post-COLG = post-collisional granite. **(B)** Biotite crystallization temperature estimates of the Guéra Massif and Lake Fitri granites. Crystallization pressure estimates of **(C)** amphibole, and **(D)** biotite of the Guéra Massif and Lake Fitri granites.

of crystallization among the studied granites. The relatively high TiO_2 and Al^{VI} contents in the Guéra Massif granites are supportive of a mid-crustal level crystallization depth.

Uchida et al. (2007) demonstrated that the total Al content of amphibole and total Al content of biotite increase together with increasing pressure, in other words, the crystallization pressure of granitoids may be constrained by the total concentration of Al in biotite. Therefore, Al-in-biotite can be utilized instead of the Al-in-hornblende for geobarometry estimates where appropriate. Eq. (3) is used to calculate crystallization pressure of biotite in granitic rocks that contain a mineral assemblage of plagioclase + biotite + muscovite + hornblende + K-feldspar + magnetite + ilmenite.

$$P\ (\text{kbar}) = 3.33Al^{T} - 6.53\ (\pm 0.33) \quad (3)$$

Where Al^{t} designates the total number of Al atoms in biotite on the bases of 22 oxygen equivalents.

The calculated average biotite crystallization pressures are shown in **Figure 7D**. The average values for individual plutons are summarized in **Table 3** with the complete results in **Supplementary Table S1**. The data indicate that the biotite crystallization pressure of the collisional granites tends to be more restricted (0.19 ± 0.08–0.23 ± 0.03 GPa) for the older granites than that for the younger granites (0.13 ± 0.02–0.25 ± 0.09 GPa) although they overlap. The biotite from the post-collisional granites, including those from Lake Fitri, have variable average pressures (570 Ma = 0.17 ± 0.05 and 0.17 ± 0.07 GPa; 560 Ma = 0.14 ± 0.07–0.27 ± 0.05 GPa; Lake Fitri = 0.35 ± 0.03–0.39 ± 0.08 GPa) but, the Lake Fitri rocks have the highest estimates.

Oxygen Fugacity Estimates

Oxygen fugacity (fO_2) is an essential parameter constraining magmatic activities (Kilinc et al., 1983; Kress and Carmichael, 1991; Ottonello et al., 2001; Botcharnikov et al., 2005). It

TABLE 2 | The range of amphibole pressure estimates from the Gueìra Massif granites.

Pluton	Sample	Pressure (GPa)		
		Max	Min	Average
590 Ma-N	14ZA16A	0.61	0.47	0.50 ± 0.07
590 Ma-S	14ZA12D	0.33	0.02	0.20 ± 0.15
570 Ma-W	14ZA01	0.37	0.31	0.33 ± 0.03
570 Ma-E	14ZA23	0.40		
560 Ma-N	14ZA18	0.44	0.32	0.39 ± 0.06
560 Ma-N	14ZA19B	0.43	0.12	0.37 ± 0.15
560 Ma-N	14ZA20B	0.36	0.05	0.29 ± 0.15
560 Ma-N	14ZA21B	0.37	0.25	0.33 ± 0.06

GPa = gigapascal. The uncertainty for all calculations is ±0.05 GPa (Johnson and Rutherford, 1989). Sample 14ZA23 only has one analysis. Average = average value of the pressure (GPa) including the uncertainty in the average.

TABLE 3 | The range of biotite pressure estimates of the Gueìra Massif and Lake Fitri granites.

Pluton	Sample	Biotite Pressure (GPa)		
		Max	Min	Average
595 Ma	14ZA02	0.317	0.153	0.21 ± 0.08
595 Ma	14ZA06	0.261	0.208	0.23 ± 0.03
595 Ma	14ZA25C	0.279	0.122	0.18 ± 0.08
590 Ma-N	14ZA16A	0.164	0.104	0.13 ± 0.02
590 Ma-S	14ZA12D	0.305	0.123	0.25 ± 0.09
570 Ma-W	14ZA01	0.225	0.121	0.17 ± 0.05
570 Ma-E	14ZA23	0.262	0.136	0.18 ± 0.06
560 Ma-S	14ZA10	0.315	0.216	0.27 ± 0.05
560 Ma-N	14ZA18	0.166	0.096	0.14 ± 0.03
560 Ma-N	14ZA19B	0.245	0.110	0.14 ± 0.07
560 Ma-N	14ZA20B	0.202	0.095	0.14 ± 0.06
560 Ma-N	14ZA21B	0.222	0.160	0.19 ± 0.03
550 Ma Ngoura	NA01	0.430	0.344	0.39 ± 0.05
550 Ma Ngoura	NA03	0.427	0.349	0.39 ± 0.04
550 Ma Ngoura	NA06	0.465	0.312	0.39 ± 0.08
550 Ma Moyto 2	NA18	0.378	0.318	0.35 ± 0.03

GPa = gigapascal. The uncertainty of each calculation is ±0.033 GPa (Uchida et al., 2007). Average = average value of the pressure (GPa) including the uncertainty in the average.

is considered to be a useful tool for determining the redox condition of melts during petrogenesis, due to its effect on crystallization, differentiation, and geophysical properties (e.g., melt structure and viscosity) of magma (Carmichael, 1991; Jayasuriya et al., 2004).

Equation (4) is used to calculate the oxygen fugacity estimate of Eugster and Wones (1962). It is based upon the Fe^{2+}-Fe^{3+}-Mg^{2+} composition of biotite, and the P and T for various oxygen buffers.

$$LogfO2 = -\frac{A}{T} + B + C\frac{(P-1)}{T} \quad (4)$$

Where T is the temperature in K, P is the pressure in bar, and A, B, and C are corresponding coefficients for different oxygen fugacity buffers. Temperature is calculated using equation (1), and P is calculated using equation (3).

The calculation of fO_2 depends on the value of coefficients A, B, and C that represent different oxygen fugacity buffers (Eugster and Wones, 1962). The coefficients are chosen based on the proportions of Fe^{2+}, Fe^{3+}, and Mg^{2+} in biotite, which for this study, are calculated using the methods of Nenova (1997). Wones and Eugster (1965) established the Fe^{2+}-Fe^{3+}-Mg^{2+} ternary diagram using the contents of biotite, where the QFM (quartz-fayalite-magnetite), NNO (Ni–NiO), and HM (hematite-magnetite) buffers are defined based on experimental data. In ideal cases, the A, B, and C values are able to be directly obtained from Eugster and Wones (1962) for a given buffer, if the data plot directly on one of the buffers. In fact, there are many cases of biotite straddling two buffers in this study. The corresponding value of the coefficient was assigned to the buffer that is closest to the data point (Yavuz, 2003a,b; Ayati et al., 2013; Li et al., 2017). In this study, all samples plot along with the QFM and NNO buffers (**Figure 8**), therefore, the value of A, B, and C coefficients are interpolated between these buffers. In which, the QFM buffer is used for Moyto (Lake Fitri), 560 Ma-N (northern) pluton, 570 Ma-E (eastern pluton), and the 590 Ma pluton whereas the NNO buffer is designated for Ngoura (Lake Fitri), 560 Ma-S (southern) pluton, 570 Ma-W (western) pluton, and 595 pluton (**Table 4**). The average values of $\log fO_2$ and their corresponding values to ΔQFM are summarized in **Table 4** and the results are listed in **Supplementary Tables S2, S3**.

The estimates do not indicate a secular variation but it seems that the granites around Mongo are generally more oxidizing (ΔQFM +0.3 to +0.5) whereas the granites to the east and south are generally more reducing (ΔQFM − 1). The granites from Lake Fitri shows a similar range of estimates with the Ngoura rocks (ΔQFM + 0.3) being moderately oxidizing and the Moyto rocks (ΔQFM − 1) being reducing.

Secular Variation in the Guéra Massif Granites

The estimated temperatures and to some extent pressures of the biotite from the Guéra Massif granites show a systematic variation from higher to lower values with decreasing age. The biotite crystallization temperatures from the Guéra Massif and the Lake Fitri region show a secular variation as they drop from 696 ± 37–607 ± 7°C over time (**Figure 7B**). The low temperatures of some biotite (<650°C) is indicative of late stage crystallization. Experimental studies show that granitic magma will become solid when the solidification temperature cools to 650–700°C (Tuttle and Bowen, 1958; Luth et al., 1964; Piwinskii, 1968; Freiberg et al., 2001). However, recent studies suggest that the crystallization of many minerals, in particular K-feldspar megacrysts, in calc-alkalic granites can be lower than 650°C and argue for lower consolidation temperatures due to repeated cycles of heating and fluxing by water-rich fluids (Glazner and Johnson, 2013; Challener and Glazner, 2017).

In comparison, the zircon saturation temperature estimates (TZr°C ± 40°C) do not show a secular variation as the temperatures for all rocks ranges from 714°C to 587°C

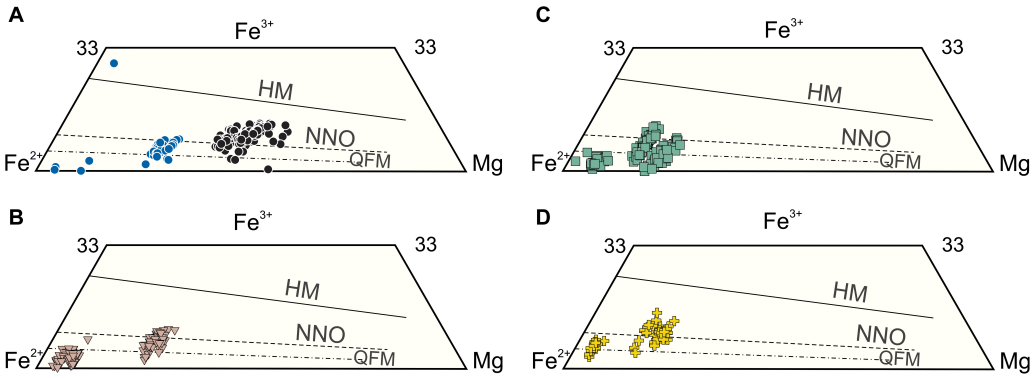

FIGURE 8 | Plot of biotite redox conditions from the **(A)** 595–590 Ma granitic rocks, **(B)** 570 Ma granitic rocks, **(C)** 560 Ma granitic rocks of the Guéra Massif, and **(D)** the Lake Fitri (554–545 Ma) granitic rocks. Lake Fitri data from Shellnutt et al. (2018). The redox buffers of Eugster and Wones (1962) are HM = hematite-magnetite; NNO = Ni-NiO; QFM = quartz-fayalite-magnetite.

TABLE 4 | The range of biotite oxygen fugacity estimates from the Gueìra Massif and Lake Fitri granites.

Pluton	Sample	LogfO_2			ΔQFM (Average)	Buffer
		Max	Min	Average		
595 Ma	14ZA02	−15.80	−17.73	−16.5 ± 1.0	+0.30 ± 0.03	NNO
595 Ma	14ZA06	−17.50	−18.77	−18.2 ± 0.6	+0.41 ± 0.05	NNO
595 Ma	14ZA25C	−16.17	−18.51	−17.3 ± 1.2	+0.37 ± 0.09	NNO
590 Ma-N	14ZA16A	−19.17	−20.63	−20.2 ± 0.7	−0.99 ± 0.02	QFM
590 Ma-S	14ZA12D	−19.97	−20.51	−20.3 ± 0.3	−1.00 ± 0.01	QFM
570 Ma-W	14ZA01	−17.47	−19.09	−18.3 ± 0.8	+0.44 ± 0.07	NNO
570 Ma-E	14ZA23	−18.73	−20.67	−20.1 ± 1.0	−0.99 ± 0.03	QFM
560 Ma-S	14ZA10	−17.87	−19.11	−18.4 ± 0.6	+0.40 ± 0.05	NNO
560 Ma-N	14ZA18	−20.34	−20.79	−20.6 ± 0.2	−1.00 ± 0.01	QFM
560 Ma-N	14ZA19B	−19.63	−20.76	−20.2 ± 0.6	−0.99 ± 0.02	QFM
560 Ma-N	14ZA20B	−19.87	−20.71	−20.3 ± 0.4	−1.00 ± 0.02	QFM
560 Ma-N	14ZA21B	−19.69	−20.67	−20.3 ± 0.5	−1.00 ± 0.02	QFM
550 Ma Ngoura	NA01	−17.45	−18.69	−18.1 ± 0.6	+0.32 ± 0.05	NNO
550 Ma Ngoura	NA03	−17.38	−18.41	−17.9 ± 0.5	+0.31 ± 0.04	NNO
550 Ma Ngoura	NA06	−17.79	−18.96	−18.4 ± 0.6	+0.34 ± 0.04	NNO
550 Ma Moyto 2	NA18	−19.50	−20.47	−20.2 ± 0.5	−1.00 ± 0.02	QFM

Average = average values of the logfO_2 and ΔQFM including the uncertainty in the averages.

(**Supplementary Table S1**; Boehnke et al., 2013). The low TZr(°C) temperatures are consistent with the inheritance-rich granites described by Miller et al. (2003). It is postulated that inheritance-rich granites require infiltration of water-rich fluids that could be derived by dehydration of crust in the zone of melting. The granites from Guéra Massif and Lake Fitri are known to contain a significant amount of inherited zircons, and partial melting (∼800–720°C) and fractional crystallization models (∼910–740°C) of the collisional (e.g., 595–590 Ma rocks Guéra Massif) and post-collisional (e.g., Lake Fitri) systems indicate that water-saturated or near water-saturated conditions yield the best results (Shellnutt et al., 2017, 2018, 2019a). Consequently, it is possible that some of the low biotite temperature estimates are not necessarily due to sub-solidus re-equilibration during metamorphism or hydrothermal alteration (Ackerson et al., 2018). Indeed, the biotite and whole rock TZr(°C) temperature estimates in this study lend support to this conclusion and they were likely derived from inheritance- and water-rich parental magmas. The reason for the secular temperature change is uncertain, although the biotites from the 595 Ma rocks have the highest temperatures, the host rock does not contain amphibole whereas the lower temperatures biotites are found in rocks with amphibole. Therefore, it is possible that the low biotite temperature estimates may be due to their later crystallization (i.e., post amphibole).

The oxygen fugacity of the investigated granites does not show a secular trend but the granite bodies in the northern portion of the Guéra Massif around Mongo tend to be oxidizing whereas those to the east and south are reducing. The only exception is samples 14ZA10 (560 Ma-S) which is relatively oxidizing. A similar relationship is observed in the Lake Fitri granites where the Ngoura granites are oxidizing

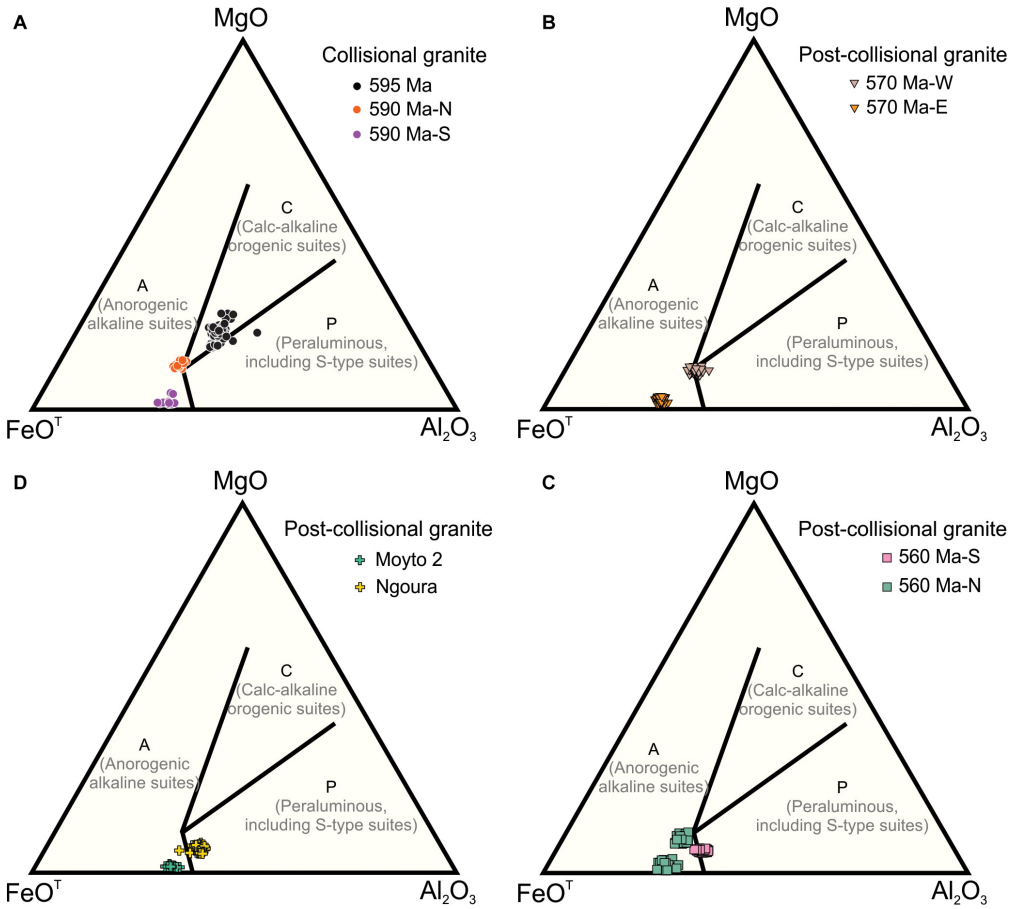

FIGURE 9 | Classification of biotite using the FeO-MgO-Al_2O_3 tectonomagmatic discrimination diagram of Abdel-Rahman (1994). **(A)** Collisional granites, **(B)** 570 Ma post-collisional granites, **(C)** 560 Ma post-collisional granites, and **(D)** post-collisional granites from Lake Fitri. Lake Fitri data from Shellnutt et al. (2018).

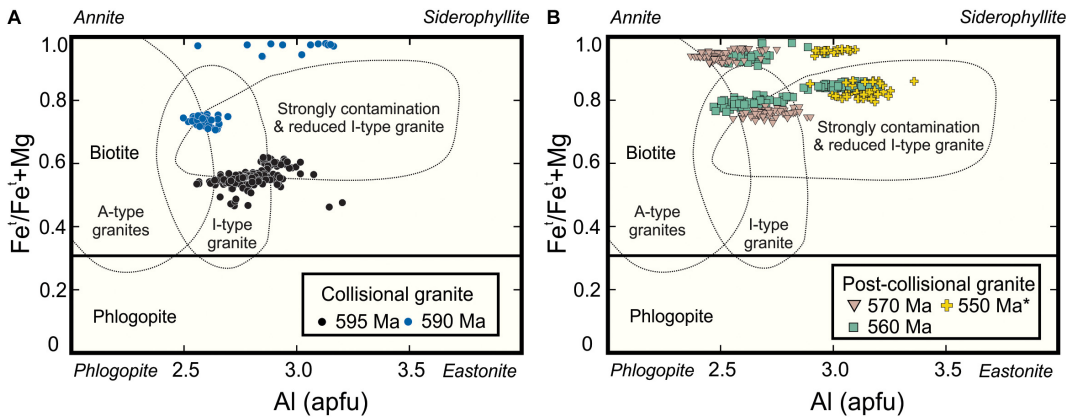

FIGURE 10 | Discrimination of biotite using Fe/(Fe + Mg) vs. ∑Al (apfu) (Shabani et al., 2003). **(A)** Collisional granites, and the **(B)** ~570 Ma post-collisional granites, ~560 Ma post-collisional granites, and ~550 post-collisional granites from Lake Fitri. Lake Fitri data from Shellnutt et al. (2018).

and the Moyto granites are reducing. In general, the biotites that have low Ti content also have low fO_2 estimates. The concentration of ferrous iron usually varies among different sample suites that differ in redox conditions, and the oxidation state of magma activity controls the extent of Fe^{2+}-enrichment in the magma sequence during is evolution (e.g., Larsen, 1976). In this case, the biotite of 590 Ma-S, 570 Ma-E, and 560 Ma-N plutons are more enriched in Fe^{2+} which

is associated with relatively reducing magmatic conditions; the Fe^{2+}-poor biotites of 595 Ma, 590 Ma-N, 570 Ma-W, and 560 Ma-S plutons are associated with relatively oxidizing magmatic conditions.

High fO_2 magmatic systems usually crystallize Fe-Ti oxide minerals such as ilmenite, hematite, and magnetite and that the appearance of hematite indicates the culmination in oxidation state in felsic rocks (Lindsley, 1991). The petrography and scanning electron microscopy investigation of this study did not identify primary hematite and the rocks have the extremely low abundance of ilmenite and magnetite which are primarily observed as inclusions within biotite or amphibole. The concentration of SiO_2 in the collisional granites is variable (59.7–74.8 wt%), whereas the post-collisional granites (69.3–76.9 wt%) is less variable but both can be very high (Pham, 2018; Shellnutt et al., 2018), which may be the reason for the low abundance of Fe-Ti oxide minerals.

The change in estimated pressure of the biotites from Guéra Massif generally shows a flat to slightly decreasing trend from oldest to youngest rocks (**Figure 7D**), possibly reflecting a decline of pressure associated with the tectonic transition from compressional to extensional stress. Our results show that there is significant pressure variation for some plutons. The 560 and 590 Ma-S plutons have higher biotite pressure estimates (0.27 ± 0.05, 0.25 ± 0.09 GPa) compared to the 560 Ma-N (0.14 ± 0.07–0.19 ± 0.03 GPa) and 590 Ma-N (0.13 ± 0.02 GPa) granites. The barometric dichotomy could be due to a pressure gradient in the 560 and 590 Ma plutons related to their location within the magma body as it was emplaced. In other words, the exhumed southern regions of the plutons correspond to the base of the intrusions whereas the northern region represents the upper portions of the pluton. However, the amphibole pressure estimates from the northern portions of the 590 and 560 Ma plutons are significantly different than the biotite estimates (**Figures 7C,D**). The higher amphibole (590 Ma-N = 0.50 ± 0.07 GPa; 560 Ma-N = 0.29 ± 0.15–0.39 ± 0.06 GPa) and lower biotite (590 Ma-N = 0.13 ± 0.02 GPa; 560 Ma-N = 0.14 ± 0.07–0.19 ± 0.03 GPa) pressure estimates are in contrast to the estimates from the southern portion of the 590 Ma pluton which have similar values (P_{Am} = 0.20 ± 0.15 GPa; P_{Bt} = 0.25 ± 0.09 GPa). A possible explanation for the pressure difference is that the amphibole is older and initially crystallized at higher pressure and was subsequently redistributed before magma consolidation after reaching neutral buoyancy in the crust (lower pressure). Consistent with this interpretation is the fact that the high pressure amphibole has higher TiO_2, Al_2O_3, CaO, Na_2O, and K_2O and lower FeO^t than the low pressure amphibole suggesting that it probably crystallized before significant feldspar crystallization occurred.

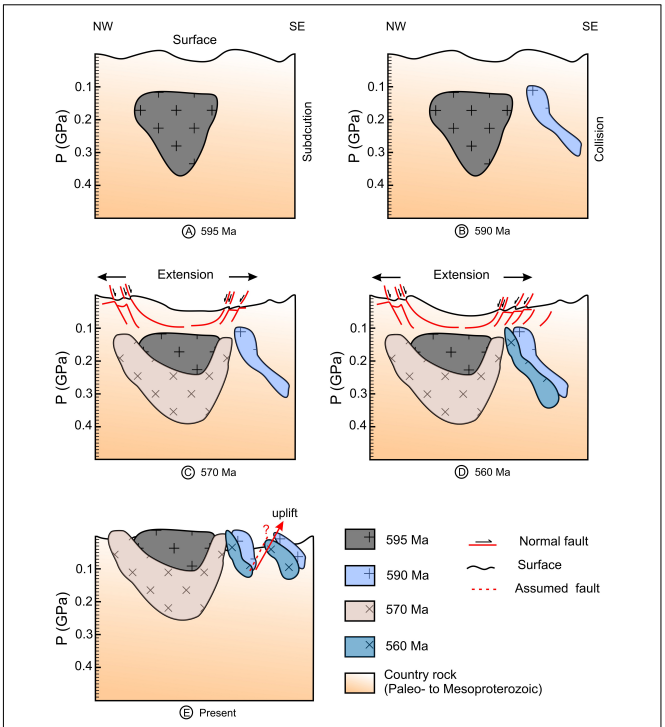

FIGURE 11 | A conceptual tectonomagmatic scenario for the crustal evolution of the Guéra Massif. **(A)** Emplacement of the (~595 Ma) subduction-related collisional granites. **(B)** Emplacement of the (~590 Ma) syn-collision granites. **(C)** Emplacement of the first generation (~570 Ma) of post-collisional granites. **(D)** Emplacement of the second generation (~560 Ma) of post-collisional granites. **(E)** Period of post-collisional uplift either immediately after emplacement (~560 Ma) or possibly during faulting related to the Late Cretaceous West and Central African rift system (WCARS).

Tectonomagmatic Evolution of Guéra Massif Granites

Biotite composition can be used to determine the tectonic environment of host rocks (Abdel-Rahman, 1994; Shabani et al., 2003; Machev et al., 2004; Bónová et al., 2010; Kumar and Pathak, 2010; Zhang et al., 2016). In this study we use the biotite tectonomagmatic characterization of Abdel-Rahman (1994) and Shabani et al. (2003). The older (595 Ma) collisional granites classify as calc-alkaline orogenic suites, and strongly contaminated and reduced (SCR) I-type granite (**Figures 9A**, **10A**). In comparison, the younger (590 Ma) collisional granite is similar to anorogenic granite (anorogenic alkaline suite) in the diagram of Abdel-Rahman (1994) but straddle the fields of A-type granite, I-type granite, and SCR I-type (590 Ma-N) of Shabani et al. (2003) (**Figures 9A**, **10A**). Indeed, the older (595 Ma) pluton is compositionally characteristic of volcanic-arc granite and was likely derived from a subduction modified mantle wedge source (Shellnutt et al., 2019a). In contrast, the 590 Ma plutons are different as they appear to be similar rocks associated with post-collisional extensional settings rather than collisional settings. Moreover, they have significant Mesoproterozoic (~1.0–1.9 Ga) inherited zircons suggesting they are likely derived from the crust (Shellnutt et al., 2019a). The overlapping and transition of biotite compositions and magmatic conditions suggest the younger (590 Ma) collisional rocks were likely related to the terminal stages of collisional. In other words, the first generation of collisional granites was emplaced at 595 Ma and related to subduction of oceanic crust beneath the Saharan

Metacraton whereas the 590 Ma plutons are probably related to syn-collisional magmatism that occurred during continent-continent collision between the Congo-São Francisco Craton and the Saharan Metacraton (Shellnutt et al., 2017, 2019a).

Post-collisional granites tend to be difficult to classify as they are commonly derived by melting of diverse (i.e., juvenile and ancient) crustal sources (Pearce, 1996). The post-collisional granites from Guéra Massif and Lake Fitri fall mostly within the field of anorogenic granites (A-field) but many straddle the boundary with peraluminous (P-field) granites (**Figure 9**; Abdel-Rahman, 1994). In comparison, nearly all data fall within the fields of I-type or SCR I-type granite in the classification of Shabani et al. (2003) (**Figure 10**). The seemingly contradictory results between the classification schemes of Abdel-Rahman (1994) and Shabani et al. (2003) is consistent with classification of post-collisional granite as Pearce (1996) demonstrates that these rocks overlap between the fields of volcanic-arc and within-plate granites with respect to Rb, Y, and Nb concentrations (**Figure 7A**). The first period of post-collisional granitic magmatism occurred at ∼570 Ma and is probably related to crustal relaxation after oblique collision and shearing between the Congo-São Francisco Craton and the Saharan Metacraton (Ferré et al., 2002; Toteu et al., 2004). The second period of post-collisional magmatism was likely emplaced after an episode of regional crustal shortening (Ferré et al., 2002; Toteu et al., 2004). The timing of exhumation and exposure is unknown as it could be related to faulting either immediately after emplacement or possibly related to fault movement associated with the Cretaceous Western and Central African rift system (**Figure 11**; Genik, 1992).

In comparison to the Guéra Massif post-collisional granites, the Lake Fitri granites are different. The Lake Fitri granites tend to overlap between the anorogenic alkaline suites (A-field) and the peraluminous suites (P-field) but more importantly the higher pressure estimates indicate that they crystallized at greater depth. It is known that the Lake Fitri granites are isotopically more depleted [$\varepsilon_{Nd}(t)$ +1.3 to +2.9] than the Guéra Massif post-collisional granites [$\varepsilon_{Nd}(t) < -1.2$] and suggest different sources were involved in their origin (Pham, 2018; Shellnutt et al., 2018, 2019a). Therefore, we conclude that the two regions probably represent separate domains/terranes and indicate that the crust near Late Fitri rocks was thicker and more juvenile whereas crust of the Guéra Massif was likely thinner and more radiogenic.

CONCLUSION

This study reports the compositions of biotite and hornblende from granitic rocks of the Guéra Massif and estimates of their likely crystallization conditions. The results offer new insight into the regional tectonic setting as well. The main conclusions are as follows:

1. The amphibole and biotite compositions show a trend of increasing total iron and decreasing magnesium content with decreasing age.
2. The biotites from the collisional granites tend to have higher crystallization temperatures, and crystallization pressure, and are derived from parental magmas that were relatively oxidizing with redox conditions between NNO and QFM buffers.
3. The biotites from the post-collisional granites tend to yield lower crystallization temperatures and pressures but have similar redox conditions as the collisional rocks.
4. The biotite from the post-collisional granites from the Lake Fitri region crystallized at moderate to low temperatures, at high pressure with redox conditions at or near the NNO to QFM buffers.
5. The older (595 Ma) collisional granites have biotite compositions similar to rocks from orogenic suites whereas the younger (590 Ma) collisional granites have biotite compositions similar to anorogenic suites.
6. All biotites from the post-collisional rocks are characteristic of anorogenic suites although the crystals from the Lake Fitri granites have more variability and straddle the boundary with the peraluminous suites.
7. The post-collisional granites from Lake Fitri region and Guéra Massif have different emplacement depths and source composition. Thus, the Lake Fitri granites are probably unrelated to the Guéra Massif and were emplaced within a separate terrane/domain of the Saharan Metacraton.

DATA AVAILABILITY STATEMENT

All datasets generated for this study are included in the article/**Supplementary Material**.

AUTHOR CONTRIBUTIONS

CP wrote the manuscript, created the figures, and processed the data. JS conceived of the study and assisted with the writing and interpretations. M-WY collected the samples. YI analyzed the samples and wrote the method details. All authors contributed to the manuscript, read, and approved the submitted version.

FUNDING

This project received support from Ministry of Science and Technology (Taiwan) through grant 107-2628-M-003-003-MY3 to JS.

ACKNOWLEDGMENTS

Scott Whattam is thanked for editorial handling.

SUPPLEMENTARY MATERIAL

The Supplementary Material for this article can be found online at: https://www.frontiersin.org/articles/10.3389/feart.2020.00318/full#supplementary-material

REFERENCES

Abdel-Rahman, A. M. (1994). Nature of biotites from alkaline, calc-alkaline, and peraluminous magmas. *J. Petrol.* 35, 525–541. doi: 10.1093/petrology/35.2.525

Abdelsalam, M. G., and Dawoud, A. S. (1991). The kabus ophiolite melange, sudan and its bearing on the western boundary of the nubian shield. *J. Geol. Soc. Lond.* 148, 83–92. doi: 10.1144/gsjgs.148.1.0083

Abdelsalam, M. G., Liégeois, J.-P., and Stern, R. J. (2002). The saharan metacraton. *J. Afr. Earth Sci.* 34, 119–136. doi: 10.1016/s0899-5362(02)00013-1

Abdelsalam, M. G., and Stern, R. J. (1996). Mapping precambrian structures in the sahara desert with SIR-C/X-SAR radar: the neoproterozoic keraf suture. *NE Sudan. J. Geophys. Res.* 101, 23063–23076. doi: 10.1029/96je01391

Ackerson, M. R., Mysen, B. O., Tailby, N., and Watson, E. B. (2018). Low-temperature crystallization of granites and the implications for crustal magmatism. *Nature* 559, 94–97. doi: 10.1038/s41586-018-0264-2

Anderson, D. J., Lindsley, D. H., and Davidson, P. M. (1993). QUILF: a PASCAL program to assess equilibria among Fe-Mg-Mn-Ti oxides, pyroxenes, olivine, and quartz. *Comput. Geosci.* 19, 1333–1350. doi: 10.1016/0098-3004(93)90033-2

Ayati, F., Yavuz, F., Asadi, H. H., Richards, J. P., and Jourdan, F. (2013). Petrology and geochemistry of calc-alkaline volcanic and subvolcanic rocks, Dalli porphyry copper-gold deposit, Markazi, Province, Iran. *Int. Geol. Rev.* 55, 158–184. doi: 10.1080/00206814.2012.689640

Black, R. (1992). *Mission Géologique au Tchad du 14 Janvier au 08 Féverier 1992*. Rapport inedit. N'Djamena: PNUD/DRGM, 15.

Boehnke, P., Watson, E. B., Trail, D., Harrison, T. M., and Schmitt, A. K. (2013). Zircon saturation re-revisited. *Chem. Geol.* 351, 324–334. doi: 10.1016/j.chemgeo.2013.05.028

Bónová, K., Broska, I., and Petrík, I. (2010). Biotite from Èierna hora Mountains granitoids (Western Carpathians, Slovakia) and estimation of water contents in granitoid melts. *Geol. Carpath.* 61, 3–17. doi: 10.2478/v10096-009-0040-1

Bora, S., and Kumar, S. (2015). Geochemistry of biotites and host granitoid plutons from the Proterozoic Mahakoshal Belt, central India tectonic zone: implication for nature and tectonic setting of magmatism. *Int. Geol. Rev.* 57, 1686–1706. doi: 10.1080/00206814.2015.1032372

Botcharnikov, R. E., Koepke, J., Holtz, F., and McCammon, C. (2005). The effect of water activity on the oxidation and structural state of Fe in a ferro-basaltic melt. *Geochim. Cosmochim. Ac.* 69, 5071–5085. doi: 10.1016/j.gca.2005.04.023

Buddington, A. F., and Lindsley, D. H. (1964). Iron-titanium oxide minerals and synthetic equivalents. *J. Petrol.* 5, 310–357. doi: 10.1093/petrology/5.2.310

Burkhard, D. J. M. (1991). Temperature and redox path of biotite-bearing intrusives: a method of estimation applied to S- and I-type granites from Australia. *Earth Planet. Sci. Lett.* 104, 89–98. doi: 10.1016/0012-821x(91)90240-i

Burkhard, D. J. M. (1993). Biotite crystallization temperatures and redox states in granitic rocks as an indicator for tectonic setting. *Geol. Mijnbouw* 71, 337–349.

Carmichael, I. S. E. (1991). The redox state of basic and silicic magmas: a reflection of their source regions? *Contrib. Mineral. Petrol.* 106, 129–141. doi: 10.1007/bf00306429

Challener, S. C., and Glazner, A. F. (2017). Igneous or metamorphic? Hornblende phenocrysts as greenschist facies reaction cells in the Half Dome granodiorite, California. *Am. Mineral.* 102, 436–444. doi: 10.2138/am-2017-5864

Eugster, H. P., and Wones, D. R. (1962). Stability reactions of the ferruginous biotite, annite. *J. Petrol.* 3, 82–125. doi: 10.1093/petrology/3.1.82

Ferré, E., Gleizes, G., and Caby, R. (2002). Obliquely convergent tectonics and granite emplacement in the Trans-Saharan belt of Eastern Nigeria: a synthesis. *Precambrian Res.* 114, 199–219. doi: 10.1016/s0301-9268(01)00226-1

Foster, M. D. (1960). "Interpretation of the composition of trioctahedral micas," in . *US Geological Survey Professional Paper 354-B*, (Washington: United States Government Printing Office), 49.

Freiberg, R., Hecht, L., Cuney, M., and Morteani, G. (2001). Secondary Ca-Al silicates in plutonic rocks and implications for their cooling history. *Contrib. Mineral. Petrol.* 141, 415–429. doi: 10.1007/s004100100241

Frost, B. R., Barnes, C. G., Collins, W. J., Arculus, R. J., Ellis, D. J., and Frost, C. D. (2001). A geochemical classification for granitic rocks. *J. Petrol.* 42, 2033–2048. doi: 10.1093/petrology/42.11.2033

Genik, G. J. (1992). Regional framework, structural and petroleum aspects of rift basins in Niger, Chad and the Central African Republic (CAR). *Tectonophysics* 213, 169–185. doi: 10.1016/b978-0-444-89912-5.50036-3

Ghent, E. D., Nicholls, J., Siminy, P. S., Sevigny, H. H., and Stout, M. Z. (1991). Hornblende Geobarometry of the Nelson Batholith, Southeastern British Columbia: tectonic implications. *Can. J. Earth Sci.* 28, 1982–1991. doi: 10.1139/e91-180

Ghiorso, M. S., and Sack, O. (1991). Fe-Ti oxide geothermometry: thermodynamic formulation and the estimation of intensive variables in silicic magmas. *Contrib. Mineral. Petrol.* 108, 485–510. doi: 10.1007/bf00303452

Glazner, A. F., and Johnson, B. R. (2013). Late crystallization of K-feldspar and the paradox of megacrystic granites. *Contrib. Mineral. Petrol.* 166, 777–779.

Hammarstrom, J. M., and Zen, E. (1986). Aluminum in hornblende: an empirical igneous geo-barometer. *Am. Mineral.* 71, 1297–1313.

Hecht, L. (1994). "The chemical composition of biotite as an indicator of magmatic fractionation and metasomatism in Sn-specialised granites of the Fichtelgebirge (NW Bohemian Massif, Germany)," in *Metallogeny of Collisional Orogens*, eds R. Seltmann, H. Kämpf, and P. Möller (Praha: Czech Geological Survey), 295–300.

Henry, B., Liégeois, J.-P., Nouar, O., Derder, M. E. M., Bayou, B., Bruguier, O., et al. (2009). Repeated granitoid intrusions during the Neoproterozoic along the western boundary of the Saharan Metacraton, Eastern Hoggar, Tuareg shield, Algeria: an AMS and U-Pb zircon age study. *Tectonophysics* 474, 417–434. doi: 10.1016/j.tecto.2009.04.022

Hollister, L. S., Grissom, G. C., Peters, E. K., Stowell, H. H., and Gisson, V. B. (1987). Confirmation of the empirical correlation of Al in hornblende with pressure of solidification of calc-alkaline plutons. *Am. Mineral.* 72, 231–239.

Isseini, M., Hamit, A., and Abderamane, M. (2013). The tectonic and geological framework of the Mongo area, a segment of the Pan-African Guera Massif in Central Chad: evidences from field observations and remote sensing. *Rev. Sci. Tchad.* 1, 4–12.

Jayasuriya, K. D., O'Neill, H. S. C., Berry, A., and Campbell, S. J. (2004). A Mössbauer study of the oxidation state of fe in silicate melts. *Am. Mineral.* 89, 1597–1609. doi: 10.2138/am-2004-11-1203

Johnson, C. M., and Rutherford, M. J. (1989). Experimental calibration of the aluminum-in-hornblende geobarometer with applicable to Long Valley Caldera (California) volcanic rocks. *Geology* 17, 837–841.

Kilinc, A., Carmichael, I. S. E., Rivers, M. L., and Sack, R. O. (1983). The ferric-ferrous ratio of natural silicate liquids equilibrated in air. *Contrib. Mineral. Petrol.* 83, 136–140. doi: 10.1007/bf00373086

Klerkx, J., and Deutsch, S. (1977). Resultats preliminaires obtenus par la methode Rb/Sr sur l'age des formations Precambriennes de la region d'Uweinat (Libye). *Musee R. l'Afr. Centrale. Déepart. Géeol. Minéeral. Rapp. Ann.* 83–94.

Kress, V. C., and Carmichael, I. S. E. (1991). The compressibility of silicate liquids containing Fe2O3 and the effect of composition, temperature, oxygen fugacity and pressure on their redox states. *Contrib. Mineral. Petrol.* 108, 82–92. doi: 10.1007/bf00307328

Kumar, S., and Pathak, M. (2010). Mineralogy and geochemistry of biotites from Proterozoic granitoid of western Arunachal Himalaya: evidence of bimodal granitogeny and tectonic af?nity. *J. Geol. Soc., India* 75, 715–730. doi: 10.1007/s12594-010-0058-0

Kusnir, I., and Moutaye, H. A. (1997). Ressources minérales du Tchad: une revue. *J. Afr. Earth Sci.* 24, 549–562. doi: 10.1016/s0899-5362(97)00080-8

Kusnir, I., and Schneider, J.-L. (1995). *Geìologie, Ressources Mineìrales et Ressources en eau du Tchad*. N'Djameìna: Centre national d'appui aÌ la recherche, 1.

Larsen, L. M. (1976). Clinopyroxenes and coexisting mafic minerals from the alkaline Ilímaussaq intrusion. South Greenland. *J. Petrol.* 17, 258–290. doi: 10.1093/petrology/17.2.258

Li, X., Chi, G., Zhou, Y., Deng, T., and Zhang, J. (2017). Oxygen fugacity of Yanshanian granites in South China and implications for metallogeny. *Ore Geol. Rev.* 88, 690–701. doi: 10.1016/j.oregeorev.2017.02.002

Liégeois, J.-P., Abdelsalam, M. G., Ennih, N., and Ouabadi, A. (2013). Metacraton: nature, genesis and behavior. *Gondwana Res.* 23, 220–237. doi: 10.1016/j.gr.2012.02.016

Liégeois, J.-P., Black, R., Navez, J., and Latouche, L. (1994). Early and late pan-african orogenies in the air assembly of terranes (Tuareg Shield. Niger). *Precambrian Res.* 67, 59–88. doi: 10.1016/0301-9268(94)90005-1

Liégeois, J.-P., Latouche, L., Boughrara, M., Navez, J., and Guiraud, M. (2003). The LATEA metacraton (Central Hoggar, Tuareg shield, Algeria): behaviour of

an old passive margin during the Pan-African orogeny. *J. Afr. Earth Sci.* 37, 161–190. doi: 10.1016/j.jafrearsci.2003.05.004

Lindsley, D. H. (1991). Oxide minerals: petrologic and magnetic significance. *Rev. Mineral.* 25, 1–509.

Luhr, J. F., Carmichael, I. S. E., and Varekamp, J. C. (1984). The 1982 eruptions of El Chichon volcano, Chiapas, Mexico-Mineralogy petrology of the anhydrite bearing pumices. *J. Volcanol. Geoth. Res.* 23, 69–108. doi: 10.1016/0377-0273(84)90057-x

Luth, W. C., Jahns, R. H., and Tuttle, O. F. (1964). The granite system at pressures of 4 to 10 kilobars. *J. Geophys. Res.* 69, 759–773. doi: 10.1029/jz069i004p00759

Machev, P., Klain, L., and Hecht, L. (2004). Mineralogy and chemistry of biotites from the belogradchik pluton-some petrological implications for granitoid magmatism in northwest Bulgaria. *Bulg. Geol. Soc. Annu. Sci. Conf. Geol.* abstract. 48–50.

Miller, C. F., McDowell, S. M., and Mapes, R. W. (2003). Hot and cold granites? Implications of zircon saturation temperatures and preservation of inheritance. *Geology* 31, 529–532.

Nachit, H., Ibhi, A., Abia, E. H., and Ohoud, M. B. (2005). Discrimination between primary magmatic biotites, reequilibrated biotites and neoformed biotites. *CR Geosci.* 337, 1415–1420. doi: 10.1016/j.crte.2005.09.002

Nachit, H., Razafimahefa, N., Stussi, J. M., and Carron, J. P. (1985). Composition chimiques des biotite et typologie magmatique des granitoïdes. *CR Acad. Sci. II* 301, 813–818.

Nenova, P. I. (1997). "Fe23": a computer program for calculating the number of Fe2+ and Fe3+ ions in minerals. *Comput. Geosci.* 23, 215–219. doi: 10.1016/s0098-3004(97)85445-3

Nkouandou, O. F., Bardintzeff, J. M., Mahamat, O., Mefire, A. F., and Ganwa, A. A. (2017). The dolerite dyke swarm of Mongo, Guéra Massif (Chad, Central Africa): geological setting, petrography, and geochemistry. *Open Geosci.* 9, 138–150.

Ottonello, G., Moretti, R., Marini, L., and Zuccolini, M. V. (2001). Oxidation state of iron in silicate glasses and melts: a thermochemical model. *Chem. Geol.* 174, 157–179. doi: 10.1016/s0009-2541(00)00314-4

Pearce, J. A. (1996). Source and settings of granitic rocks. *Episodes* 19, 120–125. doi: 10.18814/epiiugs/1996/v19i4/005

Pham, T. N. H. (2018). *Timing and Petrogenesis of Collisional and Post-Collisional Rocks of Guéra Massif, Republic of Chad*. master's thesis, National Taiwan Normal University, Taipei, TW.

Pin, C., and Poidevin, J. L. (1987). U-Pb zircon evidence for a Pan-African granulite facies metamorphism in the Central African Republic. A new interpretation of the high-grade series of the northern border of the Congo Craton. *Precambrian Res.* 36, 303–312. doi: 10.1016/0301-9268(87)90027-1

Piwinskii, A. J. (1968). Experimental studies of igneous rock series, central Sierra Nevada batholith. *California. J. Geol.* 76, 193–215.

Poidevin, J. L. (1994). Boninite-like rocks from the Paleoproterozoic greenstone belt of Bogoin, Central African Republic: geochemistry and petrogenesis. *Precambrian Res.* 68, 97–113. doi: 10.1016/0301-9268(94)90067-1

Schlüter, T. (2008). *Geological Atlas of Africa*. Berlin: Springer-Verlag.

Schmidt, M. W. (1992). Amphibole composition in tonalite as a function of pressure: an experimental calibration of the Al-in-hornblende barometer. *Contrib. Mineral. Petrol.* 110, 304–310. doi: 10.1007/bf00310745

Shabani, A. A. T., Lalonde, A. E., and Whalen, J. B. (2003). Composition of biotite from granitic rocks of the Canadian Appalachian orogen: a potential tectonomagmatic indicator? *Can. Mineral.* 41, 1381–1396. doi: 10.2113/gscanmin.41.6.1381

Shang, C. K., Satir, M., Morteani, G., and Taubald, H. (2010). Zircon and titanite age evidence for coeval granitization and migmatization of the early Middle and early Late Proterozoic Saharan Metacraton; example from the central North Sudan basement. *J. Afr. Earth Sci.* 57, 492–524. doi: 10.1016/j.jafrearsci.2009.12.006

Shellnutt, J. G., Pham, T. N. H., Denyszyn, S., Yeh, M.-W., and Lee, T.-Y. (2017). Timing of collisional and post-collisional Pan-African Orogeny silicic magmatism in south-central Chad. *Precambrian Res.* 301, 113–123. doi: 10.1016/j.precamres.2017.08.021

Shellnutt, J. G., Yeh, M.-W., Lee, T.-Y., Iizuka, Y., Pham, N. H. T., and Yang, C.-C. (2018). The origin of late ediacaran post-collisional granites near the Chad Lineament, Saharan Metacraton, South-Central Chad. *Lithos* 304-307, 450–467. doi: 10.1016/j.lithos.2018.02.020

Shellnutt, J. G., Pham, N. H. T., Yeh, M.-W., and Lee, T.-Y. (2019a). "Two series of Ediacaran collision-related granites in the Guéra Massif (Chad): tectonomagmatic constraints on the terminal collision of the eastern Central African Orogenic Belt," in *Fall Meeting (No. V31D-0160)*, Washington, DC: American Geophysical Union.

Shellnutt, J. G., Yeh, M.-W., Pham, N. H. T., and Lee, T.-Y. (2019b). Cryptic regional magmatism in the southern Saharan Metacraton at 580 Ma. *Precambrian Res.* 332:105398. doi: 10.1016/j.precamres.2019.105398

Stern, R. J. (1994). Arc assembly and continental collision in the Neoproterozoic E African Orogen: implication for the consolidation of Gondwanaland. *Annu. Rev. Earth Pl. Sci.* 22, 319–351. doi: 10.1146/annurev.ea.22.050194.001535

Stern, R. J., Kröner, A., Bender, R., Reischmann, T., and Dawoud, A. S. (1994). Precambrian basement around Wadi Halfa, Sudan: a new perspective on the evolution of the East Saharan Craton. *Geol. Rundsch.* 83, 564–577. doi: 10.1007/bf01083228

Suayah, I. B., Miller, J. S., Miller, B. V., Bayer, T. M., and Rogers, J. W. (2006). Tectonic significance of Late Neoproterozoic granites from the Tibesti massif in southern Libya inferred from Sr and Nd isotopes and U-Pb zircon data. *J. Afr. Earth Sci.* 44, 561–570. doi: 10.1016/j.jafrearsci.2005.11.020

Sultan, M., Tucker, R. D., El Alfy, Z., Attia, R., and Ragab, A. G. (1994). U-Pb (zircon) ages for the gneissic terrane west of the Nile, southern Egypt. *Geol. Rundsch.* 83, 514–522. doi: 10.1007/bf00194158

Tindle, A. G., and Webb, P. C. (1990). Estimation of lithium contents in trioctahedral micas using microprobe data: applications to micas from granitic rocks. *Eur. J. Mineral.* 2, 595–610. doi: 10.1127/ejm/2/5/0595

Tindle, A. G., and Webb, P. C. (1994). Probe-AMPH – a spreadsheet program to classify microprobe-derived amphibole analyses. *Comput. Geosci.* 20, 1201–1228. doi: 10.1016/0098-3004(94)90071-x

Toteu, S. F., Fouateu, R. Y., Penaye, J., Tchakounte, J., Mouangue, A. C. S., Van Schumus, W. R., et al. (2006). U-Pb dating of plutonic rocks involved in the nappe tectonic in southern Cameroon: consequence for the Pan-African orogenic evolution of the central African fold belt. *J. Afr. Earth Sci.* 44, 479–493. doi: 10.1016/j.jafrearsci.2005.11.015

Toteu, S. F., Penaye, J., and Djomani, Y. H. P. (2004). Geodynamic evolution of the Pan-African belt in central Africa with special reference to Cameroon. *Can. J. Earth Sci.* 41, 73–85. doi: 10.1139/e03-079

Tuttle, O. F., and Bowen, N. L. (1958). *Origin of Granite in the Light of Experimental of Studies in the System NaAlSi3O8-KAlSi3O8-SiO2-H2O*. Boulder, CO: Geological Society of America.

Uchida, E., Endo, S., and Makino, M. (2007). Relationship between solidification depth of granitic rocks and formation of hydrothermal ore deposits. *Resour. Geol.* 57, 47–56. doi: 10.1111/j.1751-3928.2006.00004.x

Wones, D., and Eugster, H. (1965). Stability of biotite: experiment, theory, and application. *Am. Mineral.* 50, 1228–1272.

Wones, D. R. (1981). Mafic silicates as indicators of intensive variables in granitic magmas. *Min. Geol.* 31, 191–212.

Yavuz, F. (2003a). Evaluating micas in petrologic and metallogenic aspect: I-definitions and structure of the computer program MICA+. *Comput. Geosci.* 29, 1203–1213. doi: 10.1016/s0098-3004(03)00142-0

Yavuz, F. (2003b). Evaluating micas in petrologic and metallogenic aspect: Part II-Applications using the computer program Mica+. *Comput. Geosci.* 29, 1215–1228. doi: 10.1016/s0098-3004(03)00143-2

Zen, E. (1988). Plumbing the depths of batholiths. *Am. J. Sci.* 289, 1137–1157. doi: 10.2475/ajs.289.10.1137

Zhang, W., Lentz, D. R., Thorne, K. G., and McFarlane, C. (2016). Geochemical characteristics of biotite from intrusive felsic rocks around the Sisson Brook W-Mo-Cu deposit, west-central New Brunswick: an indicator of halogen and oxygen fugacity of magmatic systems. *Ore Geol. Rev.* 77, 82–96. doi: 10.1016/j.oregeorev.2016.02.004

Conflict of Interest: The authors declare that the research was conducted in the absence of any commercial or financial relationships that could be construed as a potential conflict of interest.

frontiers in Earth Science

ORIGINAL RESEARCH
published: 07 August 2020
doi: 10.3389/feart.2020.00242

Early Jurassic Rare Metal Granitic Pluton of the Central Asian Orogenic Belt in North-Central Mongolia: Tungsten Mineralization, Geochronology, Petrogenesis and Tectonic Implications

Jaroslav Dostal[1], Martin Svojtka[2], Ochir Gerel[3] and Randolph Corney[1]*

[1] Department of Geology, Saint Mary's University, Halifax, NS, Canada, [2] Institute of Geology, Czech Academy of Sciences, Prague, Czechia, [3] Mongolian University of Science and Technology, Ulaanbaatar, Mongolia

The Tukhum granitic pluton is a part of the Mesozoic composite Khentei batholith of north-central Mongolia, which belongs to the Central Asian Orogenic Belt. The shallow-seated pluton (~900 km^2) is made up of two distinct biotite granite intrusions dated at ~191 and 183 Ma and hosts a tungsten deposit associated with the younger phase. Both intrusions are composed of ferroan A2-type granites, which are fractionated and silica-rich (>71 wt.%). Their mantle-normalized plots are relatively enriched in Cs, Rb, U, and Th and depleted in Ba, Sr, Eu, Nb, and Ti. They have $\varepsilon_{Nd}(t)$ ranging from ~0 to +1 and Nd model ages ~650–900 Ma. The granites were derived by partial melting of a Neoproterozoic middle/lower crustal source of felsic/intermediate composition, followed by fractional crystallization. The younger intrusion also contains leucogranites with a trace element composition indicative of a combined crystal and fluid fractionation. The source of this younger intrusion was enriched in rare metals (W, Sn). The tungsten deposit is associated with the last stages of the evolution of the granitic magma. The origin of the pluton as well as the Khentei batholith is related to a mantle plume, which provided the heat triggering a crustal melting. The plume resulted in the eastward movement of large-scale magmatism over time, from the Tarim traps (300–275 Ma) through the large Khangai magmatic center (270–240 Ma) to the Khentei batholith (230–180 Ma) in north-central Mongolia.

Keywords: Rare metal granite, tungsten deposit, Central Asian Orogenic Belt, U-Pb zircon dating, petrogenesis, mantle plume, Mongolia, Mesozoic

OPEN ACCESS

Edited by:
J. Gregory Shellnutt, National Taiwan Normal University, Taiwan

Reviewed by:
Ali Polat, University of Windsor, Canada
Changqian Ma, China University of Geosciences (Wuhan), China

****Correspondence:***
Jaroslav Dostal
jarda.dostal@smu.ca

Specialty section:
This article was submitted to Petrology, a section of the journal Frontiers in Earth Science

Received: *13 February 2020*
Accepted: *03 June 2020*
Published: *07 August 2020*

Citation:
Dostal J, Svojtka M, Gerel O and Corney R (2020) Early Jurassic Rare Metal Granitic Pluton of the Central Asian Orogenic Belt in North-Central Mongolia: Tungsten Mineralization, Geochronology, Petrogenesis and Tectonic Implications. Front. Earth Sci. 8:242. doi: 10.3389/feart.2020.00242

INTRODUCTION

Many tin-tungsten mineralization and deposits are spatially, temporally, and genetically associated with highly differentiated granitic intrusions worldwide (e.g., Sillitoe et al., 1975; Dostal and Chatterjee, 1995; Förster et al., 1999; Baker et al., 2005; Černý et al., 2005; Romer and Kroner, 2016; Korges et al., 2017). One of the regions with such an economically important association is north-central Mongolia where mineralized granitic bodies (e.g., Yarmolyuk and Kuzmin, 2012; Syritso et al., 2018) are a part of the huge Central Asian Orogenic Belt (CAOB), which is characterized

by voluminous juvenile crust unlike most Phanerozoic orogenic belts including Caledonides and Hercynides (e.g., Jahn et al., 2000). This study focuses on the granites associated with a *W* deposit in north-central Mongolia, where the genetic relationship of the mineralization with the granites is not clear. An investigation of the petrology, geochronology, and geochemical characteristics of the granitic pluton can constrain the petrogenesis of the granitic rocks as well as the origin of the mineralization. It can also be useful for mineral exploration, particularly if it can help to distinguish between fertile and barren granites. This is an important issue as granitic intrusions of the CAOB provide large exploration targets for W-Sn mineralization. A better understanding of the geochemical characteristics and petrogenesis of the mineralized intrusions is a significant step toward developing a strategy for mineral exploration in this region. In this paper, we present whole-rock major and trace element and Nd isotopic data as well as the U-Pb zircon ages for the granitic rocks from the Tukhum pluton (TP; north-central Mongolia) and discuss their origin and tectonic settings. In addition, the paper contributes to the current discussion on the role of a mantle plume under this part of the CAOB (e.g., Donskaya et al., 2013; Yarmolyuk et al., 2013). The composite intrusion, situated about 100 km NW of Ulaanbaatar, hosts a tungsten deposit.

GEOLOGICAL SETTING

The CAOB, a large accretionary orogen bounded by the Siberian craton to the west and north and the North China and Tarim cratons to the south, stretches from the Ural Mountains to the Pacific Ocean (**Figure 1**). It consists of numerous orogenic belts (e.g., Sengör et al., 1993; Jahn et al., 2000), some of which are characterized by widespread granitoid magmatism ranging in age from the Late Precambrian to the Mesozoic. In northern Mongolia and southern Siberia, along the southern border of the Siberian craton, the CAOB contains voluminous Late Paleozoic to Mesozoic granitoid rocks including large batholiths (such as Khangai and Khentei) surrounded by Permian–Early Cretaceous rift zones (**Figure 1**). In north-central Mongolia, the CAOB features the Daurian-Khentei megadome or uplift, a northeast-trending bulge about 600 km long and 200 to 220 km wide that has been uplifting from the early Mesozoic to the Recent. The megadome contains mainly Paleozoic turbidites intruded by the Khentei batholith, the largest Late Triassic–Early Jurassic intrusion in north-central Mongolia. The batholith is composed of numerous Mesozoic plutons, which were emplaced between 230 and 180 Ma (Yarmolyuk et al., 2013; this paper). The individual plutons vary in composition from granodiorite to leucogranite with minor amounts of gabbro and diorite as well as small bodies of Li-F-rich granite occurring along the margins of the batholith. Some of the Li-F-rich granites host the W-Sn mineralization. The intrusions of the megadome show a concentrically zoned arrangement (**Figure 2**) where the Khentei batholith is in the center of the bulge and is surrounded by three rift zones: Western Transbaikalian, Kharkhorin (Karakorum), and North Gobi. The rift zones consist of horsts, grabens, and depressions containing Upper Permian to Upper Triassic clastic sedimentary rocks and bimodal volcanic suites (Yarmolyuk et al., 2002) and Mesozoic granitic plutons (e.g., Dostal et al., 2014, 2015b; Antipin et al., 2016). The age of the plutons of the rift zones range typically between 221 and 186 Ma (Yarmolyuk et al., 2002; Dostal et al., 2014).

The rift zones and adjoining marginal parts of the Khentei batholith host mineralized granites. One of such plutons in north-central Mongolia is the TP which hosts a tungsten deposit (Tsagaan Davaa). Unlike some weakly mineralized granitic bodies such as Janchivlan and Avdar (Antipin et al., 2016), which occur in the rift zones along the margins of the Khentei batholith, Early Jurassic TP is located within the batholith but along its margins (**Figure 2**). It is one of the shallow-seated granitic intrusions, which are discordant and are surrounded by contact-metamorphic aureoles. The TP intruded into slightly metamorphosed Cambrian to Ordovician sedimentary rocks (mainly sandstones). The contact metamorphic aureole around the TP is up to 1.5 to 2 km wide. Close to the pluton, the aureole contains quartz-biotite-feldspar hornfels. The pluton is elongated and exposed over an area of ∼900 km^2. The internal structure of the TP suggests a dome-shaped intrusion. Our research focused on the southeastern part of the pluton (**Figure 3**), which hosts a tungsten deposit.

An unusual structure of the Daurian-Khentei megadome is not unique in the area. A large magmatic complex with a zonal concentric structure similar to that of the Khentei batholith occurs southwest of the study area (**Figure 1**). This Permian–Early Triassic body of comparable size consists of a granitoid core surrounded by rift zones (Yarmolyuk et al., 2008, 2013; Yarmolyuk and Kuzmin, 2011, 2012). The core of the structure, the Khangai batholith (>120,000 km^2), is composed mainly of granites and granodiorites emplaced between 270 and 240 Ma (Yarmolyuk et al., 2013). It lies between the Gobi-Altai and Northern Mongolian rift zones, which are similar to those around the Khentei batholith.

PETROGRAPHY

The pluton is composed mainly of fine- to coarse-grained biotite granites (**Figure 4**) and is composed of two intrusive phases (**Figure 3**). The first phase (including dated sample WOL-12) is made up of gray and yellowish gray fine- to medium-grained porphyritic granite with feldspar phenocrysts typically 1–3 cm in size that are enclosed in a groundmass composed of K-feldspar, plagioclase, quartz, and subordinate biotite (up to ∼10%). Amphibole, Fe-Ti oxides, secondary minerals (including carbonates), and accessory minerals occur in trace amounts. Phenocrysts, which are microcline-perthite and subordinate plagioclase, account for about 25% of the volume of the rocks. This intrusive phase contains numerous xenoliths of country rocks, particularly metasedimentary rocks. The second intrusive phase (encompassing dated samples WOL-14 and WOL-15) includes dominant porphyritic coarse-grained biotite granite and subordinate leucogranite. Porphyritic biotite granite contains feldspar phenocrysts, which are also mainly microcline-perthite

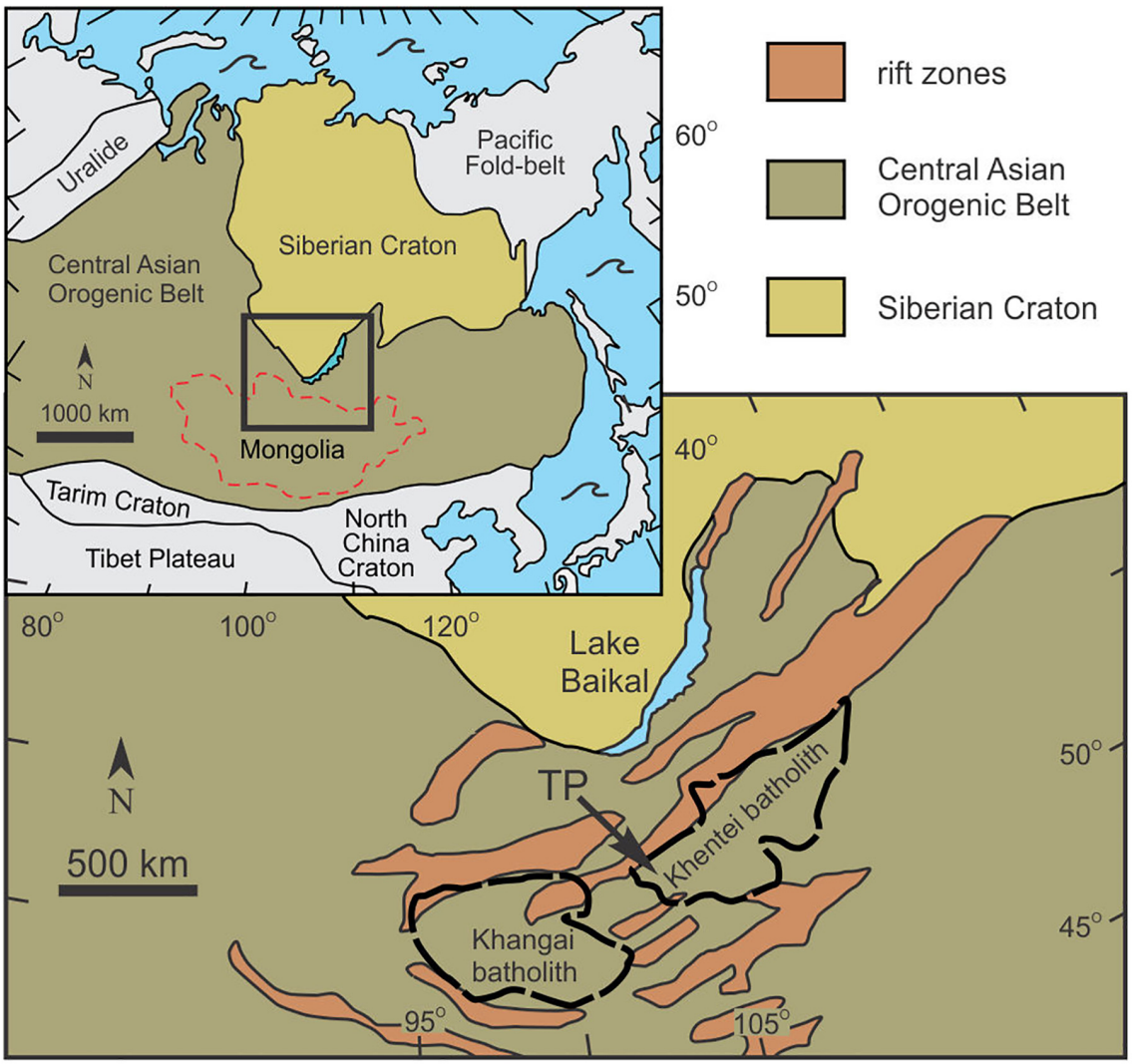

FIGURE 1 | Simplified geologic map of parts of the Central Asian Orogenic Belt and Siberian Craton showing the occurrence of two Late Paleozoic–Early Mesozoic batholiths and rift zones (modified after Yarmolyuk and Kuzmin, 2011) and the Tukham pluton (TP). Inset is a sketch map of the Central Asian Orogenic Belt, Siberian Craton, and surrounding geological provinces (modified after Jahn et al., 2009) showing the location of **Figure 1**.

and subordinate plagioclase. The groundmass is made up of plagioclase, microcline, quartz, and minor biotite and accessory minerals (titanite, zircon, Fe-Ti oxides, and pyrite). The rocks also contain minor but variable amounts of secondary minerals (chlorite, sericite, and carbonate). Compared to the rocks of the first phase, these granites have notably larger grain size. The leucogranite is composed of plagioclase (albite, albite-oligoclase), K-feldspar, quartz, secondary, and accessory minerals. These rocks mostly form bands ranging in width from a few meters to ∼100 m, which pass gradationally into the biotite granite. Some leucogranites contain dominantly primary magmatic mineral assemblages while other leucogranites, namely, those that are close to the mineralization, were affected by silicification and other alteration processes such as greisenization (quartz, dark mica, and minor fluorite). We have subdivided the altered leucogranites into moderately altered and strongly altered. Moderately altered leucogranites typically contain secondary quartz and smaller amounts of Li-bearing mica, fluorite and topaz, while the strongly altered rocks are composed mainly of a secondary mineral assemblage. It is possible that precursors of some of these strongly altered rocks were biotite granites. Porphyritic biotite granite of the second phase and leucogranite are assumed to be approximately coeval (also, e.g., Ivanova, 1976; Khasin, 1977).

TUNGSTEN MINERALIZATION

The Tsagaan Davaa tungsten deposit (Ivanova, 1976; Khasin, 1977; Jargalsaikhan, 1996) consists of wolframite-bearing quartz veins and associated greisen, which occur in the upper (apical) part (probably cupola) of the pluton. They are hosted in

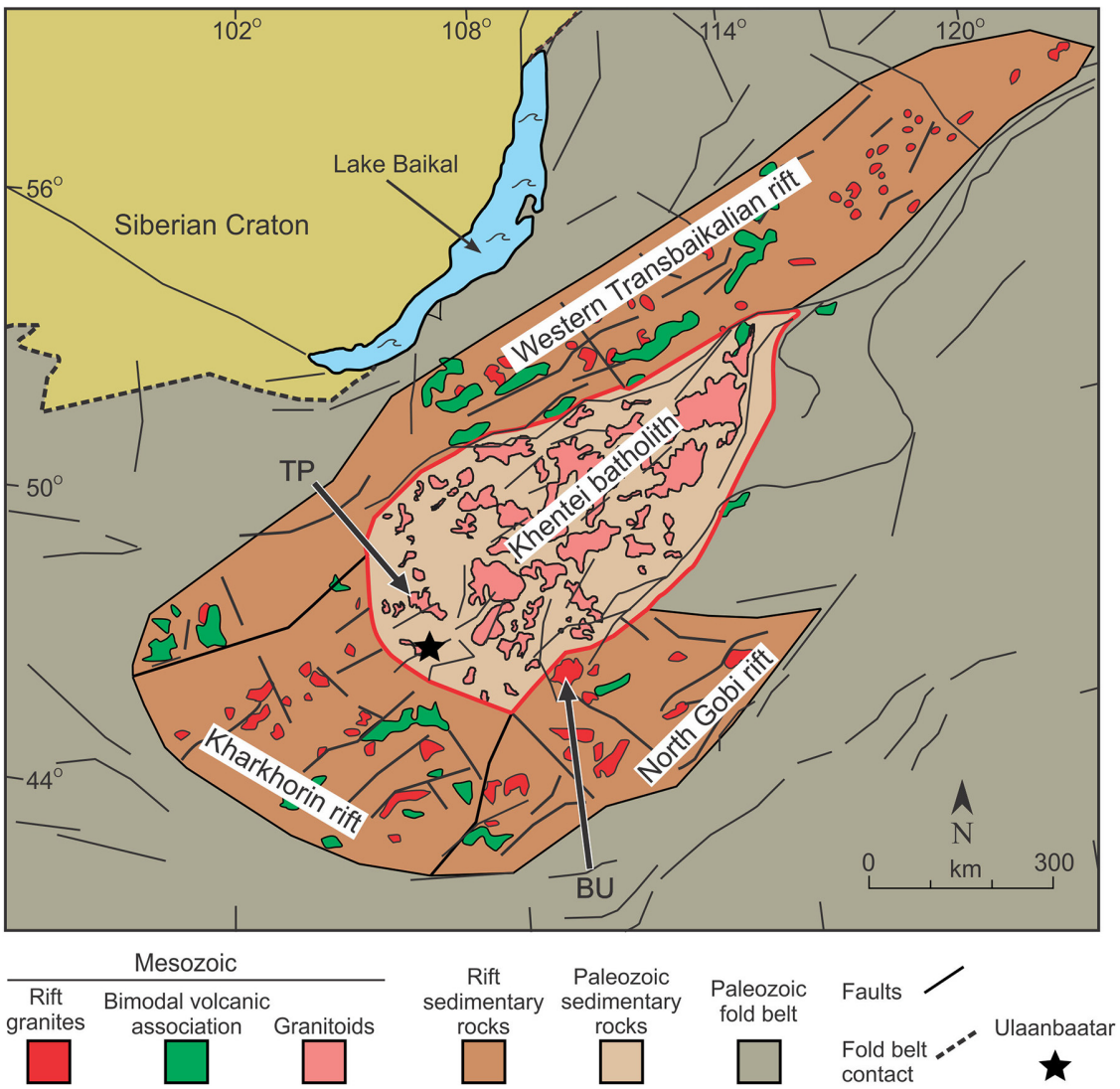

FIGURE 2 | Geologic map of the Daurian-Khentei megadome or uplift composed of the Early Mesozoic Khentei batholith, North Gobi, Kharkorin, and Western Transbaikalian rifts (modified after Yarmolyuk and Kuzmin, 2011, 2012). TP—Tukham pluton; BU—Bayan-Ulan pluton.

leucogranites, which are altered around the mineralization. Hydrothermal alteration and mineralization appear to be controlled by faults. The main mineralized zone is >1 km long and 200–500 m wide. The individual mineralized quartz veins range in thickness from <1 cm to >1 m but on an average they are ∼0.5 m thick and can be traced for tens of meters. The tungsten-bearing veins are mostly sub-horizontal bodies, gently dipping, which are parallel with the roof of the pluton and are typically accompanied by greisen and silica alteration. Greisen is the common hydrothermal alteration type associated with mineralization and is characterized by Li-F-bearing micas, fluorite, wolframite, cassiterite, and dominant quartz. The main ore mineral in the deposit is wolframite accompanied by subordinate cassiterite and molybdenite and minor scheelite, malachite, azurite, and beryl. Some veins consist almost entirely of quartz and wolframite. The deposit contained ∼3100 t of WO_3 in ore grading 1.52% WO_3 and 740 t of WO_3 in ore grading 0.72% WO_3. The grade ranges from 0.1 to 12.6% WO_3. The mine went into production in 1978.

ANALYTICAL METHODS

Whole-Rock Analyses

The analyses of whole-rock major and trace elements of the TP samples (**Table 1**) were done using lithium metaborate–tetraborate fusion at the Activation Laboratories Ltd. in Ancaster, ON, Canada. Major elements were analyzed by an inductively coupled plasma-optical emission spectrometer, whereas trace elements were determined by an inductively coupled plasma mass spectrometer (ICP-MS; Perkin Elmer Optima 3000). The accuracy for each element was monitored by analyzing

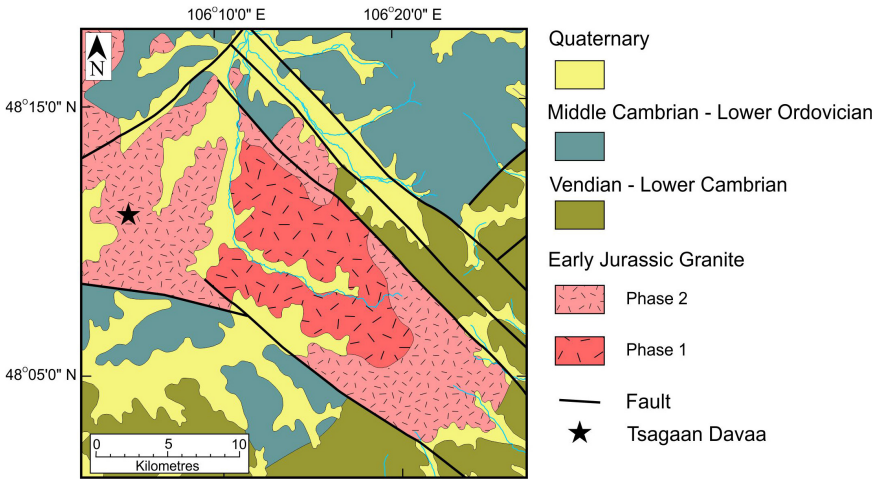

FIGURE 3 | Geological map of the southeastern part of the Tukhum pluton and surrounding units (modified after Dejidmaa, 2003; Dorjsuren and Bujinlkham, 2004) showing the location of the Tsagaan Davaa tungsten deposit.

FIGURE 4 | Photo showing a typical outcrop of the biotite granite of the Tukhum pluton (photo courtesy of Yo. Majigsuren).

international standards, which were run as unknown. Based on replicate analyses, the precision is generally better than 3% for most major elements and between 5 and 10% for trace elements. Major and some trace elements in the Bayan-Ulan samples (**Supplementary Table S2**) were determined by X-ray fluorescence at the Regional Geochemical Center at Saint Mary's University. Analytical precision as determined on replicate analyses is generally better than 5% for the major oxides and between 5% and 10% for minor and trace elements. Iron was determined as total Fe (**Table 1 Supplementary Table S2**).

Sm and Nd concentrations and Nd-isotope ratios of the granitic rocks (**Table 2**) were determined at the Atlantic Universities Regional Facility at the Department of Earth Sciences of Memorial University of Newfoundland (St. John's, Newfoundland, Canada) using a multi-collector Finnigan MAT 262 thermalionization mass spectrometer (Pollock et al., 2015). Replicate analyses of JNdi-1 yield a mean $^{143}Nd/^{144}Nd = 0.512100 \pm 6$. The 2σ values are given in **Table 2**. $\varepsilon_{Nd}(t)$ values were calculated with respect to CHUR using a present-day $^{143}Nd/^{144}Nd$ ratio of 0.512638 and a $^{147}Sm/^{144}Nd$ ratio of 0.196593, and were subsequently age-corrected. A T_{DM} model age (**Table 2**) was calculated according to the model of DePaolo (1988).

Zircon U-Pb Dating

Whole-rock samples, ca 1–2 kg in weight, were collected for mineral separation. Zircons were separated using conventional techniques: crushing, Wilfley concentration table, magnetic, and, finally, heavy liquid separations. Handpicked zircon grains were mounted in 1-inch epoxy-filled blocks, ground, and polished. Internal zircon structures were checked by cathodoluminescence (CL) imaging using scanning electron microscope at Charles University in Prague (Czech Republic). An Element 2 high-resolution sector field mass spectrometer (Thermo Scientific, Waltham, MA, United States) coupled with a 193-nm ArF Analyte Excite (Teledyne/Cetac) excimer laser ablation system at the Institute of Geology of the Czech Academy of Sciences in Prague was used to acquire the Pb/U isotopic ratios in zircons. The laser is equipped with a HelEx II active 2-volume ablation cell. The laser was fired at a repetition rate of 5 Hz, using a spot size of 25 μm. Acquisitions for standards and unknown samples consisted of a 15-s measurement of a blank followed by U and Pb signals from zircons for another 35 s. The signal was tuned for maximum sensitivity of Pb and U, Th/U ratios close to unity, and a low oxide level, commonly below 0.2%. The total of 420 mass scans data were acquired in time-resolved–peak jumping–pulse counting/analog mode with 1 point measured per peak for masses $^{204}Pb + Hg$, ^{206}Pb, ^{207}Pb, ^{208}Pb, ^{232}Th, ^{235}U, and ^{238}U. Due to a non-linear transition between the counting and analog acquisition modes of the ICP instrument and the fact that ^{238}U is usually measured in "both" mode, the raw data were preprocessed using a Python module called ExctractDat for decoding the Thermo Element ICP-MS data files (Hartman et al., 2017) and also an in-house Excel macro. As a result, the

TABLE 1 | Major and trace element compositions of granites from the Tukhum pluton.

	Phase 1			Phase 2									
Rock Type	**Granite**		**Aplite**	**Granite**				**Leucogranite**		**Altered leucogranite**		**Strongly altered granite**	
Sample	**WOL-12**	**WOL-12-1**	**WOL-13-1**	**WOL-14**	**WOL-14-1**	**WOL-15**	**WOL-15-1**	**WOL-6**	**WOL-10**	**WOL-4**	**WOL-5**	**WOL-7**	**WOL-8**
SiO_2 (wt.%)	71.99	72.86	75.07	71.86	72.96	74.36	73.71	75.27	74.79	76.86	77.08	82.47	65.85
TiO_2	0.32	0.31	0.17	0.25	0.28	0.24	0.21	0.15	0.16	0.05	0.04	0.17	0.18
Al_2O_3	13.49	13.39	12.33	13.38	13.43	12.41	13.13	12.67	12.38	12.37	12.51	7.75	18.56
$Fe_2O_3^{(t)}$	2.40	2.34	2.01	2.35	2.12	2.05	2.08	1.64	1.67	1.14	0.76	2.95	4.02
MnO	0.04	0.04	0.02	0.05	0.05	0.04	0.04	0.04	0.04	0.02	0.03	0.14	0.20
MgO	0.29	0.29	0.14	0.31	0.32	0.28	0.25	0.13	0.15	0.15	0.05	0.16	0.26
CaO	1.22	1.25	0.32	1.08	1.12	0.93	0.91	0.73	0.57	0.50	0.37	0.79	0.41
Na_2O	4.13	4.16	2.64	3.62	3.62	3.26	3.53	3.76	2.92	3.73	3.86	0.13	0.22
K_2O	4.24	4.26	6.39	4.91	4.84	4.76	5.19	4.57	5.43	4.88	4.65	2.79	6.52
P_2O_5	0.09	0.09	0.01	0.07	0.08	0.07	0.05	0.03	0.03	0.01	0.01	0.03	0.03
LOI	0.33	0.33	0.46	0.66	0.59	0.69	0.68	0.47	0.89	0.88	0.51	1.60	3.10
Σ	98.54	99.32	99.57	98.54	99.40	99.09	99.77	99.45	99.04	100.59	99.87	98.98	99.34
Sc (ppm)	2	2	1	3	3	3	3	2	2	2	2	3	7
V	10	12	8	16	21	12	12	9	6	6	2	14	20
Cu	5	5	5	5	5	10	5	150	260	460	390	590	770
Pb	27	28	37	32	33	34	34	31	32	24	39	6	13
Zn	60	60	40	50	50	50	40	140	380	710	100	590	720
Sn	2	2	3	9	9	8	6	4	27	13	4	331	374
W	0.1	0.1	0.7	3.8	2.9	2.3	2.3	2.7	9.6	3.8	3.5	12.8	53.5
Rb	155	149	181	289	293	286	293	267	471	402	303	904	1100
Cs	7.4	7.3	3.3	16.4	17.3	8.9	8.1	8.3	19.4	12.3	10.8	29.5	51.8
Ba	509	509	203	378	371	313	345	245	260	124	83	158	312
Sr	141	134	55	95	93	78	82	66	60	46	32	8	9
Ga	22	23	22	22	22	21	21	20	23	18	18	53	109
Ta	1.25	1.29	1.53	3.72	3.97	3.51	2.95	1.57	1.66	3.02	2.02	1.15	1.75
Nb	13.2	13.6	16.3	21.3	23.2	22.7	19.2	17.6	12.2	11.3	7.6	7.3	15.3
Hf	9.0	8.1	4.2	6.0	6.2	6.8	5.9	5.1	5.7	3.1	2.7	6.3	4.7
Zr	345	305	113	199	203	223	190	170	184	75	64	208	124
Y	23	24	28	51	53	38	35	53	57	59	30	68	72
Th	12.7	14.6	30.2	31.6	33.1	33.9	29.2	33.6	29.7	23.4	18.4	21.5	26.3
U	2.08	2.05	2.24	5.25	6.17	3.72	3.53	5.33	5.80	7.65	7.79	6.04	15.6
La	45.8	54.7	53.0	45.7	47.5	48.7	44.2	41.6	38.2	13.4	10.5	38.9	34.3
Ce	86.6	108	120	96.6	105	82.7	71.8	91.3	88.1	30.1	24.0	88.2	75.9
Pr	9.2	11.5	12.9	11.3	11.9	11.5	10.5	10.3	10.3	3.71	2.72	10.5	9.09
Nd	32.1	39.0	45.5	40.2	42.4	40.6	37.0	36.7	40.8	14.2	9.88	37.9	34.3
Sm	5.64	6.32	8.38	9.12	9.44	8.32	7.58	8.23	8.99	4.23	2.73	8.37	10.2
Eu	1.30	1.28	0.61	0.85	0.87	0.68	0.70	0.64	0.63	0.32	0.21	0.57	0.73
Gd	4.58	4.99	6.47	8.26	9.06	6.75	6.31	7.93	8.50	5.63	2.98	7.85	10.7
Tb	0.65	0.71	0.89	1.39	1.50	1.06	0.99	1.33	1.41	1.18	0.60	1.43	1.97
Dy	3.68	4.09	4.77	8.44	8.77	6.24	5.65	8.31	8.94	8.26	4.19	9.44	11.8
Ho	0.75	0.78	0.94	1.64	1.75	1.22	1.09	1.71	1.81	1.83	0.86	1.95	2.29
Er	2.14	2.24	2.75	4.93	5.28	3.58	3.24	5.20	5.60	5.85	2.84	6.18	6.78
Tm	0.31	0.33	0.41	0.73	0.79	0.52	0.51	0.79	0.85	0.97	0.48	0.95	1.02
Yb	2.17	2.20	2.73	4.98	5.21	3.52	3.37	4.88	5.73	6.89	3.33	6.54	6.80
Lu	0.35	0.36	0.43	0.75	0.78	0.54	0.52	0.73	0.87	1.07	0.53	0.97	1.02
Be	5	5	3	8	8	7	7	5	6	6	8	5	11
M	1.47	1.49	1.34	1.44	1.43	1.38	1.43	1.38	1.32	1.38	1.33		
T_{Zr} (°C)	813	797	711	757	761	776	753	748	763	670	661		

T_{Zr} (°C)—zircon saturation temperature estimate in °C calculated according to Boehnke et al. (2013); M = (Na + K + 2Ca)/(Al × Si).

TABLE 2 | Nd isotopic composition of granitic rocks of the TSP and BU intrusions.

Sample	Age (Ma)	Phase	Nd (ppm)	Sm (ppm)	$^{147}Sm/^{144}Nd$	$^{143}Nd/^{144}Nd_{(m)}$	2σ	$^{143}Nd/^{144}Nd_{(i)}$	$\varepsilon_{Nd(t)}$	T_{DM} (Ma)
WOL-12	191	1	32.94	5.43	0.0998	0.512560	6	0.512435	0.84	659
WOL-12–1	191	1	39.11	6.68	0.1033	0.512548	6	0.512419	0.52	695
WOL-14	183	2	40.25	8.75	0.1314	0.512558	7	0.512401	−0.04	905
WOL-15	183	2	41.37	8.42	0.1231	0.512568	8	0.512421	0.35	809
BU-1	221		26.3	6.75	0.1552	0.512648	6	0.512424	1.37	1032
BU-5	221		42.6	9.82	0.1394	0.512631	6	0.512429	1.48	849
BU-9	221		23.2	5.27	0.1373	0.512631	8	0.512432	1.54	832
BU-13	221		17.3	4.23	0.1478	0.512642	6	0.512428	1.46	934
BU-16	221		7.2	1.39	0.1167	0.512609	6	0.512440	1.69	695
BU-19	221		28.8	7.24	0.152	0.51265	6	0.512433	1.55	976
BU-25	221		27.2	5.39	0.1198	0.512642	6	0.512468	2.23	667
BU-34	221		44.5	9.01	0.1224	0.512617	6	0.512440	1.69	724

T_{DM}—depleted mantle model age calculated using the model of DePaolo (1988). $\varepsilon_{Nd}(t)$—age-corrected values calculated for the respective crystallization age; $^{143}Nd/^{144}Nd_{(m)}$—measured value; and $^{143}Nd/^{144}Nd_{(i)}$—initial, calculated, age-corrected. TSP: WOL samples; BU: Bayan-Ulan samples—data from Dostal et al. (2015b).

intensities of ^{238}U were left unchanged, if measured in a counting mode, and recalculated from ^{235}U intensities, if the ^{238}U was acquired in analog mode. No common Pb correction was applied to the data due to the high Hg contamination of the commercially available He carrier gas, which precludes accurate correction of the interfering ^{204}Hg on the very small signal of ^{204}Pb (common lead). The Hg impurities in the carrier He gas were reduced by using an in-house made gold-coated sand trap.

Elemental fractionation and instrumental mass bias were corrected by the normalization of an internal natural zircon reference material Plešovice for samples WOL-12 and WOL-14 (337 Ma, Sláma et al., 2008) and 91500 (1065 Ma, Wiedenbeck et al., 1995) for sample WOL-15. Zircon reference materials GJ-1 (609 Ma, Jackson et al., 2004; 603 Ma, Kylander-Clark et al., 2013) were periodically analyzed during the measurement for quality control, and the values for the natural standard correspond well and are less than 1.5% accurate within the published reference values. Raw data reduction and age calculations, including corrections for baseline, instrumental drift, mass bias, and down-hole fractionation, were carried out using the computer program Iolite (v. 3.5; Paton et al., 2011) with the VizualAge utility (Petrus and Kamber, 2012). All presented ages are quoted at 2σ absolute. The discordance limit for the concordant population was taken as 1.5% (**Supplementary Table S1**) and was calculated as follows: $D < 1\text{Ga} = [1 - (((^{206}Pb/^{238}U)/(^{207}Pb/^{235}U))] \times 100$.

GEOCHRONOLOGY

The age of the TP was not well established. The K-Ar whole-rock dating for the granite of the TP yielded a cooling age of 190.5 ± 4.7 Ma, whereas the whole-rock Rb-Sr gave an age range of 225 to 188 Ma (Smirnov et al., 1977). In order to refine the age, we have dated the pluton by a U-Pb zircon laser ablation ICP-MS technique.

The U-Pb isotopic ratios in zircons were measured in three samples (see **Supplementary Table S1** and **Figure 5** for dating results). Sample WOL-12 is biotite granite from the first intrusive phase while samples WOL-14 and WOL-15 are biotite granites from the second intrusive pulse. Most of the zircon grains from WOL-12, WOL-14, and WOL-15 are slightly pale brown or clear and are predominantly prismatic grains, and their fragments or rarely needles have a length of ∼200 to 500 μm. Internal crystal interiors visible in CL imaging revealed that the most of crystals show well-developed magmatic oscillatory (or sector) zoning with only slight alteration with rare featureless unzoned cores (**Figure 6**). All studied samples show uniform Th/U 0.1–0.6 (average value of 0.4; see **Supplementary Table S1**) in both the rims and cores. This Th/U ratio is typical of a magmatic origin (Hoskin and Schaltegger, 2003 and references therein).

U-Pb zircon dating of sample WOL-12 yielded a scatter in concordant ages between c. 185 Ma and 195 Ma that constitute a single concordia age of *c*. 191 ± 2 Ma (2σ; 25 analyses; **Figure 5**). The majority of zircon crystals extracted from samples WOL-14 and WOL-15 yielded a well-defined concordia magmatic age of ∼183 ± 2 Ma (2σ; 25 analyses; **Figure 5**) and 183 ± 2 Ma (2σ; 21 analyses; **Figure 5**), respectively. Inherited ages do not significantly differ from those obtained in zircon domains with magmatic growth zoning (**Figure 6**). Thus, the first phase intruded at ∼191 Ma while the second phase was emplaced at ∼183 Ma.

GEOCHEMISTRY

Sampling and Alteration

The analyzed set of representative samples from TP pluton (**Table 1**) consists of two biotite granites (WOL-12 and WOL-12-1) and an aplite (WOL-13-1) from the first intrusive phase, four biotite granites (WOL-14,WOL-14-1, WOL-15, and WOL-15-1), two leucogranites (WOL-6 and WOL-10), and two moderately altered leucogranites (WOL-4 and WOL-5) of the second intrusive phase and two strongly altered granitic samples (WOL-7 and WOL-8).

The chemical compositions of the biotite granites were not significantly modified by secondary processes. On the other

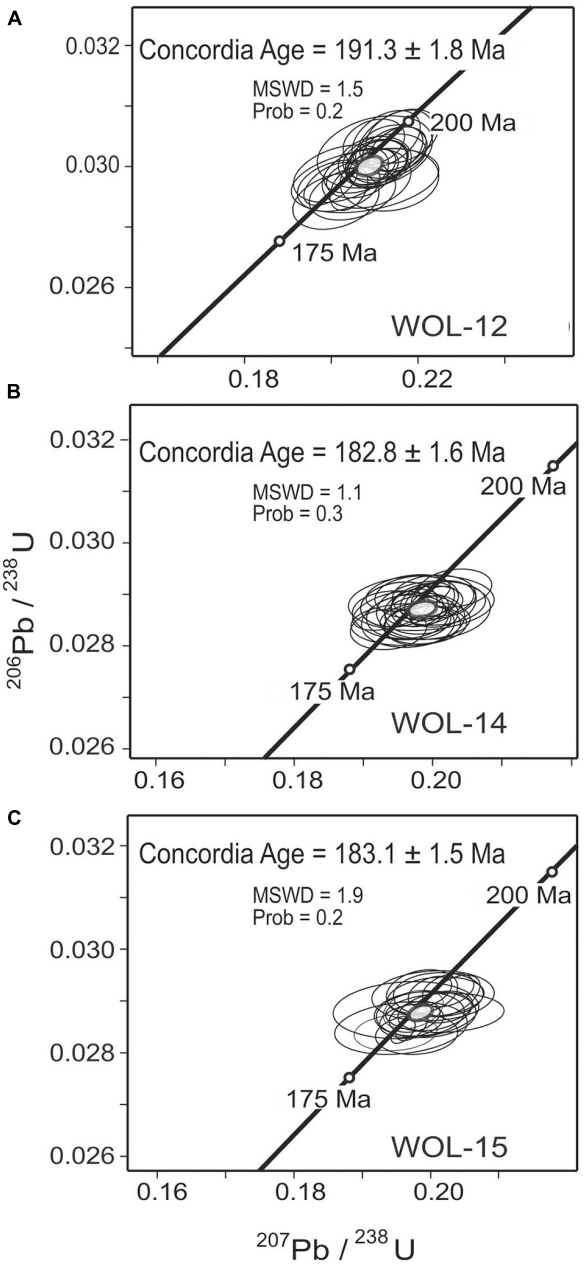

FIGURE 5 | Concordia diagrams with U-Pb isotopic data of studied samples **(A)** WOL-12, **(B)** WOL-14, and **(C)** WOL-15. All ages are quoted with 2σ uncertainties.

hand, there are notable differences among the leucogranites. Leucogranites (WOL-6 and WOL-10) probably retained most of their original composition while the moderately altered leucogranites (WOL-4 and WOL-5) were silicified, leading mainly to an addition of silica. The other two samples (WOL-7 and WOL-8) were strongly hydrothermally altered and accompanied by a notable change of the chemical composition. These two samples were not consequently plotted on some diagrams.

In addition to the TP rocks, 12 samples from the Bayan-Ulan granitic intrusion (see section "Relationship between petrogenesis and mineralization") were also analyzed (**Supplementary Table S2**). These samples do not appear to be noticeably affected by secondary processes (Dostal et al., 2015b).

Major and Trace Elements

The granitic rocks of the TP are highly siliceous and fractionated with silica contents ranging from 71 to 77 wt.% (**Figure 7**). The silica contents of the first intrusion vary between 72 and 75 wt.% in contrast to the second phase with 71 to 77 wt.%. On the normative quartz-alkali feldspar-plagioclase (QAP) graph (**Figure 8A**), they plot into the field of granite. Although there are differences between the two intrusive phases, all the rocks have molar $Al_2O_3/(Na_2O + K_2O) \sim 1–1.2$ and $Al_2O_3/(CaO + Na_2O + K_2O) \sim 1$, indicative of their mildly peraluminous character with the exception of the granites of the first phase, which are mildly metaluminous (**Figure 8B**). The granites also have a high $FeO^*/(FeO^* + MgO)$ ratio (**Figure 7A**) and correspond to ferroan granites of Frost and Frost (2011). According the modified alkali-lime index [MALI = $(Na_2O + K_2O\text{-}CaO)$] of Frost and Frost (2011), the rocks are mostly alkali-calcic (**Figure 7B**); the granites also have high contents of K_2O (**Figure 7C**). The variations of major and several trace elements relative to silica (**Figure 7**), particularly for the second phase, indicate that the granites underwent fractional crystallization. The TP granites, particularly those of the first phase, are comparable to those of numerous other intrusions of the Khentei batholith (Yarmolyuk et al., 2013).

The chondrite-normalized REE patterns of all the studied granites are enriched in light REE (LREE) and have relatively flat unfractionated heavy REE (HREE) and negative Eu anomalies. However, there are subtle differences among the rocks of the two intrusive phases. The patterns of phase 1 (**Figure 9**) have a relatively high $(La/Yb)_n$ ratio (∼14–18) accompanied by $(La/Sm)_n \sim 4$ to 6 and slightly sloping HREE with low $(Gd/Yb)_n$ ratios (∼1.8). They are closely comparable to the average of the granitic rocks of the whole Khentei batholith (**Figure 9**) reported by Yarmolyuk et al. (2013). The second intrusive phase has patterns with $(La/Yb)_n$ ranging from ∼7 to ∼10 and a more pronounced negative Eu anomaly than the first intrusive pulse. The leucogranites of the second pulse have variable REE patterns including a nearly flat one with $(La/Yb)_n \sim 1.2$ and $(Gd/Yb)_n \sim 0.7$. The altered leucogranites have patterns comparable to those of leucogranites. The flat HREE patterns imply that garnet was not in the source of the granites.

The primitive mantle-normalized plots of the TP granites (**Figure 10**) are distinctly enriched in several large ion lithophile elements, namely, Cs, Rb, Th, and U and depleted in Ba, Sr, Eu, Nb, and Ti. The altered leucogranites also have distinct positive anomalies for W and Sn. Relative to the granites of the first phase, the second-phase granites have lower Ba and Sr (**Figure 7**) but higher Rb, Ta, W, and Sn (**Figure 10**). An enrichment of Rb in the second-phase granites is reflected by the relatively low K/Rb ratio (mostly 50–150) compared to typical crustal values of ∼230

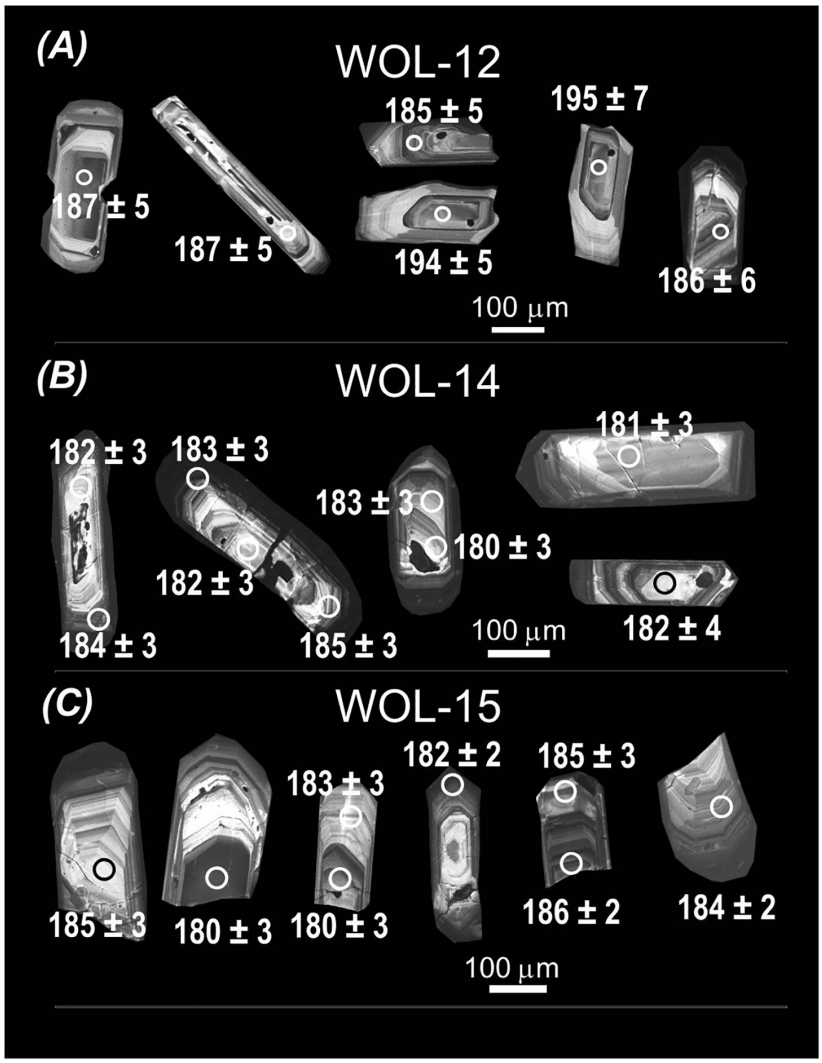

FIGURE 6 | Representative cathodoluminescence images of the dated zircons grains. The spots (25 μm) where laser ablation analysis was performed are indicated together with obtained $^{206}Pb/^{238}U$ ages in Ma (±2σ uncertainties). **(A)** zircons from sample WOL-12; **(B)** zircons from sample WOL-14; **(C)** zircons from sample WOL-15.

(Shaw, 1968; Taylor and McLennan, 1985). These rocks also have anomalous Ba/Rb and Rb/Sr ratios.

The temperatures of zircon saturation (T_{Zr}), estimated from relating the concentration of Zr to the bulk composition of the magma (Watson and Harrison, 1983; Hanchar and Watson, 2003; Boehnke et al., 2013), are variable for the various TP rocks (**Table 1**). The average temperature estimates range from a relatively high value (∼805°C) for the granites of the first phase through the granites of the second phase (∼762°C) and leucogranites (∼755°C) to low values for the moderately altered leucogranites (∼665°C) and aplite (∼710°C).

Nd Isotopes

The Nd isotopic data are given in **Table 2**. The initial isotopic ratios and $\varepsilon_{Nd}(t)$ values are age-corrected to the ages of the emplacement (phase 1 = 191 Ma; phase 2 = 183 Ma). $\varepsilon_{Nd}(t)$ values of the TP granitic rocks are close to chondritic values (0 to +0.8), indicating that they were derived from a reservoir with a long-term history of near-chondritic Sm-Nd values. The values are similar to those of Jahn et al. (2009) for the Early Mesozoic A-type granitoid rocks from this part of the CAOB (0 to +4) and are within the range of the granitoids of the Khentei batholith (+2 to −4; Yarmolyuk et al., 2013). The Nd model ages (T_{DM}) ranging from 650 to 900 Ma suggests a Neoproterozoic source.

DISCUSSION

Petrogenesis

According to the chemical composition, the TP granitic rocks correspond to the A-type granites (**Figure 11A**). Specifically, they resemble the A2 group (*sensu* Eby, 1992),

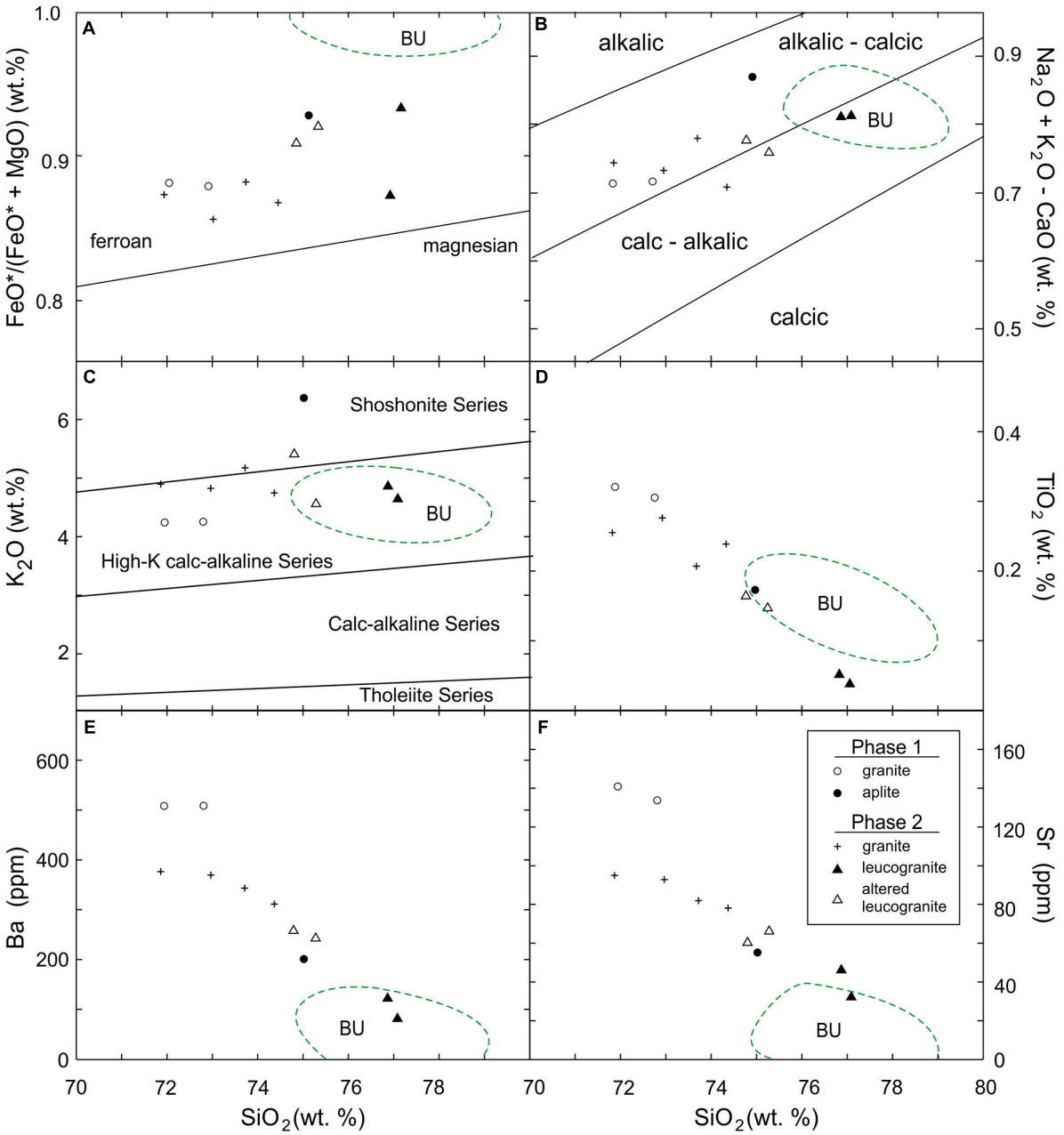

FIGURE 7 | Variations of SiO_2 (wt.%) versus **(A)** FeO*/(FeO*/MgO) showing the separation of ferroan and magnesian suites based on the relative degree of iron enrichment during differentiation (after Frost and Frost, 2011). **(B)** Modified alkali-lime index (MALI = $Na_2O + K_2O$-CaO) with fields defined by Frost and Frost (2011). **(C)** K2O (wt.%) with fields after Peccerillo and Taylor (1976). **(D)** TiO_2 (wt.%), **(E)** Ba, and **(F)** Sr (ppm) in the granitic rocks of the Tukham pluton. Dashed green curves outline the field (BU) for the Bayan-Ulan pluton.

which typically represents magmas derived from lower to middle continental crust, or underplated crust (**Figure 11B**). These characteristics are consistent with their ferroan and alkali-calcic features (Frost and Frost, 2011). Collectively in the TP granites, TiO_2, FeO*, Al_2O_3, MgO, CaO, P_2O_5, Ba, and Sr decrease with increasing SiO_2 (**Figure 7**), indicating crystallization of plagioclase, ferromagnesian minerals (biotite), and accessories (Fe-Ti oxides and apatite). Negative anomalies of Sr, Ba, Eu, Nb, and Ti on the primitive mantle normalized plots also support such a process (**Figure 10**). Covariations of Ba versus Sr (**Figure 12**) indicate that the fractionation of feldspars played a major role during the magma evolution. However, the TP granitic rocks represent two magma pulses derived from distinct sources at different times. While the rocks of the first intrusion closely resemble the average composition of the Khentei batholith,

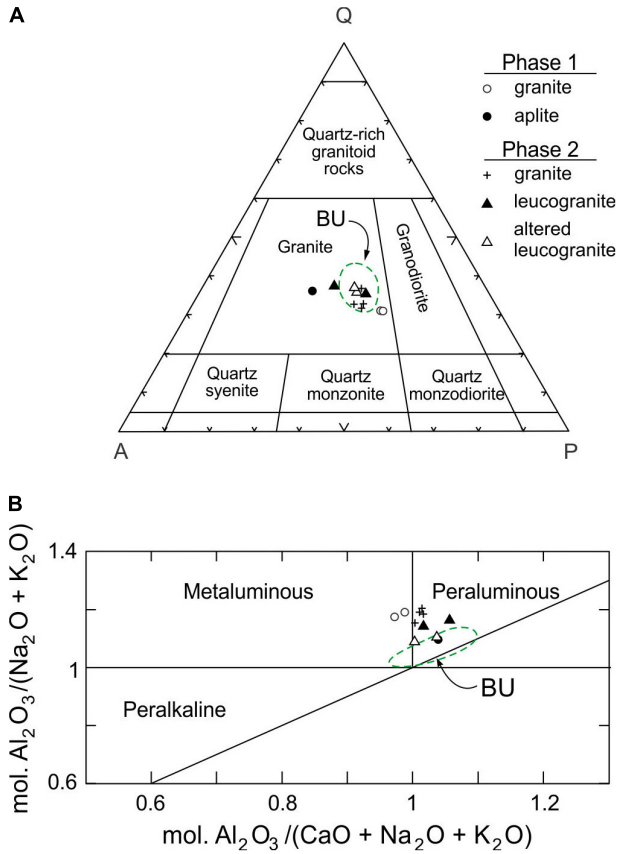

FIGURE 8 | (A) Mesonormative quartz-alkali feldspar-plagioclase (QAP) ternary classification diagram used to characterize the modal composition of the plutonic rocks. It shows the Tukhum granitic rocks whereas the dashed green curve outlines the field (BU) for the Bayan-Ulan pluton. **(B)** $Al_2O_3/(Na_2O + K_2O)$ versus $Al_2O_3/(CaO + Na_2O + K_2O$; in mole%) diagram for TP granitic rocks defining the ranges of peraluminous, metaluminous, and peralkaline plutonic rocks. The dashed green line delineates the field (BU) for the rocks from Bayan-Ulan pluton.

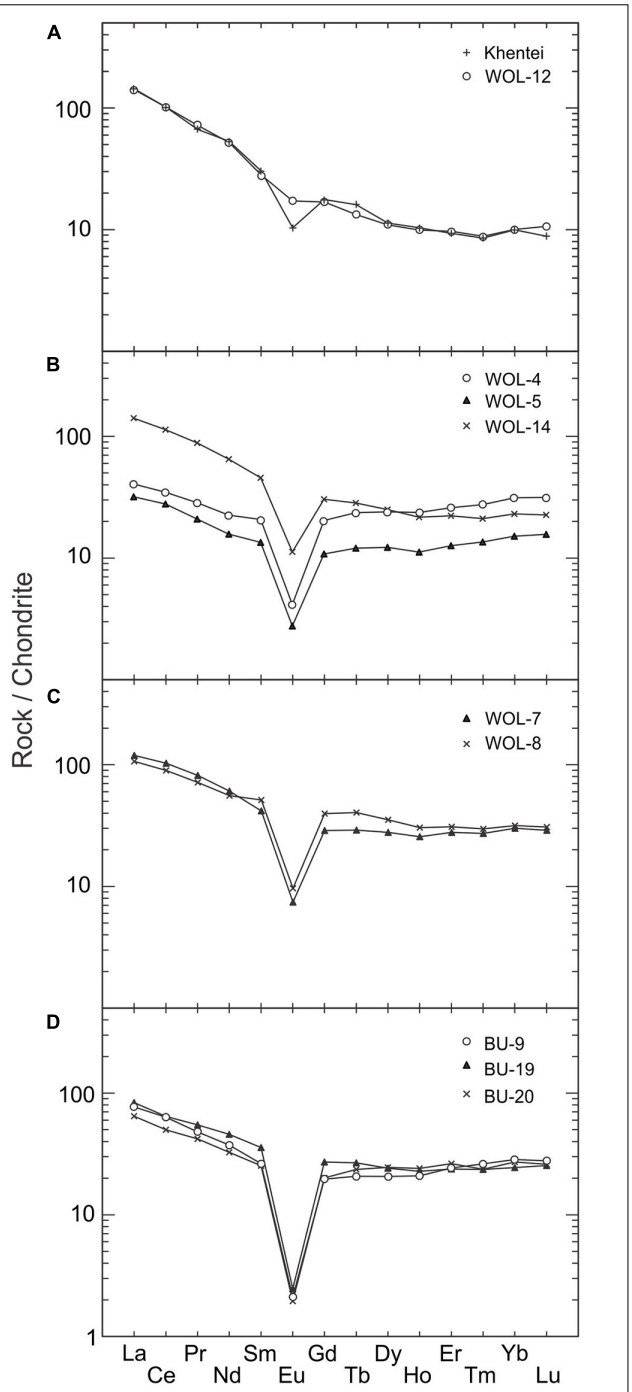

FIGURE 9 | Chondrite-normalized rare-earth element diagrams for **(A)** phase 1 TP granite (WOL-12) and the average of granitic rocks of the Khentei batholith (Yarmolyuk et al., 2013); **(B)** phase 2 TP granites (WOL-14 typical biotite granite; WOL-4 and 5-altered leucogranites); **(C)** TP strongly altered granites; and **(D)** granites of the Bayan-Ulan pluton. Normalizing values are after Sun and McDonough (1989).

the granites of the second phase have different geochemical characteristics (including T_{Zr}) and underwent more extensive fractional crystallization.

The origin of A2-type granitic rocks has been typically attributed to either fractional crystallization or crustal melting (Eby, 1992; Bonin, 2007). These processes can also be invoked for the generation of the TP granitic rocks, which intruded during the last stages of the emplacement of the Khentei batholith and of the plutons of the rift zones surrounding the megadome. More specifically, the petrogenetic processes are (1) extensive fractional crystallization of a mantle-derived mafic or intermediate magma with or without crustal contamination and (2) partial melting of middle or lower crustal source rocks.

Compositional similarities of the granites of the first intrusion to the average of the Khentei batholith and to an estimate of the total crust of East China (**Figures 9**, **10**), peraluminous/metaluminous characteristics of the granitic rocks, and the lack of intermediate rock types (Daly gap) negate an origin by fractional crystallization of mantle-derived mafic or intermediate magma but are consistent with a process where rising mafic magma triggers partial melting of the crustal material

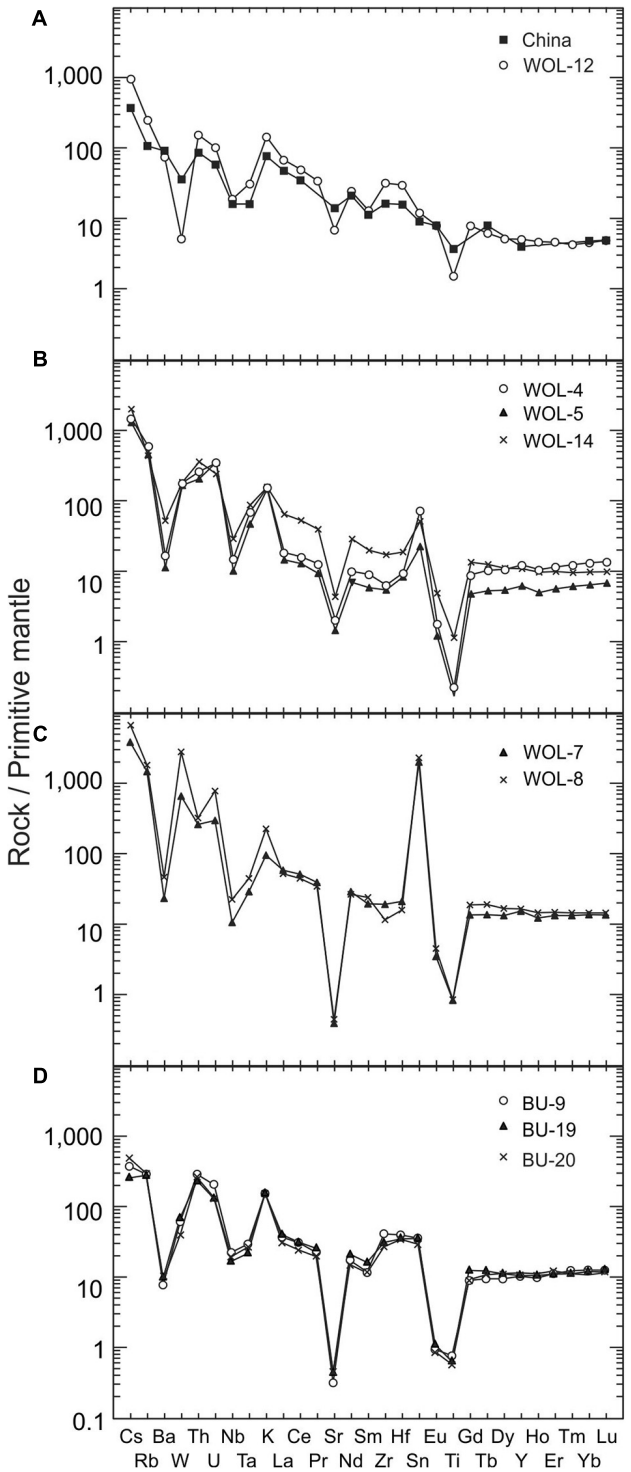

FIGURE 10 | Primitive-mantle normalized incompatible element abundances for the granitic rocks of the Tukham and Bayan-Ulan plutons. **(A)** Phase 1 TP granite (WOL-12) and an estimate of total crust of Eastern China (Gao et al., 1998); **(B)** phase 2 TP granites (WOL-14 typical biotite granite; WOL-4 and WOL-5 altered leucogranites); **(C)** TP strongly altered granites; and **(D)** granites of the Bayan-Ulan pluton. Elements are arranged in the order of decreasing incompatibility from left to right. Normalizing values are after Sun and McDonough (1989).

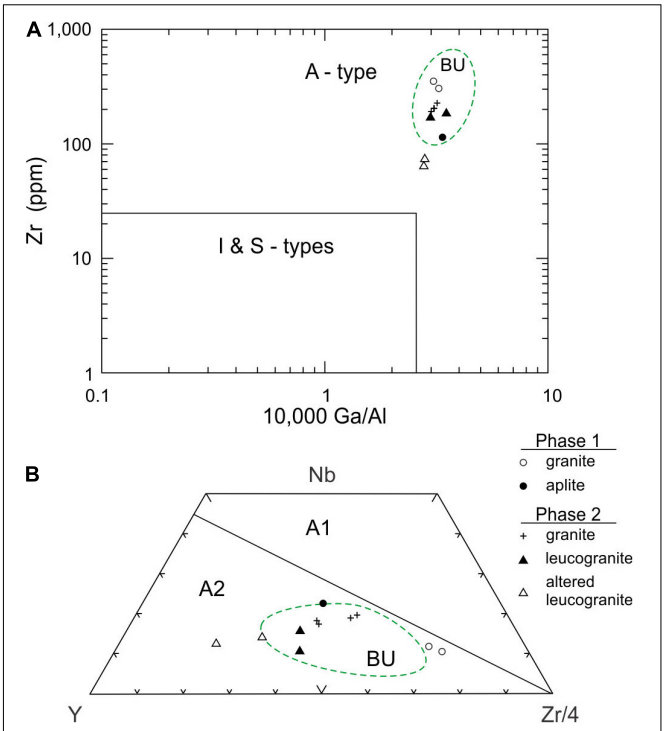

FIGURE 11 | (A) Plot of 10^4 Ga/Al versus Zr (ppm) of Whalen et al. (1987) showing the A-type characteristics of the granitic rocks of the Tukham pluton. I and S field is for I- and S-type granites. **(B)** Y-Nb-Zr/4 diagram of Eby (1992) for the granitic rocks of the Tukham pluton showing the fields of the A1 and A2 granitoids. The dashed green curves show the fields (BU) for the Bayan-Ulan pluton.

from which the granitic magma inherit their geochemical characteristics. This is a common process during lithospheric extension and is a consequence of magmatic underplating and crustal melting (e.g., Huppert and Sparks, 1988). Thus, the TP granites are probably the results of partial melting of the middle/lower crust of granodioritic–tonalitic composition (cf. Frost and Frost, 2011). The Nd model ages (**Table 2**) suggest that the sources were of Neoproterozoic age. The differences in the T_{Zr} between the two intrusive phases reflect, in part, different melting conditions. The low T_{Zr} (<800°C) of felsic magma of the second phase is considered to reflect water-fluxed melting as opposed to the relatively high temperature (>800°C) during anhydrous melting of magma of the first phase (Miller et al., 2003; Collins et al., 2016). The low T_{Zr} for the mineralized leucogranites (~665°C) is probably due to the activities of fluids.

Relationship Between Petrogenesis and Mineralization

The petrogenesis of peraluminous fluorine-rich leucogranites such as those of TP is still under dispute, although these rocks can be associated with Sn-W-U-Ta mineralization (Linnen, 1998; Černý et al., 2005; Linnen and Cuney, 2005). These rocks are enriched in incompatible trace elements such as Rb, Cs, Th, U, W, and Sn and depleted in Ti, Ba, Sr, Nb, and Eu. They also

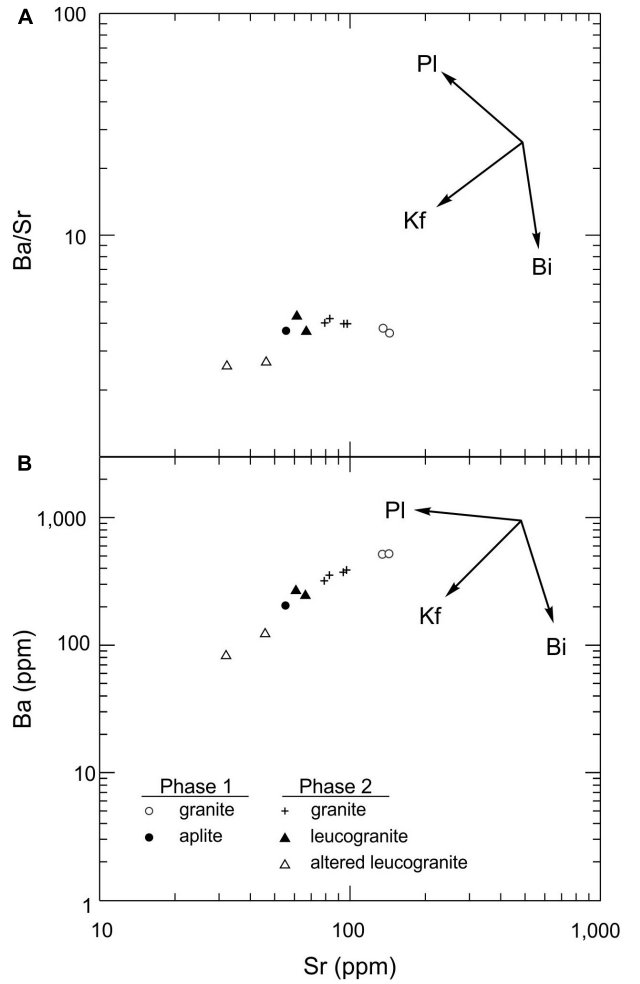

FIGURE 12 | (A) Ba/Sr and **(B)** Ba versus Sr (in ppm) diagrams for the granitic rocks of the Tukham pluton. Vectors depict the fractionation trends of the compositional changes in the residual liquid when the specified phase is progressively removed from the magma during fractional crystallization; Pl—plagioclase; Kf—K-feldspar; and Bi—biotite.

have unusual mineralogical characteristics, such as the presence of topaz and fluorite. These rocks commonly represent the late phase of late-orogenic or anorogenic granite plutons. Two main genetic hypotheses are magmatic and metasomatic, i.e., whether their geochemical characteristics are due to magmatic processes or to post-magmatic fluid–rock interaction. Furthermore, if the characteristics are due to magmatic activities, then the chemical composition could reflect either a distinct source or unusual evolution, involving, e.g., fluorine-rich fluids.

The smooth variation trends for some major and trace elements of the granites and leucogranites of the second intrusion (**Figure 7**) and their similarities to those from non-mineralized plutons indicate that most of the chemical compositions reflect primary magmatic evolution, including extensive fractional crystallization. On the other hand, the enrichment of some elements such as Rb (accompanied by low K/Rb), a kinked shape REE pattern, and the occurrence of topaz and fluorite among others probably reflect fluid fractionation/interaction involving fluorine. This suggests that trace elements in some rocks were modified by late or post-magmatic fluid–rock interaction (Webster et al., 2004; Salvi and Williams-Jones, 2005; Thomas et al., 2005; Dostal et al., 2015a). The petrographic observations (such as the presence of various pseudomorphs and replacement textures; Ivanova, 1976) also indicate that mineral assemblages of the leucogranites are the results of both magmatic processes as well as late- or post-magmatic fluid–melts interactions. The interaction of the leucogranites with fluids led to the enrichment and redistribution of several incompatible trace elements but has not modified their major and some trace element composition. These highly evolved melts commonly moved/escaped into the apical part of the pluton along the fracture zones and are now represented by the leucogranites.

The experimental studies (e.g., Syritso et al., 2018) indicate that the W preferentially partitions into the fluid phase, which commonly escapes from a magma chamber to the host rocks forming wolframite-bearing quartz veins or greisen that are typically structurally controlled. Their frequent association with fractionated granites indicates that they are closely related, although the W mineralization is post-magmatic and related to the hydrothermal solutions. They were probably derived from the same highly fractionated magma chamber. The W mineralization is also associated with greisen. Greisen represents granites, which were altered by fluids released from the magma during the late stages of its evolution. The geochronological study of Syritso et al. (2018) on several similar tungsten deposits from eastern Transbaikalia concluded that tungsten mineralization took place almost synchronously with the crystallization of associated granites. It also appears that in this part of CAOB including TP, the W mineralization is related mainly to Mesozoic plutons, where it was emplaced along the faults in apical parts of intrusions (Syritso et al., 2018).

Comparison With Granites of the Rift Zones

To evaluate the differences between the granitic rocks of the TP, a representative intrusion of the Khentei batholith, and those of the rift zones, the TP rocks are compared with those of the Bayan-Ulan pluton (221 Ma; Dostal et al., 2015b) from the North Gobi rift zone (**Figure 2**). For comparison, which might also reveal a contrast between the ore-bearing and barren granites, we have augmented the Bayan-Ulan whole-rock analyses of Dostal et al. (2015b) with the new data (**Supplementary Table S2**). The Bayan-Ulan pluton (BU), located about 200 km east of Ulaanbaatar, outcrops over an area of ∼1000 km^2. The intrusion (Dostal et al., 2015b) is composed mainly of coarse-grained leucocratic granite containing mesoperthite with interstitial quartz and minor to trace amounts of Fe-rich alkali amphiboles and, rarely, Fe-rich biotite. The granites have relatively uniform chemical compositions; they are highly fractionated alkaline A2-type granites with silica ranging from 75 to 78.5 wt.% (**Figure 7**). Compared to the TP, the BU granites are lower in MgO, CaO, and MnO but have a higher FeO*/(FeO* + MgO) ratio (>0.95). They are predominantly peraluminous (**Figure 8**). Chondrite-normalized REE plots display a slight LREE enrichment with $(La/Yb)_n$ ∼ 2–7 and a

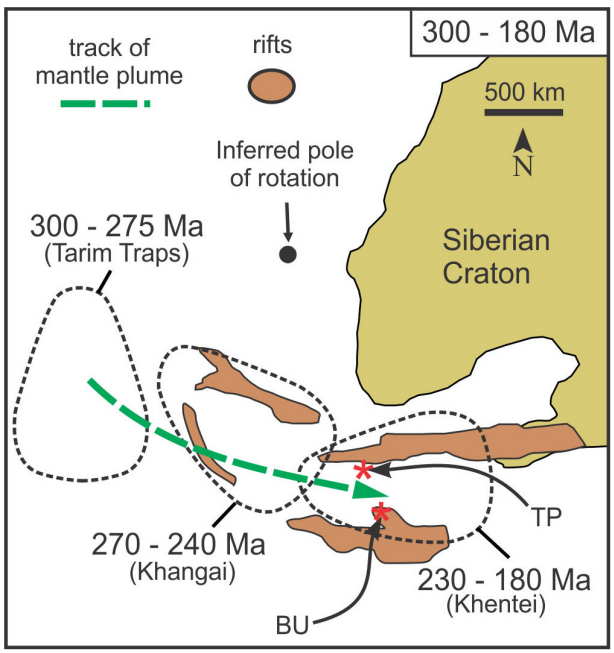

FIGURE 13 | Reconstruction of the movement of the Mongolian mantle plume and the location of the magmatic complexes in northern Mongolia and Transbaikalia (modified after Yarmolyuk and Kuzmin, 2011, 2012; Dostal et al., 2014). Dashed lines show the migration of magmatism and the positions of the Mongolian plume at 300 to 275 Ma, 270 to 240 Ma, and 230 to 180 Ma. The arrow is a tracer of Mongolian plume. TP—Tukhum pluton; BU—Bayan Ulan pluton.

distinct negative Eu anomaly (**Figure 9**). The primitive mantle-normalized patterns (**Figure 10**) are enriched in Th, U, and Rb and relatively more depleted in Ba, Sr, Eu, and Ti. Most BU granites have $\varepsilon_{Nd}(t)$ values of +1.4 to +1.7 and T_{DM} model ages ~650–1050 Ma (**Table 2**). Whereas the BU model ages overlap those of TP rocks, their $\varepsilon_{Nd}(t)$ are higher. The BU rocks were derived from a different source and underwent a different fractionation path. Dostal et al. (2015b) inferred that they were formed by the partial melting of underplated Neoproterozoic mildly alkaline basalts in the lower crust, followed by fractional crystallization. In addition, the fluids and fluid fractionation played a significantly smaller role during the evolution of the BU intrusion compared to the TP. The main Fe-Mg mineral in the BU rocks is alkali amphibole, while in the TP rocks, it is biotite. The BU rocks are not associated with a W or Sn mineralization. A comparison of the three intrusions (two TP pulses and BU) implies that the granites hosting rare metal mineralization required a distinct crustal source enriched in these elements, a high degree of fractionation, and an involvement of fluorine-rich fluids during their evolution.

Tectonic Implications

After the collision of the Siberian and North China cratons, which led to the closure of the Mongol-Okhotsk basin, north-central Mongolia and an adjoining part of southern Siberia (eastern Transbaikalia) witnessed, during the Late Permian to Early Jurassic, an emplacement of large, concentrically zoned magmatic structures. One of these magmatic structures is the Khentei (Daurian-Khentei) megadome (**Figure 2**).

The emplacement of the A2-type granitic plutons of the Khentei batholith and of the surrounding rift zones is related to rifting and partial melting. The origin of the granitic rocks requires a heat source to produce an elevated temperature. Such a heat source is usually attributed to one of the following processes: (1) delamination of the lower lithosphere, (2) thinning of lithosphere during rifting, and (3) rising of a mantle plume. The application of these tectonic models to the region has been under discussion (e.g., Yarmolyuk and Kuzmin, 2011; Donskaya et al., 2013; Li et al., 2013). We favor the mantle plume as the heat source for magmatic activities in the area as it explains well the spatial and temporal variations in Eastern Mongolia and Transbaikalia, particularly the eastward movement of large-scale magmatism over time. Yarmolyuk and Kuzmin (2011) and Dostal et al. (2014) among others noted the eastward migration of the magmatic centers through time from the Tarim traps (300–275 Ma; >250,000 km^2) through the Khangai magmatic center at 270 to 240 Ma to the Khentei (230–183 Ma) in central Mongolia (**Figure 13**). The Tarim traps are Permian continental flood basalts, which form a main part of the Tarim Large Igneous Province located in the Tarin Basin. The migration of the magmatic activities is consistent with the movement of Mongolia over a stationary mantle plume (Mongolian plume of Kuzmin et al., 2010; Yarmolyuk and Kuzmin, 2011) and is supported by paleomagnetic data (Kuzmin et al., 2010).

The plume model can also account for the zonal arrangement of the Khentei magmatic center ranging from granites and granodiorites in the core of the batholith through Li-F-rich granites along the margin of the batholith (either within or just outside of the batholith) and finally to alkaline and peralkaline lavas and alkaline granitoid intrusions in the outer margin of the rifts (Yarmolyuk and Kuzmin, 2011). A larger degree of melting that took place at a shallower depth above the core of the magmatic center generated granites, while a deeper and smaller degree of melting took place at the margins and produced alkaline and peralkaline rocks.

CONCLUSION

The TP, one of the constituent bodies of the Mesozoic Khentei batholith, is made up of two distinct intrusions dated at ~191 and 183 Ma, suggesting that the magmatic activity of the batholith lasted longer than the range of 230 to 195 Ma proposed by Yarmolyuk and Kuzmin (2011). The TP rocks are silica-rich A2-type granites, which are mainly alkali-calcic. On the primitive mantle normalized plots, they are enriched in Rb, Cs, U, and Th and depleted in Ba, Sr, Eu, Nb, and Ti. The TP rocks have $\varepsilon_{Nd}(t)$ ~ 0 to +1 and Nd model ages ~650–900 Ma. The isotopic values are within the range of other Mesozoic granites of the Khentei batholith. The granites were derived by the partial melting of middle/lower crustal Neoproterozoic rocks, followed by fractional crystallization. However, the presence of F-rich minerals in the rocks of the second intrusion as well as W-Sn

mineralization suggests that the source of the parent magma of this intrusion was enriched in several rare metals including W and Sn. The younger second intrusion also contains leucogranites with trace element compositions indicative of combined crystal and fluid fractionation during the late stages of the evolution. The bulk of the tungsten mineralization of the TP is hosted in quartz veins and resulted from an escape of fluids from a magma chamber. The mineralization is associated with the evolution of the granitic magma. An increase of the pressure of the fluids in the magma chamber and their escape caused a brecciation of the rocks and triggered an emplacement of quartz veins hosting the W mineralization.

The partial melting required a heat source. The Late Paleozoic to Early Mesozoic granitic province in north-central Mongolia, which includes two batholiths, Khangai and Khentei, and the eastward migration of the magmatic center through time, is consistent with a mantle plume as a heat source for magmatism. The eastward migration of the magmatic centers over time from the Tarim Large Igneous Province (South Mongolia-Tarim traps) at 300–275 Ma through the Khangai magmatic center with the Khangai batholith at 270–240 Ma to the Khentei area of Eastern Mongolia and Transbaikalia (230–180 Ma) can be explained by the movement over a stationary mantle plume (the Mongolian plume of Yarmolyuk and Kuzmin, 2011).

DATA AVAILABILITY STATEMENT

All datasets generated for this study are included in the article/**Supplementary Material**.

AUTHOR CONTRIBUTIONS

JD developed the idea, wrote the bulk of the manuscript, processed data, and collected samples. MS wrote a part of the manuscript, processed data, and created figures. OG contributed to the ideas and concept and wrote a part of the manuscript. RC collected and prepared samples and created figures. All authors contributed to the article and approved the submitted version.

FUNDING

This study was supported by NSERC Canada Discovery grant to JD and by the institutional support RVO67985831 to MS.

ACKNOWLEDGMENTS

We thank reviewers Ali Polat and Changqian Ma and co-editor Greg Shellnutt for constructive reviews that significantly improved the manuscript. We are also grateful to Yo. Majigsuren for providing assistance during fieldwork and for field photos and to J. Batsukh for help with a map compilation.

SUPPLEMENTARY MATERIAL

The Supplementary Material for this article can be found online at: https://www.frontiersin.org/articles/10.3389/feart.2020.00242/full#supplementary-material

REFERENCES

Antipin, V., Gerel, O., Perepelov, A., Odgerel, D., and Zolboo, T. (2016). Late Paleozoic and Early Mesozoic rare-metal granites in Central Mongolia and Baikal region: review of geochemistry, possible magma sources and related mineralization. *J. Geosci.* 61, 105–125. doi: 10.3190/jgeosci.211

Baker, T., Pollard, P. J., Mustard, R., Markl, G., and Graham, J. L. (2005). A comparison of granite-related tin, tungsten and gold-bismuth deposits: implication for exploration. *SEG Newslett.* 61, 5–17.

Boehnke, P., Watson, E. B., Trail, D., Harrison, T. M., and Schmitt, A. K. (2013). Zircon saturation revisited. *Chem. Geol.* 351, 324–334. doi: 10.1016/j.chemgeo.2013.05.028

Bonin, B. (2007). A-type granites and related rocks: evolution of a concept, problems and prospects. *Lithos* 97, 1–29. doi: 10.1016/j.lithos.2006.12.007

Černý, P., Blevin, P. L., Cuney, M., and London, D. (2005). Granite-related ore deposits. *Econ. Geol.* 350, 337–370.

Collins, W. J., Huang, H. Q., and Jiang, X. (2016). Water-fluxed crustal melting produces Cordilleran batholiths. *Geology* 44, 143–146. doi: 10.1130/g37398.1

Dejidmaa, G. (2003). *State Geological Complete Map*. Ulaanbaatar: Government of Mongolia. Report 5567.

DePaolo, D. J. (1988). *Neodymium Isotope Geochemistry: An Introduction*. New York, NY: Springer, 187.

Donskaya, T. V., Gladkochub, D. P., Mazukabzov, A. M., and Ivanov, A. V. (2013). Late Paleozoic - Mesozoic subduction-related magmatism at the southern margin of the Siberian continent and the 150 million-year history of the Mongol-Okhotsk Ocean. *J. Asian Earth Sci.* 62, 79–97. doi: 10.1016/j.jseaes.2012.07.023

Dorjsuren, B., and Bujinlkham, B. (2004). *State Geological Complete Map*. Ulaanbaatar: Government of Mongolia. Report 5668.

Dostal, J., and Chatterjee, A. K. (1995). Origin of topaz-bearing and related peraluminous granites of Late Devonian Davis Lake pluton, Nova Scotia, Canada: crystal versus fluid fractionation. *Chem. Geol.* 123, 67–88. doi: 10.1016/0009-2541(95)00047-p

Dostal, J., Owen, J. V., Gerel, O., Keppie, J. D., Corney, R., Shellnutt, J. G., et al. (2014). The 186 Ma Dashibalbar alkaline granitoid pluton in the North-Gobi rift of Central Mongolia: evidence for melting of Neoproterozoic basement above a plume. *Am. J. Sci.* 314, 613–648. doi: 10.2475/02.2014.06

Dostal, J., Kontak, D. J., Gerel, O., Shellnutt, J. G., and Fayek, M. (2015a). Cretaceous ongonites (topaz-bearing albite-rich microleucogranites) from Ongon Khairkhan, Central Mongolia: products of extereme magmatic fractionation and pervasive metasomatic fluid: rock interaction. *Lithos* 236-237, 173–189. doi: 10.1016/j.lithos.2015.08.003

Dostal, J., Owen, J. V., Shellnutt, J. G., Keppie, J. D., Gerel, O., and Corney, R. (2015b). Petrogenesis of the Triassic Bayan-Ulan alkaline granitic pluton in the North Gobi rift of central Mongolia: implications for the evolution of the Early Mesozoic granitoid magmatism in the Central Asian Orogenic Belt. *J. Asian Earth Sci.* 109, 50–62. doi: 10.1016/j.jseaes.2015.04.021

Eby, G. N. (1992). Chemical subdivision of the A-type granitoids: petrogenetic and tectonic implications. *Geology* 20, 641–644.

Förster, H. J., Tischendorf, G., Trumbull, R. B., and Gottesmann, B. (1999). Late-collisional granites in the Variscan Erzgebirge, Germany. *J. Petrol.* 40, 1613–1645. doi: 10.1093/petroj/40.11.1613

Frost, C. D., and Frost, B. R. (2011). On ferroan (A-type) granitoids: their compositional variability and mode of origin. *J. Petrol.* 52, 39–53. doi: 10.1093/petrology/egq070

Gao, S., Luo, T. C., Zhang, B. R., Zhang, H. F., Han, Y. W., Zhao, Z. D., et al. (1998). Chemical composition of the continental crust as revealed by studies in East China. *Geochim. Cosmochim. Acta* 62, 1959–1975. doi: 10.1016/s0016-7037(98)00121-5

Hanchar, J. M., and Watson, E. B. (2003). Zircon saturation thermometry. *Rev. Mineral. Geochem.* 53, 89–112. doi: 10.1515/9781501509322-007

Hartman, J., Franks, R., Gehrels, G., Hourigan, J., and Wenig, P. (2017). *Decoding Data Files from a Thermo ElementTM ICP Mass Spectrometer*. Available online at: https://github.com/jhh67/extractdat.git (accessed October 20, 2019).

Hoskin, P. W. O., and Schaltegger, U. (2003). The composition of zircon and igneous and metamorphic petrogenesis. *Rev. Mineral. Geochem.* 53, 27–62. doi: 10.1515/9781501509322-005

Huppert, H. E. and Sparks, R. S. J. (1988). The generation of granite magmas by intrusions of basalts into continental crust. *J. Petrol.* 29, 599–624. doi: 10.1093/petrology/29.3.599

Ivanova, G. F. (1976). *Mineralogy and Geochemistry of The Tungsten Deposits in Mongolia*. Moscow: Nauka.

Jackson, S. E., Pearson, N. J., Griffin, W. L., and Belousova, E. A. (2004). The application of laser ablation-inductively coupled plasma-mass spectrometry to in situ U–Pb zircon geochronology. *Chem. Geol.* 211, 47–69. doi: 10.1016/j.chemgeo.2004.06.017

Jahn, B. M., Litvinovsky, B. A., Zanvilevich, A. N., and Rechow, M. (2009). Peralkaline granitoid magmatism in the Mongolian-Transbaikalian Belt: evolution, petrogenesis and tectonic significance. *Lithos* 113, 521–539. doi: 10.1016/j.lithos.2009.06.015

Jahn, B.-M., Wu, F. Y., and Chen, B. (2000). Granitoids of the Central asian orogenic belt and continental growth in the phanerozoic. *Trans. R. Soc. Edinburgh Earth Sci.* 91, 181–193. doi: 10.1017/s0263593300007367

Jargalsaikhan, D. (1996). "Metallic mineral deposits," in *Guide to the Geology and Mineral resources of Mongolia*, eds D. Jargalsaikhan, M. Kazmer, and D. Sanjaadorj (Ulaanbaatar: MUST), 157–158.

Khasin, R. A. (1977). "Tin, tungsten and molybdenum," in *Geology of Mongolian People's Republic* (Moscow: Nedra), 270–436.

Korges, M., Weis, P., Lüders, V., and Laurent, O. (2017). Depressurization and boiling of a single magmatic fluid as a mechanism for tin-tungsten deposit formation. *Geology* 46, 75–78. doi: 10.1130/g39601.1

Kuzmin, M. I, Yarmolyuk, V. V., and Kravchinsky, V. A. (2010). Phanerozoic hot spot traces and paleogeographic reconstructions of the Siberian continent based on interaction with the African large low shear velocity province. *Earth Sci. Rev.* 102, 29–59. doi: 10.1016/j.earscirev.2010.06.004

Kylander-Clark, A. R. C., Hacker, B. R., and Cottle, J. M. (2013). Laser-ablation split-stream ICP petrochronology. *Chem. Geol.* 345, 99–112. doi: 10.1016/j.chemgeo.2013.02.019

Li, S., Wang, T., Wilde, S. A., and Tong, Y. (2013). Evolution, source and tectonic significance of Early Mesozoic granitoid magmatism in the Central Asian Orogenic Belt (central segment). *Earth Sci. Rev.* 126, 206–234. doi: 10.1016/j.earscirev.2013.06.001

Linnen, R. B. (1998). The solubility of Nb-Ta-Zr–Hf-W in granitic melts with Li and Li + F: constraints for mineralization in rare metal granites and pegmatites. *Econ. Geol.* 93, 1013–1025. doi: 10.2113/gsecongeo.93.7.1013

Linnen, R. L., and Cuney, M. (2005). "Granite-related rare-element deposits and experimental constraints on Ta-Nb-W-Sn-Zr-Hf mineralization," in *Rare-Element Geochemistry and Mineral Deposits*, eds R. L. Linnen and I. M. Samson (Newfoundland: Geological Association of Canada), 45–68.

Miller, C. F., McDowell, S. M., and Mapes, R. W. (2003). Hot and cold granites? Implications of zircon saturation temperatures and preservation of inheritance. *Geology* 31, 529–532.

Paton, C., Hellstrom, J., Paul, B., Woodhead, J., and Hergt, J. (2011). Iolite: freeware for the visualisation and processing of mass spectrometric data. *J. Anal. Atom. Spectr.* 26, 2508–2518.

Peccerillo, A., and Taylor, S. R. (1976). Geochemistry of Eocene calc-alkaline volcanic rocks from the Kastamonu area, Northern Turkey. *Contrib. Mineral. Petrol.* 58, 63–81. doi: 10.1007/BF00384745

Petrus, J. A., and Kamber, B. S. (2012). VizualAge: a novel approach to laser ablation ICP-MS U-Pb geochronology data reduction. *Geostand. Geoanal. Res.* 36, 247–270. doi: 10.1111/j.1751-908x.2012.00158.x

Pollock, J.C., Sylvester, P. J. and Barr, S. M. (2015). Lu-Hf zircon and Sm-Nd whole-rock isotope constraints on the extent of juvenile arc crust in Avalonia: examples from Newfoundland and Nova Scotia, Canada. *Can. J. Earth Sci.* 52, 161–181. doi: 10.1139/cjes-2014-0157

Romer, R. I., and Kroner, U. (2016). Phanerozoic tin and tungsten mineralization-tectonic control on the distribution of enriched protoliths and heat sources for crustal melting. *Gondwana Res.* 31, 60–95. doi: 10.1016/j.gr.2015.11.002

Salvi, S., and Williams-Jones, A. E. (2005). "Alkaline granite-syenite deposits," in *Rare-Element Geochemistry and Mineral Deposits*, eds R. L. Linnen and I. M. Samson (Newfoundland: Geological Association of Canada), 315–341.

Sengör, A. M. C., Natal'in, B. A., and Burtman, V. S. (1993). Evolution of Altaid tectonic collage and Paleozoic crustal growth in Eurasia. *Nature* 364, 299–307. doi: 10.1038/364299a0

Shaw, D. M. (1968). A review of K-Rb fractionation trends by covariation analysis. *Geochim. Cosmochim. Acta* 32, 573–601. doi: 10.1016/0016-7037(68)90050-1

Sillitoe, R. H., Halls, C., and Grant, J. N. (1975). Porphyry tin deposits in Bolivia. *Econ. Geol.* 70, 913–927. doi: 10.2113/gsecongeo.70.5.913

Sláma, J., Košler, J., Condon, D. J., Crowley, J. L., Gerdes A., Hanchar, J. M., et al. (2008). Plešovice zircon- new natural reference material for U-Pb and Hf isotopic microanalysis. *Chem. Geol.* 249, 1–35. doi: 10.1016/j.chemgeo.2007.11.005

Smirnov, V. N., Koval, P. V., Tsypulov Yu, P., Kovalenko, V. I, and Antipin, V. S. (1977). K-Ar age of granitoid associations in Khentei (Mongolia). *Dokl. Russ. Acad. Sci.* 232, 192–195.

Sun, S. S., and McDonough, W. F. (1989). "Chemical and isotopic systematics of oceanic basalts: implications for mantle composition and processes," in *Magmatism in the Ocean Basins*, eds A. D. Saunders and M. J. Norry (London: Geological Society London), 313–345. doi: 10.1144/gsl.sp.1989.042.01.19

Syritso, L. F., Badanina, E. V., Abusshkevich, V. S., Volkova, E. V., and Terekhov, A. V. (2018). Fertility of rare-metal peraluminous granites and formation conditions of tungsten deposits. *Geol. Ore Deposits* 60, 33–51. doi: 10.1134/s1075701518010063

Taylor, S. R., and McLennan, S. M. (1985). *The Continental Crust: Its Composition and Evolution*. Oxford: Blackwell Scientific, 312.

Thomas, R., Förster, H. J., Rickers, K., and Webster, J. D. (2005). Formation of extremely F-rich hydrous melt fractions and hydrothermal fluids during differentiation of highly evolved tin-granite magmas: a melt/fluid-inclusion study. *Contrib. Mineral. Petrol.* 148, 582–601. doi: 10.1007/s00410-004-0624-9

Watson, E. B., and Harrison, T. M. (1983). Zircon saturation revisited: temperature and composition effects in a variety of crustal magma types. *Earth Planet. Sci. Lett.* 64, 295–304. doi: 10.1016/0012-821x(83)90211-x

Webster, J., Thomas, R., Förster, H. J., Seltman, R., and Tappen, C. (2004). Geochemical evolution of halogen-enriched granite magmas and mineralizing fluids of the Zinwald tin-tungsten mining district, Erzgebirge, Germany. *Mineral. Deposita* 39, 452–472.

Whalen, J. B., Currie, K. L., and Chappell, B. W. (1987). A-type granites: geochemical characteristics, discrimination and petrogenesis. *Contrib. Mineral. Petrol.* 95, 407–419. doi: 10.1007/bf00402202

Wiedenbeck, M., Alle, P., Corfu, F., Griffin, W. L., Meier, M., Oberli, F., et al. (1995). Three natural zircon standards for U–Th–Pb, Lu–Hf, trace element and REE analyses. *Geostand. Newslett.* 19, 10–23.

Yarmolyuk, V. V., Kovalenko, V. I., Kozakov, I. K., Salnikova, E. B., Bibikova, E. V., Kovach, V. P., et al. (2008). The age of the Khangai batholith and the problem of batholith formation in Central Asia. *Doklady Earth Sci.* 423, 1223–1228. doi: 10.1134/s1028334x08080096

Yarmolyuk, V. V., Kovalenko, V. I., Salnikova, E. B., Budnikov, S. V., Kovach, V. P., Kotov, A. B., et al. (2002). Tectono-magmatic zoning, magma sources, and geodynamic of the Early Mesozoic Mongolo-Transbaikalian magmatic area. *Geotectonics* 36, 293–311.

Yarmolyuk, V. V., and Kuzmin, M. I. (2011). *Rifting and Silicic Large Igneous Provinces of the Late Paleozoic - Early Mesozoic in the Central Asia: Large Igneous Provinces Commission*. Available online at: http://www.largeigneousprovinces.org/11dec (accessed January 15, 2020).

Yarmolyuk, V. V., and Kuzmin, M. I. (2012). Late Paleozoic and Early Mesozoic rare-metal magmatism of Central Asia: stages, provinces, and formation settings. *Geol. Ore Deposits* 54, 313–333. doi: 10.1134/s1075701512050054

Yarmolyuk, V. V., Kuzmin, M. I., and Kozlovsky, A. M. (2013). Late Paleozoic-Early Mesozoic within-plate magmatism in North Asia: traps, rifts, giant batholiths, and the geodynamics of their origin. *Petrology* 21, 101–126. doi: 10.1134/s0869591113010062

Conflict of Interest: The authors declare that the research was conducted in the absence of any commercial or financial relationships that could be construed as a potential conflict of interest.

The handling editor declared a past co-authorship with one of the authors, JD.

frontiers in Earth Science

ORIGINAL RESEARCH
published: 21 August 2020
doi: 10.3389/feart.2020.00354

Petrogenesis of the Late Oligocene Takht batholith, Southeastern Iran: Implications for the Diachronous Nature of the Arabia–Eurasia Collision

Kwan-Nang Pang[1†], Abdolnaser Fazlnia[2*], Wei-Qiang Ji[3], Susan Jamei[2,4] and Amin Jafari[2,5]*

[1] Institute of Earth Sciences, Academia Sinica, Taipei, Taiwan, [2] Department of Geology, Urmia University, Urmia, Iran, [3] State Key Laboratory of Lithospheric Evolution, Institute of Geology and Geophysics, Chinese Academy of Sciences, Beijing, China, [4] Faculty of Earth Sciences, Shahid Beheshti University, Tehran, Iran, [5] Department of Geology, Faculty of Natural Sciences, University of Tabriz, Tabriz, Iran

OPEN ACCESS

Edited by:
Paterno Castillo,
University of California, San Diego,
United States

Reviewed by:
Zi-Fu Zhao,
University of Science and Technology of China, China
Simone Tommasini,
University of Florence, Italy

***Correspondence:**
Kwan-Nang Pang
knpang@earth.sinica.edu.tw
Abdolnaser Fazlnia
a.fazlnia@urmia.ac.ir

†ORCID:
Kwan-Nang Pang
orcid.org/0000-0003-0369-395X

Specialty section:
This article was submitted to Petrology, a section of the journal Frontiers in Earth Science

Received: 01 May 2020
Accepted: 29 July 2020
Published: 21 August 2020

Citation:
Pang K-N, Fazlnia A, Ji W-Q, Jamei S and Jafari A (2020) Petrogenesis of the Late Oligocene Takht batholith, Southeastern Iran: Implications for the Diachronous Nature of the Arabia–Eurasia Collision. Front. Earth Sci. 8:354. doi: 10.3389/feart.2020.00354

Zircon U-Pb age, mineral compositional, elemental and Sr-Nd isotopic data are documented for intermediate to felsic rocks in the Takht batholith, a Late Oligocene igneous complex in the southeastern segment of the Urumieh-Dokhtar belt, Iran, to investigate magma genesis in the context of regional tectonics. A large part of the magmatic belt formed by northward subduction of the Neotethys before the Arabia–Eurasia continental collision. Zircon U-Pb age data indicate the batholith crystallized at ∼25 Ma, an age consistent with previous results. Geochemical data indicate that the rocks share features typical of calc-alkaline magmas and I-type granitoids. The least evolved magma inferred from the data has basaltic andesite composition, consistent with either of the following origins: (i) a partial melt of the mantle followed by differentiation, or (ii) a partial melt of the lower crust. With increasing SiO_2, $(^{87}Sr/^{86}Sr)_{25Ma}$ increases from 0.7053 to 0.7073, and εNd_{25Ma} decreases from −0.3 to −2.9, consistent with increasing effects of assimilation–fractional crystallization, although processes such as magma mixing and melting of heterogeneous source rocks cannot be entirely ruled out. Aluminum-in-hornblende thermometry indicates that the batholith might have emplaced at ∼6.5 km or shallower paleo-depths. Moho depth proxies Sr/Y and $(La/Yb)_N$ yield crustal thickness of ∼20–30 km, showing no evidence for magma processing within thick crust. Overall, our results indicate that the Takht batholith is a Cordilleran-type batholith formed beneath a continental or transitional arc of normal crustal thickness. This is consistent with the notion that Arabia and Eurasia have collided in a diachronous manner, propagating from the northwest to the southeast since the Late Eocene–Early Oligocene.

Keywords: granitoids, geochemistry, Urumieh-Dokhtar, Arabia, Eurasia, Neotethys

INTRODUCTION

Subduction and collision are important tectonic processes that take part in orogenic cycles. These processes not only bring together continental masses but also create and shape mountain belts, playing a key role in ocean and atmospheric circulation (Yin and Harrison, 2000; Allen and Armstrong, 2008; Jagoutz et al., 2016). Also, subduction and collision lead to development of thick crust that resists recycling, contributing to continent formation (Cawood et al., 2013; Hawkesworth et al., 2017; Moyen et al., 2017). Despite the above importance, tracking subduction and collision events in orogens is harder than generally appreciated. In a given orogenic system, there could be multiple events of subduction and collision in different time and space, superimposed and variably preserved in the geologic record. Unraveling details of the record requires studies within and across sub-disciplines of earth sciences.

In magmatic orogens, igneous record gives useful constraints on magma genesis, which could yield indirect clues in tracking subduction and collision. For example, thick lithosphere generated by collision might facilitate formation of alkaline magmas either by relatively low degrees of mantle melting (Aldanmaz et al., 2000) and/or increased influence of continent-derived materials in magma genesis (Wang et al., 2017). Magmas formed over thick crust in subduction and collision zones tend to have high Sr/Y, La/Yb, and Dy/Yb because of increased influence of residual garnet over plagioclase in magma genesis (Chung et al., 2003; Topuz et al., 2005; Ji et al., 2012; Goss et al., 2013; Ducea et al., 2015). For instance, Sr/Y and La/Yb of intermediate to felsic magmas have been taken as indicators of Moho depths in arcs and continental collision zones (Chapman et al., 2015; Profeta et al., 2015; Hu et al., 2017).

This study is focused on the petrology and geochemistry of the Late Oligocene Takht batholith (Fazlnia et al., 2014; Hosseini et al., 2017a), which crops out in the southeastern segment of the Urumieh-Dokhtar belt, Iran within the Arabia–Eurasia collision zone. The Late Oligocene is a critical timing in this particular collision zone because it coincides with most estimates for the age of initial collision. Here, we use zircon U-Pb ages, mineral composition, geochemical and Sr-Nd isotopic data to (i) describe the mineralogical and geochemical variations of different rocks from the batholith, (ii) constrain the petrogenesis of these rocks, and (iii) explore the potential implications of magma genesis in the context of regional tectonics. Our data indicate that the Takht batholith formed in an arc setting, showing no signs of any collision-induced crustal thickening. Because the Arabia–Eurasia collision has initiated at the Turkish-Iranian borderlands by the time the batholith formed, our results hint that the collision might have occurred in a diachronous manner.

GEOLOGICAL BACKGROUND

Mountain ranges of Iran are parts of the Alpine-Himalayan orogenic system. In particular, the Zagros orogen has received much attention because it formed by colliding continents of Arabia and Eurasia. The orogen consists of three sub-parallel, NW-SE-trending structural elements including (i) the Urumieh-Dokhtar belt, (ii) the Sanandaj-Sirjan zone, and (iii) the Zagros fold and thrust belt (**Figure 1**). A conventional wisdom regarding Zagros orogeny is that the Arabia–Eurasia collision has followed Neotethyan subduction from the Jurassic to the Tertiary (Berberian and King, 1981; Alavi, 1994; Hassanzadeh and Wernicke, 2016). Increasing evidence points to the Late Eocene to the Early Oligocene as the initial age of collision (Allen and Armstrong, 2008; Mouthereau et al., 2012; McQuarrie and van Hinsbergen, 2013; Gholami Zadeh et al., 2017; Koshnaw et al., 2018), along what is now the Bitlis-Zagros suture (or the Main Zagros Fault), the major tectonic boundary between the Sanandaj-Sirjan zone and the Zagros fold and thrust belt.

The Zagros orogen has an extensive igneous record, particularly focused in the Sanandaj-Sirjan zone and the Urumieh-Dokhtar belt. The latter is a ∼1800–2000-km-long and ∼50–80-km-wide belt composed mainly of volcanic and intrusive rocks of calc-alkaline and to a lesser extent tholeiitic or alkaline affinities (Berberian and Berberian, 1981; Alavi, 1994; Shahabpour, 2005, 2007; Honarmand et al., 2013, 2016; Kananian et al., 2014; Babazadeh et al., 2017; Sarjoughian et al., 2018). It is generally accepted that a large portion of the Urumieh-Dokhtar belt represents an Andean-type paleo-arc formed by northward subduction of the Neotethys beneath terranes that had accreted to the southern margin of Eurasia (Berberian and King, 1981; Alavi, 1994; Aftabi and Atapour, 2000). Neotethyan subduction might also be responsible for Eocene magmatism that affected the northwestern part of the Sanandaj-Sirjan zone (Fazlnia, 2019). In the southeastern segment of the Urumieh-Dokhtar belt where the Takht batholith crops out, published ages of igneous rocks range between ∼82 and ∼5.4 Ma (Chiu et al., 2013; Hosseini et al., 2017b), although magmatism likely peaked over the Eocene (Verdel et al., 2011).

The Takht batholith was dated at ∼25 Ma using *in situ* zircon U-Pb isotopic analysis on a granitic rock (Hosseini et al., 2017a). In that study, an age of ∼24.2 Ma was also reported for a granodiorite porphyry associated with high-grade Cu mineralization at the Takht-e-Gonbad mine. These ages are consistent with not only information shown on geological maps (Khan-Nazer and Emami, 1996) but also field relations indicating that the batholith intruded Eocene strata and was cut in places by dykes with inferred Miocene ages (Dimitrijevic, 1973; Hassanzadeh, 1993; Shafiei, 2008). Yet, the hosts to other porphyry Cu deposits in the southwestern segment of the Urumieh-Dokhtar belt, including Sarcheshmeh and Meiduk to the northwest of the Takht batholith, appeared to have formed slightly later at the Middle Miocene (McInnes et al., 2005; Zarasvandi et al., 2018 and references therein).

The Takht batholith consists of a wide spectrum of intermediate to felsic intrusive rocks (e.g., Dargahi, 2007; Shafiei, 2008), a view ascertained during our field work. In general, the rocks tend to be richer in mafic minerals at the margin of the batholith and in felsic minerals toward its center (**Figure 1**). According to aerial view, the intermediate and felsic units make up about 65 and 35%, respectively, of the exposed batholith. Although generally richer in mafic minerals, the intermediate

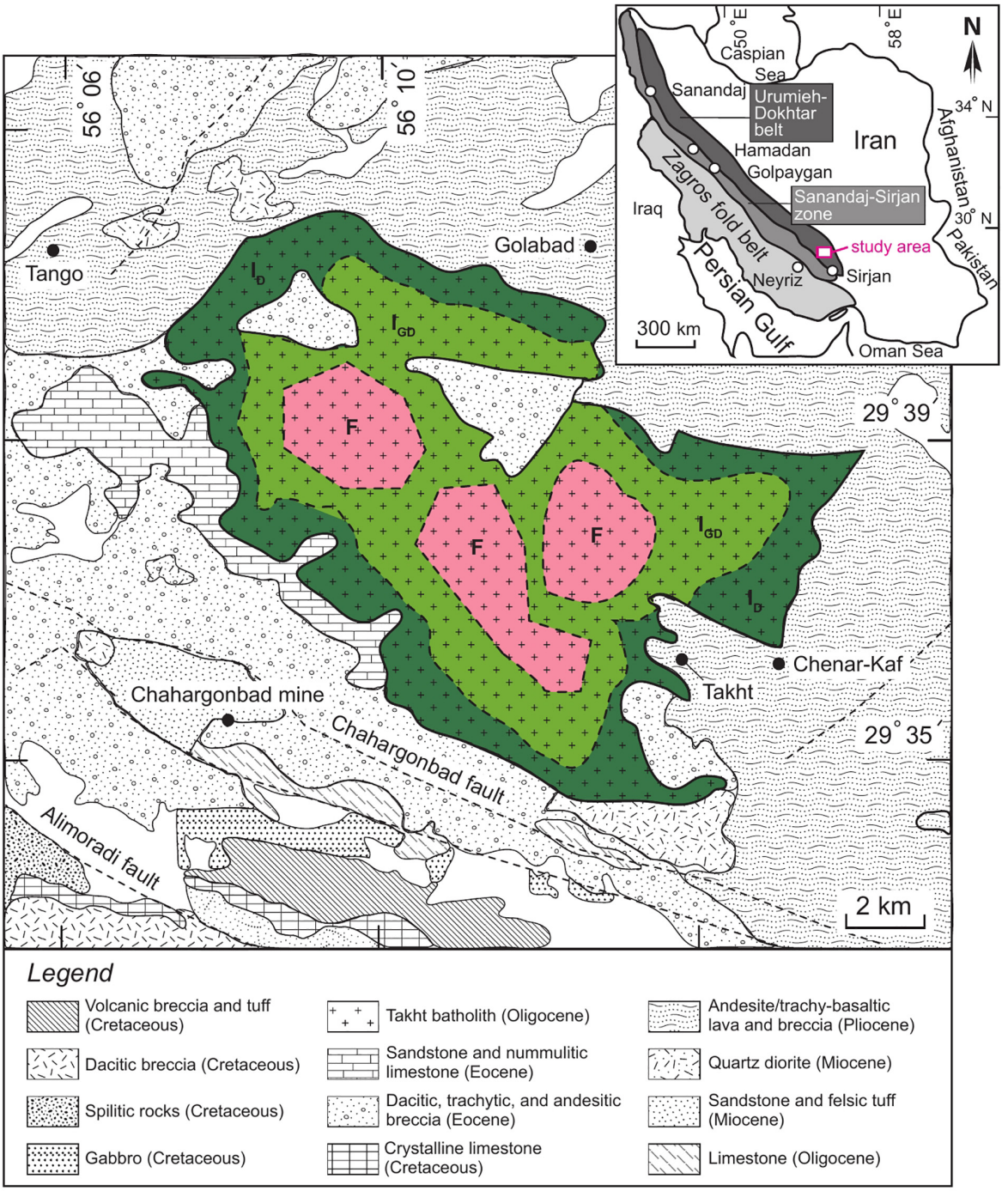

FIGURE 1 | Simplified geological sketch map showing the geology of the Takht batholith and adjacent areas, southeastern Iran (modified after Khan-Nazer and Emami, 1996). I_D = intermediate unit dominated by diorite, I_{GD} = intermediate unit dominated by granodiorite, F = felsic unit. Inset shows the main tectonic units of the Zagros orogen (Stöcklin, 1968).

unit show complex contact relationships between dioritic and granitic rocks in places (**Figure 2A**). In addition, mafic to felsic enclaves of various sizes are locally observed in outcrops (**Figure 2B**). Hereafter, rocks from the intermediate and felsic units are referred to as intermediate and felsic suites, respectively.

PETROGRAPHY

Intermediate Suite

Rocks of the intermediate suite are fine- to medium-grained. Granular texture is the most common (**Figures 3A,B**) although

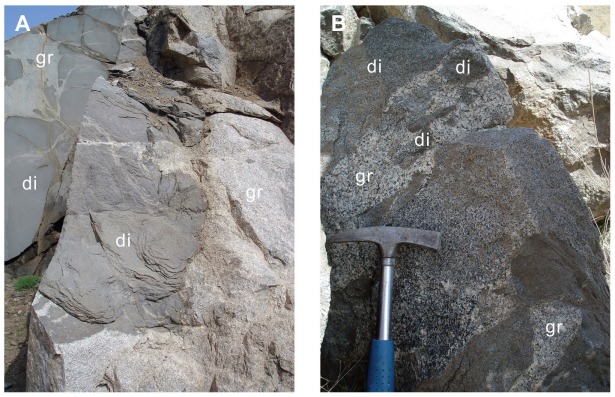

FIGURE 2 | Contact relations between dioritic (di) and granitic (gr) rocks of the Takht batholith. **(A)** Dioritic rock in sharp contact with and apparently cut by granitic rock; note the network of dikelets connecting to the main mass of granitic rock. **(B)** Centimeter-sized enclaves of diorite occur in granitic rock.

cumulate texture is observed in some samples (**Figures 3C,D**). Mineral assemblage comprises plagioclase (∼15–55 vol.%) and hornblende (∼5–25 vol.%) with subordinate amounts of orthoclase (∼0–20 vol.%), clinopyroxene (∼0–15 vol.%), biotite (∼3–10 vol.%), and quartz (∼0–25 vol.%). Apatite, zircon, titanite, and Fe-Ti oxides are common accessory minerals. Plagioclase occurs as euhedral or subhedral grains of various sizes, some of which show oscillatory zoning with margins replaced by sericite, calcite, and epidote (**Figure 3D**). Hornblende occurs as euhedral to subhedral grains of various sizes, and some of them form poikilitic masses enclosing grains of Fe-Ti oxides (**Figure 3A**) and plagioclase (**Figure 3B**). Orthoclase is commonly intergrown with plagioclase, hornblende and biotite, and many orthoclase grains display perthitic texture (**Figure 3E**). Clinopyroxene is subhedral or anhedral, and commonly shows signs of uralitization. Biotite and quartz occur as fine to medium grains intergrown with other minerals (**Figure 3E**).

Felsic Suite

Rocks of the felsic suite commonly exhibit granular texture (**Figures 3F–H**). Mineral assemblage comprises orthoclase (∼25–65 vol.%), quartz (∼20–40 vol.%), plagioclase (∼5–15 vol.%), hornblende (∼3–10 vol.%), and biotite (∼2–5 vol.%). Titanite, zircon, and Fe-Ti oxides are common accessory minerals. Orthoclase occurs as a fine- to medium-grained, ubiquitous mineral in most monzogranites and syenogranites (**Figures 3F–H**). Perthitic texture is common in orthoclase (**Figure 3H**). Quartz grains are subhedral with a range of sizes. Plagioclase is euhedral or subhedral, and some grains exhibit oscillatory zoning (**Figure 3G**). Biotite is subhedral, occurring either with hornblende or as discrete grains. Graphic intergrowths of fine-grained orthoclase and quartz are commonly observed in a subset of samples almost totally dominated by quartz and feldspar (**Figure 3H**).

ANALYTICAL METHODS

A large set of samples was collected from outcrops of the Takht batholith. Samples that are generally fresh and representative were selected for geochronological, mineral chemical and geochemical analyses.

Zircon was extracted from the samples by conventional methods involving heavy-liquid and magnetic separation, and hand-picking under binocular microscope. Zircon grains were mounted in epoxy, polished, and analyzed for cathodoluminescence (CL) imaging and U-Pb isotopes by laser ablation-ICP-MS at the Beijing Quick-Thermo Science & Technology, Co., Ltd. Details of the analytical procedures are similar as described by Ji et al. (2020). The instrument used is an ESI New Wave NWR 193UC (TwoVol2) laser ablation system connected to an Agilent 8900 ICP-QQQ. The analytical spots are 20 μm in diameter. 91500 zircon and Plešovice zircon were used as primary and secondary reference materials, respectively. The latter yielded a mean age of 336.3 ± 2.0 Ma (MSWD = 0.8, n = 22), consistent with the recommended values within errors (Sláma et al., 2008). The zircon U-Pb age data are given in **Supplementary Table 1**.

Six samples were selected for electron probe microanalysis (EPMA) at the University of Kiel, Germany. Using a JEOL JXA8900 microprobe, compositions of feldspar and amphibole were determined at a probe current of 15 or 20 nA and an accelerating voltage of 15 kV. The EPMA data are given in **Supplementary Tables 2**, **3**.

Sixteen samples were selected for whole-rock major and trace element analysis, which was performed at the ACME Analytical Laboratories, Canada. Samples were crushed into small chips and pulverized in an agate mill. Loss-on-ignition (LOI) was determined by heating 1 g of dried rock powder at 1000°C for 2 h. Major element oxides were measured by X-ray fluorescence (XRF) spectrometry and trace elements were analyzed by inductively coupled plasma-mass spectrometry (ICP-MS) followed by lithium borate fusion. Precision and accuracy were monitored by replicate analyses of samples and in-house standards (**Supplementary Table 4**). The major and trace element data are given in **Table 1**.

Eight samples were analyzed for whole-rock Sr-Nd isotopic analysis at the ACME Analytical Laboratories, Canada. A 200–400 mg aliquot of rock powder was dissolved using mixed hydrofluoric, nitric, and hydrochloric acids. Strontium was purified using cation exchange resin and 2.5 N HCl. Sample solution was loaded onto pre-outgassed and clean rhenium filaments with phosphoric acid and tantalum oxide. Strontium isotope analysis was performed using a thermal ionization mass spectrometer with five Faraday collectors in dynamic mode and ^{88}Sr = 3.0 V. Strontium isotopes were normalized to $^{86}Sr/^{88}Sr$ = 0.1194. Neodymium was purified using HDHEP-coated resin and 0.25N HCl, and its isotopes were analyzed using multi-collector ICP-MS with seven Faraday collectors after dissolution in 2% HNO_3. Neodymium isotopes were normalized to $^{146}Nd/^{144}Nd$ = 0.7219. The whole-rock Sr-Nd isotopic data are given in **Table 2**.

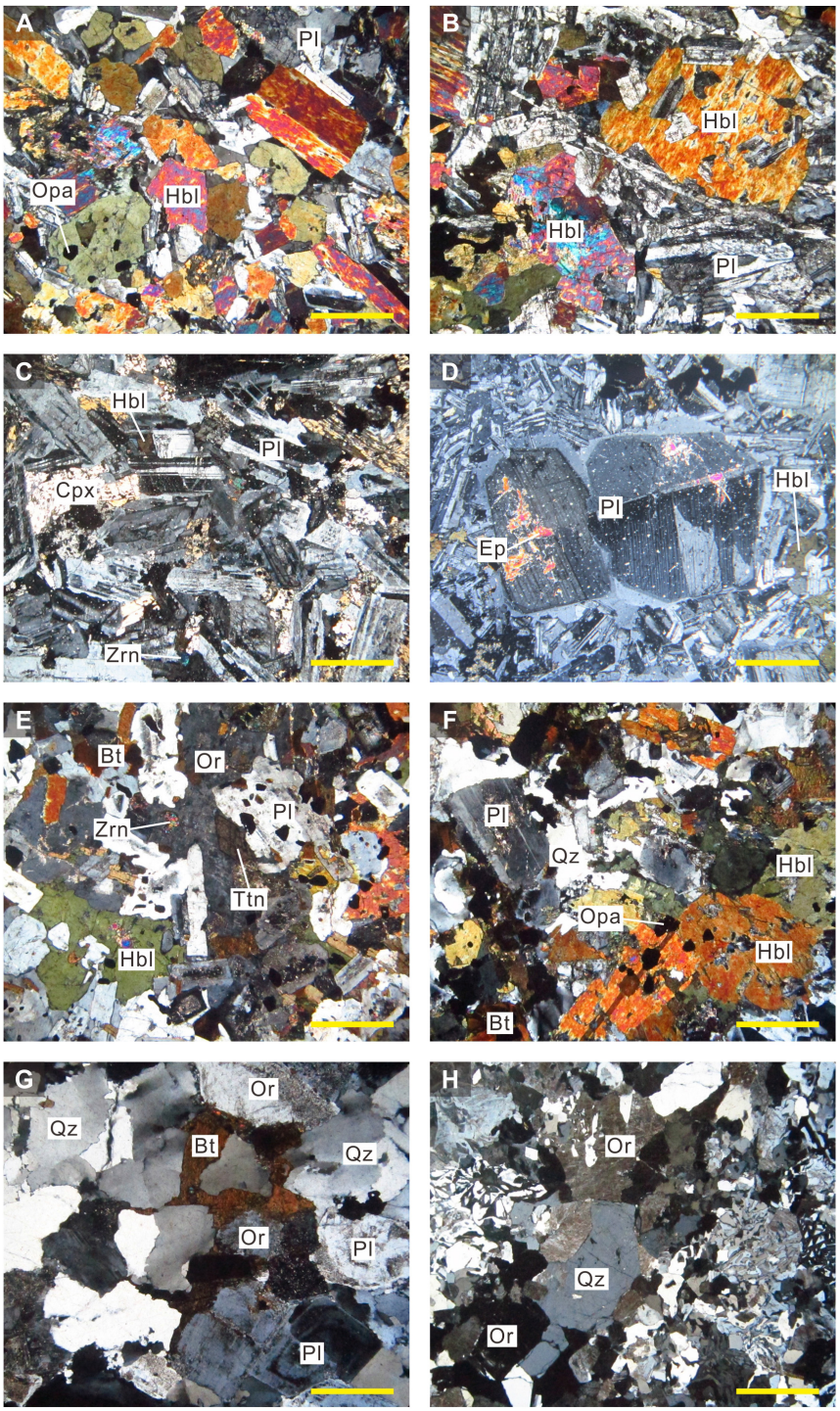

FIGURE 3 | Photomicrographs of rocks from the Takht batholith. **(A)** Granular texture shown by diorite consisting of interlocking grains of hornblende and plagioclase. **(B)** Poikilitic hornblende enclosing plagioclase in a diorite. **(C)** Cumulate texture shown by diorite consisting of a framework of cumulus plagioclase with intercumulus clinopyroxene and hornblende. **(D)** Coarse plagioclase crystals showing resorbed boundaries in a fine-grained matrix of plagioclase and hornblende in a diorite sample. **(E)** Granular texture shown by granodiorite consisting of interlocking grains of hornblende, biotite, plagioclase, and orthoclase. **(F)** Granular texture shown by monzogranite consisting of interlocking grains of hornblende, biotite, plagioclase and quartz. **(G)** Granular texture shown by monzogranite consisting of interlocking grains of biotite, plagioclase, orthoclase, and quartz. **(H)** Graphic texture, which is made up of intergrown orthoclase and quartz, shown by syenogranite. Perthite texture is observed in some orthoclase grains (upper center). All photomicrographs were taken under cross-polarized light and the yellow bars in the lower right of each frame denote length of 1 mm. Mineral abbreviations are used after Whitney and Evans (2010), except for minerals that have no recommended abbreviations: Bt = biotite, Cpx = clinopyroxene, Ep = epidote, Hbl = hornblende, Opa = Fe-Ti oxides, Or = orthoclase, Pl = plagioclase, Qz = quartz, Ttn = titanite, Zrn = zircon.

TABLE 1 | Geochemical data for the studied samples from the Takht batholith.

	Intermediate suite								Felsic suite							
Sample	**E-17-2**	**I-10**	**I-9**	**B-14**	**D-18**	**E-16-1**	**E-10**	**G-7**	**A-5-2**	**E-14-1**	**A-4**	**A-5-1**	**B-2**	**C-7**	**B-12**	**C-6**
Rock	**D[1]**	**D**	**D**	**D**	**GD[1]**	**GD**	**GD**	**GD**	**MG[1]**	**MG**	**MG**	**MG**	**MG**	**MG**	**SG[1]**	**SG**
Major oxides (wt.%)																
SiO_2	56.68	55.44	55.29	58.55	61.56	64.44	63.79	62.29	68.31	71.17	69.02	69.34	71.38	71.82	76.28	76.76
TiO_2	0.73	0.82	0.91	0.70	0.72	0.56	0.59	0.68	0.41	0.25	0.36	0.33	0.30	0.33	0.13	0.07
Al_2O_3	17.15	17.54	18.46	17.22	16.20	15.92	15.52	15.89	14.84	13.87	14.69	14.63	14.90	15.13	12.48	12.44
Fe_2O_3[2]	8.10	8.53	1.44	7.18	6.52	5.42	5.73	5.82	3.74	1.77	3.18	3.18	2.58	1.93	0.94	0.85
MnO	0.18	0.10	0.02	0.12	0.20	0.15	0.12	0.09	0.06	0.02	0.06	0.05	0.03	0.01	0.01	bdl[4]
MgO	3.54	3.93	4.88	3.25	2.24	1.75	2.31	2.58	0.87	0.61	0.96	0.80	0.80	0.17	0.20	0.04
CaO	6.61	7.35	12.11	6.75	4.94	4.04	5.01	5.28	1.62	2.26	2.87	2.11	3.4	2.42	0.92	0.61
Na_2O	3.27	3.36	4.51	3.37	4.06	3.93	2.94	3.34	4.46	5.75	3.73	3.67	5.14	3.96	3.51	3.2
K_2O	1.44	1.33	0.30	1.63	2.20	2.45	2.94	2.56	3.62	0.35	3.44	3.97	0.52	3.00	4.36	5.35
P_2O_5	0.19	0.14	0.20	0.15	0.14	0.13	0.13	0.13	0.11	0.06	0.10	0.08	0.09	0.08	0.02	0.02
LOI	1.90	1.20	1.70	0.90	1.10	1.00	0.70	1.10	1.80	3.80	1.40	1.70	0.70	1.00	0.90	0.60
Total	99.84	99.81	99.8	99.82	99.87	99.88	99.84	99.84	99.89	99.94	99.84	99.88	99.92	99.91	99.81	99.95
Mg#[3]	46.4	47.7	87.0	47.3	40.5	39.0	44.4	46.8	31.5	40.6	37.4	33.3	38.0	14.9	29.6	8.5
Trace elements (ppm)																
Sc	17.0	24.0	25.0	22.0	16.0	10.0	16.0	18.0	9.00	3.00	7.00	7.00	5.00	5.00	2.00	bdl
V	174	227	284	183	131	87	127	147	52.0	26.0	51.0	44.0	55.0	45.0	13.0	8.00
Co	21.4	22.0	2.70	18.7	13.0	9.70	13.6	14.1	5.20	2.10	34.6	4.60	3.00	2.00	47.5	1.10
Ni	5.60	7.40	1.60	3.80	1.70	2.70	6.20	5.60	4.10	3.00	1.40	4.20	4.00	4.60	0.30	2.70
Cu	50.6	145	6.00	84.6	69.6	23.7	81.9	23.9	50.2	7.60	31.4	36.2	8.00	10.6	4.50	15.9
Zn	53.0	18.0	13.0	25.0	40.0	37.0	25.0	19.0	27.0	4.00	25.0	22.0	25.0	13.0	13.0	4.00
Ga	17.3	17.6	16.2	16.0	16.5	15.3	13.3	14.1	14.1	12.4	14.5	12.6	12.7	13.2	12.3	10.4
Rb	58.8	27.2	5.60	37.5	89.7	88.1	67.3	73.8	98.5	7.50	106	108	9.40	81.4	129	188
Sr	353	352	536	329	230	276	235	257	223	222	205	192	239	221	86.0	37.9
Y	14.5	16.8	19.5	18.4	25.0	17.1	22.0	20.2	20.8	12.0	17.6	14.2	10.9	7.30	8.30	9.20
Zr	75.4	80.5	70.0	128	115	118	151	149	134	131	154	148	120	150	98.5	88.6
Nb	2.90	2.60	2.60	3.40	5.00	3.60	3.70	3.40	4.90	4.10	4.10	4.00	3.60	4.50	6.70	6.00
Cs	2.30	2.20	0.80	1.20	3.90	4.20	4.50	3.40	1.20	bdl	1.80	1.20	0.20	4.00	1.40	3.00
Ba	150	237	103	284	277	255	427	319	379	91.0	431	423	135	369	412	307
La	9.10	9.80	8.10	11.9	10.7	14.4	15.1	15.2	14.3	18.6	18.5	18.6	10.4	17.1	24.9	22.9
Ce	18.2	20.8	19.9	25.2	22.3	26.6	30.0	30.6	26.6	34.5	35.1	34.1	23.9	29.7	45.5	40.9
Pr	2.25	2.63	2.79	3.05	3.05	3.08	3.73	3.65	3.22	3.81	3.88	3.84	2.65	3.07	4.63	4.02
Nd	10.0	11.8	13.4	12.3	12.8	11.4	14.9	15.1	13.0	13.0	14.7	14.1	9.10	10.6	15.1	12.7
Sm	2.22	2.59	3.04	2.93	3.34	2.61	3.45	3.22	2.75	2.22	2.98	2.54	1.71	1.83	2.42	2.07
Eu	0.81	0.81	0.82	0.83	0.83	0.78	0.81	0.76	0.69	0.51	0.64	0.61	0.56	0.57	0.27	0.19
Gd	2.48	2.93	3.55	3.23	3.74	2.81	3.50	3.48	2.88	1.88	2.68	2.38	1.65	1.39	1.86	1.61
Tb	0.39	0.47	0.56	0.50	0.62	0.45	0.58	0.56	0.51	0.30	0.44	0.38	0.27	0.21	0.26	0.22
Dy	2.53	2.95	3.84	3.23	3.96	2.94	3.51	3.65	3.48	1.92	2.77	2.49	1.64	1.08	1.35	1.25
Ho	0.52	0.60	0.72	0.67	0.87	0.57	0.80	0.72	0.68	0.39	0.63	0.49	0.34	0.22	0.24	0.28
Er	1.60	1.65	2.16	1.80	2.60	1.74	2.23	2.07	2.14	1.24	1.83	1.63	1.09	0.76	0.79	0.86
Tm	0.22	0.26	0.31	0.29	0.41	0.28	0.33	0.32	0.38	0.19	0.31	0.28	0.18	0.11	0.14	0.17
Yb	1.42	1.68	2.05	1.90	2.93	1.85	2.17	2.25	2.60	1.36	2.25	1.80	1.26	0.89	1.14	1.29
Lu	0.22	0.28	0.31	0.30	0.43	0.30	0.38	0.35	0.39	0.23	0.34	0.30	0.21	0.14	0.20	0.21
Hf	2.10	1.90	1.80	3.20	3.50	3.40	4.30	4.20	4.20	3.60	4.10	4.30	3.40	4.40	3.80	3.80
Ta	0.20	0.20	0.20	0.30	0.40	0.40	0.30	0.40	0.30	0.40	0.50	0.40	0.50	0.40	1.10	0.70
Pb	6.30	1.90	1.10	1.50	8.10	6.70	4.40	1.80	21.9	1.10	8.00	20.8	5.80	9.80	3.70	3.10
Th	2.80	3.90	2.80	3.40	6.40	7.60	8.50	7.10	11.6	14.6	10.9	11.7	11.1	9.20	16.1	19.4
U	0.50	0.50	0.50	0.50	1.00	1.20	1.30	1.20	2.20	1.50	1.70	1.50	1.40	0.90	1.40	2.40

[1]D = diorite sensu lato, GD = granodiorite, MG = monzogranite, SG = syenogranite. [2]Total iron as Fe_2O_3. [3]Mg# = [molar 100 x Mg/(Mg + Fe^{2+})], assuming 10% of total iron oxide is ferric. [4]bdl = below detection limit.

TABLE 2 | Sr-Nd isotopic data for a subset of the studied samples from the Takht batholith.

Sample	Rock[1]	Rb[2] (ppm)	Sr (ppm)	$^{87}Sr/^{86}Sr$	$\pm 2\sigma_m$[3]	$(^{87}Sr/^{86}Sr)_{25Ma}$[4]	Sm (ppm)	Nd (ppm)	$^{143}Nd/^{144}Nd$	$\pm 2\sigma_m$	$(^{143}Nd/^{144}Nd)_{25Ma}$	εNd_{25Ma}
I-10	D	27.2	352	0.705421	0.000013	0.7053	2.59	11.8	0.512612	0.000008	0.51259	−0.3
D-18	D	89.7	230	0.705751	0.000011	0.7054	3.34	12.8	0.512598	0.000010	0.51257	−0.7
E-16-1	GD	88.1	276	0.706785	0.000012	0.7065	2.61	11.4	0.512557	0.000010	0.51253	−1.4
G-7	GD	73.8	257	0.706756	0.000010	0.7065	3.22	15.1	0.512512	0.000009	0.51249	−2.2
A-5-2	MG	98.5	223	0.706624	0.000010	0.7062	2.75	13.0	0.512521	0.000009	0.51250	−2.1
A-4	MG	106	205	0.707451	0.000012	0.7069	2.98	14.7	0.512512	0.000011	0.51249	−2.2
C-7	MG	81.4	221	0.707652	0.000013	0.7073	1.83	10.6	0.512495	0.000011	0.51248	−2.5
B-12	SG	129	86.0	0.706781	0.000023	0.7053	2.42	15.1	0.512475	0.000010	0.51246	−2.9

[1]D = diorite sensu lato, GD = granodiorite, MG = monzogranite, SG = syenogranite. [2]Ratios $^{87}Rb/^{86}Sr$ and $^{147}Sm/^{144}Nd$ are computed from trace element data based on the following equations: $^{87}Rb/^{86}Sr = Rb/Sr \times [2.69295 + 0.28304 \times (^{87}Sr/^{86}Sr)]$, $^{147}Sm/^{144}Nd = Sm/Nd \times [0.53149 + 0.14252 \times (^{143}Nd/^{144}Nd)]$. [3]The values refer to 2σ standard error of the mean. [4]$(^{87}Sr/^{86}Sr)_t$ and εNd(t) values were calculated based on t = 25 Ma, $\lambda(^{87}Rb) = 1.42 \times 10^{-11}$ year^{-1}, $\lambda(^{147}Sm) = 6.54 \times 10^{-12}$ year^{-1}, $^{87}Rb/^{86}Sr$ and $^{147}Sm/^{144}Nd$ calculated as above, and present day chondritic values of $^{143}Nd/^{144}Nd = 0.512638$, $^{147}Sm/^{144}Nd = 0.1967$, $^{87}Sr/^{86}Sr = 0.7045$, and $^{87}Rb/^{86}Sr = 0.0827$ (Faure and Mensing, 2005).

RESULTS

Geochemical Classification

The geochemical data obtained are useful in characterizing rock types and magma affinity. Major element data are recalculated to millications and casted on a P-Q diagram of Debon and Le Fort (1988), on which fields for rock types are used after Bonin et al. (2020). Samples of the intermediate suite plot in fields of quartz diorite, tonalite, and granodiorite (**Figure 4A**); however, those classified as tonalites contain too much orthoclase to be tonalite in a strict petrographic sense. For simplicity, therefore, the former two are grouped as diorite *sensu lato*. Samples of the felsic suite plot above all the fields of Bonin et al. (2020) (**Figure 4A**). Two samples are classified as syenogranite based on relatively low molar [K − (Na + Ca)] compared with the others, which are all grouped as monzogranite. This classification, although imperfect, appears justified with respect to petrographic observations (**Figure 3**). Besides, all samples display calc-alkaline affinity on a binary diagram of modified alkali lime index (MALI) versus SiO_2 (**Figure 4B**). In addition, samples of the intermediate suite are metaluminous, whereas those of the felsic suite are either metaluminous or slightly peraluminous (**Figure 4C**). This feature, together with the occurrence of hornblende and titanite in the majority of samples, indicates an affinity to I-type granites (Chappell and White, 1974).

Zircon U-Pb Geochronology

Most zircon grains in sample I-12 (diorite) are euhedral and prismatic, showing simple oscillatory zoning typical of igneous zircon. According to Corfu (2013), igneous zircon commonly has Th/U greater than 0.2. Relatively high Th/U of zircon grains in sample I-12 (∼0.5–1.1) is thus consistent with an igneous origin (**Supplementary Table 1**). Nineteen spot analyses yield a mean $^{206}Pb^*/^{238}U$ age of 26.2 ± 0.6 Ma with MSWD of 1.3 (**Figures 5A,B**). While zircon grains in sample E-15 (monzogranite) are also prismatic, euhedral form is less common. Oscillatory zoning is evident from CL images for most grains, yet zoning pattern appears complex for some grains. The igneous origin of the grains is indicated by relatively high Th/U (∼0.4–1.9) (**Supplementary Table 1**). Twenty spot analyses yield a mean $^{206}Pb^*/^{238}U$ age of 25.2 ± 0.4 Ma with MSWD of 1.18 (**Figures 5C,D**). In summary, the zircon U-Pb data support a crystallization age of the Takht batholith at ∼25 Ma, consistent with earlier age results reported by Hosseini et al. (2017a).

Mineral Composition

Compositions of plagioclase and orthoclase are given in **Supplementary Table 2**. For samples of the intermediate suite, most analyzed feldspar grains are plagioclase (An_{37-55}), plotting in the fields of labradorite and andesine on a ternary feldspar diagram (**Figure 6A**). The anorthite content of the plagioclase appears to vary negatively with K_2O, which ranges from about 0.2 to 0.8 wt.%. The FeO_T content ranges from about 0.2 to 0.7 wt.%, showing no correlation with anorthite content. For samples of the felsic suite, the feldspar displays substantial compositional variations. For example, a monzogranite sample has plagioclase with An_{46} composition, whereas a syenogranite sample contains coexisting plagioclase (An_{12}) and orthoclase (**Figure 6A**). The BaO content of the orthoclase is about 0.4 wt.%.

Compositions of amphibole are given in **Supplementary Table 3**. All analyzed amphibole grains can be classified as magnesiohornblende (**Figure 6B**). For samples of the intermediate suite, amphibole displays relatively restricted variations in TiO_2 (∼1.2–2.4 wt.%), CaO (∼10.6–11.8 wt.%), and Na_2O (∼1.4–2.0 wt.%). In contrast, its Al_2O_3 (∼6.6–10.4 wt.%), FeO_T (∼11.0–16.6 wt.%), and MgO (∼11.7–15.0 wt.%) vary over a range of several weight percent. Magnesium number of the amphibole ranges from about 67 to 81, showing no correlations with the above major elements. For samples of the felsic suite, amphibole is characterized by relatively high SiO_2 (∼48.2–48.5 wt.%), and relatively low TiO_2 (∼0.7–1.1 wt.%), Al_2O_3 (∼4.0–6.5 wt.%), and Na_2O (∼0.8–1.3 wt.%). Yet, amphibole in both intermediate and felsic suites have overlapping ranges in Mg# (**Figure 6B**).

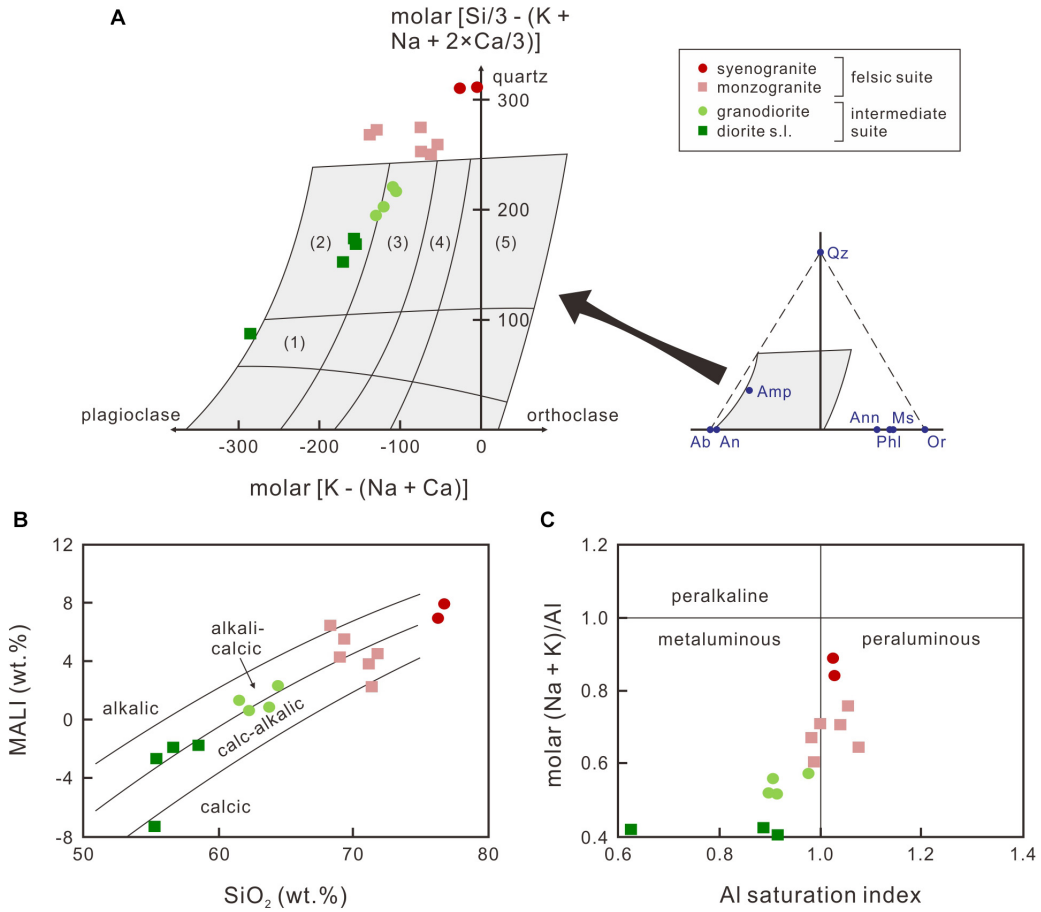

FIGURE 4 | Geochemical classification for the studied samples. **(A)** The P-Q diagram based on millications (Debon and Le Fort, 1988). Fields for selected rock types are after Bonin et al. (2020), including: (1) quartz diorite, (2) tonalite, (3) granodiorite, (4) monzogranite, (5) granite and syenogranite. **(B)** Covariation of MALI and SiO_2. Solid lines separating different series are after Frost et al. (2001). **(C)** Covariation of molar (Na + K)/Al and aluminum saturation index.

Whole-Rock Geochemistry

The studied samples have variable SiO_2 contents from ~55 to ~76 wt.% in the following order: diorite *sensu lato* < granodiorite < monzogranite < syenogranite (**Table 1**). As shown in **Figure 7**, the studied samples display continuous trends in the Harker diagrams. Most major elements, including TiO_2, Al_2O_3, Fe_2O_{3T}, MgO, CaO and P_2O_5, decrease with increasing SiO_2 (**Figures 7A–F**). The combined concentrations of Na_2O and K_2O show an increasing trend with SiO_2 (**Figure 7G**), excluding two monzogranites with low K_2O contents (samples E-14-1 and B-2, **Table 1**). The above trends are consistent with fractionation of ferromagnesian silicates, plagioclase, Fe-Ti oxides (and/or titanite) and apatite in generating the major element variations. Covariations of minor or trace elements and SiO_2 provide additional clues into the probable fractionated phase(s). Decreasing trends of V and Sr with increasing SiO_2 (**Figures 8A,B**) are consistent with fractionation of Fe-Ti oxides and plagioclase. Yttrium increases with SiO_2 in the intermediate suite and plummets in the felsic suite (**Figure 8C**), suggesting Y-bearing accessory minerals such as xenotime might have started to fractionate from the magma at a late stage of differentiation. Zirconium exhibits a similar trend as Y (**Figure 8D**), consistent with zircon fractionation. Niobium, La and Th display increasing trends with SiO_2 (**Figures 8E–G**), suggesting that these elements, like Na and K, are incompatible during the entire course of magma differentiation.

Trace element patterns shown on primitive mantle-normalized diagrams for the intermediate suite (**Figure 9A**) have the following features: (i) enrichment of large-ion-lithophile elements (LILE) in the order of 30 to 100 times primitive mantle abundances, (ii) negative Nb-Ta-(Ti) anomalies relative to K and La, (iii) positive Pb anomaly, and (iv) limited fractionation between middle to heavy rare-earth elements (REEs). A diorite sample (sample I-9) has a different pattern compared with the above in having lower abundances of Rb, Ba, and K (**Figure 9B**). Generally, trace element patterns for the felsic suite share similar features as those for the intermediate suite (**Figure 9C**). Within the felsic suite, the syenogranites in particular have low abundances of Sr, P, Eu, Ti and the heavy REE compared with monzogranites, a feature presumably related to fractionation of feldspars, Fe-Ti oxides (and/or titanite) and apatite (**Figure 9C**). The two monzogranites showing low K_2O contents display

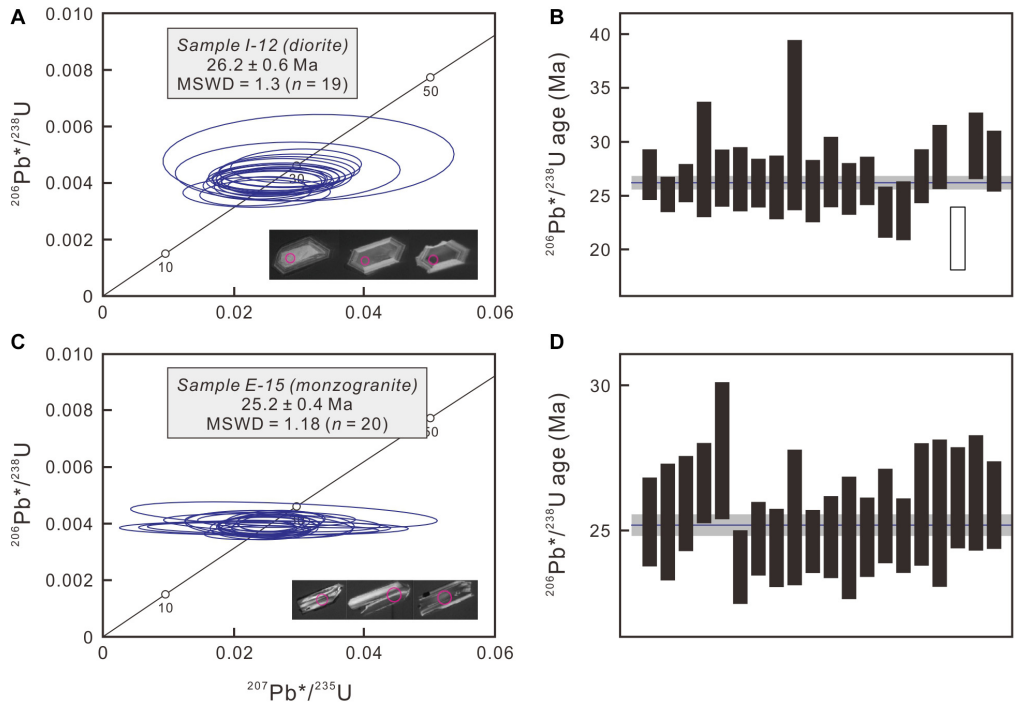

FIGURE 5 | Diagrams illustrating zircon U-Pb geochronologic results for two selected samples. **(A)** Wetherill concordia diagram and representative zircon CL images for sample I-12 (diorite). **(B)** $^{206}Pb^*/^{238}U$ age for individual spot analysis for sample I-12 (diorite). **(C)** Wetherill concordia diagram and representative zircon CL images for sample E-15 (monzogranite). **(D)** $^{206}Pb^*/^{238}U$ age for individual spot analysis for sample E-15 (monzogranite). Red circles on CL images denote analyzed spots of 20 μm. The diagrams are generated by IsoplotR (Vermeesch, 2018). Asterisk denotes correction for unradiogenic lead by isochron regression by the Ludwig (1998) algorithm. In frames **(B,D)**, filled bars denote analyses used for mean age calculation and empty ones do not.

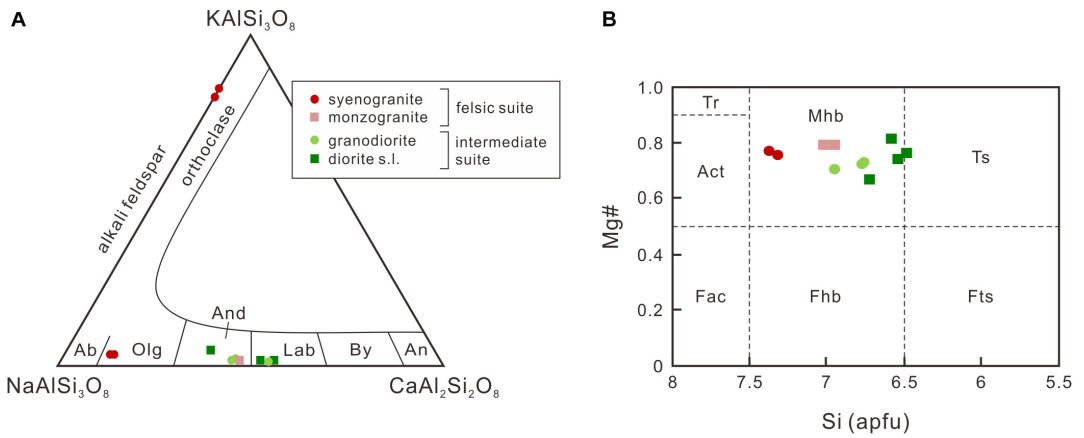

FIGURE 6 | Compositions of plagioclase and amphibole in a subset of the selected samples. **(A)** $KAlSi_3O_8$–$NaAlSi_3O_8$–$CaAl_2Si_2O_8$ ternary diagram for feldspars. **(B)** Mg# versus Si binary diagram for amphibole (after Leake et al., 1997). Mineral abbreviations are used after Whitney and Evans (2010), except for minerals that have no recommended abbreviations: Ab = albite, Act = actinolite, An = anorthite, And = andesine, By = bytownite, Fac = ferroactinolite, Fhb = ferrohornblende, Fts = ferrotschermakite, Lab = labradorite, Mhb = magnesiohornblende, Olg = oligoclase, Tr = tremolite, Ts = Tschermakite.

relatively low abundances of Rb and Ba in trace element patterns (**Figure 9D**).

The Sr-Nd isotopic data for samples chosen for analysis show limited variability. In detail, $^{87}Sr/^{86}Sr$ ranges from 0.7054 to 0.7077, and $^{143}Nd/^{144}Nd$ ranges from 0.5125 to 0.5126 (**Table 2**). After age correction to 25 Ma, the isotopic data plot in the lower right quadrant of a Sr-Nd isotope space characteristic of high time-integrated Rb/Sr and low time-integrated Sm/Nd relative to Bulk Silicate Earth (BSE) (**Figure 10A**). Using equations of Ickert (2013), the maximum errors propagated for the calculation of initial isotopic ratios are estimated to be ± 0.0005 for $(^{87}Sr/^{86}Sr)_{25Ma}$ and ± 0.30 for εNd_{25Ma}.

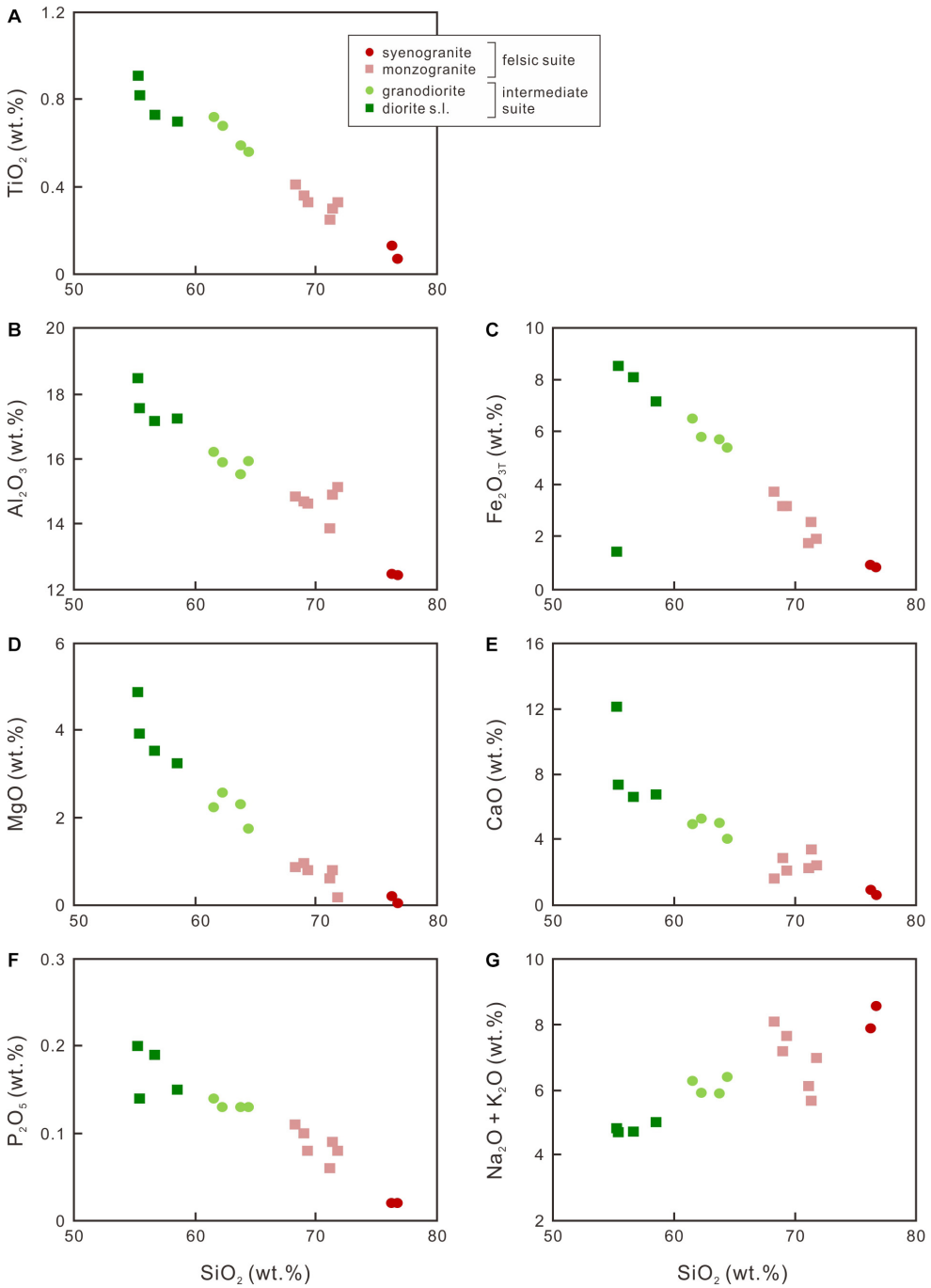

FIGURE 7 | Harker diagrams showing the variations of major element oxides against silica for the studied samples. **(A)** TiO_2; **(B)** Al_2O_3; **(C)** Fe_2O_{3T}; **(D)** MgO; **(E)** CaO; **(F)** P_2O_5; **(G)** $Na_2O + K_2O$.

Generally, the Sr and Nd isotopic ratios are negatively correlated except a syenogranite (sample B-12) having lower $^{87}Sr/^{86}Sr$ than expected. A probable reason is that the Sr isotopic ratio of this sample is over-corrected due to post-magmatic Rb-gain or Sr-loss, consistent with its high Rb/Sr (∼1.5). Besides, there exists a negative correlation between Nd isotopic ratios and SiO_2 concentration (**Figure 10B**).

DISCUSSION

Depth of Magma Emplacement

We estimate the crustal level at which the Takht batholith was emplaced using the aluminum-in-hornblende geobarometer (Hammarstrom and Zen, 1986), a tool which was widely applied to calc-alkaline intrusive rocks (Putirka, 2016 and references

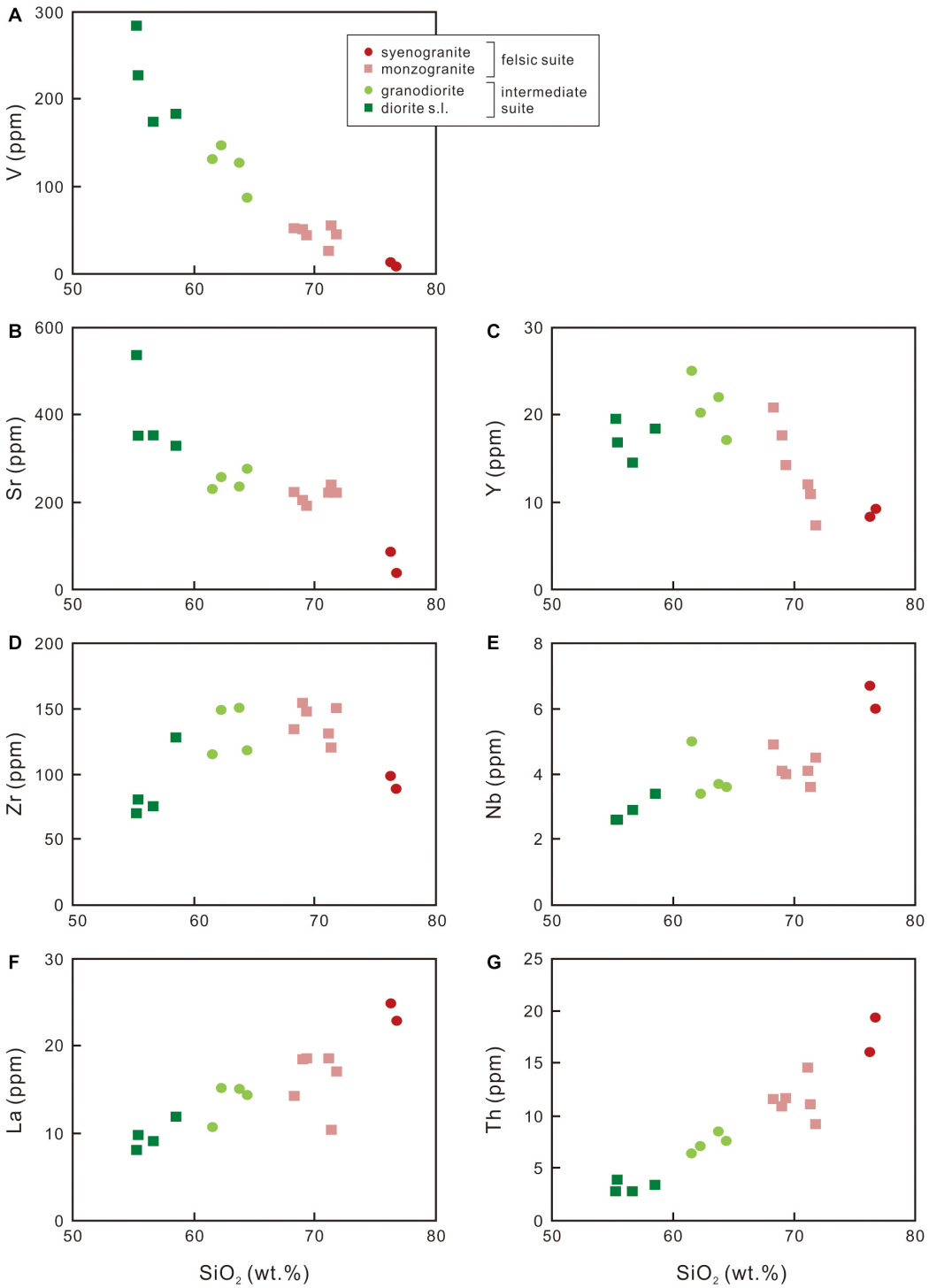

FIGURE 8 | Variations of minor or trace elements against silica for the studied samples. **(A)** V; **(B)** Sr; **(C)** Y; **(D)** Zr; **(E)** Nb; **(F)** La; **(G)** Th.

therein). Since its original formulation, the geobarometer was calibrated by various researchers including Hollister et al. (1987); Johnson and Rutherford (1989), Blundy and Holland (1990), Schmidt (1992), among many others. For most hornblende compositions obtained in this study (**Supplementary Table 3**), these calibrations yield pressure estimates between 1.3 and 5.5 kbar, with a spread of ∼1–1.5 kbar for a given hornblende analysis using different calibrations. Generally, the median of pressure resulted from different calibrations appears to follow the order: diorite *sensu lato* (∼2.7–5.1 kbar), granodiorite (∼1.8 kbar),

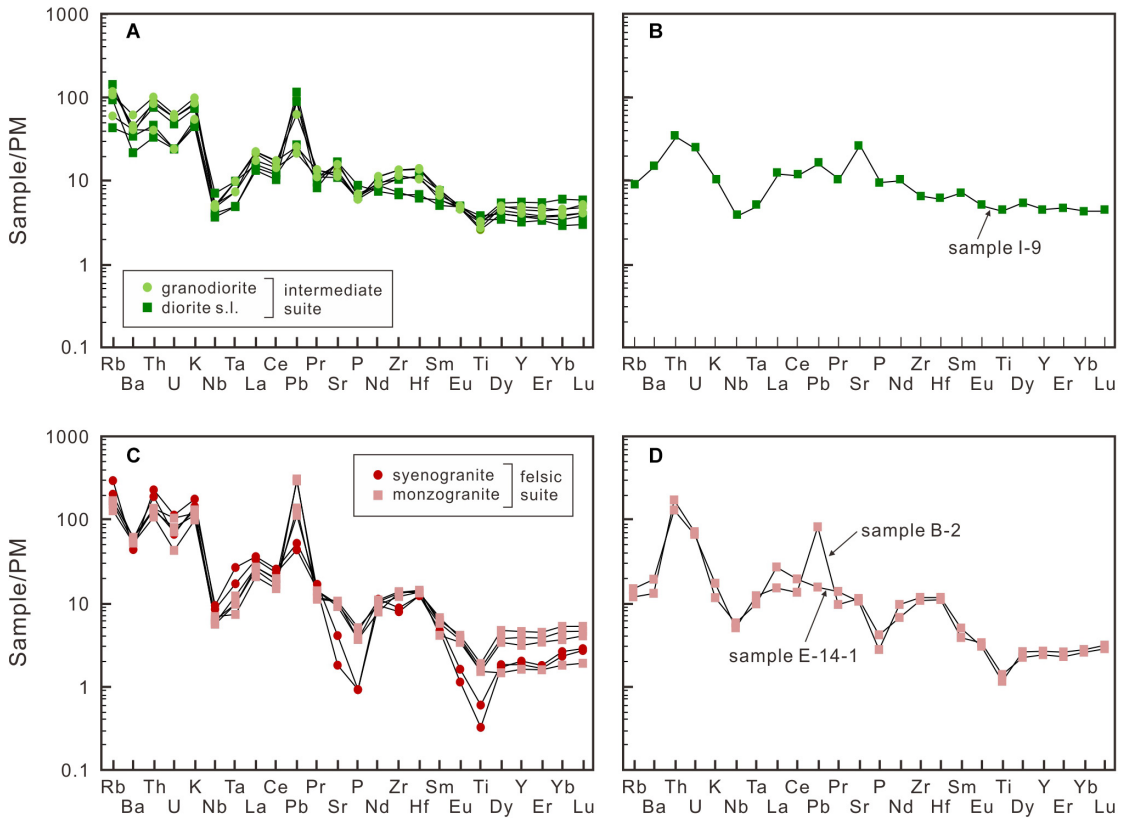

FIGURE 9 | Primitive mantle-normalized extended trace element patterns for the studied samples. **(A)** Intermediate suite. **(B)** A diorite (sample I-9) showing a different pattern from other samples of the intermediate suite. **(C)** Felsic suite. **(D)** Two monzogranites (samples E-14-1 and B-2) showing different patterns from other samples of the felsic suite. Normalizing values are after Sun and McDonough (1989).

and monzogranite (∼1.5 kbar). Given the maximum distance between the mafic and felsic units in the field (**Figure 1**), however, it is unlikely that the entire pressure range reflects magma solidification at different paleo-depths. Instead, it is more likely that hornblende in the diorites might have formed at mid-crustal levels and were entrained by magma(s) that ascent and eventually froze at the final emplacement depth. If that is the case, the final emplacement of the Takht batholith might occur at 2 kbar or less, equivalent to about 6.5 km or shallower paleo-depths, an estimate close to the lower bound of ∼5–10 km made by Fazlnia et al. (2014).

Petrogenetic Constraints

It is important to evaluate the effect of alteration on the geochemical data obtained in this study, for some of these data are used to derive constraints related to magma genesis at high temperature. Petrographic observations indicate that most studied samples are essentially fresh with little or no signs of post-magmatic alteration (**Figure 3**). Almost all samples have LOI lower than 2 wt.% (**Table 1**), except in a monzogranite (sample E-14-1) where higher LOI (∼3.8 wt.%) might be due to partial alteration of plagioclase to sericite as observed in thin section. Further, the trace element patterns for most studied samples are coherent (**Figures 9A,C**), suggesting mobilization of particular trace elements, as would be expected for extensive post-magmatic alteration, did not occur.

Sample I-9, a diorite as mentioned above, requires a special note because of its unusual major and trace element features. It has low Fe_2O_3 (∼1.4 wt.%), high CaO (∼12.1 wt.%) compared with other diorites (**Figures 7C,E**). Also, its trace element pattern is different from other diorites in showing low abundances of Rb, Ba, and K (**Figure 9B**). After a detailed petrographic check, we note several unique features: (i) a high content of plagioclase compared with the other diorites, (ii) plagioclase occurs as a framework of coarse grained crystals commonly observed in cumulates (**Figure 3C**), and (iii) the rare presence of hornblende and absent of biotite. Based on these observations, we suggest the unusual geochemical features of sample I-9 might be related to its probable origin as a plagioclase-rich cumulate.

Next, we examine probable processes responsible for generating the geochemical variations observed in the studied samples. As noted earlier, the elemental trends shown by the samples are consistent with fractionation of ferromagnesian silicates, plagioclase, Fe-Ti oxides (and/or titanite) and apatite, presumably with zircon and/or xenotime joining the fractionating assemblage at a late stage (**Figures 7**, **8**). Fractionation in a closed system, however, cannot explain the

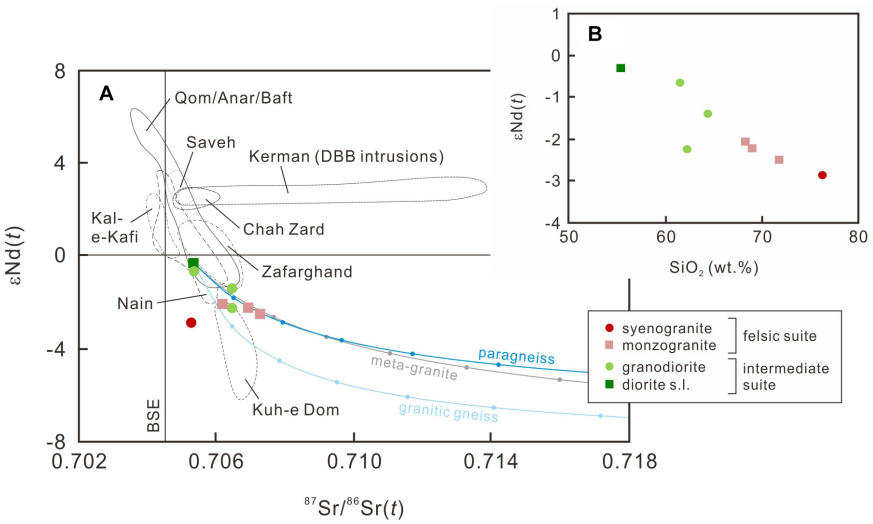

FIGURE 10 | Covariations involving Sr and Nd isotopes for the studied samples. **(A)** A binary diagram of εNd versus $^{87}Sr/^{86}Sr$. **(B)** A binary diagram of εNd versus SiO_2. Shown in frame **(A)** are fields of published data obtained from the Urumieh-Dokhtar belt, including Qom/Anar/Baft (Omrani et al., 2008), Kerman (DBB intrusions, Dargahi et al., 2010), Nain (Yeganehfar et al., 2013), Kuh-e Dom (Sarjoughian et al., 2012; Kananian et al., 2014), Kal-e-Kafi (Ahmadian et al., 2016), Chah Zard (Kouhestani et al., 2017), Saveh (Nouri et al., 2018), and Zafarghand (Sarjoughian et al., 2018). Also shown are AFC trajectories assuming sample I-10, which has the lowest $^{87}Sr/^{86}Sr_{25Ma}$ and εNd_{25Ma} among the studied samples, underwent concurrent fractional crystallization and assimilation of different crustal rocks from the ChahJam-Biarjmand metamorphic complex, Iran (Shafaii Moghadam et al., 2015): metagranite (sample BJ10-20, gray), paragneiss (sample CHJ09-12, deep blue), and granitic gneiss (sample CHJ09-18, light blue). The trajectories are computed using equations of DePaolo (1981) with the following parameters: crystal-liquid partition coefficients of Sr (2 for plagioclase, 0.096 for clinopyroxene, and 0.0022 for olivine) and Nd (0.14 for plagioclase, 0.173 for clinopyroxene, and 0.001 for olivine) [compiled by Ersoy and Helvacı (2010)], a fractionating assemblage consisting of plagioclase, clinopyroxene and olivine at 6:2:2, and a ratio of assimilation rate to fractional crystallization rate of 0.5. Dots on the trajectories denote 10% intervals for the fraction of remaining liquid.

negative correlation between Nd isotopes and SiO_2 (**Figure 10B**). The trend appears to require increasing contribution of isotopically enriched materials to the magma as it became more differentiated. To model the process, we calculate assimilation–fractional crystallization (AFC) trajectories using data from the ChahJam-Biarjmand metamorphic complex, which was exhumed from and likely representative of the lower to middle crust of Iran (Shafaii Moghadam et al., 2015). Three major rock types in that study are used as end-member assimilants, including a metagranite, a paragneiss and a granitic gneiss. As shown in **Figure 10A**, the least evolved diorite would have undergone ∼10–15% AFC to explain the observed Sr-Nd isotopic variations. We then explore whether the intermediate and felsic units of the Takht batholith satisfy mass balance by undertaking energy-constrained (EC)-AFC simulations (Bohrson and Spera, 2001; Spera and Bohrson, 2001) with similar compositional parameters for the initial magma and the assimilants as the classical AFC models presented above (**Supplementary Table 5**). The results indicate that, for all three assimilants, the initial dioritic magma would have undergone ∼42% differentiation (mainly by fractional crystallization) before being able to form rocks with Sr-Nd isotopes observed in the felsic unit due to significant addition of anatectic melt from the wallrocks. Also, the mass ratios of the intermediate unit to the felsic unit predicted by these models range from 6:1 to 9:1 (**Supplementary Table 6**). Thus, it appears that the current exposure of these units (65 to 35%, ∼2:1) requires a considerable amount of dioritic rocks be hidden at a deeper level of the batholith. Another possibility is that mechanisms apart from AFC might have played a role in the formation of the felsic suite, such as crustal melting, which is discussed below.

We then consider additional magmatic processes such as mingling or mixing of magmas, which is hinted by field observations (**Figures 2A,B**) and complex zoning seen from plagioclase in diorites (**Supplementary Figures S1–S3**), even though available data point to a coherent age of ∼25 Ma for the batholith (**Figure 5** and Hosseini et al., 2017a). As magma mixing generates linear trends shown by covariation of elements and isotopes, one could argue that, for example, granodiorites and monzogranites are solidified products of mixing between dioritic and syenogranitic magmas (**Figures 7, 8**). However, mixing alone is hard to explain the kinked trends of Y or Zr versus SiO_2 (**Figures 8C,D**), which appear to record fractionation of accessory minerals such as xenotime and zircon (Förster, 1998; Lee and Bachmann, 2014). Another possibility is that differences in rock types are results of melting heterogeneous source rocks in the crust with limited mixing of the resultant magmas. That has to imply that not only the kinked trends note above but also the εNd_{25Ma}–SiO_2 trend (**Figure 10A**) are fortuitous. If heterogeneous source rocks were to be melted in the crust, however, scattered data in terms of Sr-Nd isotopes and SiO_2 seem to be more likely. Yet, melting heterogeneous source rocks might be responsible for second-order geochemical variations in the dataset. For example, differences in major and trace element geochemistry among the monzogranites might be related to source rocks with variable contents of K-bearing phases such as

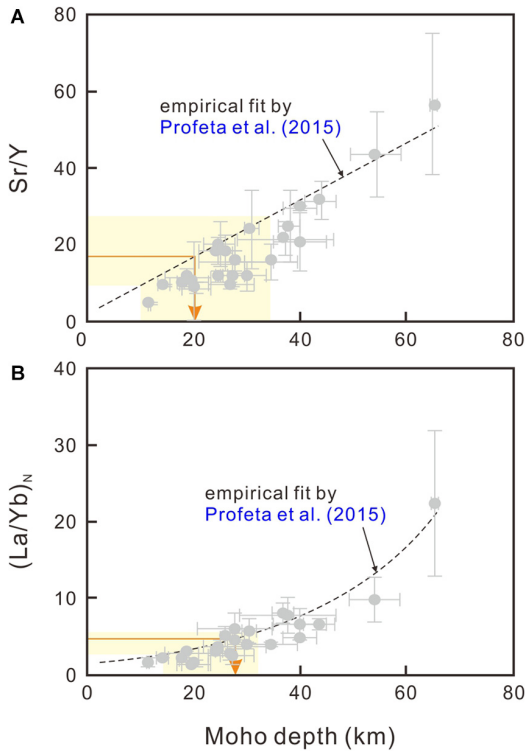

FIGURE 11 | Estimation of crustal thickness using Moho depth proxies **(A)** Sr/Y and **(B)** $(La/Yb)_N$ where subscript N denotes normalization against CI chondrite (Sun and McDonough, 1989). Dotted line denotes empirical fits of data for a given volcanic arc shown by gray symbols (Profeta et al., 2015). The yellow band and orange line denote the range and median, respectively, of data for the intermediate suite, which generally satisfy the filters proposed by Profeta et al. (2015) including ranges of SiO_2 (55–68 wt.%) and MgO (1–6 wt.%). If data for monzogranites are included, the median for Sr/Y remains unchanged (~17) while that for $(La/Yb)_N$ is slightly higher (~6.9).

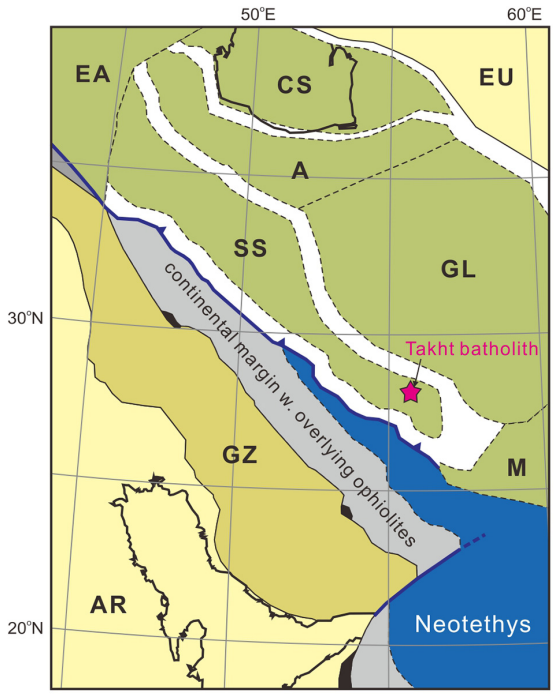

FIGURE 12 | Paleogeographic reconstruction of the Arabia–Eurasia collision zone at ~27 Ma (McQuarrie and van Hinsbergen, 2013). Gray regions denote the northeastern margin of Arabia with overlying ophiolites (shown in black, including Kermanshah, Neyriz and Semail from north to south). White regions denote areas that were shortened among continental blocks situated between Eurasia and Arabia. Red star denotes the location where the Takht batholith might have formed. A = Alborz, AR = Arabia, EA = East Anatolia, EU = Eurasia, GL = Greater Lut, GZ = Greater Zagros, M = Makran, SC = South Caspian, SS = Sanandaj-Sirjan.

biotite, muscovite and orthoclase (**Figures 9C,D**). Also, the Sr-Nd isotopic composition of the syenogranite hints derivation from source rocks that are probably different from the monzogranites (**Figure 10A**). In summary, we maintain that AFC exerts the dominant control of the geochemical variations observed from the samples, while processes such as mingling and mixing of magmas, and melting of heterogeneous source rocks, cannot be completed excluded.

Next, we examine the origin of the diorite *sensu lato*, the arguably least evolved rock type in the Takht batholith. As a group it has the highest MgO (~3.5–4.9 wt.%), the lowest SiO_2 (~55.3–56.7 wt.%) and, relative to BSE, the least unradiogenic Nd isotopes and the least radiogenic Sr isotopes (**Figure 10A**). Hosseini et al. (2017a) analyzed a range of igneous rocks related to the Takht-e-Gonbad deposit and their dataset includes a sample with basaltic composition (i.e., sample TAM12 with ~6 wt.% MgO and ~49 wt.% SiO_2). However, that sample belongs to Eocene volcanic/volcaniclastic rocks, which were intruded by Oligocene and Miocene igneous rocks. Thus, there is no direct evidence for magmas that are more primitive than the studied diorites in the formation of the ~25 Ma Takht batholith. If our inference for an intermediate parental magma is correct, then two possible origins apply. First, it might be a residual liquid of a mantle-derived magma that had undergone differentiation prior to emplacement. This explains the general lack of mafic-ultramafic rocks at the current exposure. Second, the intermediate parental magma might have a lower crustal origin. Blatter et al. (2013) demonstrated by melting experiments that intermediate magmas with similar MgO and SiO_2 as the studied diorites could form by partial melting of hydrous arc basalts over a wide range of oxygen fugacity at lower crustal pressure. Importantly, hybrid mechanisms involving a combination of the two end-member scenarios are also permissive; for instance, mixing of lower crustal melts and variably fractionated mantle-derived magmas in zones of melting, assimilation, storage and homogenization (MASH) close to the Moho (e.g., Hildreth and Moorbath, 1988), or lower crustal hot zones (Annen et al., 2006).

Tectonic Implications

As illustrated above, the Takht batholith possesses typical subduction-related geochemical signatures (**Figure 9**). A straightforward explanation for these is that the Takht batholith formed in a subduction zone, an interpretation mostly

adapted in earlier studies (Shahabpour, 2005, 2007; Shafiei et al., 2009; Mohajjel and Fergusson, 2014; Shafaii Moghadam et al., 2015; Rasouli et al., 2016). Another possibility is that the batholith formed in a setting without active subduction, for example, where subduction-modified domains of the mantle lithosphere and/or the lower crust were perturbed by processes unrelated directly to subduction (e.g., upwelling of the asthenosphere). If that is the case, variable magma types and chemistry (e.g., alkalinity, trace elements, and radiogenic isotopes) is expected because of the variety of source rocks that might be involved and the range of depths where partial melting might occur. In this study, however, we do not observe such variations and the geochemical data illustrated above are consistent in most aspects with arc magmas. Therefore, it is appropriate to consider the Takht batholith as a Cordilleran-type batholith, forming as part of a continental arc in the Late Oligocene at ∼25 Ma.

Our inference that the Takht batholith is of Cordilleran-type sheds indirect lights on how Arabia and Eurasia might have collided. Available data in northwestern Iran and southern Lesser Caucasus indicate that Late Oligocene magmatic rocks show geochemical features characteristic of formation over relatively thick crust, such as relatively high Sr/Y and La/Yb (Moritz et al., 2016; Rezeau et al., 2016, 2017). In view of growing evidence suggesting that the Arabia–Eurasia collision initiated between the Late Eocene and the Early Oligocene (Allen and Armstrong, 2008; Mouthereau et al., 2012; McQuarrie and van Hinsbergen, 2013; Gholami Zadeh et al., 2017; Koshnaw et al., 2018), these features have been interpreted in the context of collision-induced crustal thickening (e.g., Moritz et al., 2016). We note that none of the rocks in this study display such geochemical features. For instance, the ranges of Sr/Y and $(La/Yb)_N$ of these rocks could be used to indicate modest crustal thickness, probably between 20 and 30 km (**Figure 11**). Here, an intriguing question is, at a given time, how the Takht batholith with an inferred arc origin can be reconciled in a tectonic setting where continental collision appeared to have started. One possibility is that collision did initiate in northwestern Iran and southern Lesser Caucasus, but not so to the southeast of the collision zone, where the Neotethys was still subducting beneath central Iran, as depicted by Chiu et al. (2013). This is consistent with paleogeographic reconstruction by McQuarrie and van Hinsbergen (2013) (**Figure 12**), and the view that post-collisional magmatism propagated from northwest to southeast along the Arabia–Eurasia collision zone (Pang et al., 2015; Lin et al., 2020). While we remain open to other possible tectonic scenarios that could explain the aforementioned spatial variations in magma composition, the simplest explanation hitherto appears to be diachronous collision.

CONCLUSION

A field, petrologic and geochemical study of the Late Oligocene Takht batholith, Iran yields the following conclusions:

- The batholith was solidified at ∼25 Ma and the depth of magma emplacement was likely 6.5 km or less. It consists mainly of intermediate to felsic rocks, showing subalkaline, dominantly metaluminous compositions and I-type affinity.
- The rocks display geochemical and Sr-Nd isotopic variations consistent with concurrent fractional crystallization and assimilation of lower to middle crustal rocks.
- The least evolved magma indicated by the data has intermediate composition, and might represent a differentiated liquid of a mantle-derived magma, or a partial melt of the lower crust, or any combination between them as predicted by models involving MASH or lower crustal hot zones.
- The batholith is most likely of Cordilleran-type related to northward subduction of the Neotethys. In the context of regional tectonics, the paleogeographic position of the batholith can be reconciled if Arabia and Eurasia have been colliding in a diachronous manner since the Late Eocene–Early Oligocene.

DATA AVAILABILITY STATEMENT

The original contributions presented in the study are included in the article/**Supplementary Material**, further inquiries can be directed to the corresponding authors.

AUTHOR CONTRIBUTIONS

K-NP analyzed the data and wrote the manuscript. AF designed the study, participated in field work, and analyzed the data. W-QJ obtained zircon U-Pb isotopic data and analyzed the data. SJ and AJ participated in field work. All authors contributed to the article and approved the submitted version.

FUNDING

Financial support from Urmia University (Iran), Ministry of Science and Technology, Taiwan, China (105-2628-M-001-002-MY4 to K-NP), and Career Development Award, Academia Sinica (AS-CDA-109-M07 to K-NP) are acknowledged.

ACKNOWLEDGMENTS

The authors thank the reviewers for comments and suggestions, improving the presentation of many arguments. The authors also thank P. R. Castillo for editorial handling.

SUPPLEMENTARY MATERIAL

The Supplementary Material for this article can be found online at: https://www.frontiersin.org/articles/10.3389/feart.2020.00354/full#supplementary-material

REFERENCES

Aftabi, A., and Atapour, H. (2000). Regional aspects of shoshonitic volcanism in Iran. *Episodes* 23, 119–125.

Ahmadian, J., Sarjoughian, F., Lentz, D., Esna-Ashari, A., Murata, M., and Ozawa, H. (2016). Eocene K-rich adakitic rocks in the Central Iran: implications for evaluating its Cu–Au–Mo metallogenic potential. *Ore Geol. Rev.* 72, 323–342. doi: 10.1016/j.oregeorev.2015.07.017

Alavi, M. (1994). Tectonic of the Zagros orogenic belt of Iran: new data and interpretations. *Tectonophysics* 229, 211–238. doi: 10.1016/0040-1951(94)90030-2

Aldanmaz, E., Pearce, J. A., Thirlwall, M. F., and Mitchell, J. G. (2000). Petrogenetic evolution of late Cenozoic, post-collision volcanism in western Anatolia, Turkey. *J. Volcanol. Geotherm. Res.* 102, 67–95. doi: 10.1016/s0377-0273(00)00182-7

Allen, M. B., and Armstrong, H. A. (2008). Arabia-Eurasia collision and the forcing of mid-Cenozoic global cooling. *Palaeogeogr. Palaeoclimatol. Palaeoecol.* 265, 52–58. doi: 10.1016/j.palaeo.2008.04.021

Annen, C., Blundy, J. D., and Sparks, R. S. J. (2006). The genesis of intermediate and silicic magmas in deep crustal hot zones. *J. Petrol.* 47, 505–539. doi: 10.1093/petrology/egi084

Babazadeh, S., Ghorbani, M. R., Bröcker, M., D'Antonio, M., Cottle, J., Gebbing, T., et al. (2017). Late oligocene–miocene mantle upwelling and interaction inferred from mantle signatures in gabbroic to granitic rocks from the Urumieh–Dokhtar arc, south Ardestan, Iran. *Int. Geol. Rev.* 59, 1590–1608. doi: 10.1080/00206814.2017.1286613

Berberian, F., and Berberian, M. (1981). Tectono-plutonic episodes in Iran. *Geol. Surv. Iran Rep.* 52, 566–593.

Berberian, M., and King, G. C. P. (1981). Towards a paleogeography and tectonic evolution of Iran. *Can. J. Earth Sci.* 18, 210–265. doi: 10.1139/e81-019

Blatter, D. L., Sisson, T. W., and Hankins, W. B. (2013). Crystallization of oxidized, moderately hydrous arc basalt at mid- to lower-crustal pressures: implications for andesite genesis. *Contrib. Mineral. Petrol.* 166, 861–886. doi: 10.1007/s00410-013-0920-3

Blundy, J. D., and Holland, T. J. B. (1990). Calcic amphibole equilibria and a new amphibole-plagioclase geothermometer. *Contrib. Mineral. Petrol.* 104, 208–224. doi: 10.1007/bf00306444

Bohrson, W. A., and Spera, F. J. (2001). Energy-constrained open-system magmatic processes II: application of energy-constrained assimilation–fractional crystallization (EC-AFC) model to magmatic systems. *J. Petrol.* 42, 1019–1041. doi: 10.1093/petrology/42.5.1019

Bonin, B., Janoušek, V., and Moyen, J.-F. (2020). Chemical variation, modal composition and classification of granitoids. *Geol. Soc. Lond. Spec. Publ.* 491, 9–51. doi: 10.1144/sp491-2019-138

Cawood, P. A., Hawkesworth, C. J., and Dhuime, B. (2013). The continental record and the generation of continental crust. *Geol. Soc. Am. Bull.* 125, 14–32. doi: 10.1130/b30722.1

Chapman, J. B., Ducea, M. N., DeCelles, P. G., and Profeta, L. (2015). Tracking changes in crustal thickness during orogenic evolution with Sr/Y: an example from the North American Cordillera. *Geology* 43, 919–922. doi: 10.1130/g36996.1

Chappell, B. W., and White, A. J. R. (1974). Two contrasting granite types. *Pac. Geol.* 8, 173–174.

Chiu, H.-Y., Chung, S.-L., Zarrinkoub, M. H., Mohammadi, S. S., Khatib, M. M., and Iizuka, I. (2013). Zircon U-Pb age constraints from Iran on the magmatic evolution related to Neotethyan subduction and Zagros orogeny. *Lithos* 162-163, 70–87. doi: 10.1016/j.lithos.2013.01.006

Chung, S.-L., Liu, D., Ji, J., Chu, M.-F., Lee, H.-Y., Wen, D.-J., et al. (2003). Adakites from continental collision zones: melting of thickened lower crust beneath southern Tibet. *Geology* 31, 1021–1024.

Corfu, F. (2013). A century of U-Pb geochronology: the long quest towards concordance. *Geol. Soc. Am. Bull.* 125, 33–47. doi: 10.1130/b30698.1

Dargahi, S. (2007). *Post-Collisional Miocene Magmatism in the Sarcheshmeh-Shahrebabak Region NW of Kerman: Isotopic Study, Petrogenetic Analysis and Geodynamic Pattern of Granitoid Intrusives and the Role of Adakitic Magmatism in Development of Copper Mineralization*. PhD thesis. Kerman: Shahid Bahonar University of Kerman.

Dargahi, S., Arvin, M., Pan, Y., and Babaei, A. (2010). Petrogenesis of Post-collisional A-type granitoid from the Urumieh-Dokhtar magmatic assemblage, Southwestern Kerman, Iran: constraints on the Arabian-Eurasian continental collision. *Lithos* 115, 190–204. doi: 10.1016/j.lithos.2009.12.002

Debon, F., and Le Fort, P. (1988). A cationic classification of common plutonic rocks and their magmatic associations: principles, method, applications. *Bull. Minéral.* 111, 493–510. doi: 10.3406/bulmi.1988.8096

DePaolo, D. J. (1981). Trace element and isotopic effects of combined wallrock assimilation and fractional crystallization. *Earth Planet. Sci. Lett.* 53, 189–202. doi: 10.1016/0012-821x(81)90153-9

Dimitrijevic, M. D. (1973). *Geology of the Kerman Region. Report* 52. Tehran: Geological Survey of Iran.

Ducea, M. N., Saleeby, J. B., and Bergantz, G. (2015). The architecture, chemistry, and evolution of continental magmatic arcs. *Annu. Rev. Earth Planet. Sci.* 43, 299–331. doi: 10.1146/annurev-earth-060614-105049

Ersoy, Y., and Helvacı, C. (2010). FC–AFC–FCA and mixing modeler: a Microsoft® Excel© spreadsheet program for modeling geochemical differentiation of magma by crystal fractionation, crustal assimilation and mixing. *Comput. Geosci.* 36, 383–390. doi: 10.1016/j.cageo.2009.06.007

Faure, G., and Mensing, T. M. (2005). *Isotopes: Principles and Applications*. Hoboken, NJ: John Wiley and Sons, 897.

Fazlnia, A. (2019). Petrogenesis and tectonic significance of Sardasht syenite–monzonite–gabbro–appinite intrusions, NW Iran. *Int. J. Earth Sci.* 108, 49–66. doi: 10.1007/s00531-018-1641-7

Fazlnia, A. N., Jamei, S., and Jafari, A. (2014). Penetrative conditions and tectonomagmatic setting of the Takht granitic batholith, Sirjan. *Petrology* 5, 33–50.

Förster, H.-J. (1998). The chemical composition of REE-Y-Th-U-rich accessory minerals in peraluminous granites of the Erzgebirge-Fichtelgebirge region, Germany. Part II: xenotime. *Am. Mineral.* 83, 1302–1315. doi: 10.2138/am-1998-11-1219

Frost, B. R., Barnes, C. G., Collins, W. J., Arculus, R. J., Ellis, D. J., and Frost, C. D. (2001). A geochemical classification for granitic rocks. *J. Petrol.* 42, 2033–2048. doi: 10.1093/petrology/42.11.2033

Gholami Zadeh, P., Adabi, M. H., Hisada, K.-I., Hosseini-Barzi, M., Sadeghi, A., and Ghassemi, M. R. (2017). Revised version of the Cenozoic collision along the Zagros Orogen, insights from Cr-spinel and sandstone modal analyses. *Sci. Rep.* 7:10828.

Goss, A. R., Kay, S. M., and Mpodozis, C. (2013). Andean adakite-like high-Mg andesites on the northern margin of the Chilean–Pampean flat-slab (27–28.5°S) associated with frontal arc migration and fore-arc subduction erosion. *J. Petrol.* 54, 2193–2234. doi: 10.1093/petrology/egt044

Hammarstrom, J. M., and Zen, E. (1986). Aluminum in hornblende: an empirical igneous geobarometer. *Am. Mineral.* 71, 1297–1313.

Hassanzadeh, J. (1993). *Metallogenic and Tectono-Magmatic Events in the SE Sector of the Cenozoic Active Continental Margin of Iran (Shahr-e-Babak area, Kerman province)*. Ph.D. thesis. Los Angeles, CA: University of California.

Hassanzadeh, J., and Wernicke, B. P. (2016). The Neotethyan Sanandaj-Sirjan zone of Iran as an archetype for passive margin-arc transitions. *Tectonics* 35, 586–621. doi: 10.1002/2015tc003926

Hawkesworth, C. J., Cawood, P. A., Dhuime, B., and Kemp, T. I. S. (2017). Earth's continental lithosphere through time. *Annu. Rev. Earth Planet. Sci.* 45, 169–198. doi: 10.1146/annurev-earth-063016-020525

Hildreth, W., and Moorbath, S. (1988). Crustal contributions to arc magmatism in the Andes of Central Chile. *Contrib. Mineral. Petrol.* 98, 455–489. doi: 10.1007/bf00372365

Hollister, L. S., Grisson, G. C., Peters, E. K., Stowell, H. H., and Sisson, V. B. (1987). Confirmation of the empirical correlation of Al in hornblende with pressure of solidification of calc-alkaline plutons. *Am. Mineral.* 72, 231–239.

Honarmand, M., Rashidnejad Omran, N., Corfu, F., Hashem Emami, M., and Nabatian, G. (2013). Geochronology and magmatic history of a calc-alkaline plutonic complex in the Urumieh-Dokhtar Magmatic Belt, Central Iran: zircon ages as evidence for two major plutonic episodes. *Neues Jahrbuch für Mineral.* 190, 67–77. doi: 10.1127/0077-7757/2013/0230

Honarmand, M., Rashidnejad Omran, N., Neubauer, F., Nabatian, G., Hashem Emami, M., Bernroider, M., et al. (2016). Mineral chemistry of a Cenozoic igneous complex, the Urumieh-Dokhtar magmatic belt, Iran: petrological

implications for the plutonic rocks. *Island Arc* 25, 137–153. doi: 10.1111/iar.12148

Hosseini, M. R., Ghaderi, M., Alirezaei, S., and Sun, W. (2017a). Geological characteristics and geochronology of the Takht-e-Gonbad copper deposit, SE Iran: a variant of porphyry type deposits. *Ore Geol. Rev.* 86, 440–458. doi: 10.1016/j.oregeorev.2017.03.003

Hosseini, M. R., Hassanzadeh, J., Alirezaei, S., Sun, W., and Li, C.-Y. (2017b). Age revision of the neotethyan arc migration into the southeast Urumieh-Dokhtar belt of Iran: geochemistry and U-Pb zircon geochronology. *Lithos* 284-285, 296–309. doi: 10.1016/j.lithos.2017.03.012

Hu, F., Ducea, M. N., Liu, S., and Chapman, J. B. (2017). Quantifying crustal thickness in continental collisional belts: global perspective and a geologic application. *Sci. Rep.* 7:7058.

Ickert, R. B. (2013). Algorithms for estimating uncertainties in initial radiogenic isotope ratios and model ages. *Chem. Geol.* 340, 131–138. doi: 10.1016/j.chemgeo.2013.01.001

Jagoutz, O., Macdonald, F. A., and Royden, L. (2016). Low-latitude arc–continent collision as a driver for global cooling. *Proc. Natl. Acad. Sci. U.S.A.* 113, 4935–4940. doi: 10.1073/pnas.1523667113

Ji, W.-Q., Wu, F.-Y., Liu, C.-Z., and Chung, S.-L. (2012). Early Eocene crustal thickening in southern Tibet: new age and geochemical constraints from the Gangdese batholith. *J. Asian Earth Sci.* 53, 82–95. doi: 10.1016/j.jseaes.2011.08.020

Ji, W.-Q., Wu, F.-Y., Wang, J.-M., Liu, X.-C., Liu, Z.-C., Zhang, Z., et al. (2020). Early evolution of himalayan orogenic belt and generation of middle eocene magmatism: constraint from Haweng granodiorite porphyry in the tethyan himalaya. *Front. Earth Sci.* 8:236. doi: 10.3389/feart.2020.00236

Johnson, M. C., and Rutherford, M. J. (1989). Experimental calibration of an aluminum-in-hornblende geobarometer applicable to Long Valley caldera (California) volcanic rocks. *Geology* 17, 837–841.

Kananian, A., Sarjoughian, F., Nadimi, A., Ahmadian, J., and Ling, W. (2014). Geochemical characteristics of the Kuh-e Dom intrusion, Urumieh–Dokhtar Magmatic Arc (Iran): implications for source regions and magmatic evolution. *J. Asian Earth Sci.* 90, 137–148. doi: 10.1016/j.jseaes.2014.04.026

Khan-Nazer, N. A., and Emami, H. (1996). *Geological Map of Chahar Gonbad (scale: 1:100000)*. Tehran: Geological Survey of Iran.

Koshnaw, R. I., Stockli, D. F., and Schlunegger, F. (2018). Timing of the Arabia-Eurasia continental collision – evidence from detrital zircon U-Pb geochronology of the Red Bed Series strata of the northwest Zagros hinterland, Kurdistan region of Iraq. *Geology* 47, 47–50. doi: 10.1130/g45499.1

Kouhestani, H., Ghaderi, M., Emami, M. H., Meffre, S., Kamenetsky, V., McPhie, J., et al. (2017). Compositional characteristics and geodynamic significance of late Miocene volcanic rocks associated with the Chah Zard epithermal gold–silver deposit, southwest Yazd, Iran. *Island Arc* 27:e12223. doi: 10.1111/iar.12223

Leake, B. E., Woolley, A. R., Arps, C. E. S., Birch, W. D., Gilbert, M. C., Grice, J. D., et al. (1997). Nomenclature of amphiboles; report of the subcommittee on amphiboles of the international mineralogical association, commission on new minerals and mineral names. *Am. Mineral.* 82, 1019–1037.

Lee, C.-T. A., and Bachmann, O. (2014). How important is the role of crystal fractionation in making intermediate magmas? Insights from Zr and P systematics. *Earth Planet. Sci. Lett.* 393, 266–274. doi: 10.1016/j.epsl.2014.02.044

Lin, Y.-C., Chung, S.-L., Bingöl, A. F., Yang, L., Okrostsvaridze, A., Pang, K.-N., et al. (2020). Diachronous initiation of post-collisional magmatism in the Arabia-Eurasia collision zone. *Lithos* 356-357, 105394. doi: 10.1016/j.lithos.2020.105394

Ludwig, K. R. (1998). On the treatment of concordant uranium-lead ages. *Geochim. Cosmochim. Acta* 62, 665–676. doi: 10.1016/s0016-7037(98)00059-3

McInnes, B. I. A., Evans, N. J., Fu, F. Q., and Garwin, S. (2005). Application of thermochronology to hydrothermal ore deposits. *Rev. Mineral. Geochem.* 58, 467–498. doi: 10.1515/9781501509575-020

McQuarrie, N., and van Hinsbergen, D. J. J. (2013). Retrodeforming the Arabia-Eurasia collision zone: age of collision versus magnitude of continental subduction. *Geology* 41, 315–318. doi: 10.1130/g33591.1

Mohajjel, M., and Fergusson, C. L. (2014). Jurassic to Cenozoic tectonics of the Zagros Orogen in northwestern Iran. *Int. Geol. Rev.* 56, 263–287. doi: 10.1080/00206814.2013.853919

Moritz, R., Rezeau, H., Ovtcharova, M., Tayan, R., Melkonyan, R., Hovakimyan, S., et al. (2016). Long-lived, stationary magmatism and pulsed porphyry systems during Tethyan subduction to post-collision evolution in the southernmost Lesser Caucasus, Armenia and Nakhitchevan. *Gondwana Res.* 37, 465–503. doi: 10.1016/j.gr.2015.10.009

Mouthereau, F., Lacombe, O., and Vergés, J. (2012). Building the Zagros collisional orogen: timing, strain distribution and the dynamics of Arabia/Eurasia plate convergence. *Tectonophysics* 532-535, 27–60. doi: 10.1016/j.tecto.2012.01.022

Moyen, J.-F., Laurent, O., Chelle-Michou, C., Couzinié, S., Vanderhaeghe, O., Zeh, A., et al. (2017). Collision vs. subduction-related magmatism: two contrasting ways of granite formation and implications for crustal growth. *Lithos* 277, 154–177. doi: 10.1016/j.lithos.2016.09.018

Nouri, F., Azizi, H., Stern, R. J., Asahara, Y., Khodaparast, S., Madanipour, S., et al. (2018). Zircon U-Pb dating, geochemistry and evolution of the Late Eocene Saveh magmatic complex, central Iran: partial melts of sub-continental lithospheric mantle and magmatic differentiation. *Lithos* 314-315, 274–292. doi: 10.1016/j.lithos.2018.06.013

Omrani, J., Agard, P., Whitechurch, H., Benoit, M., Prouteau, G., et al. (2008). Arc-magmatism and subduction history beneath the Zagros Mountains, Iran: a new report of adakites and geodynamic consequences. *Lithos* 106, 380–398. doi: 10.1016/j.lithos.2008.09.008

Pang, K.-N., Chung, S.-L., Zarrinkoub, M. H., Wang, F., Kamenetsky, V. S., and Lee, H.-Y. (2015). Quaternary high-Mg ultrapotassic rocks from the Qal'eh Hasan Ali maars, southeastern Iran: petrogenesis and geodynamic implications. *Contribut. Mineral. Petrol.* 170:27.

Profeta, L., Ducea, M. N., Chapman, J. B., Paterson, S. R., Marisol Henriquez, Gonzales, S., et al. (2015). Quantifying crustal thickness over time in magmatic arcs. *Sci. Rep.* 5:17786.

Putirka, K. (2016). Amphibole thermometers and barometers for igneous systems and some implications for eruption mechanisms of felsic magmas at arc volcanoes. *Am. Mineral.* 101, 841–858. doi: 10.2138/am-2016-5506

Rasouli, J., Ghorbani, M., Ahadnejad, V., and Poli, G. (2016). Calk-alkaline magmatism of Jebal-e-Barez plutonic complex, SE Iran: implication for subduction-related magmatic arc. *Arab. J. Geosci.* 9, 287–306.

Rezeau, H., Moritz, R., Leuthold, J., Hovakimyan, S., Tayan, R., and Chiaradia, M. (2017). 30 Myr of Cenozoic magmatism along the Tethyan margin during Arabia–Eurasia accretionary orogenesis (Meghri–Ordubad pluton, southernmost Lesser Caucasus). *Lithos* 288-289, 108–124. doi: 10.1016/j.lithos.2017.07.007

Rezeau, H., Moritz, R., Wotzlaw, J.-F., Tayan, R., Melkonyan, R., Ulianov, A., et al. (2016). Temporal and genetic link between incremental pluton assembly and pulsed porphyry Cu-Mo formation in accretionary orogens. *Geology* 44, 627–630. doi: 10.1130/g38088.1

Sarjoughian, F., Kananian, A., Haschke, M., Ahmadian, J., and Ling, W. (2012). Magma mingling and hybridization in the Kuh-e Dom pluton, Central Iran. *J. Asian Earth Sci.* 54-55, 49–63. doi: 10.1016/j.jseaes.2012.03.013

Sarjoughian, F., Lentz, D., Kananian, A., Ao, S., and Xiao, W. (2018). Geochemical and isotopic constraints on the role of juvenile crust and magma mixing in the UDMA magmatism, Iran: evidence from mafic microgranular enclaves and cogenetic granitoids in the Zafarghand igneous complex. *Int. J. Earth Sci.* 107, 1127–1151. doi: 10.1007/s00531-017-1548-8

Schmidt, M. W. (1992). Amphibole composition in tonalite as a function of pressure: an experimental calibration of the Al-in-hornblende barometer. *Contrib. Mineral. Petrol.* 110, 304–310. doi: 10.1007/bf00310745

Shafaii Moghadam, H., Khademi, M., Hu, Z., Stern, R. J., Santos, J. F., and Wu, Y. (2015). Cadomian (Ediacaran–Cambrian) arc magmatism in the ChahJam-Biarjmand metamorphic complex (Iran): magmatism along the northern active margin of Gondwana. *Gondwana Res.* 27, 439–452. doi: 10.1016/j.gr.2013.10.014

Shafiei, B. (2008). *Metallogenic Model of Kerman Porphyry Copper Belt and its Exploratory Approaches*. Ph.D. thesis. Kerman: Shaheed Bahonar University of Kerman.

Shafiei, B., Haschke, M., and Shahabpour, J. (2009). Recycling of orogenic arc crust triggers porphyry Cu mineralization in Kerman Cenozoic arc rocks, southeastern Iran. *Mineral. Depos.* 44, 265–283. doi: 10.1007/s00126-008-0216-0

Shahabpour, J. (2005). Tectonic evolution of the orogenic belt in the region located between Kerman and Neyriz. *J. Asian Earth Sci.* 24, 405–417. doi: 10.1016/j.jseaes.2003.11.007

Shahabpour, J. (2007). Island-arc affinity of the Central Iranian volcanic belt. *J. Asian Earth Sci.* 30, 652–665. doi: 10.1016/j.jseaes.2007.02.004

Sláma, J., Košler, J., Condon, D. J., Crowley, J. L., Gerdes, A., Hanchar, J. M., et al. (2008). Plešovice zircon–a new natural reference material for U–Pb and Hf isotopic microanalysis. *Chem. Geol.* 249, 1–35. doi: 10.1016/j.chemgeo.2007.11.005

Spera, F. J., and Bohrson, W. A. (2001). Energy-constrained open-system magmatic processes I: general model and energy-constrained assimilation and fractional crystallization (EC-AFC) formulation. *J. Petrol.* 42, 999–1018. doi: 10.1093/petrology/42.5.999

Stöcklin, J. (1968). Structural history and tectonics of Iran: a review. *Am. Assoc. Petrol. Geol. Bull.* 52, 1229–1258.

Sun, S.-S., and McDonough, W. F. (1989). "Chemical and isotopic systematics in ocean basalt: implication for mantle composition and processes," in *Magmatism in the Ocean Basins. Geological Society of London Special Publications 42*, eds A. D. Saunders and M. J. Norry (Oxford: Blackwell Scientific Publication), 313–345. doi: 10.1144/gsl.sp.1989.042.01.19

Topuz, G., Altherr, R., Schwarz, W. H., Siebel, W., Satır, M., and Dokuz, A. (2005). Post-collisional plutonism with adakite-like signatures: the Eocene Saraycık granodiorite (Eastern Pontides, Turkey). *Contrib. Mineral. Petrol.* 150, 441–455. doi: 10.1007/s00410-005-0022-y

Verdel, C., Wernicke, B. P., Hassanzadeh, J., and Guest, B. (2011). A Paleogene extensional arc flare-up in Iran. *Tectonics* 30:TC3008. doi: 10.1029/2010TC002809

Vermeesch, P. (2018). IsoplotR: a free and open toolbox for geochronology. *Geosci. Front.* 9, 1479–1493. doi: 10.1016/j.gsf.2018.04.001

Wang, Y., Foley, S. F., and Preleviæ, D. (2017). Potassium-rich magmatism from a phlogopite-free source. *Geology* 45, 467–470. doi: 10.1130/g38691.1

Whitney, D. L., and Evans, B. (2010). Abbreviations for names of rock-forming minerals. *Am. Mineral.* 95, 185–187. doi: 10.2138/am.2010.3371

Yeganehfar, H., Ghorbani, M. R., Shinjo, R., and Ghaderi, M. (2013). Magmatic and geodynamic evolution of Urumieh–Dokhtar basic volcanism, Central Iran: major, trace element, isotopic, and geochronologic implications. *Int. Geol. Rev.* 55, 767–786. doi: 10.1080/00206814.2012.752554

Yin, A., and Harrison, T. M. (2000). Geologic evolution of the Himalayan-Tibetan orogen. *Annu. Rev. Earth Planet. Sci.* 28, 211–280. doi: 10.1146/annurev.earth.28.1.211

Zarasvandi, A., Rezaei, M., Raith, J. G., Pourkaseb, H., Asadi, S., Saed, M., et al. (2018). Metal endowment reflected in chemical composition of silicates and sulfides of mineralized porphyry copper systems, Urumieh-Dokhtar magmatic arc, Iran. *Geochim. Cosmochim. Acta* 223, 36–59. doi: 10.1016/j.gca.2017.11.012

Conflict of Interest: The authors declare that the research was conducted in the absence of any commercial or financial relationships that could be construed as a potential conflict of interest.

frontiers in Earth Science

ORIGINAL RESEARCH
published: 09 September 2020
doi: 10.3389/feart.2020.00363

The Pan-African High-K I-Type Granites From Batié Complex, West Cameroon: Age, Origin, and Tectonic Implications

Maurice Kwékam[1], Victor Talla[2], Eric Martial Fozing[1], Jules Tcheumenak Kouémo[3], István Dunkl[4] and Eammanuel Njonfang[5]*

[1] Laboratoire de Géologie de l'Environnement, Faculté des Sciences, Université de Dschang, Dschang, Cameroon, [2] Département Sciences de la Terre, Université de Yaoundé I, Yaoundé, Cameroon, [3] Département Sciences de la Terre, Université de Douala, Douala, Cameroon, [4] Department of Sedimentology, Geowissenschaftliches Zentrum Göttingen, Georg-August-Universität Göttingen, Göttingen, Germany, [5] Laboratoire de Géologie de l'Ecole Normale Supérieure, Université de Yaoundé I, Yaoundé, Cameroon

The Batié granitic massif in western Cameroon is NE–SW elongated, follows the regional foliation, and is parallel to the Kekem–Fotouni shear zone, which is the southwestern extension of the Tcholliré–Banyo Fault (TBF). This massif comprises two petrographic units: biotite granite and amphibole granite. Major, trace, REE, Sr–Nd isotopic, and new U–Pb data are used to constrain their nature and origin. The results indicate that they are high-K alkali-calcic with shoshonite affinity. The amphibole granite is metaluminous, whereas biotite granite is weakly peraluminous. Both granites are high-temperature I-type granites and crystallized under oxidizing conditions. Initial $(^{87}Sr/^{86}Sr)_{620\ Ma}$ ratios (0.7062–0.7080) and $\varepsilon Nd_{620\ Ma}$ (−12.6 to −8.9) indicate that the parental magmas were produced by partial melting of thick Paleoproterozoic crust and were mixed with felsic magma from the upper continental crust. Their Nd T_{DM} typically varies from 1.68 to 1.96 Ga. The massif was mostly emplaced between 630 and 547 Ma during the transitional period between the crustal thickening (630–610 Ma) and the development of the shear zones, which began with sinistral movements (610–580 Ma) and continued with dextral movements (585–540 Ma). Plutonism continued during the dextral movements. The Batié granite is geochemically and isotopically similar to other post-collisional pan-African granitic massifs located along the TBF.

Keywords: Batié massif, Pan-African, Paleoproterozoic crust, collision, high-K granite

OPEN ACCESS

Edited by:
J. Gregory Shellnutt, National Taiwan Normal University, Taiwan

Reviewed by:
M. P. Manu Prasanth, National Taiwan Normal University, Taiwan
Dominique Gasquet, Université Savoie Mont Blanc, France

****Correspondence:***
Maurice Kwékam
maurice.kwekam@univ-dschang.org; mkwekam@yahoo.fr

Specialty section:
This article was submitted to Petrology, a section of the journal Frontiers in Earth Science

Received: *16 April 2020*
Accepted: *04 August 2020*
Published: *09 September 2020*

Citation:
Kwékam M, Talla V, Fozing EM, Tcheumenak Kouémo J, Dunkl I and Njonfang E (2020) The Pan-African High-K I-Type Granites From Batié Complex, West Cameroon: Age, Origin, and Tectonic Implications. Front. Earth Sci. 8:363. doi: 10.3389/feart.2020.00363

INTRODUCTION

The Pan-African domain of Western Central Cameroon shows many plutonic massifs emplaced following the extensive remobilization and granitization during the collision between the São Francisco–Congo and West African cratons and the Saharan metacraton at 640–580 Ma (Liégeois et al., 1998; Abdelsalam et al., 2002; Ngako et al., 2008). The Pan-African geological history of this domain indicates that there have been several magmatic episodes of rock formation from various sources (crustal or mantle) in different tectonic settings (pre- to post-collision). Plutonic rocks were emplaced into shear zones and are either foliated or unfoliated. Deformation usually occurred either

during or immediately after the consolidation of the magma. The elongated NE–SW Batié plutonic massif outcrops at the southern edge of the Kekem–Fotouni shear zone, which is the southwestern extension of the Tcholliré–Banyo Fault (TBF). Along this shear zone and on either side, several granitic massifs were studied. They are mainly I- or S-type, which are high-K calc-alkaline granites emplaced between 680 and 580 Ma (Nzolang et al., 2003; Tagne-Kamga, 2003; Toteu et al., 2004; Tchameni et al., 2006; Djouka-Fonkwé et al., 2008; Kwékam et al., 2010, 2013, 2020).

In this study, we focus on the Batié magmatic complex, along with a large number of similar Pan-African granitoids, emplaced along the TBF that separates the Central from the Northern domain. The field associations, combined with geochemical, zircon U–Pb, and whole-rock Sr–Nd isotopic studies, provide important constraints on the source nature and mechanism for the formation of this pluton, which in turn might have great significance in understanding the Neoproterozoic Pan-African belt in West Cameroon. Our results show that the partial melting of materials of mixed origin at the continental crust during the Pan-African orogeny would be a plausible process in the formation of Batié granite.

GEOLOGICAL SETTING

The convergence between the São Francisco–Congo and West African craton and the Saharan metacraton during the late Neoproterozoic gave rise to the Pan-African Central African Fold Belt (CAFB) (Abdelsalam et al., 2002). The edges of the cratons were brittle and remobilized by the various metamorphic episodes and deep faults that segmented the continental lithosphere into blocks delineated by post- to late-collisional shear zones. Liégeois et al. (2013) distinguish metacratonized and non-metacratonized domains (**Figure 1**).

Three main successive tectonic events, associated with the Pan-African collisional and post-collisional evolution, are defined in Cameroon (Ngako et al., 2008): (i) crustal thickening (630–610 Ma) marked by refolded thrust tectonics and widespread stretching lineation, (ii) left lateral wrench movements (610–580 Ma), and (iii) right lateral wrench movements mainly presented in the Central Cameroon shear zone (CCSZ) and dated at 585–540 Ma (Toteu et al., 2004). This evolution ends with the development of the molassic basins and the emplacement of alkaline granitoids at 545 Ma in the context of distension (Toteu et al., 2004; Dawaï et al., 2013; Bouyo-Houketchang et al., 2016). Many regional syntheses distinguish three tectonic domains in the CAFB: West Cameroon, Central Cameroon, and South Cameroon. The West Cameroon domain, defined as an active margin, is characterized by a calc-alkaline magmatism from 800 to 600 Ma (Toteu et al., 2001). It is marked by elongated granitic massifs aligned in the NE–SW direction parallel to the regional schistosity (Tetsopgang et al., 2008; Fozing et al., 2014; Njanko et al., 2017; Kwékam et al., 2020). The Central Cameroon domain is an intermediate continental domain and consists of Pan-African granitoids intruding gneissic basement. This domain is also highlighted by many shear zones along which outcrops granitic massifs with associated amphibolite enclaves (Fozing et al., 2019). Granitic massifs are generally elongated parallel to the NE–SW shear zones and are emplaced in transpression or transtension fault relay zones (pull-apart basins). This is the case of the Lom granite (Ngako et al., 2003), the Bandja granite (Nguiessi-Tchankam et al., 1997; Tcheumenak Kouémo et al., 2014), and the Bangangté syenite (Tchouankoué et al., 2016). Most of these massifs are calc-alkaline and strongly potassic, which are I- or S-type with shoshonitic affinity (Nzolang et al., 2003; Djouka-Fonkwé et al., 2008). The central domain is separated from the western domain by the TBF. The southern domain represents a syntectonic basin (Toteu et al., 2006). It includes meta-sediments and pre- to syntectonic intrusions metamorphosed in the granulite facies (Nzenti et al., 1992) before exhumation and thrusting over the Congo craton (Barbey et al., 1990).

The Kekem–Fotouni shear zone, which separates the Fomopéa granite from the Bandja and Batié massifs, is marked by a mylonite band affecting Paleoproterozoic gneisses (ca. 2.1 Ga; Penaye et al., 1993) and the edges of the granitic massifs. In this mylonite band, small plutons of gabbronorite (Kwékam et al., 2013) and charnockite are also observed (Nguiessi-Tchankam et al., 1997; Tcheumenak Kouémo et al., 2014). These formations, as well as the granites from the remobilized gneisses, are largely covered by the Tertiary transitional basalt of Mount Bangou and the Cenozoic volcanic rocks of Mount Bambouto (**Figure 2A**).

FIELD GEOLOGY AND PETROGRAPHY

The Batié granitic complex is elongated NE–SW and parallel to the other granitic massifs that outcrop along the Kekem–Fotouni shear zone (**Figure 2A**). This syn-kinematic characteristic is underlined within the massif by NNE–SSW elongated micro-enclaves parallel to the preferential orientation of the feldspar megacrystals and granitic dykes (pegmatite) with oblique internal prismation, suggesting a sinistral NNE–SSW syn-magmatic shear. The Batié granite massif intrudes an orthogneiss complex, but the contact is entirely concealed by Tertiary volcanic formations of Mount Bangou (**Figure 2B**). Its northwestern edge is affected by the Kekem–Fotouni shear zone. Petrographically, it primarily consists of biotite granite and amphibole granite. The amphibole granite is exposed to the southeast and northwest of the massif. The Batié granite is leucocratic with an oriented porphyritic structure, which is characterized by the abundance of K-feldspar megacrystals that range in size from 5 to 8 cm length and from 2.5 to 5 cm width. These crystals show mostly symmetrical Carlsbad's twin and preferentially NNE–SSW orientation. In addition to K-feldspar, this granite consists of quartz, plagioclase, biotite, and/or amphibole. Titanite, allanite, apatite, zircon, and magnetite are identified as accessory minerals. Quartz (24–40%) is interstitial and occurs in polycrystalline clusters frequently wedged between the feldspar megacrystals. K-feldspar (15–38%) is orthoclase, which is sometimes transformed into microcline at the edge or entirely. It is euhedral to sub-euhedral and develops exsolutions

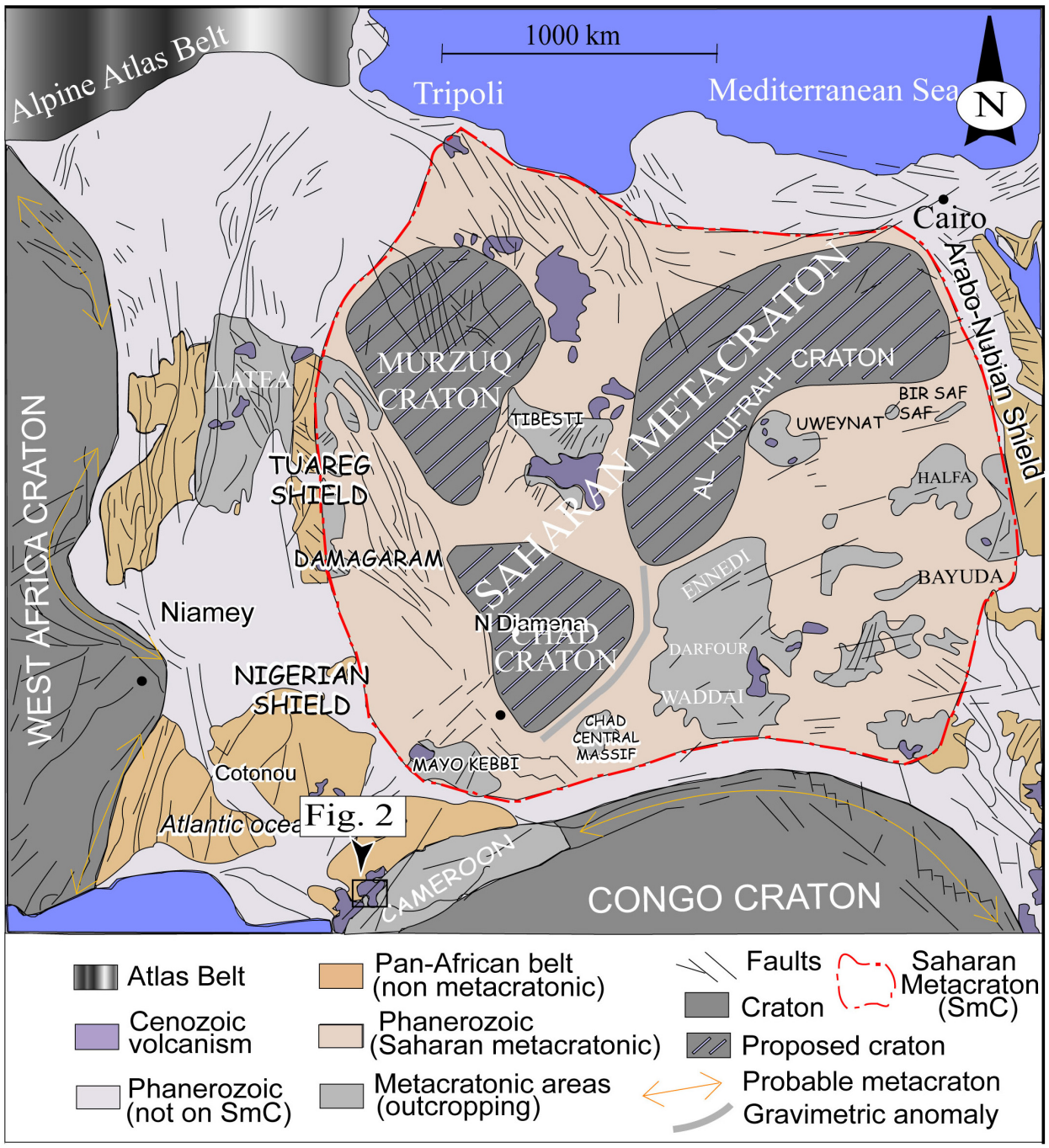

FIGURE 1 | Geological sketch map of west-central Africa with cratonic areas and the Pan-African–Brasiliano provinces of the Pan-Gondwana belt in a Pangea reconstruction; modified from Castaing et al. (1994) and Abdelsalam et al. (2002) after Liégeois et al. (2013).

of plagioclase (lamellae and staining perthite). It encloses titanite, biotite, apatite, and magnetite crystals. It is replaced by sericite. Plagioclase (22–31%) occurs as euhedral to sub-euhedral crystals (2 cm × 1 cm), which is classified as oligoclase (An_{26-17}). It often displays albite and Carlsbad's twin and has normal zoning. Alteration is frequent, especially from the core. Plagioclase in the amphibole granite (northwestern edge) displays mechanical twinning and kink-band deformation. Biotite (2–13%) occurs as flakes with frayed ends and corroded by quartz and feldspars. The biotite flakes form isolated crystals and discontinuous lines surrounding the feldspar megacrystals. Biotite also contains apatite, titanite, zircon, magnetite, and allanite. Some flakes are altered to chlorite. Amphibole (0.7–4%) is a green hornblende found only in the amphibole granite. It occurs in euhedral to

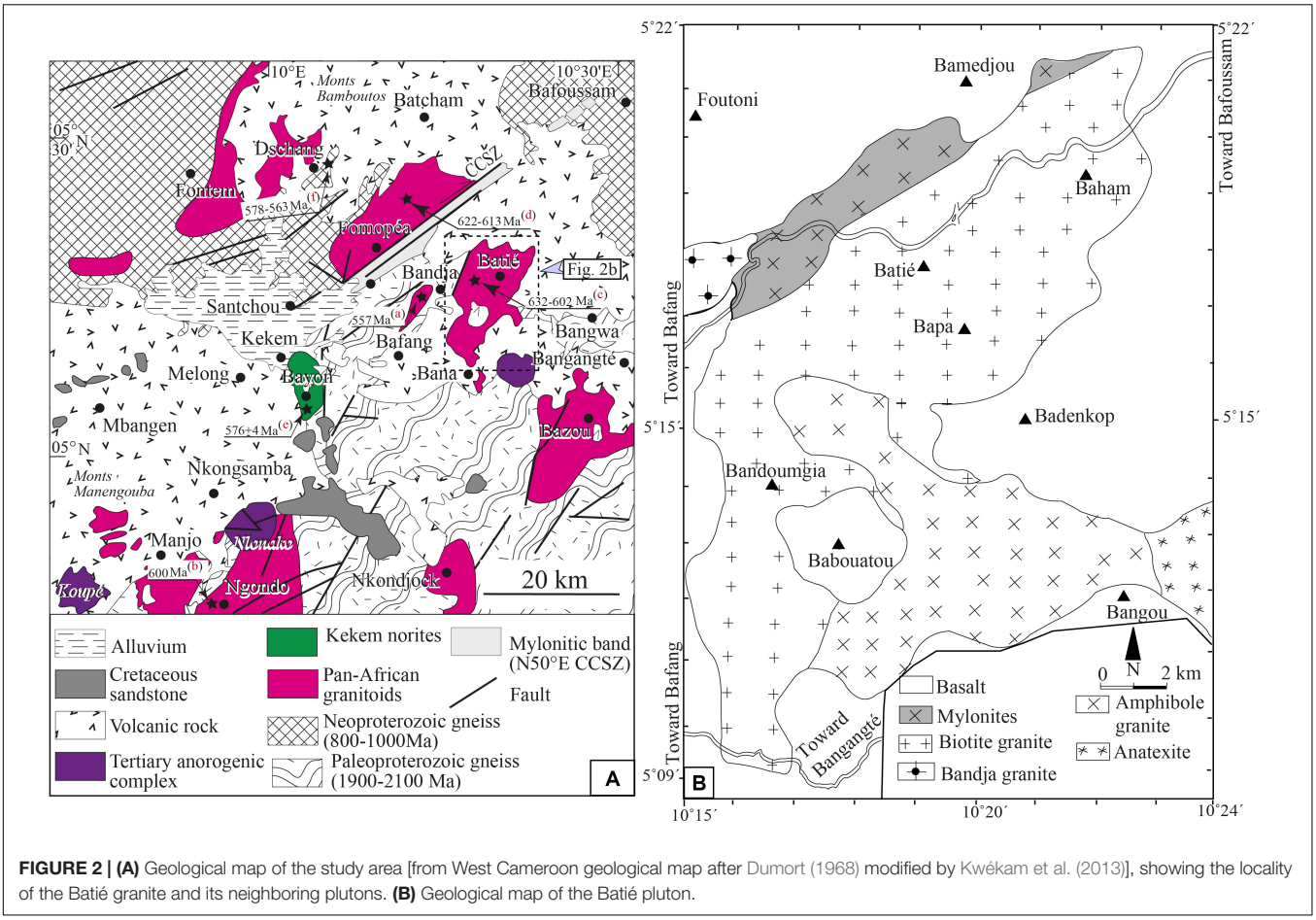

FIGURE 2 | (A) Geological map of the study area [from West Cameroon geological map after Dumort (1968) modified by Kwékam et al. (2013)], showing the locality of the Batié granite and its neighboring plutons. **(B)** Geological map of the Batié pluton.

sub-euhedral cross-sections with frequent h1 (100) twinning and generally sub-euhedral longitudinal sections.

Secondary, epidote, chlorite, and sericite are present in minor abundances.

ANALYTICAL METHODS

Mineral Analyses

The chemical composition of amphiboles, biotite, and feldspar is determined on 10 thin polished slides using the Cameca SX50 automated electron microprobe at the Institute of Mineralogy and Petrography of the Swiss Federal Institute of Technology in Zurich. Natural and synthetic silicates were used as calibration standards, and the raw data are automatically corrected for deviation, dead time, and background noise using the ZAF correction process (Pouchou and Pichoir, 1984). The conditions of analysis are set at 15 kV and 20 nA with 200 s counting time for one element.

Laser Ablation U–Th–Pb Analyses

Sample BT901 of the amphibole granite collected for U–Th–Pb geochronology by laser ablation was crushed, and the zircon crystals were separated by the heavy liquid and magnetic separation method using conventional techniques (e.g., Bosch et al., 1996). The non-magnetic zircon crystals were hand sorted and mounted on double-sided adhesive tape and embedded in a 25 mm diameter epoxy support. The crystal supports were coated with 2,500 mesh *SiC* paper and polished with 9, 3, and 1 μm diamond suspensions.

The analytical method is described in detail by Kwékam et al. (2020). The age calculation and quality control are based on the drift and fractionation corrections by standard-sample bracketing using GJ-1 zircon reference material (Jackson et al., 2004). Deviations, splitting corrections, and data reductions were performed using the Geozentrum Göttingen, Georg-August Universität, Abteilung Geochemie's UranOS software (Dunkl et al., 2008). The quality and accuracy of the method was verified by analyses of secondary reference materials: the Plešovice zircon yielded a concordia age of 337.1 ± 1.0 Ma (Sláma et al., 2008) and the 91500 zircon yielded a concordia age of 1,059.6 ± 3.8 Ma (reference age of 1,065.4 ± 0.3 Ma; Wiedenbeck et al., 1995). The concordia curve was obtained using the Isoplot software (Ludwig, 2012).

Whole-Rock Geochemical Analyses

The whole-rock geochemical analysis was performed by X-ray fluorescence (XRF) and inductively coupled plasma mass

spectrometry (ICP-MS) at the Institute for Mineralogy and Petrography (IMP) of the Swiss Federal Institute of Technology Zurich (ETH Zurich) and at the Geozentrum Göttingen, Georg-August Universität, Abteilung Geochemie, Germany. Major and some trace elements (Sc, V, Cr, Co, Ni, Zn, Ga, Rb, Sr, Zr, and Ba) are measured by XRF analysis on glass disks (see detail in Kwékam et al., 2020).

Rb–Sr and Sm–Nd Isotopic Analyses

Hundred milligram of the samples was dissolved by an acid mixture of HNO_3 and HF at 180°C. The separation of Sr and REE was performed on columns filled with the cation exchange resin AG 50W-X8 with 2.5 M HCl. Nd separation from the REE was performed on a column filled with hexyl di-ethyl hydrogen phosphate (HDEHP) coated Teflon with 0.18 M HCl. Sr, Nd, Rb, and Sm isotopes were measured with a Finnigan TRITON mass spectrometer at the Geowissenschaftliches Zentrum Göttingen, Georg-August Universität, Abteilung Geochemie. Measurements were performed in static and in the peak-jumping multicollector mode for Sr and for Nd, respectively. Sr analyses were corrected for mass fractionation by normalization to $^{88}Sr/^{86}Sr = 8.375209$, whereas Nd analyses were normalized to $^{146}Nd/^{144}Nd = 0.7219$. Repeated measurements of the standard NBS987 gave on average a value of 0.710244, with a reproducibility of 0.000007 (2σ). The Nd standard La Jolla was determined with an average of 0.511845 ± 0.000005 (see detail in Kwékam et al., 2020).

RESULTS

Zircon U–Pb Dating

BT901 From AG

Twenty-one zircons extracted from the BT901 amphibole granite sample have been treated, and data are reported in **Supplementary Table S1**. Zircon crystals are usually in an elongated pyramidal shape. The zircons are translucent and light pink. Th/U is >0.1 and ranges from 0.2 to 1.6, which is the feature of magmatic zircon. The U–Pb ages obtained on the individual grains are Neoproterozoic (683–547 Ma), and we can distinguish two families of zircons. The first is made up of old zircons obtained from two grains (682 and 634 Ma), and the second major group has ages ranging from 612 to 547 Ma. On the concordia diagram, data are scattered and do not permit a reliable age to be determined (**Figure 3A**). However, the "Zircon Age Extractor" method by Ludwig (2012) gives an average age of 561 + 8/−5 Ma with 97.9% confidence coefficient by a coherent group of 10 points (**Figure 3B**). This age is comparable to the Neoproterozoic ages obtained on the neighboring granitic massifs of the central domain of the Pan-African orogeny from Central Africa in Cameroon (Li et al., 2017; Kwékam et al., 2020).

Sample From BG

U–Pb ages on zircons from the biotite granite have already been determined by Njiekak et al. (2008) in an extensive study of the Bangwa and Foumbot areas. The old inherited (634–628 Ma) and Neoproterozoic (602–503 Ma) ages were presented on 10 zircon crystals. The authors had interpreted these data as contamination by the gneissic host rocks for the former (634–628 Ma) and emplacement age (602 Ma) and deformation (mylonitization) age after emplacement of the Batié massif (575 Ma from Talla, 1995). Thus, data obtained for both granites (AG and BG) seem to reflect the geological history of the region, especially the CAFB. Considering the results and the ages of similar massifs in the same region (e.g., Fomopéa granites; 621–613 Ma; Kwékam et al., 2010), we propose the age of intrusion at ∼630 to ∼602 Ma.

Whole-Rock Sr–Nd Isotopic Compositions

Eleven Sr isotope analyses were performed (**Supplementary Table S2**). Five BG samples and three AG samples define an isochron at 627 ± 35 Ma with $^{87}Sr/^{86}Sr$ initial ratio = 0.7065 ± 0.0014 and mean squares of weighted deviates (MSWD = 4.2). Another isochron obtained by five samples of BG indicates 627 ± 21 Ma with $^{87}Sr/^{86}Sr$ initial ratio = 0.7062 ± 0.0012 and a really good MSWD = 2.0. The isochron ages have significant uncertainty (**Figures 3C,D**) but cover the range from the zircon U–Pb ages, as well as the ages of the other massifs of the CAFB domain. Initial $(^{87}Sr/^{86}Sr)_{620\ Ma}$ ratios (0.7019–0.7080) of analyzed samples are low and vary only slightly.

Nd isotope data were obtained from four biotite granite samples and one amphibole granite sample (**Supplementary Table S2**). The $\varepsilon Nd_{620\ Ma}$ (−8.9 to −12.6) isotope parameters and the older model age T_{DM} (1,685–1,963 Ma) suggest a crustal component in the source.

Geochemical Compositions

The SiO_2 contents range from 53 to 68 wt.% in the AG and from 56.3 to 76 wt.% in the BG (**Supplementary Table S1**). Both granites have high K_2O contents of 4.1–8.1 wt.%. In the SiO_2 vs. K_2O diagram (**Figure 4A**), these granites plot mostly within high-K calc-alkaline to shoshonite series fields. K_2O contents decrease in BG with increasing SiO_2. They also classify as alkali-calcic and alkalic granites (**Figure 4B**; Frost et al., 2001). AG are mostly metaluminous (A/CNK = 0.78–1.02), whereas BG are metaluminous to weakly peraluminous (A/CNK = 0.95–1.10); therefore, these are typical I-type granitoids (**Figure 4C**; Chappell and White, 1992). The FeO* (0.72–1) indicates that the rocks of the Batié massif belong to the ferroan series (**Figure 4D**; Frost et al., 2001). MgO, CaO, Al_2O_3, Fe_2O_3, P_2O_5, and TiO_2 contents decrease with increasing SiO_2 (**Figure 5**). However, no significant correlations were noticed in the Na_2O vs. SiO_2 diagram (**Figure 5**). Normalized REE patterns of all samples are generally parallel to each other and to the crust (**Figure 6**). The LREE exhibit moderate to strong enrichment [$(La/Yb)_N$ = 19–68] relative to the primitive mantle, whereas the HREE patterns are almost flat [$(Dy/Yb)_N$ = 1.2–2.2]. BG have strong negative europium anomalies (Eu/Eu* = 0.53–0.14), whereas AG have weak europium anomalies (Eu/Eu* = 0.71). Primitive mantle-normalized trace element diagram shows Th, U, K, and Zr enrichment and Ba, Nb, Sr, P, and Ti depletion (**Figure 6**).

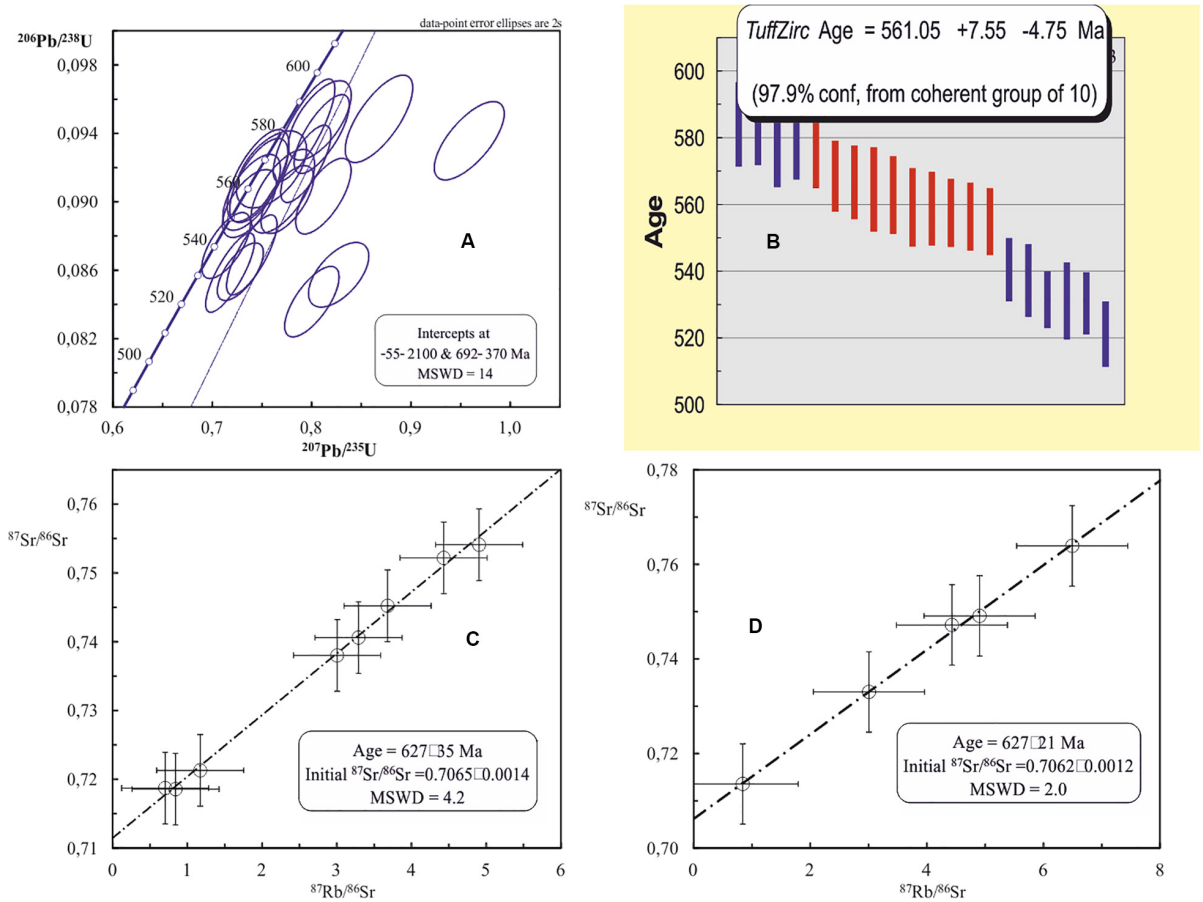

FIGURE 3 | Zircon U–Pb results obtained on the amphibole granite sample BT901: **(A)** concordia plot, **(B)** the result of the algorithm "Zircon age extractor" of Isoplot (Ludwig, 2012), **(C)** Sr–Rb isochrones for eight samples (AG and BG), and **(D)** Sr–Rb isochrones for five samples (BG only).

Mineralogy

The amphiboles of the GA of the Batié massif give distinct chemical compositions (**Supplementary Table S3**). The values for Ca (1.67–1.96 a.p.f.u.) and Na (0.04–0.13 a.p.f.u.) in the B-site and their $(Ca + Na)_B$ indicate that these amphiboles belong to the calcium amphibole sub-group after Leake et al. (1997). In addition, the values of Si^{IV} (6.27–7.23) in site T and the sums of $(Na + K)_A$ in site A (0.21–0.66), as well as their Mg/(Mg + Fe) ratios of 0.44–0.79, indicate that the amphiboles of the AG of the Batié massif are magnesio-hornblende, magnesio-hastingsite hornblende, and edenite hornblende in accordance with the classification by Leake et al. (1997). Some crystals of the deformed AG have actinolite and hornblende affinities (**Supplementary Table S3**).

Biotites are present in both granites (AG and BG) and have fairly distinct chemical compositions (**Supplementary Table S4**). The biotites in AG are more magnesian (MgO = 9.84–15.12%) and depleted in Al_2O_3 (13.75–14.88%) and FeO (15.35–21.79%), whereas the biotites in BG are richer in Al_2O_3 (15.96–16.63%) and FeO (22.40–25.07%) and poor in MgO (5.82–7.55%). Their $Mg/(Mg + Fe^{2+} + Mn^{2+})$ ratios make it possible to distinguish between the two groups of biotites (0.45–0.66 for AG and 0.29–0.36 for BG). Therefore, the biotites in BG are plotted at the Fe-biotite pole, whereas the biotites in AG extend from the transitional zone between Fe-biotite and Mg-biotite to the Mg-biotite pole in triangular diagram (**Figure 7A**) after Foster (1960). These characteristics of the biotites from the Batié massif are similar to those of the biotites of the metaluminous calc-alkaline granitoids (**Figures 7B,C**; Abdel-Rahman, 1994).

The composition of feldspar varies from labradorite An_{58} to oligoclase An_{13}. Plagioclases are generally oligoclase (An_{26-23}) in the AG; however, zoned crystals show a core of labradorite–andesine (An_{58-48}) composition. The plagioclases in the deformed AG are predominantly albite–oligoclase (An_{23-5}). In the BG, the plagioclases are usually of oligoclase (An_{27-17}) composition.

DISCUSSION

Age

Data obtained for the Batié granite massif is used to reveal the geological history of the CCSZ. The geochronological data (634–503 Ma) by Njiekak et al. (2008) and this work (683–547 Ma)

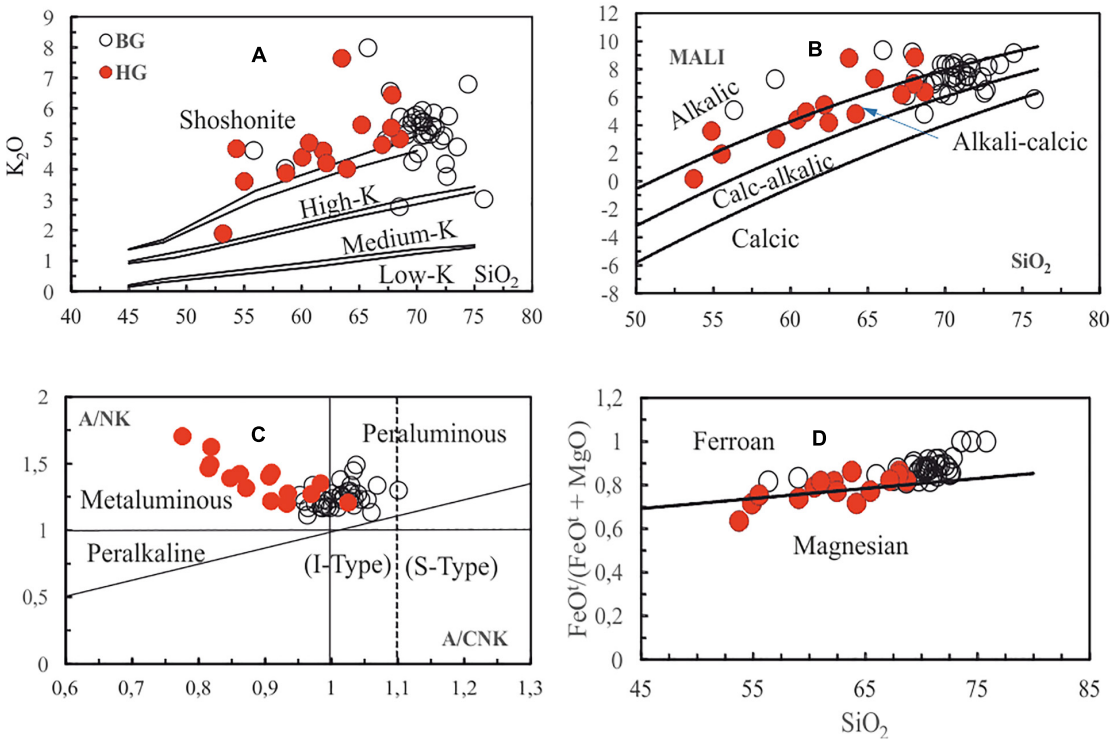

FIGURE 4 | Nature of Batié granites. **(A)** K_2O vs. SiO_2 diagram after Peccerillo and Taylor (1976), showing the high-K calc-alkaline to shoshonitic affinity of the Batié granites; boundary lines (bands) are from Rickwood (1989). **(B,D)** MALI ($K_2O + Na_2O$–CaO vs. SiO_2) and FeO* vs. SiO_2 diagrams from Frost et al. (2001), showing the alkali-calcic and ferroan character of the Batié granites. **(C)** [A/NK ($Al_2O_3/Na_2O + K_2O$) vs. A/CNK ($Al_2O_3/CaO + N_2O + K_2O$) molecular ratios] diagram after Maniar and Piccoli (1989).

indicate that the emplacement of the massif lasted at least 100 Ma. The oldest ages (683–634 Ma) can be considered as those of inherited zircons. Wherever a silicic magma is saturated in water, zircon crystallization begins early in the magmatic period and continues up to the end with the development of trace elements rich in hydrozircon (Pupin, 1980). The large size of the feldspar crystals, as well as the mineralogical assemblage of the Batié granites, indicates that the magma was very rich in water. This explains the age range of the zircons of these granites. Considering the Rb/Sr data (627 ± 21 Ma) and the ages obtained in the neighboring massifs (630–572 Ma for Fomopéa, 590–550 Ma for Bandja), the age of the Batié massif can be constrained between 630 Ma and 547 Ma. U–Pb zircon results suggest that the emplacement of the Batié granite began at the end of crustal thickening and, together with the Fomopéa complex, represents the first generation of high-K Pan-African calc-alkaline plutons from western Cameroon. They are thus older than most of the Pan-African plutons that are being emplaced at ca. 580 Ma during the second tectonic period (Kwékam et al., 2010). The age interval likely identifies distinctly the deformation phases that the massif experienced. Indeed, the BT901 sample of amphibole granite was collected in the mylonite band in the NW of the massif, and the ages between 561 and 547 Ma may correspond to the mylonitization phase as suggested by Nguiessi-Tchankam et al. (1997), Njiekak et al. (2008), and Kwékam et al. (2013).

Magma Evolution Conditions

The mineralogical composition of the granites, as well as the chemical composition of their ferromagnesian minerals, is generally a function of the evolution conditions of the magma (e.g., degree of oxidation and water content) (Wones, 1981; Bonin, 1990; Ridolfi et al., 2010; Chen et al., 2016). The grain size of the rock is also influenced by the evolution conditions of the magmas (Marre, 1982). The large size of feldspars in the Batié granite, some of which reach more than 5 cm, and the presence of titanite, magnetite, and allanite suggest an oxidizing and H_2O-rich environment. The coexistence of titanite and quartz also suggests high oxygen fugacity (Wones, 1989). For instance (**Figure 8**), amphibole crystallized from oxidizing magmas would possess higher $Fe^{3+}/(Fe^{3+} + Fe^{2+})$ and lower Fe/(Fe + Mg) ratios than those from the reducing ones (Wones, 1981). The amphiboles from AG are characterized by high $Fe^{3+}/(Fe^{3+} + Fe^{2+})$ ratios of 0.18–0.41 and relatively low to moderate Fe/(Fe + Mg) ratios of 0.44–0.60 and 0.61–0.79, suggesting crystallization under an oxidizing condition (Wones, 1981; Clowe et al., 1988; Chen et al., 2016). On the other hand, total rock K/Rb ratios are relatively low in the biotite granite (49–315) and moderate in the amphibole granite (140–311), indicating a highly evolved magma for the biotite granite to moderately evolved magma for the amphibole granite (**Figure 8**).

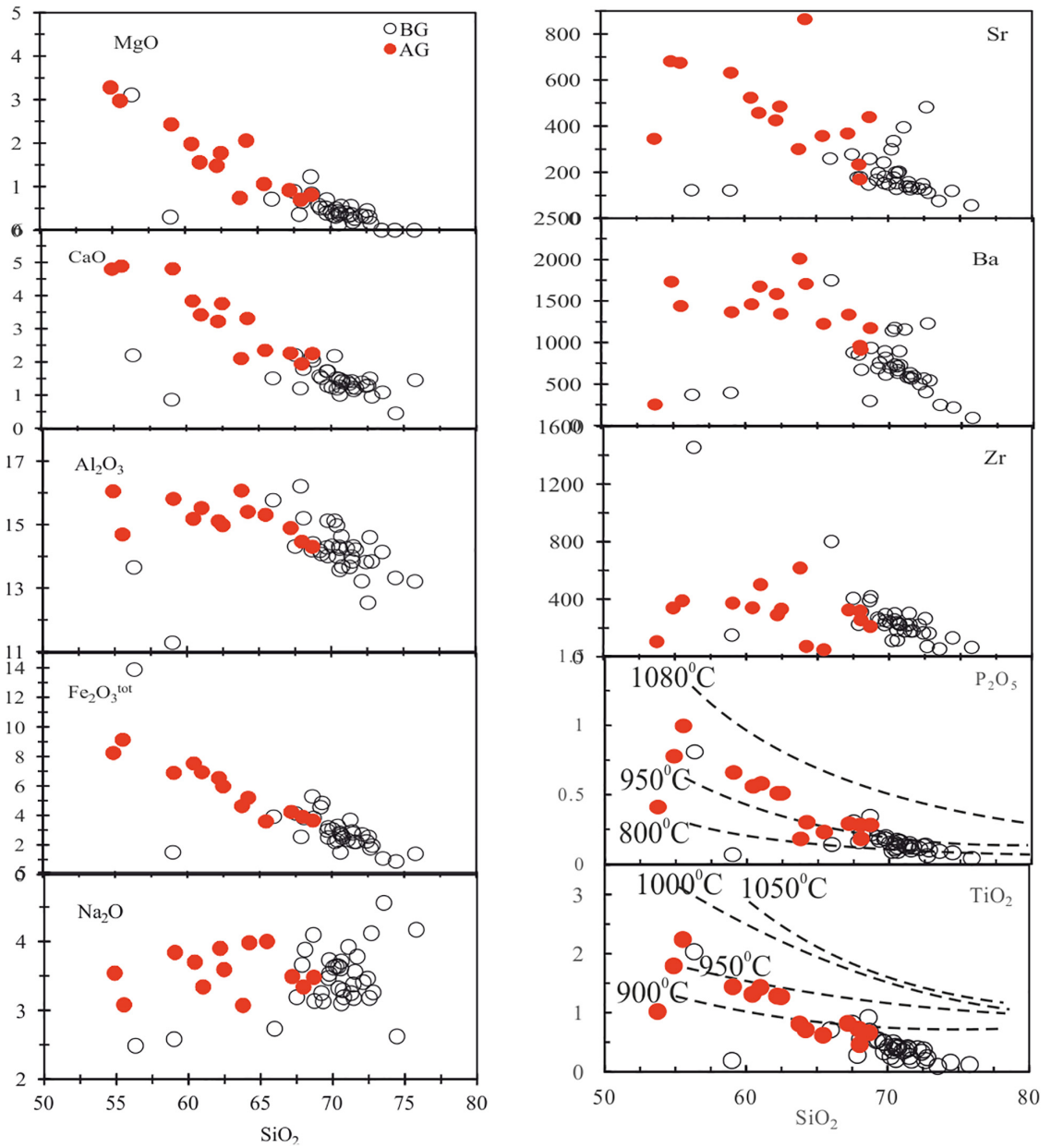

FIGURE 5 | Harker diagrams of selected major and trace elements. P_2O_5 and TiO_2 are used for evaluating the temperature of crystallization. In P_2O_5 vs. SiO_2, the evolution trend is similar to I-type granitoids (Chappell et al., 1998) and mixing melts line (Lee and Bachmann, 2014).

Various authors have shown that there is a linear relationship between the total aluminum of the hornblende and its crystallization pressure (Hollister et al., 1987; Johnson and Rutherford, 1989). The pressures of the AG amphiboles were calculated using the equations proposed by Schmidt (1992), whereas the temperatures were calculated using the thermometry by Blundy and Holland (1990). The AG yielded crystallization temperatures and pressures ranging from 682 to 822°C and from 1.12 to 6.8 kbar, respectively. The temperatures and pressures calculated on the amphiboles are much more representative of the final emplacement conditions. Temperatures obtained using whole-rock P_2O_5 and TiO_2 contents indicate values well above 950°C (**Figure 5**). These values, which are related to those of apatite and titanite minerals, suggest that the magma of the granites of the Batié massif started to crystallize at temperatures above 950°C and indicate that these granites are high-temperature I-type granites (Chappell et al., 1998).

Petrogenesis

High-temperature granites are more prospective for mineralization because they have a greater capacity to undergo extended fractional crystallization and concentrate incompatible

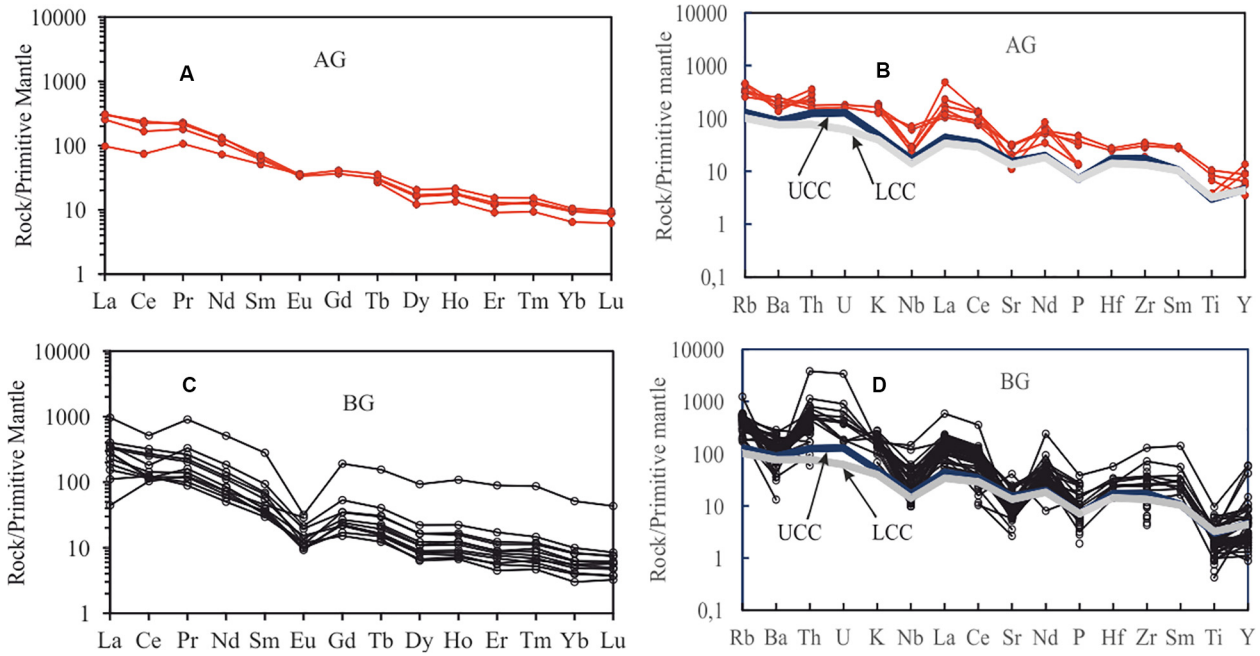

FIGURE 6 | Primitive mantle-normalized REE patterns **(A,C)** and primitive mantle-normalized spidergrams **(B,D)**. Normalizing values are from Sun (1982) and McDonough et al. (1992) (AG, amphibole granite; BG, biotite granite; UCC, upper continental crust; LCC, lower continental crust after Rudnick and Gao, 2003).

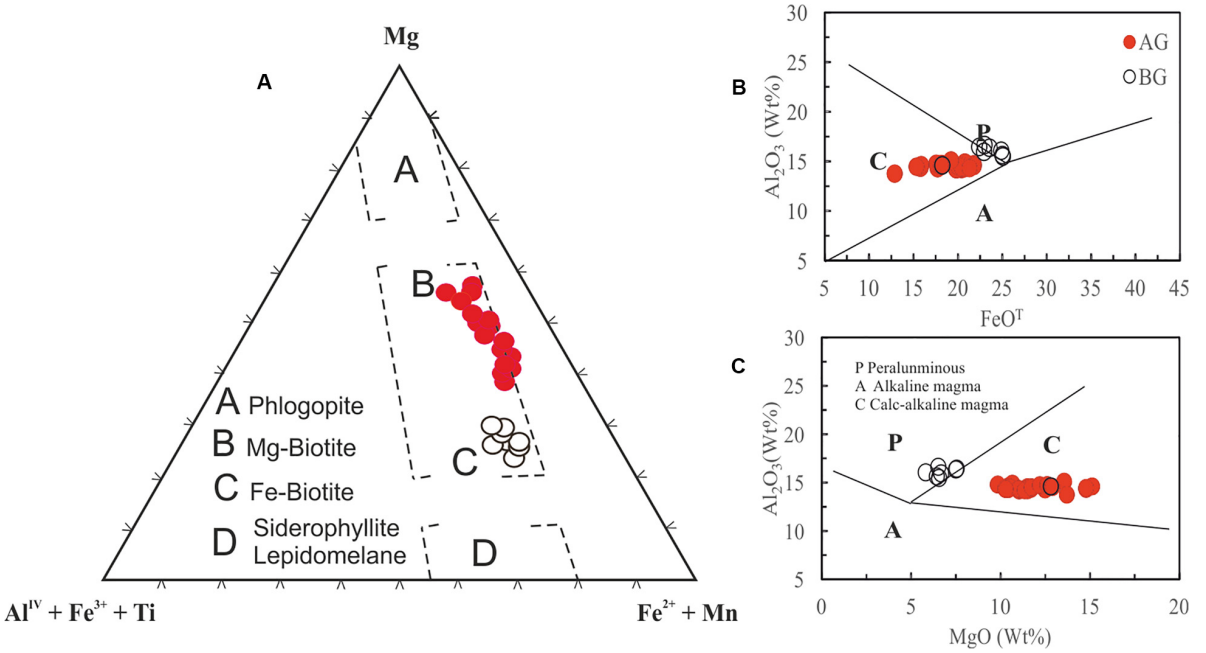

FIGURE 7 | Compositions of biotites from Batié granites in **(A)** triangular diagram after Foster (1960) and **(B,C)** after Abdel-Rahman (1994).

components, including progressive increase in the activity of H_2O (Chappell et al., 1998). Barium variation in Batié granite illustrates that the compositional variation resulted from fractional crystallization. The Ba contents in the AG increased up to 2,000 ppm before decreasing. In the BG, Ba decreases progressively and indicates biotite and K-feldspar crystallization. Negative Eu, Nb, Ta, P, and Ti anomalies indicate crystallization of minerals, such as plagioclase, hornblende, biotite, apatite, allanite, and titanite, in the magma of the Batié granites. The general decrease of certain elements, such as Fe_2O_3, MgO, CaO,

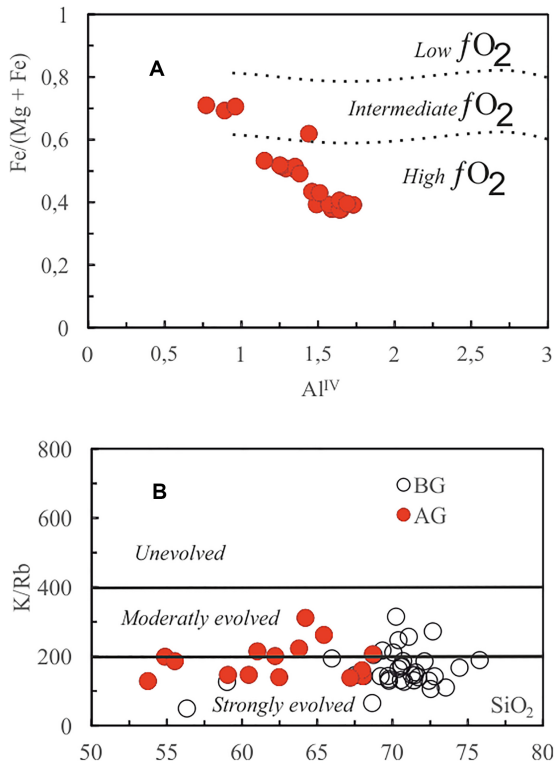

FIGURE 8 | (A) Al^{IV} values vs. Fe/(Fe + Mg) ratios of amphiboles from the amphibole granites. Low, intermediate, and high oxygen fugacity (fO_2) fields are after Anderson and Smith (1995). **(B)** K/Rb vs. SiO_2 diagram showing moderately to strongly evolved character of Batié granites after Blevin (2004).

TiO_2, and Al_2O_3, with increasing SiO_2 of the rocks can also be interpreted as evidence of fractional crystallization and/or magma mixing. However, the SiO_2 contents in both granites (AG and BG) exhibit linear correlations with P_2O_5 and Zr (Lee and Bachmann, 2014), indicating that magma mixing occurred rather than fractional crystallization. Mineralogical and geochemical compositions of Batié granites are similar to those of K-rich and K-feldspar porphyritic Calc-alkaline Granitoids (KCG) of mixed origin (Barbarin, 1999). However, the correlation between the initial ratios of Sr in the $^{87}Sr/^{86}Sr$ vs. SiO_2 or $1/Sr*10^3$ diagrams (**Figures 9A,B**) suggests a more complex process. Some samples of the biotite granite are arranged on a horizontal line, indicating fractional crystallization. On the other hand, the majority of samples have a negative correlation in both diagrams. According to Benito et al. (1999), this negative correlation is related to metasomatism caused by fluids from sediments.

High-temperature I-type granites are usually formed by the partial melting of mafic rocks in the deep crust or perhaps from a subduction modified mantle (Chappell et al., 1998). The diagram $Al_2O_3 + Fe_2O_3 + MgO + TiO_2$ vs. $Al_2O_3/(Fe_2O_3 + MgO + TiO_2)$ from Patiño Douce (1999) indicates that the amphibole granite melt was from amphibolite melts, whereas the biotite granite melt was from greywacke melts (**Figure 9C**). These melts are formed in the lower lithospheric crust. The isotopic data are not sufficient enough to decide the origin of the magma of these granites. The initial Sr ratios (0.7019–0.7080; **Supplementary Table S2**) suggest a modified mantle source, whereas the εNdt values (−12.6 to −8.9) support a crustal source, although the value (−8.9) of the AG sample alone would indicate the possible mixing of amphibolite magmas and crustal felsic source. Moreover, the initial ratio $^{87}Sr/^{86}Sr = 0.7062 \pm 0.0012$ obtained by the isochron is that of the continental crust (**Figure 3D**). The Nd model ages (1,815–1,963 Ma for BG and 1,685 Ma for AG; **Supplementary Table S2**) probably suggest the age of the protolith rock source or mixing between juvenile mantle-derived material and melt from old (Eburnian) crust. Indeed, alkali-calcic granites are considered to be derived from hybrid sources, which are granites of crustal + mantle origin (Pupin, 1980; Barbarin, 1999). Furthermore, two samples of the amphibole granite are plotted around the lower continental crust, whereas the other samples (BG and AG) are around the upper continental crust in the Th/Nb vs. La/Nb diagram (**Figure 9D**). According to Barbarin (1999), KCG is derived from the mixing of mantle-derived basaltic magmas and crustal melts with varying proportions. Th/Nb ratios suggest the interaction between low continental crust (LCC) and upper continental crust (UCC) (**Figure 9D**). The crustal component is very important in the Batié granite than the other calc-alkaline granites of the West Cameroon region that are formed by magmatic mixing processes. The geological environment of the region also supports this hypothesis. In the Batié area, the continental basement is represented by Eburnian garnet gneiss (ca. 2.1 Ga) and Archaean rocks of the Congo craton. It is possible that one of these rocks participated in the formation of the magma of the Batié granite. Furthermore, recent work by Fozing et al. (2019) mentions amphibolite enclaves (with Nd T_{DM} = 1.7 Ga; see Kwékam et al., 2010) along the Kekem–Fotouni shear zone in the Fomopéa complex. These amphibolites may be representative of the type of basaltic magma from the lower crust that mixed with felsic magma derived from the upper crust. The most likely source for the granites of the Batié massif would be a crustal source resulting from the partial melting of heterogeneous materials from the deep basalt layer (amphibolite) of the crust and the upper continental crust.

Geodynamic Context

The strongly potassic alkali-calcic characteristic with a shoshonite affinity and its high-temperature I-type granite feature show that the rocks of the Batié massif are derived from magma formed in an environment related to a subduction zone. Previous work along the TBF (Nguiessi-Tchankam et al., 1997; Njonfang et al., 2006; Kwékam et al., 2010, 2013; Fozing et al., 2019) suggested an old plate boundary subducted during the assembling of blocks to form Gondwana. Liégeois et al. (2013) also indicate that this Pan-African structure represents the northern edge of the Congo craton (**Figure 1**). However, the ages obtained on the Batié granites make it possible to propose their emplacement during the Pan-African orogeny, which is more precisely at the end of crustal thickening (ca. 630–620 Ma) and continued to the left lateral wrench movements (610–580 Ma) (Ngako et al., 2008). This hypothesis is supported by the position of the samples of the two granites (AG and BG) in the geotectonic

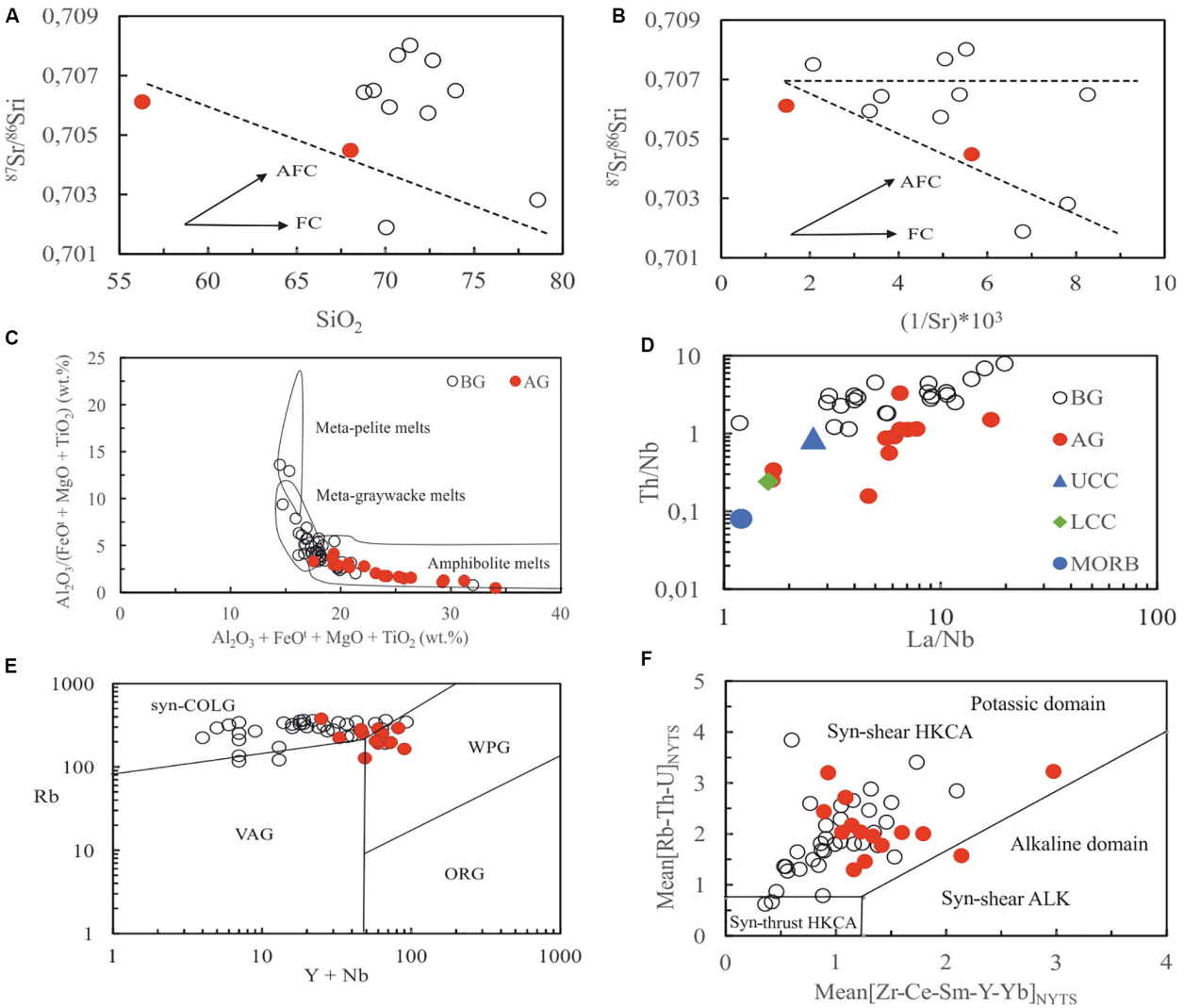

FIGURE 9 | (A) Plots of $(^{87}Sr/^{86}Sr)_{620\ Ma}$ vs. SiO_2 and **(B)** $(^{87}Sr/^{86}Sr)_{650\ Ma}$ vs. $1/Sr*10^3$ show that Batié granites are not only controlled by fractional crystallization (FC). The oblique line indicates the metasomatism trend. **(C)** Compositional comparison between the Batié granites with those partial melts from metapelites, metagreywackes, and amphibolites (after Patiño Douce, 1999). **(D)** Diagram Th/Nb vs. La/Nb showing mainly the crust contribution of Batié granite magmas [upper continental crust (UCC) and lower continental crust (LCC) values are from Rudnick and Gao (2003), and Mid-Ocean ridge basalt (MORB) values are from Saunders and Tarney (1984)]. **(E)** Discrimination diagrams for the tectonic interpretation of granitic rocks after Pearce et al. (1984) (syn-collisional granites, syn-COLG; volcanic-arc granites, VAG; ocean-ridge granites, ORG; within-plate granites, WPG). **(F)** Sliding normalization diagram comparing the Batié pluton to the reference syn-shear high-K calc-alkaline (HKCA) of the Yenchichi–Telabit series (Liégeois et al., 1998). The Batié pluton displays a strong potassic trend (NYTS, normalization to Yenchichi–Telabit series).

diagram Rb vs. (Y + Nb) of **Figure 9E**, where they mainly occupy the domains of syn-collision granites (syn-COLG) and post-collision granites by Pearce et al. (1984). Similarly in the diagram by Liégeois et al. (1998), the Batié rocks follow the potassic trend in the syn-shear high-K calc-alkaline (HKCA) domain (**Figure 9F**). At the end of its emplacement, the Batié massif was affected by right lateral wrench movements (ca. 585–540 Ma) marked at the northwestern edge by a NE–SW mylonite band (see **Supplementary Table S1** and **Figures 1**, **2**). The right lateral wrench movements are mainly marked by the CCSZ (Ngako et al., 2008). The model for the emplacement of the Batié massif is very close to that proposed by Ferré et al. (1998) for the granites of eastern Nigeria and Kwékam et al. (2010) for the Fomopéa pluton. The geodynamic context of the magma emplacement, starting with convergence and high-heat production, can last longer than in frontal collision orogeny and continue by strike-slip shear zones, which provide an ascent path. The origin of the Batié massif could be associated with the Pan-African convergence between the Congo craton and the Saharan metacraton that initiated the metacratonization of the northern boundary of the Congo craton. Post-collisional transpressive movements (Ngako et al., 2003; Tagne-Kamga, 2003; Kwékam et al., 2013) along the CCSZ induce linear lithospheric delamination, followed

by the upwelling of mantle magmas, triggering the partial melting of the old lower continental crust of the Congo craton's northern boundary. However, high-K alkali-calcic metaluminous granites are associated with delamination of over thickened crust (Frost et al., 2001).

CONCLUSION

The Pan-African post-collisional Batié granite at the southern edge of the Kekem–Fotouni shear zone (TBF fragment) in West Cameroon comprises biotite granite and amphibole granite, which is emplaced between 630 and 547 Ma during the transitional period between the crustal thickening (ca. 630–610 Ma) and the development of the shear zones first (610–580 Ma) sinistral and then dextral movements (585–540 Ma) and exhumed in a transpressive dextral NE–SW strike-slip tectonic setting. The presence of titanite, allanite, and magnetite associated with quartz shows that these highly potassic alkali-calcic granites are derived by partial melting of lower amphibolite deep crust and crystallized in a highly oxidizing H_2O-rich environment. Indeed, the granites of Batié were formed from highly evolved magma for the biotite granite to moderately evolved magma for the amphibole granite. These are high-temperature granites susceptible to mineralization. The mainly low initial $(^{87}Sr/^{86}Sr)_{620\ Ma}$ ratios (0.7062–0.7080) in combination with $\varepsilon Nd_{620\ Ma}$ (-12.6 to -8.9) suggest an abundant proportion of crustal material, supporting the participation of the old Paleoproterozoic crust in the formation of the Batié granite magma as indicated by their Nd T_{DM} ages (1.68–1.96 Ga). The results of this work indicate that there were successive phases of movement along the CCSZ, and that at each phase, it is associated with one granite series.

DATA AVAILABILITY STATEMENT

All datasets presented in this study are included in the article/**Supplementary Material**.

AUTHOR CONTRIBUTIONS

MK: conceptualization (lead), data curation (equal), formal analysis (equal), funding acquisition (equal), methodology (equal), validation (lead), visualization (lead), writing – original draft (lead), and writing – review and editing (lead). VT: formal analysis (equal), investigation (equal), and writing. EF: data curation (equal), formal analysis (equal), investigation (equal), and writing – review and editing (equal). JT: data curation (equal), investigation (equal), software (equal), and writing – review (equal). ID: data curation (equal), formal analysis (equal), methodology (equal), software (equal), validation (equal), and writing – review and editing (equal). EN: conceptualization (equal), formal analysis (supporting), project administration (supporting), and writing – review. All authors contributed to the article and approved the submitted version.

ACKNOWLEDGMENTS

We thank the Germany Academic Exchange Organisation (DAAD) for its financial support. MK thanks Gerhard Wörner of the Universität Göttingen for his supervision and his team, especially Andreas Kronz for his help on electron microprobe and Gerald Hartman for additional isotope analyses. We are grateful to the anonymous reviewers whose pertinent remarks contributed to improving the quality of the manuscript. We are grateful to GS (co-editor of this special issue), Ana Rodrigues (Frontiers fee support), and Ursuala Rabar (Frontiers liaison manager) for their assistance in obtaining funding for publishing fees.

SUPPLEMENTARY MATERIAL

The Supplementary Material for this article can be found online at: https://www.frontiersin.org/articles/10.3389/feart.2020.00363/full#supplementary-material

TABLE S1 | Laser ablation ICP-MS U-Pb data on zircon from Amphibole granite, sample BT901.

TABLE S2 | Rb-Srand Sm-Ndwhole-rock data (Model age calculated after Michard et al. (1985).

TABLE S3 | Major and trace elements analyses.

TABLE S4 | Selected microprobe analyses of amphibole from amphibole granite.

TABLE S5 | Selected microprobe analyses of biotite.

REFERENCES

Abdel-Rahman, A. F. M. (1994). Nature of biotites from alkaline, calc-alkaline, and peraluminous magmas. *J. Petrol.* 35, 525–541. doi: 10.1093/petrology/35.2.525

Abdelsalam, M. G., Liégeois, J. P., and Stern, R. J. (2002). The saharan metacraton. *J. Earth Sci.* 34, 119–136. doi: 10.1016/S0899-5362(02)00013-1

Anderson, J. L., and Smith, D. R. (1995). The effects of temperature and (O_2 on the Al-in-hornblende barometer. *Am. Mineral.* 80, 549–559. doi: 10.2138/am-1995-5-614

Barbarin, B. (1999). A review of the relationships between granitoid types, their origins and their geodynamic environments. *Lithos* 46, 605–626. doi: 10.1016/S0024-4937(98)00085-1

Barbey, P., Macaudière, J., and Nzenti, J. P. (1990). High-pressure dehydratation melting of metapelites: evidence from the migmatites of Yaoundé (Cameroon). *J. Petrol.* 31, 401–427. doi: 10.1093/petrology/31.2.401

Benito, R., Lopez-Ruiz, J., Cebria, J. M., Hertogen, J., Doblas, M., Oyarzun, R., et al. (1999). Sr and O isotope constraints on source and crustal contamination in the high-K calc-alkaline and shoshonitic neogene volcanic rocks of SE Spain. *Lithos* 46, 773–802. doi: 10.1016/S0024-4937(99)00003-1

Blevin, P. L. (2004). Redox and composional parameters for interpretating the granitoid metallogeny of Eastern Austria: implications for gold-rich ore system. *Resour. Geol.* 54, 241–252. doi: 10.1111/j.1751-3928.2004.tb00205.x

Blundy, J. D., and Holland, T. J. B. (1990). Calcic amphibole equilibrium and a new amphibole-plagioclase geothermometer. *Contribut. Mineral. Petrol.* 104, 208–224. doi: 10.1007/BF00306444

Bonin, B. (1990). From orogenic to anorogenic setting: evolution of granitic suites after a major orogenesis. *Geol. J.* 25, 261–270. doi: 10.1002/gj.3350250309

Bosch, D., Bruguier, O., and Pidgeon, R. T. (1996). The evolution of an Archaean metamorphic belt: a conventional and SHRIMP U-Pb study of accessory minerals from the Jimperding metamorphic belt, Yilgarn craton, Western Australia. *J. Geol.* 104, 695–711. doi: 10.1086/629863

Bouyo-Houketchang, M., Penaye, J., Njel, U. O., Moussango, A. P. I., Sep, J. P. N., Nyama, B. A., et al. (2016). Geochronological, geochemical and mineralogical constraints of emplacement depth of TTG suite from the Sinassi batholith in the central African Fold Belt (CAFB) of northern Cameroon: Implications for tectonomagmatic evolution. *J. African Earth Sci.* 116, 9–41. doi: 10.1016/j.jafrearsci.2015.12.005

Castaing, C., Feybesse, J. L., Thieblemont, D., Triboulet, C., and Chevremont, P. (1994). Palaeogeographical reconstructions of the Pan-African/Brasiliano Orogen; closure of an oceanic domain or intracontinental convergence between major blocks? *Precamb. Res.* 69, 327–344. doi: 10.1016/0301-9268(94)90095-7

Chappell, B. W., Bryant, C. J., Wyborn, D., White, A. J. R., and Williams, I. S. (1998). High- and Low-temperature I-type granites. *Ressour. Geol.* 48, 225–235. doi: 10.1111/j.1751-3928.1998.tb00020.x

Chappell, B. W., and White, A. J. R. (1992). I- and S-type granites in the Lachlan Fold Belt. *Trans. R. Soc. Edinburg. Earth Sci.* 83, 1–26. doi: 10.1017/S0263593300007720

Chen, M., Sun, M., Buslov, M. M., Cai, K., Zhao, G., Kulikova, V. A., et al. (2016). Crustal melting and magma mixing in a continental arc setting: evidence from the Yaloman intrusive complex in the Gorny Altai terrane, Central Asian Orogenic Belt. *Lithos* 252–253, 76–91. doi: 10.1016/j.lithos.2016.02.016

Clowe, C. A., Popp, R. K., and Fritz, S. J. (1988). Experimental investigation of the effect of oxygen fugacity on ferric-ferrous ratios and unit-cell parameters of four natural clinoamphiboles. *Am. Mineral.* 73, 487–499.

Dawaï, D., Bouchez, J. L., Paquette, J. L., and Tchameni, R. (2013). The Pan-Afrcan quartz-syenite of Guider (North-Cameroon): magnetic fabric and U-Pb dating of a late-orogenic emplacement. *Precamb. Res.* 236, 132–144. doi: 10.1016/j.precamres.2013.07.008

Djouka-Fonkwé, M. L., Schulz, B., Schüssler, U., Tchouankoué, J.-P., and Nzolang, C. (2008). Geochemistry of the Bafoussam Pan-African I- and S-type granitoids in western Cameroon. *J. African Earth Sci.* 50, 148–167. doi: 10.1016/j.jafrearsci.2007.09.015

Dumort, J.-C. (1968). Carte Géologique de Reconnaissance à L'échelle du 1/50000, République Fédérale du Cameroun, Notice Explicative Sur la Feuille Douala-Ouest, Direction des Mines et de la Géologie du Cameroun.

Dunkl, I., Mikes, T., Simon, K., and von Eynatten, H. (2008). "Brief introduction to the windows program Pepita: data visualization, and reduction, outlier rejection, calculation of trace element ratios and concentrations from LA-ICP-MS data," in *Laser Ablation ICP-MS in the Earth Sciences: Current Practices and Outstanding Issues. Mineralogical Association of Canada, Short Course*, ed. P. Sylvester (Quebec City, QC: Mineralogical Association of Canada), 334–340.

Ferré, E., Caby, R., Peucat, J. J., Capdevila, R., and Monié, P. (1998). Pan-African, post-collisional, ferro-potassic granite and quartz-monzonite plutons of Eastern Nigeria. *Lithos* 45, 255–279. doi: 10.1016/S0024-4937(98)00035-8

Foster, M. (1960). Interpretation of the composition of trioctahedral micas. *U.S. Geol. Surv. Prof. Pap.* 354, 11–49. doi: 10.3133/pp354B

Fozing, E. M., Kwékam, M., Gountié Dedzo, M., Asaah Asobo, N. E., Njanko, T., Tcheumenak Kouémo, J., et al. (2019). Petrography and geochemistry of amphibolites from the Fomopéa Pluton (West Cameroon): origin and geodynamic setting. *J. African Earth Sci.* 154, 181–194. doi: 10.1016/j.jafrearsci.2019.03.024

Fozing, E. M., Kwékam, M., Njanko, T., Njonfang, E., Séta, N., Yakeu Sandjo, A. F., et al. (2014). Structural evolution of the Pan-African Misajé pluton (Northwestern Cameroon). *Syllab. Rev. Sci. Ser.* 5, 12–26.

Frost, B. R., Barnes, C. G., Collins, W. J., Arculus, R. J., Ellis, D. J., and Frost, C. D. (2001). A geochemical classification for granitic rocks. *J. Petrol.* 42, 2033–2048. doi: 10.1093/petrology/42.11.2033

Hollister, L. S., Grisson, G. C., Peters, E. K., Stowell, H. H., and Sisson, S. B. (1987). Confirmation of the empirical correlation of Al in hornblende with pressure of solidification of calc-alkaline plutons. *Am. Mineral.* 72, 231–239.

Jackson, S., Pearson, N., Griffin, W., and Belousova, E. (2004). The application of laser ablation-inductively coupled plasma-mass spectrometry to in situ U-Pb zircon geochronology. *Chem. Geol.* 211, 47–69. doi: 10.1016/j.chemgeo.2004.06.017

Johnson, M. C., and Rutherford, M. J. (1989). Experimental calibration of the aluminium-in-hornblende geobarometer with application to Long valley caldera (California) volcanic rocks. *Geology* 17, 841–867. doi: 10.1130/0091-7613(1989)017<0837:ECOTAI>2.3.CO;2

Kwékam, M., Affaton, P., Bruguier, O., Liégeois, J.-P., Hartmann, G., and Njonfang, E. (2013). The Pan-African Kekem gabbro-norite (West-Cameroon), U-Pb zircon age, geochemistry and Sr-Nd isotopes: geodynamical implication for the evolution of the Central African fold belt. *J. African Earth Sci.* 84, 70–88. doi: 10.1016/j.jafrearsci.2013.03.010

Kwékam, M., Dunkl, I., Fozing, E. M., Hartmann, G., Njanko, T., Tcheumenak Kouémo, J., et al. (2020). Syn-kinematic ferroan high-K I-type granites from Dschang in South-western Cameroon: U-Pb age, geochemistry and implications for crustal growth in the late Pan-African orogeny. *Geol. Soc.* 502:19. doi: 10.1144/sp502-2019-19

Kwékam, M., Liégeois, J.-P., Njonfang, E., Affaton, P., Hartmann, G., and Tchoua, F. (2010). Nature, origin, and significance of the Fomopéa Pan-African high-K calc-alkaline plutonic complex in the Central African fold belt (Cameroon). *J. African Earth Sci.* 54, 79–95. doi: 10.1016/j.jafrearsci.2009.07.012

Leake, B. E., Woolley, A. R., Arps, C. E. S., Birch, W. D., Grice, M. C., Hawthorne, F. C., et al. (1997). Nomenclature of amphiboles: report of the subcommitte on amphiboles of the international mineralogical association, commission on new minerals and mineral names. *Can. Mineral.* 35, 219–246.

Lee, C.-T. A., and Bachmann, O. (2014). How important is the role of crystal fractionation in making intermediate magmas? Insights from Zr and P systematics. *Earth Planet. Sci. Lett.* 393, 266–274. doi: 10.1016/j.epsl.2014.02.044

Li, X. H., Chen, Y., Tchouankoué, J. P., Liu, C. Z., and Li, J. (2017). Improving geochronological framework of the Pan-African orogeny in Cameroon: new SIMS zircon and monazite U-Pb age constraints. *Precamb. Res.* 294, 307–321. doi: 10.1016/j.precamres.2017.04.006

Liégeois, J. P., Abdelsalam, M. G., Ennih, N., and Ouabadi, A. (2013). Metacraton: nature, genesis and behavior. *Gondw. Res.* 23, 220–237. doi: 10.1016/j.gr.2012.02.016

Liégeois, J.-P., Navez, J., Hertogen, J., and Black, R. (1998). Contrasting origin of post-collisional high-K calc-alkaline and shoshonotic versus alkaline and peralkaline granitoids. The use of sliding normalization. *Lithos* 45, 1–28. doi: 10.1016/S0024-4937(98)00023-1

Ludwig, K. R. (2012). User's Manual for Isoplot 3.75: A Geochronological Toolkit for Microsoft Excel. Berkeley Geochronology Center Special Publication, no. 4, p. 70. Available online at: http://www.bgc.org/isoplot_etc/isoplot/Isoplot3_75-4_15manual.pdf

Maniar, P. D., and Piccoli, P. M. (1989). Tectonic discrimination of granitoids. *Geol. Soc. Am. Bull.* 101, 635–643. doi: 10.1130/0016-7606(1989)101<0635:TDOG>2.3.CO;2

Marre, J. (1982). Méthodes d'analyse structurale des granitoïdes. *B.R.G.M. Manuels et Méthodes* 3:128.

McDonough, W. F., Sun, S.-S., Ringwood, A. E., Jagoutz, E. A. W., and Hofmann, A. W. (1992). Potassium, rubidium, and cesium in the Earth and Moon and the evolution of the mantle of the Earth. *Geochim. Cosmochim. Acta* 56, 1001–1012. doi: 10.1016/0016-7037(92)90043-I

Michard, A., Gurriet, P., Soudan, M., and Albarède, F. (1985). Nd isotopes in French Phanerozoic shales: external vs internal aspects of crustal evolution. *Geochim. Cosmochim. Acta* 49, 601–610. doi: 10.1016/0016-7037(85)90051-1

Ngako, V., Affaton, P., and Njonfang, E. (2008). Pan-African tectonic in northwestern Cameroon: implication for history of Western Gondwana. *Gondw. Res.* 14, 509–522. doi: 10.1016/j.gr.2008.02.002

Ngako, V., Affaton, P., Nnange, J. M., and Njanko, T. (2003). Pan-African tectonic evolution in central and southern Cameroon: transpression and transtension during sinistral shear movements. *J. African Earth Sci.* 36, 207–214. doi: 10.1016/S0899-5362(03)00023-X

Nguiessi-Tchankam, Cl, Nzenti, J. P., Nsifa, E. N., Tempier, P., and Tchoua, F. (1997). A calc-alkaline magmatic complex from Bandja in the north-equatorial fold belt; a synkinematic emplacement of plutonic rocks in a sinistral strike-slip shear zone from Pan-African age. *Compt. Rend. Acad. Sci. Paris* 325, 95–101. doi: 10.1016/S1251-8050(97)83969-9

Njanko, T., Njiki Chatué, C., Kwékam, M., Bella Nké, B. E., Yakeu Sandjo, A. F., and Fozing, E. M. (2017). The Numba ductile deformation zone (northwest Cameroon): a geometric analysis of folds based on the Fold Profiler method. *J. Earth Syst. Sci.* 126, 23–33. doi: 10.1007/s12040-017-0801-7

Njiekak, G., Dörr, W., Tchouankoué, J.-P., and Zulauf, G. (2008). U-Pb zircon and microfabric data of (meta) granitoids of western Cameroon: constraints on the timing of pluton emplacement and deformation in the Pan-African belt of central Africa. *Lithos* 102, 460–477. doi: 10.1016/j.lithos.2007.07.020

Njonfang, E., Ngako, V., Kwékam, M., and Affaton, P. (2006). Les orthogneiss calco-alcalins de Foumban-Bankim: témoins d'une zone interne de marge active panafricaine en cisaillement. *Compt. Rend. Geosci.* 338, 606–616. doi: 10.1016/j.crte.2006.03.016

Nzenti, J. P., Ngako, V., Kambou, R., Penaye, J., Bassahak, J., and Njel, U. O. (1992). Structures regionals de la chaîne panafricaine au Nord-Cameroun. *Compt. Rend. Acad. Sci. Paris* 611, 115–119.

Nzolang, C., Kagami, H., Nzenti, J. P., and Holtz, F. (2003). Geochemistry and preliminary Sr-Nd isotopic data on the neoproterozoic granitoids from the Bantoum area, west Cameroon: evidence for a derivation from a Paleoproterozoic to Archean crust. *Pol. Geosci.* 16, 196–226.

Patiño Douce, A. E. (1999). What do experiments tell us about the relative contributions of crust and mantle to the origin of granitic magmas? *Geol. Soc. Lond. Spec. Public.* 168, 55–75. doi: 10.1144/GSL.SP.1999.168.01.05

Pearce, J. A., Harris, N. B. W., and Tindle, A. G. (1984). Trace element discrimination diagrams for the tectonic interpretation of granitic rocks. *J. Petrol.* 25, 956–983. doi: 10.1093/petrology/25.4.956

Peccerillo, A., and Taylor, S. R. (1976). Geochemistry of eocene calc-alkaline volcanic rocks from the Kastamonu area, Northern Turkey. *Contribut. Mineral. Petrol.* 58, 63–81. doi: 10.1007/BF00384745

Penaye, J., Toteu, S. F., Van Schumus, W. R., and Nzenti, J. P. (1993). U-Pb and Sm-Nd Preliminary geologic data on the Yaoundé séries Cameroon. Reinterpretation of the granulitic rocks as suture of a collision in the "Central African" belt. *Compt. Rend. Acad. Sci. Paris* 317, 789–794.

Pouchou, J. L., and Pichoir, F. (1984). A new model for quantitative X-ray microanalysis of homogeneous samples. *Rech. Aérosp.* 5, 13–38.

Pupin, J. P. (1980). Zircon and granite petrology. *Contribut. Mineral. Petrol.* 73, 207–220. doi: 10.1007/BF00381441

Rickwood, P. C. (1989). Boundary lines within petrologic diagrams which use oxides of major and minor elements. *Lithos* 22, 247–263. doi: 10.1016/0024-4937(89)90028-5

Ridolfi, F., Renzulli, A., and Puerini, M. (2010). Stability and chemical equilibrium of amphibole in calc-alkaline magmas: an overview, new thermobarometric formulations and application to subduction-related volcanoes. *Contribut. Mineral. Petrol.* 160, 45–66. doi: 10.1007/s00410-009-0465-7

Rudnick, R. L., and Gao, S. (2003). "Composition of the continental crust," in *The Crust, Treatise in Geochemistry*, Vol. 3, eds R. L. Rudnick, H. D. Holland, and K. K. Turekian (Amsterdam: Elsevier), 1–16. doi: 10.1016/B0-08-043751-6/03016-4

Saunders, A. D., and Tarney, J. (1984). "Geochemical characteristic of basaltic volcanism within back-arc basins," in *Marginal Basin Geology*, eds B. P. Kokelaar and M. F. Howells (London: Geology Society), 59–76. doi: 10.1144/GSL.SP.1984.016.01.05

Schmidt, M. (1992). Amphibole composition in tonalite as a function of pressure: an experimental calibration of the Al-in-hornblende barometer. *Contribut. Mineral. Petrol.* 110, 304–310. doi: 10.1007/BF00310745

Sláma, J., Košler, J., Condon, D. J., Crowley, J. L., Gerdes, A., Hanchar, J. M., et al. (2008). Plešovice zircon - A new natural reference material for U-Pb and Hf isotopic microanalysis. *Chem. Geol.* 249, 1–35. doi: 10.1016/j.chemgeo.2007.11.005

Sun, S. S. (1982). Chemical composition and origin of the earth's primitive mantle. *Geochim. Cosmochim. Acta* 46, 179–192. doi: 10.1016/0016-7037(82)90245-9

Tagne-Kamga, G. (2003). Petrologenesis of the neoproterozoic ngondo plutonic complex (Cameroon, west central Africa): a case of late-collisional ferro-potassic magmatism. *J. African Earth Sci.* 36, 149–171. doi: 10.1016/S0899-5362(03)00043-5

Talla, V. (1995). *Le Massif Granitique Panafricain de Batié (Ouest Cameroun): Pétrologie-Pétrostructurale-Géochimie*. Thèse Doctorat 3ème cycle, Université de Yaoundé I, Yaoundé.

Tchameni, R., Pouclet, A., Penaye, J., Ganwa, A. A., and Toteu, S. F. (2006). Petrology and geochemistry of the Ngaoundéré Pan-African granitoids in central north Cameroon: implications for their sources and geological setting. *J. African Earth Sci.* 44, 511–529. doi: 10.1016/j.jafrearsci.2005.11.017

Tcheumenak Kouémo, J., Njanko, T., Kwékam, M., Naba, S., Bella Nké, B. E., Yankeu Sandjo, A. F., et al. (2014). Kinematic evolution of the Fodjomekwet-Fotouni Shear Zone (West-Cameroon): implication on the emplacement of the Fomopéa and Bandja plutonic massifs. *J. African Earth Sci.* 99, 261–275. doi: 10.1016/j.jafrearsci.2014.07.018

Tchouankoué, J. P., Li, X. H., Ngo Belnoun, R. N., Mouafo, L., and Ferreira, V. P. (2016). Tinning and tectonic implications of the Pan-African Bangangté syenomonzonite: constraints from in-situ zircon U-Pb age and Hf-O isotopes. *J. African Earth Sci.* 124, 94–103. doi: 10.1016/j.jafrearsci.2016.09.009

Tetsopgang, S., Suzuki, K., and Njonfang, E. (2008). Petrology and CHIME geochronology of Pan-African high-K and Sr/Y granitoids in the Nkambé area, Cameroon. *Gondw. Res.* 14, 686–699. doi: 10.1016/j.gr.2008.01.012

Toteu, S. F., Fouateu, Y. R., Penaye, J., Tchakounté, J., Mouangue, S. C. A., Van Schmus, R. W., et al. (2006). U-Pb dating of plutonic rocks involved in the nape tectonic in Southern Cameroon: consequence for the Pan-African orogenic evolution of the central African fold belt. *J. African Earth Sci.* 44, 479–493. doi: 10.1016/j.jafrearsci.2005.11.015

Toteu, S. F., Penaye, J., and Poudjoum-Djomani, Y. H. (2004). Geodynamic evolution of the Pan-African belt in Central Africa with special reference to Cameroon. *Can. J. Earth Sci.* 41, 73–85. doi: 10.1139/e03-079

Toteu, S. F., Van Schmus, W. R., Penaye, J., and Michard, A. (2001). New U-Pb and Sm-Nd data from north-central Cameroon and its bearing on the pre-Pan African history of central Africa. *Precamb. Res.* 108, 45–73. doi: 10.1016/S0301-9268(00)00149-2

Wiedenbeck, M., Allé, P., Corfu, F., Griffin, W. L., Meier, M., Oberli, F., et al. (1995). Three natural zircon standards for U-Th-Pb, Lu-Hf, trace element and REE analyses. *Geostand. Newslett.* 19, 1–23. doi: 10.1111/j.1751-908X.1995.tb00147.x

Wones, D. R. (1981). Mafic silicates as indicators of intensive variables in granitic magmas. *Min. Geol.* 31, 191–212.

Wones, D. R. (1989). Significance of the assemblage titanite + magnetite + quartz in granitic rocks. *Am. Mineral.* 74, 744–749.

Conflict of Interest: The authors declare that the research was conducted in the absence of any commercial or financial relationships that could be construed as a potential conflict of interest.

frontiers in Earth Science

ORIGINAL RESEARCH
published: 01 October 2020
doi: 10.3389/feart.2020.551097

Schedule of Mafic to Hybrid Magma Injections Into Crystallizing Felsic Magma Chambers and Resultant Geometry of Enclaves in Granites: New Field and Petrographic Observations From Ladakh Batholith, Trans-Himalaya, India

Santosh Kumar[1]*

[1] Department of Geology, Centre of Advanced Study, Kumaun University, Nainital, India

OPEN ACCESS

Edited by:
J. Gregory Shellnutt, National Taiwan Normal University, Taiwan

Reviewed by:
Koushik Sen, Wadia Institute of Himalayan Geology, India
Fatemeh Sarjoughian, University of Kurdistan, Iran

***Correspondence:**
Santosh Kumar
skyadavan@yahoo.com

Specialty section:
This article was submitted to Petrology, a section of the journal Frontiers in Earth Science

Received: *11 April 2020*
Accepted: *01 September 2020*
Published: *01 October 2020*

Citation:
Kumar S (2020) Schedule of Mafic to Hybrid Magma Injections Into Crystallizing Felsic Magma Chambers and Resultant Geometry of Enclaves in Granites: New Field and Petrographic Observations From Ladakh Batholith, Trans-Himalaya, India. Front. Earth Sci. 8:551097. doi: 10.3389/feart.2020.551097

Diorites, granites, and associated magmatic enclaves and dykes constitute the bulk of the Ladakh Batholith, which is an integral part of the Trans-Himalayan magmatic arc system. In this paper geometry of microgranular enclaves hosted in the granites has been examined from the Leh-Sabu-Chang La and surrounding regions of the eastern Ladakh Batholith to infer the mechanism and schedule of mafic to hybrid magma injections into evolving felsic magma chambers and the resultant enclave geometry. Mafic or hybrid magmas inject into felsic magma at low volume fraction (<0.35) of crystals and form the rounded to elongated microgranular enclaves in the Ladakh Batholith. Angular to subangular (brecciated), rounded to elongated pillow-like microgranular enclave swarms can also be documented as disrupted synplutonic mafic to hybrid dykes and sheets, when intruding the felsic magma with high volume fraction (>0.65) of crystals. A large rheological difference between coeval felsic and mafic magmas inhibits much interaction. Mafic magma progressively crystallizes and evolves while minimizing thermal and rheological differences. Consequently, the felsic-mafic magma interaction process gradually becomes more efficient causing the dispersion of enclave magma globules and undercooling into the partly crystalline felsic host magma. Thus the evolution of the Ladakh Batholith should be viewed as multistage interactions of mafic to hybrid magmas coeval with felsic magma pulses in plutonic conditions from its initial to waning stages of evolution.

Keywords: enclaves, synplutonic dykes, granites, Ladakh Batholith, Trans-Himalaya, India

INTRODUCTION

Granites (*sensu lato*) may contain any type of lithic inclusion or fragment, which is commonly referred to as *enclave* (a French term, Lacroix, 1890 in Didier, 1973). The diverse nature and origin of enclaves hosted in granites are described in many studies (e.g., Didier, 1984; Vernon, 1984; Furman and Spera, 1985; Castro et al., 1991a; Castro et al., 1991b; Shellnutt et al., 2010; Kumar et al., 2004a; Kumar et al., 2004b; Kumar et al., 2005; Clemens et al., 2016; Kumar et al., 2017), and are considered

to represent: 1) xenolith (Sollas, 1894) as solid fragment of country rocks mostly confined to the margins of a pluton or may represent enroute deeper-derived lithology or unmelted source material, 2) surmicaceous enclave (Lacroix, 1933) as segregation of refractory source materials (restite) left after partial melting, 3) cognate or autolith (Pabst, 1928) as early-crystallized cumulus phases or segregation of mafic clots or fragments of chilled border rock series of cogenetic felsic magma, 4) microgranular (Didier and Roques, 1959) or microgranitoid (Vernon, 1983) enclaves representing felsic, mafic, and mafic-felsic (intermediate) hybridized magmas entrained, mingled, and undercooled into relatively cooler partly crystalline felsic host magma at any stage of its evolution. However, when mafic or hybrid magma is injected into a largely crystallized felsic magma chamber, it is commonly distributed as swarms of microgranular enclave together with synplutonic dykes (Barbarin, 1989; Kumar, 2014). In the present paper, the term enclave refers to the mafic and mafic-felsic (hybrid) varieties of microgranular or microgranitoid enclaves.

Enclaves in granites can offer significant insight into the understanding of operative physical and chemical processes during the evolution of a felsic plutonic system. The similar ages, chemical, and isotopic signatures of enclaves and host granites have been interpreted in various ways. Some favor the cogenetic relation between the enclave and host granites (e.g., Pin et al., 1990; Shellnut et al., 2010) whereas some argue their derivation from common crustal sources (e.g., Güraslan and Altunkaynak, 2019; Lu et al., 2020); and some advocate mafic-felsic magma mixing, mingling, chemical modification, and isotopic re-equilibration at varying degrees responsible for their partial to nearly equivocal chemical and isotopic features (e.g., Holden et al., 1987; Eberz and Nicholls, 1990; Elburg, 1996; Kumar and Rino, 2006; Adam et al., 2019). The geochemical and isotopic features do not provide unambiguously a viable model of enclave origin. Therefore in most cases, discussion on the origin of enclaves in granites largely revolves around the interpretations of megascopic and microscopic features (e.g., Didier, 1973; Sparks et al., 1977; Vernon, 1983; Eberz and Nicholls, 1988; Vernon et al., 1988; Barbarin, 1989, Castro, 1990; Didier and Barbarin, 1991; Fernandez and Gasquet, 1994; Kumar, 1995; Kumar et al., 2004a; Kumar et al., 2004b; Kumar, 2010a; Wiebe et al., 2007; Vernon, 2014).

The enclaves are usually ubiquitous in metaluminous (I-type), calc-alkaline granites, but are also found in other granite types such as anorogenic A–, hybrid H–, and shoshonitic SH-types. However, the enclaves are relatively rare in peraluminous (S-type) granites and absent in anatectic or leucogranite. The surmicaceous enclaves are rare in anorogenic (A-type), post-collisional granites (Didier, 1984). The enclaves may also enclose xenoliths and are considered to be double enclaves (Didier, 1987), however, large enclaves can enclose several other smaller enclaves, which can be referred to as composite enclaves (e.g., Kumar, 2010a). Zoned enclaves with different cooling history are also reported in the granites (e.g., Adam et al., 2019).

Felsic and associated magmatic rocks constitute the bulk of the Ladakh Batholith (600 km long, 20–80 km wide) roughly trending NW-SE covering an area of ca 30,000 sq km, which is an integral part of the Trans-Himalayan calc-alkaline magmatic arc system located in the north of Indus Tsangpo Suture Zone (ITSZ) (**Figure 1A**). The Ladakh Batholith is largely formed by the melting of Neo-Tethyan ocean crust subducted below the Asian plate during early Cretaceous-Lower Eocene (Thakur, 1992), and is characterized by mafic to felsic composite intrusions of variable compositions. The mafic-felsic magmatic suites range from gabbro-diorite-tonalite to granodiorite-granite-leucogranite of magnetite (oxidized) and ilmenite (reduced) series granites corresponding to metaluminous (I-type) and peraluminous (S-type) granites, respectively, which are crosscut by several post-plutonic mafic dykes (Auden, 1935; Wadia, 1937; Frank et al., 1977; Rai, 1980; Honegger et al., 1982; Ahmad et al., 1998, Kumar, 2008, Kumar, 2010b). Felsic magmatic rocks forming the Ladakh Batholith are collectively referred as granites unless stated for a specific rock type. Earlier mafic (diorite) stock-like bodies are also found disrupted by intruding granite magma that is more pronounced in the eastern parts of Ladakh Batholith (e.g., Weinberg, 1997; Kumar, 2010a; Kumar et al., 2016). Enclaves as xenoliths of older mafic volcanics in granites are also reported (Rai, 1980; Ahmad et al., 1998; Jain et al., 2003; Singh et al., 2007). Redox conditions of Ladakh granites and related rocks have been assessed in terms of magnetic susceptibility and phase petrology (Kumar, 2008; Kumar 2010b). The occurrence and origin of mafic to hybrid microgranular enclaves hosted in Ladakh Batholith are reported and discussed (Kumar, 2010a).

In this paper, new spectacular field and petrographic features of microgranular enclaves, and dyke- and sheet-like enclave swarms, referred as synplutonic dykes, hosted in the granites exposed in and around Leh, Sabu, and Chang La regions of Ladakh Batholith have been documented and examined in order to understand the style and schedule of mafic to hybrid magma injections into felsic magma chambers from its initial to waning stages of evolution (i.e., with increasing crystallinity and rheology).

Geology, Geochemistry, and Geochronology

In the Trans-Himalaya, the Kohistan–Ladakh-Karakoram Batholiths have evolved as a single entity during the late Cretaceous and early Palaeogene (Pundir et al., 2020, and references therein). The Ladakh Batholith represents an integral part of the Trans-Himalayan calc-alkaline magmatic belt extending from east of Nanga Parbat to Lhasa (**Figure 1A**) and is bounded by Shyok Suture Zone (SSZ) in the north and ITSZ in the south (**Figure 1B**). The Asian plate in the north and Indian plate in the south are juxtaposed and accreted along the ITSZ with the closure of Neo-Tethyan Ocean. Ahmad et al. (1998) stated that the enclaves in the granites probably represent the initial pulses of magmatism in response to intra-oceanic northward subduction of Neo-Tethyan Ocean beneath an immature arc, and subsequently, a huge amount of felsic magmatism was generated as the arc matured forming the Ladakh Batholith.

The Ladakh Batholith is differentially unroofed in the western (p = 3.35–4.27 kbar), central (p = 2.99 kbar), and eastern (p = 2.17 kbar) parts, as inferred from Al-in-hornblende geobarometer (Kumar, 2010b). The FeO^t/MgO ratio of biotites

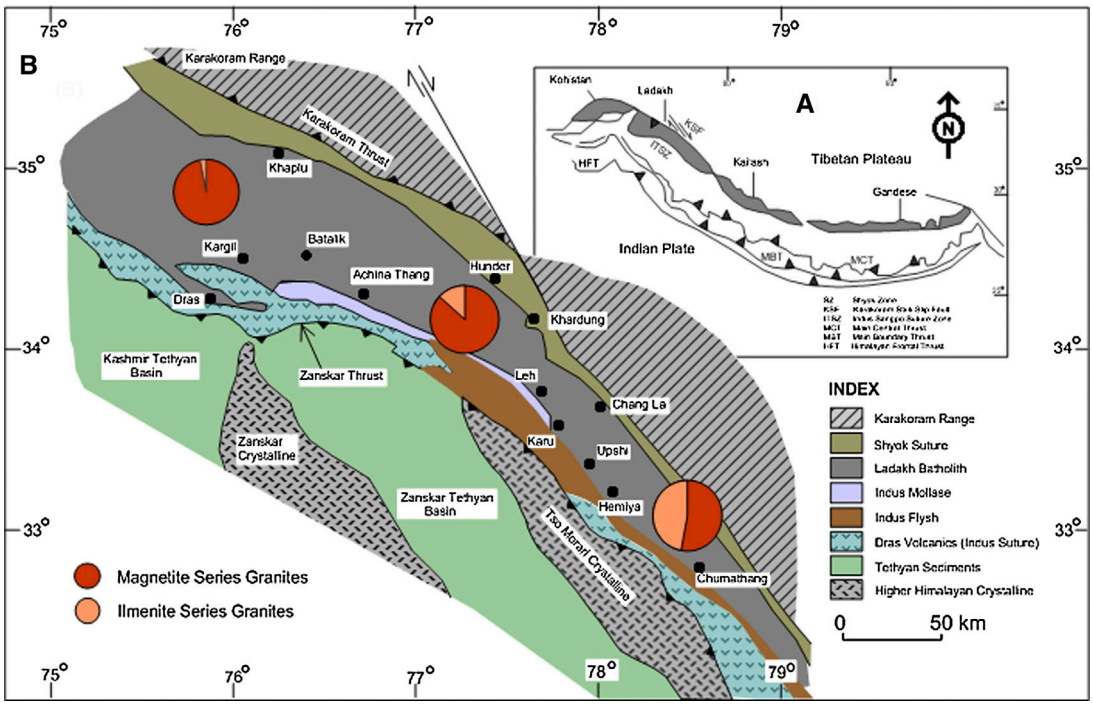

FIGURE 1 | (A) Geological structure of Himalaya showing the tectonic elements, Trans-Himalayan magmatic arc and location of the Ladakh Batholith (after Gansser, 1977). **(B)** Geological map of Ladakh Himalaya (after Sharma and Chaubey, 1983; Thakur, 1987). Relative abundance of magnetite series and ilmenite series granites in western, central and eastern parts of the Ladakh Batholith is shown by wheel diagrams (Kumar, 2008; Kumar, 2010b).

from the granites of western (1.44–2.19), central (1.31–1.90), and eastern (1.71–2.63) parts suggests the contribution of dominant calc-alkaline, metaluminous (I-type), and subordinate amount of peraluminous (S-type) felsic magmas in the evolution of Ladakh Batholith. Ahmad et al. (1998) observed that the enclaves and mafic dykes in granites of the Ladakh Batholith are basaltic-andesite and andesite belonging to subalkaline, calc-alkaline series in terms of major and trace elements. The negative relationship of MgO, $Fe_2O_3^t$, MnO, TiO_2, CaO, Al_2O_3 against SiO_2, and positive trends of TiO_2, CaO, CaO/Al_2O_3 against MgO may indicate fractionation of gabbroic assemblage, however, the absence of negative chondrite normalized Eu and primitive mantle normalized Sr anomalies shows that plagioclase was not an important fractionating phase. Based on geochemical features of enclaves, Ahmad et al. (1998) proposed the cognate or autolith origin for some selected enclaves sampled from western Ladakh, as inferred by Honegger et al. (1982), and others as entrained xenoliths of pre-existing mafic rock into the granites. However, Kumar and Singh (2008) suggest that the enclaves and host granites are largely as calc-alkaline, mildly to strongly metaluminous (molar $Al_2O_3/CaO + Na_2O + K_2O$ = 0.9–1.05), which are compositionally different from diorite, gabbro, and mafic dykes. Near linear to curvilinear variation trends observed for TiO_2, CaO, $Fe_2O_3^t$, MgO, MnO, and TiO_2 against SiO_2 of enclaves and host granites can be attributed to synchronous mafic-felsic magma mixing and fractionation. The large data scatter for Al_2O_3, Na_2O, K_2O, P_2O_5, Rb, Ba, Nb, Yb, and Zr against SiO_2 is, however, a combined outcome of elemental diffusion at varying degrees and sorting of minerals hosting these elements during mixing-fractionation events.

The extent and duration of calc-alkaline felsic magmatism constituting the Ladakh Batholith have been constrained based on a variety of chronological database, without taking into account the mafic to hybrid magma contributions. Magmatism within the Ladakh Batholith was most intense during Late Cretaceous to Early Paleogene (67 and 45 Ma) (Singh et al., 2007; Upadhyay et al., 2008; Jain and Singh, 2009; Ravikant et al., 2009; White et al., 2011a; White et al., 2011b; Kumar et al., 2012; Shellnutt et al., 2013; Jain 2014) with early discrete pulses at *ca.* 102 and 97 Ma identified in the western part (Honegger et al., 1982). Some sporadic geochronological data (Singh et al., 2007) on coarse grained diorite (58.4 ± 1.0 Ma) and granodiorite (60.1 ± 0.5 Ma) from Karu and Chang La regions of the Ladakh Batholith suggest a coeval nature between the diorite and granodiorite. A subvolcanic mafic dyke (45.7 ± 0.8 Ma) and granites (45.27 ± 0.56 Ma) at Daah-Hanu (Weinberg and Dunlop, 2000) provide the same ages of their formation. The likely reasons for synchronous diorite and granodiorite magmatism are not yet described. However, in and around the Leh and Sabu regions, stock-like dioritic bodies are also found as pre-existing older lithological units as compared to the granites (Kumar et al., 2016; Weinberg, 1997).

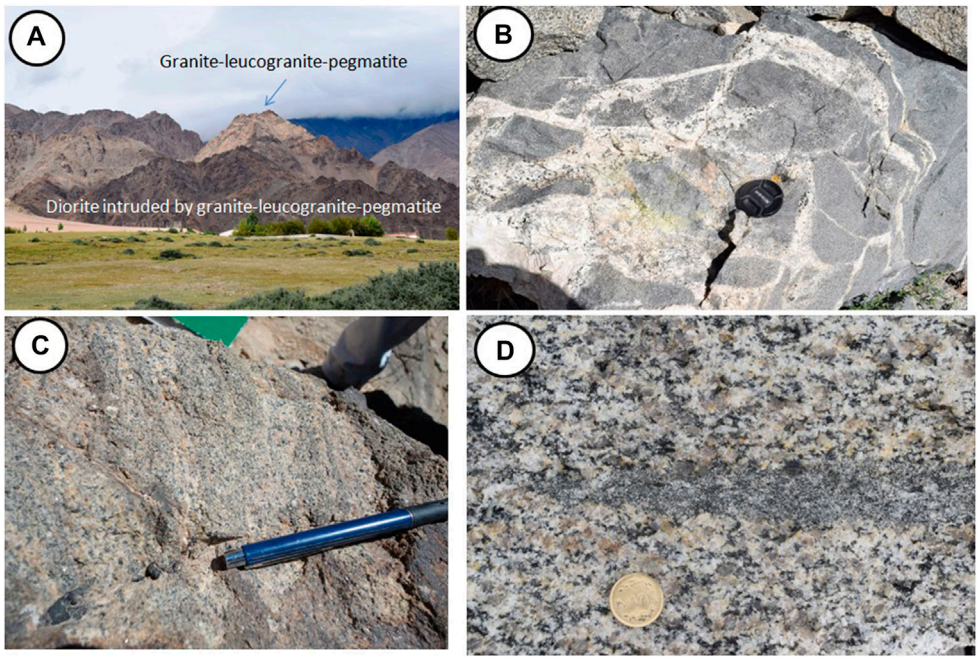

FIGURE 2 | (A) Panoramic view of diorite and granite-leucogranite-pegmatite hills near Sabu, showing the intrusive relationships between them. **(B)** Diorite is dismembered as xenoliths and partially assimilated by the intruding granite-leucogranite-pegmatite system. **(C)** Modally graded crude igneous layering shown by alternate bands of mafic and felsic minerals in the granite. **(D)** Biotite granite contains elongated mesocratic fine grained facies with diffused boundaries.

MATERIALS AND METHODS

More than 35 outcrops along planned traverses exposed in and around the Leh-Sabu-Chang La regions of eastern Ladakh Batholith have been investigated in order to establish the field relationships between mafic lithological units including the enclaves and host granites. The enclave typology, synplutonic dykes and sheets, and their morphology, size, and contact relations with host granites were recorded and documented. The preferred criteria in classifying the enclave types are their macro- and micro-structures (shapes: spheroidal to ellipsoidal; roundness: as their corners, and edges are rounded, subrounded or angular; contact relationships: sharp, diffused, crenulated to highly convoluted; primary igneous flow-lamination, fine- to coarse-grained phenocryst-bearing or phenocryst-free, cumulates, and solid-state deformation defined by foliation, schistosity, gneissosity, etc.). Representative rock thin sections were prepared for petrographic study and estimating the modal volume percentage of constituting minerals to assign the name of the rocks. The petrographic features relevant to infer the physical properties and processes such as viscosity contrast, magma-mixing, mingling, and undercooling have also been documented.

Megascopic and Microscopic Results

Field Observations

The Ladakh Batholith is mainly composed of diorite, granodiorite (±enclaves), leucogranite, and pegmatite. Granodiorite is the most dominant rock type among all of the observed varieties of granitic rocks. The granite hillocks with melanocratic bodies and patches of diorites are widespread in and around the Leh and Sabu regions. Such diorite outcrops as stock-like bodies are exposed widely at several sq meters to a hundred sq km scale, which can be seen even from far distances. The granite-leucogranite-pegmatite system intrudes the diorites (**Figure 2A**). Leucogranites and pegmatites are devoid of microgranular enclaves. The intrusive relationships are very well displayed by the presence of partially assimilated xenoliths of diorites and network of leucogranite-pegmatite veins (**Figure 2B**). At several places, the granite exhibits linear sharp contacts with the diorites. Near Sabu, the granite shows a rare feature of modally graded, crudely layered igneous structures with alternate bands of coarse grained mafic (hornblende, biotite) and felsic (quartz, feldspars) minerals (**Figure 2C**). At Leh, near the western end of town, undeformed, equigranular medium to coarse grained biotite granites are widely exposed, which occasionally host elongated fine grained mesocratic lithic materials showing diffuse boundaries with the host granites (**Figure 2D**). At this particular outcrop, amphibole is absent or rare and is devoid of enclaves.

At places, the fine grained mafic rock with devitrified glassy xenocrysts shows jigsaw-like crenulated margins (**Figure 3A**). A mesocratic porphyritic enclave of nearly circular shape with sharp and slightly diffused margins contains variable proportion of mafic-felsic xenocrysts that appear as phenocrysts (**Figure 3B**). The felsic xenocrysts, in particular, are rounded to subhedral that indicate their partial resorption in hybrid magma. Fine grained mafic enclaves commonly having subrounded to elongate shapes (up to 15 cm across) are intimately linked with fine mafic schlierens and aggregates.

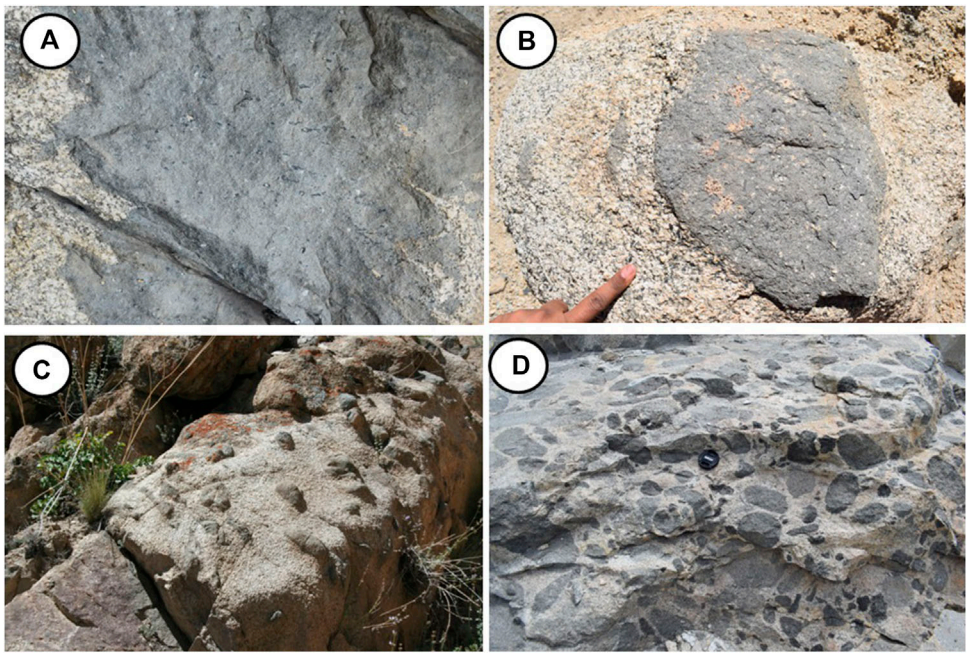

FIGURE 3 | (A) Fine grained mafic body contains frequent quartz (glass) xenocrysts and shows serrated contacts with host granite. **(B)** A large enclave containing mafic-felsic phenocrysts showing sharp contact with host granite. Partial diffuse contact can also be noted. **(C)** Elongated mafic enclave swarms follow a particular direction in the host granite. Note the enclaves form monadnock ridge. **(D)** Randomly oriented closely spaced holomelanocratic, melanocratic to mesocratic enclaves with variable shapes and sizes are hosted in granite from northern margin of Ladakh Batholith.

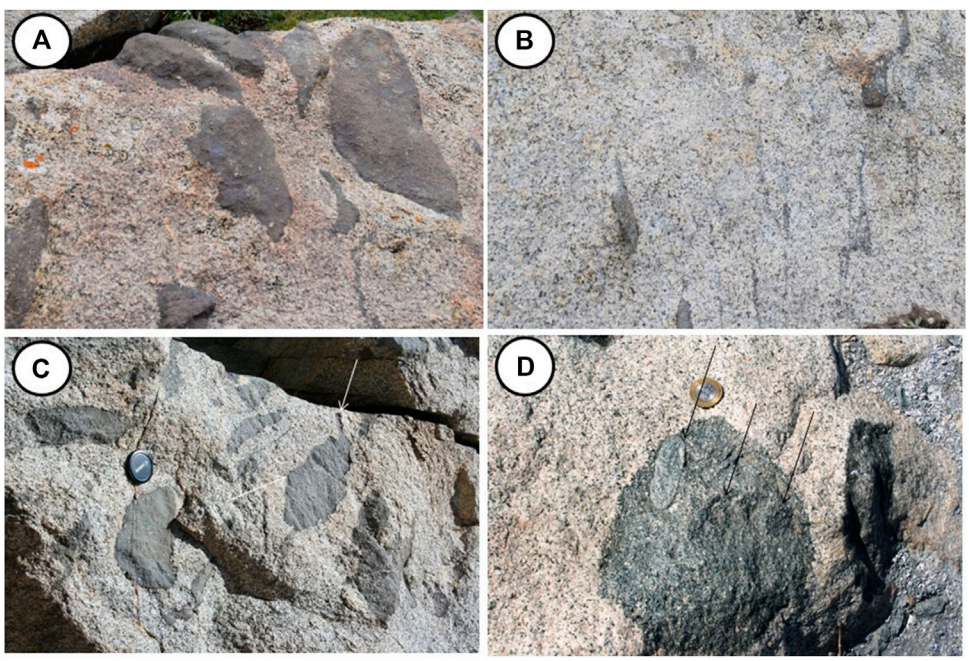

FIGURE 4 | (A) Mafic enclaves with variable shapes and sizes showing the common sharp and occasional cuspate margins. Note the presence of minor mafic schlierens. **(B)** Mafic schlierens correlate well with mostly digested enclaves within the host granite. **(C)** Mafic enclaves of variable shapes and sizes. Note an enclave shows viscous finger texture and cuspate margin (white arrows). These features of enclaves are from a large part of outcrop as shown in Kumar (2010a). **(D)** A nearly circular composite enclave encloses circular melanocratic to elongate mesocratic enclaves (shown by black arrows).

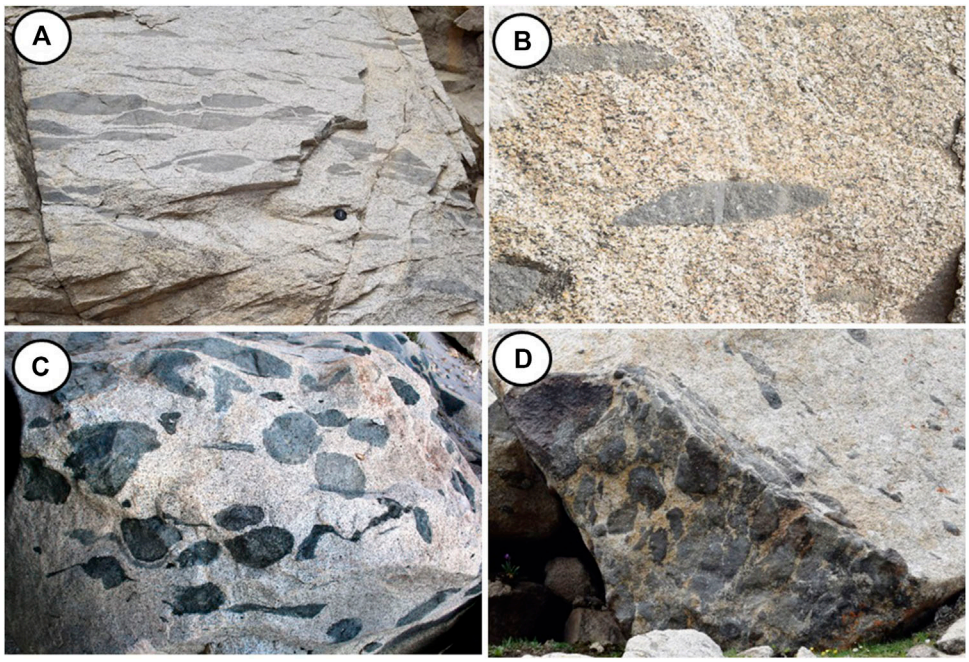

FIGURE 5 | (A,B) Elongated and stretched enclaves follow a flow direction of host granite magma. **(C, D)** Transverse and longitudinal sections of outcrops showing diverse geometry of numerous enclaves that suggest the chaotic nature of some enclaves.

These mafic enclave swarms are oriented in a particular direction of magmatic flowage within the host granite, and they exhibit monadnock like features (**Figure 3C**). The enclaves showing all kinds of diverse geometry (rounded to subrounded, elliptical, angular to subangular, moderately to highly curved, platy and small spotted) and color index (holomelanocratic, melanocratic, and mesocratic) are randomly distributed and embayed within the host granite without any marked flowage pattern (**Figure 3D**). Some of them are closely spaced. At some outcrops, a few fine grained mafic enclaves (maximum up to 30 cm across) of variable shapes and sizes with sharp and irregular boundaries follow wavy trails of mafic schlierens that appear to be detached or disaggregated fragments of large enclave magma body (**Figure 4A**). Some moderately to highly stretched enclaves with or without diffused margins connected with straight and curvilinear mafic schlierens indicate an arrested (frozen) state of magmatic flowage and comingling structures (**Figure 4B**). These are typical magmatic features resulted from the disaggregation of enclaves during progressive stages from mingling to mixing.

An enclave showing viscous fingering texture (**Figure 4C**) also exhibits a crenulated boundary outline with a concave contact outline toward the felsic host, a kind of pillowing structure that is the result of differences in temperatures and viscosities between the interacting mafic and felsic magmas. A circular, relatively large, mesocratic hybrid (felsic-mafic xenocryst-bearing) enclave has sharp contact with felsic host granite (**Figure 4D**). A few small-sized fine grained, rounded to elongated, melanocratic to mesocratic enclaves are enclosed within the hybrid enclave (**Figure 4D**), which together form a composite enclave. The small enclaves yet again show sharp contacts with the enclosing hybrid enclave (**Figure 4D**). The composite enclaves can be seen at several outcrops in the Ladakh Batholith. Few elongated and stretched enclaves (**Figures 5A,B**) may give the wrong impression of solid-state deformational objects that are commonly considered suitable for marking the brittle or ductile strain. However, these features were most likely formed during synchronous mafic-felsic magmatic flowage under the influence of a prevailing convection current in the magma chamber.

A few outcrops of enclaves were preferably chosen, which can exhibit 3D geometry (longitudinal section across the horizontal plane) of the enclaves (**Figures 5C,D**). On both the surfaces, the enclaves show irregular to chaotic, subrounded, curvilinear, and extreme elongate geometry. Moreover, the enclaves exhibit variable color indices and sharp contacts with host granites (**Figure 5C**). On the horizontal surface, the enclave swarms display elongate, and spindle shaped geometry whereas on the longitudinal section they manifest closely spaced, platy, and irregular shapes (**Figure 5D**). Hence, the true geometry of enclaves cannot be easily discerned in the field.

Synplutonic (or synmagmatic) fine grained (mafic) to porphyritic (hybrid) composite dykes intrude the granites at some places. Some of them appear as pillow-like sheets. These are the spectacular field features formed by the injection of mafic or hybrid magmas into the mostly crystallized (>65%) host granite magma (**Figures 6A–D**). These composite dykes and sheets are emplaced and exposed on both sides of a hillock covering a small area of about 5,000 sq meters. These dykes and sheets are discontinuous and disrupted to form platy and

FIGURE 6 | (A) Hillock showing disrupted mafic to hybrid synplutonic dykes and sheets injected into most crystallized granite. Note that synplutonic dykes and sheets are discontinuous and have got disrupted appearing pillowed but they broadly follow the same strike direction (NE-SE). **(B)** There are numerous mafic to hybrid enclave globules that are offset from dykes and sheets. **(C)** Closer view of part of mafic and hybrid synplutonic dykes. **(D)** Closer view of parts of hybrid synplutonic dykes. Note the sharp contact and straight contact outline of dyke with host granite, and felsic (quartz and K-feldspar) phenocrysts (xenocrysts) present in the hybrid synplutonic dyke.

parallel enclave swarms, which are oriented along the dyke strike direction (NE-SW). They commonly have sharp contacts with host granites (**Figure 6A**). A closer view of the dykes reveals their mafic (**Figure 6C**) and hybrid (**Figures 6C,D**) characteristics. Some offset of these injections form rounded to elliptical shaped enclaves (**Figure 6B**), because of the heterogeneous viscosity of host granite magma. This is primarily governed by differential crystal contents that may allow dispersal of injecting mafic to hybrid magmas as enclave globules. The synplutonic hybrid dykes contain abundant felsic xenocrysts (**Figure 6D**) that are sourced and injected from mafic-felsic mixed zone hidden at depth below the host felsic magma. The host granite shows medium to coarse grained equigranular textures.

A synplutonic mafic injection into partly crystalline (>65%) granite is moderate to highly disrupted to form clusters of angular (brecciated), subrounded, and elliptical enclave swarms (**Figure 7C**), which are commonly aligned, disposed, and broadly meander in the strike directions of N-S, E-W, and NE-SW. The disruption of synplutonic mafic dykes (nearly crystallized) into enclave swarms within the granite matrix depends upon the rheology of felsic host magma. This determines the yield strength (crystal-mush plus residual-melt), viscous passages of mafic intrusion, and flow departure of enclave swarms likely under the influence of tensional stress applied to the felsic magma chamber with heterogeneous crystal contents, as demonstrated in the model (**Figures 7A,B**). It is remarkable that at this outcrop only a mafic synplutonic dyke has intruded the granite whereas in the previously described outcrop both the mafic and hybrid synplutonic dykes have injected into the granite.

Microstructural Features

The modal mineralogy of the studied granites represents quartz diorite, granodiorite, and monzogranite whereas enclaves are micro-monzodiorite, micro-quartz diorite, micro-tonalite, and micro-monzogranite. The granites and enclaves have a common mineral assemblage (hbl-bt-pl-Kf-qtz-ap-zrn-mag ± ilm; mineral symbols are after Kretz, 1983) but they differ in modal proportion, the enclaves being enriched in mafic minerals.

Microscopically, the enclaves exhibit typical magmatic textures such as fine grained, equigranular, hypidiomorphic to porphyritic (**Figures 8, 9**). The contacts between the enclaves and host granites are sharp and wavy without any reaction signature (**Figures 8A,B**). In some instances, the contact outline between them is marked by the grain boundaries of either plagioclase or poikilitic amphibole crystallized in the host granite (**Figures 8A,B**). The grain boundaries of these minerals are devoid of any thermal effect and probably served as surfaces against which the enclave magma globules might have undercooled uniformly, and hence produced fine grained equigranular texture. In some enclaves, biotite dominates over the amphiboles and vice versa (**Figures 8A,B**). The presence of magnetite both in the enclave and granite indicates oxidizing condition, which is a

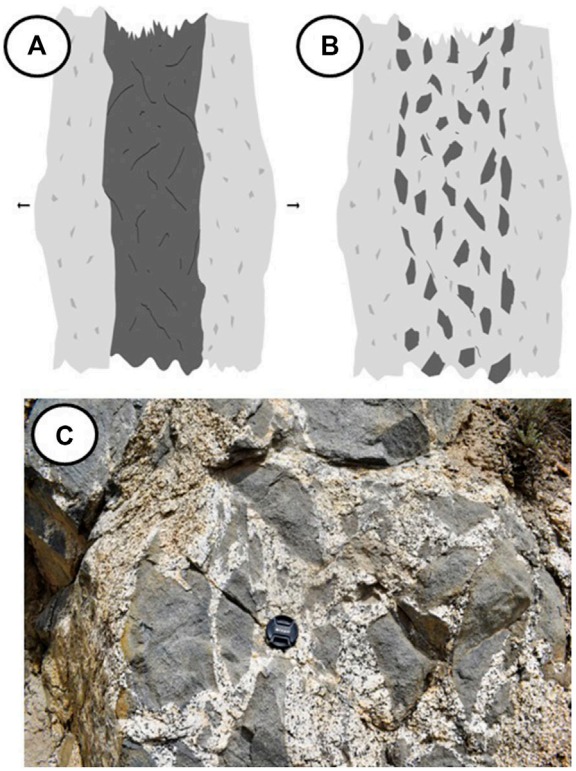

FIGURE 7 | Hypothetical model illustrating the likely mechanism of **(A)** injection of mafic magma into highly crystallized (>65%) felsic granite magma that **(B)** ruptured and brecciated into angular mafic enclave swarms under the extensional environment of granite magma, which is very well demonstrated **(C)** at outcrop scale, similar to as shown in Kumar et al. (2016).

characteristic of calc-alkaline subduction zone magmatism. The small flaky and platy biotites are commonly aligned along the contact outline (**Figure 8A**), and hence could not penetrate the semi-solid enclaves during the mingling event.

In a few enclaves, subhedral to euhedral amphiboles along with a minor amount of biotite are clustered and form the mafic aggregates (**Figure 8C**) that are in close association with tabular plagioclase, interstitial quartz, and K-feldspar. Subhedral to anhedral elongate amphiboles along with magnetite, quartz, and plagioclase show magmatic flowage texture (**Figure 8D**). Small acicular (needle-shaped) apatite crystals can also be observed poikilitically enclosed within the interstitial felsic minerals, which result from the undercooling of enclave magma globules. Porphyritic enclaves frequently contain plagioclase phenocrysts with normal, patchy, and oscillatory zonings (**Figures 9A,B**). They exhibit resorption surfaces as a corroded (dissolution) feature over which albitic rims are grown (**Figure 9B**). In some cases, the albitic rim appears to be replaced by sericite (**Figure 9A**). Synplutonic mafic dykes and sheets (partly pillow-like) show a typical interlocking subpoikilitic texture where plagioclase laths are partially enclosed by anhedral to subhedral amphiboles and less frequently by biotite, commonly associated with granular magnetite (**Figures 9C,D**).

DISCUSSION

Diorite Xenoliths, Layered Granite, and Cognate Enclave

Pre-existing stock-like dioritic bodies (Weinberg, 1997) are intruded by the granite-leucogranite-pegmatite system, as evident from the presence of dioritic xenoliths hosted in the intruding lithological units (**Figures 2A,B**). It is likely that the Neo-Tethyan oceanic subduction-related magmatism may have been initiated with the emplacement of diorite followed by profuse granite magmatism in the Ladakh Himalaya. The rarely occurring layered structure (**Figure 2C**) in the granite, exposed close to Sabu, is likely due to mafic-felsic mineral sorting under the influence of double diffusion convection and gravity settling operated in a magma chamber (e.g., McBirney, 1985), and not due to the enclave-forming magmatic pulse. The hornblende biotite granite is a major rock constituent of the Ladakh Batholith, which commonly hosts the microgranular enclaves. However, a biotite granite exposure (**Figure 2D**) contains a fine grained mesocratic enclave with diffused contacts (**Figure 2D**), which possibly represents cognate enclave of early crystallized fine grained cumulus phases of host magma.

Evidence Against Restite Origin of Enclaves in Ladakh Batholith

The origin of igneous enclaves hosted in the granites is still debated (Clemens et al., 2018, and references therein). The presence of mafic clots, inherited and metamorphic zircons, and Ca-rich patchy zoned (resorbed) plagioclase in enclaves favors the restite origin of enclaves (e.g., Chappell et al., 1987; Chen et al., 1989; Huang et al., 2018). The studied enclaves from Ladakh Batholith, however, lack partial melting textures, deformational, or recrystallization features. In contrast, the enclaves show typical fine grained to porphyritic textures, acicular apatite, some elongated amphiboles (**Figures 8C,D, 9A,B**), sharp, and lobate enclave-granite contact outlines (**Figures 3–5**), and patchy zoned core with a corrosive surface of plagioclase phenocrysts (**Figures 9A,B**), which together oppose the restite origin of enclaves. The observed anorthite rim (bright gray zone) grown over the corroded margin of plagioclase xenocrysts (**Figures 9A,B**) likely crystallized in a new mafic-felsic magma mixed (high-T) environment (e.g., Hibbard, 1981; Andersson, 1988; Andersson and Eklůnd, 1994; Kumar et al., 2017). The enclave-bearing granite may have, however, experienced later tectono-thermal deformation (e.g., Siebel et al., 2012).

Disproving the Cognate or Cumulate Model of Enclave Origin

The cognate model states that the enclave is a cumulate rock of early crystallized cumulus phases or rapidly cooled (chilled) border rock series of the host granite magma or more mafic cogenetic fractions with trapped interstitial melts (e.g., Phillips et al., 1981; Dodge and Kistler, 1990; Dahlquist, 2002; Esna-Ashari et al., 2011; Xiao et al., 2020). The cumulate hypothesis appears valid where the evidence of excessive nucleation of

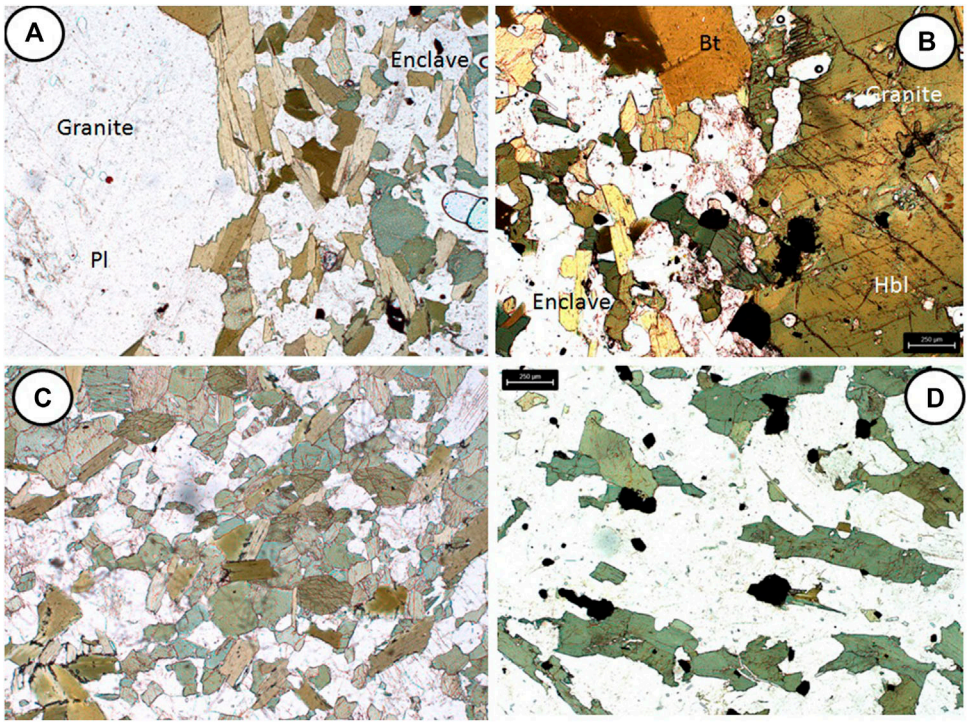

FIGURE 8 | (A) Microphotographs showing magmatic textures and contact relationships between the enclave and host granite. Note the sharp contact of enclave against the plagioclase of granite. Plane polarized. **(B)** Contact between the enclave and host granite is sharp and crenulated without any reaction signature even at the microscopic level. Crossed polar. The base of the photograph equals 2.5 mm. **(C)** Mafic enclave enriched in amphibole and biotite, which are aggregated at places with interstitial quartz and feldspars. **(D)** Elongated and anhedral crystals of amphiboles exhibit magmatic flowage. Note the acicular apatite in the interstitial felsic minerals. Plane polarized. The base of the photograph equals to 2.5 mm.

ferromagnesian minerals by rapid cooling at the margins of a shallow magma chamber and later its fragmentation and dispersal by dynamic arc plutonism is preserved (e.g., Esna-Ashari et al., 2011). Similarly, reheating and remelting of the mafic chilled margin in the ascent conduits can be dislocated by dyke injection and the host rocks can be fragmented to sizes similar to the enclaves (e.g., Fernandez and Castro, 2018). However, in the present case, numerous features such as sharp and crenulate contact outline (**Figures 3–5**), xenocrystic-bearing (hybrid) enclaves (**Figures 9A,B**), and large grain size contrast between the enclave and host granite (**Figures 8A,B**) strongly oppose cognate origin of enclaves. Coarse grained plutonic xenoliths have been reported in the volcanic system (Cooper et al., 2019) but in the felsic plutonic system, they represent early formed crystal mush pooled at the base of the magma chamber (e.g., Wiebe et al., 1997).

Evidence of Mafic-Felsic Magma Interaction, Mingling, and Undercooling

The mafic-felsic magma interacting system truly represents a composite mafic-silicic intrusive system (Wiebe, 1980; Wiebe, 1994) typical to those observed in the present study.

Most magmas experience three rheological states during crystallization, 1) Newtonian state at a low fraction of crystals ($F < 0.35$), 2) Bingham behavior or stress thinning state with yield stress ($F = 0.35–0.65$), and 3) solid-like behavior ($F > 0.65$) (Fernandez and Gasquet, 1994, and references therein). Coeval mafic and felsic magmas with contrasting temperatures and compositions achieve thermal equilibration at which crystallization is more advanced in the mafic magma rather than the felsic magma. At this point, an inversion temperature exists that governs relative viscosities of magmas such as mafic magma becomes less viscous than felsic magma at a temperature higher than the inversion temperature, and vice versa. Thus, the generated inversion of viscosity between the coeval mafic and felsic magmas can explain most of the features described here (e.g., Frost and Mahood, 1987; Fernandez and Gasquet, 1994). However, an open felsic magma chamber intermittently recharged by mafic to hybrid magma pulses may behave in a different and more complex manner. Magma convection ceases once the magma chamber develops a crystallinity of ca 40–50% (Chen et al., 2018).

Enclaves of variable shapes and sizes are formed within the host granite magma with a low crystallinity at an initial stage of its evolution. The enclaves may lack a chilled margin because small size enclaves (ca. 15 cm) are not capable to generate a thermal gradient within it, and hence undercooled at a uniform rate. The large sized enclave globules may, however, generate a thermal gradient forming the chilled margin and coarser core, because they behave as micro-plutons. It is therefore suggested that each enclave partially crystallizes as a discrete body with a unique cooling history (e.g., Rooyakkers et al., 2018). Numerical modeling of deformation of a crystal-rich enclave in a pure shear regime suggests that enclave particles pack early, quickly erasing

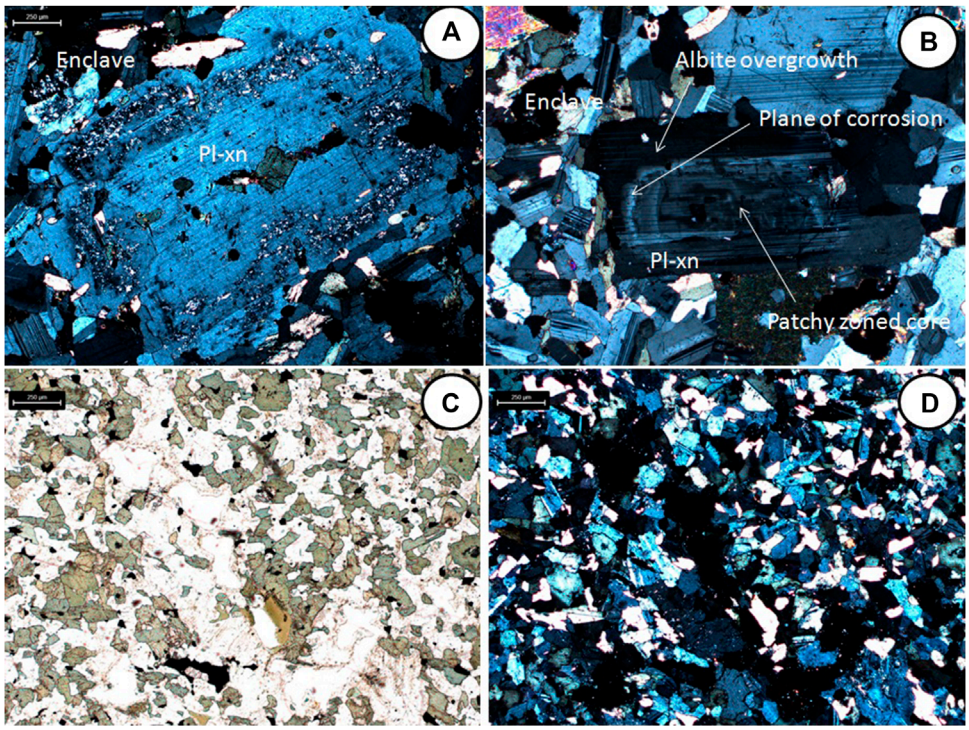

FIGURE 9 | (A) Plagioclase xenocryst (Pl-xn) in the porphyritic (hybrid) enclave. Note the sericitization along the plane of corrosion shown by a white arrow. Crossed polar. **(B)** Plagioclase xenocryst (Pl-xn) in porphyritic (hybrid) enclave showing patchy zoned core, corroded margin with the growth of An-rich plagioclase (bright gray) and albite rim. Crossed polar. The base of the photograph equals 2.5 mm. **(C)** Predominating amphibole and subordinate biotite show subpoikilitic relation with plagioclase laths in mafic synplutonic dyke. Note the quartz rinds in the center surrounded by minute dusty mafic grains. Plane Polarized. **(D)** Crossed polar view of the same as **(C)**. The base of the photograph equals 2.5 mm.

differences in initial content and building a force chain parallel to the compression axis that transmits stresses to the host granite (Burgisser et al., 2020). It is observed that the enclaves are not deformed under solid state and display similar magnetic fabrics that imply mafic magma globules coexisted and flowed with felsic host magma (Zhu et al., 2018). The mineral constituents of the studied enclaves of the Ladakh Batholith are solely unaffected by deformation, recrystallization, and solid-liquid reaction rims (**Figures 8, 9**). Vernon (1983) advocated if the magmatic flowage passes through the enclaves, the homogeneity may approach partial to complete disappearance of enclaves, as observed at some places in the present case (**Figures 4A,B**). This is a process leading to homogenization under a flow-favoured magma mixing environment (e.g., Reid and Hamilton, 1987; Reid et al., 1983; Castro, 1990).

How are the enclaves with diverse geometry and nature brought together at one place (**Figures 3D, 5C**) in a felsic magma chamber? The most plausible reason is either whole body convection current in the magma chamber or due to gravity settling at an early stage of granite evolution (e.g., Wiebe et al., 2007). However, over the time scale of magma mixing and mingling, convective patterns are difficult to recognize (Montagna et al., 2015). The absence of mafic schlierens among the randomly distributed enclave population indicates the transportation of enclaves in a much weaker medium (low viscosity) of host granite magma. Igneous lamination and schlieren in granites (**Figures 3B, 4A,B**) are, however, an expression of concurrent magma injection, aggregation with or without mingling/hybridization, hydrodynamic processes coupled with fractional crystallization, and deformation during the growth of plutons (Barbey, 2009). Thus, within a given volume of Ladakh granites and based on the type and behavior of enclaves, one can recognize the comingling and hybrid zones (e.g., Mariano and Sial, 1988; Perugini et al., 2003). Although enclaves do not provide precise information on the depth (pressure) where the felsic-mafic magmas were mixed, the enclaves appear to have ascended from greater depths than their surrounding host granites (Didier et al., 1989).

Schematic Model of Enclave Origin

Water content, crystal size, degree of crystallinity, mass fraction, composition, and temperature determine the rheology of interacting mafic and felsic magmas (Frost and Mahood, 1987). Low viscosity, minimal rheological differences, and thermal equilibrium between the coeval mafic and felsic magmas will produce convective overturn (Huppert et al., 1984; Sparks and Marshall, 1986) forming a hybrid magma zone hidden below the felsic magma at crustal depth. Under the influence of turbulent convection, the hybrid magma may also be injected into the overlying felsic magma, forming either rounded to elongated hybrid enclave globules or disrupted as angular brecciated to dyke-/sheet-like enclave swarms depending upon the schedule of

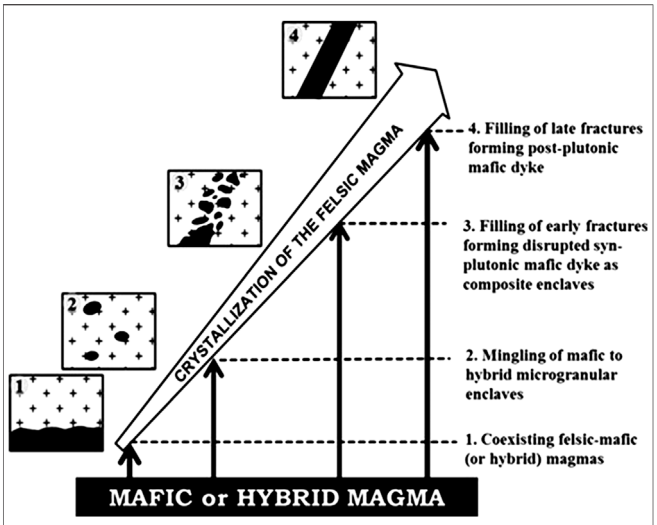

FIGURE 10 | Schematic presentation of mafic to hybrid magma injections into the progressively crystallizing felsic magma chamber and the resultant geometry of enclaves (after Barbarin, 1989; Barbarin and Didier, 1992, with the addition of "hybrid" by Kumar, 2014).

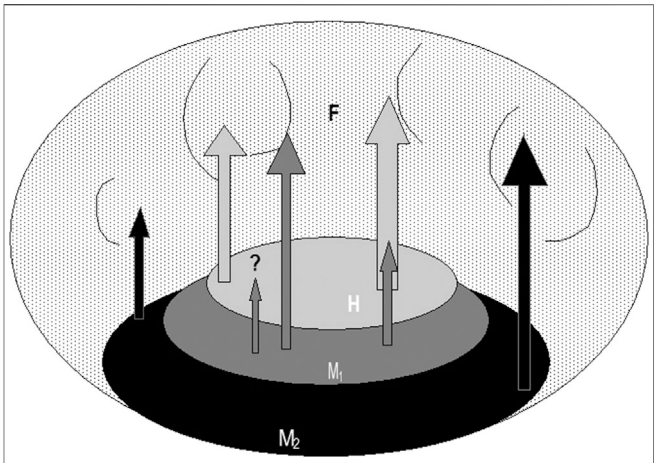

FIGURE 11 | A simplified schematic cartoon showing the most viable genetic model of mafic to hybrid and composite enclaves in granites. Mafic magma (M_1) pooled below and mixed with the partly crystalline felsic magma chamber to form hybrid magma (H) zone. Both the mafic and felsic magmas were crystal charged. Another pulse of mafic magma (M_2) accumulated below the M1. The mafic to hybrid magmas were injected into the overlying felsic magma chamber during its initial to waning stages of crystallization and formed the various enclave types observed in the studied granites of Ladakh Batholith (Based on Kumar, 2010a, and references therein). Post plutonic dyke intrudes after the consolidation of granite magma.

its injection into evolving felsic magma with changing rheology (e.g., Barbarin, 1989; Fernandez and Barbarin, 1991; Barbarin and Didier, 1992; Fernandez and Gasquet, 1994; Kumar, 2014), as shown by a schematic model (**Figure 10**). A large fine grained circular composite enclave (**Figure 4D**) lacks zoning. Zoned enclaves are commonly formed either by internal differentiation mechanism or multiple magma mixing and mingling events from magma source to emplacement level (Castro et al., 1990; Zhang et al., 2014; Zhang et al., 2016) or in two different, deep and shallower, magma chambers (Adam et al., 2019). However, the observed composite enclaves (**Figure 4D**) appear to have formed in an open felsic magma chamber that was essentially recharged intermittently by mafic to hybrid magmas pooled just below the felsic magma chamber (**Figure 11**), as similarly suggested for the origin of composite and other types of enclaves found in the granites of western Ladakh Batholith (Kumar, 2010a).

A few sheet-like bodies appear to be pillowed against relatively cooler host granite magma (**Figure 6A**), similar to as described elsewhere (e.g., Clemens et al., 2016). Mafic synplutonic dykes contain a high volume of crystal content (**Figures 9C,D**) and hence behaved more like a solid and become brecciated angular enclaves (**Figures 7A–C**). Depending upon the viscosity of enclave-hosting felsic magma and prevailing local strain, the structures like flowing or static breccias may develop (Fernandez and Gasquet, 1994). Brecciation and disruption (break-up) of mafic to hybrid synplutonic dykes (**Figures 6A, 7C**) might have occurred within a transition zone between the crystal mush (>65%) and melt condition of host felsic magma (Janoušek et al., 2000; Rooyakkers et al., 2018). However, the hybrid dyke magma might have been sourced from the felsic-mafic hybrid magma zone from where the other hybrid enclave globule types were also derived (e.g., Kumar and Rino, 2006), and hence they could be genetically linked (Zhang et al., 2014). These aspects need to be tested further using geochemical and isotopic investigations.

CONCLUSIONS

- Melanocratic to mesocratic, mafic to hybridized, rounded to elliptical microgranular enclaves hosted in the granites of Ladakh Batholith are considered products of mingling and undercooling of enclave magma globules against a relatively cooler, partly crystalline felsic host magma in a plutonic environment.
- It is more likely that felsic magma chambers were fed intermittently by mafic to hybrid magma pulses throughout its crystallization history with progressively changing rheology, and formed the enclave globules, synplutonic mafic dykes, sheets, and disrupted enclave swarms.
- Large sized enclave globules may get disaggregated into several smaller ones or partly to completely homogenize within the host granites depending upon the crystal content (<35%) and intensity of convection current prevailed in the chamber.
- The Ladakh Batholith is formed by composite plutons evolved through multistage interactions of coeval mafic to hybrid and felsic magma pulses.

DATA AVAILABILITY STATEMENT

All datasets presented in this study are included in the article/ supplementary material.

AUTHOR CONTRIBUTIONS

SK is the sole author of the paper and the principal investigator, fund manager, and administrator of the research project on

Ladakh Batholith. He is responsible for the conceptualization, data curation, validation, visualization, format analysis, methodology, writing, review, and editing of the article.

FUNDING

DST-Science and Engineering Research Board (SERB), New Delhi Grant (EMR/2017/002420).

ACKNOWLEDGMENTS

The infrastructural facilities developed under UGC-CAS-I & II and DST-FIST-II programmes in the Department of Geology, Kumaun University are gratefully acknowledged. Rajeev K. Mahajan, Rajwant, and Prahlad Ram, SERB, Delhi are thanked for the continuous encouragement. C. P. Dorjey, Karma, and Kapil S. Panwar helped during the geological fieldwork. Manjari Pathak, Saurabh Gupta, and Anjali Solanki helped to document the microstructural features and digitizing the figures. The generous scientific comments from two reviewers helped to improve the earlier versions of the manuscript. J. G. Shellnutt is also thanked for thorough editorial works and correcting the English and grammar of the manuscript. A few remarks from Catherine Annen, Specialty Chief Editor, Petrology Section, also helped improving the manuscript.

REFERENCES

Adam, M. S. M., Kim, T., Song, Y.-S., and Kim, Y.-S. (2019). Occurrence and origin of the zoned microgranular enclaves (MEs) within the Cretaceous granite in Taejongdae, SE Korea. *Lithos* 324–325, 537–550. doi:10.1016/j.lithos.2018.11.008

Ahmad, T., Thakur, V. C., Islam, R., Khanna, P. P., and Mukherjee, P. K. (1998). Geochemistry and geodynamic implications of magmatic rocks from the trans-Himalayan arc. *Geochem. J.* 32, 383–404. doi:10.2343/geochemj.32.383

Andersson, U. B., and Eklund, O. (1994). Cellular plagioclase intergrowths as a result of crystal-magma mixing in the Proterozoic Åland rapakivi batholith, SW Finland. *Contrib. Mineral. Petrol.* 117, 124–136. doi:10.1007/bf00286837

Andersson, U. B. (1988). Evidence of plutonic magma mixing, Southern Sweden. *Rec. Soc. Ital. Mineral. Petrol.* 43, 609–618

Auden, J. B. (1935). Traverses in the Himalaya. *Rec. Geol. Surv. India* 69, 123–167.

Barbarin, B. (1989). Importance des différents processus d'hybridation dans les plutons granitiques du batholite de la Sierra Nevada, Californie. *Schweiz Mineral Petrogr. Mitt.* 69, 303–315.

Barbarin, B., and Didier, J. (1992). Genesis and evolution of mafic microgranular enclaves through various types of interaction between coexisting felsic and mafic magmas. *Earth Sci.* 83, 145–153. doi:10.1017/S0263593300007835

Barbey, P. (2009). Layering and schlieren in granitoids: a record of interactions between magma emplacement, crystallization and deformation in growing plutons. *Geol. Belg.* 12, 109–133.

Burgisser, A., Carrara, A., and Annen, C. (2020). Numerical simulations of magmatic enclave deformation. *J. Volcanol. Geoth. Res.* 392, 106790. doi:10.1016/j.jvolgeores.2020.106790

Castro, A. (1990). Microgranular enclaves of the quintana granodiorite (los pedroches batholith): petrogenetic significance. *Rev. Soc. Geol. España* 3, 7–21.

Castro, A., de la Rosa, J. D., and Stephens, W. E. (1990). Magma mixing in the subvolcanic environment: petrology of the Gerena interaction zone near Seville, Spain. *Contrib. Mineral. Petr.* 106, 9–26. doi:10.1007/bf00306405

Castro, A., Moreno-Ventas, I., and de la Rosa, J. D. (1991a). H-type (hybrid) granitoids: a proposed revision of the granite-type classification and nomenclature. *Earth Sci. Rev.* 31, 237–253. doi:10.1016/0012-8252(91)90020-g

Castro, A., Moreno-Ventas, I., and de la Rosa, J. D. (1991b). Multistage crystallization of tonalitic enclaves in granitoid rocks (Hercynian belt, Spain): implications for magma mixing. *Geol. Rundsch.* 80, 109–120. doi:10.1007/bf01828770

Chappell, B. W., White, A. J. R., and Wyborn, D. (1987). The importance of residual source material (restite) in granite petrogenesis. *J. Petrol.* 28, 1111–1138. doi:10.1093/petrology/28.6.1111

Chen, C., Xing, D., Rui, L., Qi, Z. W., Jian, O. D., Lei, Y., et al. (2018). Crystal fractionation of granitic magma during its non-transport processes: a physical-based perspective. *Sci. China Earth Sci.* 61, 190–204. doi:10.1007/s11430-016-9120-y

Chen, Y. D., Price, R. C., and White, A. J. R. (1989). Inclusions in three S-type granites from southeastern Australia. *J. Petrol.* 30, 1181–1218. doi:10.1093/petrology/30.5.1181

Clemens, J. D., Elburg, M. A., and Harris, C. (2017). Origins of igneous microgranular enclaves in granites: the example of Central Victoria, Australia. *Contrib. Mineral. Petrol.* 172, 88. doi:10.1007/s00410-017-1409-2

Clemens, J. D., Regmi, K., Nicholls, I. A., Weinberg, R., and Maas, R. (2016). The Tynong pluton, its mafic synplutonic sheets and igneous microgranular enclaves: the nature of the mantle connection in I-type granitic magmas. *Contrib. Mineral. Petrol.* 171, 35. doi:10.1007/s00410-016-1251-y

Cooper, F. G., Blundy, J. D., Macpherson, C. G., Humphreys, M. C. S., and Davidson, J. P. (2019). Evidence from plutonic xenoliths for magma differentiation, mixing and storage in a volatile-rich crystal mush beneath St. Eustatius, Lesser Antilles. *Contrib. Mineral. Petrol.* 174, 39. doi:10.1007/s00410-019-1576-4

Dahlquist, J. A. (2002). Mafic microgranular enclaves: early segregation from metaluminous magma (Sierra de Chepes), Pampean Ranges, NW Argentina. *J. S. Am. Earth Sci.* 15, 643–655. doi:10.1016/s0895-9811(02)00112-8

Didier, J. (1973). "Granites and their enclaves: the bearing of enclaves on the origin of granites," in *Developments in petrology*. Amsterdam: Elsevier, Vol. 3.

Didier, J. (1984). "The problem of enclaves in granitic rocks: a review of recent ideas on their origin," in *Proceedings of international symposium on Geology of granites and their metallogenetic relations*. Editors K. Q. Xu and G. C. Tu (Nanjing and Beijing, China: Nanjing University, Science Press), 137–144.

Didier, J. (1987). Contribution of enclave studies to the understanding of origin and evolution of granitic magmas. *Geol. Rundsch.* 76, 41–50. doi:10.1007/bf01820572

Didier, J., and Barbarin, B. (1991). "Enclaves and granite petrology," in *Developments in petrology*. Amsterdam: Elsevier, Vol. 13, 625.

Didier, J., Fernandez, A., and Elmouraouah, A. (1989). *A model for the genesis of granitic magmas by crustal melting around mafic inclusions: the Peyron near Burzet (Ardeche, Massif Central, France)*. Athens: Theophrastus Publication Sa, 163–192.

Didier, J., and Roques, M. (1959). Sur les enclaves des granites du Massif Central Français. Comptes rendus de l'Académie des sciences, Paris [On the enclaves of the granites of the French Massif Central. *Proc. Acad. Sci.* 228, 1839–1841.

Dodge, F. C. W., and Kistler, R. W. (1990). Some additional observations on inclusions in the granitic rocks of the Sierra Nevada. *J. Geophys. Res.* 95, 17841–17848. doi:10.1029/jb095ib11p17841

Eberz, G. W., and Nicholls, I. A. (1988). Microgranitoid enclaves from the Swifts Creek Pluton SE-Australia: textural and physical constraints on the nature of magma mingling processes in the plutonic environment. *Geol. Rundsch.* 77, 713–736. doi:10.1007/bf01830179

Eberz, G. N. W., and Nicholls, I. A. (1990). Chemical modification of enclave magma by post-emplacement crystal fractionation, diffusion and metasomatism. *Contrib. Mineral. Petrol.* 104, 47–55. doi:10.1007/bf00310645

Elburg, M. A. (1996). Genetic significance of multiple enclave types in a peraluminous ignimbrite suite, Lachlan fold belt, Australia. *J. Petrol.* 37, 1385–1408. doi:10.1093/petrology/37.6.1385

Esna-Ashari, A., Hassanzadeh, J., and Valizadeh, M.-V. (2011). Geochemistry of microgranular enclaves in Aligoodarz Jurassic arc pluton, western Iran: implications for enclave generation by rapid crystallization of cogenetic granitoid magma. *Miner. Petrol.* 101, 195. doi:10.1007/s00710-011-0149-7

Fernandez, A. N., and Barbarin, B. (1991). "Relative rheology of coeval mafic and felsic magmas: nature of resulting iteration processes and shape and mineral fabrics of mafic microgranular enclaves," in *Enclaves and granite petrology. Developments in petrology*, Editors Didier, J., and Barbarin, B. (Amsterdam: Elsevier), Vol. 13, 263–275.

Fernandez, A. N., and Gasquet, D. R. (1994). Relative rheological evolution of chemically contrasted coeval magmas: example of the Tichka plutonic complex (Morocco). *Contrib. Mineral. Petrol.* 116, 316–326. doi:10.1007/bf00306500

Fernández, C., and Castro, A. (2018). Mechanical and structural consequences of magma differentiation at ascent conduits: a possible origin for some mafic microgranular enclaves in granites. *Lithos* 320–321, 49–61. doi:10.1016/j.lithos.2018.09.004

Frank, W., Thoni, M., and Purtscheller, F. (1977). Geology and petrography of Kullu-south Lahul area. *Sci. Terre Himal. CNRS* 268, 147–160.

Frost, T. P., and Mahood, G. A. (1987). Field, chemical, and physical constraints on mafic-felsic magma interaction in the Lamarck Granodiorite, Sierra Nevada, California. *Geol. Soc. Am. Bull.* 99, 272–291. doi:10.1130/0016-7606(1987)99<272:fcapco>2.0.co;2

Furman, T., and Spera, F. J. (1985). Co-mingling of acid and basic magma with implications for the origin of mafic I-type xenoliths: Field and petrochemical relations of an unusual dike complex at eagle lake, Sequoia National Park, California, U.S.A. *J. Volcanol. Geoth. Res.* 24, 151–178. doi:10.1016/0377-0273(85)90031-9

Gansser, A. (1977). The great suture zone between Himalaya and Tibet: a preliminary account. *Sci. Terre Himal. CNRS.* 268, 181–192.

Güraslan, I. N., and Altunkaynak, Ş. (2019). Role of mantle and lower continental crust in the genesis of Eocene post-collisional granitoids: insights from the Topuk pluton (NW Turkey). *J. Asian Earth Sci.* 179, 365–384. doi:10.1016/j.jseaes.2019.05.012

Hibbard, M. J. (1981). The magma mixing origin of mantled feldspars. *Contrib. Mineral. Petrol.* 76, 158–170. doi:10.1007/bf00371956

Holden, P., Halliday, A. N., and Stephens, W. E. (1987). Neodymium and strontium isotope content of microdiorite enclaves points to mantle input to granitoid production. *Nature.* 330, 53–56. doi:10.1038/330053a0

Honegger, K., Dietrich, V., Frank, W., Gansser, A., Thöni, M., and Trommsdorff, V. (1982). Magmatism and metamorphism in the Ladakh Himalayas (the Indus-Tsangpo suture zone). *Earth Planet Sci. Lett.* 60, 253–292. doi:10.1016/0012-821x(82)90007-3

Huang, X.-D., Lu, J.-J., Sizaret, S., Wang, R.-C., Wu, J.-W., and Ma, D.-S. (2018). Reworked restite enclave: Petrographic and mineralogical constraints from the Tongshanling intrusion, Nanling Range, South China. *J. Asian Earth Sci.* 166, 1–18. doi:10.1016/j.jseaes.2018.07.001

Huppert, H. E., Stephen, R., Sparks, J., and Turner, J. S. (1984). Some effects of viscosity on the dynamics of replenished magma chambers. *J. Geophys. Res.* 89, 6857–6877. doi:10.1029/jb089ib08p06857

Jain, A. K. (2014). When did India–Asia collide and make the Himalaya? *Curr. Sci.* 106, 254–266.

Jain, A. K., and Singh, S. (2009). *Geology and tectonics of the southeastern Ladakh and karakoram*. Bangalore: Geological Society of India.

Jain, A. K., Singh, S., Manickavasagam, R. M., Joshi, M., and Verma, P. K. (2003). Himprobe programme: integrated studies on geology, petrology, geochronology and geophysics of the Trans-Himalaya and Karakoram. *Mem. Geol. Soc. India.* 53, 1–56.

Janoušek, V., Bowes, D. R., Braithwaite, C. J. R., and Rogers, G. (2000). Microstructural and mineralogical evidence for limited involvement of magma mixing in the petrogenesis of Hercynian high-K calc-alkaline intrusion: the Kozárovice granodiorite, Central Bohemian pluton, Czech Republic. *Earth Environ. Sci. Trans. R. Soc. Edinburgh.* 91, 15–26. doi:10.1017/S0263593300007264

Kretz, R. (1983). Symbols for rock-forming minerals. *Am. Mineral* 68, 277–279.

Kumar, S. (1995). Microstructural evidence of magma quenching inferred from enclaves hosted in the Hodruša Granodiorites, Western Carpathians. *Geol. Carpath.* 46, 379–382.

Kumar, S. (2008). Magnetic susceptibility mapping of Ladakh granitoids, northwest higher Himalaya: implication to redox series of felsic magmatism in the subduction environments. *Mem. Geol. Soc. India.* 72, 83–102.

Kumar, S. (2010a). Mafic to hybrid microgranular enclaves in the Ladakh batholith, northwest Himalaya: implications on calc-alkaline magma chamber processes. *J. Geol. Soc. India* 76, 5–25. doi:10.1007/s12594-010-0080-2

Kumar, S. (2010b). Magnetite and ilmenite series of granitoids of Ladakh Batholith, Northwest Indian Himalaya: implications on redox conditions of calc-alkaline felsic magma chambers. *Curr. Sci.* 99, 1260–1264. doi:10.2307/24068524

Kumar, S. (2014). "Magmatic processes: review of some concepts and models," in *Modelling of magmatic and allied processes*. Editors S Kumar and R. N. Singh (Cham, Switzerland: Springer-Switzerland), 1–22.

Kumar, S., Bora, S., and Sharma, U. K. (2016). Geological appraisal of Ladakh and Tirit granitoids in the Indus-Shyok Suture Zones of Northwest Himalaya, India. *J. Geol. Soc. India.* 87, 737–746. doi:10.1007/s12594-016-0446-1

Kumar, S., Pieru, T., Rino, V., and Hayasaka, Y. (2017). Geochemistry and U–Pb SHRIMP zircon geochronology of microgranular enclaves and host granitoids from South Khasi Hills of the Meghalaya Plateau, NE India: evidence of synchronous mafic–felsic magma mixing–fractionation and diffusion in a post-collision tectonic environment during the Pan-African orogenic cycle. *Geol. Soc. Lond. Spec. Publ.* 457, 253–289. doi:10.1144/SP457.10

Kumar, S., Pieru, T., Rino, V., and Lyngdoh, B. C. (2005). Microgranular enclaves in Neoproterozoic granitoids of south Khasi Hills, Meghalaya plateau, Northeast India: field evidences of interacting coeval mafic and felsic magmas. *J. Geol. Soc. India.* 65, 629–633.

Kumar, S., and Rino, V. (2006). Mineralogy and geochemistry of microgranular enclaves in Palaeoproterozoic Malanjkhand granitoids, central India: evidence of magma mixing, mingling, and chemical equilibration. *Contrib. Mineral. Petrol.* 152, 591–609. doi:10.1007/s00410-006-0122-3

Kumar, S., Rino, V., and Pal, A. B. (2004a). Field evidence of magma mixing from microgranular enclaves hosted in Palaeoproterozoic Malanjkhand granitoids, central India. *Gondwana Res.* 7, 539–548. doi:10.1016/s1342-937x(05)70804-2

Kumar, S., Rino, V., and Pal, A. B. (2004b). Typology and geochemistry of microgranular enclaves hosted in Malanjkhand granitoids, Central India. *J. Geol. Soc. India.* 64, 277–292.

Kumar, S., and Singh, B. (2008). Mineralogy and Geochemistry of mafic to hybrid microgranular enclaves and felsic host of Ladakh batholith, Northwest Himalaya: Evidence of multistage complex magmatic processes. *Himal. J. Sci.* 5, 130–131. doi:10.3126/hjs.v5i7.1315

Kumar, S., Singh, B., Wu, F. Y., and Ji, W. Q. (2012). Timing of Asia–India collision evident from U–Pb–Lu–Hf isotopes of zircons from granitoids and enclaves of Ladakh Batholiths, NW Himalaya. *J. Nepal Geol. Soc.* 45, 164–165.

Lacroix, A. (1933). Sur Quelques granites des environs de Porto. *An fac. Cienc. Porto.* 18, 35–68.

Lacroix, A. (1890). Sur les enclaves du trachyte de Menet (Cantal), sur leurs modifications et leur origin. Paris: C R Academy of Science, 11, 1003–1006.

Le Maitre, R. W. (2002). "A classification and glossary of terms," in *Recommendations of the IUGS Subcommission on the systematics of igneous rocks*. 2nd Edn. Cambridge: Cambridge University Press, 236.

Lu, Y. H., Gao, P., Zhao, Z. F., and Zheng, Y. F. (2020). Whole-rock geochemical and zircon Hf–O isotopic constraints on the origin of granitoids and their mafic enclaves from the Triassic Mishuling pluton in West Qinling, central China. *J. Asian Earth Sci.* 189, 104136. doi:10.1016/j.jseaes.2019.104136

Mariano, G., and Sial, A. C. (1988). Evidence of magma mixing in the Itaporanga Batholith, NE Brazil. *Rec. Soc. Ital. Mineral. Petrolo.* 43, 555–568.

McBirney, A. R. (1985). Further considerations of double-diffusive stratification and layering in the Skaergaard Intrusion. *J. Petrol.* 26, 993–1001. doi:10.1093/petrology/26.4.993

Montagna, C. P., Papale, P., and Longo, A. (2015). "Timescales of mingling in shallow magmatic reservoirs," in *Chemical, physical and temporal evolution of magmatic systems*. Editors L Caricchi and J. D. Blundy (London, UK: Geological Society, London, Special Publications), Vol. 422.

Pabst, A. (1928). *Observation on inclusions in the granitic rocks of the Sierra Nevada*. California, United States: University of California Geological Sciences, 17, 325–388.

Perugini, D., Poli, G., Christofides, G., and Eleftheriadis, G. (2003). Magma mixing in the Sithonia Plutonic Complex, Greece: evidence from mafic microgranular enclaves. *Mineral. Petrol.* 78, 173–200. doi:10.1007/s00710-002-0225-0

Phillips, G. N., Wall, V. J., and Clemens, J. D. (1981). Petrology of the Strathbogie Batholith: a cordierite-bearing granite. *Can. Mineral.* 19, 47–63.

Pin, C., Binon, M., Belin, J. M., Barbarin, B., and Clemens, J. D. (1990). Origin of microgranular enclaves in granitoids: equivocal Sr-Nd evidence from Hercynian rocks in the Massif Central (France). *J. Geophys. Res.* 95, 17821–17828. doi:10.1029/JB095iB11p17821

Pundir, S., Adlakha, V., Kumar, S., and Singhal, S. (2020). Closure of India–Asia collision margin along the Shyok suture zone in the eastern Karakoram: new geochemical and zircon U–Pb geochronological observations. *Geol. Mag.* 157, 1451–1472. doi:10.1017/s0016756819001547.

Rai, H. (1980). Origin and emplacement of Ladakh Batholith: present day knowledge. *Himal. Geol.* 10, 78–93.

Ravikant, V., Wu, F. Y., and Ji, W. Q. (2009). Zircon U–Pb and Hf isotopic constraints on petrogenesis of the Cretaceous–Tertiary granites in eastern Karakoram and Ladakh, India. *Lithos.* 110, 153–166. doi:10.1016/j.lithos.2008.12.013

Reid, J. B., Jr, Evans, O. C., and Fates, D. G. (1983). Magma-mixing in granitic rocks of the Central Sierra Nevada, California. *Earth Planet Sci. Lett.* 66, 243–261. doi:10.1016/0012-821X(83)90139-5

Reid, J. B., Jr, and Hamilton, M. A. (1987). Origin of Sierra Nevada granite: evidence from small scale composite dikes. *Contrib. Mineral. Petrol.* 96, 441–454.

Rooyakkers, S. M., Wilson, C. J. N., Schipper, C. I., Barker, S. J., and Allan, A. S. R. (2018). Textural and micro-analytical insight into mafic-felsic interactions during the Oruanui eruption, *Contrib. Mineral. Petrol.* 173, 35. doi:10.1007/s00410-018-1461-6.

Sharma, K. K., and Choubey, V. M. (1983). "Petrology, geochemistry, and geochronology of the southern margin of the Ladakh Batholith between Upshi and Chumathang," in *Geology of Indus suture zone of Ladakh*. Editors V. C. Thakur and K. K. Sharma (Dehradun: Wadia Institute of Himalayan Geology), Vol. 240, 41–60.

Shellnutt, J. G., Jahn, B.-M., and Dostal, J. (2010). Elemental and Sr-Nd isotopes geochemistry of microgranular enclaves from peralkaline A-type granite plutons of the Emeishan large igneous province, SW China. *Lithos.* 119, 34–46. doi:10.1016/j.lithos.2010.07.011

Shellnutt, J. G., Lee, T.-Y., Brookfield, M. E., and Chung, S.-L. (2013). Correlation between magmatism of the Ladakh Batholith and plate convergence rates during the India–Eurasia collision. *Gondwana Res.* 26, 1051–1059. doi:10.1016/j.gr.2013.09.006

Singh, S., Kumar, R., Barley, M. E., and Jain, A. K. (2007). SHRIMP U-Pb ages and depth of emplacement of Ladakh Batholith, Eastern Ladakh, India. *J. Asian Earth Sci.* 30, 490–503. doi:10.1016/j.jseaes.2006.12.003

Sollas, J. W. (1894). On the volcanic district of Calingford and Slieve Gullion. I: On the relation of the granite to the gabbro of Barnavarve. *Trans. R. Irish Acad.* 30, 477–512.

Siebel, W., Shang, C. K., Thern, E., Danišík, M., and Rohrmüller, J. (2012). Zircon response to high-grade metamorphism as revealed by U–Pb and cathode-luminescence studies. *Int. J. Earth Sci.* 101, 2105–2123. doi:10.1007/s00531-012-0772-5

Sparks, R. J. S., and Marshall, L. A. (1986). Thermal and mechanical constraints on mixing between mafic and silicic magmas. *J. Volcanol. Geoth. Res.* 29, 99–124. doi:10.1016/0377-0273(86)90041-7

Sparks, R. J. S., Sigurdson, H., and Wilson, L. (1977). Magma mixing: a mechanism for triggering acid explosive eruptions. *Nature.* 267, 6337–6344. doi:10.1038/267315a0

Thakur, V. C. (1987). Plate tectonic interpretation of the western Himalaya. *Tectonophysics.* 134, 91–102. doi:10.1016/0040-1951(87)90251-4

Thakur, V. C. (1992). *Geology of the western Himalaya*. Oxford: Pergamon Press, 366.

Turner, A. K. (2014). When did India–Asia collide and make the Himalaya? *Curr. Sci.* 106, 254–266.

Upadhyay, R., Frisch, W., and Siebel, W. (2008). Tectonic implication of U-Pb zircon ages of the Ladakh Batholith, Indus suture zone, northwest Himalaya, India. *Terra. Nova.* 20, 309–317. doi:10.1111%2Fj.1365-3121.2008.00822.x

Vernon, R. H. (1983). "Restite, xenoliths and microgranitoid enclaves in granites," in *Clarke memorial lecture*. NSW: Journal Proceeding Royal Society, Vol. 116, 77–103.

Vernon, R. H. (1984). Microgranitoid enclaves in granites-globules of hybrid magma quenched in a plutonic environment. *Nature.* 309 (5967), 438–439. doi:10.1038/309438a0

Vernon, R. H. (2014). Microstructures of microgranitoid enclaves and the origin of S-type granitoids. *Aust. J. Earth Sci.* 61, 227–239. doi:10.1080/08120099.2014.886623

Vernon, R. H., Etheridge, M. A., and Wall, V. J. (1988). Shape and microstructures of microgranitoid enclaves: indicators of magma mingling and flow. *Lithos.* 22, 1–11. doi:10.1016/0024-4937(88)90024-2

Wadia, D. N. (1937). The Cretaceous volcanic series of Astor-Deosai Kashmir and is intrusion. *Record Geol. Surv. India.* 72, 151–161.

Weinberg, R. F. (1997). The disruption of a diorite magma pool by intruding granite: the Sobu body, Ladakh Batholith, Indian Himalayas. *J. Geol.* 105, 87–98. doi:10.1086/606149

Weinberg, R. F., and Dunlop, W. J. (2000). Growth and deformation of the Ladakh Batholith, northwest Himalayas: implications for timing of continental collision and origin of calc-alkaline Batholith. *J. Geol.* 108, 303–320. doi:10.1086/314405

White, L. T., Ahmad, T., Ireland, T. R., Lister, G. S., and Forster, M. S. (2011a). Deconvolving episodic age spectra from zircons of the Ladakh Batholith, northwest Indian Himalaya. *Chem. Geol.* 289, 179–196. doi:10.1016/j.chemgeo.2011.07.024

White, L. T., Ahmad, T., Lister, G. S., and Ireland, T. R. (2011b). Where does Indian plate and the Eurasian plate begin? *Geol. Geochem. Geophys.* 12 (Q10013), 6–201. doi:10.1029/2011GC003726

Wiebe, R. A. (1980). Comingling of contrasted magmas in the plutonic environment: examples from the Nain anorthositic complex. *J. Geol.* 88, 197–209. doi:10.1086/628491

Wiebe, R. A. (1994). Silicic magma chambers a trap for basaltic magmas: The Cadillac mountain intrusive complex, Mount Desert island, Maine. *J. Geol.* 102, 423–427. doi:10.1086/629684

Wiebe, R. A., Jellinek, M., Markley, M. J., Hawkins, D. P., and Snyder, D. (2007). Steep schlieren and associated enclaves in the Vinalhaven granite, Maine: possible indicators for granite rheology. *Contrib. Mineral. Petrol.* 153, 121–138. doi:10.1007/S00410-006-0142-Z

Wiebe, R. A., Manon, M. R., Hawkins, D. P., and McDonough, W. F. (2004). Late-stage mafic injection and thermal rejuvenation of the Vinalhaven granite, Coastal Maine. *J. Petrol.* 45, 2133–2153. doi:10.1093/petrology/egh050

Wiebe, R. A., Smith, D., Sturn, M., King, E. M., and Seckler, M. S. (1997). Enclaves in the Cadillac mountain granite (Coastal Maine): samples of hybrid magma from the base of the chamber. *J. Petrol.* 38, 393–426. doi:10.1093/petroj/38.3.393

Xiao, Y., Chen, S., Niu, Y., Wang, X., Xue, Q., Wang, G., et al. (Forthcoming 2020). Mineral compositions of syn-collisional granitoids and their implications for formation of juvenile continental crust and adakitic magmatism. *J. Petrol.*

Zhang, Y-J., Ma, C-Q., Zhang, C., and Li, J.-W. (2014). Fractional crystallization and magma mixing: evidence from porphyritic diorite-granodiorite dyke and mafic microgranular enclaves within the Zhoukoudian pluton, Beijing. *Mineral. Petrol.* 108, 777–800. doi:10.1007/s00710-014-0336-4.

Zhang, J., Wang, T., Castro, A., Zhang, L., Shi, X., Tong, Y., et al. (2016). Multiple mixing and hybridization from magma source to final emplacement in the Permian Yamatu pluton, the Northern Alexa Block. China. *J. Petrol.* 57, 933–980. doi:10.1093/PETROLOGY/EGW028

Zhu, K.-Y., Shen, Z.-Y., Li, M.-Y., and Yu, Y.-H. (2018). Interaction between mingling mafic and felsic magmas: its role in differentiation of a quartz monzonite and MMEs from eastern South China. *Lithos.* 318–319, 60–77. doi:10.1016/j.lithos.2018.07.033

Conflict of Interest: The authors declare that the research was conducted in the absence of any commercial or financial relationships that could be construed as a potential conflict of interest.

frontiers in Earth Science

ORIGINAL RESEARCH
published: 28 January 2021
doi: 10.3389/feart.2020.602870

Petrogenesis of Mesoproterozoic Granites of the Swartoup Hills Region, Kakamas Domain, Namaqua Belt, South Africa

Steffen Hermann Büttner, Stephen Anthony Prevec and Graeme Alvin Schmeldt*

Department of Geology, Rhodes University, Makhanda (Grahamstown), South Africa

The Swartoup and Polisiehoek plutons in the Swartoup Hills (South Africa) formed during an episode of significant magma emplacement in the Mesoproterozoic Namaqua Sector of the Namaqua Metamorphic Province. They intruded into mid-crustal metasedimentary rocks of the metapelitic Koenap and mafic to carbonate-bearing Bysteek Formations during and shortly after the ~1,200–1,220 Ma regional metamorphic peak that reached ultrahigh temperatures. Subsequent to pluton emplacement, the crust underwent regional high-temperature deformation during slow near-isobaric cooling. A further episode of pluton emplacement associated with fluid circulation truncated the first-order regional tectonic structures at ~1,100 Ma. Based on their petrography, the Swartoup pluton is subdivided into leuco-granitoids with biotite as the sole mafic phase, pyroxene granitoids, and garnet-bearing granitoids, which may contain significant biotite. These subgroups display distinctive geochemical variations from one another, and from the Koenap Formation migmatites and the Polisiehoek granites, which are exposed nearby. Incompatible trace element distributions suggest that the Swartoup and Polisiehoek granitoids represent modified A-type granite magma, consistent with derivation from partial melting of quartzo-feldspathic crust. The magmas incorporated significant amounts of juvenile mantle-derived magma ($\varepsilon_{Nd}{}^{1200}$ of ~−5, and LREE-depleted), but do not require older, early to late Paleoproterozoic crust. Particularly close to contacts to the calcic Bysteek Formation, localized contamination of the Swartoup granites by supracrustal carbonates is evident. A relatively pervasive alkali metasomatic effect is manifested strongly in the initial $^{87}Sr/^{86}Sr$ and LILE profiles of the Polisiehoek granites in particular, as well as in some of the Swartoup pyroxene granitoids, which could be either a symptom of CO_2 metasomatism related to the Bysteek Formation carbonates, or to post-magmatic fluid metasomatism, perhaps linked to regional shearing. The comparison of our results with literature data suggests that similar sources, A-type granitic, Meso- to Paleoproterozoic crustal, and enriched mantle, have contributed, in locally differing proportions, to granites in most parts of the Namaqua Sector. Most likely, these plutons were generated during crustal and mantle melting in a long-lived hot continental back-arc environment.

Keywords: A-type granite, migmatite, melt mixing, Kakamas Domain, radiogenic isotopes, Proterozoic crust

OPEN ACCESS

Edited by:
Steven W. Denyszyn, University of Western Australia, Australia

Reviewed by:
J. Gregory Shellnutt, National Taiwan Normal University, Taiwan
Kwan-Nang Pang, Academia Sinica, Taiwan
Jaroslav Dostal, Saint Mary's University, Canada

****Correspondence:***
Stephen Anthony Prevec
s.prevec@ru.ac.za

Specialty section:
This article was submitted to Petrology, a section of the journal Frontiers in Earth Science

Received: *04 September 2020*
Accepted: *16 November 2020*
Published: *28 January 2021*

Citation:
Büttner SH, Prevec SA and Schmeldt GA (2021) Petrogenesis of Mesoproterozoic Granites of the Swartoup Hills Region, Kakamas Domain, Namaqua Belt, South Africa. Front. Earth Sci. 8:602870. doi: 10.3389/feart.2020.602870

INTRODUCTION

During its formation and evolution, granitic magma may be exposed to processes and factors that influence its mineral, chemical, and isotope composition, grain size, texture, and contact relationships with the host rocks into which the pluton is emplaced and where it solidifies. These parameters include the variably homogenous or heterogeneous source rocks from which the granite magma is generated, the lithospheric level in which the primary magma is formed, and the contribution of different magmas that may mix or mingle during ascent or emplacement (e.g., Vernon et al., 1988; Baxter and Feeley, 2002). Assimilation of, and chemical reaction with, host rocks may contaminate granitic magma, causing local compositional and textural variations (e.g., Clemens et al., 1986; Clemens and Vielzeuf, 1987; Clemens, 2003; Chappell et al., 2004; Clemens and Stevens, 2012). The extent of interaction that is possible with the host rock depends on further factors, such as the mineral composition of the host rock, its temperature and physical state, and the capacity of the intruding magma to react with the host rock, depending on the composition, shape, size, and temperature of the magma chamber.

The petrogenetic importance of each of these parameters and processes can be identified and evaluated *via* the analysis of the mineralogical and geochemical variability of the chemical and isotopic compositions of the pluton, the field relationships between pluton and host rocks, comparison with other plutons of equal age nearby, and the understanding of the evolution of the crust hosting these plutons (Clarke, 1992).

The crustal evolution of the Namaqua Metamorphic Province in South Africa and Namibia (**Figure 1A**) is characterized by a long-standing high-temperature regime in the Mesoproterozoic, particularly between ~1,230 and ~1,080 Ma, with further episodes of early (~1,300 Ma) and late (~1,000 – 1,030 Ma) magmatism in some parts of the belt (Robb et al., 1999; Raith et al., 2003; Clifford et al., 2004; Bial et al., 2015a; Bial et al., 2015b; Abrahams and Macey, 2020; Groenewald and Macey, 2020). Granitic to charnockitic plutonism is predominant and widespread

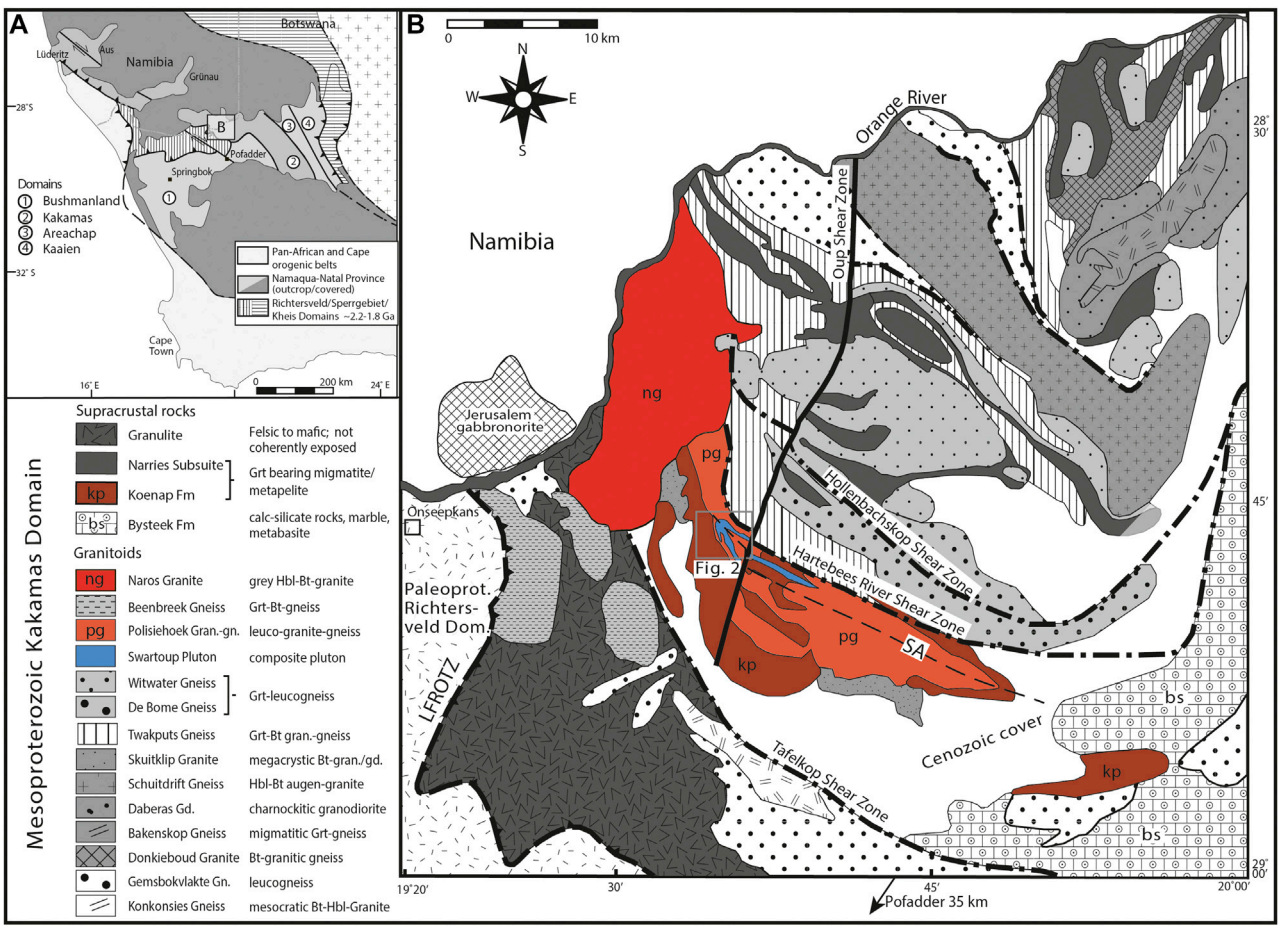

FIGURE 1 | Regional geology of the Namaqua Sector of the Namaqua-Natal Metamorphic Province. **(A)**. The four Mesoproterozoic domains of the Namaqua Sector and the Palaeoproterozoic basement of the Richtersveld, Sperrgebiet, and Kheis Domains in southwestern Africa. **(B)** The central Namaqua Sector in South Africa with its main granitic and supracrustal entities and regional shear zones. Along the Lower Fish River-Onseepkans Shear Zone (LFROTZ; Macey et al., 2015), the rocks of the Kakamas Domain are thrusted over the Paleoproterozoic Richtersveld Domain. The position of the map in **Figure 2** is highlighted. Maps A and B are modified after Bial et al. (2015b) and references therein. SA: Swartmodder antiform.

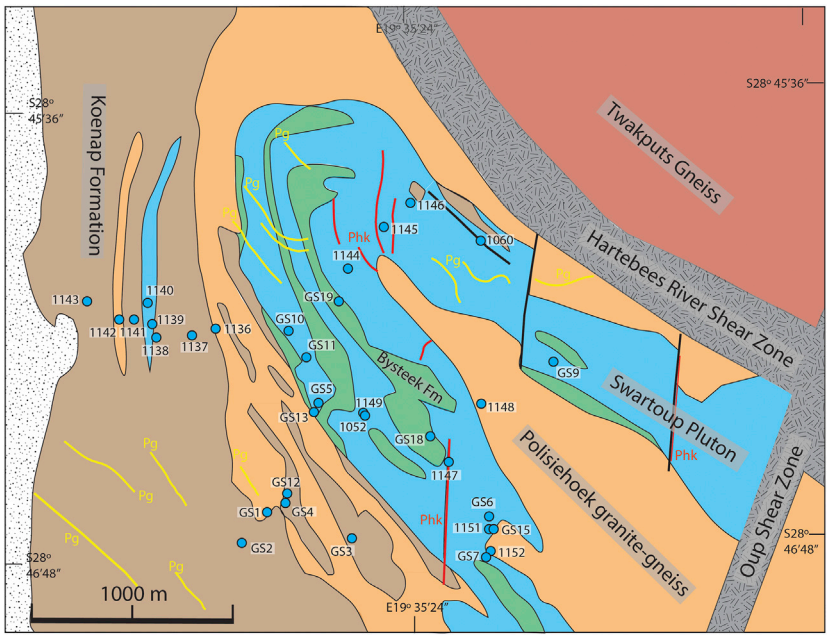

FIGURE 2 | Simplified geological map of the study area (**Figure 1B**) showing the distribution of lithological entities, main structures, and sample locations. Pg, pegmatites (in yellow); Phk, Polisiehoek Granite dykes (in red). Pegmatites are post-orogenic and undeformed. Polisiehoek Granite dykes commonly show sheared boundaries or, in some places, penetrative mylonitization.

throughout the orogen. Mafic or bimodal magmatism, such as the Jerusalem gabbronorite (**Figure 1B**), the Kum-Kum norite, and the Tantalite Valley Complex (Miller, 2008), emplaced between ~1,210 and 1,225 Ma (unpublished data; pers. comm. Paul Macey, 2020), basaltic lavas in the Bushmanland Group (~1,130 ± 35 Ma; Cornell et al., 2009), the ~1,100 Ma Koras Group (Bailie et al., 2012), or the ~1,030 Ma Koperberg Suite (Clifford et al., 1995; Robb et al., 1999), indicate fertile mantle sources throughout much of the evolution of the lithosphere in the Namaqua Sector.

The tectonic setting of the Namaqua Metamorphic Province, particularly its Namaqua Sector (**Figure 1**), is a matter of debate. The traditional model developed in the 1980s (Joubert, 1986; Stowe, 1986; and reviewed by Miller, 2012) proposes multiple oceanic basins separating small continental fragments in the early Mesoproterozoic, presuming multiple subduction zones and eventual terrane collisions at ~1,200 Ma in the context of Rodinia assembly. More recently, this model has been challenged (Bial et al., 2015a; Bial et al., 2015b; Macey et al., 2016; Büttner, 2020), particularly on the basis of the lack of convincing indicators for subduction- or collision-related metamorphism, or evidence for the existence of oceanic basins once separating crustal entities in the region at that time. Bial et al. (2015a) proposed a long-lived continental back-arc, with regionally and chronologically variable heat and magma transfer into thin lithosphere, as the most likely tectonic setting for the Namaqua Sector in the Mesoproterozoic. Although the Namaqua Metamorphic Province evolved in the time period during which Rodina formed, there appears to be no evidence that the Namaqua Sector was involved in the collision of pre-Rodinia cratons or lithospheric fragments, and it may well have formed along the margin of the evolving supercontinent.

Granite petrogenesis is a monitor of processes during the high-temperature episodes in the Namaqua Sector, and a number of studies, particularly by Bailie (Bailie et al., 2010; Bailie et al., 2012; Bailie et al., 2017; Bailie et al., 2019), have used the geochemistry and isotopic signatures of granitoid rocks for the interpretation of the regional crustal evolution. The current study adds new complementary data from the Swartoup and Polisiehoek plutons in the central part of the Namaqua Sector, in the Kakamas Domain (**Figures 1A,B**).

In the field, the Swartoup Pluton (**Figure 1B**) shows compositional heterogeneity and locally significant metasomatic or magmatic interaction with pelitic and calcic host rocks of the supracrustal Koenap and Bysteek Formations, indicated by transitional contacts or hybrid rock types. By contrast, the spatially associated Polisiehoek granite gneiss, which according to crosscutting relationships is younger than the Swartoup Pluton, shows sharp boundaries with the Swartoup Pluton and the supracrustal host rocks along pluton and dyke contacts. At the scale of hundreds of meters (**Figure 2**), both, the Swartoup and the Polisiehoek plutons intrude the Bysteek and the Koenap Formations along irregular contacts, forming lenses of host rock within the plutons. These lenses show compositions, structural trends, and shapes that are compatible with the regional geological structure and lithology, and therefore are most likely roof pendants.

In this study, we investigate the field relationships, the compositional and geochemical variations, and Nd and Sr isotope signatures of the Swartoup and Polisiehoek plutons

and their host rocks. We discuss potential magma sources, petrogenetic processes, and possible genetic relationships, and the extent and nature of interactions between intrusive magma and host rocks, in the context of the regional evolution of the Mesoproterozoic crust. The compositional variations of these plutons are compared with data from other parts of the Namaqua Sector, and their petrogenesis is evaluated in the context of the tectonic setting of the region in Mesoproterozoic time.

Geological Context and Regional Crustal Evolution

The Mesoproterozoic Kakamas Domain (**Figure 1**) consists of medium- to high-grade metamorphic supracrustal metamorphic rocks which commonly show extensive anatexis. Predominantly granitoid plutons intruded this basement between ~1,220 and ~1,180 Ma, and in a second episode at ~1,100 Ma (Bial et al., 2015a; Bial et al., 2015b). The region of the Swartoup Hills, east of the Lower Fish River-Onseepkans Thrust Zone (LFROTZ; **Figure 1B**), along which the Kakamas Domain has been thrusted over the Paleoproterozoic Richtersveld Magmatic Arc in the west (Thomas et al., 2016; Macey et al., 2017) is arguably the highest grade metamorphic region within the Kakamas Domain. In this area, the Swartoup and Polisiehoek plutons and their metamorphic host rocks formed and developed in a high- to ultrahigh temperature (HT/UHT) and low-pressure environment reaching up to about 900°C, at pressures not exceeding 500–550 MPa (Bial et al., 2015a; Bial et al., 2015b). Spinel–quartz– and osumilite-bearing parageneses in felsic host rocks indicate the UHT increment of the P–T path. Regional anatexis and diatexis in rocks of pelitic and psammopelitic bulk composition are associated with the thermal maxima (Bial et al., 2015a).

The ages of magmatic zircon in migmatites indicate two episodes of anataxis in the metamorphic basement in the region, an early phase around ~1,300–1,350 Ma and a second phase around 1,200 Ma (Bial et al., 2015a). It is not evident which of these episodes is responsible for the growth of the UHT mineral assemblages, but Bial et al. (2015a) consider the ~1,200 Ma anataxis as the dominant melt-forming episode in the supracrustal rocks of the region.

The metamorphic history is characterized by slow isobaric cooling over at least ~120 m.y. between ~1,200 Ma to 1,070–1,090 Ma that alternates with episodic reheating, but only minor pressure variation. For this time period, there is no indication of temperatures of metamorphism of less than upper amphibolite facies conditions or pressure increments higher than 550 MPa. In the Aus region of Namibia (**Figure 1A**), the crust of the Kakamas Domain reached high temperature and low pressure conditions associated with granitic plutonism much later, at about 1,030 – 1,060 Ma (Diener et al., 2013). At this time, the crust in the Swartoup Hills already had cooled down to lower amphibolite facies conditions (Büttner et al., 2013). The most likely tectonic setting of this long-lasting high-temperature/low-pressure evolution with episodic plutonism and thermal peaks is the thin and hot lithosphere of a Mesoproterozoic continental back-arc (Bial et al., 2015a; Büttner, 2020).

The long-lasting high-temperature metamorphic history of the Swartoup Hills region correlates in time with two main episodes of crustal plutonism, an earlier one at 1,230–1,180 Ma during regional anatexis, and a later pronounced event at ~1,100 Ma, during which one of the largest bodies in the region, the Naros pluton, was emplaced (Bial et al., 2015b; Macey et al., 2015; Macey et al., 2016).

The main episode of crustal deformation is bracketed by the ages of regional anataxis and pluton emplacement episodes. The dominant structural inventory consists of large-scale dome-and-basin structures and regional ductile shear zones (Moen and Toogood, 2007). Both structure types overprint migmatites and the ~1,200 Ma plutons, but the ~1,101 Ma Naros pluton truncates regional dome-and-basin structures and the main shear zones, such as the Hartebees River or the Hollenbachskop shear zones (**Figures 1B**, **2**; Bial et al., 2015a; Bial et al., 2015b). Locally, magmatic foliation suggests the late-tectonic emplacement of the Naros pluton (Bial et al., 2015b). A similar situation exists further east along the Hartebees River shear zone, where the Karama'am Granite (1,106 ± 8 Ma) truncates its mylonitic structure (Colliston et al., 2015). For the Grünau area in neighboring Namibia, Bial et al. (2016) provide a more accurate estimate of the time of deformation along regional shear zones. In the Grünau shear zone, a younger monazite generation, compositionally distinct compared to monazite related to the regional ~1,200 Ma metamorphic peak, formed between ~1,130 and 1,120 Ma. This age is interpreted to date the mylonitization along this shear zone (Bial et al., 2016). The same age of 1,125 ± 5 Ma is found in zircon rims, interpreted as high-temperature growth in the solid state in granites nearby major shear zones, such as the 1,195 ± 16 Ma Skuitklip Granite (Bial et al., 2015b; **Figure 1B**). The Polisiehoek granite gneiss has been dated as 1,203 ± 11 Ma (Pettersson, 2008), with a T_{DM} age of 2,244 Ma indicating a significant Paleoproterozoic component in its source (Pettersson et al., 2009).

In the wider area of the Swartoup pluton, Bial et al. (2015b) identify three distinct groups of granitoid plutons: 1) mesocratic granites, 2) leucocratic granites, and 3) leucogranites. Mesocratic granitoids are high-K, ferroan granites and tonalities, enriched in large-ion lithophile elements (LILEs) and rare-earth elements. They characterized these plutons as A- and I-type granitoids (e.g., Whalen et al., 1987; King et al., 1997; Zhang et al., 2019). Bial et al. (2015b) proposed that these granites formed by fractional crystallization of a hot (~900°C), mafic parental magma. The leucocratic granitoids and leucogranites vary from granitic to syenitic compositions, and were interpreted as products of low temperature (<730°C), fluid-present partial melting of a felsic metasedimentary source, classifying them as S-type granitoids. All mesocratic and leuco-/leucocratic granitoids, except the ~1,101 Ma Naros granodiorite, were emplaced between ~1,220 and ~1,180 Ma (Bial et al., 2015b). Mafic and ultramafic plutons in southernmost Namibia intruded between ~1,225 and 1,210 Ma (Paul Macey, unpublished data, pers. comm., 2020). Accordingly, for this time frame, both the crust and the mantle must be considered possible sources for granitoid plutonism. At the

same time, major anataxis affected the pluton-hosting supracrustal rocks (Bial et al., 2015a), which created the possibility of anatectic melt contributing to the formation of plutons in the Kakamas Domain. Given a period of regional magmatic zircon growth in metamorphic rocks between ~1,225 and ~1,175 Ma (Bial et al., 2015a), an age bracket for the metamorphic peak in the Koenap migmatites of ~1,200 ± 25 Ma can be proposed.

Following a protracted period of high crustal temperatures, a second heat pulse around 1,100 Ma facilitated zircon growth in older plutons and production of the younger granite suite (Naros pluton, the Donkieboud Granodiorite, and smaller bodies such as the Beenbreek pluton; Pettersson, 2008; Bial et al., 2015b; Abrahams and Macey, 2020). This renewed plutonic activity around 1,100 Ma is associated with reheating of the crust and fluid circulation, manifested in the renewed growth of monazite and garnet (Bial et al., 2015a). Crustal cooling below mid-amphibolite facies conditions took at least an additional 75–115 m.y. Such crustal temperatures in the Swartoup Hills area are estimated for ~985–1,026 Ma (Pettersson, 2008; Büttner et al., 2013; Bial et al., 2015a).

ANALYTICAL METHODS

A total of forty-four representative rock samples were collected from the study area: ten from the Koenap Formation migmatites, three from the Bysteek Formation, twenty-one from the Swartoup Pluton, and nine from the Polisiehoek granite gneisses. Sampling localities are shown in **Figure 2**.

Major elements were determined by XRF analysis at the Central Analytical Facility at Stellenbosch University (South Africa) on fused glass discs using a PANalytical Axios wavelength dispersive spectrometer. The spectrometer utilized a 2.4-kW Rh-tube and LIF200, LIF220, PE 002, Ge 111, and PX1 crystals, and used a gas-flow (90% argon–10% methane gas mixture) proportional counter and a scintillation detector. Matrix effects in the samples were corrected for using theoretical alpha factors and measured line overlap factors using SuperQ PANalytical software. Calibration standards included the NIM-G (granite from the Council for Mineral Technology, South Africa) and BE-N (basalt from the International Working Group). Trace element analysis was conducted on the same fused discs by LA-ICP-MS at the same facility, using a Resonetics 193 nm excimer laser connected to an Agilent 7700 ICP-MS. Trace elements are quantified using NIST612 for calibration and the silica content from XRF as an internal standard, and BCR-2 and BHVO 2G as external standards. Duplicate measurements were made on each sample.

Rb/Sr and Sm/Nd isotopic ratios were measured for twenty-seven samples using Nu Instruments HR MC-ICP-MS at the University of Cape Town, South Africa, using the methods described by Harris et al. (2015). For strontium, the reference granite standard JG-2 gave a value of $^{87}Sr/^{86}Sr = 0.76014 \pm 3$, consistent with the internal reproducibility of 0.760 ± 1 (n = 6), compared to a literature reported value of ~0.75805 (Ma et al., 2013). Strontium isotope compositions were corrected for Rb interference and normalized to $^{86}Sr/^{88}Sr = 0.1194$ to correct for thermal fractionation. For Nd, analyses were monitored relative to a standard value for JG-2 of $^{143}Nd/^{144}Nd = 0.512250 \pm 12$, as compared to an internal value of 0.512232 ± 24 (n = 17) and a literature value of ~0.51221 (e.g., Miyakazi and Shuto, 1998). Mass interference from Sm was corrected based on natural Sm isotopic composition, and thermal fractionation of Nd isotopic composition was corrected during analysis by normalization to $^{146}Nd/^{144}Nd = 0.7219$.

OBSERVATIONS AND ANALYTICAL DATA

Field observations and field relationships of the Swartoup Pluton, the Polisiehoek granite gneiss, and their host rocks

Swartoup Pluton

The Swartoup Pluton forms a narrow, up to 600-m thick plutonic layer that stretches approximately 10 km along strike (**Figure 1B**). Subsequent folding in its solid state affected the pluton and its host rocks, producing a first-order NW-SE trending and NE plunging antiformal structure, to which Moen and Toogood (2007) refer as the Swartmodder antiform (**Figure 1B**). Localized ductile deformation formed mylonite or ultramylonite zones up to ~1 m thick in the Swartoup Pluton. Away from these zones, the pluton shows macroscopically undeformed granitic texture and, in some places, minor magmatic foliation.

The pluton consists of different lithological varieties including granites, granodiorites, and less commonly, monzonites, quartz-monzonites, and monzo-diorites. Orthopyroxene is rare and in the current study has been found in only one location in a monzo-diorite (Loc. 1,151; **Figure 2**), allowing the classification as enderbite. Bial et al. (2015b) describe another occurrence, but these rocks appear to form only a small proportion of the pluton. Alkali feldspar phenocrysts, typically between 0.5 and 2.5 cm in size are, irrespective of the extent of weathering, visible in most parts of the Swartoup Pluton (**Figure 3A**), suggesting that the most abundant rock type is granodiorite or granite. In addition to quartz and the feldspars, the mineralogy of the Swartoup Pluton typically consists of biotite and accessory phases such as apatite and zircon. Garnet is typically rare, but can be locally abundant, and pyroxene is typically absent. The rocks are medium- to coarse-grained and, where fresh, medium to dark gray. The boundaries between the different granitoid varieties are often not exposed or are masked by weathering. Where they are exposed, they are gradational, suggesting coexistence of different granitoid magmas.

The 1:250,000 geological map of the region shows the Swartoup Pluton as "Swartoup Enderbite" (Moen and Toogood, 2007). However, since orthopyroxene-bearing tonalitic material is present in only a few small domains of the pluton, and overwhelmingly the pluton is alkali feldspar-rich and mostly pyroxene-free, we deem the name "Swartoup Pluton" more appropriate for this intrusion.

Close to, and in contact with, the calcic rocks of the Bysteek Formation, the Swartoup Pluton grades into a several meter thick zone of clinopyroxene-rich granodiorites, granites, and tonalites that contain variable amounts of alkali feldspar, plagioclase, and quartz. Plagioclase phenocrysts may reach up to 4 cm in size. The dominant morphotype is a leucocratic feldspathic granitoid, but it can be locally melanocratic and/or gneissose, with leucosome

FIGURE 3 | Field appearance of the Swartoup and Polisiehoek plutons and their host rocks. **(A)** Alkali feldspar-rich Swartoup leucogranite from the interior of the pluton with undeformed magmatic texture. **(B)** Magmatic megabreccia in mafic granulites of the Bysteek Formation. The intruding facies of the Swartoup Pluton is leucocratic and may be alkali feldspar or plagioclase dominated, but always shows large magmatic clinopyroxene. This type of granitoid is restricted to the contact zone of the Swartoup pluton with the metabasites of the Bysteek Formation. Inset: Centimeter-sized magmatic clinopyroxene in leucocratic matrix at the contact to a fine-grained metabasite fragment. Gradational contacts indicate the interaction of the intruding magma with the breccia clasts. **(C)** Dyke of Polisiehoek Granite cutting the Swartoup Pluton at sharp intrusive boundaries. Elswhere, such contacts are commonly sheared. **(D)** Convoluted folding of marble and calc-silicate rock layers of the Bysteek Formation. **(E)** Stromatic to nebulitic migmatite of the Koenap Formation with abundant garnet in alkali feldspar-rich leucosome. Cordierite and sillimanite, or biotite are commonly present. **(F)** Alkali feldspar phenocrystic Swartoup Pluton overprinted during regional deformation at high temperature along a shear zone parallel to the Hartebees River shear zone (Loc. 1,060; **Figure 1B**).

veins, and significant accessory clinopyroxene (the latter as distinctive phenocrysts up to 2 cm in diameter; **Figure 3B**), or garnet present. This rock type is therefore distinguished from the homogeneous granitoids with biotite as the sole mafic mineral that typifies the Swartoup Pluton rocks. Accordingly, three petrologic based subtypes of the Swartoup intrusion are designated in this study, consisting of 1) Swartoup leucogranitoids, which are the quartzo-feldspathic, felsic granitoids with biotite as the sole mafic phase; 2) Swartoup pyroxene granitoids, which are typically more melanocratic, and contain clinopyroxene except in sample 1,151 that contains orthopyroxene; and finally 3) Swartoup garnet granitoids, which contain macroscopically visible garnet present in variable but in places significant quantity. Where the Swartoup Pluton intrudes the metabasites of the Bysteek Formation, up to meter-sized angular clasts of mafic granulites and the Swartoup clinopyroxene granitoid form distinctive magmatic mega-breccias with macroscopically evident interaction between intruding magma and granulite fragments are observed (**Figure 3B**).

Polisiehoek Granite Gneiss

The Polisiehoek granite gneiss is one of the largest plutons in the region, with an outcrop size of ~40 × 8 km (**Figure 1**). It is a largely uniform leucocratic rock with medium- to coarse-grained alkali feldspar and quartz as the dominant phases, minor plagioclase, and in places some garnet. Biotite is rare or absent. Significant ductile deformation formed up to several hundred-meter-thick zones with a characteristic penetrative continuous schistosity, particularly in an area immediately to the southwest of the boundary between Polisiehoek gneiss and the Swartoup Pluton (**Figure 2**). On foliation planes, transport lineations are rare, suggesting deformation predominantly in the oblate field of strain. In such zones, the magmatic mineral assemblage is entirely recrystallized with alkali feldspar grain sizes of 100–400 μm, but small rheological contrasts between feldspar and quartz prevent the formation of augen-shaped clasts. Other areas in the Polisiehoek granite gneiss remained undeformed and show medium- to coarse-grained magmatic textures without significant flow textures. The pink alkali feldspar in undeformed Polisiehoek granite dominates the color of the rock in the field. In sheared domains, the recrystallized alkali feldspar is white. Weathering and minor iron oxide or hydroxide precipitation in the sheared domains is characterized by its orange weathering color, which is an indicative and obvious feature of the Polisiehoek granite gneiss in the field.

The Polisiehoek granite gneiss forms the core and the outer margin of the Swartmodder antiform (**Figures 1B**, **2**), which indicates its pre-tectonic emplacement and its intrusion on either side of the Swartoup Pluton layer. Prominent Polisiehoek granitic dykes, up to ~2 m thick, crosscut the Swartoup Pluton (**Figure 3C**), indicating the relative age relationship of the two plutons. Some connect the inner and outer Polisiehoek granite layers of the Swartmodder antiform. Commonly, but not always, the dyke margins are intensely sheared in the solid state, causing mylonites and ultramylonites to form.

Along the northeastern limb of the Swartmodder antiform, shearing along the Hartebees River Shear Zone (HRSZ; **Figures 1B**, **2**) overprints the Polisiehoek granite gneiss, and, less commonly, parts of the Swartoup Pluton and the supracrustal host rocks. The HRSZ offsets the lithological sequence, juxtaposing the rock sequence that is the focus of the current study with the Twakputs gneiss to the northeast of the shear zone (**Figures 1B**, **2**). The Twakputs gneiss formed as an in situ low-temperature S-type granite (Bial et al., 2015b).

Supracrustal Rocks: Koenap and Bysteek Formations

Metapelitic diatexites of the Koenap Formation and granulite-facies calc-silicates, marbles, and metabasites of the Bysteek Formation (**Figures 3B,D**) form the immediate host rocks of the Swartoup and Polisiehoek plutons (**Figure 2**). The protolith ages of these supracrustal metamorphic host rocks are not accurately known. Moen and Toogood (2007) deem the Bysteek Formation stratigraphically older than the Koenap Formation, but due to the intense deformation and metamorphism in the region, this age relationship could not be verified in the field. Common inherited Paleoproterozoic (~1.8–2.0 Ga) and early Mesoproterozoic zircon (Moen and Toogood, 2007), in some cases showing indication of detrital transport (Bial et al., 2015a; Bial et al., 2015b), indicate the Paleoproterozoic heritage and possible sediment sources of that age. Moen and Toogood (2007) estimate the depositional age of the Koenap Formation's protolith as between 1.3 and 1.8 Ga.

The carbonate, calcic-pelitic, and pelitic composition of the Bysteek and Koenap Formations suggest variable, gradually changing deposition of carbonate grading into marls and eventually psammopelitic/pelitic material. Moen (2001) emphasizes the transitional nature of the carbonatic Bysteek and pelitic/psammopelitic Koenap Formations. Accordingly, the metabasites of the Bysteek Formation may have formed either from marls or mafic igneous protoliths. In the study area, the Bysteek Formation forms only narrow outcrops that form contacts with the Koenap Formation and both plutons (**Figure 2**). The main outcrop of the Bysteek Formation is 20–50 km to the southeast of the study area (**Figure 1B**).

The Koenap Formation forms topographic highs as small hills of several tens of meters in diameter within the intrusive Polisiehoek granite gneiss but forms coherent basement further to the southwest (**Figures 1B**, **2**). A black oxide layer of desert varnish disguises the typically lighter color of the fresh rocks. The Koenap Formation shows a variety of high-grade metamorphic rocks ranging from stromatic to nebulitic migmatites (**Figure 3E**), diatexites, and pockets of in situ granite. Moen and Toogood (2007) refer to these rocks as "kinzigites." In other domains, the migmatites and diatexites grade into homogenous medium-grained gray granofelsic granulites without layering or separation of leucocratic and mafic material. Their composition and texture is consistent with that of restitic felsic granulite.

Leucosome dykes, up to decimeter thickness, transecting the layering in stromatic migmatites along diffuse and gradual boundaries suggest some melt mobility during anatexis. In some places, such dykes are connected to granitic pools of several meters in diameter. However, there is no indication that such dykes have transported magma over larger distances (e.g., tens or hundreds of meters) or in large volumes.

The composition of the anatexites and granulites of the Koenap Formation consists of quartz, alkali feldspar, plagioclase, garnet, and minor cordierite, sillimanite, biotite, and spinel. Plagioclase and alkali feldspar may show euhedral faces suggesting their crystallization in melt (Vernon, 1986). Biotite and sillimanite commonly occur as inclusions in cordierite, which is always a minor phase, but neither in cordierite nor in the melanosome are biotite and sillimanite in contact with each other. Most samples contain either sillimanite or biotite. These relationships suggest biotite–sillimanite consuming melting reactions forming the leucosome of the migmatites. Garnet is commonly present and almost always associated with the leucosome. Poikilitic cores containing quartz and feldspar, and in places sillimanite and biotite, might have grown in the solid state at the upper end of the prograde P–T path. The rim zones are largely inclusion free. Euhedral faces are rare; typically, the garnet shape is irregular. Crystals may reach up to 4 mm in size. The rim zones of garnet

are in textural equilibrium with leucosome phases and are likely to have formed as a cotectic phase during biotite and sillimanite breakdown. Spinel–quartz associations and pseudomorphs after osumilite, as described in Bial et al. (2015a), are also present in the Koenap Formation close to the Polisiehoek and Swartoup plutons. Samples described by Bial et al. (2015a) show similar features and assemblages, and we consider their P–T–t paths applicable to the Koenap Formation in the study area.

The Bysteek Formation contains three prominent rock types: metabasite, calc-silicate rocks, and marbles (**Figures 3B,D**). Metabasites are typically massive and fine- to medium-grained, but layered in some places. Leucosome veins are rare, and, where present, they are typically folded. The mineral assemblage is typically simple, showing clinopyroxene and anorthitic plagioclase. Ca-rich garnet is present in places. Biotite and orthopyroxene are rare, and accessories are titanite and apatite. Leucosome veins are less than 1 cm thick and contain plagioclase, minor alkali feldspar, and quartz. The melt forming reaction is unclear, but the presence of alkali feldspar suggests biotite breakdown. The melanosome seams contain clinopyroxene. The mineral assemblage of the metabasites and the presence of leucosome veins are consistent with the ultrahigh-temperature P–T conditions of the regional metamorphism (Bial et al., 2015a).

Calc-silicates are light brown fine-grained and plagioclase–quartz–dominated rocks that may contain alkali feldspar, clinopyroxene, garnet, and titanite. In addition, Moen and Toogood (2007) describe green amphibole, scapolite, and epidote, which have not been found in the current study. In places, the calc-silicate rocks contain minor calcite. The calc-silicate rocks form centimeter to several meters thick layers, interlayered with marble. Where marble and calc-silicate rocks are thinly (~<dm scale) interlayered, convoluted folding is common, and boudinage may contort the layering to form calc-silicate nodules and lenses in a marble matrix (**Figure 3D**).

Marble layers are commonly pure calcite but may contain accessory small (<2 mm) silicate grains, including orange grossularite, green olivine, or clinopyroxene. Epidote has been described by Moen and Toogood (2007) but has not been encountered in the current study. Two of the marble layers in the study area are up to ~10 m thick but more commonly they are thinner and interlayered and interfolded with calc-silicates.

Contacts and Transitions

Relevant for this study are the contact relationships between 1) the supracrustal metamorphic rocks of the Koenap and Bysteek Formations with the Swartoup Pluton, 2) the Polisiehoek granite gneiss and the Swartoup Pluton, and 3) between the Polisiehoek Gneiss and the Koenap and Bysteek Formations.

Along the contact of the Koenap Formation with the Swartoup Pluton diffuse transitions between anatexites and plutonic rocks suggest the interaction of both rocks in their partially molten state. Furthermore, the presence of garnet-bearing granitoids within the Swartoup Pluton, about 3 m away from the contact, suggests the flow of garnet-bearing magma from the anatexites into the Swartoup Pluton's marginal zone. The interior of the Swartoup Pluton is typically garnet-free.

Restricted to a several meter-wide zone along the contact to the marbles and calc-silicates of the Bysteek Formation, the Swartoup Pluton shows a texturally distinctive lithological variety with large up to 2-cm–sized clinopyroxene in a white plagioclase- and alkali feldspar-rich matrix. This material, but not other Swartoup Pluton varieties, intrude the Bysteek granulitic metabasites, forming magmatic megabreccias (**Figure 3B**).

The contacts of the Polisiehoek granite gneiss with the supracrustal rocks and with the Swartoup Pluton are markedly different. This contact zone with both the migmatites of the Koenap Formation and the Bysteek Formation is commonly sheared. Where such deformation is absent, the contacts are planar or irregular, but always sharp. No megabreccias are related to the emplacement of the Polisiehoek magma. Abundant Polisiehoek granite dykes in both the Koenap Formation and the Swartoup Pluton show sharp and planar contacts. There is no evidence of metasomatic or melt interaction of Polisiehoek melt with any of its host rocks.

Regional Shear Zones and Brittle Deformation

The Hartebees River shear zone, an up to ~400-m thick regional scale structure to the northeast (**Figure 2**), leaves the Swartoup Pluton largely unaffected, except of minor shear zones that are parallel to the HRSZ and are likely genetically related (**Figure 3F**). The Oup shear zone crosscuts the pluton at high angle (**Figure 2**) but in the study area is poorly exposed. Further north in the Twakputs gneiss, the Oup shear zone forms highly ductile mylonite zones.

Brittle faults are commonly associated with coarse-grained and often euhedral epidote and calcite mineralization, indicating the percolation of Ca-rich fluids. Pseudotachylyte is present in the regolith but has not been seen in situ. Büttner et al. (2013) describe similar faults and mineralizations in the Twakputs Gneiss north of the Hartebees River shear zone.

Geochemistry

This chapter presents the results of the XRF major elemental and LA-ICPMS trace elemental analysis. Average compositions of the main lithological groups are provided with the full data set in the **Supplementary Material**.

Basic classification of the granitoids using major element geochemistry according to Middlemost (1994) is illustrated in **Figure 4**. The Swartoup granite samples form two clusters in the fields of granites and granodiorites, but display a scatter to lower silica and less alkaline granodiorite compositions. These variations can be explored by plotting the Swartoup samples according to their mineralogical criteria, such that the leucogranitoids with biotite as the sole mafic mineral plot within a restricted alkali content range, but with variable silica contents, falling into the fields of granite, granodiorite, and quartz monzonite. The pyroxene granitoids show a wider chemical variation, plotting from granite all the way to monzodiorite. The garnetiferous Swartoup granitoids show the least variation in this plot, consistently plotting in the granodiorite field.

The Polisiehoek granites fall into the field of granite, with a small compositional range (**Figure 4**). The Polisiehoek granite samples plot close to the high silica samples of Swartoup

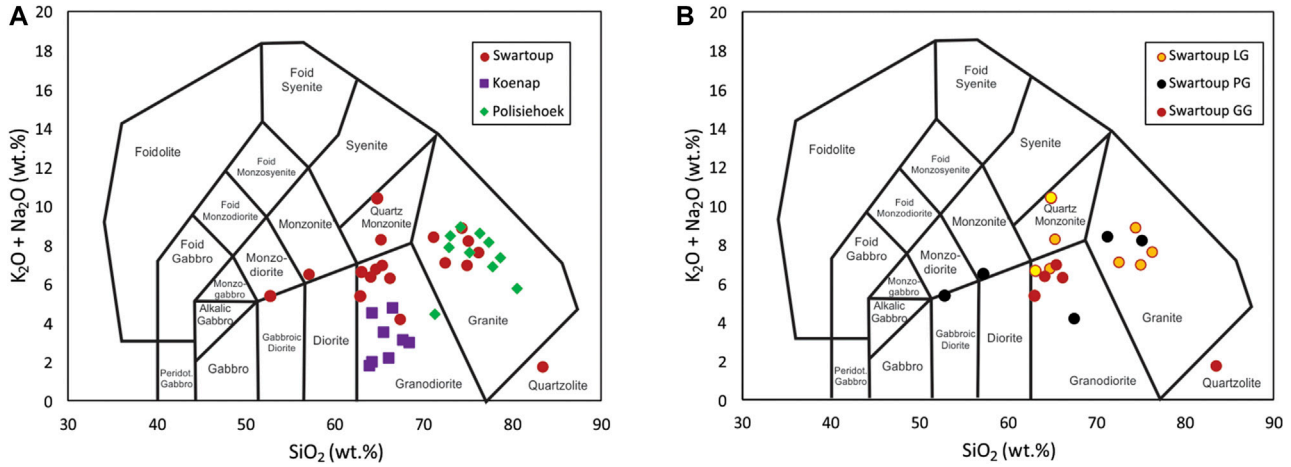

FIGURE 4 | (A) Total alkali vs. silica (TAS) diagram (after Middlemost, 1994) for classification of Swartoup Pluton granitoids and the Polisiehoek granite gneisses. Koenap Formation migmatites are plotted for compositional reference (as opposed to classification) purposes only. In **(B)**, the Swartoup granitoids are subdivided according to their modal compositions into leucogranitoids (LG) with biotite as the sole mafic phase, pyroxene-bearing granitoids (PG), and garnet-bearing granitoids (GG). See text for discussion.

leucogranitoids and some of the pyroxene granitoids. The Koenap migmatites and diatexites plot in the granodiorite field, with distinctly lower total alkali contents than average Polisiehoek or Swartoup plutons (**Figure 4A**). In their SiO_2 contents, they are similar to garnet-bearing material from the Swartoup Pluton.

Incompatible Trace Elements

Incompatible trace elements, which can be used to illustrate genetic relationships between components potentially related by partial melting, are presented in **Figure 5**. The Swartoup granitoids are presented as the three petrologically distinguished groups (**Figures 5A–C**). Of these, the leucogranitoids and the garnet-bearing granitoids show similar trace element profiles, featuring relatively consistent patterns within the groupings, with some exceptions among the leucogranitoids. Most samples feature small negative spikes for Ba relative to Rb and Th, and show significant negative anomalies for Ta, Sr, and Ti. The garnet granitoids include samples that are distinguished from all other rocks in this study by the presence of a hump in the profile between the middle and heavy REE at the far right side of the profile, consistent with garnet accumulation in those rocks. The pyroxene granitoids are relatively heterogeneous in terms of profile patterns and element concentrations, with relatively high abundances of LILE on the left of the profile (compared to the other Swartoup groups), and samples showing either positive or negative spikes for Th, Nd, and Sm. The variation in the LREE is consistent with control by modal variation (fractionation or addition) of pyroxenes in these samples, as the main LREE-concentrating phase.

The Polisiehoek granitoids (**Figure 5D**) show large variability in some HFSE (Th, Nb, and Ta) and in Cs and Rb of one to two orders of magnitude. Sr is uniformly low, which correlates with low Ca contents in the alkali feldspar-rich and plagioclase-poor granitoid. The Koenap migmatite samples (**Figure 5E**) are characterized by uniform abundance profiles, with some variation evident in mobile large ion lithophile elements (LILE; Cs, K, and Rb, specifically).

The Bysteek Formation samples are shown for reference (**Figure 5F**). Most trace elements in the calc-silicate sample are below detection limits, while the marble shows prominent enrichment in Nb and low concentrations of LILE (including K) generally.

REE Variations

Figures 6A–6F show chondrite-normalized rare-earth diagrams of the various units. The $[La/Yb]_N$ and Eu/Eu* ratios of the sample set, calculated from the data in the Supplement Material, are shown in **Table 1**.

The Swartoup leucogranitoids (**Figure 6A**) and Koenap migmatites (**Figure 6E**) show similar enrichments in REE to one another, with Ce averaging around 20–30× chondrites, and with similar magnitudes of LREE enrichment. Compared to the leucogranitoids, the HREE profiles of the migmatites (**Figure 6E**) are flat. Koenap migmatites are also characterized by distinct negative Eu anomalies, whereas Swartoup Pluton leucogranites exhibit a mixture of negative and positive Eu anomalies. The mixture of both positive and negative Eu anomalies in rocks with otherwise broadly similar REE profiles is most consistent with local redistribution of feldspar crystals in the crystallizing magma, as feldspars are the only phases which strongly concentrate Eu (as Eu^{+2}) relative to the other REE (Henderson, 1984). In sharp contrast, the Swartoup pyroxene granitoids (**Figure 6B**) show nonuniform REE abundances, profile slopes, and Eu anomaly size and direction, consistent with the variability displayed in their major and trace element chemistry. The garnet granitoids show distinctive patterns (**Figure 6C**), featuring enrichments in the heavy middle to heavy rare-earth elements, and distinctive depletions in the light middle rare-earth elements in two samples, with no or small negative Eu anomalies in those

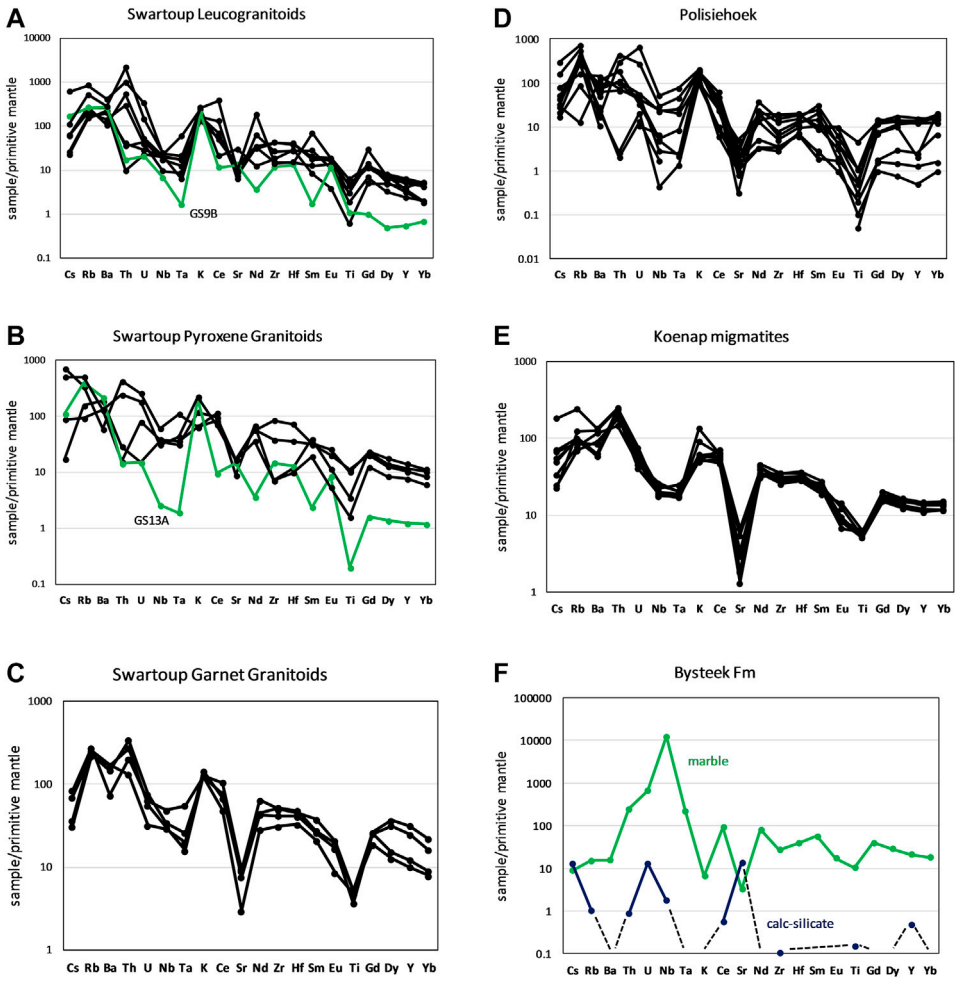

FIGURE 5 | Incompatible element spidergrams, normalized to Primitive Mantle (Bulk Silicate Earth pyrolite) of McDonough and Sun (1995). See text for additional information.

samples. Sample GS16A, which is from a garnet-rich quartzofeldspathic zone, is accordingly poor in LREE with a prominent enrichment in HREE consistent with garnet accumulation.

Most Polisiehoek granitic gneisses (**Figure 6D**) have REE profiles similar to those of Koenap Formation migmatites, showing relatively uniform profiles characterized by LREE enrichment at about 100–200× chondritic values, well-defined negative Eu anomalies, and flat to gently increasing HREE profiles. The REE profile of the Bysteek Formation marble shows fairly flat LREE contents between 200× chondrite concentrations, a small negative Eu anomaly, and a shallow and uniform decline in HREE. One of the clinopyroxene-bearing Swartoup granites (**Figure 6B**) from nearby the contact to the Bysteek Formation shows a similar REE pattern.

Radiogenic Isotopic Compositions

Sr and Nd isotopic compositions were determined for 19 granitoid samples, as well as four migmatites and one marble sample. The Rb-Sr isotopic compositional data are presented in **Table 2**, and the distributions for the granitoids are shown on a $^{87}Rb/^{86}Sr$ vs. $^{87}Sr/^{86}Sr$ isochron diagram in **Figure 7**. Some linear arrays are evident, but none of the suites can statistically be classified as isochrons based on their Model 3 solutions according to Ludwig (2012). Hence, the data are shown relative to reference lines with the corresponding ages and initial $^{87}Sr/^{86}Sr$ ratios (labeled as R*i*) indicated for each unit.

The Rb–Sr isotopic compositions show a set of subparallel aligned arrays defined by samples from the Koenap Formation migmatites, the Polisiehoek granitoids, and most of the Swartoup granitoids, corresponding to slope ages of around 1,200 Ma. The Koenap Formation data correspond to a slope age of ~1,200 Ma (**Figure 7B**) albeit with a regression imprecision of ±150 Ma and an MSWD of 41. The Sr initial isotope ratio is 0.716 ± 8. The Polisiehoek sample set shows a wide range in Rb/Sr ratio attributable to the highly variable Rb concentrations, which range from 51 to 423 ppm (**Table 2**), whereas Sr shows a restricted concentration range (32–81 ppm). The Swartoup Pluton samples show a high variability, with the leucogranitoid samples aligned along a linear trend consistent with their expected age of ~1,200 Ma.

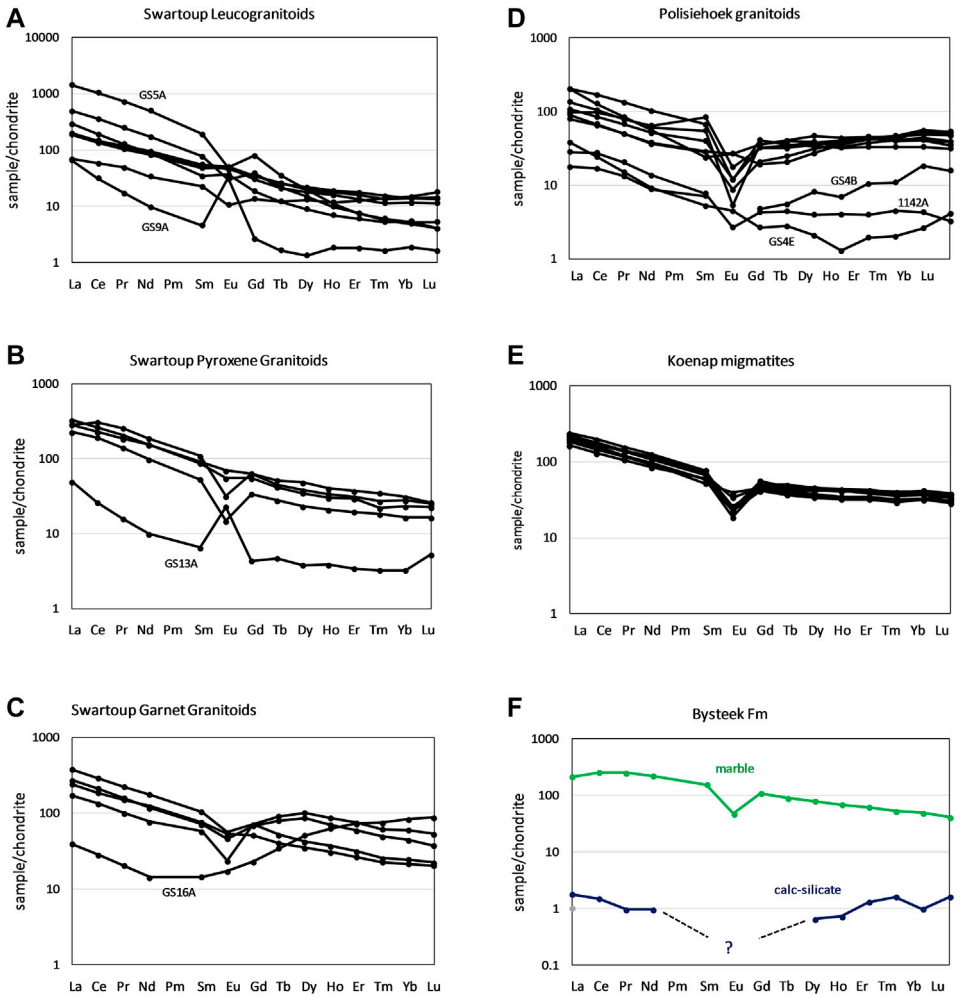

FIGURE 6 | Chondrite-normalized rare-earth diagrams of the Swartoup and Polisiehoek plutons and their host rocks. Compositionally distinct samples are labeled and/or distinguished using color.

The Sm–Nd isotopic compositions (**Figure 8**; **Table 3**) contrast with the Rb–Sr isotopic dataset, inasmuch as the Sm–Nd data show linear arrays constrained between reference lines corresponding to ages of ~900 Ma and around 760 Ma. Five Swartoup granitoids and all four Polisiehoek granitoid samples lie near the 900 Ma reference line. The Koenap Formation migmatites and many of the Swartoup leucogranitoids lie near the 760 Ma reference line. Neither of these trends bears any close relationship to a slope derived from the intrusion age at ~1,200 Ma.

DISCUSSION

In its exposed shape, the Swartoup pluton forms a small body amongst significantly larger younger plutons, such as the ~1,203 Ma Polisiehoek or ~1,101 Ma Naros plutons (Pettersson, 2008; Bial et al., 2015b). It was emplaced as a layer not more than a few hundred meters thick. Dykes of the Polisiehoek pluton cut the Swartoup Pluton (**Figure 3C**) and the UHT metamorphic supracrustal migmatites and granulites of the Koenap and Bysteek Formations along sharp intrusive contacts. By contrast, the contacts between the Swartoup Pluton and the migmatites of the Koenap Formation are transitional or gradational in places where they were not affected by the tectonic overprint. Garnet-rich patches with gradational boundaries to Swartoup leucogranites likely formed from proximal Koenap Formation magma injections, and may be present several meters within the Swartoup Pluton. This indicates the emplacement of the Swartoup Pluton during the presence of melt in the Koenap Formation. The main phase of anatexis has been dated as ~1,225–1,175 Ma, with the highest temperature (spinel–quartz and osumilite stability) reached early in this time interval (Bial et al., 2015a). The emplacement of the Swartoup magma into (ultra-) hot crust is also indicated by the transitional contacts of mafic Bysteek Formation granulites and intruding melt (**Figure 3B**).

TABLE 1 | $[La/Yb]_N$ ratios and Eu*/Eu ratios.

Rock type	Sample	$[La/Yb]_N$	Eu*/Eu	Rock type	Sample	$[La/Yb]_N$	Eu*/Eu
Swartoup Leucogran	GS5A	86.90	1.91	Koenap migmatite	1137A	5.99	1.70
	GS9A	5.03	1.74		1138A	4.22	2.44
	GS9B	40.40	0.11		1141A	4.93	2.89
	GS15B	2.80	2.70		1143A	7.46	2.23
	1144A	12.90	0.97		1143B	6.79	2.21
	1145A	14.70	0.88		1147B	6.80	1.72
	1146A	16.30	0.81		GS4C	5.93	2.80
	1149A	54.60	0.72		GS4D	5.92	1.24
Swartoup Px Gran	GS10B	15.00	1.30				
	GS11D	8.14	2.72	Polisiehoek Granitoid	1136A	3.29	2.12
	GS13A	15.10	0.24		1142A	6.33	2.24
	GS13B	12.50	2.92		1147C	6.12	4.56
Swartoup Gt Gran	1139A	14.80	1.55		1148A	1.87	2.81
	1140A	10.70	1.20		1148B	2.35	2.99
	GS7A	5.50	1.51		1152A	4.40	0.80
	GS15C	235	2.73		GS1A	2.30	1.19
	GS16A	0.53	1.57		GS4B	1.62	—
Bysteek	GS10A	4.02	2.77		GS4E	18.90	0.90
Fm	GS19A	1.12	—		GS11B	2.42	8.59

Eu/Eu is defined as $[(0.5\times(Sm + Gd))/Eu]_N$. Samples GS19A (Bysteek marble specimen) and GS4B (Polisiehoek granite gneiss) contain no detectable Eu. Samples were normalized to CI carbonaceous chondrite of McDonough and Sun (1995).*

The significantly larger Polisiehoek pluton was emplaced after the migmatites and the Swartoup Pluton solidified, but prior to cooling to low temperature. Folds related to the formation of the Swartoup antiform, and the mylonite zones parallel to the Hartebees and Oup shear zones in both plutons and the supracrustal host rocks formed above the stability of white mica or other phases indicating temperatures of the mid-amphibolite facies or lower. Bial et al. (2015b), Bial et al. (2016) propose the formation of first-order structures in the Kakamas Domain at about 1,120–1,130 Ma, which is in agreement with the 1,101 ± 6 Ma Naros Pluton truncating the Hartebees River shear zone and large-scale fold structures (Bial et al., 2015b). All these suggest slow cooling of the crust after the regional metamorphic peak.

These field relations, with evident interaction between the Swartoup magma and the melt in the hosting Koenap migmatites and the Bysteek mafic/calcic granulites, bear the potential of a local origin of the Swartoup Pluton. The diatectic Koenap Formation forms a large outcrop in the region (**Figures 1**, **2**), and may well have generated a several hundred-meter-thick granitic pluton. The much larger Polisiehoek granite gneiss was emplaced at a later time, and no field observation indicates any direct (i.e., transitional) relationship between the granite and its host rocks. In the following sections, we assess the potential sources of both the Swartoup and Polisiehoek plutons and the possible contributions of the Koenap and Bysteek Formations to their composition.

Radiogenic Isotopic Constraints on Granitoid Source Rocks

The radioisotopic compositional variation can provide first-order estimates on timing and contributions from various prospective chemical reservoirs. **Figure 9** shows the distribution of the granitoid rocks in $\varepsilon_{Nd}{}^{1200\ Ma}$ vs. $^{87}Sr/^{86}Sr^{1200\ Ma}$ space, as well as the Koenap migmatites, relative to Bulk Earth, the Depleted Mantle, and approximated Kakamas Domain area crustal reservoir. Isotopic compositions have been calculated for 1,200 Ma, based on the existing age of ~1,203 Ma for the Polisiehoek intrusion, and an estimated age of ~1,215–1,225 Ma for the Koenap migmatite.

The least variable data, the Koenap migmatite samples, plot with a restricted range of Nd and Sr isotopic compositions, which is consistent with their derivation from melting of Mesoproterozoic crust (**Figures 9A,B**). While a, at the time, very young crust (~1.3 Ga) would not have evolved enough by 1.2 Ga to account for the Koenap Formation data, contributions from older crustal material, such as a mixture of ~1.6 and 1.3 Ga crust, would be appropriate. Equally possible is a mixture of 1.3 Ga crust with a small contribution from ~2.4 Ga crust, as invoked by Eglington (2006) and Bailie et al. (2017) as the preferred crustal contamination end-member for granitoids in the central Namaqua Sector. Abundant inherited zircon of Paleoproterozoic (1.8–2.1 Ga) and early Mesoproterozoic (1.4–1.6 Ga) ages in granites and migmatites in the region (Bial et al., 2015a; Bial et al., 2015b) support the presence of such sources in the Kakamas Domain.

The Swartoup leucogranitoids and garnet granitoids (LG, GG in **Figure 9**) plot as distinctly less evolved compositions than the Koenap Formation, and therefore these Swartoup granitoids cannot represent a pure (closed system) partial melt of the Koenap migmatite. These samples overlap directly with the least-radiogenic samples from the coeval to slightly younger Keimoes Suite in the eastern Kakamas Domain (**Figure 9A**; Bailie et al., 2017) and the southern Bushmanland Domain (Bailie et al., 2019). They are consistent with derivation from a mixture of Koenap Formation and a juvenile depleted mantle-

TABLE 2 | Radiogenic isotopic data for this study. (Rb–Sr isotopic compositional data).

Rock type	Sample	Rb (ppm)	Sr (ppm)	$^{87}Rb/^{86}Sr$	$^{87}Sr/^{86}Sr$	±2σ	$^{87}Sr/^{86}Sr$ at 1200 Ma
Koenap migmatite	1137A	74.26	135.17	1.5490	0.74403	15	0.71785
	1138A	41.85	37.84	3.1183	0.76847	20	0.71575
	1143B	56.24	68.20	2.3248	0.75723	9	0.71792
	1147B	146.06	66.64	6.1801	0.82536	11	0.72088
Bysteek marble	GS19A	0.62	271.90	0.0064	0.70660	10	0.70649
Swartoup Leucogran.	GS5A	161.20	124.10	3.7817	0.76766	13	0.70373
	GS9A	499.20	588.85	2.4627	0.74523	12	0.70360
	GS9B	156.50	261.00	1.7399	0.73342	13	0.70401
	GS15B	311.10	195.25	4.6468	0.78548	11	0.70693
	1145A	88.39	263.75	0.9715	0.72345	13	0.70703
	1146A	157.46	248.65	1.8381	0.73661	15	0.70554
	1149A	124.28	146.64	2.4624	0.74727	14	0.70564
Swartoup Px Gran.	1151A	55.51	339.36	0.4738	0.71459	13	0.70658
	GS11D	204.65	175.20	3.3972	0.75712	11	0.69969
	GS10B	93.50	337.80	0.8015	0.71245	13	0.69890
Swartoup Gt Gran.	GS13A	236.70	291.05	2.3625	0.74540	11	0.70546
	GS13B	304.60	323.40	2.7372	0.74952	10	0.70325
	GS7A	137.55	150.65	2.6553	0.75649	10	0.71160
Polisiehoek granite gneiss	1136A	131.18	81.31	4.7136	0.80462	14	0.72494
	1142A	51.06	34.53	4.3129	0.78507	24	0.71215
	1148A	216.99	30.71	21.202	1.08293	41	0.72451
	1152A	171.20	65.15	7.7135	0.85279	25	0.72239
	GS1A	94.15	100.05	2.7376	0.75988	10	0.71360
	GS11B	423.20	31.75	40.866	1.31344	16	0.62259

Rb/Sr calculated from Sr and Rb concentrations determined by LA-ICP-MS on fused beads. See Analytical Methods section for further details.

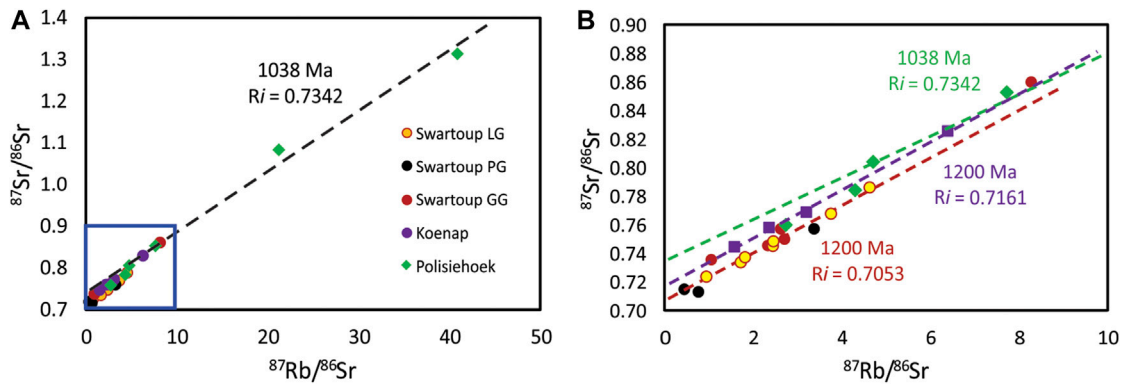

FIGURE 7 | Rb–Sr isochron diagram for the granitoids. **(A)** All samples from the Polisiehoek granite gneiss, extending to high Rb/Sr ratios in a near-linear array. The lower left of the diagram containing the Swartoup Pluton and Koenap Fm. samples is expanded in **(B)**, showing the linear arrays with best-fit reference lines, with age and initial $^{87}Sr/^{86}Sr$ ratios shown corresponding to their slope. The reference line for the Swartoup pluton is based on five samples only. See text for discussion. Swartoup LG, PG, and GG = leucogranitoid, pyroxene granitoid, and garnet granitoid, respectively.

derived melt (**Figure 9B**), or alternatively with the remelting of a source which contained a mixture of juvenile crust and older granitoid crust.

The observed initial $^{87}Sr/^{86}Sr$ ratios for the Swartoup pyroxene granitoids and Polisiehoek granitoids (**Figure 9A**) show a wide range in initial ratio, but are largely consistent with the compositional range reported by Bailie et al. (2017) and Bailie et al. (2019), both in terms of anomalously radiogenic and anomalously (improbably) unradiogenic compositions. This range in $^{87}Sr/^{86}Sr$ values from ~Bulk Earth (or lower) to ~0.77 is not correlated to complementary ε_{Nd}^{1200} compositional variation. It cannot be readily attributable to bulk crustal contamination based on the compositional range of the known reservoirs, and is therefore most readily attributable to post-crystallizational mobility of Rb in these rocks. This is consistent with the evidence for LILE enrichment shown in the incompatible trace element spidergrams for the Swartoup pyroxene granitoids and the Polisiehoek granitoids (**Figures 5B,D**). The related implications will be discussed in more detail below.

Based on initial $^{87}Sr/^{86}Sr$ and ε_{Nd}^{1200}, a juvenile mantle melt contribution cannot be excluded as the least-radiogenic end-member, but it is not required to explain the data. The effect of the variable Rb-Sr systematics can be eliminated by plotting the chondrite-normalized $^{147}Sm/^{144}Nd$ ratio ($f_{Sm/Nd}$) against ε_{Nd}^{1200}.

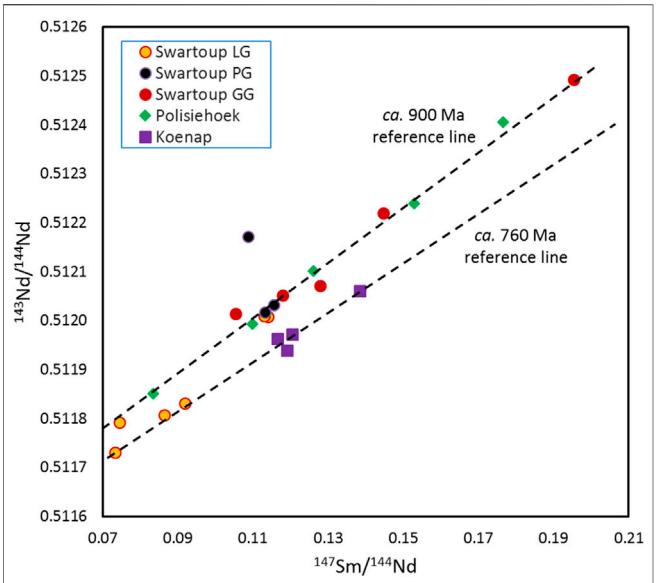

FIGURE 8 | Sm–Nd "isochron" diagram for the Swartoup Hills granitoid suite. See text for details.

Figure 10 shows the dataset from this study in the context of the data range of local crust (Yuhara et al., 2002; Eglington, 2006; Pettersson et al., 2009; Bailie et al., 2017). Based on this diagram, the Kakamas Domain granitoid compositions potentially could be derived from three contributing components. 1) A mantle-derived partial melt, originating between around 1.6 to 1.5 Ga (i.e., Mesoproterozoic isotopically enriched mantle-derived partial melt); 2) LREE-enriched rocks which are slightly (perhaps 100–200 million years) older than the intrusions; and 3) much older, early Paleoproterozoic crust. Key points here include the following:

(1) A juvenile partial melt of an isotopically enriched mantle could explain end-member 1, or a mafic crust significantly older than the formation of the granites. Constraints on the possible involvement of an enriched mantle source will be discussed further below. Note that, critically, the depleted mantle end-member (end-member 1 in **Figure 10**) cannot be a juvenile (i.e., ~1,200 Ma) melt derived from partial melting of the depleted mantle asthenosphere; the $\varepsilon_{Nd}{}^{1200\ Ma}$ vs. $^{87}Sr/^{86}Sr^{1200\ Ma}$ plot in **Figure 9** is deceiving in this context, as the isotopically depleted component is not, in fact, the LREE-depleted component.
(2) The isotopically depleted but LREE-enriched end-member (end-member 2 in **Figure 10**) is strongly represented in multiple data sets (Bailie et al., 2017; this study), in the Swartoup Hills most prominently reflected in the Polisiehoek granitoid dataset, which displays a linear mixing line.
(3) Minimal contribution from much older crust (end-member 3 in **Figure 10**) is required to explain the composition of granitoids in the Swartoup Hills.

Late Paleoproterozoic (~2.4–2.2 Ga) crustal rocks have been invoked to explain local isotopic compositions (Eglington, 2006; Bailie et al., 2017; 2019), and as modeled in **Figure 9** for the Namaqua Metamorphic Complex data of Yuhara et al. (2002), which lie comfortably along a Paleoproterozoic mixing curve in **Figure 9A**. However, still older crustal rocks, such as potentially

TABLE 3 | Radiogenic isotopic for the Swartoup Hills. (Sm–Nd isotopic compositional data).

Rock type	Sample	Nd (ppm)	Sm (ppm)	$^{143}Nd/^{144}Nd$	2σ	$^{147}Sm/^{144}Nd$	ε_{Nd}, at 1200 Ma
Koenap migmatite	1137A	49.8	9.96	0.511972	12	0.1204	−1.3
	1138A	38.6	8.86	0.512061	14	0.1383	−2.3
	1143B	44.3	8.57	0.511962	17	0.1164	−0.9
	1147B	49.8	9.84	0.511940	15	0.1190	−1.7
Swartoup Leucogran.	GS5A	80.4	15.3	0.511807	28	0.1145	−3.6
	GS9B	40.4	7.81	0.511831	22	0.1163	−3.4
	GS15B	37.7	7.08	0.511731	21	0.1130	−4.8
	1145A	42.9	8.11	0.512007	10	0.1139	+0.4
	1146A	37.7	7.08	0.512101	11	0.1130	+0.6
	1149A	40.8	5.05	.0511792	9	0.0744	+2.3
	1151A	70.0	13.5	0.512032	14	0.1156	+0.6
Swartoup Px Gran.	GS11D	85.1	16.0	0.512017	22	0.1131	+0.7
	GS10B	42.9	8.11	0.512171	13	0.1139	+3.6
Swartoup Ga Gran.	GS13A	4.52	0.96	0.512071	15	0.1279	−0.5
	GS13B	44.5	7.77	0.512015	17	0.1052	+1.9
	GS15C	35.3	8.47	0.512219	15	0.1446	−0.2
	GS16A	6.56	2.13	0.512492	19	0.1953	−2.6
	GS7A	53.4	10.5	0.512052	17	0.1178	+0.7
Polisiehoek granite gneiss	1136A	16.5	4.20	0.512101	11	0.1260	+0.4
	1142A	25.4	3.52	0.511993	16	0.1099	+0.8
	1148A	27.8	8.15	0.512239	16	0.1530	−1.1
	1152A	6.25	2.33	0.511851	23	0.0833	+2.1
	GS1A	17.3	4.22	0.512182	15	0.1466	−1.2
	GS11B	40.8	5.05	0.512405	12	0.1765	−1.5

Sm/Nd calculated from Sm and Nd concentrations determined by LA-ICP-MS on fused beads. See Methodology section for further details.

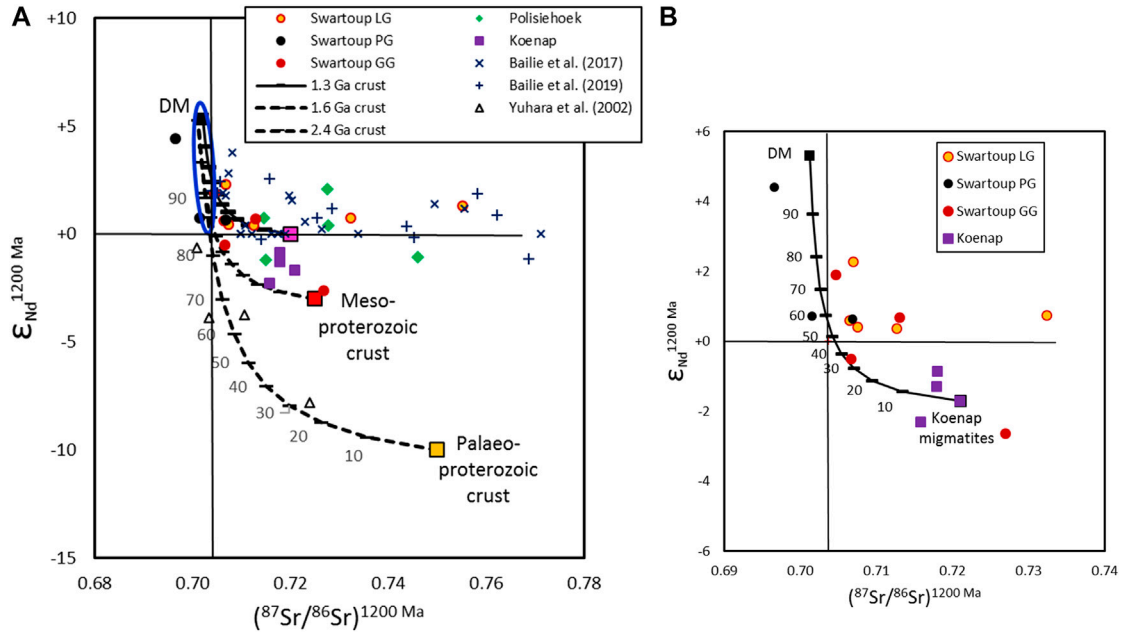

FIGURE 9 | Initial Sr and Nd isotopic compositions, corrected to 1,200 Ma, the approximate age of the Polisiehoek granite emplacement. Bulk Earth composition indicated by black lines. **(A)** Approximate positions for the depleted mantle (DM, in the blue ellipse), and Mesoproterozoic (1.3 Ga, magenta square; 1.6 Ga red square) and Paleoproterozoic (1.9 Ga; orange square) crustal rocks. Mixing models corresponding to addition of a mantle-derived end-member to crustal reservoirs of ~1.3, 1.6, and a 2.4 Ga ages are indicated by the graduated curves. In **(B)**, the mixing of Koenap sample 1147B, compositions with depleted mantle is modeled with reference to the Swartoup granitoid samples. Data for Bulk Earth from McCulloch and Wasserburg (1978), depleted mantle from DePaolo (1981) and Faure (1986) for Nd and Sr, respectively. Regional crustal reservoir compositions are based on Namaqua Province datasets from Yuhara et al. (2002), Eglington (2006), and Bailie et al. (2017) for combined Sm–Nd and Rb–Sr data, Sm–Nd data from Pettersson et al. (2009), and Rb–Sr from Clifford et al. (1975). See text for additional details.

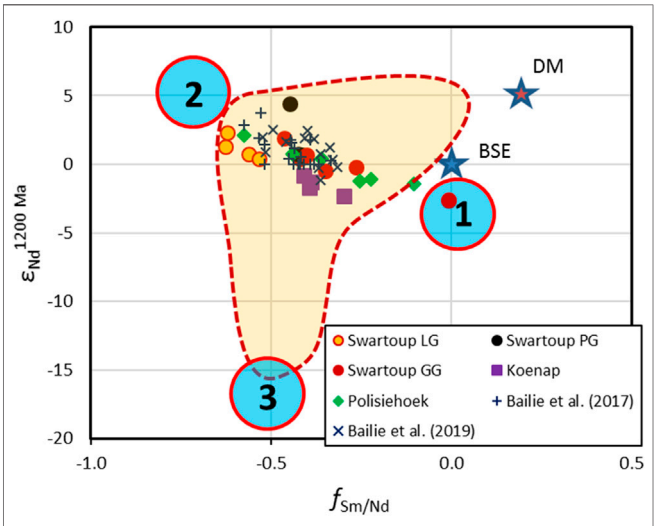

FIGURE 10 | Chondrite-normalized Sm/Nd ratio ($f_{Sm/Nd}$) plotted against ε_{Nd}^{1200}. Pale orange field with dashed border: Namaquan crust based on Yuhara et al. (2002), Eglington (2006) and Pettersson et al. (2009). DM, depleted mantle; BSE, bulk silicate Earth, as represented here by the Chondritic Uniform Reservoir (CHUR) composition to which the plot is normalized. The three blue circles indicate the minimum number and suggested compositional characteristics of end-members required to explain the distribution of data for the Swartoup Hills granitoids. See text for discussion.

recycled late Archaean rocks, are required in order to accommodate $\varepsilon_{Nd}^{1200\ Ma}$ values < −15, as reported (and so interpreted) by Pettersson et al. (2009). However, for the Swartoup Hills (this study), Keimoes Suite (Bailie et al., 2017), and Kliprand Dome (Bailie et al., 2019) datasets, there is minimal, if any, contribution of this older crust evident. However, the presence of a Paleoproterozoic heritage in the crust of the Kakamas Domain in general, as indicated by abundant T_{DM} data (Pettersson et al., 2009) and by inherited zircon, is not disputed.

Derivation of the LREE-Enriched Non-radiogenic Nd Component

A source region capable of generating melts with LREE enrichment and isotopically depleted Nd (positive $\varepsilon_{Nd}^{1200\ Ma}$) is typically one involving a significant component of partial melt derived from a juvenile depleted mantle. Given that according to DePaolo (1981) depleted mantle has a composition around $\varepsilon_{Nd}^{1200\ Ma}$ = +5.2, and the most depleted samples from this study are between +1.9 and +3.6, there is some allowance for a small amount of mixing between a mantle source and existing crust. Bailie et al. (2017) reported two samples from the nearby Keimoes Suite with similarly isotopically depleted Nd ($\varepsilon_{Nd}^{1200\ Ma}$ of +2.8 to +3.8) and low Sm/Nd ($^{147}Sm/^{144}Nd < 0.095$).

Depleted mantle signatures are associated with A-type ("anorogenic") granites and form from a combination of

differentiated basaltic melts and/or remelted quartzo-feldspathic crust (Eby, 1992; Whalen et al., 1996; Frost and Frost, 2011). Such melts are only moderately and locally modified by metasomatism or crystal fractionation. A-type melts occur worldwide throughout geological time in a variety of tectonic settings and do not necessarily indicate an anorogenic or rifting environment. In the Namaqua Sector, coeval flood basalts (or voluminous mafic dyke swarms or any other component of a Large Igneous Province) are entirely absent, arguing against an M-type (mantle-derived; Eby, 1992) differentiate origin. By contrast, the abundant zircon formation around ~1.3 Ga in the central Namaqua Sector provides evidence for the presence of slightly older high-grade metamorphic basement rocks. An unspecified modified (by virtue of having non–mantle-like Sr isotopic compositions) A-type granite source is therefore proposed as the compositional end-member 2 of **Figure 10**.

Alkali Metasomatism

Samples of the Polisiehoek and the Swartoup pyroxene granitoids, as well as most of the Keimoes Suite of Bailie et al. (2017) and the Kliprand Dome (Bailie et al., 2019) datasets, display prominent age-corrected $^{87}Sr/^{86}Sr$ enrichment (**Figure 9A**). The effects of alkali enrichment can be illustrated in a plot of Rb against Sr, a less mobile alkaline earth element (in aqueous solutions), in **Figure 11A**. For reference to an even less mobile element, Rb variation with the high field strength element (HFSE) Nd is also shown (**Figure 11B**). In both plots, enrichment in Rb evident in samples of Polisiehoek and the Swartoup pyroxene granitoids is not correlated to increases in the HFSE.

The lack of correlation between LILE and HFSE enrichment means that the enrichment process could involve an aqueous solution in which the LILE are soluble but not the HFSE, as distinct from a partial melt, where both chemical groups would be expected to be mobilized equally. In **Figure 11A**, the enrichment in Rb for (some) samples of the Polisiehoek and Swartoup pyroxene granitoids, as well as numerous samples from the Keimos and Kliprand suites, with over 200 ppm Rb, are contrasted with the Swartoup leucogranites, garnet granitoids, and the Koenap migmatites, all of which show relatively restricted variation in Rb and in Sr, suggesting less secondary Rb enrichment.

The LREE enrichment evident in **Figure 10** is evidently not a consequence of LREE enrichment in absolute terms. **Figure 11B** shows that the samples that show Rb enrichment are typically those low in Nd. This process is thus not linked to bulk crustal contamination by radiogenic older crust, for example, where enrichment in Rb and LREE would be correlated with increased $^{87}Sr/^{86}Sr$ and increasingly negative $\varepsilon_{Nd}{}^{1200}$ values. The LILE enrichment evident in the spidergrams for the Polisiehoek granite gneiss (**Figure 5D**) and Swartoup pyroxene granitoids (**Figure 5B**) is therefore interpreted as a response to alkali metasomatism, through which Rb (along with other alkali and mobile alkaline earth elements) was introduced as a post-magmatic open system event, thereby interfering with the Rb–Sr systematics of those samples. The samples featuring the highest Rb concentrations also have very high measured $^{87}Sr/^{86}Sr$, indicating that the metasomatic process probably occurred not long after crystallization, rather than in recent times, where the Rb enrichment would not be supported by any additional radiogenic Sr accumulation. Nonetheless, back-calculation of $^{87}Sr/^{86}Sr$ for these samples shows both anomalously low or high values at 1,200 Ma, consistent with an artifact of age correction based on modified Rb/Sr ratios.

There are a number of potential events following granite emplacement which represent possible fluid metasomatic episodes. During the prolonged and slow cooling of the crust after the ~1,200 Ma thermal peak, secondary monazite in metapelitic host rocks formed at ~1,090–1,070 Ma, possibly related to fluid mobility and a late heating event during the ~1,100 Ma Naros Pluton emplacement (Bial et al., 2015a). At ~1,000 Ma, the emplacement of the late-Mesoproterozoic pegmatite belt in the Namaqua Sector was a further episode that may have caused widespread fluid mobility in the crust (Bial et al., 2015a; Doggart, 2019). Such pegmatites are abundant in the study area. Furthermore, during the waning stages of the Neoproterozoic Pan-African orogeny, the area was affected by brittle faulting and foreland seismicity, leading to the formation of pseudotachylyte (~512 Ma) and epidote mineralization along faults (Büttner et al., 2013), features that are also present in the Swartoup Pluton. However, in the absence of petrographic evidence for a pervasive low-temperature hydrothermal event, our preference from these options would be to attribute the alkali metasomatism to fluid activity in the ~100 million years following Swartoup granite emplacement, associated with prolonged elevated temperatures.

The Rb enrichment in the Polisiehoek and some of the Keimoes samples corresponding to an Rb/Sr ratio around 10 is not correlated to Sr enrichment, so is not obviously explained by metasomatism or contamination related to carbonate supracrustal rocks, which suggests that two separate processes are required to explain the alkali enrichment and the Ca enrichment. However, Marcantonio et al. (1990) modeled between 10 and 30% contamination of their granites by host-rock marble, which was manifested as distinctively heavy $\delta^{18}O$ values (~+10), but was not evident in Sr or Nd isotopic compositions nor in Ca enrichments. They note that effective modeling of this is made more uncertain by the generally low REE concentrations and heterogeneous isotopic compositions of the marbles. They suggested that this apparent contradiction could perhaps be accounted for by fluid metasomatism involving CO_2-rich fluids in the granite source area, rather than by bulk marble assimilation during emplacement. This explanation could allow that both the alkali enrichment and the Ca enrichment events could be attributed to carbonate contamination, in the form of separate geochemically distinct processes. A regional fluid metasomatism may explain the alkali enrichment, which locally takes place in combination with physical assimilation effects explaining the bulk contamination. The data of Marcantonio et al. (1990) do not show any of the characteristic heterogeneity in initial $^{87}Sr/^{86}Sr$ ratio which features in this study and those of Bailie et al. (2017, 2019), nor is their fluid contamination event specifically characterized by alkali enrichment. On these grounds, two distinct contamination processes are indicated for the Swartoup and Polisiehoek plutons.

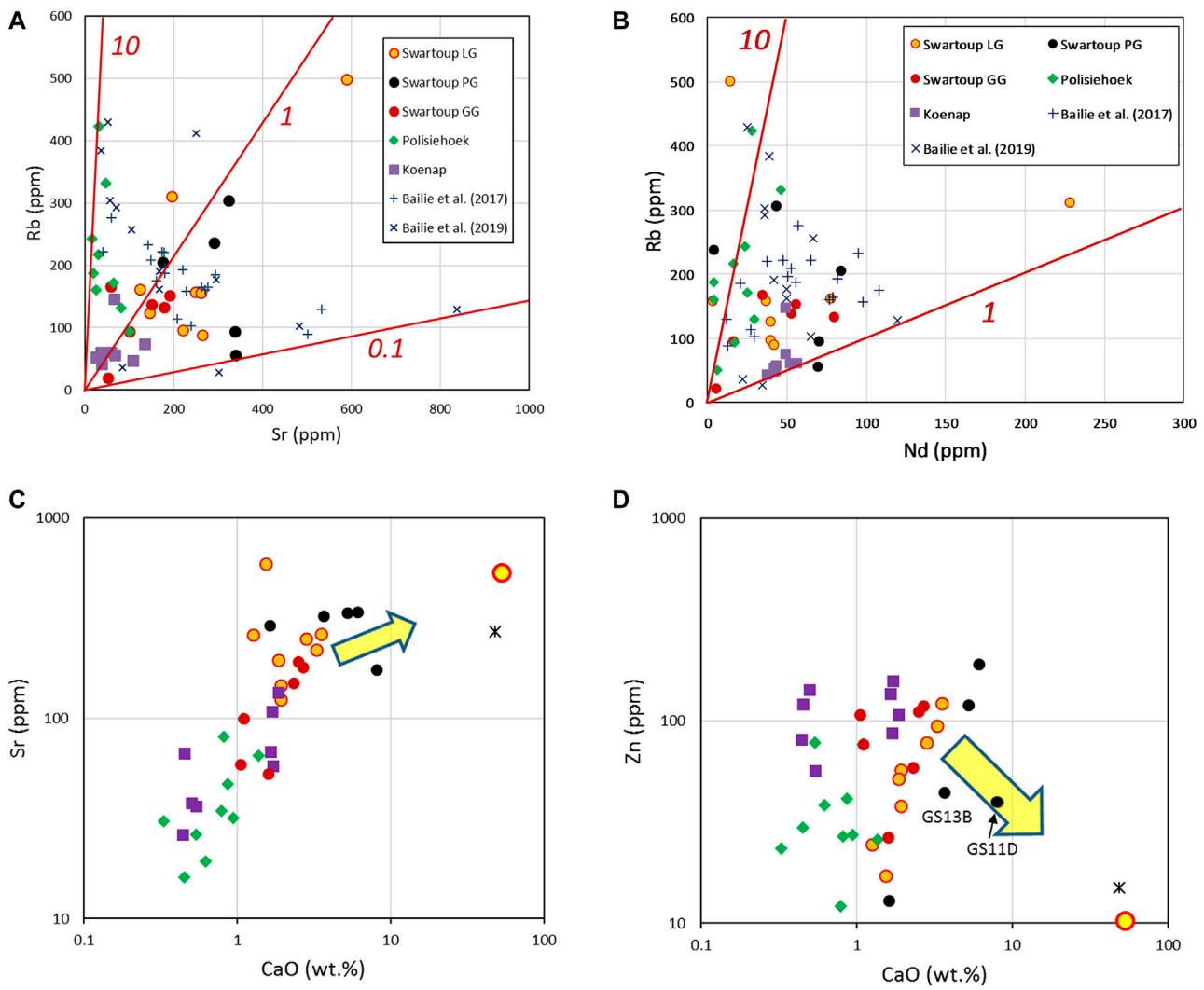

FIGURE 11 | Variation of Rb vs. **(A)** Rb vs. Sr and **(B)** Rb vs. Nd, for the Swartoup Hills granitoids and migmatite, as well as the granitoids of Bailie et al. (2017) and Bailie et al. (2019). Lines of constant Rb/Sr or Rb/Nd ratio are shown in red, with values indicated. In **(C)** CaO vs Sr and **(D)** CaO vs. Zn data are plotted, with reference to a sample of the Bysteek Formation marble (plotted as an asterisk) and average back-arc limestones (yellow symbol; Zhang et al., 2017). The arrows indicate direction of mixing from an average Swartoup granitoid toward the carbonate compositions.

Carbonate Contamination

The Rb enrichment in the pyroxene granitoids and some of the Keimoes and Kliprand rocks shown in **Figure 11A** do show correlated increases in Rb and Sr along trends corresponding to Rb/Sr ratios of around 1 and 0.1. These latter trends could be linked to the effects of syn-emplacement carbonate (marble or calc-silicate) assimilation or fluid mobilization processes, as manifested in the petrology of some of the Swartoup pyroxene granitoids. The marbles of the Bysteek Formation in the immediate vicinity of the Swartoup pluton provide the obvious source for this process.

Geochemically, the trace element compositions of the granitoids are not prominently influenced by elemental enrichments or depletions typically related to carbonates, as noted in the text accompanying **Figures 5**, **6**, except that the REE profiles for Swartoup pyroxene granitoid samples GS-13B, and in particular GS-11D, are virtually identical in both profile shape and elemental abundances to the Bysteek marble profile in **Figure 8F**. Samples GS-11D and -13B were collected from nearby the pluton contact to the Bysteek Formation (**Figure 2**).

Geochemical evidence for local contributions from the marbles to the Swartoup granitoids can be seen more clearly in plots of CaO against Sr and Zn (**Figures 11C,D**). The compositional trends here suggest that only a few samples of pyroxene granitoid, collected in sight of the Bysteek Formation calcic and carbonate rocks, actually reflect direct compelling chemical evidence for carbonate contamination.

Incompatible Trace Element Constraints on Granitoid Source Rocks

Given the demonstrated open system behavior in the alkali and alkaline earth metals, and the potential effects of carbonates,

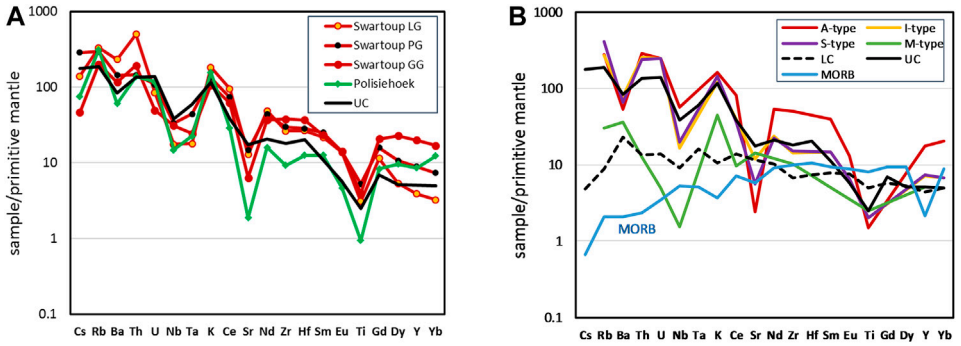

FIGURE 12 | Primitive mantle-normalized trace element spidergrams. **(A)** Average Swartoup Hills granitoid compositions (this study), and **(B)** I-, S-, M-, and A-type granites from Whalen et al. (1987) and Collins et al. (1982). Reference compositions of Upper and Lower Crust and average MORB from Taylor and McLennan (1995).

classification diagrams based on major element oxide ratios are probably not reliable as petrogenetic indicators for these intrusions in this setting. The trace element distribution patterns (including both LILE and HFSE; **Figure 12**) of Swartoup Hills granitoids can, however, usefully be compared to those of granitoids from subduction settings (Whalen et al., 1987) and intraplate A-type settings (Collins et al., 1982; Whalen et al., 1987). The trace element profiles for S- (sedimentary rock protolith) and I- (igneous origins) type granites are similar to one another, with the most pronounced distinction being the more prominent negative Sr anomaly for I-type granitoids. Contrastingly, the A-type (anorogenic, within-plate) granitoids feature a significantly larger negative Sr anomaly than the other types, and significant relative enrichment in REE and Zr. Bial et al. (2015b) interpreted the characteristics of the Schuitdrift granite gneiss (**Figure 1B**), a hornblende-biotite mesocratic granitoid, as the product of fractional crystallization from a mafic mantle-derived source melt. These rocks show relative enrichment in Th, high REE, modest relative depletions in Nb and Ti, and a strong negative anomaly for Sr. In contrast, the associated leuco-granitoid rocks show prominent negative anomalies for Nb and Ti, and were interpreted as the products of partial melting of sedimentary protoliths with no mantle-derived melt contributions.

In this context, all of the granitoids analyzed in this study show some affinities to the A-type profile, specifically with regard to the high Th/U ratios, prominent negative anomalies for Sr, and high REE contents (**Figures 12A,B**). The absence of a prominent Zr depletion in the Swartoup granitoids is also consistent with the A-type granitoid profile. However, the Nb anomaly of the rocks in this study is comparable to that typical of I- and S-type granitoids, and is significantly smaller than that observed in the leucogranitic paragneisses further north described by Bial et al. (2015b). This combination of diagnostic features is therefore consistent with the mixed protolith origins that have been proposed, such that neither a purely anorogenic-type protolith nor a metasedimentary one is appropriate for any of these intrusions. The Polisiehoek granite gneiss (**Figure 12B**), which shows the most prominent negative Ba, Nb, and Sr anomalies, but almost MORB-like REE and Zr, perhaps best exemplifies this mix of diagnostic features. Because this geochemical pattern represents a heavily modified A-type granite signature, it cannot easily be accommodated directly into the compositional subclassifications of A-type granites. None of the Swartoup Hills samples actually plot convincingly within the A-type granite fields of Eby (1992), or within the ferroan granite fields of Frost and Frost (2011). However, their Y/Nb ratios are all >1, with elevated Rb/Nb and Sc/Nb ratios, more consistent with A-type granites derived from I-type protoliths (A_2 granites of Eby, 1992), rather than as mantle melt fractionation products (A_1 granites of Eby, 1992). According to the alternative classification scheme of Frost and Frost (2011), the Polisiehoek granite samples largely qualify as ferroan, consistent with the siliceous members of other A-type granites. By contrast, the Swartoup and Polisiehoek samples are modified to varying extents toward more calcic and calc-alkalic compositions. Given that the correlation of A-type granite geochemistry with specific petrogenetic and tectonic settings is problematic at best (Whalen et al., 1996), an origin involving a mixture of crustal- and mantle-derived sources appears to be the most defensible interpretation for A-type granites broadly, with the Swartoup and Polisiehoek plutons showing much stronger affiliations to remelted granitic crust rather than to basaltic differentiates.

Heterogeneity of Granitoid Source Rocks in the Namaqua Sector

Neodymium isotope diagrams for different domains and sub-domains in the Namaqua Sector (**Figure 13**) suggest that different compositional reservoirs were accessed to different extents in different places. The ages of granitoid emplacement, between ~1,230 and 950 Ma (Thomas et al., 1994, 2016; Macey et al., 2015), are broadly consistent across the Namaqua Sector, so no temporal evolution of sources is indicated from these data. Five potential source components are identified here, characterized as follows:

(1) Depleted mantle; characterized by positive values of $\varepsilon_{Nd}{}^{1200}{}_{Ma}$, unradiogenic $^{87}Sr/^{86}Sr$, and LREE-depletion relative to HREE.

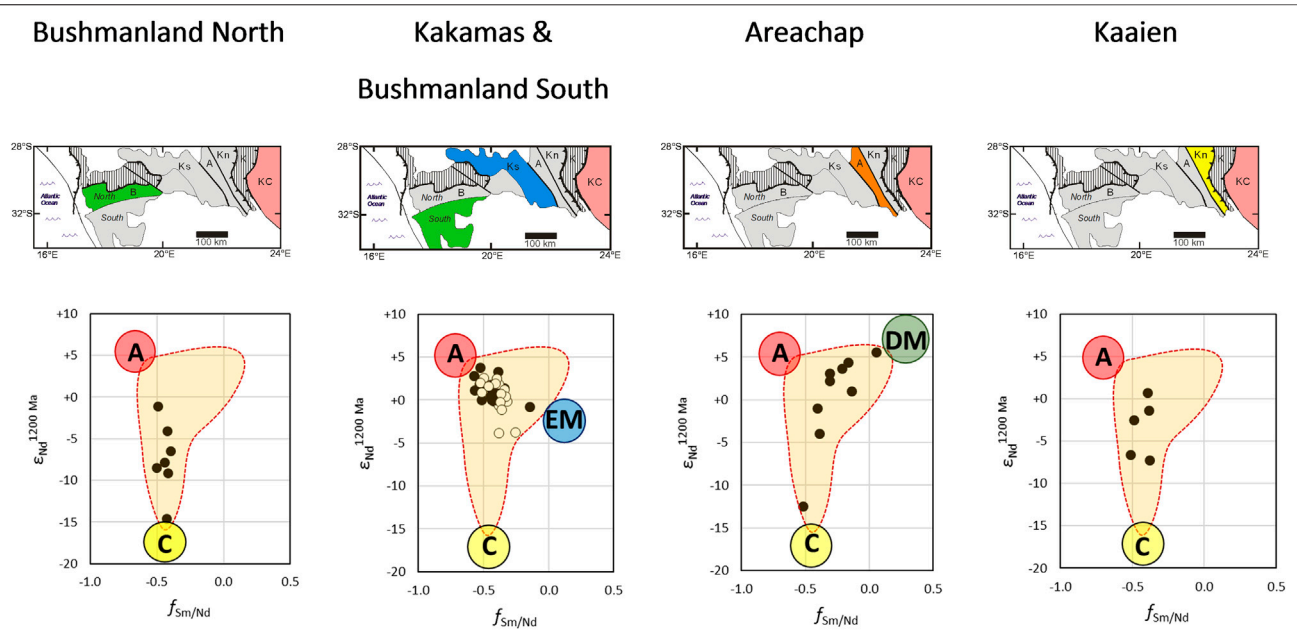

FIGURE 13 | Source variation with geographic position and different domains. Bushmanland North data from Yuhara et al. (2002) and Pettersson et al. (2009); Bushmanland South data from Yuhara et al. (2002), Pettersson et al. (2009), and Bailie et al. (2019); Kakamas (Ks) data from Bailie et al. (2017) and this study; Areachap and Kaaien data from Pettersson et al. (2009). B, Bushmanland; Ks, Kakamas; A, Areachap; Kn, Kaaien; K, Kheis; KC, Kaapvaal Craton. Vertically-lined fields are 2.4–2.2 Ga pre-Namaquan regions (see also **Figure 1**). Granite magma sources: A, anorogenic granite source; C, Paleo-/Mesoproterozoic crust; EM, enriched mantle; DM, depleted mantle.

(2) Mesoproterozoic mafic magma, which has the characteristics of an enriched mantle; weakly negative values of $\varepsilon_{Nd}^{1200\ Ma}$, moderately enriched $^{87}Sr/^{86}Sr$, and LREE-depletion relative to HREE (end-member 1 in **Figure 10**).
(3) Anorogenic granite source, characterized by positive values of $\varepsilon_{Nd}^{1200\ Ma}$, unradiogenic $^{87}Sr/^{86}Sr$, and LREE enrichment relative to HREE (end-member 2 in **Figure 10**).
(4) Mesoproterozoic felsic crust, with $\varepsilon_{Nd}^{1200\ Ma}$ of ~-5 to -10, radiogenic $^{87}Sr/^{86}Sr$, and LREE enrichment relative to HREE (end-member 3 in **Figure 10**, which has been separated into younger and older Proterozoic crust here).
(5) Paleoproterozoic felsic crust, with $\varepsilon_{Nd}^{1200\ Ma}$ of ~−15 to −20, radiogenic $^{87}Sr/^{86}Sr$, and LREE enrichment relative to HREE.

Bushmanland North

The northern Bushmanland Domain is proximal to the Paleoproterozoic Richtersveld Domain and contains a significant proportion of Paleoproterozoic rocks, such as the Steinkopf gneiss and the Gladkop Suite (Nke et al., 2020). According to Bailie et al. (2019), the proportion of Mesoproterozoic crust formation decreases from the south to the north in the Bushmanland Domain. The spread of $\varepsilon_{Nd}^{1200\ Ma}$ between ~0 and −15 indicates mixing between relatively old crustal source and an anorogenic granite source. The older components are likely Paleoproterozoic rocks similar to those in the Richtersveld Domain, for which Pettersson et al. (2009) report $\varepsilon_{Nd}^{1200\ Ma}$ of −13. There is no evidence for the involvement of any mafic, LREE-depleted crust, or mantle sources. We may tentatively conclude that the source rocks for these granitoids consisted mainly of felsic crustal rocks only, with no juvenile or older mafic sources providing significant contributions.

Kakamas and Bushmanland South

The Kakamas Domain, where the largest dataset is available, shows a strong clustering adjacent to the anorogenic granite source (**Figure 13**), with a significant contribution (more evident in **Figure 10**) from an enriched mafic mantle source. These data are consistent with the partial melting of a granulitic lower crust, forming the A-type component, and the addition of coeval juvenile isotopically enriched mafic mantle magmas. Significant early Mesoproterozoic (~1.5 Ga) or Paleoproterozoic crustal sources are not required to explain the data distribution in the Kakamas or southern Bushmanland Domains.

Areachap

In their $\varepsilon_{Nd}^{1200\ Ma}$ and $f_{Sm/Nd}$ patterns, the data from the Areachap Domain (**Figure 13**), approaching the Kaapvaal Craton, overlap with those from the adjacent Kakamas Domain, but in addition some data points support the involvement of a depleted mantle source, combining mainly with Mesoproterozoic felsic crust. Arguably, the anorogenic granite source is represented here as well. A few of the samples from the Keimoes granitoid suite of Bailey et al. (2017), plotted here as part of the Kakamas Domain, actually lie within the Areachap Domain, and strongly show the influence of the A-type source here as well. There are no compositional

distinctions evident between samples from either side of the domain boundary. One sample, collected from the interior of the domain, just south of the town of Upington (Pettersson et al., 2009), has an $\varepsilon_{Nd}^{1200\ Ma}$ of −12.5, which requires the involvement of a significantly older crustal source, probably representing the Paleoproterozoic heritage indicated for the entire Namaqua Sector by T_{DM} and zircon ages. In this domain, the source rocks incorporated a significant component of juvenile mantle melt, along with older felsic crust. This would be consistent with the interpretations of Pettersson et al. (2009), who note the distinctive presence in this domain of arc-related supracrustal sequences without mature metasediments, and a provenance combining juvenile and older rocks.

Kaaien

The few data available from the Kaaien Domain, close to the Paleoproterozoic rocks of the Kheis Subprovince, show a pattern similar to those of the northern Bushmanland Domain, which is also adjacent to a Paleoproterozoic domain. The data show the involvement of early Mesoproterozoic crust and the anorogenic granite source, with no requirement for early Paleoproterozoic crust nor any LREE-depleted mafic source.

What stands out as broad observations from these data sets is that there is no clear geographical trend of increasing or decreasing involvement of any one source component, such as might be anticipated from west to east with increasing proximity to the Kaapvaal Craton. Interpretations of this type are restricted by the fact that magmatic rocks of different ages in a dynamic tectonic evolution are combined within the data sets. The northern Bushmanland Domain shows prominent involvement of older crust, consistent with its proximity to the Richtersveld Domain immediately to the north, as noted by Bailie et al. (2019) and Nke et al. (2020). However, the data currently available from domains which parallel the Archean Kaapvaal Craton boundary to the east show no such systematic affinities to old source rocks. However, without more extensive data, this cannot be meaningfully assessed.

Source Heterogeneity in Granitoids of the Namaqua Sector

The processes and sources of granitoids in the Swartoup Hills reflect the larger scale processes active in other domains in the Namaqua Sector. The dominant magma sources are, with variable proportions, an A-type granite source, a mafic magma contribution generated from an isotopically enriched source, and magma generated form early Mesoproterozoic or Paleoproterozoic crust. The isotopic characteristics of the A-type component indicate that the source rocks were not significantly older (e.g., early Meso- or Paleoproterozoic) than the age of their partial melting event. Bial et al. (2015a) report magmatic zircon of ~1,300–1,350 Ma in metapelites from the Swartoup Hills, attributed to a high-temperature metamorphic stage predating the ~1,200 Ma episode of crustal anatexis. Similar ages are reported for volcanic rocks in the Areachap Domain (~1,275–1,371 Ma; Pettersson et al., 2007; Bailie et al., 2010), for orthogneiss slices along the Lower Fish River Onseepkans Thrust Zone (1,320–1,270 Ma; Macey et al., 2016), and for the Konkiep Domain in central Namibia (1,330–1,380 Ma; Hoal and Heaman, 1995; Becker, 2008; Cornell et al., 2015), indicating the large scale of intense heat influx into the continental crust at that time. Potentially, the source of the A-type granite component formed at that time.

Isotopically, the mafic melt component could have formed either from crust that had formed several hundred million years prior to its partial melting, or from a juvenile partial melt from an enriched mantle source. There is no evidence in the Namaqua Sector of abundant presence of mafic crust, neither of Mesoproterozoic nor Paleoproterozoic age. By contrast, mafic plutonism and volcanism across the Namaqua Sector and during several episodes of the crustal evolution indicate mantle melting. For example, the Jerusalem gabbronorite (**Figure 1B**), in nearby southernmost Namibia, intruded the crust of the Kakamas Domain at the same time as the bulk of the granitic plutons (pers. commun. Paul Macey, 2020). Abundant partial melting of an enriched asthenospheric mantle and the effective mixing of such melts with coeval felsic lower crustal melts are possible, and likely to occur, in a continental back-arc setting (Bial et al., 2015a; Büttner, 2020), where hot crust is underlain by thin lithospheric mantle, and partial asthenospheric mantle melting is common, particularly during extensional episodes. Conversely, neither terrane accretion or continent–continent collisions, nor volcanic arcs, provide such a setting, as they both typically display thickened crust and lithosphere, and do not support the long-standing high-temperature/low-pressure regime that is observed in the Namaqua Sector (Büttner, 2020).

Granitoids with ε_{Nd} signatures indicating early Mesoproterozoic or Paleoproterozoic crustal sources are unproblematic to explain in the Namaqua Sector. U-Pb ages of inherited zircon components of such age and T_{DM} ages spreading from ~1.4 to 2.4 Ga (e.g., Eglington, 2006; Pettersson et al., 2007, 2009; Bial et al., 2015a,b; Macey et al., 2015) testify to the presence of rocks of this age and active crust forming processes at that time.

Granite Emplacement in the Swartoup Hills

The Swartoup granitoid and Polisiehoek granite plutons in the Kakamas Domain were emplaced into host rocks of variably metapelitic, calc-silicate, mafic and carbonatic compositions during a high-temperature orogenic episode. Along its margin, the Swartoup Pluton shows significant contamination by its host rocks. Contamination by calcic host rocks of the Bysteek Formation formed macroscopically conspicuous features such as the growth of millimeter- to centimeter-sized clinopyroxene. This is consistent with geochemical evidence for localized carbonate contamination of the granitoid. The Polisiehoek pluton, although significantly larger than the Swartoup Pluton, and therefore arguably with a higher potential to interact with its host rocks, does not show evidence of significant chemical or physical interaction with its host rocks during its emplacement. Although the crust at that time of emplacement was still at granulite facies conditions, intrusive contacts are sharp. The Polisiehoek magma, without contribution of melt contamination from its host rocks, was generated in deeper

crustal and mantle levels. We attribute the more intense contamination of the Swartoup Pluton magma by its host rocks to the magma emplacement at the regional ultrahigh temperature metamorphic peak with abundant anatectic melt present in the host rock, temperatures that allowed even the mafic granulites of the Bysteek Formation to react with the intruding granitic melt. Conversely, the larger Polisiehoek granite was much more pervasively affected by alkali metasomatism that resulted in significant mobility of Rb and heterogeneous apparent initial $^{87}Sr/^{86}Sr$ as a result.

SUMMARY AND CONCLUSIONS

The Swartoup Hills granitoid suite and associated migmatites, as a component of the Kakamas Domain, show the following characteristics:

The Swartoup granites, granodiorites, and quartz monzonites intruded the felsic migmatitic gneisses of the Koenap Formation and marbles and calc-silicates of the associated Bysteek Formation. Radiogenic isotopic evidence requires that the Swartoup Pluton rocks could not have been derived solely by partial melting of the Koenap Formation metapelites. The main source material for the Swartoup Pluton is geochemically and isotopically consistent with an A-type granitic source, mixed with an isotopically enriched LREE-depleted, and hence mantle-derived contribution. The variable composition of the Swartoup granitoids seems to imply composite pluton characteristics. However, contamination from the proximal supracrustal Bysteek Formation carbonates, forming clinopyroxene granitoids, or the presence of garnet, possibly entrained in melt injections from nearby Koenap Formation migmatites, are restricted to narrow marginal zones. We attribute these contaminations to the emplacement of the Swartoup Pluton during the regional metamorphic peak, with the associated anatectic melt mobility and high reactivity of the host rocks. The narrow shape of the layer forming the Swartoup Pluton, causing a high surface/volume ratio, likely promoted the proportional abundance of magma contamination from the host rocks.

The Polisiehoek granites, which have intruded the Swartoup granitoids, were derived from a mixture of the A-type granite source and a larger component of the enriched mantle source. They show no evidence of contamination from their host rocks, which is in agreement with the sharp intrusive contacts to all other rock types. This indicates that at the time of pluton emplacement, most likely around 1,203 Ma (Pettersson et al., 2009), the Swartoup Pluton, and the Koenap Formation migmatites had solidified. Neither the Swartoup nor the Polisiehoek granitoids require the contribution of significantly older crustal (i.e., early Meso- or Paleoproterozoic) material in their sources.

The Polisiehoek granites and some Swartoup leucogranitoids have been strongly but heterogeneously affected by alkali metasomatism that is not obviously linked to carbonate assimilation or metasomatism, but which cannot be eliminated as a possible source of CO_2-rich alkaline aqueous fluids. This has significantly influenced the Rb–Sr isotope systematics in the Kakamas Domain. This is also evident in the Keimoes Suite rocks further to the east, as well as in the southern Bushmanland Domain, but is not evident in any of the Koenap Formation migmatite samples from the Swartoup Hills. Repeated heating and/or magma emplacement between ~1,100 and ~1,000 Ma, or Pan-African fault bound fluid influx may explain possible fluid sources, although the absence of a hydrothermal mineralogical overprint suggests that this metasomatism occurred as a late-magmatic high temperature process, rather than in association with a discrete lower temperature hydrothermal process.

The main magma sources of plutons in the Swartoup Hills, comprising a mantle magma generated by partial melting of enriched subcontinental asthenosphere, and an A-type magma generated from Mesoproterozoic crust, are compatible with the sources of granitoids across the entire Namaqua Sector. The consistency of magma sources for granitic plutons across the Namaqua Sector suggests a uniform tectonic setting across the belt, in which Mesoproterozoic crust generates partial melt at times when also fertile mantle sources and conditions are present to contribute melt that is blended with the crustal melts in the lower crust. The longevity of plutonism in the Namaqua Sector between ~1,300 and ~1,000 Ma points to a tectonic setting in which the main magma sources remain regionally available, and in which the required high temperatures were maintained or regenerated over long periods in relatively thin lithosphere. A mobile continental back-arc appears to be the only setting in which this is possible.

DATA AVAILABILITY STATEMENT

The original contributions presented in the study are included in the article/**Supplementary Material**, and further inquiries can be directed to the corresponding author.

AUTHOR CONTRIBUTIONS

SB: Geological context and introduction, field mapping and field relationships, sample collection, petrography, discussion and interpretations. SP: Geochemical and isotope data processing, data documentation, interpretation and writeup, petrological model of magma evolution, discussion and interpretation. GS: Fieldwork, sample collection, some petrography and data processing, parts of the Analytical Methods section.

ACKNOWLEDGMENTS

Constructive reviews by G Shellnut, K-N Pang and J Dostal are gratefully acknowledged for improvements to the manuscript. Fieldwork and analytical costs for this project were supported *via* Rhodes University RC Grants to SB.

SUPPLEMENTARY MATERIAL

The Supplementary Material for this article can be found online at: https://www.frontiersin.org/articles/10.3389/feart.2020.602870/full#supplementary-material.

REFERENCES

Abrahams, Y., and Macey, P. H. (2020). Lithostratigraphy of the Mesoproterozoic Donkieboud granodiorite (Komsberg Suite), South Africa and Namibia. *S. Afr. J. Geol.* 123, 421–430. doi:10.25131/sajg.123.0028

Bailie, R., Abrahams, G., Bokana, R., van Bever-Donker, J., Frei, D., and Le Roux, P. (2019). The geochemistry and geochronology of the upper granulite facies Kliprand Dome: comparison of the southern and northern parts of the Bushmanland Domain of the Namaqua Metamorphic Province, southern Africa and clues to its evolution. *Precam. Res.* 330, 58–100. doi:10.1016/j.precamres.2019.04.011

Bailie, R., Gutzmer, J., and Rajesh, H. (2010). Lithogeochemistry as a tracer of the tectonic setting, lateral integrity and mineralization of a highly metamorphosed Mesoproterozoic volcanic arc sequence on the eastern margin of the Namaqua Province, South Africa. *Lithos* 119, 345–362.

Bailie, R., Macey, P. H., Nethenzheni, S., Frei, D., and le Roux, P. (2017). The Keimoes Suite redefined: the geochronological and geochemical characteristics of the ferroan granites of the eastern Namaqua Sector, Mesoproterozoic Namaqua-Natal Metamorphic Province, southern Africa. *J. Afr. Earth Sci.* 134, 737–765. doi:10.1016/j.jafrearsci.2017.07.017

Bailie, R., Rajesh, H. M., and Gutzmer, J. (2012). Bimodal volcanism at the western margin of the Kaapvaal Craton in the aftermath of collisional events during the Namaqua-Natal Orogeny: the Koras Group, South Africa. *Precam. Res.* 200-203, 163–183. doi:10.1016/j.precamres.2012.01.017

Baxter, S., and Feely, M. (2002). Magma mixing and mingling textures in granitoids: examples from the Galway Granite, Connemara, Ireland. *Mineral. Petrol.* 76, 63–74. doi:10.1007/s007100200032

Becker, T. (2008). "The Kairab Formation east of Sesriem and the associated subvolcanic intrusive rocks." In *The geology of Namibia*., Editor R. M. G. Miller (Windhoek, Namibia: Geological Survey), Vol. 2, 8-10–8-16.

Bial, J., Büttner, S. H., and Appel, P. (2016). Timing and conditions of regional metamorphism and crustal shearing in the granulite facies basement of south Namibia: implications for the crustal evolution of the Namaqualand metamorphic basement in the Mesoproterozoic. *J. Afr. Earth Sci.* 123, 145–176. doi:10.1016/j.jafrearsci.2016.07.011

Bial, J., Büttner, S. H., and Frei, D. (2015b). Formation and emplacement of two contrasting late-Mesoproterozoic magma types in the central Namaqua Metamorphic Complex (South Africa, Namibia): evidence from geochemistry and geochronology. *Lithos* 224–225, 272–294. doi:10.1016/j.lithos.2015.02.021

Bial, J., Büttner, S. H., Schenk, V., and Appel, P. (2015a). The long-term high-temperature history of the central Namaqua Metamorphic Complex: evidence for a Mesoproterozoic continental back-arc in southern Africa. *Precam. Res.* 268, 243–278. doi:10.1016/j.precamres.2015.07.012

Büttner, S. H. (2020). Comment on "Evidence for Mesoproterozoic collision, deep burial and rapid exhumation of garbenschiefer in the Namaqua front, South Africa" by Valby Van Schijndel, David H. Cornell, Robert Anczkiewicz, Anders Schersten, Geoscience Frontiers, Volume 11, Issue 2, Pages 511–531. *Geosci. Front.* 11, 1889–1894. doi:10.1016/j.gsf.2020.04.007

Büttner, S. H., Fryer, L., Lodge, J., Diale, T., Kazondunge, R., and Macey, P. (2013). Controls of host rock mineralogy and H_2O content on the nature of pseudotachylyte melts: evidence from Pan-African faulting in the foreland of the Gariep Belt, South Africa. *Tectonophys* 608, 552–575. doi:10.1016/j.tecto.2013.08.024

Chappell, B. W., White, A. J. R., Williams, I. S., and Wyborn, D. (2004). Low- and high-temperature granites. *Earth Sci.* 95, 125–140. doi:10.1017/S0263593300000973

Clarke, D. B. (1992). *Granitoid rocks*. London, UK: Chapman & Hall.

Clemens, J. D., Holloway, J. R., and White, A. J. R. (1986). Origin of an A-type granite: experimental constraints. *Am. Mineral.* 71, 317–324.

Clemens, J. D. (2003). S-Type granitic magmas – petrogenetic issues, models and evidence. *Earth-Sci. Rev.* 61, 1–18. doi:10.1016/S0012-8252(02)00107-1

Clemens, J. D., and Stevens, G. (2012). What controls chemical variation in granitic magmas. *Lithos* 134-135, 317–329. doi:10.1016/j.lithos.2012.01.001

Clemens, J. D., and Vielzeuf, D. (1987). Constraints on melting and magma production in the crust. *Earth and Planet. Sci. Letters* 86, 287–306. doi:10.1016/0012-821X(87)90227-5

Clifford, T. N., Barton, E. S., Retief, E. A., Rex, D. C., and Fanning, C. M. (1995). A crustal progenitor for the intrusive anorthosite–charnockite kindred of the cupriferous Koperberg Suite, O'okiep district, Namaqualand, South Africa; new isotope data for the country rocks and the intrusives. *J. Petrol.* 36, 231–258. doi:10.1093/petrology/36.1.231

Clifford, T. N., Barton, E. S., Stern, R. A., and Duchesne, J.-C. (2004). U-Pb zircon calendar for Namaquan (Grenville) crustal events in the granulite-facies terrane of the O'okiep Copper District of South Africa. *J. Petrol.* 45, 669–691. doi:10.1093/petrology/egg097

Clifford, T. N., Gronow, J., Rex, D. C., and Burger, A. J. (1975). Geochronological and petrogenetic studies of high-grade metamorphic rocks and intrusives in Namaqualand, South Africa. *J. Pet.* 16, 154–188. doi:10.1093/petrology/16.1.154

Collins, W. J., Beams, S. D., White, A. J. R., and Chappell, B. W. (1982). Nature and origin of A-type granites with particular reference to southeastern Australia. *Contrib. Mineral. Petrol.* 80, 189–200. doi:10.1007/BF00374895

Colliston, W. P., Cornell, D. H., Schoch, A. E., and Praekelt, H. E. (2015). Geochronological constraints on the Hartbees River Thrust and Augrabies Nappe: new insights into the assembly of the Mesoproterozoic Namaqua-Natal Province of southern Africa. *Precambr. Res.* 265, 150–165. doi:10.1016/j.precamres.2015.03.008

Cornell, D. H., Pettersson, Å., Whitehouse, M. J., and Scherstén, A. (2009). A new chronostratigraphic paradigm for the age and tectonic history of the Mesoproterozoic Bushmanland Ore District, South Africa. *Econ. Geol.* 104, 1277–1281. doi:10.2113/gsecongeo.104.8.1277

Cornell, D. H., van Schijndel, V., Simonsen, S. L., and Frei, D. (2015). Geochronology of Mesoproterozoic hybrid intrusions in the Konkiep terrane, Namibia, from passive to active continental margin in the Namaqua-Natal Wilson Cycle. *Precambr. Res.* 265, 166–188. doi:10.1016/j.precamres.2014.11.028

DePaolo, D. J. (1981). Neodymium isotopes in the Colorado Front Range and crust–mantle evolution in the Proterozoic. *Nature* 291, 193–196. doi:10.1038/291193a0

Diener, J. F. A., White, R. W., Link, K., Dreyer, T. S., and Moodley, A. (2013). Clockwise, low-P metamorphism of the Aus granulite terrain, southern Namibia, during the Mesoproterozoic Namaqua Orogeny. *Precam. Res.* 224, 629–652. doi:10.1016/j.precamres.2012.11.009

Doggart, S. (2019). Geochronology and isotopic characterisation of LCT pegmatites from the Orange River Pegmatite Province. MSc thesis, Stellenbosch, South Africa: Stellenbosch University, 234.

Eby, G. N. (1992). Chemical subdivision of the A-type granitoids: petrogenetic and tectonic implications. *Geology* 20, 641–644. doi:10.1130/0091-7613(1992)020<0641:CSOTAT>2.3.CO

Eglington, B. M. (2006). Evolution of the Namaqua-Natal Belt, southern Africa – a geochronological and isotope geochemical review. *J. Afr. Earth Sci.* 46, 93–111. doi:10.1016/j.jafrearsci.2006.01.014

Faure, G. (1986). *Principles of isotope geology*. 2nd Edition, Hoboken, NJ: John Wiley & Sons, Inc. 588 pp.

Frost, C. D., and Frost, B. R. (2011). On ferroan (A-type) granitoids: their compositional variability and modes of origin. *J. Pet.* 52, 39–53.

Groenewald, C. A., and Macey, P. A. (2020). Lithostratigraphy of the Mesoproterozoic Yas-Schuitdrift Batholith, South Africa and Namibia. *S. Afr. J. Geol.* 123, 431–440. doi:10.25131/sajg.123.0029

Harris, C., Le Roux, P., Cochrane, R., Martin, L., Duncan, A.R., Marsh, J.S., Le Roex, A.P., and Class, C. (2015). The oxygen isotope composition of Karoo and Etendeka picrites: High δ18O mantle or crustal contamination? Contrib. Mineral. Petrol. 170, 8, doi:10.1007/s00410-015-1164-1

Henderson, P. (1984). "General geochemical properties and abundances of the rare earth elements", in *Rare earth element geochemistry*., Editor P. Henderson (Amsterdam, Netherlands: Elsevier Science Publishers B. V.), 1–32.

Hoal, B. G., and Heaman, L. M. (1995). The Sinclair sequence: U–Pb age constraints from the Awasib Mountain area. *Commun. Geol. Surv. Namib.* 10, 83–91.

Joubert, P. (1986). Namaqualand - a model of Proterozoic accretion? *Transact. Geol. Soc. South Africa.* 89, 79–96.

King, P. L., White, A. J. R., Chappel, B. W., and Allen, C. M. (1997). Characterization and origin of aluminous A-type granites from the Lachland Fold Belt, southeastern Australia. *J. Pet.* 38, 371–391. doi:10.1093/petroj/38.3.371

Ludwig, K. R. (2012). *User's manual for Isoplot 3.75: a geochronological toolkit for Microsoft Excel*. Berkeley, CA: Berkeley Geochronology Center, Special Publication No. 5.

Ma, J.-L., Wei, G.-J., Liu, Y., Ren, Z.-Y., Xu, Y.-G., and Yang, Y.-H. (2013). Precise measurement of stable ($\delta^{88/86}$Sr) and radiogenic (^{87}Sr/^{86}Sr) strontium isotope

ratios in geological standard reference materials using MC-ICP-MS. *Chin. Sci. Bull.* 58, 3111–3118. doi:10.1007/s11434-013-5803-5

Macey, P. H., Lambert, C. W., Kisters, A. F. M., Gresse, P. G., Thomas, R., Miller, J. A., et al. (2016). *Towards a new geodynamic model for the western Namaqua Province*. Cape Town, South Africa: 35th International Geological Congress.

Macey, P. H., Minnaar, H., Miller, J. A., Lambert, C., Kisters, A. F. M., Diener, J., et al. (2015). *The Precambrian geology of the Warmbad region, southern Namibia. An interim explanation to 1:50 000 geological map sheets of the 1: 250 000 2818 Warmbad sheet*. Geological Survey of Namibia and Council for Geoscience of South Africa, Windhoek, Pretoria.

Macey, P. H., Thomas, R. J., Minnaar, H. M., Gresse, P. G., Lambert, C. W., Groenewald, C. A., et al. (2017). Origin and evolution of the ~1.9 Ga Richtersveld Magmatic Arc, SW Africa. *Precam. Res.* 292, 417–451. doi:10.1016/j.precamres.2017.01.013

Marcantonio, F., McNutt, R. H., Dickin, A. P., and Heaman, L. M. (1990). Isotopic evidence for the crustal evolution of the frontenac arch in the Grenville Province of Ontario, Canada. *Chem. Geol.* 83, 297–314. doi:10.1016/0009-2541(90)90286-G

McCulloch, M. T., and Wasserburg, G. J. (1978). Sm-Nd and Rb-Sr chronology of continental crust formation. *Science* 200, 1003–1011. doi:10.1126/science.200.4345.1003

McDonough, W. F., and Sun, S.-S. (1995). The composition of the Earth. *Chem. Geol.* 120, 223–253. doi:10.1016/0009-2541(94)00140-4

Middlemost, E. A. K. (1994). Naming materials in the magma/igneous rock system. *Earth Sci. Rev.* 37, 215–224. doi:10.1016/0012-8252(94)90029-9

Miller, R. Mc. G. (2008). *The geology of Namibia*. Vol. 1. *Archaean to Mesoproterozoic. Minestry of Mines and Energy*., Geological Survey, Windhoek.

Miller, R. McG. (2012). Review of Mesoproterozoic magmatism, sedimentation and terrane amalgamation in southwestern Africa. *S. Afr. J. Geol.* 115, 417–448.

Miyakazi, T., and Shuto, K. (1998). Sr and Nd isotope ratios of twelve GSJ rock reference samples. *Geochem. J.* 32, 345–350. doi:10.2343/geochemj.32.345

Moen, H. F. G. (2001). *Geological map 2818 Onseepkans, 1:250,000*. Council for Geoscience, Pretoria.

Moen, H. F. G., and Toogood, D. J. (2007). *Explanation: sheet 2818: the geology of the Onseepkans area (1:250,000)*. Council for Geoscience, South Africa.

Nke, A. Y., Bailie, R. H., Macey, P. H., Thomas, R. J., Frei, D., Roux, P. L., et al. (2020). The 1.8 Ga Gladkop suite: the youngest Palaeoproterozoic domain in the Namaqua-Natal Metamorphic Province, South Africa. *Precam. Res.* 350, 105941. doi:10.1016/j.precamres.2020.105941

Pettersson, Å., Cornell, D. H., Moen, H. F. G., Reddy, S., and Evans, D. (2007). Ion-probe dating of 1.2 GA collision and crustal architecture in the Namaqua-Natal Province of southern Africa. *Precam. Res.* 158, 79–92. doi:10.1016/j.precamres.2007.04.006

Pettersson, Å., Cornell, D. H., Yuhara, M., and Hirahara, Y. (2009). Sm–Nd data for granitoids across the Namaqua sector of the Namaqua–Natal Province, South Africa. *Geol. Soc. Lon.* 323, 219–230. doi:10.1144/SP323.10

Pettersson, Å. (2008). Mesoproterozoic crustal evolution in South Africa. Ph.D. thesis. Göteborg, Sweden. University of Göteborg.

Raith, J. G., Cornell, D. H., Frimmel, H. E., and De Beer, C. H., (2003). New insights into the geology of the Namaqua Tectonic Province, South Africa, from ion probe dating of detrital and metamorphic zircon. *J. Geol.* 111, 347–366. doi:10.1086/373973

Robb, L. J., Armstrong, R. A., and Waters, D. J. (1999). The history of granulite-facies metamorphism and crustal growth from single zircon U–Pb geochronology: Namaqualand, South Africa. *J. Petrol.* 40, 1747–1770. doi:10.1093/petroj/40.12.1747

Stowe, C.W. (1986). Synthesis and interpretation of structures along the north-eastern boundary of the Namaqua tectonic Province, South Africa. *Trans. Geol. Soc. S. Afr.* 89, 185–198.

Taylor, S. R., and McLennan, S. M. (1995). The geochemical evolution of the continental crust. *Rev. Geophys.* 33, 241–265. doi:10.1029/95RG00262

Thomas, R. J., Agenbacht, A. L. D., Cornell, D. H., and Moore, J. M. (1994). The Kibaran of southern Africa: tectonic evolution and metallogeny. *Ore Geol. Rev.* 9 131–160. doi:10.1016/0169-1368(94)90025-6

Thomas, R. J., Macey, P. H., Spencer, C., Dhansay, T., Diener, J. F. A., Lambert, C. W., et al. (2016). The Sperrgebiet Domain, Aurus Mountains, SW Namibia: a ~2020 to 850 Ma window within the Pan-African Gariep Orogen. *Precambr. Res.* 286, 35–58. doi:10.1016/j.precamres.2016.09.023

Vernon, R. H., Etheridge, M. A., and Wall, V. J. (1988). Shape and microstructure of microgranitoid enclaves: indicators of magma mingling and flow. *Lithos* 22 1–11. doi:10.1016/0024-4937(88)90024-2

Vernon, R. H. (1986). Potassium feldspar megacrysts in granites—phenocrysts, not porphyroblasts. *Earth Sci. Rev.* 23, 1–63. doi:10.1016/0012-8252(86)90003-6

Whalen, J. B., Curries, K. L., and Chappell, B. W. (1987). A-type granites: geochemical characteristics, discrimination and petrogenesis. *Contrib. Mineral. Petrol.* 95, 407–419. doi:10.1007/BF00402202

Whalen, J. B., Jenner, G. A., Longstaffe, F. J., Robert, F., and Gariépy, C. (1996). Geochemical and isotopic (O, Nd, Pb and Sr) constraints on A-type granite petrogenesis based on the Topsails Igneous Suite. *Newfoundland Appalachians. J. Pet.* 37, 1463–1489.

Yuhara, M., Miyazaki, T., Ishioka, J., Suzuki, S., Kagami, H., and Tsuchiya, N. (2002). Rb-Sr and Sm-Nd mineral isochron ages of the metamorphic rocks in the Namaqualand Metamorphic Complex, South Africa. *Gond. Res.* 5, 771–779. doi:10.1016/S1342-937X(05)70912-6

Zhang, K-J., Li, Q.-H., Yana, L.-L., Zeng, L., Lua, L., Zhang, Y.-X., et al. (2017). Geochemistry of limestones deposited in various plate tectonic settings. *Earth Sci. Rev.* 167, 27–46. doi:10.1016/j.earscirev.2017.02.003

Zhang, L.-X., Wang, Q., Zhu, D.-C., Li, S.-M., Zhao, Z.-D.,, Zhang, L.-L., et al. (2019). Generation of leucogranites via fractional crystallization: a case from the Late Triassic Luoza batholith in the Lhasa Terrane, southern Tibet. *Gond. Res.* 66, 63–76. doi:10.1016/j.gr.2018.08.008

Conflict of Interest: The authors declare that the research was conducted in the absence of any commercial or financial relationships that could be construed as a potential conflict of interest.

Advantages of publishing in Frontiers

OPEN ACCESS
Articles are free to read for greatest visibility and readership

FAST PUBLICATION
Around 90 days from submission to decision

HIGH QUALITY PEER-REVIEW
Rigorous, collaborative, and constructive peer-review

TRANSPARENT PEER-REVIEW
Editors and reviewers acknowledged by name on published articles

Frontiers
Avenue du Tribunal-Fédéral 34
1005 Lausanne | Switzerland

Visit us: www.frontiersin.org
Contact us: frontiersin.org/about/contact

REPRODUCIBILITY OF RESEARCH
Support open data and methods to enhance research reproducibility

DIGITAL PUBLISHING
Articles designed for optimal readership across devices

FOLLOW US
@frontiersin

IMPACT METRICS
Advanced article metrics track visibility across digital media

EXTENSIVE PROMOTION
Marketing and promotion of impactful research

LOOP RESEARCH NETWORK
Our network increases your article's readership